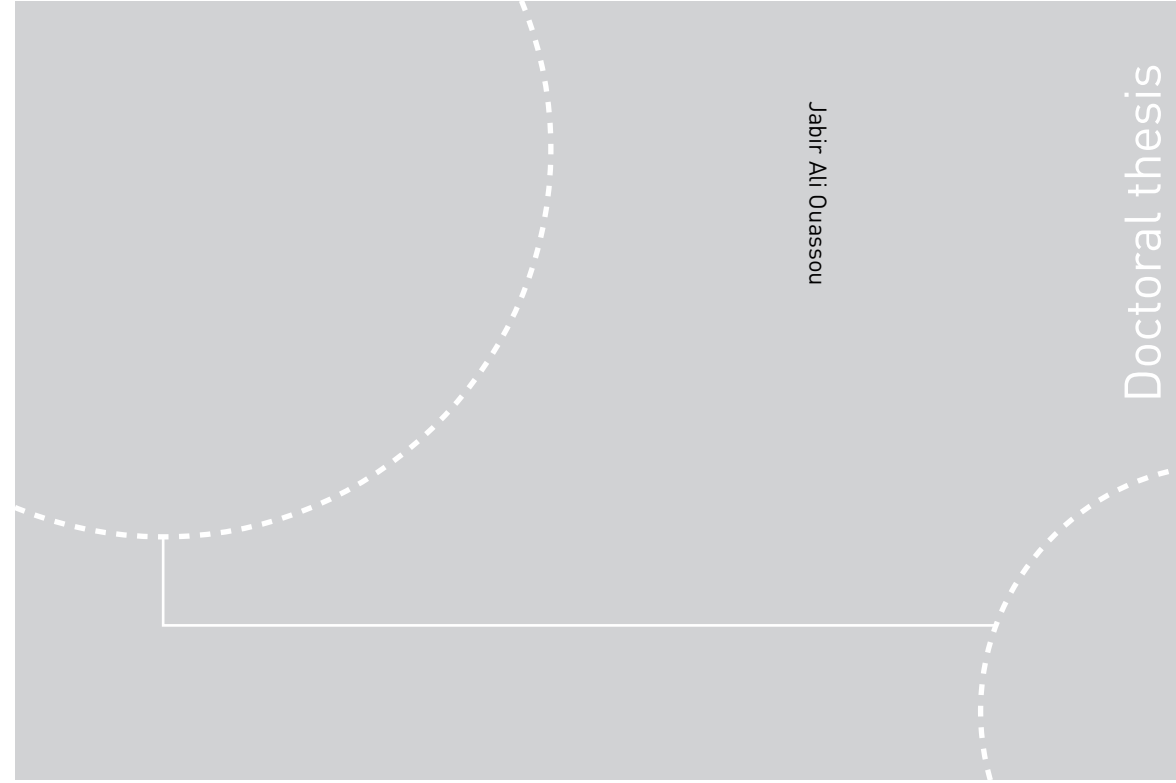


ISBN 978-82-326-3718-8 (printed ver.)
ISBN 978-82-326-3719-5 (electronic ver.)
ISSN 1503-8181



Doctoral theses at NTNU, 2019:57

Jabir Ali Ouassou

Manipulating superconductivity in magnetic nanostructures in and out of equilibrium

 **NTNU**
Norwegian University of
Science and Technology

Doctoral theses at NTNU, 2019:57

 NTNU

NTNU
Norwegian University of Science and Technology
Thesis for the Degree of
Philosophiae Doctor
Faculty of Natural Sciences
Department of Physics

 **NTNU**
Norwegian University of
Science and Technology

Jabir Ali Ouassou

Manipulating superconductivity in magnetic nanostructures in and out of equilibrium

Thesis for the Degree of Philosophiae Doctor

Trondheim, March 2019

Norwegian University of Science and Technology
Faculty of Natural Sciences
Department of Physics



Norwegian University of
Science and Technology

NTNU
Norwegian University of Science and Technology

Thesis for the Degree of Philosophiae Doctor

Faculty of Natural Sciences
Department of Physics

© Jabir Ali Ouassou

ISBN 978-82-326-3718-8 (printed ver.)
ISBN 978-82-326-3719-5 (electronic ver.)
ISSN 1503-8181

Doctoral theses at NTNU, 2019:57

Printed by NTNU Grafisk senter

Abstract

We consider nanostructures that are constructed from superconducting, ferromagnetic, and spin-orbit-coupled materials. These structures are analyzed both theoretically and numerically, under both equilibrium and nonequilibrium conditions. Special emphasis is placed on how one can exert control over the superconducting properties of these systems. For instance, this includes developing new ways to toggle superconductivity on and off via electric or magnetic input signals, and new ways to shape the charge and spin supercurrents flowing through these systems. The thesis itself provides an introduction to how we performed our calculations, as well as a summary of some interesting research results. The main body of research consists of 15 enclosed publications, where we go into more detail on each specific project.

Preface

This document is submitted as a doctoral thesis in theoretical condensed matter physics at the Center for Quantum Spintronics (QuSpin), Norwegian University of Science and Technology (NTNU). The research presented herein was conducted as part of a 3.5-year doctoral program, which included 1 year of courses and teaching duties. The doctoral research has been supervised by Prof. Jacob Linder, and builds directly on a previous 1-year master project [1, 2]. This research was funded by the Research Council of Norway, under grants 240806 and 262633.

In addition to the thesis and research papers, a significant part of the doctoral work has been to develop a general numerical solver for the Usadel equation, which is available at github.com/jabirali/GENEUS. The thesis itself was written in LUALATEX, using a custom-made template available at github.com/jabirali/ThesisTemplate. Most illustrations and plots were created in Adobe Illustrator and Gnuplot, respectively.

Acknowledgments

First of all, I'm grateful to my supervisor Jacob Linder, without whom this thesis would not have been possible. He enthusiastically introduced me to the theory of superconductivity as a master student, and has since then carefully guided my development as a researcher. In addition to being a world-class scientist, he is adept at communicating his ideas, and it is clear that he takes his job as a supervisor seriously. Whenever I had a question or new result, he would be there to offer surprisingly quick and insightful feedback, as well as constructive criticism when appropriate. I also appreciate the liberty I've had to pursue ideas that I myself found interesting—at whatever strange times and places that suited me best. This academic freedom has helped me develop my own scientific independence and confidence. So Jacob: thank you for providing me with excellent supervision over the years.

I also have to thank the rest of our research group. First of all, I've had the pleasure of sharing an office with two fellow doctoral students, Vetle Risinggård and Morten Amundsen. I have fond memories of our many discussions—sometimes productive ones, where we brainstorm new ideas and collectively attack problems, other times just drifting off-topic and having fun when we really ought to get back to work. Except for my supervisor, my first scientific collaboration was with Sol H. Jacobsen. Especially when I was entering the field as a master student, comparing notes with her proved quite helpful, and we have since collaborated on a few other publications too. Other colleagues that deserve special mention are Tom Vethaak and Akash Kamra. I have enjoyed our many chats over coffee or beer, and value our continued friendship outside of work. Finally, thanks to all the other students and researchers at the department for providing a stimulating environment.

Outside NTNU, we have had a very productive relationship with the experimental groups at Cambridge and in Leiden. I have had the pleasure of working closely with Kaveh Lahabi, Angelo Di Bernardo, Niladri Banerjee, Avradeep Pal, Jason W.A. Robinson, Mark G. Blamire, and Jan Aarts. Thanks to all of you for providing valuable discussions and productive collaborations. I should also thank Marco Aprili at Paris-Sud for insightful discussions during the workshop in Les Arcs.

I am also grateful to Wolfgang Belzig for our discussions during his sabbatical, for our collaboration afterwards, and of course for inviting me to visit his research group in Konstanz. I had a really nice stay there, and appreciate the warm welcome that I received from the group.

Outside of work, I also wish to thank all my friends and family for being there for me. My girlfriend Kristine has especially helped me just relax, enjoy life, and be happy. My flatmates Einar Karlsen and Ådne Nyberg have also done a good job of distracting me when I needed it. Einar also proved to be a good “rubber duck”, and could probably get his own PhD after listening to my monologues for a few years. Inge Madshaven has been a good friend and coadventurer—I’m not sure whether I’d have ended up on a horse in Kyrgyzstan on my own. Eirik S. Nilssen, Carina Norvik, Christian Tangene, and Christian Jakobsen also deserve special mentions for our many pleasant conversations over coffee or beer during the past years. Finally, I wish to thank my family for encouraging me to pursue my studies and work hard.

Notation

Most notation in this thesis follows the usual conventions in condensed matter physics. For instance, real and complex scalars are written in *italics*, geometric vectors and tensors are written in ***bold italics***, while chemical elements and physical units are written in an upright font. Matrix transposition is denoted with a superscript^T, complex conjugation with an asterisk^{*}, and Hermitian conjugation with a dagger[†]. In the thesis itself, we use $:=$ for definitions, \sim for proportionalities, and \approx for approximations. In the papers, we sometimes use \equiv for definitions and identities, \sim for orders of magnitude, and \simeq or \cong for approximations. Differentiation operators are abbreviated to $\partial_x := \partial/\partial x$, while commutators and anticommutators are denoted $[A, B] := AB - BA$ and $\{A, B\} := AB + BA$. Finally, the expectation value of Ω is written $\langle \Omega \rangle$.

Geometric vectors and tensors are described using the Cartesian unit vectors $\mathbf{e}_x, \mathbf{e}_y, \mathbf{e}_z \in \mathbb{R}^3$, and the associated derivative operator is $\nabla := \partial_x \mathbf{e}_x + \partial_y \mathbf{e}_y + \partial_z \mathbf{e}_z$. Rank-2 spinors are described using the Pauli matrices $\sigma_0, \sigma_1, \sigma_2, \sigma_3 \in \mathbb{C}^{2 \times 2}$. Spin-dependent phenomena can often be analyzed either in terms of vectors or spinors, and these representations are connected via the Pauli vector $\boldsymbol{\sigma} := \sigma_1 \mathbf{e}_x + \sigma_2 \mathbf{e}_y + \sigma_3 \mathbf{e}_z$. Notably, an inner product $\omega = \mathbf{w} \cdot \boldsymbol{\sigma}$ projects a vector onto the spinor basis, while a trace $\mathbf{w} = \text{Tr}(\omega \boldsymbol{\sigma})/2$ projects it back onto the vector basis. To avoid notational clutter, we denote these spinors in the same way as scalars.

The interactions between electrons and holes in a superconductor can also be modelled using spinors. This is referred to as having a structure in *Nambu space*, and is described by Pauli matrices $\hat{\tau}_0, \hat{\tau}_1, \hat{\tau}_2, \hat{\tau}_3$ with the same definitions as the basis σ_n that spans spin space. We use hats to denote that an object has a Nambu structure. The propagators used to model superconducting proximity systems are in general rank-2 bispinors with both Nambu and spin structures, which can be described using the 16 basis matrices $\hat{\tau}_n \otimes \sigma_m \in \mathbb{C}^{4 \times 4}$ that arise from the Kronecker products of Pauli matrices. We use the convention that sums and products between incompatible spinors should be resolved by taking Kronecker products with appropriate identity elements. Specifically, the product $\hat{\tau}_n \sigma_m \mapsto (\hat{\tau}_n \otimes \sigma_0)(\hat{\tau}_0 \otimes \sigma_m) = \hat{\tau}_n \otimes \sigma_m$, while the sum $a + b\sigma_1 + c\hat{\tau}_2 \mapsto a(\hat{\tau}_0 \otimes \sigma_0) + b(\hat{\tau}_0 \otimes \sigma_1) + c(\hat{\tau}_2 \otimes \sigma_0)$. It is also useful to define $\hat{\boldsymbol{\sigma}} := \text{diag}(\boldsymbol{\sigma}, \boldsymbol{\sigma}^*) \in \mathbb{C}^{3 \times 4 \times 4}$, which takes the role of the Pauli vector for spin-dependent processes involving both electrons and holes.

Units

In this thesis and the enclosed papers, we use *rationalized natural units*. These units are defined by normalizing fundamental physical constants to one: the speed of light c , Planck's reduced constant \hbar , Boltzmann's constant k_B , and the rationalized gravitational constant $1/4\pi G$. Since the vacuum permittivity ϵ_0 and permeability μ_0 are related to the speed of light via $c = 1/\sqrt{\epsilon_0\mu_0}$, it is also possible to set ϵ_0 and μ_0 to one. Thus, the unit system itself can be summarized by the following equation:

$$c = \epsilon_0 = \mu_0 = \hbar = k_B = 1/4\pi G = 1.$$

Natural units make derivations in theoretical physics much simpler than e.g. SI units, and can prevent the unit system from obscuring the natural relationships between physical quantities. For instance, $k_B = 1$ makes it slightly clearer that temperature is a measure of energy, how entropy can be measured in bits, and that the ideal gas constant is just an artifact of an unnatural unit system. If required for clarity, these constants are written explicitly even though we use natural units; for example, explicit factors $\hbar/2$ can be useful when discussing spins. It is also worth mentioning that we take $e < 0$ to mean the *electron charge*.

The units above are convenient for theoretical derivations, and can also be useful for describing e.g. the conditions in the early universe. However, the magnitudes of the base units are impractical for describing low-energy phenomena in condensed matter physics. For instance, the energy unit $\sqrt{\hbar c^5/4\pi G} \approx 10^{30}$ meV is extremely large compared to the order parameter $\Delta \approx 0.1\text{--}10$ meV of a conventional superconductor, while the length unit $\sqrt{4\pi G\hbar/c^3} \approx 10^{-25}$ nm is correspondingly small compared to the superconducting coherence length $\xi \approx 10\text{--}1000$ nm. When discussing physical observables, we therefore tend to restore an appropriate unit system by comparing quantities with similar physical interpretations. For example, in superconductors, we compare energies to the order parameter Δ , temperatures to the critical temperature T_c , and lengths to the coherence length ξ . These material-dependent units make it easy to provide material-independent theoretical predictions, and the results can easily be translated to e.g. SI units by looking up values for the characteristic scales Δ , T_c , ξ for a given superconductor.

Errata

After publication, some errors have been discovered in the enclosed papers. Luckily, none of these affect any published physical predictions. Below, we list the mistakes that have been discovered so far.

- In equation (A17) of paper II, the identities $N\gamma = \gamma\tilde{N}$ and $\tilde{N}\tilde{\gamma} = \tilde{\gamma}N$ are correct, but the similar-looking $N\tilde{\gamma} = \tilde{\gamma}\tilde{N}$ and $\tilde{N}\gamma = \gamma N$ are not. These erroneous identities are not used in the derivations.
- In equations (B16) and (B18) of paper II, two $f_{\uparrow\downarrow}^K$ should be replaced by $f_{\downarrow\uparrow}^K$. However, the following equation (B19) is correct.
- In equations (1–2) and (5–6) of paper IV, there is a factor 1/2 missing in front of each ∇^2 . These equations are only used to qualitatively discuss the spin–orbit-induced spin-valve effect, and are not used for the numerical fits presented afterwards.
- In equation (4) of paper IX, an imaginary unit i is missing in front of α_{sf} and α_{so} . However, these terms had been correctly implemented in the numerical code, and this i does not affect the analytical argument for conservation of spin supercurrents.
- In figure 4 of paper X, the vertical axis should be labeled J/J_c and not $J(z)/J_c$. As the horizontal axis correctly indicates, the charge current is plotted as function of phase difference, and is of course conserved as function of position in a 1D system.

In some cases, what may appear to be mistakes are rather just cases of inconsistent notation between the papers, which have been written at different stages in the learning process and with different coauthors. For instance, depending on the paper, the matrix current has been defined as $\check{I} = DN_F \check{g}\tilde{V}\check{g}$, $\check{I} = +D\check{g}\tilde{V}\check{g}$, $\check{I} = -D\check{g}\tilde{V}\check{g}$, and $\check{I} = \check{g}\tilde{V}\check{g}$.

Publications

- I. **S.H. Jacobsen, J.A. Ouassou, J. Linder.**
Superconducting order in magnetic heterostructures.
Advanced magnetic and optical materials, ch. 1 (2016).
DOI: [10/GFGR9J](https://doi.org/10/GFGR9J)
- II. **S.H. Jacobsen, J.A. Ouassou, J. Linder.**
Critical temperature and tunneling spectroscopy of
superconductor–ferromagnet hybrids with intrinsic
Rashba–Dresselhaus spin–orbit coupling.
Physical review B 92, 024510 (2015).
DOI: [10/GC4M3J](https://doi.org/10/GC4M3J)
- III. **J.A. Ouassou, A. Di Bernardo, J.W.A. Robinson, J. Linder.**
Electric control of superconducting transition
through a spin–orbit coupled interface.
Scientific reports 6, 29312 (2016).
DOI: [10/GFGR9S](https://doi.org/10/GFGR9S)
- IV. **N. Banerjee, J.A. Ouassou, Y. Zhu, et al.**
Controlling the superconducting transition by spin–orbit coupling.
Physical review B 97, 184521 (2018).
DOI: [10/GFGR9V](https://doi.org/10/GFGR9V)
- V. **J. Linder, M. Amundsen, J.A. Ouassou.**
Microwave control of the superconducting proximity
effect and minigap in magnetic and normal metals.
Scientific reports 6, 38739 (2016).
DOI: [10/GFGR9T](https://doi.org/10/GFGR9T)
- VI. **M. Amundsen, J.A. Ouassou, J. Linder.**
Analytically determined topological phase
diagram of the proximity-induced gap in
diffusive n -terminal Josephson junctions.
Scientific reports 7, 40578 (2017).
DOI: [10/F9K69K](https://doi.org/10/F9K69K)
- VII. **A. Pal, J.A. Ouassou, M. Eschrig, J. Linder, M.G. Blamire.**
Spectroscopic evidence of odd frequency superconducting order.
Scientific reports 7, 40604 (2017).
DOI: [10/GFGR9X](https://doi.org/10/GFGR9X)

- VIII. **J.A. Ouassou, A. Pal, M. Blamire, M. Eschrig, J. Linder.**
Triplet Cooper pairs induced in diffusive *s*-wave superconductors interfaced with strongly spin-polarized magnetic insulators or half-metallic ferromagnets.
Scientific reports 7, 1932 (2017).
DOI: [10/F99CHF](https://doi.org/10/F99CHF)
- IX. **J.A. Ouassou, S.H. Jacobsen, J. Linder.**
Conservation of spin supercurrents in superconductors.
Physical review B 96, 094505 (2017).
DOI: [10/GC4M2N](https://doi.org/10/GC4M2N)
- X. **J.A. Ouassou, J. Linder.**
Spin-switch Josephson junctions with magnetically tunable $\sin(\delta\varphi/n)$ current–phase relation.
Physical review B 96, 064516 (2017).
DOI: [10/CMN8](https://doi.org/10/CMN8)
- XI. **K. Lahabi, M. Amundsen, J.A. Ouassou, et al.**
Controlling supercurrents and their spatial distribution in ferromagnets.
Nature communications 8, 2056 (2017).
DOI: [10/GCRHMZ](https://doi.org/10/GCRHMZ)
- XII. **M. Amundsen, J.A. Ouassou, J. Linder.**
Field-free nucleation of antivortices and giant vortices in nonsuperconducting materials.
Physical review letters 120, 207001 (2018).
DOI: [10/GDG3KD](https://doi.org/10/GDG3KD)
- XIII. **J.A. Ouassou, T.D. Vethaak, J. Linder.**
Voltage-induced thin-film superconductivity in high magnetic fields.
Physical review B 98, 144509 (2018).
DOI: [10/GFGR9W](https://doi.org/10/GFGR9W)
- XIV. **J.A. Ouassou, J. Linder.**
Voltage control of superconducting exchange interaction and anomalous Josephson effect.
ARXIV: [1810.02820](https://arxiv.org/abs/1810.02820)
- XV. **J.A. Ouassou, J.W.A. Robinson, J. Linder.**
Controlling spin supercurrents via nonequilibrium spin injection.
ARXIV: [1810.08623](https://arxiv.org/abs/1810.08623)

Contents

1	Introduction	1
1.1	Background and motivation	1
1.2	Fundamental concepts	4
1.3	Recent developments	10
2	Theoretical framework	13
2.1	Propagators	13
2.2	Quasiclassical limit	15
2.3	Diffusive limit	17
2.4	Energy matrices	20
2.5	Boundary conditions	25
2.6	Physical observables	28
2.7	Parametrization	32
2.8	Reservoirs	35
3	Numerical algorithms	39
3.1	Discretization strategy	39
3.2	Steady-state calculations	44
3.3	Convergence acceleration	48
3.4	Homotopy continuation	52
3.5	Phase diagrams	54
3.6	Critical temperature	58
3.7	Numerical code	61
4	Research highlights	63
4.1	Current-induced vortices	63
4.2	Single-magnet spin valves	66
4.3	Half-metallic spin valves	71
4.4	Spin-switch Josephson junctions	74
4.5	Voltage-induced superconductivity	76
5	Outlook	81
	Bibliography	83

Introduction

1.1 Background and motivation

Roughly a century has passed since the discovery of superconductivity. The relevant materials are often metallic at room temperature,¹ and only transition into their superconducting state at cryogenic temperatures. Macroscopically, this state is characterized by two properties [3, 4]. The first is a complete lack of electrical resistance, as discovered by Onnes in 1911. The second is an imperviousness to magnetic fields, as discovered by Meissner and Ochsenfeld in 1933. However, a full microscopic understanding of superconductivity was not achieved until the seminal work by Bardeen, Cooper, and Schrieffer in 1957 [5, 6]. The so-called BCS theory of superconductivity won them a Nobel prize, and is by now referred to as *conventional superconductivity*—a category that covers most elemental superconductors like Nb and Al.

Since then, research and applications related to superconductivity has exploded. One long-standing goal has been to engineer materials that remain superconducting at higher and higher temperatures, with the hope of one day achieving room-temperature superconductivity. If this technology could be realized and mass-produced, it could help combat the single dominant source of energy waste: resistive heating. Initially, progress was slow, with the critical-temperature record only increasing from 4 K (Hg) to 23 K (Nb₃Ge) during the first 75 years of research [3]. However, after the discovery of superconductivity in cuprates [3, 7], the record skyrocketed—and in less than a decade, it had already reached its peak value of 133 K (HgBa₂Ca₂Cu₃O₈) [8, 9]. This remains the record at ambient pressure [9], although the mechanism behind its unconventional superconductivity is still controversial [10].

Less than a year ago, some progress was made with the discovery of superconductivity in twisted bilayer graphene [11]. Although its critical temperature was below 2 K, its phase diagram and coupling strength was reminiscent of the cuprates. Since it is also a simpler system to analyze theoretically than the cuprates, this finding has already spurred a lot of theoretical interest, and has raised hopes for understanding unconventional superconductivity in the near future.

1. High-temperature superconductors such as cuprates are notable exceptions. They are usually *bad metals* in their non-superconducting state.

Another noteworthy result was the discovery of superconductivity in high-pressure hydrides [9, 12, 13]. This technically raised the critical-temperature record to first 203 K (SH₃) and recently 250 K (LaH₁₀). In contrast to cuprates, hydrides can be understood as conventional superconductors. While interesting for fundamental-physics reasons, the hydrides are still quite far from realizing superconductivity at ambient conditions. They require pressures above 150 GPa (1.5 million atmospheres) to operate at high temperatures, which is likely more challenging for applications than liquid-nitrogen cryogenic systems.

While superconductivity at ambient conditions remains a dream for now, this has not stopped the known superconductors from finding applications. One example is superconducting electromagnets, where a superconducting coil is used to produce an intense magnetic field in an energy-efficient manner. These are routinely used for MRI machines at hospitals, NMR and MS analyses in chemistry, plasma confinement in fusion reactors, and beam control in particle accelerators [14]. The current world record for superconducting magnets is a field strength of 32 T [15]. For comparison, this is a million times the field strength of the Earth, a thousand times the field strength of a typical fridge magnet, and about twice the field strength required to diamagnetically levitate a small animal in Earth's gravitational field [16, 17].

Superconductors have also found applications in high-precision sensors. The perhaps best-known example is the SQUID, which is one of the most accurate ways to measure magnetic fields [3, 4]. In addition to being used routinely in a lab setting, these devices have been used in space missions to measure fields down to the attotesla scale by averaging measurements over a few days [18]. More recently, the SQUID has been miniaturized to the nano-SQUID, which is sufficiently sensitive to measure single-electron spins [19, 20]. Other examples include cameras that can accurately detect the color of single photons and thermometers with nanosecond time resolution [21–23].

Another application area for superconductors that is expected to become important in the near future is high-performance computing. So far, semiconductor-based computing has been extremely successful. In the period 1975–2009, the average speed and energy efficiency of semiconductor-based computers doubled roughly every 1.5 years [24]. This resulted in an exponential increase in both quantities, which since WWII has resulted in a performance increase of more than 10^{12} [24].

However, this development cannot continue for much longer. One reason is that the newest generation of semiconductor devices already have a minimum feature size of 7 nm; this corresponds to roughly one transistor per $100 \times 100 \text{ nm}^2$, and is rapidly approaching the atomic scale. At the same time as the development of semiconductor technology is getting closer to its limits, there is an ever-increasing demand for energy-efficient computation. Worldwide, data centers already consume more power than the entire United Kingdom, and their power consumption keeps doubling roughly every 4 years [25]. Even at room temperature, the energy efficiency of classical computers could in principle be improved by roughly a factor 10^5 before reaching the fundamental Landauer limit, but it has become increasingly clear that semiconductor technology cannot take us all the way there [26].

There is therefore interest in identifying a suitable technological heir, and superconductor-based computing is a popular candidate. First of all, the technology has already been proven to be realistic: a 20 GHz prototype for a superconducting CPU was realized nearly two decades ago [27]. Furthermore, superconducting computers are projected to be roughly 10^3 times more energy-efficient than conventional computers [28]. Moreover, the technology can in principle be operated at near-terahertz frequencies, resulting in a potential speed benefit as well [28]. Finally, for data centers in particular, the lack of room-temperature superconductivity is likely not a huge barrier to adoption of the technology, since they already require sophisticated cooling systems for today's solutions. For these reasons, e.g. the United States government views superconductor technology as the most promising successor to semiconductor technology [29], and China has recently invested heavily in the development of superconducting computers [30].

In this thesis, the focus is on *superconducting spintronics*, where superconducting and magnetic elements are combined to produce new device functionality [31–36]. Macroscopically, superconductivity and magnetism appear to be antagonistic: weak magnetic fields are completely expelled by superconductors, while strong magnetic fields extinguish all traces of superconductivity. However, we will see that at the nanoscale, new forms of superconductivity emerge from their interactions, with different properties from either bulk material. In addition to being interesting from a fundamental-physics perspective, this may have applications in both classical and quantum computing [37].

1.2 Fundamental concepts

Conventional BCS superconductivity arises due to a phonon-mediated attraction between electrons [3, 4]. This attractive force creates an instability in the Fermi liquid of an otherwise normal metal [3, 5]: electrons of opposite spins and momenta form bound pairs, and these *Cooper pairs* condense into a coherent state [6]. We describe this macroscopic quantum state via a complex order parameter $\Delta = |\Delta|e^{i\chi}$ [6]. The condensation energy associated with Cooper pairing is $|\Delta|$, meaning that an energy $2|\Delta|$ is required to break a Cooper pair into two excited electrons. This creates a gap $|\Delta|$ in the density of states around the Fermi level, and directly affects electron tunneling into superconductors [38]. The critical temperature T_c is by definition the highest temperature at which a finite gap $|\Delta| > 0$ exists. As for the condensate phase χ , it is directly related to any *charge supercurrents* $J_e \sim \nabla\chi$.

The attractive electron–electron interaction can be understood via a simple classical picture [39]. We can think of a metal as a positive ionic lattice inhabited by negative electrons. When an electron moves through the lattice, it attracts nearby ions via the Coulomb interaction, thus distorting the lattice. The ions can stay in this distorted state for a long time after the electron has passed. Thus, the electron leaves behind a positively charged wake, which can attract a new electron afterwards. In a way, the positive lattice overscreens the negative charge of the first electron, and this attracts the second electron [40]. The second electron can lower its energy by following the trail left by the first one, and is then protected against scattering by an energy barrier. Since the origin of electrical resistance is precisely electron scattering, this energy barrier opens for the possibility of dissipationless transport. The optimal Cooper pair consists of two electrons moving in *opposite* directions, since each electron can then follow the other’s trail. This picture also explains why this is a low-temperature phenomenon: at high temperatures the thermal vibrations of the lattice would overshadow the electron-induced distortions. The above is a satisfying explanation for the mechanism behind the attraction; but being a classical explanation, it does not highlight the importance of phase coherence. Quantum-mechanically, the lattice distortion is interpreted as a phonon, and the electron pairs form a coherent many-body state.

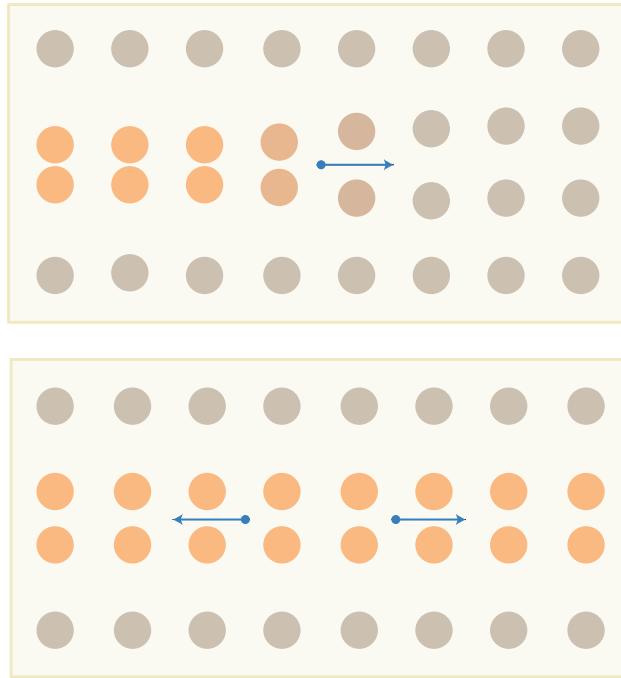


Figure 1.1: Cartoon picture of conventional superconductivity. The top panel depicts an electron (blue) moving through the ionic lattice of a metal (grey), which leaves behind a positively charged lattice distortion (orange). The bottom panel depicts a Cooper pair of two electrons following each other's lattice distortions. By following these positively charged trails, the electrons lower their energies and enter a bound state, which protects them against scattering. The quantum-mechanical treatment shows that all these individual Cooper pairs condense into a macroscopic quantum state.

Cooper pairs are born in superconductors, but are not necessarily confined to their birthplace. When a superconductor (s) is brought into contact with a normal metal (N), Cooper pairs can migrate back and forth between them. This is known as the *proximity effect*, and simultaneously induces superconductivity in N and diminishes it in s. Microscopically, the proximity effect can be understood as being mediated by *Andreev reflections* [41]. Basically, when a low-energy electron in N reaches the s/N interface, it can pick up an electron of opposite spin, and enter s in the form of a Cooper pair² This process leaves behind a hole, which is retroreflected back into N.³ Conversely, when a hole in N reaches the s/N interface, it can annihilate one electron in a Cooper pair. The other electron of the pair is then ejected from s and into N. Thus, electrons and holes in N can be converted into each other if they simultaneously create or annihilate Cooper pairs inside s.

One consequence of these interactions is the formation of *Andreev bound states*. An electron at the s/N interface can: (I) be converted into a hole; (II) move along a path that leads back to the interface; (III) be converted back into an electron; (IV) follow the time-reversed path back to the starting point. This standing wave describes a quasiparticle bound state in N, and is directly induced by the condensate in s. Each electron-hole conversion creates or annihilates a Cooper pair in s, which makes s sensitive to the properties of N. Each conversion is also a phase-coherent process, so the bound states in N involve electrons and holes with phases correlated to the condensate in s. *Andreev pairs* in N in many ways behave like Cooper pairs that have leaked out of s, which is a common and intuitive way to discuss proximity effects.

Another important process is the *Josephson effect* [42]. In Josephson's original treatment [43], it was shown that Cooper pairs could tunnel between the superconductors in an s/I/s junction, where I is an insulator. This causes a tunneling supercurrent $J_e \sim \sin(\delta\chi)$ to manifest, which depends on the phase difference $\delta\chi$ between the s's. Cooper pairs can also flow through s/N/s structures, in which case the effect may be understood via Andreev reflections. The microscopic picture is that a hole in N can annihilate a Cooper pair at the interface to the first s, and the resulting electron can move to the second s. It may then create a new Cooper pair, and be reflected as a hole again.

-
2. *Low energy* refers to an excitation energy $|\epsilon|$ below the condensation energy $|\Delta|$. These particles cannot enter a superconductor without forming a Cooper pair.
 3. *Retroreflection* means that the incoming electron and outgoing hole have opposite momenta. In contrast, *specular reflection* would conserve transverse momentum.

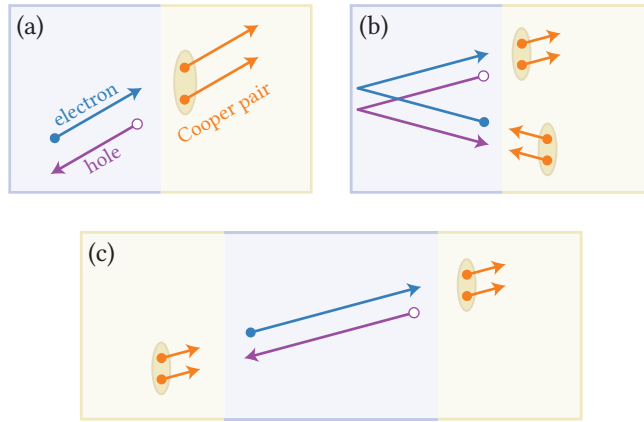


Figure 1.2: Illustration of (a) Andreev reflection, (b) an Andreev bound state, and (c) Josephson tunneling. The yellow backgrounds correspond to superconductors, and the blue backgrounds to normal metals. These figures illustrate the simplest case of clean materials with transparent interfaces. However, the same kind of processes occur in dirty materials with resistive interfaces as well.

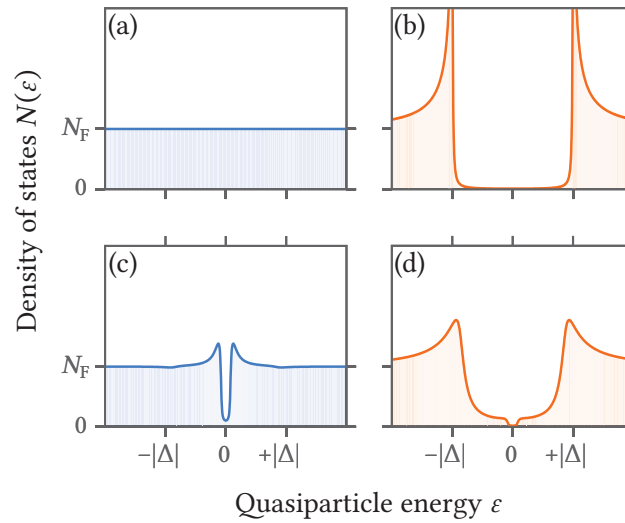


Figure 1.3: Demonstration of the proximity effect in an s/n bilayer. (a) In a bulk n, the density of states can be approximated by a constant N_F on a scale of a few meV around the Fermi level $\varepsilon = 0$. (b) In a bulk s, a gap $|\Delta|$ opens up around the Fermi level. Panels (c–d) show what happens when the two materials are placed into contact: a *minigap* opens in n, and *subgap states* appear in s. The local density of states can be probed in STM experiments [44–46].

Cooper pairs in conventional superconductors are always spinless, and the same goes for proximity structures involving normal metals. In other words, these pairs must have a singlet spin structure $|\uparrow\downarrow\rangle - |\downarrow\uparrow\rangle$,⁴ and are therefore called *singlets*. However, if a superconductor (s) is connected to a homogeneous ferromagnet (F), *opposite-spin triplets* $|\uparrow\downarrow\rangle + |\downarrow\uparrow\rangle$ are generated in a process called *spin mixing*, where we take the magnetization direction of F to be the spin-quantization axis. Note that both singlets and opposite-spin triplets consist of electrons from different spin bands, which have different Fermi momenta inside ferromagnetic metals. This momentum mismatch causes them to decay rapidly in ferromagnets, and the leakage of superconductivity into such a ferromagnet is therefore called a *short-ranged proximity effect*.

In the presence of inhomogeneous magnetism, *equal-spin triplets* $|\uparrow\uparrow\rangle$ and $|\downarrow\downarrow\rangle$ are also produced [47]. The explanation for this is simply that an opposite-spin triplet $|\uparrow\downarrow\rangle + |\downarrow\uparrow\rangle$ along one spin axis can be written as a linear combination of equal-spin triplets $|\uparrow\uparrow\rangle$ and $|\downarrow\downarrow\rangle$ along a perpendicular spin axis. Thus, if a system contains two perpendicularly magnetized layers, the opposite-spin triplets produced in the first layer correspond to equal-spin triplets in the second layer. Note that equal-spin triplets consist of electrons from the same spin band, and have the same range inside a ferromagnet as any Andreev pair would have in a normal metal. The leakage of such pairs into ferromagnets is therefore called a *long-ranged proximity effect* [47, 48]. Other ways to induce long-ranged proximity effects include spin-orbit coupling [49, 50] and time-dependent magnetizations [51]. Equal-spin triplets open for many new possibilities in superconducting spintronics devices. For instance, the state $|\uparrow\uparrow\rangle$ carries net spin, and can therefore be used to transport dissipationless *spin supercurrents* through a material. These spin supercurrents should exert torques on magnetic layers, and can in principle be used to manipulate the magnetic texture of a device.

Triplet superconductivity in s/F proximity structures has proven to be a rich research field. We will not give a complete overview here, but provide a more thorough introduction in publication I (enclosed). Pedagogical introductions can also be found in e.g. references 31 and 32; a detailed theoretical review is given in reference 33; and an experimental review is given in reference 34. Brief introductions to relevant subtopics are also provided in chapter 4 and publications II–XV.

4. Throughout this thesis, we ignore the normalization factors $1/\sqrt{2}$ of spin states.

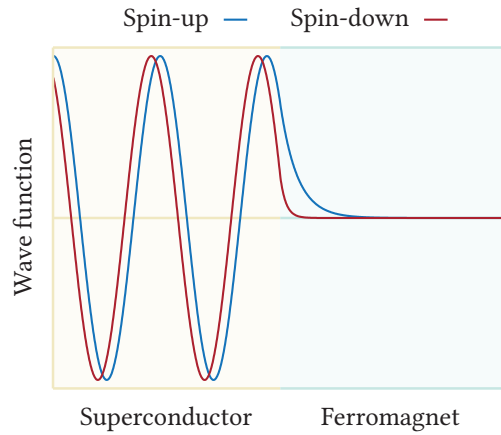


Figure 1.4: Illustration of spin-mixing at the interface between a superconductor and a ferromagnetic insulator [33]. An insulator is a classically forbidden region for low-energy quasiparticles, so incoming spin-up and spin-down electrons are both reflected. However, the energies of spin-up and spin-down particles in a *ferromagnetic* insulator can be very different due to the spin splitting of the bands. This means that spin-up particles can penetrate slightly deeper into the insulator than spin-down particles before being reflected, resulting in a spin-dependent interfacial phase shift. Thus, if the incoming wave was in a singlet state $|\uparrow\downarrow\rangle - |\downarrow\uparrow\rangle$, the outgoing wave is in the state $|\uparrow\downarrow\rangle e^{i(\varphi_{\uparrow} - \varphi_{\downarrow})} - |\downarrow\uparrow\rangle e^{i(\varphi_{\downarrow} - \varphi_{\uparrow})}$. Defining the phase difference $\delta\varphi = \varphi_{\uparrow} - \varphi_{\downarrow}$, the result can be written as an explicit singlet-triplet mixture $[|\uparrow\downarrow\rangle - |\downarrow\uparrow\rangle] \cos(\delta\varphi) + [|\uparrow\downarrow\rangle + |\downarrow\uparrow\rangle] i \sin(\delta\varphi)$. A similar process occurs in ferromagnetic metals [33]. In that case, the momentum mismatch causes spin-up and spin-down electrons to oscillate at different frequencies. This results in a spatial oscillation between singlets and triplets, in addition to an exponential decay of both.

1.3 Recent developments

Josephson junctions have been a very fruitful area of research [42]. For instance, they form the basis for the SQUID magnetometer [3, 4], the RSFQ architecture for superconducting classical computers [52], and several suggestions for superconducting quantum computers [53]. Recently, two new families of Josephson junctions have been realized experimentally, namely φ junctions [54–58] and φ_0 junctions [59–65].

The φ junction was constructed by connecting a 0 and π junction in parallel [54]. This results in a Josephson junction with a degenerate ground-state phase difference $\delta\chi = \pm\varphi$, where φ is determined by the junction parameters. While the φ junction has a nontrivial current-phase relation $J_e = J_{c1} \sin(\delta\chi) - J_{c2} \sin(2\delta\chi)$, we see that the current remains zero in the absence of phase differences $\delta\chi = 0$, just like the 0 and π junctions it is constructed from. Having a degenerate ground state that can be magnetically switched might e.g. be useful as a qubit.

The φ_0 junction was constructed using a quantum dot as the interlayer [59]. This results in a Josephson junction with a non-degenerate ground-state phase difference $\delta\chi = \varphi_0$, where φ_0 could be tuned via electrostatic gating. Other suggested interlayers include three non-collinear ferromagnets [60], spin-orbit-coupled materials [61], and topological insulators [62]. In contrast to φ junctions, the current-phase relation $J_e \sim \sin(\delta\chi - \varphi_0)$ is a direct generalization of the 0 or π junctions. This implies that an *anomalous supercurrent* $J_e \sim -\sin(\varphi_0)$ appears when the phase difference $\delta\chi = 0$, which separates this junction from 0, π , φ junctions. Note that a φ_0 junction functions as a *phase battery* when placed in a superconducting circuit: since phase gradients $\nabla\chi$ cause supercurrents to flow, and a φ_0 junction tries to set up a spontaneous phase difference, it can be used to force a supercurrent to flow through a superconducting circuit. We explore a magnetic φ_0 junction in paper XIV, where we show that the phase bias φ_0 can be tuned via a transverse voltage bias. A thermal counterpart to the anomalous charge supercurrent in a φ_0 junction was explored in reference 66.

There has been a strong focus on topology in physics recently, and the field of superconductivity is no exception. In the context of Josephson junctions, it has been demonstrated that *multiterminal junctions* exhibit topological properties [VI, 67, 68]. This may provide an accessible platform for studying topological materials in higher dimensions.

Combining superconductors with strongly polarized ferromagnets is perhaps a particularly interesting prospect for superconducting spintronics devices. One reason is that they can be used to generate spin-polarized supercurrents via spin filtering. Spin supercurrents can in principle be used to e.g. manipulate the magnetic texture of a system, and may therefore be especially interesting for applications [31–34]. The first experimental indications that the ground-state magnetic configuration is influenced by superconductivity were published last year [69]. We investigate one way to control the magnetic ground state in paper [xiv](#). Strongly polarized ferromagnets also provide a way to verify whether a long-ranged triplet proximity effect is taking place, since only $|\uparrow\uparrow\rangle$ and $|\downarrow\downarrow\rangle$ pairs can survive inside a strong ferromagnet.

Long-ranged proximity effects in half-metallic ferromagnets were realized experimentally already over a decade ago [70]. More recently, some surprising findings were found using similar materials. For instance, a critical temperature modulation of up to 1.8 K was demonstrated in a half-metallic spin-valve setup, even though the superconductor was made very large compared to its coherence length [71]. Another surprising finding was that contacting a conventional superconductor to a half-metallic ferromagnet could lead to a large zero-energy peak in the density of states deep inside the superconductor [72]. In paper [viii](#), we shed some light on these discoveries. While long-ranged proximity effects provide evidence of the spin structure of a Cooper pair, the odd-frequency nature of these pairs has also been explicitly demonstrated in the form of a paramagnetic Meissner effect [73].

Instead of using magnetic inhomogeneity to generate long-ranged proximity effects, it was shown in references [49–50](#) that spin–orbit coupling can be used. Some novel effects related to spin–orbit coupling in proximity structures were investigated in papers [ii–iv](#). It was also pointed out in reference [74](#) that long-ranged orbital effects in superconductor/ferromagnet systems can occur in more systems than previously anticipated. Some potential ramifications of this are discussed in [chapter 4](#). Finally, recent experiments on nonequilibrium spin injection in superconducting junctions has opened for a new way of controlling spin supercurrents [75]. Using spin pumping to control the triplet proximity effect had previously been theoretically explored in reference [51](#), and the effects of the associated spin injection on spin supercurrents are investigated in reference [76](#) and paper [xv](#).

Theoretical framework

In this chapter, we discuss the theoretical framework that underlies our calculations. First, we introduce the basic theoretical formalism: matrix propagators and matrix currents, which encapsulate information about all physical observables in a system. We then discuss how these propagators and currents can be calculated for physical systems of interest, and how to extract physical predictions from them.

2.1 Propagators

Modern treatments of quantum field theory are often expressed in the language of *propagators*. Their precise definitions vary between authors and contexts. However, they usually have the same basic structure, namely an expectation value of a product of field operators:

$$G(\mathbf{r}, t|\mathbf{r}', t') := \langle \Psi(\mathbf{r}, t)\Psi^\dagger(\mathbf{r}', t') \rangle = \langle \Omega|\Psi(\mathbf{r}, t)\Psi^\dagger(\mathbf{r}', t')|\Omega \rangle. \quad (2.1)$$

Here, Ψ^\dagger is a *creation operator*, which places a particle at position \mathbf{r}' at time t' ; Ψ is an *annihilation operator*, which removes a particle of the same kind from position \mathbf{r} at time t ; and $|\Omega\rangle$ is the state of the physical system. Thus, $\langle \Omega|\Psi(\mathbf{r}, t)\Psi^\dagger(\mathbf{r}', t')|\Omega \rangle$ may be interpreted as injecting a particle at \mathbf{r}' , letting it propagate on its own from t' to t , then attempting to measure it at \mathbf{r} . Intuitively, the result should then describe the probability of a particle propagating from (\mathbf{r}', t') to (\mathbf{r}, t) . Particles that propagate “backwards in time” are interpreted as holes.

More rigorously, we can identify the propagator $G(\mathbf{r}, t|\mathbf{r}', t')$ as an inner product between two states $\Psi^\dagger(\mathbf{r}, t)|\Omega\rangle$ and $\Psi^\dagger(\mathbf{r}', t')|\Omega\rangle$, where the former has an extra particle at position \mathbf{r} at time t , and the latter has an extra particle at position \mathbf{r}' at time t' . Since inner products in quantum mechanics are interpreted as probability amplitudes for the transition between the corresponding states, this supports the interpretation of $G(\mathbf{r}, t|\mathbf{r}', t')$ as the probability amplitude for a particle placed at (\mathbf{r}', t') to end up at (\mathbf{r}, t) . Hence, the name *propagator*.¹

1. These objects are also called *correlators*, *correlation functions*, *Green functions*, and *Gorkov functions*. These names also make sense: technically, the propagators do measure correlations between field values at different points; and mathematically, they are the Green functions that solve the Gorkov equation [77].

We wish to describe superconductor/ferromagnet hybrid systems. Superconductors induce electron–hole correlations in nearby materials via interfacial Andreev reflections. Ferromagnets, on the other hand, lift the degeneracy between spin-up and spin-down. Thus, we need to describe correlations between four kinds of quasiparticle excitations: spin-up electrons, spin-down electrons, spin-up holes, and spin-down holes. This can be done succinctly via the bispinor operator [78],²

$$\hat{\Psi} := (\Psi_{\uparrow}, \Psi_{\downarrow}, \Psi_{\uparrow}^{\dagger}, \Psi_{\downarrow}^{\dagger}), \quad (2.2)$$

where Ψ_{σ} and Ψ_{σ}^{\dagger} are the field operators for electrons with spin σ . Throughout this thesis, we employ the Keldysh formalism [80–85], which defines the following 4×4 propagators in Nambu \otimes spin space,³

$$\hat{G}^{\text{R}}(\mathbf{r}, t | \mathbf{r}', t') := -i\hat{\tau}_3 \langle \{\hat{\Psi}(\mathbf{r}, t), \hat{\Psi}^{\dagger}(\mathbf{r}', t')\} \rangle \theta(t - t'), \quad (2.3)$$

$$\hat{G}^{\text{A}}(\mathbf{r}, t | \mathbf{r}', t') := +i\hat{\tau}_3 \langle \{\hat{\Psi}(\mathbf{r}, t), \hat{\Psi}^{\dagger}(\mathbf{r}', t')\} \rangle \theta(t' - t), \quad (2.4)$$

$$\hat{G}^{\text{K}}(\mathbf{r}, t | \mathbf{r}', t') := -i\hat{\tau}_3 \langle [\hat{\Psi}(\mathbf{r}, t), \hat{\Psi}^{\dagger}(\mathbf{r}', t')] \rangle, \quad (2.5)$$

where $\hat{\tau}_3 = \text{diag}(+1, +1, -1, -1)$ is a Pauli matrix in Nambu space, and θ is the unit step function. Note that the commutators above have to be interpreted in terms of outer products between the bispinors [89]:

$$\{\hat{\Psi}, \hat{\Psi}^{\dagger}\} := \hat{\Psi} \otimes \hat{\Psi}^{\dagger} + \hat{\Psi}^{\dagger} \otimes \hat{\Psi} = \hat{\Psi} \hat{\Psi}^{\dagger} + [(\hat{\Psi}^{\dagger})^{\text{T}}(\hat{\Psi})^{\text{T}}]^{\text{T}}; \quad (2.6)$$

$$[\hat{\Psi}, \hat{\Psi}^{\dagger}] := \hat{\Psi} \otimes \hat{\Psi}^{\dagger} - \hat{\Psi}^{\dagger} \otimes \hat{\Psi} = \hat{\Psi} \hat{\Psi}^{\dagger} - [(\hat{\Psi}^{\dagger})^{\text{T}}(\hat{\Psi})^{\text{T}}]^{\text{T}}. \quad (2.7)$$

The *retarded*, *advanced*, and *Keldysh* propagators defined above are then collected into an 8×8 matrix in Keldysh \otimes Nambu \otimes spin space,

$$\check{G} := \begin{pmatrix} \hat{G}^{\text{R}} & \hat{G}^{\text{K}} \\ 0 & \hat{G}^{\text{A}} \end{pmatrix}. \quad (2.8)$$

As we will see later, the retarded and advanced components contain information on e.g. the density of states in a material, while the Keldysh component contains information on the occupation of those states.

-
2. Some authors define the bispinor operator as $\hat{\Psi} = (\Psi_{\uparrow}, \Psi_{\downarrow}, \Psi_{\downarrow}^{\dagger}, -\Psi_{\uparrow}^{\dagger})$. In that basis, time-reversal invariant quantities become proportional to the Nambu identity $\hat{\tau}_0$, and spin-independent quantities become proportional to the spin identity σ_0 , which results in more intuitive matrix structures for the propagators [79].
 3. The Keldysh formalism is the standard way to treat nonequilibrium problems in condensed matter physics. The most common alternative is the Matsubara formalism, which simplifies equilibrium calculations via analytical continuation to complex time [86]. Recently, this technique has also been extended to nonequilibrium systems by introducing complex chemical potentials [87, 88].

2.2 Quasiclassical limit

In principle, the exact propagator \check{G} can be determined directly from the Gorkov equation [77]. However, this is prohibitively difficult for all but the simplest physical systems, so one typically relies on the *quasiclassical approximation* to simplify the problem [80–84]. Mathematically, this approximation can be introduced as follows. First, the propagator is rewritten using center-of-mass coordinates, so that they describe propagation from coordinates $(\mathbf{r} - \delta\mathbf{r}/2, t - \delta t/2)$ to $(\mathbf{r} + \delta\mathbf{r}/2, t + \delta t/2)$. The propagation distance $\delta\mathbf{r}$ and time δt are then Fourier-transformed, yielding a description in terms of the quasiparticle momentum \mathbf{p} and energy ε . Herein, we only consider stationary problems, so we can also discard any dependence on the center-of-mass time t . We now have a description $\check{G}(\mathbf{r}, \mathbf{p}, \varepsilon)$ that is still exact, just parametrized differently.⁴

In this description, the quasiclassical approximation can be written

$$\check{G}(\mathbf{r}, \mathbf{p}, \varepsilon) \approx -i\pi\delta(\zeta)\check{\Gamma}(\mathbf{r}, \mathbf{p}_F, \varepsilon), \quad (2.9)$$

where $\zeta := \mathbf{p}^2/2m - \varepsilon_F$ is the kinetic energy, ε_F is the Fermi energy, and m is the effective mass. The delta function above constrains the momentum to the Fermi surface: $|\mathbf{p}| = p_F := \sqrt{2m\varepsilon_F}$. Finally, the right-hand side is expressed in terms of a *quasiclassical propagator* $\check{\Gamma}$, which depends on the transport direction \mathbf{n} via the Fermi momentum $\mathbf{p}_F = p_F\mathbf{n}$. The above can easily be inverted for $\check{\Gamma}$ by integrating over all ζ :

$$\check{\Gamma} := \frac{i}{\pi} \int d\zeta \check{G}(\mathbf{r}, \mathbf{p}, \varepsilon). \quad (2.10)$$

Starting from the Gorkov equation, one can similarly derive an equation of motion for $\check{\Gamma}$ known as the *Eilenberger equation* [80–83, 91],

$$\mathbf{v}_F \cdot \nabla \check{\Gamma} = i[\check{\Sigma}, \check{\Gamma}], \quad (2.11)$$

where $\mathbf{v}_F := \mathbf{p}_F/m$ is the Fermi velocity. The *energy matrix* $\check{\Sigma}$ describes how the effective energies of different quasiparticle species are shifted by various types of scattering and decoherence in the material, and is discussed in more detail later in this chapter. This equation can be made dimensionless by introducing either the *ballistic coherence length* $\xi_0 := v_F/\Delta_0$ or *Andreev energy* $\varepsilon_A := v_F/L$ [81], where Δ_0 is the zero-temperature gap of a bulk superconductor, and L is the material length.

4. This is sometimes called the *Wigner representation* [80], due to its similarity to the Wigner quasiprobability distribution in first-quantized quantum mechanics [90].

The quasiclassical approximation can be better understood by Fourier-transforming equation (2.9) back from momentum space:

$$\check{G}(\mathbf{r}, \delta\mathbf{r}, \varepsilon) \sim N_F \langle \check{\Gamma}(\mathbf{r}, \mathbf{p}_F, \varepsilon) e^{i\mathbf{p}_F \cdot \delta\mathbf{r}} \rangle_F, \quad (2.12)$$

where N_F is the normal-state density of states at the Fermi energy, and the angle brackets $\langle \dots \rangle_F$ denote an average over the Fermi surface. As illustrated in figure 2.1, the propagator \check{G} has been separated into a rapidly oscillating plane wave $e^{i\mathbf{p}_F \cdot \delta\mathbf{r}}$ with a slowly varying envelope $\check{\Gamma}$. Another difference is the explicit prefactor N_F , which describes the spectral density of electrons available for transport processes. In the quasiclassical formalism, this is clearly factored out, resulting in a convenient normalization condition: $\check{\Gamma}^2 = 1$ [83]. Thus, the quasiclassical approximation lets us describe the system in terms of a normalized and slowly varying propagator $\check{\Gamma}$ instead of the exact propagator \check{G} .

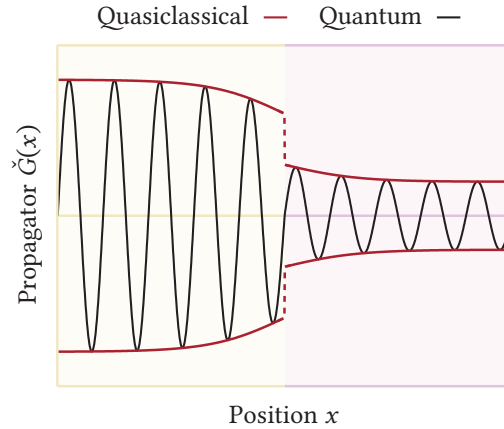


Figure 2.1: Illustration of the quasiclassical approximation in 1D, where the background colors indicate different materials. The full quantum-mechanical propagator $\check{G}(x) \sim \check{\Gamma}(x) e^{ipx}$ oscillates rapidly on the atomic scale ($\lesssim 1$ nm). The quasiclassical propagator $\check{\Gamma}(x)$ is found by integrating out these oscillations, and describes how the envelope varies on the mesoscopic scale (10–1000 nm). Note that the exact propagator $\check{G}(x)$ is continuous, while the quasiclassical propagator $\check{\Gamma}(x)$ can be discontinuous across sharp interfaces. In other words, the quasiclassical approximation breaks down at interfaces, so that appropriate boundary conditions are required.

So when is the quasiclassical approximation $\mathbf{p} \approx \mathbf{p}_F$ valid? In general, when all energy scales in the problem are much smaller than the Fermi energy ($\gtrsim 1$ eV); or equivalently, all length scales are large compared to the Fermi wavelength ($\lesssim 1$ nm). This is the case for many materials. For instance, the order parameter in a low-temperature superconductor like Nb is ~ 1 meV [92], and in a weak magnet like Pd₈₈Ni₁₂ is ~ 40 meV [93]. However, there are some materials that are far outside this regime as well. For instance, half-metallic ferromagnets have so high spin-splitting that one spin band is conducting while the other is insulating, and topological insulators have so strong spin-orbit coupling that they have perfect spin-momentum locking. However, we note that in these two specific cases, a generalized quasiclassical theory can still be defined around their unconventional Fermi surfaces [VIII, 94].

2.3 Diffusive limit

In this thesis, we focus on *dirty materials*, i.e. materials with a relatively high concentration of random impurities. Formally, this means that the mean free path for quasiparticles is much smaller than all other length scales in the problem (except the Fermi wavelength). As illustrated in figure 2.2, these frequent scatterings cause the quasiparticles to explore the entire Fermi surface as they diffuse through the material. Since all other physical properties were assumed to vary slowly compared to the mean free path, the quasiparticles effectively see a Fermi-surface average of these other properties. In other words: the quasiclassical propagator $\check{\Gamma}$ should depend only weakly on the transport direction \mathbf{v}_F .

In the dirty limit, physical observables are therefore well-described by the first two moments with respect to the transport direction:

$$\check{g} := \langle \check{\Gamma} \rangle_F, \quad \check{I} := \langle \check{\Gamma} \mathbf{v}_F \rangle_F, \quad (2.13)$$

where we have introduced the *isotropic quasiclassical propagator* \check{g} and *anisotropic quasiclassical propagator* \check{I} . From the normalization $\check{\Gamma}^2 = 1$, one can show that $\check{g}^2 \approx 1$ and $\{\check{g}, \check{I}\} = 0$. For brevity, we will simply refer to \check{g} as the *propagator*, while \check{I} is usually called the *matrix current* due to its close relationship to transport properties [53, 95, 96]. In terms of these, the Eilenberger equation splits into two coupled equations:

$$\nabla \cdot \check{I} = i[\check{\Sigma}, \check{g}], \quad \check{I} \approx -D \check{g} \nabla \check{g}, \quad (2.14)$$

where $D := \tau v_F^2/3$ is the diffusion coefficient and τ the mean free time.

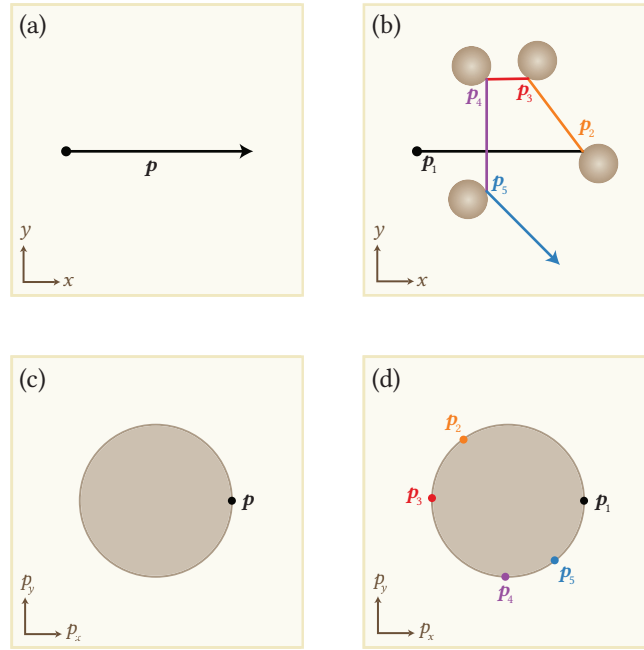


Figure 2.2: Illustration of (a) ballistic transport in clean materials and (b) diffusive transport in dirty materials. In the clean limit, there are no impurities to scatter off, so quasiparticles continue along their trajectories for long periods of time. This means that each quasiparticle sees only a small part of the Fermi surface as shown in panel (c), and is very sensitive to its initial momentum direction. In the dirty limit, the high impurity concentration causes frequent scatterings that randomize the quasiparticle momentum. The quasiparticle population therefore explores the entire Fermi surface on their journey through the material as shown in panel (d). Thus, all physical quantities transported by these quasiparticles are effectively averaged over the Fermi surface, causing only a weak dependence on the initial momentum direction.

The diffusive approximation can also be generalized to a perturbative expansion in the mean free time τ , in which case equation (2.14) can be seen to be the $\mathcal{O}(\tau)$ result. While we focus on the $\mathcal{O}(\tau)$ equation in this thesis, we note that qualitatively new physics sometimes emerge at higher orders in τ . For instance, a spin-dependent Lorentz force appears at $\mathcal{O}(\tau^2)$ in spin-orbit-coupled materials [96], and gives rise to superconducting analogues of the spin-Hall effect and its inverse.

In the presence of a $u(1)$ or $su(2)$ gauge field \mathbf{A} , the diffusion equation then takes the same basic form as equation (2.14), except that all derivatives are replaced by *gauge-covariant derivatives* [11, 49, 50, 97]

$$\tilde{\nabla}(\cdot) := \nabla(\cdot) - i[\hat{\mathbf{A}}, \cdot], \quad (2.15)$$

where $\hat{\mathbf{A}} := \text{diag}(+\mathbf{A}, -\mathbf{A}^*)$. The sign difference between the diagonal blocks can be attributed to electrons have opposite charges and spins compared to holes.⁵ One application of the gauge-covariant equations is that the orbital effects of an applied magnetic field \mathbf{B} are described via a spin-independent gauge field $\mathbf{B} = \nabla \times \mathbf{A}$. If the field is applied along e.g. the x -axis, this can be described by $\mathbf{A} = By\mathbf{e}_z$ in the Landau gauge. Another application of recent interest is that linear-in-momentum spin-orbit coupling can be described as an emergent $su(2)$ gauge field. For instance, the Rashba coupling that arises due to broken inversion symmetry along the z -axis can be described as $\mathbf{A} = \alpha(\sigma_x\mathbf{e}_y - \sigma_y\mathbf{e}_x)$.

In the diffusive limit, the matrix current $\check{\mathbf{I}}$ is a slave variable of the propagator \check{g} . This means that equation (2.14) can be written as a closed equation for \check{g} called the *Usadel equation* [80–83, 98],

$$iD\tilde{\nabla}(\check{g}\tilde{\nabla}\check{g}) = [\check{\Sigma}, \check{g}]. \quad (2.16)$$

This can be made dimensionless by introducing either the *diffusive coherence length* $\xi := \sqrt{D/\Delta_0}$ or the *Thouless energy* $\varepsilon_\tau := D/L^2$ [81], where L is the material length. Together with a model for the energy matrix $\check{\Sigma}$ of a material, and appropriate boundary conditions for the matrix current $\check{\mathbf{I}} = -D\check{g}\tilde{\nabla}\check{g}$, this provides a complete description of superconducting structures in the quasiclassical and diffusive limits.

5. The fact that holes carry opposite spins from electrons can be seen from their field operators. We define a *spin-up hole* as the quasiparticle created by the operator Ψ_\uparrow , which is actually the annihilation operator for spin-up electrons. Since annihilating a spin-up electron clearly has to *decrease* the spin of the system, we conclude that the corresponding holes must carry spin-down.

Similarly to equation (2.8), the propagator \check{g} described by the Usadel equation can be separated into components in Nambu spin space:

$$\check{g} := \begin{pmatrix} \hat{g}^R & \hat{g}^K \\ 0 & \hat{g}^A \end{pmatrix}. \quad (2.17)$$

These components are not independent. From the electron–hole symmetries of the quasiclassical propagators, one can derive the identities $\hat{g}^A = -\hat{\tau}_3 \hat{g}^{R*} \hat{\tau}_3$ and $\hat{g}^R(-\varepsilon) = -\hat{\tau}_1 \hat{g}^{R*}(+\varepsilon) \hat{\tau}_1$. Furthermore, the normalization condition $\check{g}^2 = 1$ can be expanded as $(\hat{g}^R)^2 = (\hat{g}^A)^2 = 1$ and $\hat{g}^R \hat{g}^K + \hat{g}^K \hat{g}^A = 0$, which implies that we can parametrize the Keldysh component as $\hat{g}^K = \hat{g}^R \hat{h} - \hat{h} \hat{g}^A$. Here, \hat{h} is known as the *distribution function*, and describes the occupation numbers for the different states in a material. This distribution function can be chosen block-diagonal,⁶ and satisfies the same electron–hole symmetry $\hat{h}(-\varepsilon) = -\hat{\tau}_1 \hat{h}^*(+\varepsilon) \hat{\tau}_1$. These symmetry considerations justify that it is sufficient to calculate the 4×4 matrices \hat{g}^R and \hat{h} at positive energies $\varepsilon > 0$, since this is clearly sufficient to reconstruct the full 8×8 propagator \check{g} .

2.4 Energy matrices

Most information about a material lies in its energy matrix $\check{\Sigma}$, which describes the effective energies of its quasiparticles. In this section, we summarize the contributions accounted for in our models.

The simplest case is a normal metal, meaning a material without any intrinsic superconducting or magnetic properties [80–83, 101]:

$$\check{\Sigma}_0 = \varepsilon \hat{\tau}_3. \quad (2.18)$$

In the absence of any emergent fields, external fields, or special scattering processes, it is perhaps not surprising that the effective energies are solely determined by the excitation energy ε itself. In a bulk normal metal, the solution to equation (2.16) is $\hat{g}^R = \hat{\tau}_3$. This result is energy-independent because the quasiclassical theory neglects any

6. The distribution function \hat{h} is not uniquely defined, since the Keldysh propagator $\hat{g}^K = \hat{g}^R \hat{h} - \hat{h} \hat{g}^A$ is invariant under transformations $\hat{h} \rightarrow \hat{h} + \hat{g}^R \hat{\chi} + \hat{\chi} \hat{g}^A$ for arbitrary matrices $\hat{\chi}$ [80]. We use a generalization of a convention due to Schmid and Schön [80, 81, 99, 100], and take the distribution function to be block-diagonal. Another interesting choice would be to define $\hat{g}^R \hat{h} + \hat{h} \hat{g}^A = 0$, which simplifies the parametrization of the Keldysh propagator to $\hat{g}^K = 2\hat{g}^R \hat{h}$.

variations in the electronic band structure near the Fermi level, which has been factored out as a constant prefactor N_F . On the other hand, when superconducting correlations are induced, the propagator \hat{g}^R gains off-diagonal components proportional to $\hat{\tau}_1$ or $\hat{\tau}_2$. Substituted into equation (2.16), we find that this leads to an energy-dependent decay of these correlations inside a normal metal. This effect can be understood as follows. Proximity-induced superconductivity can be described as repeated Andreev reflections between electrons at an energy $\varepsilon_F + \varepsilon$ and holes at $\varepsilon_F - \varepsilon$, where each such reflection creates or annihilates an electron pair at the Fermi level ε_F in a superconductor.⁷ These electrons and holes accumulate phases $e^{\pm i(\varepsilon_F \pm \varepsilon)\delta t}$ when they propagate for times δt in the normal metal. These propagation times are equal for the electron and hole forming each such Andreev pair, since they propagate at the Fermi velocity along time-reversed paths after each Andreev reflection. This shows that the phases they accumulate after two successive Andreev reflections cancel almost perfectly [102]. The net phase mismatch per reflection is clearly proportional to $\varepsilon \ll \varepsilon_F$, and this decoherence is captured by the energy matrix above.

In practice, we also have to let $\varepsilon \rightarrow \varepsilon + i\eta$, where the small but finite η is the *inelastic scattering rate* or *Dynes parameter* [103, 104]. Physically, this provides an approximative account of inelastic scattering processes in the material, i.e. scattering processes where quasiparticles change their kinetic energies after the collision. More precisely, the Dynes approximation provides a good description of how spectral features such as e.g. the density of states are affected by inelastic scattering. However, since it does not explicitly couple different energies ε in the Usadel equation, it does not capture the relaxation of the distribution function properly. A more rigorous approach would be to explicitly model the electron–phonon and electron–electron scattering processes [99], which however make the equations more cumbersome to solve. In this thesis, we limit our attention to the Dynes approximation. We note

7. When we say the quasiparticles exist at $\varepsilon_F \pm \varepsilon$, we refer to where in the electronic bands there is an additional or missing electron. Since Andreev reflection requires two electrons at $\varepsilon_F \pm \varepsilon$ to produce a Cooper pair at ε_F , an incoming “extra electron” at $\varepsilon_F + \varepsilon$ leads to an outgoing “missing electron” at $\varepsilon_F - \varepsilon$. Electrons and holes nevertheless have the same *excitation energy* ε ; this is because a hole excitation requires moving an electron from $\varepsilon_F - \varepsilon$ to ε_F , and an electron excitation requires moving an electron from ε_F to $\varepsilon_F + \varepsilon$, and both processes cost the same energy ε .

that in addition to its physical motivation, an infinitesimal $\eta \rightarrow 0^+$ is formally required to separate the retarded and advanced branches of the propagator mathematically,⁸ and a finite value for η also improves the convergence of numerical calculations by damping the BCS coherence peaks. In most of our calculations, we have set $\eta = 0.01\Delta_0$.

Next, we consider the mean-field description of conventional superconductors. These are described by $\check{\Sigma} = \check{\Sigma}_0 + \check{\Sigma}_{\text{sc}}$, where [80–83, 101]

$$\check{\Sigma}_{\text{sc}} = \text{antidiag}(+\Delta, -\Delta, +\Delta^*, -\Delta^*). \quad (2.19)$$

The superconducting order parameter Δ in general a complex number, where its magnitude describes the strength of the superconducting correlations, and its argument describes the condensate phase. We see that the energy matrix is antidiagonal in spin space, which is consistent with conventional superconductors hosting a condensate of opposite-spin electron pairs $|\uparrow\downarrow\rangle - |\downarrow\uparrow\rangle$. We also see that it is antidiagonal in Nambu space, corresponding to anomalous electron–hole correlations. This contribution to the effective energy opens up a gap in the density of states, shifting the lowest-energy excitations from $|\varepsilon| = 0$ to $|\varepsilon| = |\Delta|$. In general, the order parameter Δ has to be calculated self-consistently from the propagators; this will be discussed in more detail in section 2.6.

The next material class of interest is that of ferromagnets. The intrinsic magnetic field in such materials cause three distinct physical effects that are relevant in superconductor/ferromagnet proximity structures. The first is a spin-splitting effect, whereby the effective energy of an electron with spin σ is shifted from ε to $\varepsilon + \mathbf{m} \cdot \sigma$. This is parametrized in terms of a magnetic exchange field \mathbf{m} . The second is a polarization effect, whereby the density of states for spin-up and spin-down quasiparticles differ at the Fermi level. This can be parametrized in terms of a polarization $P = (D_\uparrow - D_\downarrow)/(D_\uparrow + D_\downarrow)$, where D_σ is an effective spin-dependent diffusion coefficient. Finally, there is an orbital effect which can lead to e.g. spontaneous supercurrents and vortex excitations in proximity systems. This is usually neglected in the case of materials that are magnetized in the plane of a thin film, although this approximation has recently been brought into question [74].

8. This is e.g. essential for Meissner effects in superconducting materials: the screening currents arise from contributions of the kind $\eta/[\eta^2 + f(\varepsilon)^2]$, which converge to a delta function $\pi\delta[f(\varepsilon)]$ even in the limit $\eta \rightarrow 0^+$.

In *weak ferromagnets*, the polarization effect is usually neglected. The energy matrix is then just $\check{\Sigma}_0 + \check{\Sigma}_{\text{ex}}$, where [35, 36, 101, 105]

$$\check{\Sigma}_{\text{ex}} = \mathbf{m} \cdot \hat{\boldsymbol{\sigma}}, \quad (2.20)$$

and $\hat{\boldsymbol{\sigma}} := \text{diag}(\boldsymbol{\sigma}, \boldsymbol{\sigma}^*)$. In the absence of superconductivity, this does not change the solution $\hat{g}^{\text{R}} = \hat{\tau}_3$ to the Usadel equation. When superconducting correlations are induced, on the other hand, this term is responsible for singlet–triplet mixing and a rapid decoherence of opposite-spin electron pairs. Instead of representing an actual ferromagnet, the model above can also describe the Zeeman-splitting of any metal in a strong magnetic field [106]. Recently, the same model has also been used for proximity-induced magnetism in materials near the Stoner instability, by self-consistently calculating a magnetic exchange field from the spin accumulation in the material [76].

In *strong ferromagnets*, the polarization effect becomes important, and e.g. results in a strongly spin-dependent conductivity. On the other hand, excitations in the two spin bands decouple, and the exchange effect can be neglected. The energy matrix for a strong ferromagnet polarized in the z -direction can therefore be approximated as [VIII]

$$\check{\Sigma}_{\text{pol}} = \Pi \varepsilon \hat{\tau}_3, \quad (2.21)$$

where the polarization matrix $\Pi = 2(1 - P\sigma_3)/(1 - P^2)$, and P is the polarization of the diffusion coefficient as discussed above. Note that in the half-metallic limit $P \rightarrow 1$, the polarization matrix $\Pi \rightarrow \text{diag}(1, \infty)$; substituted into the Usadel equation, one finds that this destroys all superconducting correlations involving the spin-down band. For a derivation and application of this model, see paper VIII.

This model can be understood as follows. The Usadel equation in a normal metal is $iL^2 \nabla(\check{g} \nabla \check{g}) = [\varepsilon/\varepsilon_{\text{T}}, \check{g}]$, where the Thouless energy for a material of length L is $\varepsilon_{\text{T}} := D/L^2$. Clearly, the generalization to a spin-dependent diffusion coefficient $D_{\sigma} := D(1 \pm P)/2$ leads to a spin-dependent Thouless energy as well. However, since the Usadel equation only depends on the ratio $\varepsilon/\varepsilon_{\text{T}}$, this can be reinterpreted as a spin-independent ε_{T} with spin-dependent effective quasiparticle energies $2\varepsilon/(1 \pm P)$ —which is precisely what the matrix $\Pi\varepsilon$ describes. In the half-metallic limit, the effective quasiparticle energies of one spin band become infinite, meaning that no excitations occur anymore.

The orbital effect associated with magnetic fields can be accounted for using a $U(1)$ gauge field \mathbf{A} , as shown in equation (2.15). However, when a material is thin compared to the magnetic penetration depth λ and superconducting coherence length ξ , the effects of the field can instead be approximated as an effective energy term [99, 106, 107]

$$\check{\Sigma}_{\text{orb}} = i\Delta_0(H/H_c)^\kappa \hat{\tau}_3 \check{g} \hat{\tau}_3, \quad (2.22)$$

where $\kappa = 1$ for out-of-plane and $\kappa = 2$ for in-plane fields. We parametrize the orbital decoherence via a critical field H_c , which is the magnetic field at which superconductivity vanishes even at zero temperature. This is generally much higher for in-plane than out-of-plane fields, and can be calculated from the sample geometry [107]. This model was e.g. used to fit the experimental results in paper IV.

So far, we have discussed the different energy matrix contributions that arise due to the intrinsic properties of a material. We now turn to the extrinsic properties, which arise due to various scattering processes involving random impurities. We treat these scattering processes in the Born approximation, which means that some phenomena such as YSR states [108–110] cannot be described. For a discussion of the quasi-classical theory beyond the Born approximation, see e.g. reference 111. The extrinsic contributions listed below can be added to the intrinsic energy matrices describing superconductors, ferromagnets, or normal metals in order to account for their impurities.

The first such contribution describes spin-independent scattering processes involving non-magnetic impurities [82, 83]:

$$\hat{\Sigma}_{\text{imp}} = \frac{i}{2\tau} \check{g}. \quad (2.23)$$

This contribution has to be manually included when considering moderately dirty materials using the Eilenberger equation. It has however already been accounted for in the derivation of the Usadel equation, and is the source of the mean free time τ in the diffusion coefficient.

In the case of impurities with magnetic moments or spin-orbit coupling, more exotic scattering processes are also possible. If the magnetic moments of the impurities are randomly oriented, this is described as an *isotropic spin-flip scattering* [101, 112],

$$\hat{\Sigma}_{\text{sf}} = \frac{i}{2\tau_{\text{sf}}} \hat{\sigma} \check{g} \hat{\sigma}. \quad (2.24)$$

If the magnetic moments are correlated, one obtains a *uniaxial spin-flip scattering* by letting $\hat{\sigma} \rightarrow \hat{\sigma} \cdot \mathbf{s}$ above [112], where \mathbf{s} parametrizes the magnetic ordering axis. Similarly, impurities with atomic spin-orbit coupling give rise to *spin-orbit scattering* [36, 112, 113],

$$\hat{\Sigma}_{\text{so}} = \frac{i}{2\tau_{\text{so}}} \hat{\tau}_3 \hat{\sigma} \check{g} \hat{\sigma} \hat{\tau}_3. \quad (2.25)$$

The energy matrices above are expressed in terms of a spin-flip time τ_{sf} and spin-orbit time τ_{so} . We note that in general, spin-flip scattering suppresses both singlet and triplet pairs, while spin-orbit scattering only suppresses triplet pairs [112, 114]. Materials with spin-flip and spin-orbit scattering were investigated in paper IX.

2.5 Boundary conditions

As we briefly discussed in section 2.2, the quasiclassical approximation breaks down at the interfaces between materials. Thus, to bridge the quasiclassical propagators across interfaces, one has to derive appropriate boundary conditions from the underlying non-quasiclassical theory near the interface. Typically, the results are expressed in terms of the quasiclassical matrix current $\check{I} := \check{I} \cdot \mathbf{n}$ flowing out of an interface, where \mathbf{n} is the normal vector of the interface. A trivial example would be an interface to vacuum or a bulk insulator: since no quasiparticles can exist there, the boundary conditions are simply $\check{I} = 0$.

In this thesis, we mostly focus on low-transparency interfaces, in which case we can use the boundary conditions [VIII, 115–123]

$$\begin{aligned} (L/D)\check{I} = & \left(\frac{1}{2} \frac{G_{\text{T}}}{G_{\text{N}}} \right) [\check{g}, F(\check{g}')] \\ & - \left(\frac{i}{2} \frac{G_{\varphi}}{G_{\text{N}}} \right) [\check{g}, \hat{r}] \\ & + \left(\frac{1}{4} \frac{G_{\text{T}} G_{\chi}}{G_{\text{N}} G_{\varphi}} \right) F(\check{g}') \check{g} F(\check{g}') \\ & + \left(\frac{1}{8} \frac{G_{\varphi} G_{\chi}}{G_{\text{N}} G_{\text{T}}} \right) [\check{g}, \hat{r} \check{g} \hat{r}] \\ & + \left(\frac{i}{8} \frac{G_{\chi}}{G_{\text{N}}} \right) [\check{g}, F(\check{g}') \check{g} \hat{r} + \hat{r} \check{g} F(\check{g}')] \\ & + \left(\frac{i}{8} \frac{G'_{\chi}}{G_{\text{N}}} \right) [\check{g}, F(\check{g}') \hat{r}' \check{g}' - \hat{r}'], \end{aligned} \quad (2.26)$$

where we have defined the spin-filtering function

$$F(\check{v}) := \check{v} + \frac{P}{1 + \sqrt{1 - P^2}} \{\check{v}, \hat{t}\} + \frac{1 - \sqrt{1 - P^2}}{1 + \sqrt{1 - P^2}} \hat{t} \check{v} \hat{t}. \quad (2.27)$$

These boundary conditions are valid to second order in the tunneling probabilities, second order in the spin-mixing angles, and all orders in the interface polarization, assuming that these interface parameters are not too different between the interfacial transport channels. This is a new result derived in paper VIII, which is significantly simpler than the corresponding boundary conditions presented previously in reference 115. Below, we discuss different limiting cases of these boundary conditions, and how to interpret its various parameters.

Let us first consider a non-magnetic interface: $P = G_\varphi = G_\chi = G'_\chi = 0$. The boundary conditions then reduce to a particularly simple form,

$$(2L/D) \check{I} = (G_T/G_N) [\check{g}, \check{g}'], \quad (2.28)$$

which are known as the Kuprianov–Lukichev boundary conditions in the literature [123]. Here, \check{g} is the propagator on the same side of the interface as \check{I} is being calculated, \check{g}' the propagator on the other side of the interface, L the length of the material, and G_N the normal-state conductance of the material. The remaining parameter G_T is the tunneling conductance, which is related to the tunneling probability and interfacial channel density. This description is valid to lowest order in the tunneling probabilities, and is commonly used to model imperfect interfaces to normal metals or weak ferromagnets.

Next, we include a finite spin-mixing conductance G_φ , which is associated with singlet–triplet mixing due to interfacial phase shifts, and polarization P , which is associated with a spin-filtering effect. That yields the following boundary conditions [115–122],

$$(2L/D) \check{I} = (G_T/G_N) [\check{g}, F(\check{g}')] - i(G_\varphi/G_N) [\check{g}, \hat{r}], \quad (2.29)$$

which are valid to first order in the tunneling probabilities and spin-mixing angles, and to all orders in the polarization. It has recently been shown that the same boundary conditions can also be used to describe uncompensated antiferromagnetic interfaces [124]. These boundary conditions include a matrix $\hat{t} := \mathbf{t} \cdot \hat{\sigma}$, which describes the average magnetization \mathbf{t} seen by electrons tunneling through the interface, and

another matrix $\hat{r} := \mathbf{r} \cdot \boldsymbol{\sigma}$, which describes the magnetization \mathbf{r} seen by reflected electrons. In completely homogeneous magnetic systems, these can be taken to be equal. However, if the magnetic interface is used as a model for e.g. tunneling through a thin ferromagnetic insulator that contains a domain wall, or if an otherwise homogeneous magnetic metal has its magnetization pinned in a different direction at the interface, these magnetizations can be quite different. Since magnetic inhomogeneities are associated with long-range triplet generation and spontaneous spin currents in superconducting systems, the results of such inhomogeneity can be quite important.

The full second-order boundary conditions contain a number of new terms. However, as described in paper VIII, all the new terms can be rewritten in terms of a single new parameter G_χ . This is a mixed interface conductance, in the sense that while G_T describes tunneling probabilities and G_φ describes spin-mixing processes, G_χ essentially measures the correlation between these processes. In addition, the boundary conditions involve G'_χ and \hat{r}' , which are simply the values of G_χ and \hat{r} on the other side of the interface. These new terms have relatively straight-forward interpretations: every F describes a tunneling event, every \hat{r} describes spin-mixing on this side of the interface, and every \hat{r}' spin-mixing on the other side of the interface. Thus, from top to bottom, these terms describe (I) second-order tunneling, (II) second-order spin-mixing, (III) a tunneling event combined with spin-mixing on this side, (IV) a tunneling event combined with spin-mixing on the other side. To second order in the tunneling and spin-mixing amplitudes, this is of course the contributions one would expect.

For most projects presented in this thesis, the first-order magnetic boundary conditions have been employed. A notable exception is paper VIII, where we investigated the effect of the second-order boundary conditions in superconductor/half-metal structures in figure 10. Unfortunately, the results were not that interesting: at least for that particular setup, including a finite G_χ did not yield any qualitatively new physics, but rather just resulted in behaviour that could be reproduced by slightly lowering the value of G_φ . In that paper, we also investigated the density of states in superconductor/ferromagnetic-insulator bilayers. We then treated the magnetic properties to *all* orders in spin-mixing angles, and found qualitatively new results compared to the G_φ approximation, as shown in figure 5.

In this thesis, we have focused on low-transparency interfaces. There are however boundary conditions available for higher transparencies as well: Nazarov's boundary conditions describe non-magnetic interfaces with arbitrary transparencies [53, 95], and Eschrig's boundary conditions can be series-expanded to higher orders in the tunneling probabilities and spin-mixing angles if required [115].

2.6 Physical observables

The solution to the Usadel equation is given by the retarded propagator \hat{g}^R and distribution function \hat{h} , which can be used to reconstruct the entire propagator \check{g} and matrix current $\check{I} = -D\check{g}\tilde{\nabla}\check{g}$. In this section, we discuss how to calculate physical observables from these results.

Before we proceed, it is convenient to parametrize the Nambu spin structure of the components $\hat{g}^R, \hat{g}^K, \hat{I}^K$ as follows [33]:

$$\hat{g}^R := \begin{pmatrix} (g_s^R + \mathbf{g}_t^R \cdot \boldsymbol{\sigma}) & (f_s^R + \mathbf{f}_t^R \cdot \boldsymbol{\sigma})i\sigma_2 \\ -(\tilde{f}_s^R + \tilde{\mathbf{f}}_t^R \cdot \boldsymbol{\sigma}^*)i\sigma_2 & -(\tilde{g}_s^R + \tilde{\mathbf{g}}_t^R \cdot \boldsymbol{\sigma}^*) \end{pmatrix}, \quad (2.30)$$

$$\hat{g}^K := \begin{pmatrix} (g_s^K + \mathbf{g}_t^K \cdot \boldsymbol{\sigma}) & (f_s^K + \mathbf{f}_t^K \cdot \boldsymbol{\sigma})i\sigma_2 \\ (\tilde{f}_s^K + \tilde{\mathbf{f}}_t^K \cdot \boldsymbol{\sigma}^*)i\sigma_2 & (\tilde{g}_s^K + \tilde{\mathbf{g}}_t^K \cdot \boldsymbol{\sigma}^*) \end{pmatrix}, \quad (2.31)$$

$$\hat{I}^K := \begin{pmatrix} (I_s^K + \mathbf{I}_t^K \cdot \boldsymbol{\sigma}) & (J_s^K + \mathbf{J}_t^K \cdot \boldsymbol{\sigma})i\sigma_2 \\ -(\tilde{J}_s^K + \tilde{\mathbf{J}}_t^K \cdot \boldsymbol{\sigma}^*)i\sigma_2 & -(\tilde{I}_s^K + \tilde{\mathbf{I}}_t^K \cdot \boldsymbol{\sigma}^*) \end{pmatrix}. \quad (2.32)$$

The g 's defined here are referred to as *normal components*, and the f 's as *anomalous components*. We have also introduced the notation $\tilde{u}(+\varepsilon) := u^*(-\varepsilon)$, which represents an electron-hole conjugation. For notational transparency, we consider the current $\hat{I}^K := \hat{\mathbf{I}}^K \cdot \mathbf{n}$ along the junction direction \mathbf{n} . The generalization to 3D transport problems is straight-forward: the matrix I_s^K becomes a vector \mathbf{I}_s^K that points along the transport direction, while \mathbf{I}_t^K becomes a rank-2 tensor since it has both a transport direction and spin polarization. The structures of the matrices above follow from the normalization and symmetry constraints discussed in section 2.3. The exceptions are the $i\sigma_2$ factors, which simplify the physical interpretation of anomalous correlations.⁹

9. For historical reasons, this is often referred to as *d*-vector notation [125, 126].

Once the matrices $\hat{g}^R, \hat{g}^K, \hat{I}^K$ have been calculated at positive energies, the components introduced above can easily be calculated for any energy. Using well-known identities for traces, together with the definition of the electron–hole-conjugation above, we e.g. see that:

$$g_s^K(+\varepsilon) = \frac{1}{4} \text{Tr}[(\hat{\tau}_0 + \hat{\tau}_3)\hat{g}^K(+\varepsilon)], \quad (2.33)$$

$$g_s^K(-\varepsilon) = \frac{1}{4} \text{Tr}[(\hat{\tau}_0 - \hat{\tau}_3)\hat{g}^K(+\varepsilon)]^*, \quad (2.34)$$

$$f_s^K(+\varepsilon) = \frac{1}{4} \text{Tr}[(-i\hat{\sigma}_2)(\hat{\tau}_1 - i\hat{\tau}_2)\hat{g}^K(+\varepsilon)], \quad (2.35)$$

$$f_s^K(-\varepsilon) = \frac{1}{4} \text{Tr}[(+i\hat{\sigma}_2)(\hat{\tau}_1 + i\hat{\tau}_2)\hat{g}^K(+\varepsilon)]^*. \quad (2.36)$$

In terms of these quantities, the density of states can be written [33]

$$N_s(\mathbf{r}, \varepsilon) = N_F \text{Re}[g_s^R(\mathbf{r}, \varepsilon) + \mathbf{s} \cdot \mathbf{g}_t^R(\mathbf{r}, \varepsilon)], \quad (2.37)$$

where \mathbf{s} refers to the spin-projection of the quasiparticles. In other words, the spin-independent density of states is just $N_F \text{Re}[g_s^R]$, while the spin-polarization of the density of states is given by $N_F \text{Re}[\mathbf{g}_t^R]$. This provides a simple physical interpretation of the retarded propagator \hat{g}^R .

Another important quantity is the superconducting order parameter Δ . Its magnitude determines e.g. the gap in the density of states, while its complex phase is important for e.g. Josephson effects. For a bulk superconductor at zero temperature, we can take the order parameter to be a real constant Δ_0 . For a current-carrying superconductor, we present a semi-analytical solution in paper XII. More generally, the order parameter has to be determined fully self-consistently. As shown in appendix B of paper II, the self-consistency equation for a weakly coupled conventional superconductor is

$$\Delta(\mathbf{r}) = \frac{1}{4 \log(2\omega_c/\Delta_0)} \int_{-\omega_c}^{+\omega_c} d\varepsilon f_s^K(\mathbf{r}, \varepsilon). \quad (2.38)$$

The integral is taken up to the Debye cutoff ω_c , which we in our simulations usually set to $\omega_c = 30\Delta_0$. Clearly, the anomalous component f_s^K has to describe the singlet pairs associated with conventional superconductivity. Similarly, f_t^K can be shown to describe triplet pairs.

The next observables we consider are the charge accumulation ρ_e , spin accumulation ρ_s , charge current J_e , and spin current J_s :

$$\rho_e(\mathbf{r}) = -\frac{1}{4} e N_F \int_{-\infty}^{+\infty} d\varepsilon \operatorname{Re}[g_s^K(\mathbf{r}, \varepsilon)], \quad (2.39)$$

$$\rho_s(\mathbf{r}) = -\frac{1}{4} \frac{\hbar}{2} N_F \int_{-\infty}^{+\infty} d\varepsilon \operatorname{Re}[g_t^K(\mathbf{r}, \varepsilon)], \quad (2.40)$$

$$J_e(\mathbf{r}) = -\frac{1}{4} e N_F \int_{-\infty}^{+\infty} d\varepsilon \operatorname{Re}[I_s^K(\mathbf{r}, \varepsilon)], \quad (2.41)$$

$$J_s(\mathbf{r}) = -\frac{1}{4} \frac{\hbar}{2} N_F \int_{-\infty}^{+\infty} d\varepsilon \operatorname{Re}[I_t^K(\mathbf{r}, \varepsilon)]. \quad (2.42)$$

We derive these equations from the Heisenberg equations for the field operators in the supplemental of paper xv. This provides physical interpretations for the Keldysh propagator \hat{g}^K and matrix current \hat{I}^K : the former describes the local charge and spin imbalance, and the latter the flow of charge and spin between positions.

Energy and spin-energy transport are described in a similar way [99]:

$$\rho_{\text{he}}(\mathbf{r}) = \frac{1}{4} N_F \int_{-\infty}^{+\infty} d\varepsilon \operatorname{Re}[\varepsilon g_s^K(\mathbf{r}, \varepsilon)], \quad (2.43)$$

$$\rho_{\text{hs}}(\mathbf{r}) = \frac{1}{4} N_F \int_{-\infty}^{+\infty} d\varepsilon \operatorname{Re}[\varepsilon g_t^K(\mathbf{r}, \varepsilon)], \quad (2.44)$$

$$J_{\text{he}}(\mathbf{r}) = \frac{1}{4} N_F \int_{-\infty}^{+\infty} d\varepsilon \operatorname{Re}[\varepsilon I_s^K(\mathbf{r}, \varepsilon)], \quad (2.45)$$

$$J_{\text{hs}}(\mathbf{r}) = \frac{1}{4} N_F \int_{-\infty}^{+\infty} d\varepsilon \operatorname{Re}[\varepsilon I_t^K(\mathbf{r}, \varepsilon)]. \quad (2.46)$$

The most obvious contributions to the energy and spin-energy are *heat* and *spin-heat*. Heat refers to a spin-independent excitation of electrons and holes, which can be interpreted as an effective increase in the electronic temperature. Spin-heat, on the other hand, refers to a higher effective temperature for one spin species than the other, corresponding to e.g. an excess of spin-up electrons and spin-down holes. However, the energy and spin-energy also contain contributions from charge and spin accumulation that depend on the chemical potential [127].

It is a common misconception that these equations can be derived in the same manner as the charge and spin transport equations, since the results are similar. However, the rigorous derivation actually starts from the energy–momentum tensor of the quantum fields [127–129],

$$T_{\mu\nu\sigma} = \frac{\partial L_\sigma}{\partial(\partial_\nu\Psi_\sigma)}(\partial_\mu\Psi_\sigma) + (\partial_\mu\Psi_\sigma^\dagger)\frac{\partial L_\sigma}{\partial(\partial_\nu\Psi_\sigma^\dagger)} - \delta_{\mu\nu}L_\sigma, \quad (2.47)$$

where the kinetic part of the Langrangian for spin- σ particles is

$$L_\sigma = i[\Psi_\sigma^\dagger(\partial_t\Psi_\sigma) - (\partial_t\Psi_\sigma^\dagger)\Psi_\sigma] - (1/2m)(\nabla\Psi_\sigma^\dagger)(\nabla\Psi_\sigma). \quad (2.48)$$

Here, $T_{tt\sigma}$ is the spin- σ energy density operator, which is related to the spin- σ energy accumulation. Similarly, $(T_{tx\sigma}, T_{ty\sigma}, T_{tz\sigma})$ is the spin- σ energy flux operator, which is usually interpreted as a spin- σ energy current. Such an analysis shows that e.g. the spin- σ energy current in the system can be calculated from the expectation value

$$J_{h\sigma} = (-1/2m)(\partial_t\nabla_{\mathbf{r}'} + \nabla_{\mathbf{r}}\partial_{t'})\langle\Psi_\sigma^\dagger(\mathbf{r}', t')\Psi_\sigma(\mathbf{r}, t)\rangle, \quad (2.49)$$

which after the quasiclassical approximation yields the usual expressions for the energy and spin-energy currents $J_{h\uparrow} \pm J_{h\downarrow}$.

In equilibrium, the distribution function reduces to the Fermi–Dirac form $\hat{h} = \tanh(\varepsilon/2T)\hat{\tau}_0$, where T is the temperature of the system. The components of \hat{g}^K are then directly related to those of \hat{g}^R :

$$g_s^K(\mathbf{r}, \varepsilon) = 2 \operatorname{Re}[g_s(\mathbf{r}, \varepsilon)] \tanh(\varepsilon/2T), \quad (2.50)$$

$$g_t^K(\mathbf{r}, \varepsilon) = 2 \operatorname{Re}[g_t(\mathbf{r}, \varepsilon)] \tanh(\varepsilon/2T), \quad (2.51)$$

$$f_s^K(\mathbf{r}, \varepsilon) = [f_s^R(\mathbf{r}, +\varepsilon) - f_s^R(\mathbf{r}, -\varepsilon)] \tanh(\varepsilon/2T), \quad (2.52)$$

$$f_t^K(\mathbf{r}, \varepsilon) = [f_t^R(\mathbf{r}, +\varepsilon) + f_t^R(\mathbf{r}, -\varepsilon)] \tanh(\varepsilon/2T). \quad (2.53)$$

This provides an interpretation of f_s^R and f_t^R as a kind of density of states for singlet and triplet pairs. Similarly, we see that the charge and spin accumulation can be interpreted in terms of the density of states and distribution function. It is therefore commonly stated that \hat{g}^R describes the equilibrium properties of a material, while $\hat{g}^K = \hat{g}^R\hat{h} - \hat{h}\hat{g}^A$ describes the nonequilibrium properties. This is however not entirely true: if superconductivity is treated self-consistently, \hat{g}^R and \hat{g}^A are also implicitly functions of \hat{h} via the self-consistency equation for Δ .

Another useful fact is that the matrix current $\hat{\mathbf{I}}^{\text{K}}$ can be written [80]:

$$\hat{\mathbf{I}}^{\text{K}} = \hat{\mathbf{I}}^{\text{KS}} + \hat{\mathbf{I}}^{\text{KR}}, \quad (2.54)$$

$$\hat{\mathbf{I}}^{\text{KS}} = -D[(\hat{g}^{\text{R}}\tilde{\nabla}\hat{g}^{\text{R}})\hat{h} - \hat{h}(\hat{g}^{\text{A}}\tilde{\nabla}\hat{g}^{\text{A}})], \quad (2.55)$$

$$\hat{\mathbf{I}}^{\text{KR}} = -D[(\tilde{\nabla}\hat{h}) - \hat{g}^{\text{R}}(\tilde{\nabla}\hat{h})\hat{g}^{\text{A}}]. \quad (2.56)$$

Only $\hat{\mathbf{I}}^{\text{KS}}$ depends on the phase gradients of the propagators, and only $\hat{\mathbf{I}}^{\text{KR}}$ depends on the chemical potential and temperature gradients of the distribution function. This allows us to interpret the former as condensate-driven supercurrents, and the latter as quasiparticle-driven resistive currents, which can be useful to distinguish these effects.

Finally, we note that the parametrization of the propagators used in this section can also be useful analytically. For example, if the superconducting correlations in a proximitized material are weak, one can use the approximations $|g_s^{\text{R}}| \approx 1$ and $|f_s^{\text{R}}|, |f_t^{\text{R}}|, |g_t^{\text{R}}| \ll 1$ to linearize the Usadel equation. The result can be written in the simple form [II]:

$$(iD/2)\nabla^2 f_s^{\text{R}} = \varepsilon f_s^{\text{R}} + \mathbf{m} \cdot \mathbf{f}_t^{\text{R}}, \quad (2.57)$$

$$(iD/2)\nabla^2 f_t^{\text{R}} = \varepsilon f_t^{\text{R}} + \mathbf{m} f_s^{\text{R}} + 2iD\Omega \mathbf{f}_t, \quad (2.58)$$

where \mathbf{m} is the magnetic exchange field in a material, and Ω is a 3×3 matrix that describes the spin-orbit coupling of a material [II–IV].

2.7 Parametrization

The retarded propagator \hat{g}^{R} has a normalization condition $(\hat{g}^{\text{R}})^2 = 1$ and electron-hole symmetry $\hat{g}^{\text{R}}(\varepsilon) = -\hat{\tau}_1 \hat{g}^{\text{R}*}(-\varepsilon) \hat{\tau}_1$. This implies that it has some redundant degrees of freedom that can be eliminated by a suitable parametrization, thus simplifying the task of solving the Usadel equation. For analytical calculations, many different parametrizations are in use depending on the problem at hand. For instance, one might use equation (2.30) directly; set $g_s^{\text{R}} = \varepsilon/\Omega$, $f_s^{\text{R}} = \theta e^{i\chi}/\Omega$ where $\Omega = \sqrt{\varepsilon^2 - \theta^2}$ [XII, 130, 131]; set $g_s^{\text{R}} = \cosh \theta$, $f_s^{\text{R}} = e^{i\chi} \sinh \theta$ [80, 81, 132]; or use spin-dependent generalizations of these [I, 112]. In these examples, θ and χ are complex functions of position and energy, and parametrize the size and phase of a superconducting condensate, respectively.

In this thesis, we mostly focus on numerical calculations in structures with inhomogeneous magnetism or spin-orbit coupling. A practical

way to treat such problems is the *Riccati parametrization* [II, 133, 134],¹⁰

$$\hat{g}^{\text{R}} := \begin{pmatrix} +N & 0 \\ 0 & -\tilde{N} \end{pmatrix} \begin{pmatrix} 1 + \gamma\tilde{\gamma} & 2\gamma \\ 2\tilde{\gamma} & 1 + \tilde{\gamma}\gamma \end{pmatrix}, \quad (2.59)$$

where the normalization matrix is defined as $N = (1 - \gamma\tilde{\gamma})^{-1}$. We note that in contrast to the alternatives mentioned above, the Riccati parametrization is completely general, single-valued, and bounded [I]. Some useful identities when working with this parametrization are $N\gamma = \gamma\tilde{N}$, $N(1 + \gamma\tilde{\gamma}) = 2N - 1$, and $\nabla N = N[(\nabla\gamma)\tilde{\gamma} + \gamma(\nabla\tilde{\gamma})]N$.

Starting from the retarded part of the Usadel equation $\nabla \cdot \hat{\mathbf{I}}^{\text{R}} = \hat{U}^{\text{R}}$, where $\hat{\mathbf{I}}^{\text{R}} = -D\hat{g}^{\text{R}}\nabla\hat{g}^{\text{R}}$ and $\hat{U}^{\text{R}} = i[\hat{\Sigma}^{\text{R}}, \hat{g}^{\text{R}}]$, we have derived the following identities for the derivatives of the Riccati parameter γ [VIII]:

$$\nabla^2\gamma = -(2DN)^{-1}(U_{12}^{\text{R}} - U_{11}^{\text{R}}\gamma) - 2(\nabla\gamma)\tilde{N}\tilde{\gamma}(\nabla\gamma), \quad (2.60)$$

$$\nabla\gamma = -(2DN)^{-1}(I_{12}^{\text{R}} - I_{11}^{\text{R}}\gamma), \quad (2.61)$$

where U_{12}^{R} refers to the top-right 2×2 block of \hat{U}^{R} , and so on. These equations can be used to numerically implement the Usadel equation and its boundary conditions, respectively. In the presence of a gauge field \mathbf{A} , these equations have to be adjusted as shown in paper II.

In equilibrium, it is sufficient to solve the Riccati-parametrized equations for \hat{g}^{R} to calculate all observables, since the distribution function is simply the Fermi–Dirac one: $\hat{h} = \tanh(\varepsilon/2T)\hat{\tau}_0$. Out of equilibrium, one also has to solve a kinetic equation for the distribution function \hat{h} . In the supplemental of paper XIII, we derived a new form for this equation. The approach is not entirely new [80, 81, 99, 106, 137, 138]; however, our equations are both simpler and more general than previous ones, and resulted in a very efficient numerical implementation.

First, it is convenient to introduce a set of basis matrices $\hat{\rho}_n$ that span the block-diagonal Nambu⊗spin space:

$$\begin{aligned} \hat{\rho}_0 &:= \hat{\tau}_0\hat{\sigma}_0, & \hat{\rho}_1 &:= \hat{\tau}_0\hat{\sigma}_1, & \hat{\rho}_2 &:= \hat{\tau}_0\hat{\sigma}_2, & \hat{\rho}_3 &:= \hat{\tau}_0\hat{\sigma}_3; \\ \hat{\rho}_4 &:= \hat{\tau}_3\hat{\sigma}_0, & \hat{\rho}_5 &:= \hat{\tau}_3\hat{\sigma}_1, & \hat{\rho}_6 &:= \hat{\tau}_3\hat{\sigma}_2, & \hat{\rho}_7 &:= \hat{\tau}_3\hat{\sigma}_3. \end{aligned} \quad (2.62)$$

10. It is named this way because the parametrization transforms the Eilenberger equation into a *Riccati matrix differential equation*. This allows one to use special theorems to simplify the numerical solution of the equation; in particular, one can calculate the changes to the solution $\gamma(\mathbf{r}, \varepsilon)$ as the boundary conditions $\gamma_0(\varepsilon)$ change without having to solve the differential equation itself again [135, 136].

As discussed in section 2.3, the distribution function \hat{h} can be taken to be a block-diagonal matrix. This means that it can be parametrized as

$$\hat{h} = h_n \hat{\rho}_n, \quad (2.63)$$

where we use the summation convention on the right-hand side, and the coefficients can be found from the traces $h_n = (1/4) \text{Tr}[\hat{\rho}_n \hat{h}]$. The distribution is in other words parametrized as an 8-element vector h , which describes all charge, spin, energy, and spin-energy degrees of freedom. The equation for the distribution function takes a particularly simple form when expressed in terms of these coefficients [XIII]:

$$M_{nm} \nabla^2 h_m = -(\nabla M_{nm} + \mathbf{Q}_{nm}) \cdot \nabla h_m - (\nabla \cdot \mathbf{Q}_{nm} + V_{nm} + W_{nm}) h_m. \quad (2.64)$$

Similarly, the boundary conditions can be written in the form

$$M_{nm} \partial h_m = T'_{nm} h'_m - (Q_{nm} + T_{nm} + R_{nm}) h_m, \quad (2.65)$$

where the directions of $\partial := \mathbf{n} \cdot \nabla$ and $Q_{nm} := \mathbf{n} \cdot \mathbf{Q}_{nm}$ are determined by the interface normal \mathbf{n} . The primed quantity h' refers to the distribution function on the other side. The summations over m can be identified as matrix-vector multiplications, where $\mathbf{Q}, M, V, W, T, R$, are 8×8 matrices that operate on the vector h . We note that all these coefficients are independent of h , making this an *explicit linear second-order differential equation* for the distribution function. This makes it very efficient numerically; in fact, it typically takes less time to solve this kinetic equation than the Riccati-parametrized equation for \hat{g}^R .

We now discuss the calculation of the coefficients in equations (2.64) and (2.65). For a material described by a general second-order energy matrix $\check{\Sigma} = \hat{v} + \hat{w} \hat{g} \hat{w}$, the coefficients of equation (2.64) are:

$$\mathbf{Q}_{nm} = \frac{D}{4} \text{Tr} [\hat{\rho}_m \hat{\rho}_n (\hat{g}^R \nabla \hat{g}^R) - \hat{\rho}_n \hat{\rho}_m (\hat{g}^A \nabla \hat{g}^A)], \quad (2.66)$$

$$M_{nm} = \frac{D}{4} \text{Tr} [\hat{\rho}_n \hat{\rho}_m - \hat{\rho}_n \hat{g}^R \hat{\rho}_m \hat{g}^A], \quad (2.67)$$

$$V_{nm} = \frac{i}{4} \text{Tr} \{ [\hat{\rho}_n, \hat{v}] (\hat{g}^R \hat{\rho}_m - \hat{\rho}_m \hat{g}^A) \}, \quad (2.68)$$

$$W_{nm} = \frac{i}{4} \text{Tr} \{ [\hat{\rho}_n, \hat{w}] (\hat{g}^R \hat{w} \hat{g}^R \hat{\rho}_m - \hat{\rho}_m \hat{g}^A \hat{w} \hat{g}^A + \hat{g}^R [\hat{\rho}_m, \hat{w}] \hat{g}^A) \}. \quad (2.69)$$

Every energy matrix contribution considered in this thesis is either a first-order or second-order matrix as described above (see section 2.4).

The main physical phenomena considered in this thesis that are not captured by this form of the kinetic equation would be a gauge field A , which requires that a number of new terms be added to the kinetic equation [139]. As for the boundary coefficients, these are

$$T_{nm} = \frac{D}{8L} \frac{G_T}{G_N} \text{Tr} \{ [F(\hat{g}^{A'}) \hat{\rho}_n - \hat{\rho}_n F(\hat{g}^{R'})] (\hat{g}^R \hat{\rho}_m - \hat{\rho}_m \hat{g}^A) \}, \quad (2.70)$$

$$T'_{nm} = \frac{D}{8L} \frac{G_T}{G_N} \text{Tr} \{ (\hat{g}^A \hat{\rho}_n - \hat{\rho}_n \hat{g}^R) [F(\hat{g}^{R'} \hat{\rho}_m - \hat{\rho}_m \hat{g}^{A'})] \}, \quad (2.71)$$

$$R_{nm} = \frac{D}{8L} \frac{G_\varphi}{G_N} \text{Tr} \{ [-i\hat{r}, \hat{\rho}_n] (\hat{g}^R \hat{\rho}_m - \hat{\rho}_m \hat{g}^A) \}. \quad (2.72)$$

This equation is directly derived from equation (2.29), and has the same notation and regime of validity as that equation. We have not derived higher-order boundary conditions for the kinetic equation herein. For more details about this parametrization and derivations of the coefficients listed above, see appendices B and C of paper XIII.

2.8 Reservoirs

It is often useful to include *reservoirs* in the model of a physical system. By this, we mean bulk materials with known macroscopic properties; e.g. a semi-infinite superconductor with a fixed condensate phase, or a semi-infinite normal metal at a fixed voltage bias. In equilibrium, treating a superconductor as a reservoir can significantly expedite calculations, since its order parameter does not have to be self-consistently determined. Out of equilibrium, having at least one reservoir in the model is a prerequisite, as the chemical potential and temperature of a material does not naturally emerge from the kinetic equation itself. In this section, we describe how we model these reservoirs in practice.

Let us consider a superconductor with a known macroscopic order parameter $\Delta = \Delta_0 e^{i\chi}$. When approximated as a reservoir, the superconducting state should be homogeneous ($\nabla \hat{g}^R = 0$), and the Usadel equation reduces to $[\hat{\Sigma}_0 + \hat{\Sigma}_{sc}, \hat{g}^R] = 0$. One can verify that this equation is solved by equation (2.59) for the Riccati parameters

$$\gamma_s = +e^{+i\chi} \tanh(\theta/2) i\sigma_2, \quad (2.73)$$

$$\tilde{\gamma}_s = -e^{-i\chi} \tanh(\theta/2) i\sigma_2, \quad (2.74)$$

where $\theta = \text{acoth}[(\varepsilon + i\eta)/\Delta_0]$. This also demonstrates how the Riccati parameters are bounded: even though the elements of \hat{g}^R diverge as

$\varepsilon \rightarrow \pm\Delta_0$, we see that $\|\gamma_s\| = \|\tilde{\gamma}_s\| = |\tanh(\theta/2)| \in [0, 1]$.¹¹ The solution for a normal-metal reservoir follows from the limit $\Delta_0 \rightarrow 0$,

$$\gamma_N = \tilde{\gamma}_N = 0, \quad (2.75)$$

demonstrating that γ and $\tilde{\gamma}$ parametrize superconducting correlations.

The distribution function of a quite general nonequilibrium reservoir can be described by the diagonal matrix [XIII]

$$\hat{h} = \text{diag}(h_\uparrow^+, h_\downarrow^+, h_\uparrow^-, h_\downarrow^-), \quad (2.76)$$

where $h_\sigma^\pm := \tanh[(\varepsilon \pm eV_\sigma)/2T_\sigma]$ are the distribution functions of each kind of quasiparticle. More precisely, h_\uparrow^+ describes spin-up electrons, h_\downarrow^- spin-down holes, and so on. It is worth noting that one should *not* include a Dynes parameter $\varepsilon \rightarrow \varepsilon + i\eta$ in the distribution functions; these describe the occupation numbers $n_\sigma^\pm(\varepsilon) = [1 - h_\sigma^\pm(\varepsilon)]/2$ of the quasiparticle states, which are always real quantities. Compared to equation (2.63), we see that the coefficients h_n are given by the sums and differences of these quasiparticle-resolved distribution functions h_σ^\pm :

$$\begin{aligned} h_0 &= (h_\uparrow^+ + h_\downarrow^+ + h_\uparrow^- + h_\downarrow^-)/4, \\ h_3 &= (h_\uparrow^+ - h_\downarrow^+ + h_\uparrow^- - h_\downarrow^-)/4, \\ h_4 &= (h_\uparrow^+ + h_\downarrow^+ - h_\uparrow^- - h_\downarrow^-)/4, \\ h_7 &= (h_\uparrow^+ - h_\downarrow^+ - h_\uparrow^- + h_\downarrow^-)/4. \end{aligned} \quad (2.77)$$

In this case, we have taken the spin-quantization axis to be the z -axis, so the remaining coefficients $h_1 = h_2 = h_5 = h_6 = 0$. The generalization to an arbitrary spin axis is found by applying an appropriate 3D rotation matrix to the vectors (h_1, h_2, h_3) and (h_5, h_6, h_7) . The model above allows the spin-up and spin-down bands to have different chemical potentials V_σ and temperatures T_σ ; these are parametrized by a *voltage* $V := (V_\uparrow + V_\downarrow)/2$, *temperature* $T := (T_\uparrow + T_\downarrow)/2$, *spin-voltage* $V_s := (V_\uparrow - V_\downarrow)/2$, and *spin-temperature* $T_s := (T_\uparrow - T_\downarrow)/2$ [XIII, 99, 140].

The first two parameters are well-known. An increasing temperature T means that the total excitation energy available increases, resulting in larger populations of both electrons and holes. An increasing voltage V shifts the chemical potentials of electrons and holes oppositely, resulting in an electron surplus and hole deficiency.

11. Here, $\|\Lambda\| := \sqrt{\text{Tr}(\Lambda^\dagger \Lambda)}/n$ is the normalized Frobenius norm of a matrix $\Lambda \in \mathbb{C}^{n \times n}$. This is a natural choice when using Pauli matrices as unit vectors since $\|\hat{\tau}_n \hat{\sigma}_m\| = 1$.

The other two parameters can be realized in several ways. For instance, in a half-metallic ferromagnet, the spin-splitting is so strong that e.g. the spin-up band is conducting while the spin-down band is insulating. If such a material is connected to a normal metal, spin-up quasiparticles diffuse across the interface, while the spin-down quasiparticles are trapped inside the normal metal. Thus, by controlling the voltage and temperature of the ferromagnet, one can influence the voltage and temperature of only one spin band in the normal metal, which translates to a spin-voltage and spin-temperature [141]. The same principle applies to other polarized ferromagnets [142, 143].

Another possibility is to use microwaves to excite a nonequilibrium spin population via the ferromagnetic resonance (FMR), a technique called *spin-pumping*. This technique was recently employed to investigate spin supercurrents [75], causing a renewed interest in spin injection into superconductors [xv, 76]. In the limit of weak superconductivity, an expression for the distribution function of a spin-pumped ferromagnet was derived in reference 51. When the precession frequency Ω and cone angle α are sufficiently small, the result is just a spin-voltage $eV_s = \Omega/2$ along the magnetization of the ferromagnet.¹² This is e.g. the relevant limit for the experiment in reference 75: the superconducting correlations inside $\text{Ni}_{80}\text{Fe}_{20}$ should be weak, and the precession frequency $\Omega \approx 0.5$ meV and cone angle $\alpha \approx 1^\circ$ are small.

Finally, we note that one should be careful about including superconductors with finite voltages in a model. This includes both voltages that are explicitly applied to superconductors, and charge accumulations that might arise via thermoelectric or spin-galvanic effects. This is because a finite voltage causes an AC Josephson response [4, 43], which in a bulk superconductor leads to a time-dependent order parameter $\Delta(t) = \Delta(0)e^{i\omega t}$, where the frequency $\omega = 2eV$. However, we only consider the time-independent Usadel equation here, which does not capture these oscillations. When we do consider voltage-biased superconductors, we therefore make sure to connect the superconductors to reservoirs at voltages $\pm V/2$ via tunneling contacts. Since an antisymmetric voltage configuration results in zero voltage near the center of the superconductor, and a high interface resistance minimizes the charge accumulation at the edges of the superconductor, any AC effects should be small compared to the DC effects in this limit.

12. By *small*, we mean that Ω should be much smaller than the exchange field m , and α should be small enough for the approximations $\sin \alpha \approx \alpha$ and $\cos \alpha \approx 1$.

Numerical algorithms

In chapter 2, we summarized how to model dirty superconducting structures. We now explain in more detail how these models can be handled numerically. First, we discuss some implementation details, and how to calculate the steady-state properties of 1D junctions. We then consider some higher-level techniques: skipping self-consistency iterations via convergence acceleration algorithms, critical temperature calculations via binary search algorithms, and mapping out phase diagrams via flow analysis of the order parameter. We conclude the chapter by briefly describing the numerical code itself, which is available for free under an MIT open-source licence from github.com/jabirali/geneus.

3.1 Discretization strategy

Most projects presented herein only require 1D numerical calculations.¹ Different classes of physical systems can be treated in this manner. One possibility is a *true* 1D system, where the structure is composed of nanowires. This was the case for paper vi. Another possibility is an *effective* 1D system, such as a thin-film material stack that is translation-invariant in the film plane. In that case, the physical observables only depend on the position along the direction perpendicular to the film plane, and can be described using 1D equations of motion. Most papers in this thesis belong to that category. Finally, in some cases, we consider 2D or 3D geometries where the behavior along some directions can be treated via analytical approximations. The distribution function was treated in this manner in papers xiii–xv. More complex geometries can also be realized within a 1D model using periodic boundary conditions or multiterminal boundary conditions [vi, 53].

As described in section 2.7, a complete description of each material is provided by their Riccati parameter $\gamma \in \mathbb{C}^{2 \times 2}$ and vector of distribution traces $h \in \mathbb{R}^8$. Numerically, these are described in terms of two 16-element *state vectors* $u := \text{vec}(\gamma, \tilde{\gamma}, \partial_x \gamma, \partial_x \tilde{\gamma})$ and $v := \text{vec}(h, \partial_x h)$,² where $\partial_x := \partial/\partial x$ refers to the derivative along the junction direction x .

-
1. The exceptions are papers xi and xii, where M. Amundsen performed 2D and 3D numerical calculations using a FEM approach described in reference 144.
 2. In linear algebra, *vec* refers to *vectorization* or *flattening*. For instance, $\text{vec}(\gamma, \tilde{\gamma}) := (Y_{\uparrow\uparrow}, Y_{\uparrow\downarrow}, Y_{\downarrow\uparrow}, Y_{\downarrow\downarrow}, \tilde{Y}_{\uparrow\uparrow}, \tilde{Y}_{\uparrow\downarrow}, \tilde{Y}_{\downarrow\uparrow}, \tilde{Y}_{\downarrow\downarrow})$ maps two matrices in $\mathbb{C}^{2 \times 2}$ to a vector in \mathbb{C}^8 .

The reason we include $\tilde{\gamma}$ in the state vector u is that equation (2.60) couples the equations for γ and $\tilde{\gamma}$ via $2(\partial_x \gamma) \tilde{N} \tilde{\gamma} (\partial_x \gamma)$, which makes it prudent to solve the equations for γ and $\tilde{\gamma}$ simultaneously. Including first-order derivatives in the state vectors is a standard technique for reducing the order of a differential equation [145]. For instance, equations (2.60) and (2.64) are reduced from $\partial_x^2 \gamma = \Gamma(\gamma, \tilde{\gamma}, \partial_x \gamma, \partial_x \tilde{\gamma}, x, \varepsilon)$ and $\partial_x^2 h = H(h, \partial_x h, x, \varepsilon)$ to the forms $\partial_x u = \Gamma(u, x, \varepsilon)$ and $\partial_x v = H(v, x, \varepsilon)$. These are both *explicit first-order ordinary differential equations*; a number of numerical solvers exist for this class of equations, and we employed the Fortran open-source library `BVP_SOLVER` [146–148].³ The results $u = u(x, \varepsilon)$ and $v = v(x, \varepsilon)$ are functions of position x and energy ε , where the latter only enters as a parameter in the equations.

Before discussing the equations for u and v in more detail, we briefly review how the differential-equation solver itself works. The algorithm presented here is conceptually consistent with the one used by `BVP_SOLVER`; we have however simplified it a bit, resulting in a less efficient version that is easier to understand. For a rigorous discussion of the actual algorithm behind `BVP_SOLVER`, see reference 148. Both equations above have been phrased as $\partial_x \psi = f(\psi, x)$, where ψ is a state vector and f a function that defines the differential equation. Integrating this differential equation between any two points $x = a$ and $x = b$, we find that $\varphi[\psi(x), a, b] = 0$, where the residual functional

$$\varphi[\psi(x), a, b] := \psi(b) - \psi(a) - \int_a^b dx f(\psi(x), x). \quad (3.1)$$

We now discretize the problem by introducing a mesh $X := (x_1, \dots, x_N)$ and the corresponding solution values $\Psi := (\psi_1, \dots, \psi_N)$. Furthermore, let us use the Euler approximation $(b - a)f(\psi(a), a)$ for the integral above. The discretized residuals $\varphi_n := \varphi[\psi(x), x_n, x_{n+1}]$ are then:

$$\varphi_n \approx \psi_{n+1} - \psi_n - (x_{n+1} - x_n) f(\psi_n, x_n). \quad (3.2)$$

Collecting these residuals into a vector $\Phi := (\varphi_1, \dots, \varphi_{N-1})$, the discretized differential equation reduces to a simple root-finding problem:

$$\Phi(\Psi) = 0. \quad (3.3)$$

3. The `MATLAB` solver `bvp4c` has a similar interface to `BVP_SOLVER`, and was developed by one of the same authors. The Python library `sci_kits.bvp_solver` is directly based on `BVP_SOLVER` itself. All these libraries have in common that they do not require an explicit expression for the Jacobian of the differential equation, thus significantly simplifying the numerical implementation.

It is also straight-forward to account for general nonlinear boundary conditions $g_a(\psi) = 0$ and $g_b(\psi) = 0$ within this formalism. We can simply include $\varphi_0 := g_a(\psi_1)$ and $\varphi_N := g_b(\psi_N)$ in the residual vector Φ , and the solution to $\Phi(\Psi) = 0$ will satisfy these boundary conditions. In practice, `BVP_SOLVER` uses a Runge–Kutta approximation for the integral in equation (3.1), but the procedure is otherwise the same [148].

The simplest way to approach a root-finding problem is Newton’s method [145]. In this case, we wish to determine the solution Ψ that minimizes the residual Φ . This is achieved via the iteration formula

$$\Psi \leftarrow \Psi - \left(\frac{\partial \Phi}{\partial \Psi} \right)^{-1} \Phi, \quad (3.4)$$

where the quantity in parentheses is known as the Jacobian matrix.⁴ In our implementation, this Jacobian was calculated analytically for the kinetic equation, while `BVP_SOLVER` estimated it numerically via finite-difference approximations for the Riccati-parametrized equations. This iteration process is then continued until the net residual $\|\Phi\|$ drops below some tolerance, which we in our simulations set to 10^{-10} .⁵

This brief review provides some insight into the problems that can arise numerically. Newton’s method relies on iteratively improving an initial guess for Ψ to find a nearby root. Even for simple algebraic problems, it is well-known that a good initial guess is crucial for proper convergence. One reason is that some functions have multiple roots. For instance, even the trivial $f(x) = x^2 - 4$ has two roots $x = \pm 2$, and Newton’s method converges to the root closest to its initial guess. In a physical problem, some of these roots may correspond to unphysical solutions, such as a distribution function or Riccati parameter with an anomalous norm.⁶ In other cases, the system may exhibit *multistability*,

-
4. When discussing algorithms, we use the symbol \leftarrow to denote *assignment*.
 5. In our work, we wished to determine physical observables to a precision of about 10^{-8} . These observables are usually found by summing up contributions from the Riccati parameters $\gamma(\varepsilon_n)$ calculated at 1000 energies ε_n . Assuming for simplicity that the errors in each $\gamma(\varepsilon_n)$ are uncorrelated and equally important, such a summation can be expected to amplify the numerical error from 10^{-10} to about $\sqrt{1000} \times 10^{-10} \approx 0.3 \times 10^{-8}$. This square-root formula follows from the fact that accumulation of random errors can be viewed as a 1D random walk.
 6. The norm of a distribution function is constrained by its interpretation as an occupation number. One way to justify that we need $\|\gamma\| < 1$ is the following. The density of states can be written $N(\varepsilon) = (N_F/2) \text{Re Tr}[(1 - \gamma\tilde{\gamma})^{-1}(1 + \gamma\tilde{\gamma})]$. If we for simplicity evaluate this at $\varepsilon = 0$, it is easy to check that $N(0) < 0$ for $\|\gamma\| > 1$; and a negative density of states clearly has to correspond to an unphysical solution.

which means that these solutions describe different physical states. This phenomenon is discussed in e.g. paper XIII and references 149–151. Another problem is that if the initial guess is too far away from any root, the calculation can diverge. For instance, the function $f(x) = x/(x - 1)$ has a root at $x = 0$, but Newton’s method still diverges if the initial guess $|x| \geq 1$. This is a common problem with the Usadel equation too: if the initial guess is unreasonable, the Newton iterations diverge. To summarize, the same problems that affect Newton iterations in 1D algebraic problems are relevant for the numerical solution of nonlinear differential equations. The remedy is also the same: we require an initial guess that is sufficiently close to the correct solution.

From here on, we refer to γ and h instead of explicitly bringing up their state-vector representations u and v . When we first initialize the system, we typically set the Riccati parameters in each material to the bulk solutions γ_s and γ_N presented in section 2.8. These are used to evaluate any boundary conditions. However, when we begin to solve the differential equations, we instead use $\gamma(\varepsilon_{\max}) \leftarrow 0$ and $\gamma(\varepsilon_n) \leftarrow \gamma(\varepsilon_{n+1})$ as guesses, where $(\varepsilon_1, \dots, \varepsilon_{\max})$ are the discretized energies. The fact that $\gamma \rightarrow 0$ as $\varepsilon \rightarrow \infty$ can be shown from the Usadel equation. The second equation is based on the observation that γ is usually continuous, so solutions at nearby energies should be similar. This eliminates some convergence issues during the first few self-consistency iterations compared to using a bulk solution as a guess. After a few iterations, a much better guess is however given by $\gamma_k(\varepsilon_n) \leftarrow \gamma_{k-1}(\varepsilon_n)$, where k is the self-consistency iteration. This is because as the system converges, the previous result for γ should be increasingly accurate, thus requiring fewer Newton iterations. We therefore went for a hybrid approach: we used the first strategy for the first few iterations to prevent convergence problems, and switched to the second one when $\|\gamma_k - \gamma_{k-1}\| < 0.05$ to speed up the numerics.

In practice, we usually calculate γ and h at 100 uniformly spaced positions in each material, which we will refer to as *control points*. However, the differential-equation solver often has to generate much denser meshes than this internally for the Newton iterations to converge. This causes a problem: if we only know e.g. the superconducting order parameter $\Delta(x)$ at the control points, but the numerical solver requires its values at arbitrary points, we need an efficient interpolant. A similar

situation arises for the kinetic equations for h : it is straight-forward to derive an explicit Jacobian for equation (2.64), which can significantly speed up the numerics. However, the Jacobian is a function of γ , which we only know at the control points, while the differential-equation solver has to be able to evaluate it at any point. We found Catmull–Rom splines to work very well as an interpolant for this purpose [152].

As an optimization trick, we note that it is also possible to chain multiple interpolation algorithms. For instance, we found that the most efficient alternative for the order parameter Δ was to interpolate cubically from the coarse-grained 100-point mesh to a fine-grained 400,000-point mesh before solving any differential equations, and then let the numerical solver interpolate linearly within the fine mesh. The optimal mesh size was simply determined empirically: a too large mesh is obviously a waste of space, but a too small mesh causes convergence problems in systems with e.g. large phase gradients. The reason such chaining of interpolation algorithms can be beneficial, is that linear interpolation on a uniform mesh can be implemented in a very efficient manner.⁷ Moreover, since the interpolant is typically evaluated every time a new solution for γ is evaluated, at each internal mesh point, even small optimizations here can lead to large net speed-ups.

As for the energy ε , this only appears in the equations for γ and h via the energy matrix $\check{\Sigma}$ (see section 2.4). When performing self-consistent calculations, the energy resolution required is constrained by having to get reliable results for the order parameter Δ . When performing nonequilibrium calculations, the energy resolution directly affects e.g. the system’s sensitivity to an applied voltage at low temperatures. However, in some cases—such as when calculating the density of states non-self-consistently—one can choose a lower range and density of energies without loss of accuracy. In practice, we typically solve each differential equation for 800 uniformly spaced energies in $(0, 4\Delta_0)$, and another 200 energies in the range $(4\Delta_0, 30\Delta_0)$. Finally, when calculating physical observables by integrating γ and h over energies, we note that the simple trapezoid method is far from optimal; we found e.g. interpolation and integration via **PCHIP** to be far more accurate.

7. In particular: the nearest mesh point x_n below an arbitrary point x is given by the index $n = \lfloor (N - 1)(x/L) + 1 \rfloor$, where L is the total length and N the number of mesh points. Once the nearest neighbor is known, the linear interpolation can be summarized as $\Delta(x) \approx \Delta(x_{n-1}) + [\Delta(x_n) - \Delta(x_{n-1})] [(N - 1)(x/L) - (n - 2)]$.

3.2 Steady-state calculations

In the previous section, we summarized how one can parametrize, discretize, and numerically solve the equations introduced in chapter 2. We will now discuss the larger picture: which equations should we solve, and in what order? For simplicity, we begin by considering a simple superconductor/ferromagnet (s/F) bilayer, and then discuss the generalization to arbitrary 1D models afterwards. We will also assume that we are interested in the steady-state properties, such as the density of states, charge current, or spin current. More specialized algorithms for calculating other properties are deferred to later sections.

Describing an s/F bilayer requires that we determine the Riccati parameters γ_S and γ_F in each layer, the distribution functions h_S and h_F in each layer, and the order parameter Δ in the superconductor.⁸ To determine these quantities, we have to solve the equations in table 3.1. However, these equations are interdependent. For instance, the distribution functions are found by solving equations (2.64) and (2.65); but all coefficient matrices in those equations are expressed in terms of the propagators \hat{g}^R and \hat{g}^A , which are in turn functions of the Riccati parameters. Similarly, the order parameter Δ is a function of both the Riccati parameters and distribution function via \hat{g}^K , and the parameters inside the two materials are coupled via the boundary conditions.

Table 3.1: Equations required to describe simple s/F bilayers.

Name	Symbol	Equations
Riccati parameter	γ	2.60–2.61
Distribution function	h	2.64–2.72
Energy matrix	$\check{\Sigma}$	2.18–2.20
Boundary condition	\check{I}	2.28
Superconducting order parameter	Δ	2.38
Magnetic order parameter	\mathbf{m}	N/A

8. In general, one would also have to determine the magnetic order parameter \mathbf{m} self-consistently. For instance, a spin current between two ferromagnets describes an effective exchange interaction mediated by conduction electrons [153]. Thus, electronically controlling these spin currents can change the ground-state magnetic configuration of a junction [xiv]. Another example is that some materials may exhibit proximity-induced magnetic properties [76]. Throughout this thesis, we will however assume any magnetic order parameters to be fixed.

We can visualize these interdependencies via a data dependency graph as shown in figure 3.1. This shows that there are two obvious calculation orders that optimize the information flow per iteration:

$$\gamma_F \rightarrow h_F \rightarrow \gamma_S \rightarrow h_S \rightarrow \Delta; \quad (3.5)$$

$$\gamma_F \rightarrow \gamma_S \rightarrow h_F \rightarrow h_S \rightarrow \Delta. \quad (3.6)$$

In other words, one should always calculate the γ 's before the h 's and save the order parameter for last—but whether this is done in one material at a time or not is not that important. All these calculations should then be repeated until convergence. In practice, we define *convergence* as each γ and h satisfying $\|\delta\gamma\| < 10^{-8}$ and $\|\delta h\| < 10^{-8}$, where δ denotes the change between successive iterations.⁹

The problem can be simplified via approximations. Except for paper XIII, we have consistently assumed that the distribution functions h_S and h_F are known. This simplifies the calculation loop above to $\gamma_F \rightarrow \gamma_S \rightarrow \Delta$. Usually, this entails an assumption of equilibrium conditions; but in papers XIV–XV, we used similar approximations out of equilibrium as well. It is also common to approximate the superconductor as a reservoir; in that case, both Δ and γ_S are fixed, and the problem is reduced to determining γ_F . This can be done for 1000 energies in 30 seconds using our numerical implementation.

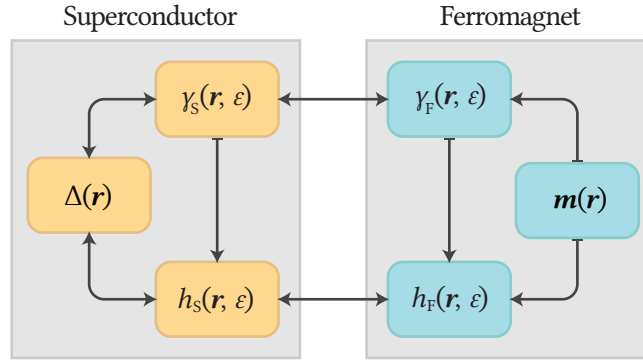


Figure 3.1: Data dependency graph for an s/F bilayer. This graph was composed from the equations listed in table 3.1.

9. The parameters γ and h are functions of position and energy; in practice, these inequalities should be interpreted as holding at every position and energy.

This scheme is easily generalized to an arbitrary number of materials: for each material, one calculates the Riccati parameters via the Usadel equation, then the distribution function via the kinetic equation, then any order parameters. This is then repeated inside one material at a time until all parameters have converged to a satisfactory degree. The optimal order for iterating over these materials follow from a similar logic as above. For instance, consider an $S_1/F_1/N/F_2/S_2$ structure, where the outer superconductors are reservoirs. The Riccati parameter γ_N in the normal metal depends on two unknowns via the boundary conditions, namely the values of γ_{F_1} and γ_{F_2} in the two ferromagnets. On the other hand, γ_{F_1} and γ_{F_2} both depend on only one unknown parameter γ_N , since the Riccati parameters γ_{S_1} and γ_{S_2} are fixed. Thus, it makes sense to iterate over the materials in the order $F_1 \rightarrow F_2 \rightarrow N$. Since the optimal iteration order tends to differ from system to system, we numerically implemented it as a general foreach-function, which allows the exact iteration order to be specified at runtime.

We note that in some cases, the equations might not converge well if one immediately attempts to solve them all at once. In that case, it makes sense to first solve the equations for the Riccati parameters, while keeping the distribution function and order parameter fixed to their initial guesses. After this non-self-consistent equilibrium calculation has converged to some degree, the complete set of equations typically converges in a more stable manner. Including such a bootstrap procedure, we summarize the solution strategy in algorithm 3.1.

Algorithm 3.1: Steady-state calculation procedure.

```

for each material  $m$ :
  Initialize  $\gamma_m, h_m, \Delta_m$  to bulk values

do until all  $\|\delta\gamma_m\| < 10^{-2}$ :
  for each material  $m$ :
     $\gamma_m \leftarrow \text{UsadelEquation}(\Delta_m, \gamma_{m-1}, \gamma_{m+1})$ 

do until all  $\|\delta\gamma_m\| < 10^{-8}$  and  $\|\delta h_m\| < 10^{-8}$ :
  for each material  $m$ :
     $\gamma_m \leftarrow \text{UsadelEquation}(\Delta_m, \gamma_{m-1}, \gamma_{m+1})$ 
     $h_m \leftarrow \text{KineticEquation}(\Delta_m, \gamma_m, h_{m-1}, h_{m+1})$ 
     $\Delta_m \leftarrow \text{SelfconsistencyEquation}(\gamma_m, h_m)$ 

```

As mentioned earlier, numerical solvers rely on initial guesses when solving differential equations—and the calculations converge faster the better these guesses are. This effect is amplified in self-consistent calculations, since the order parameter Δ exhibits a kind of numerical inertia, requiring a large number of self-consistency iterations to change significantly. One guiding principle to speed up the numerics is therefore to consider the symmetries of the physical system, and make sure that the initial guess satisfies those symmetries when applicable.

For instance, consider a simple $s/I/s/I/s$ structure, where the insulators are treated as tunneling interfaces between the superconductors. We treat the outer superconductors as reservoirs with order parameters $\Delta = \Delta_0 e^{i\chi}$, where the phase $\chi_L = 0$ for the left reservoir and $\chi_R = \pi/2$ for the right one. In equilibrium, there are then only two unknown parameters that have to be determined: the Riccati parameter γ and order parameter Δ of the central superconductor. In figure 3.2, we show the striking difference between choosing an initial guess with the phase $\chi = \chi_L = 0$ (asymmetric) and $\chi = (\chi_L + \chi_R)/2 = \pi/4$ (symmetric) for the central superconductor. The curves can be described as having error half-lives of 2.2 and 8.6 iterations, respectively, resulting in a factor 4 difference in computation time. With our numerical implementation, this is the difference between a 25 min and 90 min calculation. It is worth noting that using a normal-state solution $\Delta = 0$ as an initial guess is far more efficient than an initial guess with the wrong phase.

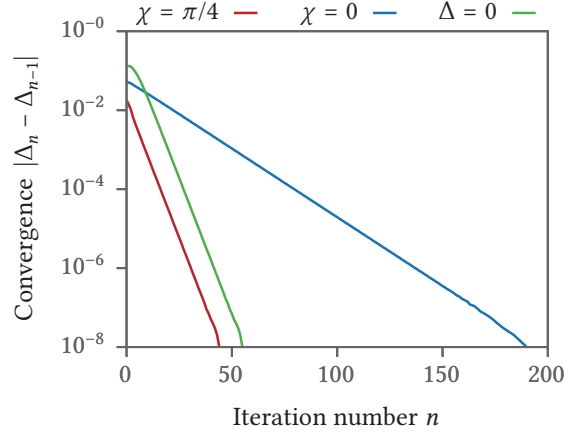


Figure 3.2: Convergence rates for a phase-biased $s/I/s/I/s$ junction. The curves correspond to different initial order parameters $|\Delta|e^{i\chi}$.

3.3 Convergence acceleration

It is not unusual for self-consistent calculations to be painstakingly slow. For instance, in an s/F bilayer, it typically takes only 30 sec to solve the equations if the superconductor is approximated as a reservoir. If we solve the equations inside the superconductor self-consistently, on the other hand, the time requirement increases to about 90 min. In complex multilayer junctions, or in junctions with high-transparency interfaces, the time requirements can be even worse.

One way to address this problem is *Steffensen's method* [154, 155].¹⁰ The starting point for our discussion is that a self-consistency iteration can be viewed as a kind of fixpoint iteration. More precisely, we are trying to solve an equation of the kind $\Delta = f(\Delta)$, where the function f abstracts away the solution of the Usadel equation and kinetic equation throughout the system. We see that algorithm 3.1 then corresponds to the naïve implementation of this fixpoint iteration scheme,

$$\Delta_{n+1} = f(\Delta_n), \quad (3.7)$$

where the subscript n refers to the iteration number. A more efficient approach would be to reformulate $\Delta = f(\Delta)$ as a root-finding problem,

$$\varphi(\Delta) := f(\Delta) - \Delta = 0, \quad (3.8)$$

and attack it via a root-finding algorithm such as Newton's method,

$$\Delta_{n+1} = \Delta_n - \frac{\varphi(\Delta_n)}{\varphi'(\Delta_n)}. \quad (3.9)$$

We can estimate the derivative above via a difference approximation $\varphi'(\Delta_n) \approx [\varphi(\Delta_{n+1}) - \varphi(\Delta_n)]/[\Delta_{n+1} - \Delta_n]$. Furthermore, substitution of equation (3.7) into (3.8) shows that we can set $\varphi(\Delta_n) = \Delta_{n+1} - \Delta_n$ if we used fixpoint iteration before we invoked Newton's method. This leads us to Steffensen's convergence acceleration equation:

$$\Delta_{n+3} = \Delta_n - \frac{(\Delta_{n+1} - \Delta_n)^2}{\Delta_{n+2} - 2\Delta_{n+1} + \Delta_n}. \quad (3.10)$$

10. I wish to thank M. Amundsen for pointing out that self-consistency iteration can be viewed as a fixpoint problem where Steffensen's method is applicable.

Equation (3.10) was derived under the assumption that $\Delta_n, \Delta_{n+1}, \Delta_{n+2}$ were calculated via fixpoint iteration. In practice, this means that we have to solve equation (3.7) at least three consecutive times between each time we can invoke equation (3.10). Empirically, we found that we in general had to perform 8 regular fixpoint iterations in-between each convergence boost to avoid numerical stability problems. We also note that to reap the full benefits of the convergence acceleration algorithm, one should solve the equations for γ and h in the superconductor immediately after each convergence boost, so that the updated order parameter Δ is reflected in the boundary conditions when we subsequently solve the equations for γ and h in neighboring materials. Finally, the order parameter $\Delta = \Delta(\mathbf{r})$ is in general a function of position; Steffensen's method should simply be applied individually at each position \mathbf{r} . An updated version of algorithm 3.1 that includes this convergence acceleration method is presented in algorithm 3.2 below.

Algorithm 3.2: Revised steady-state calculation procedure with convergence acceleration. For brevity, we use Δ'_m and Δ''_m for the values of Δ_m calculated one and two iterations earlier, respectively.

```

for each material  $m$ :
  Initialize  $\gamma_m, h_m, \Delta_m$  to bulk values
do until all  $\|\delta\gamma_m\| < 10^{-2}$ :
  for each material  $m$ :
     $\gamma_m \leftarrow \text{UsadelEquation}(\Delta_m, \gamma_{m-1}, \gamma_{m+1})$ 
do until all  $\|\delta\gamma_m\| < 10^{-8}$  and  $\|\delta h_m\| < 10^{-8}$ :
  for each material  $m$ :
     $\gamma_m \leftarrow \text{UsadelEquation}(\Delta_m, \gamma_{m-1}, \gamma_{m+1})$ 
     $h_m \leftarrow \text{KineticEquation}(\Delta_m, \gamma_m, h_{m-1}, h_{m+1})$ 
     $\Delta''_m \leftarrow \Delta'_m$ 
     $\Delta'_m \leftarrow \Delta_m$ 
     $\Delta_m \leftarrow \text{SelfconsistencyEquation}(\gamma_m, h_m)$ 
  every 8th iteration:
     $\Delta_m \leftarrow \Delta''_m - (\Delta'_m - \Delta''_m)^2 / (\Delta_m - 2\Delta'_m + \Delta''_m)$ 
     $\gamma_m \leftarrow \text{UsadelEquation}(\Delta_m, \gamma_{m-1}, \gamma_{m+1})$ 
     $h_m \leftarrow \text{KineticEquation}(\Delta_m, \gamma_m, h_{m-1}, h_{m+1})$ 

```


We show benchmarks for two different systems in figures 3.3 and 3.4. In figure 3.3, Steffensen’s method reduces the calculation from 90 iterations to 30 iterations, corresponding to a reduction in computation time from 100 min to 40 min. In figure 3.4, there is a striking reduction is from 235 to 42 iterations, reducing the computation time from almost 12 hours to 2 hours 40 min. These examples are representative of the typical speed-ups we achieved for simple and complex junctions, respectively. There are however some edge cases with much more ridiculous speed-ups. For instance, a bulk superconductor exactly at its critical temperature converges extremely slowly if we use $\Delta = \Delta_0$ as our initial guess. Without convergence acceleration, this requires almost 5000 iterations to converge to $|\Delta| < 10^{-8}$. Steffensen’s method reaches the same precision in 56 iterations with algorithm 3.2, and in 21 iterations if the boost frequency is increased to every 3rd iteration.

Figures 3.3 and 3.4 also illustrate how the convergence acceleration works: every time Steffensen’s method is invoked, there is one iteration with a larger change than usual, which reduces the numerical error by 1–2 orders of magnitude.¹¹ In-between these boosts, we perform regular fixpoint iterations, so the system usually converges at the same rate as without Steffensen’s method. We note that some numerical solvers like `BVP_SOLVER` allow the solution algorithm to be specified at run-time. In general, we found a 4th-order Runge–Kutta method to be up to twice as fast as a 6th-order method, but right after a convergence boost, the 6th-order method is both faster and more likely to converge.

Steffensen’s method for convergence acceleration is excellent when only the magnitude of the order parameter changes between iterations. However, in systems with phase-biased or voltage-biased superconducting elements, the phase winding of the order parameter changes as well. In this case, Steffensen’s method typically diverges, and we have to revert to slow fixpoint iterations. For future reference, a possible solution to this problem could be to implement a more general *quasi-Newton acceleration method* [156], which could explicitly account for the position-dependence of the order parameter during boosts.

11. Given the success we had with Steffensen’s method, we also tried to implement a number of higher-order algorithms [155]. However, on average, we found that these performed worse than Steffensen’s method, as they required more fixpoint iterations between each boost for the numerical procedure to remain stable.

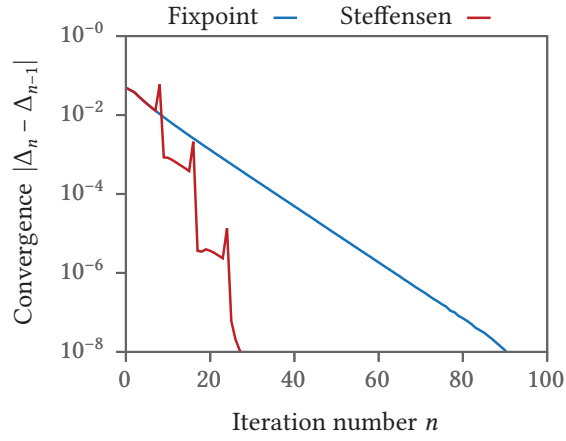


Figure 3.3: Comparison of iteration methods for an s/f bilayer with Rashba and Dresselhaus spin-orbit coupling (inspired by paper 11).

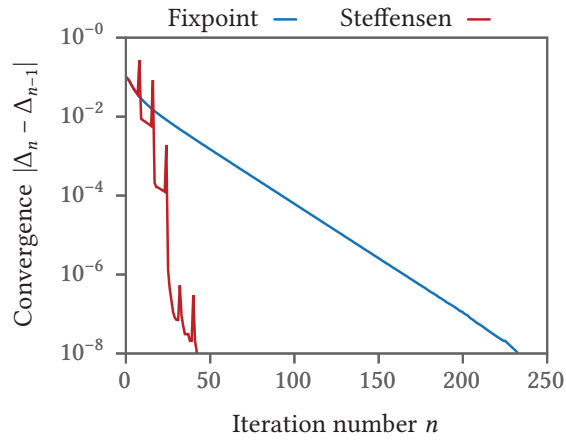


Figure 3.4: Comparison of iteration methods for a complex multi-layer junction (parameters taken from paper 1X). The junction has the structure $s/f'/s'/f'/f/s$, where the s layers are reservoirs, the f layers have a conical magnetic texture, the f' layers have high exchange fields and spin-filtering boundary conditions, and the s' layer has spin-flip and spin-orbit scattering. The order parameter is determined self-consistently in the central superconductor.

3.4 Homotopy continuation

As emphasized in previous sections, good initial guesses are essential for proper numerical convergence. Usually, a good strategy is to start with the corresponding bulk solutions in equilibrium. However, one example where this strategy failed is a superconductor connected to a very strongly polarized ferromagnetic insulator, which was considered in paper VIII. More precisely, we implemented boundary conditions to *all* orders in the spin-mixing angles φ_n at the interface [VIII, 115],

$$\begin{aligned} \hat{I} \sim \sum_n & \left[1 - \frac{i}{4} \sin(\varphi_n) \hat{a} + \frac{1}{2} \sin^2(\varphi_n/2) \hat{a} \hat{m} \right]^{-1} \\ & \times \left[-i \sin(\varphi_n) \hat{g} \hat{a} + \sin^2(\varphi_n/2) [\hat{m}, \hat{a}] \right] \\ & \times \left[1 - \frac{i}{4} \sin(\varphi_n) \hat{a} + \frac{1}{2} \sin^2(\varphi_n/2) \hat{m} \hat{a} \right]^{-1}, \end{aligned} \quad (3.11)$$

where $\hat{g} = \hat{g}^R$ depends on γ , $\hat{a} := \hat{g} \hat{m} \hat{g} - \hat{m}$, $\hat{m} := \mathbf{m} \cdot \hat{\sigma}$, and \mathbf{m} is the interface magnetization. Physically, the correct solution is quite different from a bulk superconductor, e.g. having a strong suppression of Δ at the interface [VIII]. This is also a highly nonlinear boundary condition due to the matrix inversion, making it a nontrivial task to solve. Long story short, the Newton iterations diverged for large φ_n .

The solution strategy we developed for this problem was to introduce a new boundary condition $\hat{I}' := \lambda \hat{I}$, where $\lambda = 0$ corresponds to a vacuum boundary condition, and $\lambda = 1$ restores the boundary condition we were interested in. For $\lambda = 0$, an exact solution to the problem is given by the BCS bulk solution γ_s discussed in the previous chapter, so it is legitimate to initialize the Riccati parameter $\gamma \leftarrow \gamma_s$. If we now gently increase λ between iterations, and self-consistently solve the equations for γ and Δ for each value of λ , we can gradually determine a family of physically reasonable solutions $\gamma(\lambda)$. Eventually, we reach the value $\lambda = 1$ that we were interested in, without the divergent behavior that appears if we try to solve the equations for $\lambda = 1$ right away. The above is a solution strategy which is easily generalized, and which can be useful for a variety of numerically challenging problems. We can e.g. slowly change the magnitude of any contribution in the energy matrix $\check{\Sigma}$, the voltage or phase bias across a junction, the value of a gauge field, or even the physical dimensions of a material. A suggestion for how to implement this procedure is given in algorithm 3.3.

This solution was inspired by adiabatic processes in physics [157]. In that case, the Schrödinger equation for the eigenstates can be written $H(\lambda) \Psi_n(\lambda) = E_n(\lambda) \Psi_n(\lambda)$, where λ is a parameter that changes slowly over time. If we start in a given eigenstate at $\lambda = 0$, for instance $\Psi_1(0)$, we end up in “the same” eigenstate after adiabatically deforming the Hamiltonian to $\lambda = 1$, in this case $\Psi_1(1)$. In the numerical case, the solution of the differential equation was phrased as a root-finding problem $\Phi(\Psi) = 0$ in equation (3.3). Nonlinear differential equations can have multiple solutions, so we can express this as $\Phi(\Psi_n) = 0$, where n is some index that enumerates these roots. We then generalize this to an equation $\Phi[\Psi_n(\lambda), \lambda] = 0$, where we know the solution $\Psi_n(0)$ that satisfies the equation for $\lambda = 0$. By “adiabatically” increasing λ between self-consistency iterations in the numerical simulations, we can track the same root from $\lambda = 0$ to $\lambda = 1$. This ensures that the differential-equation solver always has an initial guess that is close to a root, which increases the chance that its Newton iterations are successful. Since we know that the n 'th root was physically reasonable for $\lambda = 0$, this solution branch is also likely to be of interest for $\lambda = 1$. We arrived at this method based on an intuition from physics, but we note that the same method is known in optimization theory as a *homotopy continuation method*, based on an intuition from topology [145].

Algorithm 3.3: Homotopy continuation for divergent problems.

```

Initialize  $\gamma, h, \Delta$  to bulk values
 $\lambda \leftarrow 10^{-6}$ 
do until  $\|\delta\gamma\| < 10^{-8}$  and  $\|\delta h\| < 10^{-8}$ :
   $\gamma \leftarrow \text{UsadelEquation}(\Delta, \gamma, \lambda)$ 
   $h \leftarrow \text{KineticEquation}(\Delta, \gamma, h, \lambda)$ 
for  $\lambda \leftarrow 0.01, 0.02, \dots, 0.99$ :
  do until  $\|\delta\gamma\| < 10^{-4}$  and  $\|\delta h\| < 10^{-4}$ :
     $\gamma \leftarrow \text{UsadelEquation}(\Delta, \gamma, \lambda)$ 
     $h \leftarrow \text{KineticEquation}(\Delta, \gamma, h, \lambda)$ 
     $\Delta \leftarrow \text{SelfconsistencyEquation}(\gamma, h)$ 
 $\lambda \leftarrow 1$ 
do until  $\|\delta\gamma\| < 10^{-8}$  and  $\|\delta h\| < 10^{-8}$ :
   $\gamma \leftarrow \text{UsadelEquation}(\Delta, \gamma, \lambda)$ 
   $h \leftarrow \text{KineticEquation}(\Delta, \gamma, h, \lambda)$ 
   $\Delta \leftarrow \text{SelfconsistencyEquation}(\gamma, h)$ 

```

For simplicity, we do not explicitly iterate over materials in algorithm 3.3. Rather, when we write e.g. $\gamma \leftarrow \text{UsadelEquation}(\Delta, \gamma, \lambda)$, an iteration over materials in the same way as in algorithm 3.1 is implied. The central feature of algorithm 3.3 is the iteration over λ . Both the Usadel equation and kinetic equation can vary with λ ; this is usually the case if λ parametrizes the system's energy matrix or boundary condition. In this example, we have chosen a fixed step length $\delta\lambda = 0.01$; in practice, $\delta\lambda$ has to be empirically determined for each physical problem. A more sophisticated solution would be to use an adaptive stepping algorithm, which could adjust $\delta\lambda(\lambda)$ based on e.g. the number of self-consistency iterations required for the previous value of λ . The calculations at each λ can usually be performed with a more relaxed convergence criterion than the final calculations. This is because the goal is just to obtain a good enough result for each $\gamma(\lambda)$ to be able to solve the equations for $\gamma(\lambda + \delta\lambda)$. In this example, we use a convergence criterion of 10^{-4} for these intermediate values of λ , and increase the precision to 10^{-8} when we finally get to $\lambda = 1$. We note that the first iteration is not performed using $\lambda = 0.00$ or $\lambda = 0.01$; rather, we perform a precise calculation for $\lambda = 0.000001$. Basically, we found that the iteration where we move from $\lambda = 0$ to $\lambda > 0$ can be quite tough for the numerical solver; starting with an infinitesimal increment of λ ensures convergence of the first iteration, while the successive iterations can be performed using a much larger $\delta\lambda$.

3.5 Phase diagrams

In the previous sections, we have focused on how to calculate the steady-state properties of a superconducting structure. In general, this requires that one solve the Usadel equation, kinetic equation, and self-consistency equation repeatedly until convergence. However, not all observables of interest are of this kind. It can sometimes be equally interesting to map out *phase diagrams*, which visualize for what combination of system parameters a structure is superconducting and not. This was e.g. highly relevant for paper XIII, where we calculated phase diagrams as function of magnetic field, applied voltage, and temperature. Critical temperature calculations are a special case of phase diagrams, which were relevant for papers II–IV and paper VIII. For calculating such phase diagrams, we discovered that full convergence is rarely required, and a far more efficient algorithm exists.

To motivate our approach, let us first consider a bulk superconductor at some temperature T . The naïve way to determine whether it is superconducting would be to use a variant of algorithm 3.1 or 3.2. We initialize its state to $\Delta = \Delta_0$, and self-consistently solve all relevant equations to update Δ . If the order parameter decreases beneath some threshold $\Delta < 0.01\Delta_0$, we conclude that it is not superconducting. If the order parameter converges without this happening, we conclude that it is superconducting. To generate a phase diagram as function of temperature, we can repeat this calculation at different temperatures. By definition, the critical temperature $T = T_c$ is the lowest temperature for which $\Delta \rightarrow 0$. Using the algorithm above, it takes roughly 900 iterations to go from $\Delta = \Delta_0$ to $\Delta < 0.01\Delta_0$ at $T = T_c$ without convergence acceleration. With Steffensen’s method, the situation is drastically improved, and the process requires only 40 iterations. However, in both cases, most of these iterations are simply spent getting from $\Delta = \Delta_0$ to $\Delta = 0.01\Delta_0$. Whether the material is classified as being superconducting or not is then decided by a single iteration, which can either push Δ below $0.01\Delta_0$ or not. This is the key insight behind the more optimized algorithm: *if we simply use $\Delta = 0.01\Delta_0$ as the initial guess, we can determine in a single iteration whether the material is superconducting or not*. The order parameter Δ spontaneously increases in that iteration for $T < T_c$ and decreases for $T \geq T_c$ (see figure 3.5).

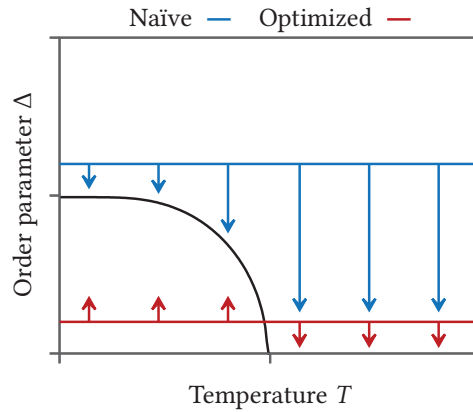


Figure 3.5: Comparison of the phase-diagram algorithms discussed above. The arrows illustrate how Δ changes during the procedures. The initial states $\Delta = \Delta_0$ (blue) and $\Delta = 0.01\Delta_0$ (red) are exaggerated.

To elucidate how a single iteration per temperature can be sufficient, we now discuss the calculations in some more detail. We can describe the self-consistency iteration scheme for a bulk superconductor as

$$\Delta_{n+1} = \Delta_n + \varphi(\Delta_n, T), \quad (3.12)$$

where n is the iteration number, and the *flow* φ of the order parameter between self-consistency iterations is defined as

$$\varphi(\Delta, T) := f(\Delta, T) - \Delta. \quad (3.13)$$

This notation was introduced in section 3.3. The function $f(\Delta, T)$ can in turn be written in closed form by combining the Usadel equation for a bulk superconductor, the self-consistency equation for the order parameter, and the equilibrium distribution function. If we take the order parameter to be real, the result can be written as:

$$f(\Delta, T) = \frac{1}{\log(2\omega_c/\Delta_0)} \int_0^{\omega_c} d\varepsilon \tanh(\varepsilon/2T) \operatorname{Re} \left(\frac{\Delta}{\sqrt{(\varepsilon + i\eta)^2 - \Delta^2}} \right).$$

Since we have assumed that we are working with a bulk superconductor here, all these quantities are position-independent. Numerically, we usually set $\eta = 0.01\Delta_0$ and $\omega_c = 30\Delta_0$, but that is not important here.

The flow $\varphi(\Delta, T)$ is a memoryless function that only depends on the *value* of Δ , and does not care whether that value was taken as an initial guess or reached via 900 fixpoint iterations. Thus, if $\varphi(0.01\Delta_0, T) > 0$, we know that Δ can never drop below $0.01\Delta_0$ via fixpoint iteration from any initial value $\Delta \geq 0.01\Delta_0$. It is therefore sufficient to calculate $\operatorname{sgn}[\varphi(0.01\Delta_0, T)]$ just once per temperature T , since this information can be used to short-circuit the naïve phase-diagram calculation.

It is important to use an infinitesimal initial guess $\Delta = 0.01\Delta_0$ instead of setting $\Delta = 0$. This is because $\Delta = 0$ technically *always* solves the equations. When $T > T_c$, the normal state corresponds to a *minimum* in the system's free energy, and is a *stable solution*. When $T < T_c$, the normal state corresponds to a *maximum* in the free energy, and is an *unstable solution*. By performing a small perturbation from $\Delta = 0$ to $\Delta = 0.01\Delta_0$, and checking whether the system converges back towards $\Delta = 0$, or diverges away from $\Delta = 0$, we can determine whether the normal-

state solution is stable or unstable.¹² Whether the system is converging towards or away from $\Delta = 0$ after a small perturbation is of course precisely what the sign of the flow function $\varphi(0.01\Delta_0, T)$ measures. This provides another interpretation of our algorithm: we are essentially checking whether $\Delta = 0$ describes a minimum or maximum in the free energy. Since the free energy is difficult to evaluate explicitly within the Usadel formalism, investigating the flow function φ is a useful alternative. The situation becomes a bit more complicated in *multistable systems*, which can exhibit a superconducting hysteresis effect with a multivalued order parameter. For a discussion of phase-diagram calculations in bistable systems, see appendix A of paper XIII.

With minor adjustments, the same algorithm can be used for arbitrary proximity structures as well. Firstly, we have to use more than 1 self-consistency iteration at each temperature, but e.g. 10 is still sufficient for most purposes. One reason is that in a proximitized superconductor, the change in the order parameter might be ambiguous during the first few iterations. For instance, in an s/F bilayer, the order parameter will likely decrease near the interface during the first iteration, even though it increases deeper inside the superconductor. It may take a couple of iterations to determine which of these effects win. Another reason is that we need to iterate over all materials in the junction a few times for information to flow back and forth. The last consideration can be alleviated via a high-precision bootstrap process, so that as much information as possible about the rest of the system reaches the superconductor before the first self-consistency iteration.

Algorithm 3.4 presents a solution procedure with these adjustments. We assume that there is only one superconductor in the system, so that it is unambiguous what we mean by the *superconducting* and *normal-state phase*, and refer to its order parameter as Δ . This Δ is of course a function of position; when used in comparison operations, we implicitly refer to its mean. We assume that the system has a known distribution function h , but the generalization to a general nonequilibrium situation is straight-forward. The algorithm is formulated in

12. We note that an analogous situation arises for a simple gravity pendulum. The equations of motion predict that the pendulum will be in equilibrium if it is either hanging straight down or straight up (i.e. it has two fixpoints). However, the latter is clearly an unstable solution, since an infinitesimal perturbation in any direction pushes the pendulum completely out of equilibrium.

terms of an abstract configuration Ω , which should include any system parameters that we wish to vary. For example, in paper XIII, we set the distribution function h to the form given in equation (2.76), and varied the temperature T and voltage V to create a phase diagram. Another example from the same paper is that we set the energy matrix to $\check{\Sigma} = \varepsilon\hat{\tau}_3 + \Delta\hat{\tau}_1 i\sigma_2 + m\sigma_3$ and varied the spin-splitting m . Both cases are incorporated into the parameter $\Omega = \{\check{\Sigma}, h\}$ referred to in the algorithm. In practice, the calculations for each Ω were performed in parallel.

Algorithm 3.4: Optimized procedure for mapping out superconducting phase diagrams. This algorithm is trivially parallelizable.

```

for each configuration  $\Omega$ :
  Initialize  $\Delta$  in the superconductor to  $0.01\Delta_0$ 
  Initialize  $\gamma$  in each material to bulk states
  do until  $\|\delta\gamma\| < 10^{-8}$ :
     $\gamma \leftarrow \text{UsadelEquation}(\Delta, \gamma, \Omega)$ 
  for  $m \leftarrow 1, \dots, 10$ :
     $\Delta \leftarrow \text{SelfconsistencyEquation}(\gamma, \Omega)$ 
     $\gamma \leftarrow \text{UsadelEquation}(\Delta, \gamma, \Omega)$ 
  if  $|\Delta| > 0.01\Delta_0$ :
     $\therefore \Omega$  corresponds to a superconducting phase
  else:
     $\therefore \Omega$  corresponds to a normal-state phase

```

3.6 Critical temperature

One common task in our research projects has been to determine the superconducting critical temperature of a junction. In general, we know that if a bulk superconductor in equilibrium has the critical temperature T_{cs} , any proximity system should have a critical temperature $T_{\text{c}} \in [0, T_{\text{cs}}]$. We will assume that there is no reentrant superconductivity, so that the critical temperature T_{c} is unambiguously defined: $|\Delta| > 0$ iff $T < T_{\text{c}}$. One straight-forward way to determine T_{c} to a precision of e.g. $0.01T_{\text{cs}}$ would then be to employ algorithm 3.4 for each of the 100 temperatures $T/T_{\text{cs}} \in \{0.00, 0.01, \dots, 0.99\}$. By checking at which temperatures the material was superconducting and not, we can infer which temperature corresponds to the critical temperature T_{c} .

However, there exists a much more efficient way to obtain the same result: a standard bisection algorithm. Since we know that $T_c \in [0, T_{cs}]$, we start by investigating the midpoint $T = T_c/2$. We initialize the system to a superconducting state with order parameter $\Delta = 0.01\Delta_0$, and perform a few self-consistency iterations to check whether $T < T_c$. If the order parameter increases, then $T < T_c$, so we conclude that $T_c \in [T_{cs}/2, T_{cs}]$. If the order parameter decreases, then $T > T_c$, which means that $T_c \in [0, T_{cs}/2]$. In either case, we have eliminated half the temperature range $[0, T_{cs}]$ via calculations at a single temperature. We then evaluate the midpoint of the revised search space, i.e. either $T = 3T_{cs}/4$ or $T = T_{cs}/4$, in order to eliminate half the remaining search space, etc. The resulting procedure is summarized in algorithm 3.5. This method determines T_c to an accuracy of $T_{cs}/2^{n+1}$ after n bisections. In practice, we usually perform 20 bisections, yielding an accuracy below 10^{-6} . For comparison, we would need calculations at over 1,000,000 temperatures to achieve the same accuracy via the naïve method.

Algorithm 3.5: Optimized critical temperature algorithm. This is based on the bisection method and the ideas behind algorithm 3.4.

```

Initialize  $\Delta$  in the superconductor to  $0.01\Delta_0$ 
Initialize  $\gamma$  in each material to bulk states
do until  $\|\delta\gamma\| < 10^{-8}$ :
     $\gamma \leftarrow \text{UsadelEquation}(\Delta, \gamma)$ 

 $T_1 \leftarrow 0$ ;
 $T_2 \leftarrow T_{cs}$ 
 $\gamma_0 \leftarrow \gamma$ 
for  $n \leftarrow 1, \dots, 20$ :
     $\gamma \leftarrow \gamma_0$ 
     $T \leftarrow (T_1 + T_2)/2$ 
    for  $m \leftarrow 1, \dots, 10$ :
         $\Delta \leftarrow \text{SelfconsistencyEquation}(\gamma, T)$ 
         $\gamma \leftarrow \text{UsadelEquation}(\Delta, \gamma)$ 
    if  $|\Delta| > 0.01\Delta_0$ :
         $T_1 \leftarrow T$ 
    else:
         $T_2 \leftarrow T$ 

 $\therefore T_c = (T_1 + T_2)/2$  to a precision below  $0.000001T_{cs}$ .

```

We have expressed algorithm 3.5 in terms of a temperature-dependent self-consistency equation. This should be interpreted as reinitializing the distribution functions at temperature T via equation (2.76), and then calculating the order parameter using these distribution functions. For the same reasons as in algorithm 3.4, we have include a high-precision bootstrap procedure before the actual bisections. Since we require a state with $\Delta = 0.01\Delta_0$ for the calculations at each temperature, we perform this bootstrap procedure once, save the resulting state to a variable γ_0 , and then restore this state every time we restart calculations at a new temperature. To calculate the critical temperature as a function of any other system parameter, we can of course just run this procedure in parallel for different configurations. The behavior of this critical temperature algorithm is illustrated in figure 3.6.

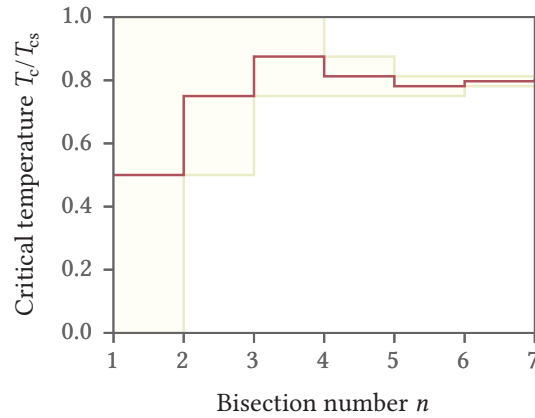


Figure 3.6: Illustration of how the critical temperature algorithm works, in this case for an example system with $T_c = 0.8T_{cs}$. The line shows the current temperature, while the shaded areas correspond to the range of possible values for the critical temperature.

3.7 Numerical code

A very large part of the doctoral work has been to develop a general numerical solver for the Usadel equation. The code was structured in a modular and object-oriented fashion, and was implemented in modern Fortran (2008+) for speed. The code itself is available on Github:

<https://github.com/jabirali/GENEUS>

It is released under an MIT open-source license, which essentially means that you are free to use it for any purpose as long as you give appropriate credit. For a description of how to compile and install the code, and a tutorial describing how to use it, see the documentation at:

<https://jabirali.github.io/GENEUS/>

The code can describe systems that contain superconductors, weak ferromagnets, strong ferromagnets, spin-orbit coupling, spin-flip and spin-orbit scattering, orbital depairing, strongly polarized magnetic interfaces, charge and spin accumulation, energy and spin-energy accumulation, and so on. It supports calculations that are both self-consistent and out of equilibrium. Basically, we have implemented all the equations, energy matrices, and boundary conditions discussed in the previous chapter, using all the algorithms presented in this chapter.

The material structure one wants to simulate is configured using simple INI-style configuration files. These are quite flexible, and can be combined with mathematical expressions and command-line arguments. For instance, let us say that we wish to perform a self-consistent equilibrium calculation for an s/F bilayer. We assume that the ferromagnet has a rotating exchange field, which we describe using an analytical function of position z . We also assume that the interface is strongly polarized. This is described by configuration 3.1. If this file is fed to the steady-state calculation program, it takes about 30 min to calculate the equilibrium state to a precision of 10^{-8} . The same file can alternatively be fed to the phase-diagram or critical-temperature calculation programs. All results are saved as tab-separated-value files (DAT files), which are easily visualized in e.g. Gnuplot. For more information about the simulation suite, see the [online documentation](#).

Configuration 3.1: Sample configuration file for an s/F bilayer.

```
[superconductor]
# Interior properties
length:      2.50
temperature: 0.10

# Right interface
conductance_b: 0.30
spinmixing_b: 1.25
polarization_b: 0.50
magnetization_b: [1,0,0]

[ferromagnet]
# Interior properties
length:      0.25
temperature: 0.10
magnetization: [cos(pi*z/2), sin(pi*z/2), 0]

# Left interface
conductance_a: 0.30
spinmixing_a: 1.25
polarization_a: 0.50
magnetization_a: [1,0,0]
```

Research highlights

In this chapter, we summarize some of the research results obtained in the enclosed papers. Clearly, reviewing every paper would be excessive, and going into full detail on each paper would be redundant. This is therefore no substitute for the papers themselves, but is rather meant as a brief introduction to some of the more interesting findings.

4.1 Current-induced vortices

It is well-known that applying a magnetic field to a thick type-II superconductor leads to the formation of *Abrikosov vortices* [3, 4, 158].¹ The field induces screening currents in the superconductor, which are associated with a phase gradient $\nabla\chi$ in the order parameter $\Delta = |\Delta|e^{i\chi}$. However, the order parameter is continuous and single-valued, which has some important ramifications. One is that the net phase winding around any point has to be quantized in units of 2π . In other words, we can define a *winding number* or *topological quantum number*

$$n := \frac{1}{2\pi} \oint_{\Omega} d\mathbf{r} \cdot \nabla\chi \in \mathbb{N}, \quad (4.1)$$

where n counts the number of vortices enclosed by the path Ω . Furthermore, since the phase χ varies around a vortex, the only way to keep $|\Delta|e^{i\chi}$ single-valued is to let $|\Delta| \rightarrow 0$ at the core. Thus, vortices have normal cores, and one *magnetic flux quantum* $\Phi_0 \approx 2 \times 10^{-15} \text{ T m}^2$ manages to traverse the superconductor through each vortex core.

Vortices also appear in thin films of proximitized normal metals [159].² In these systems, the magnetic field penetrates the film homogeneously, and is neither quantized nor confined to vortex cores. Nevertheless, the field induces phase gradients in the superconducting condensate, which nucleate into vortices with quantized phase winding. Another interesting possibility was recently pointed out in reference 160. By injecting a charge current into a superconducting wire, one can force a phase gradient to appear there. If one then contacts a normal metal

-
1. Here, *thick* means that it is large compared to the magnetic penetration depth λ .
 2. Technically, the superconducting order parameter $\Delta = 0$ in normal metals. However, there is still a superconducting condensate there that can harbor vortices, and this can be described via the anomalous propagator $f_s = |f_s|e^{i\chi}$.

to such wires, the phase gradients of the wires spread into the normal metal via the proximity effect, which in turn creates vortices. In other words, it is possible to induce vortex excitations purely electrically, in materials that do not have to be intrinsically superconducting.

In paper XII, we build on the ideas of reference 160. We consider a normal metal that is completely enveloped by a current-biased superconducting wire as shown in figure 4.1. We can then calculate a total winding number N for the proximitized normal metal by applying equation (4.1) to a path Ω along the superconducting wire. Interestingly, we find that this total vorticity nucleates into a set of vortices inside the normal metal in a pattern that satisfies three constraints. Firstly, the vortices have individual winding numbers n_i that sum up to the total winding number $N = \sum_i n_i$. Secondly, the vortices nucleate in a pattern that respects the geometric symmetries of the sample. Finally, the vortices try to minimize the quantity $E = \sum_i n_i^2$, which we show in the paper is related to the total kinetic energy of the condensate.

In figure 4.1, we show some numerical results for this system. When a total winding $N = 1$ is applied, we get a single conventional vortex with winding $n = 1$, as one would expect. If a total winding $N = 2$ is applied, we instead get a *giant vortex* with winding $n = 2$. Since this has the same kinetic energy cost as 4 conventional vortices, these excitations are usually suppressed, but for this particular geometry the symmetry constraint stabilizes it. If we increase the total winding to $N = 3$, we actually get four conventional vortices around an *antivortex*, which is spinning in the opposite direction of the applied current. This is again an excited state since annihilating a vortex and antivortex would lower the kinetic energy of the system, but in this case the symmetry constraint prevents that. Another possibility would have been to have a single $n = 3$ giant vortex; but this has a kinetic energy of $E = 3^2 = 9$, compared to $E = 4 \cdot (+1)^2 + 1 \cdot (-1)^2 = 5$ for the configuration above, so the creation of an antivortex results in a lower-energy state. Interestingly, further increasing the total winding to $N = 4$ lowers the kinetic energy, since the system can simply get rid of the antivortex.

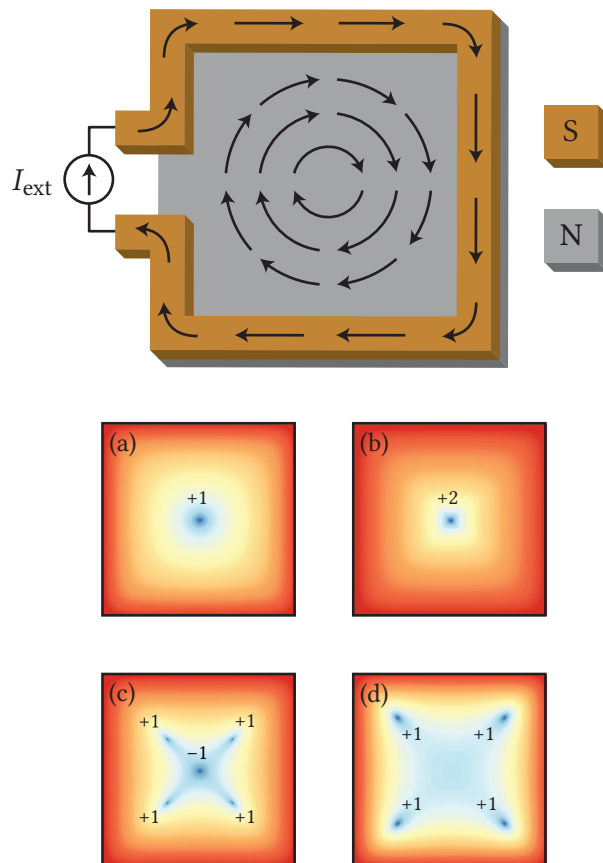


Figure 4.1: The model shows a superconducting wire (s) wrapped around a normal-metal square (N), where the superconductor is current-biased to induce a phase winding in the system. The plots below show the proximity-induced superconducting condensate, which vanishes at vortex cores (blue), and is enhanced near the surrounding superconductors (red). The labels show the winding numbers n of each individual vortex. The subplots correspond to total winding numbers of (a) $N = 1$, (b) $N = 2$, (c) $N = 3$, (d) $N = 4$.

4.2 Single-magnet spin valves

In a traditional superconducting spin valve, one requires at least two ferromagnetic layers. The simplest incarnation is an F/S/F trilayer. If the two ferromagnets have parallel magnetizations, they collaborate to induce an effective magnetic field inside the superconductor, thus suppressing superconductivity. On the other hand, if the ferromagnets have antiparallel magnetizations, their fields partially cancel inside the superconductor, thus restoring superconductivity. However, one challenge with this design is that it requires precise control over the individual magnetizations of the two ferromagnets, usually via an externally applied field. Manipulating one magnetic layer independently of the other both requires some fine-tuning of the sample parameters and restricts the magnetic field strengths at which the device can be operated. It would therefore be of interest if a similar effect could be realized in a structure with only a single homogeneous ferromagnet.

In papers II–IV, we theoretically predict and experimentally verify that this is indeed possible. More precisely, we focus on s/F bilayers with spin–orbit coupling on the ferromagnetic side of the interface. Such a ferromagnet can be described by the magnetic field vector

$$\mathbf{m} = m(\cos \varphi \cos \theta \mathbf{e}_x + \sin \varphi \cos \theta \mathbf{e}_y + \sin \theta \mathbf{e}_z), \quad (4.2)$$

while its spin–orbit coupling is given by the effective gauge field³

$$\mathbf{A} = (\alpha/\xi)(\sigma_1 \mathbf{e}_y - \sigma_2 \mathbf{e}_x) + (\beta/\xi)(\sigma_1 \mathbf{e}_x - \sigma_2 \mathbf{e}_y). \quad (4.3)$$

Here, we have assumed that the bilayer is grown in the z -direction. For the magnetization, this implies that φ parametrizes its in-plane projection and θ its out-of-plane component. As for the spin–orbit coupling, the field above describes a Rashba–Dresselhaus coupling in a film that is thin in the z -direction.⁴ The Rashba coupling α can e.g. be realized by inserting a thin layer of a metal with a strong atomic spin–orbit coupling in-between the superconductor and ferromagnet.⁵

-
3. Here, α and β are dimensionless numbers, and correspond to spin splittings in the natural unit $\hbar^2/m\xi$, where m is the electron mass. If we e.g. let $\xi = 30$ nm and take m to be the bare electron mass, this unit would correspond to 2.5 meV·nm.
 4. In papers II–III, we use the polar representation $\alpha = -A \sin \chi$ and $\beta = +A \cos \chi$. Here, we focus on the special cases $\beta = 0$ and $\beta = \alpha$, where this is less useful.
 5. An English translation of the 1959 paper by Rashba and Sheka is available as a supplemental to reference 161. That paper focuses on bulk spin–orbit coupling in wurtzite, and attributes the Hamiltonian $H \sim (\nabla V \times \mathbf{p}) \cdot \boldsymbol{\sigma}$ to a 1933 book by Pauli, where it is derived from the low-velocity limit of the Dirac equation.

The ideal material choice would be a heavy metal with a high admixture of d -orbital electrons in its conductance band, such as Pt or Au [162]. The Dresselhaus coupling β originates from the intrinsic inversion asymmetry of zincblende crystals [163].⁶ This includes many semiconductors like GaAs, InSb, and CdTe. Other ways to control the spin-orbit coupling include strain [164–166] and curvature [167, 168].

We now give a brief outline of how the novel spin-valve effect works. The defining feature of a conventional superconductor is that it has a condensate of singlet pairs $|\uparrow\downarrow\rangle - |\downarrow\uparrow\rangle$. When placed into contact with a homogeneous ferromagnet, some of these singlet pairs leak into the ferromagnet. Some of these are in turn converted into opposite-spin triplet pairs $|\uparrow\downarrow\rangle + |\downarrow\uparrow\rangle$, where we take the spin-quantization axis to be the magnetization direction of the ferromagnet. The more efficiently the ferromagnet converts singlets into triplets, the more singlets leak into the ferromagnet, thus draining the superconductor of singlets. However, the order parameter Δ in the superconductor is directly related to the singlet density, so Δ is suppressed when the triplet generation is efficient. This explains why the critical temperature T_c decreases if the triplet production increases, and vice versa.

When spin-orbit coupling is added to the problem, two new mechanisms factor into the equation. The first is that the spin-orbit coupling can convert opposite-spin triplets into equal-spin triplets $|\uparrow\uparrow\rangle$ and $|\downarrow\downarrow\rangle$. These consist of two electrons in the same spin band, and are thus immune to the pair-breaking effects of the magnetic field, making them much more stable than singlets and opposite-spin triplets inside ferromagnets [49, 50]. Generating triplets that can diffuse deep into the ferromagnet would enhance the net drainage of singlets, and therefore *suppress* the critical temperature of the system. This has no effect on the critical temperature for systems with only Rashba or only Dresselhaus coupling,⁷ and remains unimportant when both exist.⁸

-
6. The spin-orbit coupling derived by Dresselhaus is actually a cubic function of momentum. This is in contrast to equation (4.3), which is derived from a linear-in-momentum spin-orbit Hamiltonian $H \sim \mathbf{A} \cdot \mathbf{p}$. The link is that we in thin films can use the approximations $\langle p_z \rangle \approx 0$ and $\langle p_z^2 \rangle \approx \text{const.}$ to linearize it.
 7. For a justification of this claim, see equations (31–33) in paper II. Note that the linearized Usadel equation is exact in the relevant limit $T \rightarrow T_c$.
 8. This can be seen by comparing equations (31–33) and figures 20–21 in paper II. Equal-spin-triplet generation is governed by $\cos(2\varphi)$ and opposite-spin-triplet suppression by $1 - \sin(2\varphi)$. The latter explains our numerical results for $T_c(\varphi)$.

The second mechanism is that spin-orbit coupling modifies the effective energies of triplet pairs. This is an anisotropic energy penalty, and selectively suppresses triplets with certain spin projections. Which triplets are suppressed is determined by the spin-orbit coupling, which follows directly from the crystal structure and sample geometry. However, which triplets are generated is determined by the magnetization of the ferromagnet. This leads us to our novel *spin-orbit-valve effect*: we can tune to what extent the generated triplets are suppressed by rotating the magnetization of one homogeneous ferromagnet. This *enhances* the critical temperature when the triplet suppression is maximized, since this configuration closes the triplet proximity channel.

The characteristic energy scale for spin-orbit-induced energy shifts is $E_{\text{so}} := 4\Delta_0(\alpha^2 + \beta^2)$. In paper II, we showed that the effective triplet energy for systems with equal Rashba and Dresselhaus couplings is

$$E_t(\varphi) = \varepsilon + iE_{\text{so}}(1 - \sin 2\varphi)/4, \quad (4.4)$$

where ε is the quasiparticle energy, and we assume a purely in-plane rotation of the magnetic field. On the other hand, systems that only have Rashba coupling are in general invariant under in-plane rotations. However, we found in paper IV that an out-of-plane effect still exists,

$$E_t(\theta) = \varepsilon + iE_{\text{so}}(3 - \cos 2\theta)/4. \quad (4.5)$$

In figure 4.2, we demonstrate how the triplet penalties above fit together with the numerical results for the critical temperature. As anticipated in the discussion above, maxima in the triplet penalty correspond to maxima in the critical temperature, since suppressing triplets reduces the drainage of singlets from the superconductor.

Experimentally, it is difficult to engineer a structure with equally strong Rashba and Dresselhaus coupling, especially since the latter requires very specific material choices. However, figure 4.2 shows that this endeavour may well be worth the effort: it maximizes the *relative* change in triplet penalty as function of the magnetization direction, thus enabling quite dramatic T_c control. For these parameters, the resulting difference in spin-valve effect is nearly an order of magnitude. Other benefits include that in-plane rotations require less consideration of magnetic anisotropy, and that the spin-valve effect is easier to separate from any orbital-depairing effects that occur when out-of-plane magnetic fields are applied to superconducting structures.

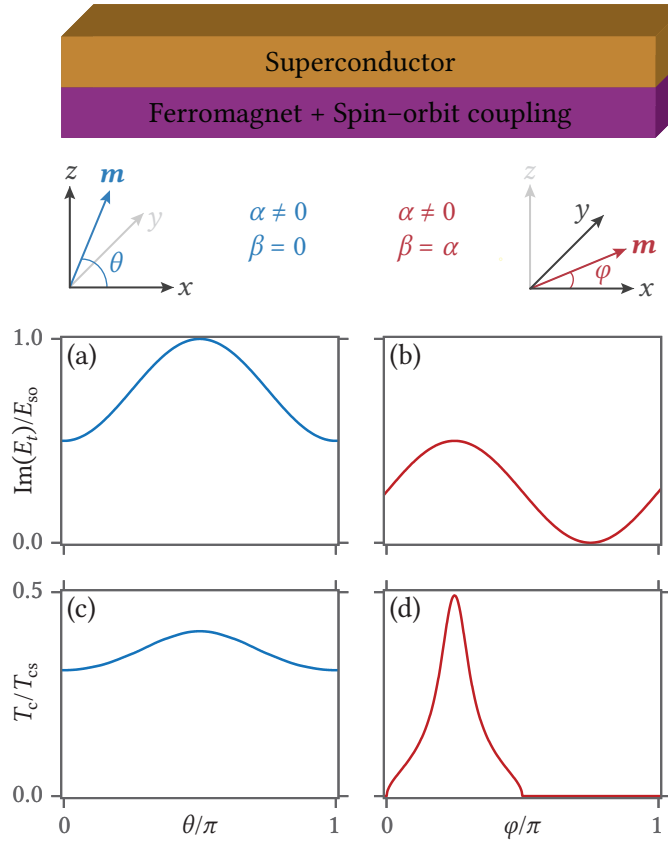


Figure 4.2: Visualization of the sample geometry, magnetization orientations, analytical results for the triplet energy penalty (a–b), and numerical results for the critical temperature (c–d). In all cases, we set the Rashba coupling $\alpha = 5$, magnetic field $m = 20\Delta_0$, superconductor length $L_S = \xi/2$, and ferromagnet length $L_F = \xi/4$. In panels (a,c), we set $\beta = 0$, and consider out-of-plane rotations θ . In panels (b,d), we set $\beta = \alpha$, and consider in-plane rotations φ .

Spin-orbit valves with both Rashba and Dresselhaus coupling have yet to be experimentally realized. One possibility was proposed in paper III, where we considered coupling a GaAs/AlGaAs-based 2DEG to a superconductor via a thin ferromagnetic insulator. Such a structure has the additional benefit that the spin-orbit coupling can be tuned via an electric gate voltage, enabling a device where superconductivity can be simultaneously controlled via magnetic and electric input signals.

Rotating from in-plane to out-of-plane magnetization in a system with only Rashba coupling was experimentally investigated in paper IV. The experiment used Nb/Pt/Co stacks to realize effective s/F bilayers with spin-orbit coupling.⁹ We found a qualitative agreement between theoretical predictions and experimental results, and concluded that the experimental observations could not be explained as either conventional s/F proximity effects or orbital-depairing effects. As discussed in the paper, the out-of-plane magnetization angle θ in this structure is finite in the absence of external magnetic fields. The maximal spin-valve effect is estimated to be around 200 mK, and corresponds to a Nb(18)/Pt(2.0)/Co(1.5) sample in a 120 mT out-of-plane field. The numbers in parentheses are thicknesses in nanometers. Stronger spin-valve effects can be expected if the superconductor is made shorter or the interface conductance enhanced. The Rashba coupling is less trivial: if it is too low, the triplet penalty is negligible for all orientations; if it is too high, triplets are completely suppressed for all orientations. Thus, the spin-valve effect is a nonmonotonic function of the Rashba coupling.

The perhaps most convincing piece of evidence for our spin-orbit-valve interpretation is the inset of figure 2c in paper IV. This shows the critical temperature modulation when the sample above is subjected to an in-plane magnetic field. The result is a suppression of about 90 mK when a 120 mT field is applied. In contrast, the Nb/Pt control sample does not show such a behavior, suggesting that the result is not caused by an orbital effect from the external field. Moreover, applying an in-plane field to Nb/Pt/Co should reduce the amount of Co flux that is injected into Nb, which would have increased not decreased the critical temperature of the system. In this case, the experimental results are consistent with the theoretical predictions, but behave oppositely from what one would have expected if orbital depairing was the culprit.

9. Technically, the stacks used in the experiment were Nb/Pt/Co/Pt. However, it was assumed that the Cooper pairs primarily “see” the spin-orbit coupling from the Pt layer between Nb and Co, since they decay rapidly with position in Co.

4.3 Half-metallic spin valves

In a *half-metallic ferromagnet*, the spin splitting of the density of states is so extreme that one spin band becomes insulating while the other remains metallic. Recently, several experiments have been performed by interfacing such magnets with conventional superconductors, and we investigated some of these numerically in paper VIII. In this section, we describe one of the experiments that *could not* be modelled by our theory, and propose some alternative explanations for their results.

In reference 71, the stacks MoGe(25)/Ni(1.5)/Cu(5.0)/CrO₂(100) and MoGe(50)/Ni(1.5)/Cu(5.0)/CrO₂(100) were grown on a TiO₂ substrate, with material thicknesses in nanometers given in parentheses. The amorphous MoGe is a conventional superconductor with an atomically short mean free path and a coherence length $\xi \approx 5$ nm. This places their experiment in the diffusive regime where the Usadel formalism is valid.¹⁰ Ni is a regular ferromagnet and CrO₂ a half-metallic ferromagnet. Cu is a normal metal that magnetically decouples the Ni and CrO₂ layers. This design was intended as a *triplet spin valve*: singlet pairs leak from the MoGe superconductor and into the Ni ferromagnet, where they are converted to opposite-spin triplets. If the CrO₂ layer is magnetized in the same direction as the Ni layer, these triplets cannot enter the CrO₂ layer, since it only has one spin band. On the other hand, if the CrO₂ layer is magnetized perpendicularly to the Ni layer, the opposite-spin triplets from the Ni layer correspond to equal-spin triplets in the CrO₂ layer. The net result is then that the thick CrO₂ layer drains superconductivity out of the MoGe layer, and this lowers the critical temperature of the system. Thus, by using an externally applied magnetic field to rotate the Ni magnetization relative to the CrO₂ magnetization, one can tune the critical temperature T_c .

The truly remarkable details in these experiments were the sizes of the superconductors employed and spin-valve effects obtained. Using a $25 \text{ nm} = 5\xi$ long superconductor, they broke the previous world record for superconducting spin-valve effects by nearly an order of magnitude, and found a critical temperature modulation $\delta T_c \approx 1.8$ K. Even for a $50 \text{ nm} = 10\xi$ long superconductor, they attributed an 800 mK modulation of the critical temperature to the triplet-spin-valve effect.

10. Strictly speaking, such a short mean free path is incompatible with the quasi-classical approximation underlying the Eilenberger and Usadel equations, where one assumes that all length scales are much longer than the Fermi wavelength.

This setup was subsequently modelled by Mironov and Buzdin [169] and by Halterman and Alidoust [170]. Both papers concluded that the triplet-spin-valve explanation seemed plausible. However, both made assumptions that were inconsistent with the actual experimental setup. Most importantly, they focused on superconductors of length $0.5-2.0\xi$, which clearly cannot explain how a spin-valve effect occurs in a 10ξ long superconductor. Furthermore, Mironov and Buzdin focused on completely transparent interfaces, which can amplify the spin-valve effect in a complex multilayer junction by up to several orders of magnitude. Halterman and Alidoust used a ballistic model for the superconductor, which is inconsistent with the extremely diffusive nature of the amorphous MoGe used in the experiment. Thus, these previous papers cannot address the most interesting aspect of the experiment: what is the mechanism behind the colossal spin-valve effect, and how can it persist even for a 10ξ long diffusive superconductor?

In paper VIII, we attempted to rigorously model the experiment. The superconductor was described using the Usadel equation, as is appropriate for a diffusive material. To accurately describe the half-metallic ferromagnet, we derived and Riccati-parametrized a model for strongly polarized ferromagnets. The interfaces were treated using the newly derived general spin-dependent boundary conditions for low-transparency interfaces [115]. We then tried to match all known material parameters in accordance with the experimental description. However, we found that *we could not reproduce any spin-valve effect at all for that setup*. The problem persisted even if we decreased the superconductor length by an order of magnitude, or varied the length and exchange field of the Ni layer. In fact, using realistic parameters, we found no critical temperature change if we removed the half-metallic layer entirely! Even if we completely suppress superconductivity at the MoGe/Ni interface, we found that the superconducting order parameter Δ recovers completely within a distance of $2-3\xi$ from the interface. Thus, it seems impossible to explain a significant critical temperature modulation in a 10ξ long superconductor via local drainage of Cooper pairs near the interface. Our theoretical results therefore suggest that *the experiment by Singh et al. cannot be fully understood as a triplet-spin-valve phenomenon, but requires a different physical mechanism*.

If the results cannot be explained as being due to a local suppression of superconductivity near the interface, the obvious alternative would be some kind of nonlocal electromagnetic effect. Amorphous MoGe is actually an extreme type-II superconductor, which according to reference 171 has a bulk magnetic penetration depth $\lambda \approx 580$ nm. The same reference points out that in films with a thickness $d < \lambda$, this is increased to the effective penetration depth $\Lambda \approx 2\lambda^2/d$. For $d = 25$ nm and $d = 50$ nm, this gives a ratio $d/\Lambda = d^2/2\lambda^2$ of about 0.1% and 0.4%, respectively. It seems more reasonable that a significant orbital effect spread over a small fraction of the magnetic penetration depth, than that a significant proximity effect spread over ten coherence lengths.

One such alternative explanation would be related to vortex physics. First of all, the experiment uses an applied out-of-plane magnetic field to reorient the magnetic configuration. Their record-breaking 1.8 K spin-valve effect was obtained at an applied magnetic field of 0.5 T. For comparison, reference 172 reported a fully developed vortex lattice for an amorphous MoGe superconductor at 0.5 T. Moreover, Singh et al. mention that the critical temperature shift continues to increase well above the fields where full collinearity has been achieved. The authors attributed this effect to surface pinning of the CrO₂ magnetization, but another explanation could be that increasing the flux injected into the superconductor continues to increase the vortex density. However, this explanation does not completely resolve the issue: Singh et al. made MoGe/Ni/Cu, MoGe/Cu/CrO₂, and MoGe control samples, and these displayed a significantly lower δT_c compared to MoGe/Ni/Cu/CrO₂.

Recently, Mironov et al. [74] showed that long-ranged electromagnetic phenomena can occur in proximity structures even for in-plane magnetizations. Furthermore, they showed that one in s/F/F' junctions can get a different electromagnetic response in the superconductor when the two ferromagnets are rotated relative to each other. Presumably, this could lead to an *orbital-valve effect* as a function of the magnetization misalignment, which would suppress superconductivity over a length scale given by Λ rather than ξ . We believe that this is a promising explanation for the experimental findings by Singh et al. Pursuing this explanation requires a self-consistent solution of the Usadel and Maxwell equations. Given the record-breaking efficiency of the device in reference 71, understanding its possibly novel physical mechanism ought to be a worthwhile goal for future research.

4.4 Spin-switch Josephson junctions

Spin valves (F/S/F) and Josephson junctions (S/F/S) are both well-studied superconducting spintronics devices. In paper [x](#) we pose the question: what happens if we combine them into a single device (S/F/S/F/S)?

To answer this question, let us review the difference between single-barrier and double-barrier junctions. A single-barrier junction $s_1/x/s_2$ consists of two superconductors s_1 and s_2 with a non-superconducting interlayer x . In the tunneling limit, the current flowing between s_1 and s_2 is given by the well-known current-phase relation [[42](#), [43](#)]

$$J_e = J_c \sin(\delta\varphi), \quad (4.6)$$

where $\delta\varphi := \varphi_2 - \varphi_1$ is the phase difference between the superconductors, and J_c depends on interface transparencies and so on. As we show in paper [x](#), a double-barrier junction $s_1/x/s_2/x/s_3$ is instead described by

$$J_e = J'_c \sin(\delta\varphi/2) \operatorname{sgn}[\cos(\delta\varphi/2)], \quad (4.7)$$

where $\delta\varphi := \varphi_3 - \varphi_1$ is the phase difference between the outer superconductors. This is qualitatively different than for a single-barrier junction: it behaves as if it had a 4π -periodic current-phase relation, but has abrupt transitions at $\delta\varphi = \pm\pi$ which ensures that the current-phase relation stays 2π -periodic. These transitions are smoothed out by any asymmetries in the system, as we explore in detail in paper [x](#).

This leads us back to our S/F/S/F/S system. If the ferromagnetic layers are parallel, superconductivity is suppressed in the central superconductor, which means that it behaves as an effective S/F/N/F/S = S/X/S single-barrier junction. On the other hand, if the ferromagnetic layers are antiparallel, superconductivity is restored in the central superconductor. We then get an S/X/S/X/S double-barrier junction. Thus, we can in situ tune the system from a $\sin(\delta\varphi)$ - to $\sin(\delta\varphi/2)$ -shaped current-phase relation by changing the orientation of one magnetic layer, as shown in figure [4.3](#). As we discuss in the paper, this argument can also be generalized to more complex n -barrier junctions, where one in principle can realize a more general $\sin(\delta\varphi/m)$ -shaped current-phase relation with a magnetically tunable integer $m \in [1, n]$.

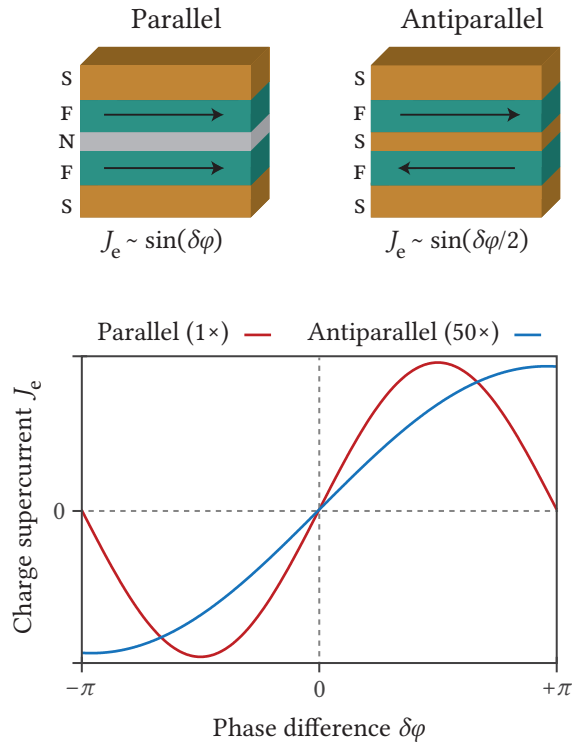


Figure 4.3: Spin-switch Josephson junction. The models illustrate how superconductivity can be turned on and off in the central layer by switching between parallel and antiparallel magnetic configurations. The numerical results below show how this switches between $\sin(\delta\varphi)$ - and $\sin(\delta\varphi/2)$ -shaped current-phase relations. The current-phase relation for the antiparallel configuration has been zoomed out 50 \times , since turning superconductivity on in the central layer obviously increases the maximal supercurrent. The material parameters used for the numerical calculations are provided in paper *x*.

This shows how a magnetic input signal can control the shape of the current-phase relation of a Josephson junction. In addition, the antiparallel configuration enhances the supercurrent compared to the parallel configuration, since suppressing superconductivity in the central layer creates a tighter bottleneck for tunneling supercurrents. Thus, by optimizing the junction parameters in a different way, the same device can be used as a Josephson junction with a magnetic on–off switch.

This research project falls into the category of Josephson junctions, which is a recurring topic in the enclosed papers. In paper [XI](#), which is an experimental project published in Nature communications, a magnetic vortex was used as the interlayer of a Josephson junction. The intrinsic inhomogeneity of the vortex created long-ranged supercurrents, which could be modulated via an external magnetic field. In paper [IX](#), we used a double-barrier Josephson junction to show that spin supercurrents are conserved in superconductors, even in the presence of spin-flip and spin–orbit impurities. This was shown both analytically and numerically for a system with both polarization and exchange contributions to the spin supercurrent. Josephson junctions also played a role in papers [II](#) and [V](#), where we among other things investigated how spin–orbit coupling and microwaves affected Josephson junctions. Papers [VI](#) and [XII](#) can be viewed as topological generalizations of non-magnetic Josephson junctions. Finally, in paper [XIV](#), we focus on how pushing magnetic Josephson junctions out of equilibrium via transverse voltages can lead to novel physical effects.

4.5 Voltage-induced superconductivity

It is a well-known fact that magnetism is harmful to superconductivity. The absolute upper limit for the magnetic spin splitting that can coexist with conventional superconductivity was derived by Chandrasekhar and Clogston in 1962: $m = \Delta_0/\sqrt{2}$. In paper [XIII](#), we demonstrate a surprising loophole in the Chandrasekhar–Clogston limit: we can stabilize superconductivity in much stronger magnetic fields $m \gg \Delta_0$ if we simply voltage bias the superconductor. Although we find that this is a low-temperature effect, it is not an extremely-low-temperature effect. For instance, taking the superconductor to be Nb, it can be realized for $m > 2\Delta_0$ up to a temperature $T \approx 1$ K, and for $m > \Delta_0$ up to $T \approx 2$ K, compared to its field-free critical temperature $T_c \approx 9.2$ K.

This research project was motivated by a simple analytical argument. Consider a bulk superconductor without voltage bias or magnetism. The self-consistency equation for its order parameter can be written

$$\Delta \sim \text{Re} \int d\varepsilon f(\varepsilon) h(\varepsilon). \quad (4.8)$$

The first factor $f(\varepsilon) = \Delta/\sqrt{(\varepsilon + i\eta)^2 - \Delta^2}$ is the singlet pair amplitude, which acts as a density of states for singlet correlations. The second factor $h(\varepsilon) = \tanh(\varepsilon/2T)$ is the energy mode of the distribution function in equilibrium. The integral of their product describes the number of occupied singlet states in a bulk superconductor in equilibrium. The prefactor and integration limits are not important for this argument.

When a magnetic spin splitting m is introduced, we have to replace $f(\varepsilon)$ by $[f(\varepsilon + m) + f(\varepsilon - m)]/2$. Rigorously, this can be shown by explicitly solving the Usadel equation. Intuitively, the spin-splitting field increases the effective energies of spin-up quasiparticles by m , and decreases the energies of spin-down quasiparticles by m , thus explaining the shifts $\varepsilon \rightarrow \varepsilon \pm m$. The self-consistency relation for a superconductor in a magnetic field is therefore modified to:

$$\Delta \sim \frac{1}{2} \text{Re} \int d\varepsilon [f(\varepsilon + m) + f(\varepsilon - m)] h(\varepsilon). \quad (4.9)$$

On the other hand, if a voltage bias V is applied via normal-metal contacts, we essentially shift the chemical potentials of the contacts by $\pm eV/2$ compared to equilibrium. Thus, the distribution function inside the contacts are effectively shifted to $h(\varepsilon \pm eV/2)$. Assuming that the superconductor is short compared to the inelastic scattering length, the distribution function deep inside the superconductor is the average $[h(\varepsilon + eV/2) + h(\varepsilon - eV/2)]/2$. This yields the self-consistency relation:

$$\Delta \sim \frac{1}{2} \text{Re} \int d\varepsilon f(\varepsilon) [h(\varepsilon + eV/2) + h(\varepsilon - eV/2)]. \quad (4.10)$$

Interestingly, if one calculates the $\Delta(m, T)$ and $\Delta(eV/2, T)$ using these two equations, the results are identical! This equivalence between magnetism and voltage bias was clarified in an elegant way by Moor, Volkov, and Efetov [173]. If we introduce the integral substitutions $\varepsilon' := \varepsilon \pm eV/2$ in equation (4.10), the equation takes the exact same form as equation (4.9), just with an effective magnetic field $m = eV/2$.

This shows manifestly that there is a symmetry between subjecting a conventional superconductor to a magnetic field or a voltage bias. A natural question that then arises is: what happens when we have *both* a magnetic field and a voltage bias? This was investigated in paper XIII, which is possibly the most important paper enclosed in this thesis. Our main result is that there is a partial cancellation between the effects of the magnetic field and voltage when $|m| \approx |eV/2|$, which leads to a stabilization of superconductivity in high magnetic fields when an appropriate voltage is applied. Our main result is shown in figure 4.4.

In addition to being interesting for fundamental physics reasons, this result has a number of wider implications for the field as a whole. Firstly, experiments in superconducting spintronics routinely rely on superconductor/ferromagnet hybrid structures, where stabilizing superconductivity in the presence of ferromagnetic elements is paramount. Secondly, we find that the physical properties of the superconductor for $m > \Delta_0$ are quite exotic compared to $m < \Delta_0$, and likely warrants further research of its own. For instance, there are *two* non-overlapping gaps in the density of states, while the density of states is not gapped at the Fermi level. This results in some curious effects, such as permitting a coexistence of supercurrents and resistive currents deep inside the superconductor. Thirdly, since superconductivity vanishes for $m > \Delta_0$ in the absence of the voltage bias, the voltage can effectively be used to turn superconductivity on and off, thus creating a bridge between conventional and superconducting electronics devices.

In figure 4.4, we show a sketch of how to experimentally realize the effect, and a phase diagram at zero temperature as function of voltage and magnetic field. Note that we have also indicated a bistable regime, where both a superconducting and normal-state solution exists. Depending on the dynamics of the system, this can manifest experimentally as either a superconducting hysteresis effect or first-order phase transition. For more discussion about bistability, more phase diagrams, rigorous numerical results for junctions of finite length with finite interface transparency, a discussion of relevant physical observables, and references to relevant literature, see paper XIII.

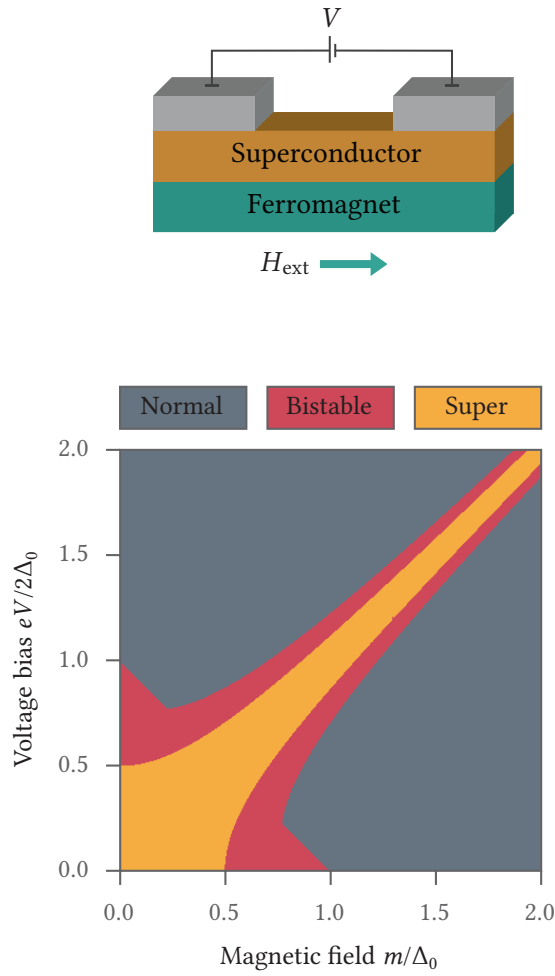


Figure 4.4: The model illustrates a possible experimental setup. A superconductor is connected to a ferromagnetic insulator, which induces a spin splitting m_0 in the superconductor. An external field H_{ext} shifts it to $m = m_0 + \mu_B H_{\text{ext}}$ via the Zeeman effect, resulting in a tunable spin splitting m . The superconductor is connected to voltage-biased normal-metal contacts, which are used to stabilize the superconducting state. The phase diagram shows how superconductivity depends on voltage bias and magnetic field at $T = 0$, demonstrating the cancellation of their effects for $|eV/2| \approx |m|$.

We note that the Chandrasekhar–Clogston limit can be explained using a simple energy argument. When a normal metal is subjected to a spin splitting, the electrons near the Fermi surface can lower their energies by flipping their spins. However, a superconductor has a gap in the density of states near the Fermi surface, thus preventing such a paramagnetic effect. When the paramagnetic energy gain obtainable by a normal metal exceeds the condensation energy associated with superconductivity, a first-order phase transition from the superconducting state to the normal state occurs. Unfortunately, while we can easily explain *that* superconductivity is stabilized when a voltage is applied, it is harder to demonstrate precisely *why*, since it is difficult to explicitly obtain the free energy of the system within the Usadel formalism. An interesting prospect for future research would be to investigate our proposed system within e.g. Bogoliubov–de Gennes formalism, where the free energy of the system is more accessible. This may provide a better understanding of the underlying mechanism.

This research on voltage-induced superconductivity in magnetic fields falls into the category of nonequilibrium superconductivity. Two other papers in this thesis also belong to this category. In paper [xiv](#), we discover two interesting physical effects. The first is that in an $S/F/N/F/S$ junction, one can apply a transverse voltage bias to the normal metal in order to change the magnetic ground state of the ferromagnetic layers from antiparallel to parallel. The second is that in an $S/F^{\uparrow}/F/S$ junction, one can apply a transverse voltage bias to the central ferromagnet in order to modulate the spontaneous charge current flowing between the superconductors. In paper [xv](#), we show that nonequilibrium spin injection can be used to manipulate spin supercurrents in an $F/S/F$ junction. We explain how this mechanism can be understood as the injected spins exerting a torque on the equilibrium spin current flowing in the junction, and discuss how it might be realized experimentally.

Outlook

In this thesis, we have investigated superconducting phenomena in nanostructures, with a focus on how to control superconductivity in low-temperature devices. The previous chapters have summarized how to theoretically describe such structures, how to numerically solve the relevant equations, and a brief description of some research highlights. The main body of research is however not contained in the thesis itself, but rather in the enclosed papers. In this chapter, we conclude the thesis by discussing some possibilities for future research.

One research topic that has proven to be fruitful is voltage-biased superconducting structures, where an energy mode of the distribution function $h(\varepsilon) = [\tanh[(\varepsilon + eV/2)/2T] + \tanh[(\varepsilon - eV/2)/2T]]/2$ is excited purely electrically. Roughly two decades ago, it was demonstrated theoretically and experimentally that this technique could be used to create a “supercurrent transistor” [81, 174–176]. In this thesis, we have shown that the same technique can be used to stabilize superconductivity in high magnetic fields, toggle the magnetic ground-state of a system, or tune the spontaneous charge current flowing in a Josephson junction [xiii, xiv]. Given the rich plethora of phenomena discovered in this area, this seems like a promising avenue for further research.

As discussed in section 4.3, a promising explanation for the record-setting spin-valve effect found by Singh et al. [71] is an orbital-valve effect, where changing the orientation of two ferromagnets might affect the critical temperature of a superconductor due to a long-ranged electromagnetic effect [74]. This can be explicitly checked via a self-consistent solution of the Maxwell and Usadel equations. Numerically, this involves adding a self-consistency equation for the gauge field A , which can probably be accelerated using Steffensen’s method in the same way as the order parameter Δ . In light of the findings in reference [74], it might also be worth revisiting many other physical systems and checking whether the observations can be explained via orbital effects. Another related research direction would be to investigate whether novel device functionality can be implemented using these long-ranged electromagnetic effects alone, such as e.g. φ_0 junctions.

Superconducting spintronics is influenced by non-superconducting spintronics. Two successful ideas from spintronics that have yet to be experimentally realized for superconducting structures are (i) spin-

current-induced magnetization switching and (ii) antiferromagnets as spintronic building blocks. Both avenues have been explored theoretically. For instance, it has been shown that the magnetic moment can in principle be modulated via superconductivity in φ_0 junctions [177] and heterostructures involving intrinsic triplet superconductors [178], and that the boundary conditions to anti- and ferromagnetic insulators are similar [124]. Recent experiments on superconductivity-mediated exchange interaction and nonequilibrium spin injection can also be expected to influence the near-future research focus [69, 75].

Another idea that could be interesting to pursue further is the one reported in reference 179. There, it was found that if a nanowire is used to bridge two superconductors with a phase difference of π , a pure odd-frequency triplet state appears in the center of the nanowire. This could e.g. be interesting to use as a building block of its own, since it provides the possibility of probing the properties of a pure odd-frequency state directly. For instance, consider two such π -biased nanowires that are bridged by another nanowire, resulting in a H-shaped geometry with superconductors at all ends. In this case, the central nanowire will act as if it was the weak link of a Josephson junction where both superconductors have purely odd-frequency states. Other scenarios like this of fundamental interest might also be worth exploring.

Finally, given the success with coupling superconductors to ferromagnets, it might be interesting to consider coupling superconductors to e.g. ferroelectrics too. Some very interesting experimental results have already been obtained for such systems, e.g. demonstrating that one can “print” Josephson junctions onto superconductor/ferroelectric bilayers via its domain structure [180]. However, there are some remaining fundamental questions that might be worth investigating. For instance, superconductivity can be suppressed using a ferroelectric domain as described in the paper above, and this results in a loss of its condensation energy. Is there an inverse effect, where a superconductor can control the spontaneous polarization direction of a weak ferroelectric? Another example is that odd-frequency triplets are known to be generated by ferromagnets. If a clean superconductor is coupled to a ferroelectric, are any new kinds of superconducting correlations induced? How about a Josephson junction where the interlayer is a thin ferroelectric—how is tunneling between the superconductors affected by the surface charge? In other words, there are many interesting questions related to superconductors and ferroelectrics.

Bibliography

1. **J.A. Ouassou.**
Full proximity effect in spin-textured superconductor/ferromagnet bilayers.
Specialization project (NTNU, Trondheim, Norway, 2014).
URL: <http://pvv.org/~jabirali/academic/master/project.pdf>
2. **J.A. Ouassou.**
Density of states and critical temperature in superconductor/ferromagnet structures with spin-orbit coupling.
Master thesis (NTNU, Trondheim, Norway, 2015).
URL: <http://hdl.handle.net/11250/2352094>
3. **K. Fossheim, A. Sudbø.**
Superconductivity (2004).
ISBN: 978-0-470-84452-6
4. **M. Tinkham.**
Introduction to superconductivity (2004).
ISBN: 978-0-486-43503-9
5. **L.N. Cooper.**
Bound electron pairs in a degenerate Fermi gas.
Physical review 104, 1189 (1956).
DOI: [10/B6WDWT](https://doi.org/10/B6WDWT)
6. **J. Bardeen, L.N. Cooper, J.R. Schrieffer.**
Theory of superconductivity.
Physical review 108, 1175 (1957).
DOI: [10/FW8K5D](https://doi.org/10/FW8K5D)
7. **J.G. Bednorz, K.A. Müller.**
Possible high- T_c superconductivity in the Ba-La-Cu-O system.
Zeitschrift für physik B 64, 189 (1986).
DOI: [10/CJ434S](https://doi.org/10/CJ434S)
8. **A. Schilling, M. Cantoni, J.D. Guo, H.R. Ott.**
Superconductivity above 130 K in the Hg-Ba-Ca-Cu-O system.
Nature 363, 56 (1993).
DOI: [10/DZZKPF](https://doi.org/10/DZZKPF)

9. **L.P. Gorkov, V.Z. Kresin.**
Colloquium: High pressure and road to room temperature superconductivity. Reviews of modern physics 90, 011001 (2018).
DOI: [10/GCRNXF](https://doi.org/10/GCRNXF)
10. **J. Zaanen, S. Chakravarty, T. Senthil, et al.**
Towards a complete theory of high T_c . Nature physics 2, 138 (2006).
DOI: [10/FV98CD](https://doi.org/10/FV98CD)
11. **Y. Cao, V. Fatemi, S. Fang, et al.**
Unconventional superconductivity in magic-angle graphene superlattices. Nature 556, 43 (2018).
DOI: [10/GC4PC9](https://doi.org/10/GC4PC9)
12. **A.P. Drozdov, M.I. Eremets, I.A. Troyan, et al.**
Conventional superconductivity at 203 K at high pressures in the sulfur hydride system. Nature 525, 73 (2015).
DOI: [10/6VJ](https://doi.org/10/6VJ)
13. **A.P. Drozdov, P.P. Kong, V.S. Minkov, et al.**
Superconductivity at 250 K in lanthanum hydride under high pressures. ARXIV: [1812.01561](https://arxiv.org/abs/1812.01561)
14. **R.M. Scanlan, A.P. Malozemoff, D.C. Larbalestier.**
Superconducting materials for large scale applications. Proceedings of the IEEE 92, 1639 (2004).
DOI: [10/C7MM53](https://doi.org/10/C7MM53)
15. **K. Coyne.**
New world-record magnet fulfills superconducting promise. News report (MAGLAB, 2017).
URL: <https://nationalmaglab.org/news-events/news/new-world-record-magnet-fulfills-superconducting-promise>
16. **M.V. Berry, A.K. Geim.**
Of flying frogs and levitrons. European journal of physics 18, 307 (1997).
DOI: [10/DR9XCD](https://doi.org/10/DR9XCD)

17. **A. Geim.**
Everyone's magnetism.
Physics today 51, 36 (2008).
DOI: [10/BZWHGC](https://doi.org/10/BZWHGC)
18. **S.K. Range.**
Gravity probe B.
Educator's guide (NASA, 2004).
URL: http://einstein.stanford.edu/content/education/GP-B_T-Guide4-2008.pdf
19. **D. Vasyukov, Y. Anahory, L. Embon, et al.**
A scanning superconducting quantum interference device with single electron spin sensitivity.
Nature nanotechnology 8, 639 (2013).
DOI: [10/GFM54W](https://doi.org/10/GFM54W)
20. **M.J. Martínez-Pérez, D. Koelle.**
NanosQUIDS.
Physical sciences reviews 2, 5001 (2017).
DOI: [10/GFMHJX](https://doi.org/10/GFMHJX)
21. **D.D.E. Martin, P. Verhoeve, A. Peacock, et al.**
A 12 × 10 pixels superconducting tunnel junction array based spectro-photometer for optical astronomy.
Nuclear instruments and methods in physics research A 520, 512 (2004).
DOI: [10/BTS6RW](https://doi.org/10/BTS6RW)
22. **P. Verhoeve, D.D.E. Martin, R.A. Hijmering, et al.**
s-CAM 3: Optical astronomy with a STJ-based imaging spectrophotometer.
Nuclear instruments and methods in physics research A 559, 598 (2006).
DOI: [10/CTZ54H](https://doi.org/10/CTZ54H)
23. **M. Zgirski, M. Foltyn, A. Savin, et al.**
Nanosecond thermometry with Josephson junctions.
Physical review applied 10, 044068 (2018).
DOI: [10/GFMCGR](https://doi.org/10/GFMCGR)

24. **J. Koomey, S. Berard, M. Sanchez, H. Wong.**
Implications of historical trends in the electrical efficiency of computing.
IEEE annals of the history of computing 33, 46 (2011).
DOI: [10/CRXBP5](https://doi.org/10/CRXBP5)
25. **T. Bawden.**
Global warming: Data centres to consume three times
as much energy in next decade, experts warn.
News report (The Independent, 2016).
URL: <http://www.independent.co.uk/environment/global-warming-data-centres-to-consume-three-times-as-much-energy-in-next-decade-experts-warn-a6830086.html>
26. **S.K. Moore.**
Computing's power limit demonstrated.
IEEE spectrum 49, 14 (2012).
DOI: [10/GFN7BV](https://doi.org/10/GFN7BV)
27. **M. Dorojevets, P. Bunyk, D. Zinoviev.**
FLUX chip: Design of a 20 GHz 16 bit ultrapipelined RSFQ
processor prototype based on 1.75 μm LTS technology.
IEEE transactions on applied super-
conductivity 11, 326 (2001).
DOI: [10/FWBFXB](https://doi.org/10/FWBFXB)
28. **D.S. Holmes, A.L. Ripple, M.A. Manheimer.**
Energy-efficient superconducting computing.
IEEE transactions on applied super-
conductivity 23, 1701610 (2013).
DOI: [10/GFN7B6](https://doi.org/10/GFN7B6)
29. **F. Bedard, N.K. Welker, G.R. Cotter, M.A. Escavage, J.T. Pinkston.**
Superconducting technology assessment.
Technical report (NSA, 2005).
URL: <https://www.nitrd.gov/pubs/nsa/sta.pdf>
30. **M. Feldman.**
China aims to be global leader in superconducting computers.
News report (TOP500, 2018).
URL: <https://www.top500.org/news/china-aims-to-be-global-leader-in-superconducting-computers/>

31. **J. Linder, J.W.A. Robinson.**
Superconducting spintronics.
Nature physics 11, 307 (2015).
DOI: [10/GC4JJV](https://doi.org/10/GC4JJV)
32. **M. Eschrig.**
Spin-polarized supercurrents for spintronics.
Physics today 64, 43 (2010).
DOI: [10/D8CJ2W](https://doi.org/10/D8CJ2W)
33. **M. Eschrig.**
Spin-polarized supercurrents for spintronics.
Reports on progress in physics 78, 104501 (2015).
DOI: [10/CWVC](https://doi.org/10/CWVC)
34. **M.G. Blamire, J.W.A. Robinson.**
The interface between superconductivity and magnetism.
Journal of physics: Condensed matter 26, 453201 (2014).
DOI: [10/GFC8KZ](https://doi.org/10/GFC8KZ)
35. **A.I. Buzdin.**
Proximity effects in superconductor–ferromagnet heterostructures.
Reviews of modern physics 77, 935 (2005).
DOI: [10/C3W2RR](https://doi.org/10/C3W2RR)
36. **F.S. Bergeret, A.F. Volkov, K.B. Efetov.**
Odd triplet superconductivity and related
phenomena in superconductor–ferromagnet structures.
Reviews of modern physics 77, 1321 (2005).
DOI: [10/BQC4VN](https://doi.org/10/BQC4VN)
37. **A.K. Feofanov, V.A. Oboznov, V.V. Bol’ginov, et al.**
Implementation of superconductor/ferromagnet/superconductor
 π -shifters in superconducting digital and quantum circuits.
Nature physics 6, 593 (2010).
DOI: [10/D728GF](https://doi.org/10/D728GF)
38. **I. Giaever.**
Energy gap in superconductors measured by electron tunneling.
Physical review letters 5, 147 (1960).
DOI: [10/FK234G](https://doi.org/10/FK234G)

39. **V.F. Weisskopf.**
The formation of Cooper pairs and the nature of superconducting currents.
Contemporary physics 22, 375 (1981).
DOI: [10/BRJR5Z](https://doi.org/10/BRJR5Z)
40. **P.-G. de Gennes.**
Superconductivity of metals and alloys (1999).
ISBN: 978-0-7382-0101-6
41. **A.F. Andreev.**
Thermal conductivity of the intermediate state of superconductors.
Soviet physics JETP 20, 1490 (1965).
42. **A.A. Golubov, M.Y. Kupriyanov, E. Il'ichev.**
The current–phase relation in Josephson junctions.
Reviews of modern physics 76, 411 (2004).
DOI: [10/BS7WMZ](https://doi.org/10/BS7WMZ)
43. **B.D. Josephson.**
Possible new effects in superconductive tunnelling.
Physics letters 1, 251 (1962).
DOI: [10/FBFM9M](https://doi.org/10/FBFM9M)
44. **A. Di Bernardo, S. Diesch, Y. Gu, et al.**
Signature of magnetic-dependent gapless odd frequency states at superconductor/ferromagnet interfaces.
Nature communications 6, 8053 (2015).
DOI: [10/F726R6](https://doi.org/10/F726R6)
45. **H. le Sueur, P. Joyez, H. Pothier, C. Urbina, D. Esteve.**
Phase controlled superconducting proximity effect probed by tunneling spectroscopy.
Physical review letters 100, 197002 (2008).
DOI: [10/D6ZDSZ](https://doi.org/10/D6ZDSZ)
46. **N. Moussy, H. Courtois, B. Pannetier.**
Local spectroscopy of a proximity superconductor at very low temperature.
Europhysics letters 55, 861 (2001).
DOI: [10/DX8JDK](https://doi.org/10/DX8JDK)

47. **F.S. Bergeret, A.F. Volkov, K.B. Efetov.**
Long-range proximity effects in superconductor–ferromagnet structures.
Physical review letters 86, 4096 (2001).
DOI: [10/BG59WR](https://doi.org/10.1073/prl.86.16.4096)
48. **M. Houzet, A.I. Buzdin.**
Long range triplet Josephson effect through a ferromagnetic trilayer.
Physical review B 76, 060504 (2007).
DOI: [10/B2VP9C](https://doi.org/10.1103/PhysRevB.76.060504)
49. **F. Bergeret, I. Tokatly.**
Singlet–triplet conversion and the long-range proximity effect in superconductor–ferromagnet structures with generic spin dependent fields.
Physical review letters 110, 117003 (2013).
DOI: [10/GC5PHK](https://doi.org/10.1103/PhysRevLett.110.117003)
50. **F. Bergeret, I. Tokatly.**
Spin–orbit coupling as a source of long-range triplet proximity effect in superconductor–ferromagnet hybrid structures.
Physical review B 89, 134517 (2014).
DOI: [10/GC5PHG](https://doi.org/10.1103/PhysRevB.89.134517)
51. **M. Houzet.**
Ferromagnetic Josephson junction with precessing magnetization.
Physical review letters 101, 057009 (2008).
DOI: [10/D95SVV](https://doi.org/10.1103/PhysRevLett.101.057009)
52. **K.K. Likharev, V.K. Semenov.**
RSFQ logic/memory family.
IEEE transactions on applied superconductivity 1, 3 (1991).
DOI: [10/D7BNV5](https://doi.org/10.1109/4227.91115)
53. **Y.V. Nazarov, Y.M. Blanter.**
Quantum transport (2009).
ISBN: 978-0-521-83246-5

54. **H. Sickinger, A. Lipman, M. Weides, et al.**
Experimental evidence of a φ Josephson junction.
Physical review letters 109, 107002 (2012).
DOI: [10/GFPHPK](https://doi.org/10/GFPHPK)
55. **E. Goldobin, D. Koelle, R. Kleiner, R.G. Mints.**
Josephson junction with a magnetic-field tunable ground state.
Physical review letters 107, 227001 (2011).
DOI: [10/BSDQMP](https://doi.org/10/BSDQMP)
56. **N.G. Pugach, E. Goldobin, R. Kleiner, D. Koelle.**
Method for reliable realization of a φ Josephson junction.
Physical review B 81, 104513 (2010).
DOI: [10/C2PG4M](https://doi.org/10/C2PG4M)
57. **A. Buzdin, A.E. Koshelev.**
Periodic alternating 0- and π -junction structures
as realization of φ -Josephson junctions.
Physical review B 67, 220504 (2003).
DOI: [10/D827WQ](https://doi.org/10/D827WQ)
58. **R.G. Mints.**
Self-generated flux in Josephson junctions
with alternating critical current density.
Physical review B 57, R3221 (1998).
DOI: [10/DFJCTJ](https://doi.org/10/DFJCTJ)
59. **D.B. Szombati, S. Nadj-Perge, D. Car, et al.**
Josephson φ_0 -junction in nanowire quantum dots.
Nature physics 12, 568 (2016).
DOI: [10/F8P7R7](https://doi.org/10/F8P7R7)
60. **M.A. Silaev, I.V. Tokatly, F.S. Bergeret.**
Anomalous current in diffusive ferromagnetic Josephson junctions.
Physical review B 95, 184508 (2017).
DOI: [10/GFPHRC](https://doi.org/10/GFPHRC)
61. **F. Konschelle, I.V. Tokatly, F.S. Bergeret.**
Theory of the spin-galvanic effect and the anomalous
phase shift φ_0 in superconductors and Josephson
junctions with intrinsic spin-orbit coupling.
Physical review B 92, 125443 (2015).
DOI: [10/GFB35S](https://doi.org/10/GFB35S)

62. **F. Dolcini, M. Houzet, J.S. Meyer.**
Topological Josephson φ_0 junctions.
Physical review B 92, 035428 (2015).
DOI: [10/GFRDWP](https://doi.org/10/GFRDWP)
63. **A. Zazunov, R. Egger, T. Jonckheere, T. Martin.**
Anomalous Josephson current through a
spin-orbit coupled quantum dot.
Physical review letters 103, 147004 (2009).
DOI: [10/D5Q9FN](https://doi.org/10/D5Q9FN)
64. **Y. Tanaka, T. Yokoyama, N. Nagaosa.**
Manipulation of the Majorana fermion, Andreev reflection,
and Josephson current on topological insulators.
Physical review letters 103, 107002 (2009).
DOI: [10/B6CN3G](https://doi.org/10/B6CN3G)
65. **A. Buzdin.**
Direct coupling between magnetism and
superconducting current in the Josephson φ_0 junction.
Physical review letters 101, 107005 (2008).
DOI: [10/BQ5GSM](https://doi.org/10/BQ5GSM)
66. **M.A. Silaev.**
 θ_0 thermal Josephson junction.
Physical review B 96, 064519 (2017).
DOI: [10/GFPHNZ](https://doi.org/10/GFPHNZ)
67. **R.-P. Riwar, M. Houzet, J.S. Meyer, Y.V. Nazarov.**
Multi-terminal Josephson junctions as topological matter.
Nature communications 7, 11167 (2016).
DOI: [10/GFJ35J](https://doi.org/10/GFJ35J)
68. **E. Strambini, S. D'Ambrosio, F. Vischi, et al.**
The ω -SQUIPT as a tool to phase-engineer Josephson topological materials.
Nature nanotechnology 11, 1055 (2016).
DOI: [10/GFPHQS](https://doi.org/10/GFPHQS)
69. **Y. Zhu, A. Pal, M.G. Blamire, Z.H. Barber.**
Superconducting exchange coupling between ferromagnets.
Nature materials 16, 195 (2017).
DOI: [10/F9GRVX](https://doi.org/10/F9GRVX)

70. **R.S. Keizer, S.T.B. Goennenwein, T.M. Klapwijk, et al.**
 A spin triplet supercurrent through the half-metallic ferromagnet CrO₂.
Nature 439, 825–827 (Feb. 2006).
 DOI: [10/BXGRGD](https://doi.org/10/BXGRGD)
71. **A. Singh, S. Voltan, K. Lahabi, J. Aarts.**
 Colossal proximity effect in a superconducting triplet spin valve based on the half-metallic ferromagnet CrO₂.
Physical review x 5, 021019 (2015).
 DOI: [10/GFKPPZ](https://doi.org/10/GFKPPZ)
72. **Y. Kalcheim, O. Millo, A. Di Bernardo, A. Pal, J.W.A. Robinson.**
 Inverse proximity effect at superconductor–ferromagnet interfaces.
Physical review B 92, 060501 (2015).
 DOI: [10/GFPMXD](https://doi.org/10/GFPMXD)
73. **A. Di Bernardo, Z. Salman, X.L. Wang, et al.**
 Intrinsic paramagnetic Meissner effect due to *s*-wave odd-frequency superconductivity.
Physical review x 5, 041021 (2015).
 DOI: [10/GFPMZJ](https://doi.org/10/GFPMZJ)
74. **S. Mironov, A.S. Mel'nikov, A. Buzdin.**
 Electromagnetic proximity effect in planar superconductor–ferromagnet structures.
Applied physics letters 113, 022601 (2018).
 DOI: [10/GDSKX4](https://doi.org/10/GDSKX4)
75. **K.-R. Jeon, C. Ciccarelli, A.J. Ferguson, et al.**
 Enhanced spin pumping into superconductors provides evidence for superconducting pure spin currents.
Nature materials 17, 499 (2018).
 DOI: [10/GC95G3](https://doi.org/10/GC95G3)
76. **X. Montiel, M. Eschrig.**
 Generation of pure superconducting spin current in magnetic heterostructures via nonlocally induced magnetism due to Landau Fermi liquid effects.
Physical review B 98, 104513 (2018).
 DOI: [10/GD83SV](https://doi.org/10/GD83SV)

77. **L.P. Gorkov.**
On the energy spectrum of superconductors.
Soviet physics JETP 34, 505 (1958).
78. **K. Maki.**
Gapless superconductivity.
Superconductivity, ch. 18 (1969).
ISBN: 978-0-8247-1521-2
79. **C. Huang, I.V. Tokatly, F.S. Bergeret.**
Extrinsic spin-charge coupling in
diffusive superconducting systems.
Physical review B 98, 144515 (2018).
DOI: [10/GFGVPZ](https://doi.org/10/GFGVPZ)
80. **V. Chandrasekhar.**
Proximity-coupled systems.
Superconductivity, ch. 8 (2008).
DOI: [10/FGT3PQ](https://doi.org/10/FGT3PQ)
81. **W. Belzig, F.K. Wilhelm, C. Bruder, G. Schön, A.D. Zaikin.**
Quasiclassical Green's function approach
to mesoscopic superconductivity.
Superlattices and microstructures 25, 1251 (1999).
DOI: [10/CN3TT8](https://doi.org/10/CN3TT8)
82. **J. Rammer, H. Smith.**
Quantum field-theoretical methods
in transport theory of metals.
Reviews of modern physics 58, 323 (1986).
DOI: [10/B8QGWH](https://doi.org/10/B8QGWH)
83. **N.B. Kopnin.**
Theory of nonequilibrium superconductivity (2009).
ISBN: 978-0-19-956642-6
84. **T. Kita.**
Introduction to nonequilibrium statistical
mechanics with quantum field theory.
Progress of theoretical physics 123, 581 (2010).
DOI: [10/BS3B5D](https://doi.org/10/BS3B5D)

85. **L.V. Keldysh.**
Diagram technique for nonequilibrium processes.
Soviet physics JETP 20, 1018 (1965).
86. **T. Matsubara.**
A new approach to quantum statistical mechanics.
Progress of theoretical physics 14, 351 (1955).
DOI: [10/CXN7H9](https://doi.org/10/CXN7H9)
87. **J.E. Han, R.J. Heary.**
Imaginary-time formulation of steady-state nonequilibrium.
Physical review letters 99, 236808 (2007).
DOI: [10/FNC7NW](https://doi.org/10/FNC7NW)
88. **J.E. Han, A. Dirks, T. Pruschke.**
Imaginary-time quantum many-body theory out of equilibrium.
Physical review B 86, 155130 (2012).
DOI: [10/GFGRRH](https://doi.org/10/GFGRRH)
89. **A. Cottet, D. Huertas-Hernando, W. Belzig, Y.V. Nazarov.**
Erratum: Spin-dependent boundary conditions for
isotropic superconducting Green's functions.
Physical review B 83, 139901 (2011).
DOI: [10/DQ7MJD](https://doi.org/10/DQ7MJD)
90. **E. Wigner.**
On the quantum correction for thermodynamic equilibrium.
Physical review 40, 749 (1932).
DOI: [10/BMW7JH](https://doi.org/10/BMW7JH)
91. **G. Eilenberger.**
Transformation of Gorkov's equation for type II
superconductors into transport-like equations.
Zeitschrift für physik A 214, 195 (1968).
DOI: [10/BHJKHR](https://doi.org/10/BHJKHR)
92. **W.L. McMillan.**
Transition temperature of strong-coupled superconductors.
Physical review 167, 331 (1968).
DOI: [10/CHBMDQ](https://doi.org/10/CHBMDQ)

93. **T.S. Khaire, W.P. Pratt, N.O. Birge.**
Critical current behavior in Josephson junctions with the weak ferromagnet PdNi. Physical review B 79, 094523 (2009).
DOI: [10/BCM2SW](https://doi.org/10/BCM2SW)
94. **H.G. Hugdal, J. Linder, S.H. Jacobsen.**
Quasiclassical theory for the superconducting proximity effect in Dirac materials. Physical review B 95, 235403 (2017).
DOI: [10/GFGR49](https://doi.org/10/GFGR49)
95. **Y.V. Nazarov.**
Novel circuit theory of Andreev reflection. Superlattices and microstructures 25, 1221 (1999).
DOI: [10/FMH3ZH](https://doi.org/10/FMH3ZH)
96. **I.V. Tokatly.**
Usadel equation in the presence of intrinsic spin-orbit coupling. Physical review B 96, 060502 (2017).
DOI: [10/GC5PHJ](https://doi.org/10/GC5PHJ)
97. **R. Raimondi, P. Schwab, C. Gorini, G. Vignale.**
Spin-orbit interaction in a two-dimensional electron gas. Annalen der physik 524, 153 (2012).
DOI: [10/C5DVNN](https://doi.org/10/C5DVNN)
98. **K.D. Usadel.**
Generalized diffusion equation for superconducting alloys. Physical review letters 25, 507 (1970).
DOI: [10/DW7KTT](https://doi.org/10/DW7KTT)
99. **F.S. Bergeret, M. Silaev, P. Virtanen, T.T. Heikkilä.**
Colloquium: Nonequilibrium effects in superconductors with a spin-splitting field. Reviews of modern physics 90, 041001 (2018).
DOI: [10/GFC3ZQ](https://doi.org/10/GFC3ZQ)
100. **A. Schmid, G. Schön.**
Linearized kinetic equations and relaxation processes of a superconductor near T_c . Journal of low temperature physics 20, 207 (1975).
DOI: [10/DR6MPQ](https://doi.org/10/DR6MPQ)

101. **J.P. Morten.**
Spin and charge transport in dirty superconductors.
Master thesis (NTNU, Trondheim, Norway, 2003).
102. **A. Altland, B.D. Simons, D.T. Semchuk.**
Field theory of mesoscopic fluctuations
in superconductor–normal-metal systems.
Advances in physics 49, 321 (2000).
DOI: [10/C68P59](https://doi.org/10.1080/0003681990883959)
103. **F. Herman, R. Hlubina.**
Thermodynamic properties of Dynes superconductors.
Physical review B 97, 014517 (2018).
DOI: [10/GC4M2M](https://doi.org/10.1103/PhysRevB.97.014517)
104. **R.C. Dynes, V. Narayanamurti, J.P. Garno.**
Direct measurement of quasiparticle-lifetime
broadening in a strong-coupled superconductor.
Physical review letters 41, 1509 (1978).
DOI: [10/DDKBD6](https://doi.org/10.1103/PhysRevLett.41.1509)
105. **L.N. Bulaevskii, A.I. Buzdin, M.L. Kulić, S.V. Panjukov.**
Coexistence of superconductivity and magnetism.
Advances in physics 34, 175 (1985).
DOI: [10/CDPWPV](https://doi.org/10.1080/0003681850883959)
106. **M. Silaev, P. Virtanen, F.S. Bergeret, T.T. Heikkilä.**
Long-range spin accumulation from heat injection in
mesoscopic superconductors with Zeeman splitting.
Physical review letters 114, 167002 (2015).
DOI: [10/F3TD6B](https://doi.org/10.1103/PhysRevLett.114.167002)
107. **R. Meservey, P.M. Tedrow.**
Spin-polarized electron tunneling.
Physics reports 238, 173 (1994).
DOI: [10/CBTZBM](https://doi.org/10.1016/0370-1571(94)90001-9)
108. **L. Yu.**
Bound state in superconductors with paramagnetic impurities.
Acta physica sinica 21 (1965).

109. **A.I. Rusinov.**
Superconductivity near a paramagnetic impurity.
Soviet physics JETP letters 9, 85 (1969).
110. **H. Shiba.**
Classical spins in superconductors.
Progress of theoretical physics 40, 435 (1968).
DOI: [10/C9JK3K](https://doi.org/10.1093/ptp/40.4.435)
111. **M.S. Kalenkov, A.D. Zaikin, L.S. Kuzmin.**
Theory of a large thermoelectric effect in
superconductors doped with magnetic impurities.
Physical review letters 109, 147004 (2012).
DOI: [10/F24W2P](https://doi.org/10.1103/PhysRevLett.109.147004)
112. **J. Linder, T. Yokoyama, A. Sudbø.**
Role of interface transparency and spin-dependent scattering in
diffusive ferromagnet/superconductor heterostructures.
Physical review B 77, 174514 (2008).
DOI: [10/CWR5GP](https://doi.org/10.1103/PhysRevB.77.174514)
113. **C. Espedal, P. Lange, S. Sadjina, A.G. Mal'shukov, A. Brataas.**
Spin Hall effect and spin swapping in diffusive superconductors.
Physical review B 95, 054509 (2017).
DOI: [10/GD4VDJ](https://doi.org/10.1103/PhysRevB.95.054509)
114. **I. Gomperud, J. Linder.**
Spin supercurrent and phase-tunable triplet
Cooper pairs via magnetic insulators.
Physical review B 92, 035416 (2015).
DOI: [10/GD84GR](https://doi.org/10.1103/PhysRevB.92.035416)
115. **M. Eschrig, A. Cottet, W. Belzig, J. Linder.**
General boundary conditions for quasiclassical
theory of superconductivity in the diffusive limit.
New journal of physics 17, 083037 (2015).
DOI: [10/GC4M5F](https://doi.org/10.1088/1751-8113/17/8/083037)

116. **P. Machon, M. Eschrig, W. Belzig.**
Nonlocal thermoelectric effects and nonlocal
Onsager relations in a three-terminal proximity-
coupled superconductor–ferromagnet device.
Physical review letters 110, 047002 (2013).
DOI: [10/GC5PG5](https://doi.org/10/GC5PG5)
117. **F.S. Bergeret, A. Verso, A.F. Volkov.**
Electronic transport through ferromagnetic and super-
conducting junctions with spin-filter tunneling barriers.
Physical review B 86, 214516 (2012).
DOI: [10/GC5PG6](https://doi.org/10/GC5PG6)
118. **F.S. Bergeret, A. Verso, A.F. Volkov.**
Spin-polarized Josephson and quasiparticle currents
in superconducting spin-filter tunnel junctions.
Physical review B 86, 060506 (2012).
DOI: [10/GFGTBJ](https://doi.org/10/GFGTBJ)
119. **A. Cottet, D. Huertas-Hernando, W. Belzig, Y.V. Nazarov.**
Spin-dependent boundary conditions for isotropic
superconducting Green’s functions.
Physical review B 80, 184511 (2009).
DOI: [10/FHJMC8](https://doi.org/10/FHJMC8)
120. **A. Cottet.**
Spectroscopy and critical temperature of diffusive superconduct-
ing/ferromagnetic hybrid structures with spin-active interfaces.
Physical review B 76, 224505 (2007).
DOI: [10/FBV93C](https://doi.org/10/FBV93C)
121. **D. Huertas-Hernando, Y.V. Nazarov, W. Belzig.**
Absolute spin-valve effect with superconducting proximity structures.
Physical review letters 88, 047003 (2002).
DOI: [10/C6737B](https://doi.org/10/C6737B)
122. **D. Huertas-Hernando, Y.V. Nazarov, W. Belzig.**
Generalized boundary conditions for the circuit
theory of mesoscopic transport.
ARXIV: [cond-mat/0204116](https://arxiv.org/abs/cond-mat/0204116)

123. **M.Y. Kuprianov, V.F. Lukichev.**
Influence of boundary transparency on the critical current of dirty ss's structures. Soviet physics JETP 67, 1163 (1988).
124. **A. Kamra, A. Rezaei, W. Belzig.**
Spin-splitting induced in a superconductor by an antiferromagnetic insulator.
DOI: [10/GFQ97S](https://doi.org/10/GFQ97S)
125. **A.J. Leggett.**
A theoretical description of the new phases of liquid ^3He . Reviews of modern physics 47, 331 (1975).
DOI: [10/DXSC69](https://doi.org/10/DXSC69)
126. **R. Balian, N.R. Werthamer.**
Superconductivity with pairs in a relative p -wave. Physical review 131, 1553 (1963).
DOI: [10/CJX5MH](https://doi.org/10/CJX5MH)
127. **A. Larkin, A.A. Varlamov.**
Theory of fluctuations in superconductors (2005).
ISBN: 978-0-19-852815-9
128. **R. Raimondi, G. Savona, P. Schwab, T. Lück.**
Electronic thermal conductivity of disordered metals. Physical review B 70, 155109 (2004).
DOI: [10/DN2FRX](https://doi.org/10/DN2FRX)
129. **L.D. Landau, E.M. Lifshitz.**
The classical theory of fields (2009).
ISBN: 978-0-7506-2768-9
130. **S.V. Bakurskiy, N.V. Klenov, I.I. Soloviev, et al.**
Theory of supercurrent transport in SIsFS Josephson junctions. Physical review B 88, 144519 (2013).
DOI: [10/GFHWMW](https://doi.org/10/GFHWMW)
131. **J. Romijn, T.M. Klapwijk, M.J. Renne, J.E. Mooij.**
Critical pair-breaking current in superconducting aluminum strips far below T_c . Physical review B 26, 3648 (1982).
DOI: [10/FSVSNK](https://doi.org/10/FSVSNK)

132. **J.P. Morten, A. Brataas, W. Belzig.**
Spin transport in diffusive superconductors.
Physical review B 70, 212508 (2004).
DOI: [10/BZMZ55](https://doi.org/10/BZMZ55)
133. **N. Schopohl.**
Transformation of the Eilenberger equations of superconductivity to a scalar Riccati equation.
ARXIV: [cond-mat/9804064](https://arxiv.org/abs/cond-mat/9804064)
134. **M. Eschrig.**
Distribution functions in nonequilibrium theory of superconductivity and Andreev spectroscopy in unconventional superconductors.
Physical review B 61, 9061 (2000).
DOI: [10/DXT85Q](https://doi.org/10/DXT85Q)
135. **M. Eschrig.**
Scattering problem in nonequilibrium quasiclassical theory of metals and superconductors.
Physical review B 80, 134511 (2009).
DOI: [10/DCKZJX](https://doi.org/10/DCKZJX)
136. **W.T. Reid.**
Riccati differential equations (2014).
ISBN: 978-0-08-095595-7
137. **I.V. Bobkova, A.M. Bobkov.**
Long-range spin imbalance in mesoscopic superconductors under Zeeman splitting.
JETP letters 101, 118 (2015).
DOI: [10/F67Z3Q](https://doi.org/10/F67Z3Q)
138. **F. Aikebaier, M.A. Silaev, T.T. Heikkilä.**
Supercurrent-induced charge–spin conversion in spin-split superconductors.
Physical review B 98, 024516 (2018).
DOI: [10/GFB34V](https://doi.org/10/GFB34V)

139. **S.H. Jacobsen, J. Linder.**
Quantum kinetic equations and anomalous nonequilibrium Cooper-pair spin accumulation in Rashba wires with Zeeman splitting. *Physical review B* 96, 134513 (2017).
DOI: [10/GFHWR2](https://doi.org/10/GFHWR2)
140. **G.E.W. Bauer, E. Saitoh, B.J. van Wees.**
Spin caloritronics. *Nature materials* 11, 391 (2012).
DOI: [10/GC4PJJ](https://doi.org/10/GC4PJJ)
141. **I.V. Bobkova, A.M. Bobkov.**
Long-range proximity effect for opposite-spin pairs in superconductor–ferromagnet heterostructures under nonequilibrium quasiparticle distribution. *Physical review letters* 108, 197002 (2012).
DOI: [10/GDQBMF](https://doi.org/10/GDQBMF)
142. **I.V. Bobkova, A.M. Bobkov.**
Recovering of superconductivity in s/F bilayers under spin-dependent nonequilibrium quasiparticle distribution. *JETP letters* 101, 407 (2015).
DOI: [10/F7FJT7](https://doi.org/10/F7FJT7)
143. **T. Wakamura, N. Hasegawa, K. Ohnishi, Y. Niimi, Y. Otani.**
Spin injection into a superconductor with strong spin–orbit coupling. *Physical review letters* 112, 036602 (2014).
DOI: [10/GD84DP](https://doi.org/10/GD84DP)
144. **M. Amundsen, J. Linder.**
General solution of 2D and 3D superconducting quasiclassical systems. *Scientific reports* 6, 22765 (2016).
DOI: [10/F8DMPK](https://doi.org/10/F8DMPK)
145. **J. Solomon.**
Numerical algorithms (2015).
ISBN: 978-1-4822-5188-3
146. **L. Shampine, P. Muir, H. Xu.**
A user-friendly Fortran BVP solver. *Journal of numerical analysis, industrial and applied mathematics* 1, 201 (2006).

147. **J.J. Boisvert, P.H. Muir, R.J. Spiteri.**
A numerical study of global error and defect control schemes for BVODES.
Technical report (SMU, Halifax, Canada, 2012).
148. **J.J. Boisvert, P.H. Muir, R.J. Spiteri.**
A Runge–Kutta BVODE solver with global error and defect control.
ACM transactions on mathematical software 39, 11 (2013).
DOI: [10/GFJ36F](https://doi.org/10/GFJ36F)
149. **I. Snyman, Y.V. Nazarov.**
Bistability in voltage-biased normal-metal/insulator/superconductor/insulator/normal-metal structures.
Physical review B 79, 014510 (2009).
DOI: [10/C5X87F](https://doi.org/10/C5X87F)
150. **I.V. Bobkova, A.M. Bobkov.**
Bistable state in superconductor/ferromagnet heterostructures.
Physical review B 89, 224501 (2014).
DOI: [10/GC4JJ7](https://doi.org/10/GC4JJ7)
151. **S.V. Bakurskiy, V.I. Filippov, V.I. Ruzhickiy, et al.**
Current–phase relations in SIsFS junctions
in the vicinity of $0-\pi$ transition.
Physical review B 95, 094522 (2017).
DOI: [10/GC4PKZ](https://doi.org/10/GC4PKZ)
152. **C. Yuksel, S. Schaefer, J. Keyser.**
Parameterization and applications of Catmull–Rom curves.
Computer-aided design 43, 747 (2011).
DOI: [10/FWVZVK](https://doi.org/10/FWVZVK)
153. **J.C. Slonczewski.**
Conductance and exchange coupling of two
ferromagnets separated by a tunneling barrier.
Physical review B 39, 6995 (1989).
DOI: [10/DWBBN2](https://doi.org/10/DWBBN2)
154. **J.F. Steffensen.**
Remarks on iteration.
Scandinavian actuarial journal 1933, 64 (1933).
DOI: [10/FX5ZBR](https://doi.org/10/FX5ZBR)

155. **M. Petković.**
 Multipoint methods for solving nonlinear equations (2013).
 ISBN: 978-0-12-397013-8
156. **R. Haelterman, A. Bogaers, J. Degroote.**
 A comparison of different quasi-Newton acceleration
 methods for partitioned multi-physics codes.
 Transactions on engineering technologies, ch. 11 (2018).
 DOI: 10/GFJ6CH
157. **D.J. Griffiths.**
 Introduction to quantum mechanics (2005).
 ISBN: 978-0-13-111892-8
158. **A.A. Abrikosov.**
 The magnetic properties of superconducting alloys.
 Journal of physics and chemistry of solids 2, 199 (1957).
 DOI: 10/D6N6T4
159. **J.C. Cuevas, F.S. Bergeret.**
 Magnetic interference patterns and vortices in diffusive SNS junctions.
 Physical review letters 99, 217002 (2007).
 DOI: 10/B54GMR
160. **D. Roditchev, C. Brun, L. Serrier-Garcia, et al.**
 Direct observation of Josephson vortex cores.
 Nature physics 11, 332 (2015).
 DOI: 10/GFKN4C
161. **G. Bihlmayer, O. Rader, R. Winkler.**
 Focus on the Rashba effect.
 New journal of physics 17, 050202 (2015).
 DOI: 10/GFKWZZ
162. **K.V. Shanavas, Z.S. Popović, S. Satpathy.**
 Theoretical model for Rashba spin-orbit interaction in *d* electrons.
 Physical review B 90, 165108 (2014).
 DOI: 10/GFKWX9
163. **G. Dresselhaus.**
 Spin-orbit coupling effects in zinc blende structures.
 Physical review 100, 580 (1955).
 DOI: 10/BF2SH3

164. **B.A. Bernevig, S.-C. Zhang.**
Spin splitting and spin current in strained bulk semiconductors.
Physical review B 72, 115204 (2005).
DOI: [10/CW6B4K](https://doi.org/10.1103/PhysRevB.72.115204)
165. **B.M. Norman, C.J. Trowbridge, J. Stephens, et al.**
Mapping spin-orbit splitting in strained (In,Ga)As epilayers.
Physical review B 82, 081304 (2010).
DOI: [10/BSR3CB](https://doi.org/10.1103/PhysRevB.82.081304)
166. **M.D. Studer.**
Spin manipulation in two-dimensional electron and hole gases.
Doctoral thesis (ETH, Zürich, Switzerland, 2010).
DOI: [10/GFKW5R](https://doi.org/10.3929/ethz-b-000145443)
167. **P. Gentile, M. Cuoco, C. Ortix.**
Curvature-induced Rashba spin-orbit interaction
in strain-driven nanostructures.
SPIN 03, 1340002 (2013).
DOI: [10/GFRD43](https://doi.org/10.1002/spin.201300002)
168. **Z.-J. Ying, M. Cuoco, C. Ortix, P. Gentile.**
Tuning pairing amplitude and spin-triplet texture
by curving superconducting nanostructures.
Physical review B 96, 100506 (2017).
DOI: [10/GFRD5B](https://doi.org/10.1103/PhysRevB.96.100506)
169. **S. Mironov, A. Buzdin.**
Triplet proximity effect in superconducting
heterostructures with a half-metallic layer.
Physical review B 92, 184506 (2015).
DOI: [10/GFKPQN](https://doi.org/10.1103/PhysRevB.92.184506)
170. **K. Halterman, M. Alidoust.**
Half-metallic superconducting triplet spin valve.
Physical review B 94, 064503 (2016).
DOI: [10/GFKPQM](https://doi.org/10.1103/PhysRevB.94.064503)
171. **N. Kokubo, S. Okayasu, A. Kanda, B. Shinozaki.**
Scanning SQUID microscope study of vortex polygons and shells
in weak-pinning disks of an amorphous superconducting film.
Physical review B 82, 014501 (2010).
DOI: [10/FVZNGZ](https://doi.org/10.1103/PhysRevB.82.014501)

172. **G.J.C. van Baarle, A.M. Troianovski, T. Nishizaki, et al.**
Imaging of vortex configurations in thin films by scanning-tunneling microscopy. Applied physics letters 82, 1081 (2003).
DOI: [10/D7BWHS](https://doi.org/10.1063/1.1548885)
173. **A. Moor, A.F. Volkov, K.B. Efetov.**
Inhomogeneous state in nonequilibrium superconductor/normal-metal tunnel structures. Physical review B 80, 054516 (2009).
DOI: [10/B5KDR5](https://doi.org/10.1103/PhysRevB.80.054516)
174. **J.J.A. Baselmans, A.F. Morpurgo, B.J. van Wees, et al.**
Reversing the direction of the supercurrent in a controllable Josephson junction. Nature 397, 43 (1999).
DOI: [10/CWRTDV](https://doi.org/10.1038/17701)
175. **F.K. Wilhelm, G. Schön, A.D. Zaikin.**
Mesoscopic superconducting-normal metal-superconducting transistor. Physical review letters 81, 1682 (1998).
DOI: [10/FHSK4H](https://doi.org/10.1103/PhysRevLett.81.1682)
176. **A.F. Volkov.**
New phenomena in Josephson SINIS junctions. Physical review letters 74, 4730 (1995).
DOI: [10/C7V95D](https://doi.org/10.1103/PhysRevLett.74.4730)
177. **F. Korschelle, A. Buzdin.**
Magnetic moment manipulation by a Josephson current. Physical review letters 102, 017001 (2009).
DOI: [10/BKKNQS](https://doi.org/10.1103/PhysRevLett.102.017001)
178. **A. Romano, P. Gentile, C. Noce, I. Vekhter, M. Cuoco.**
Control of magnetism in singlet-triplet superconducting heterostructures. Physical review B 93, 014510 (2016).
DOI: [10/GFRDZ2](https://doi.org/10.1103/PhysRevB.93.014510)

179. **S.H. Jacobsen, J. Linder.**
Giant triplet proximity effect in π -biased Josephson junctions with spin-orbit coupling. Physical review B 92, 024501 (2015).
DOI: [10/GFKX5C](https://doi.org/10.1073/pnas.1511151112)
180. **L. Bégon-Lours, V. Rouco, A. Sander, et al.**
High-temperature-superconducting weak link defined by the ferroelectric field effect. Physical review applied 7, 064015 (2017).
DOI: [10/GBPHVG](https://doi.org/10.1073/pnas.1511151112)
181. **S.H. Jacobsen, I. Kulagina, J. Linder.**
Controlling superconducting spin flow with spin-flip immunity using a single homogeneous ferromagnet. Scientific reports 6, 23926 (2016).
DOI: [10/F8GSS4](https://doi.org/10.1073/pnas.1511151112)
182. **R.C. Dynes, T.A. Fulton.**
Supercurrent density distribution in Josephson junctions. Physical review B 3, 3015 (1971).
DOI: [10/BC8VFC](https://doi.org/10.1073/pnas.1511151112)

I

Reference

S.H. Jacobsen, [J.A. Ouassou](#), J. Linder.
Superconducting order in magnetic heterostructures.
Advanced magnetic and optical materials, ch. 1 (2016).
ISBN: 978-1-119-24196-6
DOI: 10/GFGR9J

Contributions

All authors contributed to the initial discussion and planning behind the book chapter. SHJ then wrote most of the initial draft. All authors contributed to the subsequent revision and proof-reading of the draft.

Comments

This publication appeared as the first chapter of the textbook *Advanced magnetic and optical materials*, and was intended as an introduction to superconducting spintronics for the magnetism community. The book chapter is reproduced with permission from Scrivener Publishing.

Superconducting Order in Magnetic Heterostructures

Sol H. Jacobsen, Jabir Ali Ouassou and Jacob Linder*

*Department of Physics, NTNU, Norwegian University of Science and
Technology, Trondheim, Norway*

Abstract

In the rapidly developing field of spintronics, information is encoded and processed in the form of quantum spins. Although phenomena such as the giant magnetoresistance effect and spin-transfer torque have already found use in commercialized devices, two main challenges remaining in spintronic circuits based on electron transport are Joule heating and short decay lengths due to spin-flip scattering. The incorporation of superconducting elements into spintronic architectures has recently emerged as a potential solution to this problem. Recent advances in understanding the underlying physics of the interface between superconductors and ferromagnets has revealed a wealth of new features that can be enhanced and controlled to create improved spintronic devices. In this chapter, we present an introduction to the superconducting proximity effect in magnetic materials that opens the tantalizing prospect of combining the dissipationless transport offered by superconductors with the spin-polarized order existing in magnetic thin-film heterostructures. This includes an outline of theoretical frameworks and conventions in the field, as well as a discussion of some key experimental and theoretical advances that may indicate where the field is heading.

Keywords: Superconducting spintronics, proximity effect, ferromagnetism

1.1 Introduction

In the rapidly developing field of *spintronics*, information is encoded and processed in the form of quantum spins – either in place of, or in conjunction

*Corresponding author: jacob.linder@ntnu.no

with, the traditional charge-based processing schemes. This has high potential with respect to computational processing, both in terms of time and energy efficiency, as well as significantly increased stability and longer coherence times than conventional electronic components. Although several spintronic architectures have already been widely adopted, *e.g.* in hard drives and random access memory based on the giant magnetoresistive effect (GMR) [1, 2], two main challenges in spintronic circuits based on electron transport are Joule heating and short decay lengths due to spin-flip scattering. The incorporation of superconducting elements into existing spintronic architectures has recently emerged as a potential solution to this problem [3]. Recent advances in understanding the underlying physics of the interface between superconductors and ferromagnets has revealed a wealth of new features that can be enhanced and controlled to create improved spintronic devices. In this chapter, we present an introduction to the superconducting proximity effect that opens the tantalizing prospect of combining the dissipationless transport offered by superconductors with the spin-polarized order existing in magnetic thin-film heterostructures. This includes an outline of theoretical frameworks and conventions in the field, as well as a discussion of some key experimental and theoretical advances that may indicate where the field is heading.

Spin-polarized currents are typically generated by passing an electric current through a ferromagnet, such that the magnetization in the ferromagnet acts to align the electron spins. Spintronic nanostructures are designed as a series of thin-film layers of normal-metal and ferromagnetic elements, which can be incorporated into conventional semiconductor-based systems. Emergent features of such spintronic devices can then be used to harness and control aspects of the device, for which GMR provides an exemplary case. GMR manifests as a change in the electrical resistance according to the relative magnetization directions of adjacent ferromagnetic layers: the resistance is low for parallel alignment and high for anti-parallel alignment. This effect has been implemented in a wide variety of experimental structures, an important example being *spin valves* [4, 5], which switch an electric current on or off based on a magnetic input signal. Experimentally, spin valves consist of two ferromagnetic layers and an interstitial normal metal. The coercivity of one ferromagnetic layer can be enhanced due to proximity with an antiferromagnetic base layer, meaning that the application of an external magnetic field can be used to control the magnetization of the other ferromagnet. Albert Fert and Peter Grünberg shared the 2007 Nobel Prize in Physics for the discovery of the GMR effect.

In order to utilize the GMR effect, one needs a way to alter the magnetization direction of a ferromagnet. Spin-polarized electric currents

can induce magnetization dynamics via the so-called spin-transfer torque effect [6, 7], but this typically requires very large current densities of order 10^6 A/cm². This causes excessive Joule heating and ultimately destroys the properties of the thin-film structure. Recent investigations of the proximity effect, where the properties of adjacent materials leak across the interfacial barrier, have indicated that it will be possible to harness the dissipationless currents offered by superconductors to overcome the problem of excessive heating by making these supercurrents spin-polarized [3].

Superconductivity was discovered as early as 1911, when Heike Kamerlingh Onnes observed that the electrical resistivity of certain materials vanished abruptly at cryogenic temperatures [8]. Kamerlingh Onnes received the Nobel Prize in Physics in 1913 for this discovery. The temperature at which the transition to zero resistivity occurs is called the *critical temperature* (T_c) of the material, and as a material transitions into this superconducting state it displays a second characteristic feature: all magnetic fields are expelled from the material. This was discovered in 1933 by Walther Meissner and Robert Ochsenfeld [9], and subsequently became known as the *Meissner effect*.

Historically, experiments on spin transport in superconductors [10–13] predated experiments with non-superconducting materials [14]. Now that the advantage of superconducting elements in spintronics is becoming increasingly evident, the field is re-emerging as a highly active avenue of research. Recent results have exposed the tremendous potential offered by superconducting spintronics, with experiments demonstrating not only infinite magnetoresistance [15], but also strongly enhanced quasiparticle spin lifetimes [16], spin relaxation lengths [17], spin Hall effects [18], and thermoelectric currents [19] compared with non-superconducting structures. The enhancement is truly monumental: the magnitude of the superconducting spin Hall effect, for example, exceeded its non-superconducting equivalent by a factor of more than two thousand, as we will discuss further in Section 1.4.2.

This chapter is intended to provide an introduction to superconductivity in magnetic thin-film heterostructures for readers who are primarily familiar with magnetic materials. We give only a peripheral mention to examples of *bulk coexistence* of magnetic and superconducting order, as seen in certain heavy-fermion compounds, focusing instead on induced superconductivity via the proximity effect. We will explain the underlying physics and introduce the most commonly used approaches, notation and conventions, before discussing key experimental and theoretical advances and speculating on where the field is heading. The chapter is *not* intended to be a comprehensive review of the field; instead, we refer readers to the bibliography to gain a more complete overview.

In Section 1.2, we provide an introduction to superconductivity and the proximity effect in magnetic materials, and discuss the process of singlet-triplet conversion and typical experimental signatures of the proximity effect. In Section 1.3, we provide a brief introduction to the so-called *quasiclassical theory*, which is a useful theoretical framework with which one can address a vast number of physical phenomena that occur in superconductor/ferromagnet hybrid structures, and we include explanations of the different parametrizations and conventions that populate the field. In Section 1.4 we consider the frontier of current experimental research, providing first an introduction to the techniques and materials most readily available in the laboratory setting before discussing recent experimental breakthroughs in superconducting spintronics. In Section 1.5 we discuss novel predictions and speculate about future developments and technological applications before concluding in Section 1.6.

1.2 Fundamental Physics

In this section we will present a brief introduction to superconductivity, with emphasis on how superconducting correlations can manifest in other materials near an interface via the proximity effect. We give particular weight to the differences between manifestation in ferromagnetic materials compared with normal metals. We discuss the process of converting between different superconductive species, *i.e.* singlet-triplet conversion, and sources thereof, and outline the broadly applicable experimental signatures to provide an intuitive introduction to the interaction before more details are provided in the subsequent sections.

1.2.1 The Superconducting Gap

Superconductors are often categorized as conventional or unconventional, where *conventional superconductors* refer to materials that can be described fully by the Bardeen–Cooper–Schrieffer (BCS) theory [20], the Bogoliubov theory [21] and minor extensions thereof. These have an *s*-wave pairing symmetry, *i.e.* the order parameter is spherically symmetric in momentum space, and typically manifest only at very low temperatures at atmospheric pressure.¹ There are several common elemental superconductors of this kind. For instance, tin (Sn), aluminium (Al), and lead (Pb) all have critical

¹ At higher pressures, it is possible to increase the critical temperature of conventional superconductors significantly, *e.g.* the recent world record of 203 K at 150 GPa [22].

temperatures T_c in the range 0.4–7.2 K. The critical temperature is often higher in compounds and alloys compared to their constituent elements. For example, elemental titanium (Ti) and niobium (Nb) have critical temperatures of 0.4 K and 9.2 K, respectively, while the niobium-titanium alloys have critical temperatures of up to 11 K. At atmospheric pressures, the current record for highest critical temperature in a conventional bulk superconductor is 39 K for magnesium diboride (MgB_2) [23].

In the late 1970s, an unconventional superconductor dominated by d -wave pairing instead of the conventional s -wave pairing was discovered (see Figure 1.1). This turned out to be a class of materials known as high-temperature superconductors, and Johannes G. Bednorz and Karl A. Müller shared the 1987 Nobel Prize in Physics for the discovery of the first of many high-temperature cuprate superconductors [24]. Although this is a highly active research branch, a major restriction in their implementation is the requirement for extreme sample purity imposed by the d -wave pairing. Due to the prevalence and natural abundance of conventional singlet s -wave superconductors which do not suffer this restriction, it is highly desirable to use these as superconductive sources in spintronics for immediate application, and for the remainder of the chapter we shall primarily consider such sources.

Conventional superconductivity is caused by electron-phonon interactions, *i.e.* a weak coupling between the conduction electrons and the lattice vibrations of the material. This coupling distorts the lattice and causes a long-range attraction between electrons. This can therefore lead to a pair of electrons having lower energy than the Fermi energy, meaning these

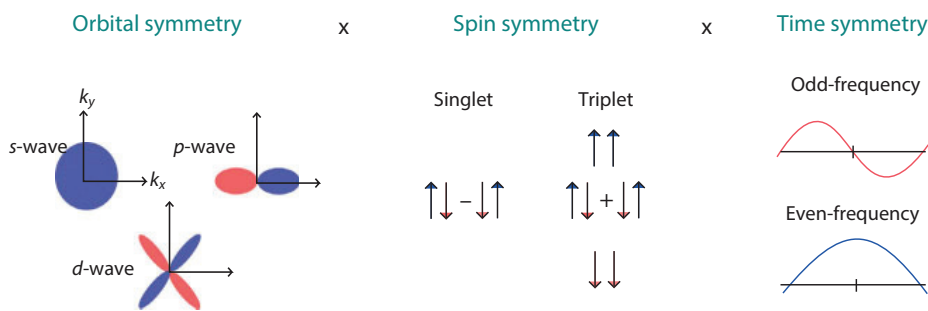


Figure 1.1 The possible symmetry combinations of a superconducting order parameter Δ . The total Cooper pair wave function must in general be antisymmetric at equal times in order to satisfy the Pauli principle, while the particular combination of underlying symmetries governs the properties and class of superconductor. The axis for the curves displaying the two types of time-symmetries (even and odd frequency) is *frequency*, essentially obtained by Fourier-transforming the relative time-coordinate $t = t_1 - t_2$ for electrons 1 and 2 in the Cooper pair.

two electrons become paired as long as they maintain the lower energy state. Since the pairing energy is typically very small, the pairs are easily destroyed by thermal lattice vibrations, which is why the materials must be cooled far below room temperature to exhibit the effect. The quasiparticle pairing of two fermions is called a Cooper pair, after Leon N. Cooper [25], and, since the range of the pairing effect far exceeds the interelectron distance, the distortion typically leads to the creation of a high number of pairs within the same volume. Individual pairs easily become unpaired due to the low pairing energy, but a new pair is just as easily created; it is the *net number* of pairs which is of importance for superconductivity, not the persistence of individual pairs over time.

The cumulative effect of many Cooper pairs in a material is to open up a gap in the continuous energy spectrum of possible electron states. This gap in the density of states means that any excitations with energies that fall within that gap, *e.g.* typical electron scattering, are forbidden. Materials in their superconducting state exhibit dissipationless charge flow precisely because these energy states are forbidden, since electron scattering is the microscopic origin of electrical resistance, and because the Cooper pairs are quantum mechanically coherent. The gap is by itself not sufficient to create superconductivity: one also needs phase coherence, as known from studies of the pseudogap phase in the high- T_c cuprates [26]. The energy threshold that delineates the gap is typically denoted by the norm $|\Delta| = \Delta_0$, which is known as the bulk *superconducting energy gap*, *i.e.* one that has not been modified due to for instance the restricted geometry of a sample or a proximity to non-superconducting materials. Note that it is nevertheless not possible to run an arbitrarily large dissipationless current through superconductors – beyond a so-called *critical current*, the current again becomes resistive.

The electron-phonon interaction and appearance of the superconducting gap are encapsulated in the mean-field Hamiltonian [20]

$$H = - \int d^3x \left[\Delta(\mathbf{x}, t) \psi_{\downarrow}^{\dagger}(\mathbf{x}, t) \psi_{\uparrow}^{\dagger}(\mathbf{x}, t) + \Delta^*(\mathbf{x}, t) \psi_{\uparrow}(\mathbf{x}, t) \psi_{\downarrow}(\mathbf{x}, t) \right]. \quad (1.1)$$

Here the operators $\psi_{\sigma}^{\dagger}(\mathbf{x}, t)$ and $\psi_{\sigma}(\mathbf{x}, t)$ create and annihilate electrons with σ spin at position \mathbf{x} and time t , respectively, and the mean-field is defined as

$$\Delta(\mathbf{x}, t) \equiv |\Delta(\mathbf{x}, t)| e^{i\varphi(\mathbf{x}, t)} \equiv \lambda \langle \psi_{\uparrow}(\mathbf{x}, t) \psi_{\downarrow}(\mathbf{x}, t) \rangle, \quad (1.2)$$

where $\lambda > 0$ is the effective coupling constant of the electron-phonon interaction. The superconducting phase φ may be removed by a U(1) gauge transformation to a gauge where Δ is real. In that case, the superconducting

phase only becomes relevant insofar as a material is affected by relative phase differences, *e.g.* due to interference between multiple superconducting elements. For a more complete introduction to superconductivity, see *e.g.* the textbook by Tinkham [27] or Sudbø and Fossheim [28].

According to Eq. (1.2), we see that the superconducting order parameter Δ originates from a finite expectation value of a two-fermion operator. As a result, the Pauli principle places restrictions on which symmetries Δ can have, as illustrated in Figure 1.1. Conventional superconductors would in this scheme be characterized as *s*-wave (even parity under exchange of spatial coordinates), spin-singlet (odd under exchange of spin coordinates), even-frequency (even under exchange of time-coordinates). This satisfies the Pauli principle at equal times of electron 1 and 2 in the Cooper pair ($t_1 = t_2$). However, as indicated in Figure 1.1 there exist other combinations. For instance, it is possible to have a spin-triplet (even under exchange of spin-coordinates) and *s*-wave order parameter if it is antisymmetric in time, meaning it vanishes when $t_1 = t_2$ [29]. This corresponds to a strong retardation effect in the correlation function of the electrons. When the order parameter is restricted to having *s*-wave symmetry in order to survive the frequent impurity scattering, which effectively leads to an averaging over the Fermi surface, it is precisely this kind of odd-frequency triplet pairing that is realized in diffusive superconductor/ferromagnet (SF) structures.

1.2.2 The Proximity Effect

By *proximity effect*, we refer to the processes by which properties of adjacent materials diffuse into one another across their mutual interface, creating a region with properties derived from both materials. In SF hybrid structures, the superconductive proximity effect therefore concerns the leakage of superconducting correlations into the ferromagnet. As well as inducing superconducting correlations in the ferromagnet, the drainage of correlations from the superconductor diminishes its superconducting properties. Furthermore, the ferromagnet may also induce magnetic order in the superconductor close to its interface. The presence of magnetic impurities causes spin-flip scattering of the constituent electrons in individual Cooper pairs, thus further suppressing the superconducting properties. The combined effect of drainage and induced magnetic order in the superconductor is called the *inverse proximity effect*, with *proximity effect* typically denoting the effect of the superconductor on the ferromagnet only. Conversely, when both effects are considered, one may refer to this as the *full proximity effect*.

In this chapter we will primarily be examining the superconductive proximity effect, but note that the inverse proximity effect typically acts to lower the superconducting gap from its bulk value, especially near the interface. When considering proximity structures where the superconductive layer is very large compared to the superconducting correlation length, and the temperature is far below the critical temperature of the hybrid structure, the inverse proximity effect can usually be neglected. In this case, to calculate physical features of the ferromagnet affected by superconductivity, such as the modification to the density of states, it is sufficient to use the bulk superconducting gap at the interface. However, ignoring the inverse proximity effect is only legitimate when it is very weak, and that is not the case in *e.g.* spin valves with thin superconducting regions of size similar to the superconducting coherence length. For such systems, the inverse proximity effect decreases the superconducting gap throughout the entire proximity structure, and therefore needs to be included in a full, self-consistent manner.

1.2.2.1 Singlet-triplet Conversion

Singlet superconducting correlations in realistic diffusive ferromagnets typically decay over distances of the order of the ferromagnetic coherence length $\xi_F = \sqrt{D/h}$, where D is the diffusion coefficient and h is the exchange strength of the ferromagnet [30]. This is because the exchange field causes the misaligned spins of the singlet Cooper pair to be energetically unequal and therefore destroys the correlation: the coherence is lost due to a difference in the phase accumulated by electrons with spin-up (\uparrow) and spin-down (\downarrow) as they propagate into the ferromagnet. The Cooper pairs thus acquire a nonzero centre-of-mass momentum, resulting in the so-called FFLO-state (after Fulde, Ferell, Larkin and Ovchinnikov [31, 32]), which is a mixture of the singlet state and the triplet state with zero spin projection along the magnetization. However, for certain configurations the superconducting correlations may instead be carried by triplet spin-pairings with a finite spin projection along the exchange field, rendering them immune to this pair-breaking effect. In this case physical quantities such as the supercurrent will decay over length scales comparable with the much longer correlation length in a normal metal $\xi_N = \sqrt{D/T}$. That is, the decay length is independent of the exchange field and instead limited by the temperature, T . At low temperatures this allows the condensate to penetrate deep into the ferromagnet, and the isolation and enhancement of this feature has been the primary focus for research into superconducting spintronics [3, 33].

Heavy-fermion compounds that display intrinsic coexistence of superconductivity and ferromagnetism garnered significant attention upon their discovery [34, 35], and by now well-established intrinsically triplet-paired superconductors such as the noncentrosymmetric cerium platinum silicon CePt_3Si [36] and the chiral strontium ruthenate Sr_2RuO_4 [37] feature regularly in the scientific literature. These materials have proven difficult to use in thin-film heterostructures for a variety of reasons to be discussed further in Section 1.4.1. They typically suffer from restrictions such as a requirement of very high pressures, exceedingly low critical temperatures (~ 1 K), or that they only superconduct at extreme sample purity because their pairing symmetry is p -wave rather than s -wave, but they are nevertheless interesting candidates for harnessing the long-range triplet pairs [38, 39]. However, it is now well known that in the presence of magnetic inhomogeneities, *i.e.* a spatially varying exchange field, singlet superconducting correlations may be converted into the long-range triplet correlations [40–42]. These magnetic inhomogeneities may arise from *e.g.* spin-polarized interfaces, multiple magnetic layers and conical-field magnets such as holmium (Ho), and enables the generation of triplet superconductivity from the wide variety of available singlet superconductors.

The conversion from singlet pairing to spin-polarized triplet pairing can be understood as a two-step process. In the first step, spin-mixing [42] occurs from for instance spin-dependent scattering at interfaces [43]. This generates the zero spin triplet projection which then coexists with the singlet component. By changing basis, the triplet component with zero spin projection can then be transformed into the triplet components with equal spin and this happens precisely in the presence of magnetic inhomogeneities. Ref. [33] provides a nice introduction to the topic.

Until recently, magnetic inhomogeneities were believed to be the primary source of the singlet-to-long-range-triplet conversion, and correspondingly the majority of research on isolating and enhancing the long-range component focused on such setups [44–55]. However, in very recent developments, it has been shown that intrinsic spin-orbit coupling can also convert the singlet pairs to long-range triplets in a ferromagnet [56, 57]. This has given rise to several novel phenomena including significant effects on the superconducting critical temperature and modification of the electronic density of states [58, 59], and this will be discussed further in Section 1.5.

1.2.2.2 *Experimental Signatures*

Before presenting the underlying theory in more detail below, we will first reinforce the intuitive picture of the superconductive proximity effect by

outlining some typical experimental signatures of the effect and the most general physical principles behind this behaviour.

Andreev Reflection. A central feature of the proximity effect is the process of Andreev reflection [60], which describes the conversion of normal current into supercurrent at a superconducting interface. Incoming electrons with energy $\epsilon < \Delta_0$ cannot be transmitted from the normal metal into the superconductor, as there are no quasiparticle states with this energy in the superconductor. There are then two possibilities: the electron can either be reflected as an electron, or it can be retroreflected as a hole with opposite spin, thereby transmitting a Cooper pair of two electrons into the superconductor in the process. Since the retroreflected hole is phase coherent with the transmitted electrons, the hole will also be phase coherent with the superconducting condensate at large, and can therefore carry information about the superconducting correlations into the normal metal, *i.e.* what we call the proximity effect.

Josephson effect. With two or more superconducting layers, such as in a Josephson junction [61, 62] where two superconducting layers sandwich one or more magnetic or non-magnetic layers, the phase difference ϕ between the superconductors becomes an important factor. Analogously to electron tunneling, the Cooper pairs can tunnel through the interstitial barrier, resulting in a flow of *supercurrent* between the two superconductors. The mechanism of multiple Andreev reflections is an intuitive candidate for explaining this tunneling effect. Consider an electron from the middle layer of a superconductor/normal-metal/superconductor structure that has an energy $\epsilon < \Delta_0$. If this electron hits the interface shared with the right superconductor, a Cooper pair may be transmitted into the superconductor, while the electron is Andreev retroreflected as a hole. The hole may then move through the normal metal to the left interface where it can annihilate a Cooper pair in this superconductor as it becomes Andreev reflected as an electron again. Through the mechanism of multiple Andreev reflections, we see that a Cooper pair can be effectively phase-coherently transmitted through a non-superconducting region from the left to right superconductor. Since the Andreev processes at both interfaces are phase-coherent processes, this tunneling phenomenon is highly sensitive to the relative phases of the two superconducting condensates. The phase difference between the superconductors therefore governs the magnitude of supercurrent that can flow in the junction via the expression $I = I_c \sin \phi$, where I_c is the critical supercurrent above which a feedback resistance enters into the system, reducing the supercurrent to conventional resistive current. Note that while $I_c > 0$ for typical superconductor/normal-metal/superconductor (SNS) structures, and $I_c < 0$ often occurs for superconductor/ferromagnet/

superconductor (SFS) structures, the current-phase relations for Josephson junctions with more involved interstitial regions can take entirely different forms. A review of the current-phase relations for a range of different Josephson junctions was given by Golubov *et al.* [63].

Oscillating superconducting order. In the presence of a large magnetic field, the FFLO state should in certain cases manifest as spatially oscillating superconducting order, but the originally proposed state has never been unambiguously observed experimentally in a superconductor due to its extreme sensitivity to impurity scattering. However, oscillation of both the order parameter and the critical temperature with the thickness of a proximized ferromagnet has been predicted and observed [64] in diffusive SF systems. From this one can infer the existence of a spatially modulated superconducting FFLO state which is also naturally manifested in other physical observables of SF systems, such as the supercurrent, as will be discussed further in Section 1.4.2.

Density of states. The density of states is a measure of the number of available microstates that a system might occupy in a particular energy range and, as discussed above, superconductors display a gap in this continuous spectrum below their critical temperature (see Figure 1.2). The normal state density of states at the Fermi level can be taken to be of the order $N_0 \sim 10^{22}/\text{eV cm}^3$ (see *e.g.* [65]). Compared to a normal metal, the presence of singlet superconductivity will lower the density of states at the Fermi level, while triplet superconductivity will increase the density of states, an effect which can be traced back to the symmetry of the superconducting order parameter [66]. The experimentally measured

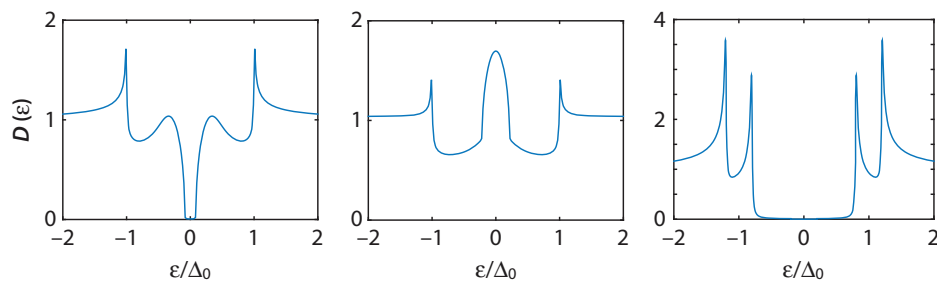


Figure 1.2 *Left panel:* Typical density of states $D(\epsilon)$ vs. quasiparticle energy ϵ measured on the non-superconducting side of an SF bilayer setup when the singlet proximity effect dominates. *Middle panel:* Typical density of states measured on the non-superconducting side of an SF bilayer setup when the triplet proximity effect dominates. *Right panel:* Spin-split density of states in a thin-film superconductor exposed to an in-plane magnetic field. Here shown for a externally induced Zeeman field of $h = 0.3\Delta_0$. In all cases the background density of states of a normal metal is here normalized as $D(\epsilon) = 1$.

enhancement of the density of states in an SF bilayer without spin-orbit coupling in the first experiments probing this effect was about 1% from the normal-state [64, 67]. On the other hand, a large effect on the density of states can be seen for a thin-film superconductor in the presence of a weak in-plane magnetic field. Meservey, Tedrow and Fulde observed a spin splitting in the electronic density of states of a superconductor with two maxima near $\Delta \pm \mu_B H$, where μ_B is the Bohr magneton and H the magnetic field [10] and showed this can be used to determine the polarization of the electron spin in a ferromagnet [13]. Such systems were recently shown to feature strong odd-frequency correlations despite the absence of a zero-energy peak [68].

In the case of a Josephson junction with an interstitial normal metal (N) or even a simpler superconductor/normal metal bilayer, the proximity effect in N manifests as a *minigap*, *i.e.* the N displays a gap $\Delta_N < \Delta_0$ [69]. This minigap extends throughout the N, even featuring on the superconducting side of the contact with the same value, and along with its dependence on phase difference this was recently measured in experiment with great accuracy [70]. When the superconductor phase difference ϕ is increased from 0 to π , the magnitude of the gap decreases. In agreement with theoretical prediction, it closes entirely at $\phi = \pi$ [71].

When the material is magnetic, the oscillating order parameter leads to a corresponding oscillation in the density of states as a function of the penetration distance into the ferromagnet due to the alternating dominance of singlet and triplet pairing [64, 72]. The density of states in the ferromagnet is *inverted* compared with SN structures when the superconducting order parameter is negative (called the π -phase) and triplet pairings dominate. Whenever the Thouless energy is much greater than the exchange field strength one expects to see a spectroscopic minigap, which closes when the resonant condition $\hbar \sim E_g$ is fulfilled, where E_g is the zero-field minigap [73, 74]. Beyond this a zero-energy peak emerges until the field strength overcomes all correlations and the density of states becomes essentially featureless [75]. In contrast to SNS junctions where the phase-difference $\phi \rightarrow \pi$ closes the gap, triplet-dominated SFS junctions can now exhibit a giant proximity effect at $\phi = \pi$, manifesting as a uniform zero-energy peak throughout the magnetic material [59].

Critical temperature. The critical temperature T_c of a superconductor is the temperature at which the superconducting correlations vanish. Mathematically, this means that the superconducting gap Δ drops to zero above the critical temperature. One of the main aspects of the inverse proximity effect is that it reduces the gap in a superconductor at all temperatures, and this in turn causes the gap to drop to zero at lower temperatures

than for a bulk superconductor. Because of this, the critical temperature of a superconductor can be directly manipulated if the inverse proximity effect can be controlled. One prime example of this is the so-called *absolute spin-valve*, which consists of a singlet superconductor sandwiched between two individually controlled ferromagnetic layers. If the ferromagnetic layers are parallel, their magnetic exchange fields add up constructively inside the superconductor. This causes strong pair-breaking and drastically lowers the critical temperature to some value $T_{c,1}$. On the other hand, if the ferromagnetic layers are antiparallel, then their magnetic fields instead partially cancel each other inside the superconductor. The superconducting condensate is thus less disturbed by the presence of magnetic order, resulting in a higher critical temperature $T_{c,2}$. Thus, by keeping the structure at a temperature $T_{c,1} < T < T_{c,2}$, whether the structure is above or below its critical temperature will depend on the relative magnetizations of the two ferromagnets. In other words, by rotating the magnetization of one (soft) ferromagnet while keeping the magnetization of the other (hard) ferromagnet fixed, superconductivity can be toggled on and off in the structure, which corresponds to an infinite GMR effect. This has been experimentally demonstrated in Ref. [15].

1.3 Theoretical Framework

One theoretical approach to examining heterostructures that combine superconducting and ferromagnetic materials is the Bogoliubov–de Gennes formalism [76]. The Bogoliubov–de Gennes equations take the form

$$\begin{pmatrix} H_0 & \Delta(x) \\ \Delta^*(x) & -H_0^* \end{pmatrix} \begin{pmatrix} \phi_e(x) \\ \phi_h(x) \end{pmatrix} = E \begin{pmatrix} \phi_e(x) \\ \phi_h(x) \end{pmatrix}, \quad (1.3)$$

where H_0 is the Hamiltonian of a single electron, including both kinetic energy and all non-superconducting interactions; ϕ_e and ϕ_h are complex wave functions that describe electron-like and hole-like excitations respectively; E is the energy of the excitations; $*$ denotes complex conjugation; and $\Delta(x)$ is a complex field that describes superconductivity. We note that this bears a lot of resemblance to the Schrödinger equation $H_0\phi_e(x) = E\phi_e(x)$ for an electron. The obvious difference is that the corresponding Bogoliubov–de Gennes equation $H_0\phi_e(x) + \Delta(x)\phi_h(x) = E\phi_e(x)$ couples electron-like and hole-like excitations. However, in the non-superconducting limit $\Delta \rightarrow 0$, we see that the Bogoliubov–de Gennes equations reduce to the Schrödinger equations.

In the ballistic limit, there is negligible resistivity due to the lack of scattering. Although seemingly a severe restriction, this can be a suitable limit when the mean free path of the conduction particles, *i.e.* the electrons and holes, is longer than the transporting medium, as can be the case for very pure metal nanowires, for example. The fewer defects there are in the medium, and the lower the temperature at which it is held, the longer the mean free path. However, the introduction of interfaces introduces an inevitable source of scattering due to the mismatch between the crystal structures of the two materials on either side of the interface. Therefore, we will focus primarily on the more widely applicable diffusive regime for the remainder of the chapter.

The Bogoliubov-de Gennes framework can be substantially simplified by making a quasiclassical approximation which in the ballistic limit provides the Eilenberger equation [77], while the diffusive limit is described by the Usadel equation [78]. Refs. [69, 79] review the use of quasiclassical Green's functions in normal-metal/superconductor heterostructures, and in this section we will provide a very brief introduction to quasiclassical theory with an overview of the primary conventions and parameterization regimes that populate the literature. The motivation for including this section is to give the reader an idea of the theoretical “toolbox” that can be used to describe the emergent quantum physics in SF systems.

1.3.1 Quasiclassical Theory

In quantum mechanics, a *Green's function* $G_{\sigma\sigma'}(\mathbf{x}, t; \mathbf{x}', t')$ can usually be thought of as a probability amplitude.² More precisely, it is a measure of the probability that a particle that was at position \mathbf{x}' with spin σ' at time t' , will appear at some other position \mathbf{x} with spin σ at some later time t . In quasiclassical theory, the two main Green's function formalisms in use are the *Keldysh real-time formalism* [81] and the *Matsubara imaginary-time formalism* [82]. Here, we will consider the Keldysh technique for ordering Green's functions, and briefly discuss the Matsubara technique in the section on conventions and notations 1.3.2.

The Keldysh technique identifies a *retarded* and *advanced* component describing particle propagation in the positive and negative temporal directions respectively, as well as a *Keldysh* component which describes any non-equilibrium component. As usual, a particle travelling backwards

² Depending on the personal preferences of the authors, the same mathematical object may be referred to as either a Green's function, Green function, or propagator [80].

in time may also be interpreted as an antiparticle travelling forwards in time, so a more natural interpretation might be that the retarded component describes the propagation of electrons while the advanced component describes the propagation of holes. The full 8×8 Green's function $\check{G} = \check{G}(\mathbf{x}, t; \mathbf{x}', t')$ is written as a combination of these,

$$\check{G} = \begin{pmatrix} \hat{G}^R & \hat{G}^K \\ 0 & \hat{G}^A \end{pmatrix}, \quad (1.4)$$

where \hat{G}^R , \hat{G}^A and \hat{G}^K refer to the retarded, advanced and Keldysh components respectively. The two 2×2 diagonal blocks of these component matrices are termed *normal* Green's functions $G_{\sigma\sigma'}$, while the off-diagonal blocks are called *anomalous* Green's functions $F_{\sigma\sigma'}$. The normal Green's functions are given by the following expectation values:

$$\begin{aligned} G_{\sigma\sigma'}^R(\mathbf{x}, t; \mathbf{x}', t') &= -i \langle \{ \psi_\sigma(\mathbf{x}, t), \psi_{\sigma'}^\dagger(\mathbf{x}', t') \} \rangle \Theta(t - t'), \\ G_{\sigma\sigma'}^A(\mathbf{x}, t; \mathbf{x}', t') &= +i \langle \{ \psi_\sigma(\mathbf{x}, t), \psi_{\sigma'}^\dagger(\mathbf{x}', t') \} \rangle \Theta(t' - t), \\ G_{\sigma\sigma'}^K(\mathbf{x}, t; \mathbf{x}', t') &= -i \langle [\psi_\sigma(\mathbf{x}, t), \psi_{\sigma'}^\dagger(\mathbf{x}', t')] \rangle, \end{aligned} \quad (1.5)$$

where $\Theta(\cdot)$ is the Heaviside step function. The anomalous counterparts $F_{\sigma\sigma'}$ are defined in the same way except for the \dagger , *i.e.* they are proportional to $\langle \{ \psi, \psi' \} \rangle$ and $\langle [\psi, \psi'] \rangle$ instead.

The Green's function displays a wavepacket-like oscillatory profile, where the relative coordinate describes the internal, rapid oscillations of the order of the Fermi wavelength λ_F , that occur due to self-interference effects. Conversely, the center-of-mass coordinate describes the spatial evolution of the wavepacket envelope. Only the average of the fast oscillations is relevant for the superconductivity of the material since the superconducting coherence length of the Cooper pairs $\xi_S \gg \lambda_F$, and thus one averages out the relative coordinate (also known as the *gradient approximation*). This is equivalent to assuming that all relevant length scales in the system must be much greater than λ_F , and is the starting point for the *quasiclassical approximation*, which goes on to consider only momenta of the order of the Fermi momentum. All physical quantities are therefore confined to the Fermi surface, and since all quasiparticles have the same magnitude of momentum in this approximation, the relevant information is the transport direction.

Explicitly, the approximation enters as an integration over the kinetic energy, such that the quasiclassical Green's function $\check{g}(\mathbf{x}, \mathbf{p}_F, \epsilon, t)$ is given by

$$\check{g}(\mathbf{x}, \mathbf{p}_F, \epsilon, t) \equiv \frac{i}{\pi} \int_{-\infty}^{\infty} d\xi_p \check{G}(\mathbf{x}, \mathbf{p}, \epsilon, t), \quad (1.6)$$

where ϵ is the quasiparticle energy, \mathbf{p} is the momentum, \mathbf{p}_F is the Fermi momentum, and $\xi_p = \mathbf{p}^2/2m - \mu$ is the kinetic energy measured from the Fermi level μ . It is straight forward to verify that this definition is equivalent to the approximation $\check{G}(\mathbf{x}, \mathbf{p}, \epsilon, t) \approx -i\pi\delta(\xi_p)\check{g}(\mathbf{x}, \mathbf{p}_F, \epsilon, t)$ where the delta function $\delta(\xi_p)$ constrains the quasiparticle momentum to the Fermi surface. In other words, this integral definition is equivalent to our previous qualitative discussion of the approximation as confining physical quantities to the Fermi surface. This integral is not well-defined for large kinetic energies ξ_p , so in practice the integral is solved by contour integration. For the details of this procedure, we refer the reader to Refs. [83–85].

The 4×4 retarded block of \check{g} has the structure:

$$\hat{g} = \begin{pmatrix} \underline{g} & \underline{f} \\ -\underline{\tilde{f}} & -\underline{\tilde{g}} \end{pmatrix}, \quad (1.7)$$

and is normalized such that $\hat{g}^2 = \hat{1}$, where $\hat{1}$ is the 4×4 unit matrix. It is worth noting that the choice of normalization convention for \hat{g} is governed by the ordering of particle creation and annihilation operators when these are combined in a convenient 4-vector form [86]. The normalization of the Green's function matrix can also be set to $\hat{g}^2 = -\hat{1}$ or $\hat{g}^2 = -\pi^2\hat{1}$ depending on the prefactor in Eq. (1.6). The advanced and Keldysh blocks have a similar structure to the retarded block, and the notation $\underline{\dots}$ denotes a 2×2 matrix. The tilde-operation $\underline{\tilde{\dots}}$ denotes a combination of complex conjugation $i \rightarrow -i$ and energy $\epsilon \rightarrow -\epsilon$. Note that the Green's functions of the system can be used to directly calculate physical observables for a superconducting system. For instance, the normalized density of states $D(\epsilon) = \frac{1}{2} \text{Re Tr } \underline{g}$ corresponds to the real part of the normal Green's function, and the critical temperature T_c can be defined as the temperature where the anomalous Green's function \underline{f} drops to zero for all energies. Moreover, a small imaginary component is often added to the energy to model inelastic scattering, such that $\epsilon \rightarrow \epsilon + i\delta$. This has the effect of smoothing out divergences in the density of states.

1.3.1.1 Diffusive Limit: Usadel Equation

In the diffusive limit, we are able to take account of particle scattering by impurities and rough interfaces. In this case the system is described by a set of second-order partial differential equations for the Green's function of a material collectively termed the Usadel equation. The Usadel equation reads:

$$D\nabla \cdot (\check{g} \nabla \check{g}) + i \left[\epsilon \hat{\rho}_3 + \hat{\Delta} + \hat{M} - \check{\sigma}_{sf} - \check{\sigma}_{so}, \check{g} \right] = 0. \quad (1.8)$$

Here we have written the equation in a quite general form, where D denotes the diffusion coefficient of the material, ϵ is the quasiparticle energy and $\hat{\rho}_3 = \text{diag}(+1, +1, -1, -1)$. Moreover, it should be noted that \check{g} in the above equation refers to the isotropic part of the quasiclassical Green's function defined in Eq. (1.6), which is independent of the direction of motion (the position on the Fermi surface). The magnetization matrix $\hat{M} = \mathbf{h} \cdot \text{diag}(\boldsymbol{\sigma}, \boldsymbol{\sigma}^*)$, where \mathbf{h} is the magnetization exchange field and $\boldsymbol{\sigma}$ is the Pauli vector. Products of matrices with incompatible dimensions should be interpreted by taking Kronecker products with the appropriate identity matrices, so that *e.g.* $\hat{\rho}_3 \check{g} = [\hat{\rho}_3 \otimes \text{diag}(1, 1)] \check{g} = \text{diag}(\hat{\rho}_3, \hat{\rho}_3) \check{g}$. The effects of spin-orbit coupling and randomly aligned magnetic spin-flip processes caused by impurities have been included via the terms

$$\begin{aligned} \check{\sigma}_{so} &= -\frac{1}{8\tau_{so}} \hat{\sigma} \hat{\rho}_3 \check{g} \hat{\rho}_3 \hat{\sigma}, \\ \check{\sigma}_{sf} &= -\frac{1}{8\tau_{sf}} \hat{\sigma} \check{g} \hat{\sigma}, \end{aligned} \quad (1.9)$$

where τ_{so} and τ_{sf} are the mean spin-flip and spin-orbit scattering times, and we have defined the matrix $\hat{\sigma} = \text{diag}(\sigma, \sigma^*)$. Impurity scattering in the Usadel equation is typically treated in the Born approximation, which means that the strength of the impurity potential (the phase-shift imposed on the electron wave function when it scatters on the impurity) is sufficiently weak, although the impurity concentration may still be high. This is in contrast to the opposite regime of the unitary limit where the scattering potential is strong, imposing a large phase-shift.

A note on the derivation and applicability of the Usadel equation

The Usadel formalism assumes that the impurity scattering rate is the largest energy scale in the system besides the Fermi level (typically several eV in metals), and may therefore be inaccurate for strong ferromagnets where

the exchange field is a significant fraction of the Fermi energy. In this case the Eilenberger equations [77] should be used instead. These are the kinetic equations for the superconductor before the standard battery of assumptions and approximations are applied in order to make more complicated scenarios tractable. A detailed derivation of the Usadel equation in the dirty limit, starting from the equation of motions for the field operators, can be found in Ref. [85]. One first finds the equation of motion for the Green's functions, and the Eilenberger equation is found by setting their difference equal to zero. This is done within the BCS mean field approximation, which reduces two-particle operators to single-particle operators by assuming short range interactions and taking the average. This is the first of many necessary approximations, and we provide a brief overview and discussion of the most common cases and the associated nomenclature typically met in the literature:

- *Mean-field Approximation:* One here assumes that electron-electron interactions can be described effectively by each electron moving in a net background field set up by the other electrons. Mathematically, this amounts to taking the average of two-particle operators to yield single-particle operators. In the case of a superconducting order parameter, this results in $\Delta(\mathbf{x}, t) = \lambda \langle \psi_{\downarrow}(\mathbf{x}, t) \psi_{\uparrow}(\mathbf{x}, t) \rangle$, where λ is the coupling constant of the effective electron-electron interaction that causes superconductivity.
- *Gradient Approximation:* This assumes all quantities vary slowly compared with the Fermi wavelength, so that one may neglect short-ranged oscillations and keep only spatial derivatives up to first order.
- *Clean Limit:* The clean limit applies to very pure materials, where the mean free path ℓ is greater than the coherence length ξ and length L of the medium, $\ell \gg \xi, L$. At low temperatures, the proximity effect is therefore long ranged. Ferromagnets with increasingly high Curie temperatures, *i.e.* the temperature beyond which it loses its permanent magnetization and becomes a paramagnet, tend towards the clean limit. Typical examples are iron (Fe) and cobalt (Co).
- *Born Approximation:* This assumes that the strength of the impurity potential is so weak that it imposes a phase-shift δ on the electron wave function upon scattering, satisfying $\delta \ll 1$. In effect one introduces a self-energy term (*i.e.* quantifying the contribution to the particle or quasiparticle's

energy given by interactions with the system) by averaging over the positions of the impurities (and averaging over spin states in the case of magnetic impurities).

- *Dirty Limit:* In contrast to the clean limit, the dirty limit is defined by $\xi \gg \ell$ or $L \gg \ell$, and the proximity effect decays exponentially because the Usadel formalism takes the ensemble average over impurities. By taking the dirty limit one assumes that the elastic scattering self-energy term from the Born approximation dominates all terms in the equation of motion for the Green's function, $1/\tau_{\text{imp}} \gg \Delta, T$, and in this way models quasiparticle diffusion.
- *Equilibrium:* In equilibrium, there are no applied voltages or temperature gradients, allowing the Keldysh component of the quasiclassical Green's function to be written purely in terms of the retarded Green's function since $\hat{g}^K = (\hat{g}^R - \hat{g}^A) \tanh(\epsilon/2k_B T)$ and $\hat{g}^A = -(\hat{\rho}_3 \hat{g}^R \hat{\rho}_3)^\dagger$, where k_B is the Boltzmann constant.
- *Weak Proximity Limit:* The limit of weak proximity effect is a reasonable approximation when the non-superconducting layers are very long, or the interface transparency is very low. Mathematically, this limit implies that the anomalous Green's function can be treated as a perturbation $\|f\| \ll 1$, since the presence of an anomalous Green's function is invariably linked to the presence of superconducting phenomena. The resultant simplification allows for analytic results which facilitates the understanding of the underlying physical mechanisms. In contrast, the strong proximity limit can typically only be solved numerically but allows for more accurate predictions of physically relevant signatures.

1.3.2 Notation and Parameterizations

The 4×4 components of the retarded Green's function $\hat{g}(\mathbf{x}, \epsilon)$ (dropping the superscript 'R' for brevity) are not all independent. Firstly, the particle-hole symmetries $\tilde{g}(\mathbf{x}, \epsilon) = g^*(\mathbf{x}, -\epsilon)$ and $\tilde{f}(\mathbf{x}, \epsilon) = f^*(\mathbf{x}, -\epsilon)$ relates the top two 2×2 blocks of the matrix to the bottom ones. Secondly, writing out the normalization condition $\hat{g}^2 = \hat{1}$ reveals two further constraints: $\underline{g}\underline{g} - \underline{f}\underline{f} = \underline{1}$ and $\underline{g}\underline{f} - \underline{f}\underline{g} = \underline{0}$. By picking a parametrization of the Green's function such that these normalization and symmetry constraints are automatically satisfied, the relevant physical equations can be significantly simplified. We will discuss two such parametrizations in this section.

In analytical treatments of superconductivity, the most popular parametrization is the so-called θ -parametrization, which is usually written

$$\hat{\mathbf{g}} = \begin{pmatrix} c_{\uparrow} & 0 & 0 & s_{\uparrow} \\ 0 & c_{\downarrow} & -s_{\downarrow} & 0 \\ 0 & s_{\downarrow} & -c_{\downarrow} & 0 \\ -s_{\uparrow} & 0 & 0 & -c_{\uparrow} \end{pmatrix}, \quad (1.10)$$

where $\sinh \theta_{\sigma} \equiv s_{\sigma}$ and $\cosh \theta_{\sigma} \equiv c_{\sigma}$. Thus, with this parametrization, the equations of motion can be recast in terms of only two scalar parameters θ_{\uparrow} and θ_{\downarrow} . While this choice can be very useful for analytical considerations, it has several limitations. Firstly, in the form presented here, it can only be used to describe singlet pairing and short-range triplet pairing, although there exists a generalization which captures all pairing components [87]. We recall that short-range triplet pairs are those which have zero spin-projection along the local magnetization direction, whereas the long-range pairs have spins aligned with the magnetization direction. When it comes to long-range triplet pairs, these would specifically be described by the elements that are set to zero in this parametrization. Secondly, the hyperbolic functions and their inverses are multi-valued. This is usually not a problem in analytical treatments, but can lead to convergence problems and instability when treating the problem numerically.

These problems bring us to the other popular parametrization, namely the Riccati parametrization [88, 89]. This parametrization is defined as

$$\hat{\mathbf{g}} = \begin{pmatrix} \underline{N} & 0 \\ 0 & -\tilde{N} \end{pmatrix} \begin{pmatrix} \underline{1} + \underline{\gamma}\tilde{\gamma} & 2\underline{\gamma} \\ 2\tilde{\gamma} & \underline{1} + \tilde{\gamma}\underline{\gamma} \end{pmatrix}, \quad (1.11)$$

where the normalization matrices³ $\underline{N} \equiv (1 - \underline{\gamma}\tilde{\gamma})^{-1}$ and $\tilde{N} \equiv (\underline{1} - \tilde{\gamma}\underline{\gamma})^{-1}$. In contrast to the multi-valued and unbounded θ -parametrization, the Riccati parametrization is both single-valued and bounded $|\underline{\gamma}| < 1$, and is therefore the most popular parametrization for numerical work. Finally, the parametrization is completely general as it can be used to analyze all combinations of singlet, short-range triplet, and long-range triplet pairing that may occur in hybrid structures.

³ In some literature, one uses the convention that $\tilde{\gamma}(\epsilon) = [-\underline{\gamma}(-\epsilon)]^*$ instead of changing the sign structure of Eq. (1.11).

We conclude this section by noting that a common alternative to the Keldysh real-time framework discussed herein is the Matsubara imaginary-time formalism. In that case, the physical equations are expressed in terms of only a single Matsubara Green's function $\hat{g}^M(\mathbf{x}, t)$, which can be related to the retarded and advanced Green's functions of the real-time formalism by analytical continuation to complex energies. We have for instance $\hat{g}^R(\epsilon) = \hat{g}^M(i\omega \rightarrow \epsilon + i\eta)$ where η is a positive infinitesimal.⁴ The imaginary energy ω is restricted to one of the discrete *Matsubara frequencies* $\omega_n \equiv (2n + 1)\pi T$, where T is the temperature of the system and n is an arbitrary integer. In superconductors, the relevant Matsubara frequencies are those below the Debye frequency ω_D , so we only need to consider $n \in (-n_D, +n_D)$ in practice, where $n_D \approx \omega_D/2\pi T$. Thus, at high temperatures, the number of Matsubara frequencies below the Debye frequency decreases, which means the Matsubara formalism becomes more computationally efficient in this regime. This explains why the formalism has become quite popular for critical temperature calculations, for example. Nevertheless, the Matsubara formalism is less general than the Keldysh formalism; the former can only be used to treat systems in thermal equilibrium, while the latter is valid also for non-equilibrium systems.

1.4 Experimental Status

In this section we will provide a brief introduction to the techniques and materials most readily available in the laboratory setting, and use the theory developed in the preceding chapter to explain the latest experimental breakthroughs in superconducting spintronics. Three comprehensive reviews of proximity effects in superconductor-ferromagnet heterostructures appeared in 2005 [29, 30, 90], as well as an overview of experimental devices in 2014 [91] and thorough review of spin-polarized supercurrents in 2015 [92]. We thus limit the scope of this section to provide a broad but brief overview of the most important experimental features affecting superconducting order in magnetic materials, primarily from the last decade.

1.4.1 Materials and Techniques

To help newcomers to superconducting spintronics or heterostructures in general, and to set the stage for the state-of-the-art experimental frontier,

⁴ Although η enters in a similar way to δ , which models the inelastic scattering in the Keldysh formalism, the mathematical equivalence here requires $\eta = 0^+$.

we provide a brief overview of the primary materials and experimental techniques typically used in the construction of such thin-film architectures. For an in-depth explanation of experimental techniques we refer readers to Ref. [93], sections of which we briefly paraphrase in 1.4.1.2. The overarching process requires an appropriate construction environment, methods of generating clean surfaces and well-formed interfaces, and methods for measuring the efficacy of all aspects of the process.

1.4.1.1 *Material Choice*

The range of available ferromagnetic and superconducting elements is too extensive to discuss all implemented combinations here with any degree of justice, so we provide just a few common examples in order to give the unfamiliar reader a feeling for the appropriate parameter range of operation. Although we assume the reader to be familiar with ferromagnetism, we highlight a few examples that work particularly well in combination with superconductivity. The common elemental ferromagnets are of course the transition metals iron (Fe), nickel (Ni) and cobalt (Co). We mentioned above that Fe and Co are in the clean limit due to their high Curie temperature, featuring an exchange field which is a substantial fraction of the Fermi energy (high polarization), and these are routinely used in their pure state in superconducting heterostructures. Ferromagnetic compounds are preferred when specifically tailored characteristics of the heterostructure, such as a desired magnitude of the exchange field, is required. Examples include PdNi and CuNi, which can feature a canted magnetization orientation relative to the film-plane due to the competition between shape- and magnetocrystalline anisotropy [49]. The diffusion constant of CuNi is of the order $D \sim 5 \text{ cm}^2/\text{s}$ [94]. Of the elemental superconductors, niobium has one of the biggest gaps at around $\Delta \approx 3 \text{ meV}$. In the diffusive limit one typically expects superconducting coherence lengths in the range $\xi_S = 10\text{--}30 \text{ nm}$, although it should be noted that its magnitude decreases when the thickness of the superconductor becomes comparable or smaller than this regime.

1.4.1.2 *Experimental Techniques*

The preparation of reasonably impurity-free nanoscale heterostructures requires extremely low ambient pressures, typically under 10^{-8} Pa , as the ambient pressure governs the rate at which external particles impinge on a surface. For this reason all operations are performed inside an ultra-high vacuum chamber, and such vacuum technology has undergone a series of steady improvements in recent years [93]. If the crystal is brittle, a

well-defined crystal surface can be prepared by cleavage, where mechanical pressure is applied to the crystal via externally controlled magnetic or electric devices. The cleavage then occurs along a particular crystallographic direction, meaning noncentrosymmetric materials are quite unsuited for cleaving due to their lack of inversion symmetry.

Since cleavage only works well for brittle crystals, and as a cleaved surface may contain rough edges or defects, an alternative preparation method is ion bombardment and annealing. In this case noble gas ions are fired at the surface of the crystal, removing the top layer along with any defects, and high-temperature annealing ($\sim 500\text{--}1200\text{ }^\circ\text{C}$) removes any noble gas remnants on the surface. The purity and crystallographic order of the remaining surface are checked by spectroscopic and diffraction methods (see more below), and the bombardment/annealing process may be repeated a number of times until a satisfactory surface is achieved.

Thin-film layers are typically deposited by simple evaporation and condensation in general, creating a transversal “pancake-stack”. When a specific crystallographic orientation is required, the evaporation-condensation conditions are chosen more carefully and deposited with a technique called Molecular Beam Epitaxy (MBE). Here a beam of the sublimated/evaporated elements or compounds from which one wishes to make a layer is directed onto the substrate, and the layer deposition can be controlled to within a single monolayer by the rapid switching of this beam. Epitaxy refers to the deposition of a thin crystalline layer on top of a crystalline substrate, where the epitaxial layer has a fixed crystallographic orientation with respect to this substrate. The substrate provides a base structure from which the epitaxial layer is “grown” – that is it acts as a so-called *seed crystal*, which lowers the interaction potential of molecules to form a crystal lattice near the surface. The quality of the interface is therefore quite dependent on the crystallographic matching/lattice constants of the two layers. The III-V semiconductor gallium arsenide (GaAs) is a commonly used substrate, which has a zincblende crystal structure, *i.e.* the atoms form two interlocked face-centered cubic lattices where the four nearest neighbours at the tetrahedral vertices are of opposite type. The epitaxy may also occur through chemical reactions, in which case the technique is called Metal-Organic MBE, or Chemical Beam Epitaxy.

For materials that have very high melting points, making the evaporation step difficult, the *sputter deposition* technique provides an alternative. This term actually denotes a range of related vapour deposition methods, many of which can still be operated at ultra-high vacuum for increased purity and epitaxial growth for structural control. In this case accelerated gaseous ions are fired onto the material from which one wishes to create a

thin-film layer (the “target”). The impact causes a number of particles to be ejected (sputtered) from the surface and are subsequently deposited as a thin-film on a substrate. By choosing reactive gases, one may also sputter compounds. The deposition with sputtering, and to a large extent also with MBE, is primarily homogeneous; patterning is significantly more of a challenge because of the lack of control over deposition direction. Thus, if particular structural features are required, these must be created by removing surface layers via etching with a focused beam of particles or by using electron-beam lithography. In the latter case, the pattern is drawn by firing an electron beam at an electron-sensitive coating, after which selective removal is possible in a solvent bath.

High-quality thin-film interfaces are crucial for efficient spin-transport between the layers, and the atomic structures of such interfaces are studied in detail using microscopy, spectroscopy and diffraction methods. Using Auger electron microscopy or X-ray photoemission spectroscopy, the intensity of the characteristic transitions or emission lines corresponding to electrons from individual atoms in the sample decays exponentially with the thin-film thickness. This is due to the often short mean free path (~tens of nm) of electrons in matter, the length of which changes according to material structure and impurity level. If the deposition occurs as an island on the substrate rather than a full monolayer, the intensity profile, which is measured as a function of the layer coverage, will instead tend to be linear [93].

Using electron diffraction techniques, bright Bragg spots show the crystallographic order of the reciprocal lattice, accurate to within the electron beam’s coherence length. If one requires a more accurate real-space image, a range of tools are available, with various advantages and drawbacks. They may yield significantly increased resolution for example, but may not be compatible with ultra-high vacuum conditions, meaning contamination of the sample might occur during transfer to the microscope. This is the case for scanning electron microscopy (SEM), which is among the most common high-resolution tools, along with transmission electron microscopy (TEM) and scanning tunneling microscopy (STM). Optical methods may also be used, such as using inelastic scattering to study vibrational properties of the lattice. For buried interfaces, ion scattering is another indispensable tool, where the subsequent analysis can yield information about the chemical composition, crystallographic quality and lattice matching between the layers. For further reading, we refer again to the book by Lüth [93] and references therein.

So far we have been concerned with the construction of thin-film architectures. Now we turn to techniques for controlling and measuring the

physical features of interest in spintronics. The practicalities of control in experimental setups can be quite unintuitive – for example, it is often easier in experiment to rotate the sample itself rather than the magnetic field source in order to probe the influence of different magnetic field orientations on the system. The pace at which interesting new features are being uncovered makes the physics of control and measurement a rapidly expanding field in itself, and this discussion will lead us naturally into the next section, where we consider the frontier of experimental research.

The differential conductance dI/dV is directly proportional to the density of states in the tunneling limit (where Andreev reflection is suppressed) and so is a common measure in which to present such analysis experimentally. It is typically normalized to the normal-state conductance at high bias (5 mV in a Nb superconductor, for a concrete example [95]). An STM can be used to generate the current-voltage sweep since the tunneling current depends on the voltage between the STM tip and the electronic structure to be probed. For this reason differential conductance and tunneling spectroscopy are sometimes used interchangeably in the literature. Numerical differentiation is very sensitive to noise, so typically an averaging over several sweeps must be taken to get an accurate mapping.

The Josephson junction (Section 1.2.2.2) is a mainstay of spintronic architectures in the context of superconducting hybrids, but the approach to its construction depends on the intended purpose. The phase difference between the superconductors can be adjusted by applying a current bias. As long as the current is smaller than the critical current I_c , the superconducting phase difference then adjusts in order to support the applied current via the relation $I = I_c \sin(\phi)$. The phase may also be modified continuously by applying an external magnetic flux in a loop geometry [70]. In an SNS junction, the superconductors have zero phase difference between them in the ground state. However, due to the oscillating behavior of the order parameter in SFS junctions described previously, the ground state in this case can occur at a phase difference equal to π . Whether 0 or π is the ground state depends on the system parameters, such as the length of the interstitial ferromagnetic layer and temperature. It has also been predicted that, in special circumstances, the ground state may be manufactured to give an arbitrary ϕ_0 -junction (see Section 1.5 for more details).

A highly influential application of Josephson junctions is their use in superconducting quantum interference devices (SQUIDs). These are typically made by joining two junctions in a loop [96], but single-junction designs which are less sensitive but more easily manufactured also exist [97, 98]. When a magnetic flux passes through the loop, it induces a circulating current. If an external current is applied to the SQUID, the induced

current will enhance the current in one arm of the loop and suppress it in the other. It will then be energetically favourable for the induced current to change direction as a function of the magnetic flux in units of $h/2e$, where h is Planck's constant and e is the electronic charge, *i.e.* in practice the induced current increases or decreases the flux through the loop. A SQUID may then in turn be used to measure properties of other thin-film heterostructures, as their high sensitivity to external flux means they function as high-precision magnetometers (equivalently magnetometers). The recently developed nanoSQUIDs can even resolve the magnetization of individual spins [99–101], and we expand on this in the following section.

1.4.2 Recent Experimental Advances

The full theoretical basis of spin transport between materials in thin-film heterostructures involving superconductors is still incomplete, but as the potential benefits have emerged the field has undergone rapid development. The race is now on to harness the full potential of superconducting correlations for spin transport in experimental devices, and a number of important steps have already been achieved in this regard. Key features include spin injection, spin accumulation, control of spin diffusion as well as dynamical detection and manipulation of the spin state of the system. Here we briefly discuss some of the superconducting counterparts to these conventional procedures from spintronics.

Spin injection and spin Hall effects. A compelling reminder of the enhanced capabilities promised by superconducting spintronics was provided recently with the report of a quasiparticle-mediated spin Hall effect – *i.e.* spin accumulation on the lateral surfaces due to spin-orbit coupling – in an *s*-wave superconductor. The magnitude of this effect exceeded its non-superconducting equivalent by a factor of more than 2000 [18]. In that experiment, a lateral superconductor-ferromagnet structure was created by using a non-magnetic Cu wire to join a ferromagnetic $\text{Ni}_{81}\text{Fe}_{19}$ wire to a wire of compound superconductor NbN, which has $T_c = 10$ K. A spin current was injected into the NbN via diffusion of spin accumulation in the Cu wire resulting from driving a current from the ferromagnet to the Cu. The inverse spin Hall effect causes scattering of the injected spin current and converts it to charge current, which below T_c is carried by quasiparticles. The electrical signatures of the inverse spin Hall effect thus manifest as a charge imbalance at the edges of the sample [102].

Spin injection in conventional spintronics typically occurs as above, through diffusion of spins across a ferromagnet/non-ferromagnet interface. At a superconducting interface, a range of novel phenomena have been shown when spin-polarized currents are injected into superconductors,

such as quasiparticle spin lifetimes close to one million times longer than the normal-state lifetime [16], which is a result of the unique properties of quasiparticles in superconductors. While they carry spin-1/2, their effective charge depends on their energy. In fact, near the gap edge $\epsilon \simeq \Delta_0$, their effective charge $Q \rightarrow 0$ at the same time as their group velocity v_g slows down. This means that close to the gap edge, one has chargeless spin-1/2 fermion excitations which should then be insensitive to processes that cause decoherence due to coupling to the charge degree of freedom. Importantly, a recent experiment has indeed given an exposition of near-chargeless spin imbalance [17], which could have interesting consequences with regard to overcoming the problem of Joule heating associated with the large charge current densities (order 10^6 A/cm²) currently required for domain wall motion and magnetization dynamics. The fact that the group velocity of quasiparticles in superconductors slows down at $\epsilon \simeq \Delta_0$ also means that it takes a much longer time for them to experience e.g. spin-orbit scattering on impurities. Spin diffusion via quasiparticles in superconductors has been shown to be strongly enhanced in Zeeman-split superconductors [103].

Spin-polarized Cooper pairs. Whereas the above examples show how spin transport in superconductors can be dramatically improved compared to its non-superconducting counterpart even at the level of quasiparticles, much attention has also been devoted to the role of spin-polarized Cooper pairs that can emerge in SF structures. This triplet component of the superconducting correlations has been enhanced in experiments both via the introduction of a ferromagnet with an inhomogeneous magnetization texture to produce long-ranged supercurrents [48, 104], and in multilayered SFS junctions [49] (see the left panel of Figure 1.3). The pioneering experiment with regard to long-ranged triplet supercurrents was done by Keizer *et al.* [105], demonstrating transfer of a supercurrent through an extreme magnetic environment: a half-metal. Half-metals are ferromagnets with so strong magnetic fields that one spin band becomes electrically insulating, while the other band is a metallic conductor. Since conventional singlet Cooper pairs consist of electrons from both spin bands, such pairs cannot exist in a half-metal. In the presence of magnetic disorder near the interfaces connecting the half-metal to a superconductor, effectively producing a local misalignment of the magnetization there compared to its direction in the bulk, a net Josephson coupling via triplet Cooper pairs can be established [106]. The history and properties of spin-polarized supercurrents has been covered in great detail in a recent review [92]. Martinez *et al.* reported recently an important step forward with regard to exerting well-defined control of such triplet supercurrents [107]. The key idea in this experiment was to use an external magnetic field to switch on and off a triplet supercurrent by controlling the relative magnetization orientation in a Ni/Co/NiFe ferromagnetic

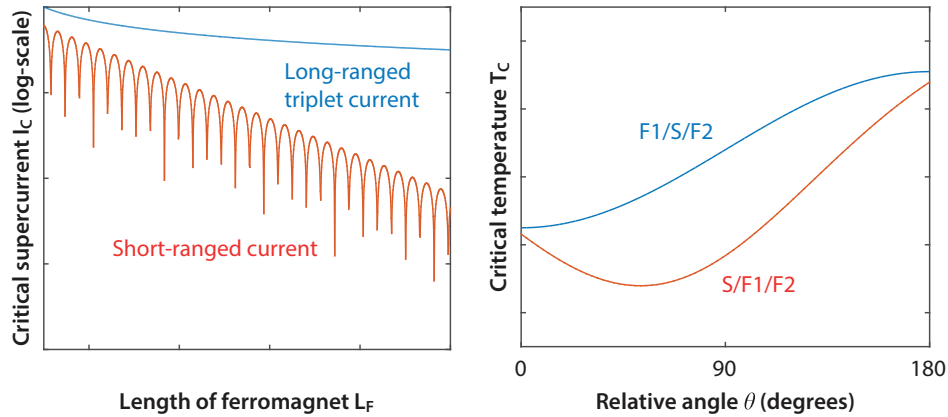


Figure 1.3 *Left panel:* The critical supercurrent can display two types of behavior in ferromagnetic Josephson junctions. If no long-ranged triplet pairs are generated (due to *e.g.* magnetic inhomogeneities), the supercurrent is suppressed very quickly with increasing junction length L_f (note the logarithmic scale). In contrast, if triplet pairs with spin-polarization aligned with the magnetization direction are created, these can carry a long-ranged current through the system which is only weakly suppressed with increasing L_f . *Right panel:* Magnetic control over the superconducting critical temperature T_c and its characteristic behaviour in two types of spin-valve junctions: FSF and SFF.

stack sandwiched between two conventional superconductors. Whereas Ni is a hard ferromagnet (high coercivity field), NiFe switches much more easily and could be rotated with a small field less than 20 mT. When the NiFe was rotated into a non-collinear orientation, a triplet supercurrent could flow through the junction, whereas it was otherwise strongly suppressed. In this way, the authors obtained “on-off ratios” up to 20 for the supercurrent.

The existence of triplet Cooper pairs is inferred indirectly via long-ranged supercurrents through ferromagnets. More direct proof can be obtained by considering how triplet Cooper pairs should influence the spectroscopic properties of superconducting structures, such as the energy-dependent density of states. The first *direct* experimental signatures of an odd-frequency triplet pairing state in a conventional superconductor was in fact reported as recently as 2015 [96], using scanning tunneling spectroscopy of a niobium/holmium bilayer. Using a sapphire substrate topped with a thin layer of non-superconducting Nb as a seed crystal,⁵ a 9.5 nm layer of Ho was grown epitaxially followed by a 20 nm layer of superconducting Nb. The sample was protected from oxidization by applying a final thin layer of

⁵ Typically, a superconducting layer needs to be longer than the order of half a coherence length of the material in order to display superconductivity, since there are otherwise insufficient Cooper pairs to form a condensate.

gold. Having noted that spin-active interfaces can enhance odd-frequency pairing on the superconducting side of an SF interface [106], the authors used the *controllable* magnetic order in Ho to gain such an amplification of the triplets. By measuring the density of states on the superconducting side, the authors also avoid the normal-state background, thus in principle getting a clearer conductance signal. By applying an external field the Ho was then driven through a metamagnetic transition from helical antiferromagnet to homogeneous ferromagnet and the authors recorded a change in the subgap density of states from a double peak indicating spin splitting to an enhanced peak at zero energy, characteristic of the behavior of odd-frequency triplets in the presence of a spin-active interface (see Figure 1.2). A similar effect was reported shortly thereafter in a superconductor/half-metal bilayer [108].

Control of T_c . In the last few years, there has been increasing activity in the quest for controlling the superconducting critical temperature T_c in spin-valve geometries, *i.e.* by changing the relative magnetization orientation of two or more ferromagnetic layers. It is also possible to alter T_c by altering the width L_F of the ferromagnetic layer. This can obviously not be done *in situ*, which is a practical hinderance, but in return the change in T_c becomes potentially much larger and in some cases fully suppresses superconductivity, $T_c \rightarrow 0$. Controlling T_c via the relative magnetization direction in an FSF spin-valve can be done with a single sample, as shown recently in Refs. [109–112]. As discussed previously, the configuration of antiparallel magnetizations should be more compatible with the superconducting state (higher T_c) compared with the parallel alignment where the fields add [113, 114]. However, there is an additional effect that must be taken into account when the fields are non-collinear. In this case, an additional proximity channel through which Cooper pairs may “leak” into the ferromagnet is opened since long-ranged Cooper pairs can now be generated. As a result, one could expect that T_c is in fact not at its lowest in the parallel alignment, but instead at misalignment angles close to $\pi/2$. This has been experimentally confirmed in [109–111]. It is worth noting that this effect becomes much more pronounced in an SFF structure than in an FSF structure, since the additive, destructive effect of the ferromagnetic layers become less severe in the former case (see the right panel of Figure 1.3).

Recently, an unusually large change in T_c of order 1 K was reported by using half-metallic ferromagnets in a spin-valve setup [115]. In their device, the authors exploited precisely the extra leakage channel via long-ranged triplet Cooper pairs which becomes of crucial importance in half-metallic ferromagnets. In this case, a proximity effect is indeed only possible when such Cooper pairs are allowed to exist. Whereas previous experiments

(mentioned above) had achieved a maximum suppression of T_c of around 100 mK, a change of 1 K was obtained in Ref. [115] by utilizing a $\text{CrO}_2/\text{Cu}/\text{Ni}/\text{MoGe}$ structure (half-metal/normal metal/ferromagnet/superconductor). The normal Cu spacer serves to reduce exchange coupling between the CrO_2 and Ni which otherwise would have their magnetizations locked to each other. Using an external magnetic field to thus accomplish rotation of the Ni layer magnetization to a 90 degree orientation relative to the CrO_2 magnetization, the large shift in T_c was observed due to the long-ranged triplet proximity effect. This finding has relevance to applications utilizing superconducting switches that are controlled magnetically, as discussed in Ref. [116]. One reason for this is that when the range of T_c varies widely, the resistance state (“off”-state) of the device is more stable with respect to thermal fluctuations. For a small change in T_c , thermal fluctuations could accidentally turn the device “on” by lowering the temperature below the T_c dictated by the magnetic configuration. A superconducting GMR device like this should be able to perform the same type of logic operations as its non-superconducting equivalent, but with much lower dissipation of energy.

Thermoelectric effects. Part of what makes the transport properties of superconductors so exciting is the strong coupling between not only the spin and charge degree of freedom, but also *heat*. In fact, quasiparticle spin accumulation in superconductors can be intimately related to thermoelectric effects. Although overall electron-hole symmetry may be preserved, spin-dependent order in superconductors induced either via a proximate magnetic host or an in-plane magnetic field in thin-film structures, breaks the spin-resolved electron-hole degeneracy. In turn, this allows for very large thermoelectric effects as predicted in [117, 118]. Interestingly, this has very recently been experimentally confirmed in [19]. In this work, the authors measured thermoelectric currents in tunnel junctions comprised of superconductor/ferromagnet layers in the presence of a high magnetic field. The resulting Seebeck coefficients were found to exceed $100 \mu\text{V}/\text{K}$, far beyond what is typically obtained in conventional metallic structures. It is encouraging to note that these results were obtained without very strongly polarized magnetic materials, alluding to the fact that even larger Seebeck coefficients might be possible when using *e.g.* strongly polarized ferromagnetic insulators such as EuO or GdN.

Imaging. SQUID technology is advancing rapidly, with nanoSQUIDs reducing noise and allowing increased magnetic field sensitivity over their traditional micrometre counterparts [99, 100]. Until very recently however, it was not possible to measure the magnetic field generated by single electron spins using a SQUID. Such precision could be gained via magnetic resonance force microscopy [119] or nitrogen-vacancy magnetometers [120],

the latter enabling imaging at atmospheric conditions, which is a considerable advantage for biological and chemical applications. However, the ubiquitous use of SQUIDS for imaging in condensed matter where low temperatures are not a practical hinderance has made this pursuit a long-standing goal. In 2013 Vasyukov *et al.* manufactured a nanoSQUID on the apex of a hollow quartz tube, with a diameter down to 56 nm [101]. This construction gives single-spin sensitivity and, being mounted on a thin tip, is straightforwardly applied as a scanning probe. They report improved flux noise due to the small effective area and increased spin sensitivity that are orders of magnitude better than previous nanoSQUIDS. By utilizing Nb and Pb, which have relatively short coherence lengths, their nanoSQUID can operate at reasonably high magnetic fields and temperatures, making this a very promising new imaging tool whose increased sensitivity will allow for much more careful experimental examination of individual spintronic architectures.

On the experimental side, Blamire and Robinson point out [92] that the missing ingredient in order to gain the required level of control of the spin transport is the ability to manipulate the spins or the magnetic state. However, there is also evidence that the underlying physics of long-range proximity effects is still not entirely understood. These are cases in which magnetic inhomogeneities and spin orbit effects both appear to be negligible, so that no known mechanism for generating the triplet component is available. In 2010, Wang *et al.* reported zero resistance for single-crystal Co nanowires up to 600 nm in length [121]. Ref. [56] argues that this could mean there exists Rashba-type coupling in the system, but this is perhaps a contentious issue. Rashba coupling is typically a surface effect (unless the lattice itself is noncentrosymmetric), and currently there exist no precise experimental estimates of how deep such effects can penetrate into the bulk of a material, although an order of ~ 1 nm is typically assumed. A recent alternative suggestion argues that giant mesoscopic fluctuations control the emergent behaviour [122].

1.5 Novel Predictions

Although triplet superconductivity may not be at the heart of all long-range effects, its generation and control has received increasing focus over the last decade due to its pivotal role in overcoming the problem of Joule heating in spintronics. The importance of combining spin-orbit coupling and magnetic materials has in this regard become increasingly apparent, and below we take a look at some of the most recent novel predictions and benefits in superconducting spintronics.

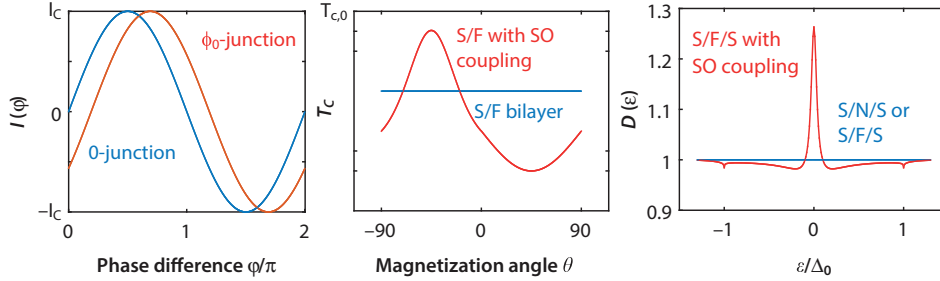


Figure 1.4 *Left panel:* In a ϕ_0 -junction, the entire current-phase relation is shifted so that a net supercurrent flows even at zero phase difference. *Middle panel:* Magnetic control of superconducting T_c in the presence of Rashba and Dresselhaus spin-orbit coupling requires only one single homogeneous ferromagnet, in contrast to all previous proposals which have required two or more magnetic materials. Here, $T_{c,0}$ is the bulk superconducting critical temperature and the angle θ is given in degrees. *Right panel:* Giant triplet proximity effect in spin-orbit coupled Josephson junction at π phase difference. Note the absence of a proximity effect without spin-orbit coupling at π phase difference for conventional SNS or SFS junctions.

1.5.1 ϕ_0 -junctions

The phase difference ϕ between the superconductors of a Josephson junction determines the supercurrent flowing in the junction according to $I = I_c \sin(\phi)$, with higher order harmonics appearing only at very low temperatures, and systems are routinely manufactured to have ground state $\phi = 0$ and $\phi = \pi$ by altering the sample length as discussed above. In principle, however, junctions may have any arbitrary single ground state between 0 and π e.g. if the superconducting state breaks time-reversal symmetry.⁶ Such junctions have been dubbed the ϕ_0 -junctions since they follow the general current-phase relation $I = I_c \sin(\phi + \phi_0)$ (see left panel of Figure 1.4). They were allowed for in Josephson's original work [61] and have been predicted to occur with unconventional superconductors [123–125]. Moreover, it was predicted by Buzdin in 2008 [126] that junctions with an interstitial noncentrosymmetric magnetic material⁷ should provide direct coupling between the supercurrent and the magnetic moment in the interstitial material. This would create a ϕ_0 -junction with ϕ_0 proportional to the strength of the spin-orbit coupling and the exchange field in

⁶ The current-phase relation must be antisymmetric if time reversal symmetry is preserved [63].

⁷ Alternatively, a centrosymmetric ferromagnet could be used if only surface properties are probed.

the metal, consequently shifting the current-phase relation as shown in the left panel of Figure 1.4 so that a net supercurrent flows even for zero phase difference between the superconductors. The model was originally formulated for pure Rashba-type spin-orbit coupling before being developed for arbitrary Rashba-Dresselhaus coupling in diffusive systems [127], and could be incorporated into spintronic circuits as a phase-shifter, to generate spin precession or utilizing precession to generate supercurrent [126]. The superconducting ϕ_0 -junction has very recently been experimentally observed [128].

1.5.2 Control of T_c

Most previous endeavours to control the critical temperature of superconducting hybrid structures have focused on the use of multiple magnetic elements. For instance, the critical temperature T_c of FSF' and SFF' junctions can be toggled between a low state $T_{c,1}$ and high state $T_{c,2}$ by rotating the magnetization of the soft F' layer relative to the hard F layer, as discussed in previous sections. However, it becomes increasingly challenging to exert control over individual layers in the presence of multiple magnetic elements, especially if these are in immediate proximity. Recently, it was discovered that inclusion of spin-orbit coupling in superconducting spintronics opens up a rich new avenue of physical phenomena. As the authors show in Ref. [58], the presence of both Rashba and Dresselhaus spin-orbit coupling in an SF bilayer causes its superconducting properties to become strongly dependent upon the magnetization direction, in contrast to the case without spin-orbit coupling. The magnetization will always suppress the triplet pairs with spin projections perpendicular to the field, *i.e.* the singlet pairs and short-range triplet pairs. The spin-orbit coupling, on the other hand, suppresses triplet pairs depending on their spin projections relative to the crystal structure, and not the magnetization direction. Depending on the direction of magnetization relative to the spin-orbit coupling then, the latter may either suppress the short-range triplet pairs, long-range triplet pairs, or both. Finally, whether the short-range triplet pairs can be converted into long-range triplet pairs or not in a homogeneous ferromagnet depends on the magnetization direction relative to the spin-orbit coupling. The net result is that the magnetization and spin-orbit coupling can either conspire to suppress or enhance the proximity effect in the ferromagnet, and these two situations result in vastly different inverse proximity effects in the superconductor. It has been shown theoretically that this can lead to a difference $T_{c,2} - T_{c,1}$ of up to $0.2T_{c,0}$, which for a niobium-titanium alloy would correspond to a 2 K change, in comparison with the current

world record for structures with multiple magnetic elements of 1 K [115] as discussed above. This result is illustrated in the middle panel of Figure 1.4, and at the time of writing it has not yet been experimentally verified.

1.5.3 Giant Proximity Effect and Control of Spin Supercurrent

In Ref. [58], the authors derive the Riccati-parameterized Usadel equation with spin-orbit coupling and go on to provide a detailed account of the effect of spin-orbit coupling on the density of states and T_c in transversal thin-films. It is shown that the density of states depends strongly on the direction of magnetization, so that in fact the direction of the exchange field can be used to tune the minigap from open to closed. Moreover, when the spin-orbit coupling direction corresponds to the transverse layering direction, the presence of spin-orbit coupling leads to an enhanced proximity effect at a phase difference $\phi = \pi$, in contrast to the well-known suppression of such effects when no spin-orbit coupling is present [59]. In fact, it is possible to fully isolate the triplet component without any contamination from singlets, and this triplet-only state persists throughout the entire interstitial layer, all the way up to the superconducting contacts. This effect is illustrated in the right panel of Figure 1.4. The density of states has a nonmonotonic dependence on the spin-orbit coupling, and, when the exchange field lies along the junction, large coupling can again lead to a magnetically tunable gap, with a gap at $\phi = 0$ and zero-energy peak at $\phi = \pi$. The significant impact of spin-orbit coupling on the density of states translates into an equally dramatic effect on the supercurrent that can flow between the superconductors of a Josephson junction. The authors have shown that for an SNFNS junction, with very thin normal-metal layers (N) and a *homogeneous* ferromagnet, it is possible generate and control a spin supercurrent that displays spin-flip immunity [129]. Normal spin currents remain polarized only up to the spin relaxation length, so the lack of spatial decay of the current is remarkable.

1.5.4 Inducing Magnetism via Superconductivity

Whereas so far we have discussed mainly how the presence of magnetic order influences superconductivity, the reciprocal phenomenon is also possible. As an example, one can consider Ref. [130] where it was proposed that it is possible to control magnetism via supercurrents. The concrete system under consideration was an SNFNS junction which supports a supercurrent when phase-biased. Due to the appearance of triplet Cooper pairs in such a junction, there exists a proximity induced magnetization

\mathbf{M} in the normal metal, which depends sensitively on the superconducting phase difference ϕ and the length d of the junction. Interestingly, the total induced magnetization $\mathbf{M} = \mathbf{M}_1 + \mathbf{M}_2$ could be decomposed into a phase-independent part $\mathbf{M}_1 = \mathbf{M}_1(d)$ and a phase-dependent part $\mathbf{M}_2 = \mathbf{M}_2(\phi, d)$. The authors found that whereas M_2 decays rapidly with the length d , the phase-independent part only weakly decreased upon increasing d . This proposal is interesting because it goes beyond discussing the long-ranged effect of triplet supercurrents and instead links Cooper pairs directly to their spin-properties, which could possibly be integrated with other magnetic components in a cryogenic spintronic device. The spin supercurrent flowing through a similar system was found to behave similarly as the magnetization [55]. The fact that a triplet proximity effect can induce a magnetization could also be a possible explanation for the remotely induced magnetism via a superconductor reported in Ref. [131], a topic which deserves further exploration.

1.6 Outlook

The field of superconducting spintronics is developing rapidly and a number of challenges can be identified from the above discussions. Theoretical models of spin-orbit coupling show great potential for enhancing features such as long-range superconducting proximity effects and realizing ϕ_0 -junctions, but a number of experimental challenges must be overcome before the effect can be adequately included in real thin-films. Consensus has not yet been reached regarding the precise penetration depth of surface Rashba-coupling into the bulk of materials. Although the relative strengths of Rashba and Dresselhaus couplings in *e.g.* semiconducting quantum wells can be measured separately [132], tuning them separately in a controllable manner has proven more challenging. We see the benefits of noncentrosymmetric materials come up again and again in the context of SF structures, and one of the most promising experimental directions to study their significance could be to make use of very thin heavy normal metals to induce Rashba coupling.

The upswing in experimental activity in the field of superconductor/ferromagnet structures has been notable over the last few years. We believe that one of the most interesting experimental directions to explore in the coming years will be the direct measurement of the triplet Cooper pair spin (as opposed to indirect via long-ranged supercurrents through ferromagnets or spectroscopic measurements of the frequency-symmetry). There are different ways in which this can be achieved. Experiments measuring effects such as domain wall motion, spin-transfer torques, and

magnetization switching due to spin-polarized supercurrents are likely to have a transformative effect on the field as it would open up a whole new avenue of possible cryogenic applications via superconducting spintronics. Moreover, the theory of equilibrium physics in SF structures is mostly well-developed at present, but there remains much work to be done on the non-equilibrium side. Spin and charge dynamics in systems combining superconducting and magnetic elements remain far less explored. Developing these aspects of the theory will be a necessary step in order to further advance the field and identify novel dynamic effects involving triplet Cooper pairs, both with regard to thermoelectric effects and magnetization dynamics.

Another interesting avenue to explore is the electromagnetic response of magnetic structures including superconducting elements. Ref. [131] demonstrated remotely induced magnetism mediated by a superconductor, leaving the question of how this phenomenon occurred open and thus also indicating that novel electromagnetic phenomena in superconductors may still lie undiscovered. Superconductivity is usually defined by its two hallmark properties of zero electrical resistance and the tendency to expel magnetic flux. Previous works have nanoengineered superconducting films with a lattice of magnetic dots in order to control the existence of superconductivity by the interplay of an applied field and the stray field of the dipole array of dots [133]. However, the role of odd-frequency superconductivity with regard to the electromagnetic response appears to be of crucial importance, as recently indicated by Di Bernardo *et al.* who reported an *inverse Meissner effect*, *i.e.* the enhancement of magnetic flux via a superconductor [134]. This finding is in agreement with theoretical predictions regarding how odd-frequency pairing in SF layers should influence the Meissner effect [135, 136]. Remarkably, this finding may cause us to rethink what the fundamental properties of superconductivity really are.

We have no doubt that the coming years will see a number of exciting experimental and theoretical advances with regard to the role of spin-orbit coupling and magnetization dynamics in SF structures, and thereby open up a rich new testing-ground for the further development of superconducting spintronics.

Acknowledgements

We have benefitted from discussions and collaborations with a number of researchers, but we would like to mention in particular M. Eschrig, J. W. A. Robinson, A. Di Bernardo, A. Pal, N. Banerjee, M. Blamire,

M. Cuoco, K. Halterman, M. Amundsen, V. Risinggård, and I. Kulagina. We acknowledge funding and support via the “Outstanding Academic Fellows” programme at NTNU, the COST Action MP-1201 and the Research Council of Norway Grant numbers 205591, 216700, and 240806.

References

1. Baibich, M.N. *et al.* Giant Magnetoresistance of (001)Fe/(001)Cr Magnetic Superlattices. *Phys. Rev. Lett.* 61, 2472, 1988.
2. Binash, G. *et al.* Enhanced magnetoresistance in layered magnetic structures with antiferro magnetic interlayer exchange *Phys. Rev. B* 39, 4828(R), 1989.
3. Linder, J. and Robinson, J.W.A. Superconducting spintronics. *Nat. Phys.* 11, 307, 2015.
4. Huertas-Hernando, D., Nazarov, Y.V., and Belzig, W. Absolute spin-valve effect with super-conducting proximity structures. *Phys. Rev. Lett.* 88, 047003, 2002.
5. Fominov, Y.V. *et al.* Superconducting triplet spin valve. *JETP Lett.* 91, 308–313, 2010.
6. Slonczewski, J.C. Mechanism of interlayer exchange in magnetic multilayers. *J. Magn. Magn. Mater.* 126, 374, 1993.
7. Slonczewski, J.C. Current-driven excitation of magnetic multilayers. *J. Magn. Magn. Mater.* 159, L1–L7, 1996.
8. Kamerlingh Onnes, H. The resistance of pure mercury at helium temperatures. *Commun. Phys. Lab. Univ. Leiden* 12, 120, 1911.
9. Meissner, W. and Ochsenfeld, R. Ein neuer Effekt bei Eintritt der Supraleitfähigkeit. *Naturwissenschaften* 21(44): 787–788, 1933.
10. Meservey, R., Tedrow, P.M. and Fulde, P. Magnetic Field Splitting of the Quasiparticle States in Superconducting Aluminium Films. *Phys. Rev. Lett.* 25, 1270, 1970.
11. Tedrow, P. M. & Meservey, R. Spin-dependent tunneling into ferromagnetic nickel. *Phys. Rev. Lett.* 26, 192–195, 1971.
12. Tedrow, P. M. & Meservey, R. Spin polarization of electrons tunneling from films of Fe, Co, Ni, and Gd. *Phys. Rev. B* 7, 318–326, 1973.
13. Tedrow, P. M. & Meservey, R. Spin-polarized electron tunneling. *Phys. Rep.* 238, 173–243, 1994.
14. Johnson, M. & Silsbee, R. H. Interfacial charge-spin coupling: Injection and detection of spin magnetization in metals. *Phys. Rev. Lett.* 55, 1790–1793, 1985.
15. Li, B. *et al.* Superconducting spin switch with infinite magnetoresistance induced by an internal exchange field. *Phys. Rev. Lett.* 110, 097001, 2013.
16. Yang, H., Yang, S.-H., Takahashi, S., Maekawa, S. & Parkin, S. S. P. Extremely long quasiparticle spin lifetimes in superconducting aluminium using MgO tunnel spin injectors. *Nature Mater.* 9, 586–593, 2010.

17. Quay, C. H. L., Chevallier, D., Bena, C. & Aprili, M. Spin imbalance and spin-charge separation in a mesoscopic superconductor. *Nature Phys.* 9, 84–88, 2013.
18. Wakamura, T., Omori, Y., Niimi, Y., Takahashi, S., Fujimaki, A., Maekawa, S. & Otani, Y. Quasiparticle-mediated spin Hall effect in a superconductor. *Nature Materials* 14, 675–678, 2015.
19. Kolenda, S., Wolf, M. J., and Beckmann, D. Observation of thermoelectric currents in high-field superconductor-ferromagnet tunnel junctions. *Phys. Rev. Lett.* 116, 097001, 2016.
20. Bardeen, J., Cooper, L.N. and Schrieffer, J.R. Microscopic Theory of Superconductivity. *Phys. Rev.* 106, 162, 1957.
21. Bogoliubov, N.N. A new method in the theory of superconductivity I. *Soviet Phys. JETP* 34, 41, 1958.
22. Drozdov, A.P. *et al.* Conventional superconductivity at 203 kelvin at high pressures in the sulfur hydride system. *Nature* 525, 73, 2015.
23. Nagamatsu, J. *et al.* Superconductivity at 39 K in magnesium diboride. *Nature* 410, 63, 2001.
24. Bednorz, J.G. and Müller, K.A. Possible high T_c superconductivity in the Ba-La-Cu-O system. *Z. Physik, B.* 64(1), 189, 1986.
25. Cooper, L.N. Bound electron pairs in a degenerate Fermi gas. *Phys. Rev.* 104(1), 1189, 1956.
26. Loram, J. W., Mirza, K. A., Cooper, J. R., and Liang, W. Y. Electronic specific heat of $\text{YBa}_2\text{Cu}_3\text{O}_{6+x}$ from 1.8 to 300 K. *Phys. Rev. Lett.* 71, 1740, 1993.
27. Tinkham, M. *Introduction to Superconductivity*, (McGraw-Hill, 1996), 2nd Edition.
28. Sudbø, A. and Fossheim, K. *Superconductivity: Physics and Applications*. Wiley, 2004.
29. Bergeret, F.S., Volkov, A.F. and Efetov, K.B. Odd triplet superconductivity and related phenomena in superconductor-ferromagnet structures. *Rev. Mod. Phys.* 77(4), 1321, 2005.
30. Buzdin, A.I. Proximity effects in superconductor-ferromagnet heterostructures. *Rev. Mod. Phys.* 77(3), 935, 2005.
31. Fulde, P. and Ferrell, R.A. Superconductivity in a strong spin-exchange field. *Phys. Rev.* 135, A550, 1964.
32. Larkin, A.I. and Ovchinnikov, Y.N. Nonuniform state of superconductors. *Sov. Phys. JETP* 20, 762, 1965.
33. Eschrig, M. Spin-polarized supercurrents for spintronics. *Phys. Today.* 64, 43, 2011.
34. Saxena, S.S. *et al.* Superconductivity on the border of itinerant-electron ferromagnetism in UGe_2 . *Nature (London)* 406, 587, 2000.
35. Aoki, D. *et al.* Coexistence of superconductivity and ferromagnetism in URhGe . *Nature (London)* 413, 613, 2001.
36. Bauer, E. *et al.* Heavy Fermion Superconductivity and Magnetic Order in Noncentrosymmetric CePt_3Si . *Phys. Rev. Lett.* 92, 027003, 2004.

37. Maeno, Y. *et al.* Superconductivity in a layered perovskite without copper. *Nature* 372, 532, 1994.
38. Mackenzie, A.P. and Maeno, Y. The superconductivity of Sr_2RuO_4 and the physics of spin-triplet pairing. *Rev. Mod. Phys.* 75, 657, 2003.
39. Annunziata, G. *et al.* Spin-sensitive long-range proximity effect in ferromagnet/spin-triplet-superconductor bilayers. *Phys. Rev. B* 83, 060508(R), 2011.
40. Bergeret, F. S., Volkov, A. F. & Efetov, K. B. Long-Range Proximity Effects in Superconductor-Ferromagnet Structures. *Phys. Rev. Lett.* 86, 4096, 2001.
41. Kadigrobov, A., Shekhter, R. and Jonson, M. Quantum spin fluctuations as a source of long-range proximity effects in diffusive ferromagnet-superconductor structures. *Europhys. Lett.* 54, 394, 2001.
42. Eschrig, M., Kopu, J., Cuevas, J.C. and Schön, G. Theory of half-metal/superconductor heterostructures. *Phys. Rev. Lett.* 90, 137003, 2003.
43. Yokuyasu, T., Sauls, J.A. and Rainer, D. Proximity effect of a ferromagnetic insulator in contact with a superconductor. *Phys. Rev. B* 38, 8823, 1988.
44. Halterman, K., Barsic, P.H. and Valls, O.T. Odd triplet pairing in clean superconductor/ferromagnet heterostructures. *Phys. Rev. Lett.* 99, 127002, 2007.
45. Cottet, A. Inducing odd-frequency triplet superconducting correlations in a normal metal. *Phys. Rev. Lett.* 107, 177001, 2011.
46. Asano, Y., Sawa, Y., Tanaka, Y. and Golubov, A.A. Odd-frequency pairs and Josephson current through a strong ferromagnet. *Phys. Rev. B* 76, 224525, 2007.
47. Kalcheim, Y. *et al.* Magnetic field dependence of the proximity-induced triplet superconductivity at ferromagnet/superconductor interfaces. *Phys. Rev. B* 89, 180506(R), 2014.
48. Robinson, J.W.A., Witt, J.D., and Blamire, M. Controlled injection of spin-triplet supercurrents into a strong ferromagnet. *Science* 329, 59, 2010.
49. Khaire, T.S. *et al.* Observation of spin-triplet superconductivity in Co-based Josephson Junctions. *Phys. Rev. Lett.* 104, 137002, 2010.
50. Alidoust, M. and Linder, J. Spin-triplet supercurrent through inhomogeneous ferromagnetic trilayers. *Phys. Rev. B* 82, 224504, 2010.
51. Sperstad, I.B., Linder, J. and Sudbø, A. Josephson current in diffusive multilayer superconductor/ferromagnet/superconductor junctions *Phys. Rev. B* 78, 104509, 2008.
52. Trifunovic, L. and Radović, Z. Long-range spin-triplet proximity effect in Josephson junctions with multilayered ferromagnets. *Phys. Rev. B* 82, 020505(R), 2010.
53. Sosnin, I., Cho, H., Petrashov, V.T. and Volkov, A.F. Superconducting phase coherent electron transport in proximity conical ferromagnets. *Phys. Rev. Lett.* 96, 157002, 2006.
54. Shomali, Z., Zareyan, M. and Belzig, W. Spin supercurrent in Josephson contacts with noncollinear ferromagnets. *New J. Phys.* 13, 083033, 2011.
55. Gomperud, I. and Linder, J. Spin supercurrent and phase-tunable triplet Cooper pairs via magnetic insulators. *Phys. Rev. B* 92, 035416, 2015.

56. Bergeret, F.S. and Tokatly, I.V. Singlet-triplet conversion and the long-range proximity effect in superconductor-ferromagnet structures with generic spin dependent fields. *Phys. Rev. Lett.* 110, 117003, 2013.
57. Bergeret, F.S. and Tokatly, I.V. Spin-orbit coupling as a source of long-range triplet proximity effect in superconductor-ferromagnet hybrid structures. *Phys. Rev. B* 89, 134517, 2014.
58. Jacobsen, S.H., Ouassou, J.A. and Linder, J. Critical temperature and tunneling spectroscopy of superconductor-ferromagnet hybrids with intrinsic Rashba-Dresselhaus spin-orbit coupling. *Phys. Rev. B* 92, 024510, 2015.
59. Jacobsen, S.H. and Linder, J. Giant triplet proximity effect in π -biased Josephson Junctions with spin-orbit coupling. *Phys. Rev. B* 92, 024501, 2015.
60. Andreev, A.F. Thermal conductivity of the intermediate state of superconductors. *Sov. Phys. JETP*. 19, 1228, 1964.
61. Josephson, B.D. Possible new effects in superconductive tunnelling. *Phys. Lett.* 1, 251, 1962.
62. Josephson, B.D. The discovery of tunnelling supercurrents. *Rev. Mod. Phys.* 46(2), 251, 1974.
63. Golubov, A.A., Kupriyanov, M.Yu. and Il'ichev, E. The current-phase relation in Josephson junctions. *Rev. Mod. Phys.* 76(2), 411, 2004.
64. Kontos, T. *et al.* Inhomogeneous superconductivity induced in a ferromagnet by proximity effect. *Phys. Rev. Lett.* 86, 304, 2001.
65. Hummel, R.E. *Electronic Properties of Materials*, Springer, New York, 2011, 4th Edition.
66. Tanaka, Y. and Golubov, A.A. Theory of the Proximity Effect in Junctions with Unconventional Superconductors. *Phys. Rev. Lett.* 98, 037003, 2007.
67. SanGiorgio, P. *et al.* Anomalous Double Peak Structure in Superconductor/Ferromagnet Tunneling Density of States. *Phys. Rev. Lett.* 100, 237002, 2008.
68. Linder, J. and Robinson, J.W.A. Strong odd-frequency correlations in fully gapped Zeeman-split superconductors. *Sci. Rep.* 5, 15483, 2015.
69. Belzig, W. *et al.* Quasiclassical Green's function approach to mesoscopic superconductivity. *Superlattices and Microstructures* 25, 1251, 1999.
70. Le Sueur, H. *et al.* Controlled Superconducting Proximity Effect Probed by Tunneling Spectroscopy. *Phys. Rev. Lett.* 100, 197002, 2008.
71. Zhou, F. *et al.* Density of States in Superconductor-Normal-Metal-Superconductor Junctions. *J. Low Temp. Phys.* 110, 841, 1998.
72. Ryazanov, V.V. *et al.* Coupling of Two Superconductors through a Ferromagnet: Evidence for a Junction. *Phys. Rev. Lett.* 86, 2427, 2001.
73. Yokoyama, T., Tanaka, Y. and Golubov, A.A. Resonant peak in the density of states in normal-metal/diffusive-ferromagnet/superconductor junctions. *Phys. Rev. B* 72, 052512, 2005.
74. Yokoyama, T., Tanaka, Y. and Golubov, A.A. Resonant proximity effect in normal metal/diffusive ferromagnet/superconductor junctions. *Phys. Rev. B* 73, 094501, 2006.

75. Kawabata, S. *et al.* Robustness of Spin-Triplet Pairing and Singlet-Triplet Pairing Crossover in Superconductor/Ferromagnet Hybrids. *J. Phys. Soc. Jpn.* 82, 124702, 2013.
76. de Gennes, P.G. *Superconductivity of Metals and Alloys*. Benjamin, New York, 1966.
77. Eilenberger, G. Transformation of Gorkov's Equation for Type II Superconductors into Transport-Like Equations. *Z. Phys.* 214, 195, 1968.
78. Usadel, K. Generalized Diffusion Equation for Superconducting Alloys. *Phys. Rev. Lett.* 25, 507, 1970.
79. Chandrasekhar, V. *An introduction to the quasiclassical theory of superconductivity for diffusive proximity-coupled systems*, book chapter in *The Physics of Superconductors: Vol. II*, Ed. K. H. Bennemann and J. B. Ketterson, Springer, Berlin, 2004.
80. Wright, M.C.M. Green function or Green's function? *Nature Physics* 2, 464, 2006.
81. Keldysh, L.V. Diagram technique for nonequilibrium processes. *Soviet Physics JETP* 20, 1018, 1965.
82. Matsubara, T. A new approach to quantum statistical mechanics. *Prog. Theor. Phys.* 14, 351, 1955.
83. Schmid, A. *Nonequilibrium Superconductivity*. Ed. K.E. Gray (Plenum, New York, 1981).
84. Rammer, J. and Smith, H. Quantum field-theoretical methods in transport theory of metals. *Rev. Mod. Phys.* 58, 323, 1986.
85. Morten, J.P. Spin and Charge Transport in Dirty Superconductors. *Norwegian University of Science and Technology*, Master thesis, 2005.
86. Maki, K. Gapless Superconductivity, in *Superconductivity*, edited by R.D. Parks, vol. 2, pages 1035–1106, Marcel Dekker, New York, 1969.
87. Ivanov, D.A. and Fominov, Ya.V. Minigap in superconductor-ferromagnet junctions with inhomogeneous magnetization. *Phys. Rev. B* 73, 214524, 2006.
88. Schopohl, N. and Maki, K. Quasiparticle spectrum around a vortex line in a d-wave superconductor. *Phys. Rev. B* 52, 490, 1995.
89. Schopohl, N. Transformation of the Eilenberger Equations of Superconductivity to a Scalar Riccati Equation. *arXiv: cond-mat/9804064*, 1998.
90. Lyuksyutov, I.F. and Pokrovsky, V.L. Ferromagnet-superconductor hybrids. *Adv. Phys.* 54, 67, 2005.
91. Blamire, M.G. and Robinson, J.W.A. The interface between superconductivity and magnetism: understanding and device prospects. *J. Phys.: Condens. Matter* 26, 453201, 2014.
92. Eschrig, M. Spin-polarized supercurrents for spintronics: a review of current progress. *Rep. Prog. Phys.* 78, 10, 2015.
93. Lüth, H. *Solid Surfaces, Interfaces and Thin Films*, (Springer, Berlin Heidelberg 2010), 5th Edition.
94. Oboznov, V. A., Bol'ginov, V. V., Feofanov, A. K., Ryazanov, V. V. & Buzdin, A. I. Thickness Dependence of the Josephson Ground States of

- Superconductor-Ferromagnet-Superconductor Junctions. *Phys. Rev. Lett.* 96, 197003, 2006.
95. Di Bernardo, A. *et al.* Signature of magnetic-dependent gapless odd frequency states at superconductor/ferromagnet interfaces. *Nat. Commun.* 6, 8053, 2015.
 96. Jaklevic, R.C. *et al.* Quantum Interference Effects in Josephson Tunneling. *Phys. Rev. Lett.* 12, 159, 1964.
 97. Silver, A.H. and Zimmerman, J.E. Quantum States and Transitions in Weakly Connected Superconducting Rings. *Phys. Rev.* 157, 317, 1967.
 98. Sternickel, K. and Braginski, A.I. Biomagnetism using SQUIDS: Status and perspectives. *Supercond. Sci. Technol.* 19, S160, 2006.
 99. Cleuziou, J.-P. *et al.* Carbon nanotube superconducting quantum interference device. *Nat. Nanotech.* 1, 53, 2006.
 100. Foley, C.P. and Hilgenkamp, H. Why NanoSQUIDS are important: an introduction to the focus issue. *Supercond. Sci. Technol.* 22, 064001, 2009.
 101. Vasyukov, D. *et al.* A scanning superconducting quantum interference device with single electron spin sensitivity. *Nature Nanotech.* 8, 639, 2013.
 102. Kimura, T. *et al.* Room-Temperature Reversible Spin Hall Effect. *Phys. Rev. Lett.* 98, 156601, 2007.
 103. Hübner, F., Wolf, M.J., Beckmann, D. and v. Löhneysen, H. Long-Range Spin-Polarized Quasiparticle Transport in Mesoscopic Al Superconductors with a Zeeman Splitting. *Phys. Rev. Lett.* 109, 207001, 2012.
 104. Sprungmann, D., Westerholt, K., Zabel, H., Weides, M. and Kohlstedt, H. Evidence for triplet superconductivity in Josephson junctions with barriers of the ferromagnetic Heusler alloy Cu_2MnAl . *Phys. Rev. B* 82, 060505(R), 2010.
 105. Keizer, R.S., Goennenwein, S.T.B., Klapwijk, T.M., Miao, G., Xiao, G. and Gupta, A. A spin triplet supercurrent through the half-metallic ferromagnet CrO_2 . *Nature* 439, 825, 2006.
 106. Eschrig, M. & Löfwander, T. Triplet supercurrents in clean and disordered half-metallic ferromagnets. *Nature Physics* 4, 138, 2008.
 107. Martinez, W., Pratt, Jr., W.P., Birge, N.O. Amplitude control of spin-triplet supercurrent in S/F/S Josephson junctions. *Phys. Rev. Lett.* 116, 077001, 2016.
 108. Kalcheim, Y., Millo, O., Di Bernardo, A., Pal, A. and Robinson, J.W.A. Inverse proximity effect at superconductor-ferromagnet interfaces: Evidence for induced triplet pairing in the superconductor. *Phys. Rev. B* 92, 060501(R), 2015.
 109. Leksin, P. V., Garif'yanov, N. N., Garifullin, I. A., Fominov, Ya. V., Schumann, J., Krupskaya, Y., Kataev, V., Schmidt, O. G., and Buchner. Evidence for Triplet Superconductivity in a Superconductor-Ferromagnet Spin Valve. *Phys. Rev. Lett.* 109, 057005, 2012.
 110. Jara, A. A., Safranski, C., Krivorotov, I., Wu, C.-T., Malmi-Kakkada, A. N., Valls, O. T., and Halterman, K. Angular dependence of superconductivity in superconductor/spin-valve heterostructures. *Phys. Rev. B* 89, 184502, 2014.

111. Wang, X. L., Di Bernardo, A., Banerjee, N., Wells, A., Bergeret, F. S., Blamire, M. G. & Robinson, J. W. A. Giant triplet proximity effect in superconducting pseudo spin valves with engineered anisotropy. *Phys. Rev. B* 89, 140508(R), 2014.
112. Banerjee, N., Smiet, C. B., Ozaeta, A., Bergeret, F. S., Blamire, M. G., and Robinson, J. W. A. Evidence for spin-selectivity of triplet pairs in superconducting spin-valves. *Nature Communications* 5, 3048, 2014.
113. Gu, J. Y., You, C.-Y., Jiang, J. S., Pearson, J., Bazaliy, Ya. B., and Bader, S. D. Magnetization-Orientation Dependence of the Superconducting Transition Temperature in the Ferromagnet-Superconductor-Ferromagnet System: CuNi/Nb/CuNi. *Phys. Rev. Lett.* 89, 267001, 2002.
114. Moraru, I. C., Pratt Jr., W. P., and Birge, N. O. Magnetization-Dependent T_c Shift in Ferromagnet/Superconductor/Ferromagnet Trilayers with a Strong Ferromagnet. *Phys. Rev. Lett.* 96, 037004, 2006.
115. Singh, A., Voltan, S., Lahabi, K. and Aarts, J. Colossal Proximity Effect in a Superconducting Triplet Spin Valve Based on the Half-Metallic Ferromagnet CrO_2 . *Phys. Rev. X* 5, 021019, 2015.
116. Robinson, J.W.A. Viewpoint: A Boost for Superconducting Logic. *Physics* 8, 49, 2015.
117. Machon, P., Eschrig, M. and Belzig, W. Nonlocal Thermoelectric Effects and Nonlocal Onsager relations in a Three-Terminal Proximity-Coupled Superconductor-Ferromagnet Device. *Phys. Rev. Lett.* 110, 047002, 2013.
118. Ozaeta, A., Virtanen, P., Bergeret, F.S. and Heikkilä, T.T. Predicted Very Large Thermoelectric Effect in Ferromagnet-Superconductor Junctions in the Presence of a Spin-Splitting Magnetic Field. *Phys. Rev. Lett.* 112, 057001, 2014.
119. Rugar, D. *et al.* Single spin detection by magnetic resonance force microscopy. *Nature* 430, 329, 2004.
120. Grinolds, M.S. *et al.* Nanoscale magnetic imaging of a single electron spin under ambient conditions. *Nature Phys.* 9, 215, 2013.
121. Wang, J. *et al.* Interplay between superconductivity and ferromagnetism in crystalline nanowires. *Nature Phys.* 6, 389, 2010.
122. Melnikov, A.S. and Buzdin, A.I., Giant Mesoscopic Fluctuations and Long-Range Superconducting Correlations in Superconductor-Ferromagnet Structures, *Phys. Rev. Lett.* 117, 077001, 2016.
123. Geschkenbein, V.B. and Larkin, A.I. The Josephson effect in superconductors with heavy fermions. *JETP Lett.* 43, 395, 1986 [*Pis'ma Zh. Eksp. Teor. Fiz.* 43, 306, 1986].
124. Yip, S. Josephson current-phase relationships with unconventional superconductors. *Phys. Rev. B* 52, 3087, 1995.
125. Sigrist, M. Time-reversal symmetry breaking states in high-temperature superconductors. *Prog. Theor. Phys.* 99, 899, 1998.
126. Buzdin, A. Direct coupling between magnetism and superconducting current in the Josephson ϕ_0 junction. *Phys. Rev. Lett.* 101, 107005, 2008.

127. Bergeret, F.S. and Tokatly, I.V. Theory of diffusive ϕ_0 Josephson junctions in the presence of spin-orbit coupling. *Euro. Phys. Lett.* 110, 57005, 2015.
128. Szombati, D.B., Nadj-Perge, S., Car, D., Plissard, S.R., Bakkers, E.P.A.M. and Kouwenhoven, L.P. Josephson ϕ_0 -junction in nanowire quantum dots. *Nature Physics* 12, 568–572, 2016.
129. Jacobsen, S.H., Kulagina, I. and Linder, J. Controlling superconducting spin flow with spin-flip immunity using a single homogeneous ferromagnet. *Sci. Rep.* 6, 23926, 2016.
130. Hikino, S. and Yunoki, S. Magnetization induced by odd-frequency spin-triplet Cooper pairs in a Josephson junction with metallic trilayers. *Phys. Rev. B* 92, 024512, 2015.
131. Flokstra, M.G. *et al.* Remotely induced magnetism in a normal metal using a superconducting spin-valve. *Nat. Phys.* 12, 57–61, 2016.
132. Ganichev, S.D. *et al.* Experimental Separation of Rashba and Dresselhaus Spin Splittings in Semiconductor Quantum Wells. *Phys. Rev. Lett.* 92, 256601, 2004.
133. Lange, M., van Bael, M.J., Bruynseraede, Y. and Moshchalkov, V.V. Nanoengineered Magnetic-Field-Induced Superconductivity. *Phys. Rev. Lett.* 90, 197006, 2003.
134. Di Bernardo, A. *et al.* Intrinsic paramagnetic Meissner effect due to *s*-wave odd frequency superconductivity. *Phys. Rev. X* 5, 041021, 2015.
135. Yokoyama, T., Tanaka, Y. and Nagaosa, N. Anomalous Meissner Effect in a Normal-Metal–Superconductor Junction with a Spin-Active Interface. *Phys. Rev. Lett.* 106, 246601, 2011.
136. Mironov, S., Mel'nikov, A. and Buzdin, A. Vanishing Meissner effect as a Hallmark of in-Plane Fulde-Ferrell-Larkin-Ovchinnikov Instability in Superconductor–Ferromagnet Layered Systems. *Phys. Rev. Lett.* 109, 237002, 2012.

II

Reference

S.H. Jacobsen, [J.A. Ouassou](#), J. Linder.
Critical temperature and tunneling spectroscopy of
superconductor–ferromagnet hybrids with intrinsic
Rashba–Dresselhaus spin–orbit coupling.
Physical review B 92, 024510 (2015).
DOI: 10/GC4M3J

Contributions

SHJ and JAO independently Riccati-parametrized the Usadel equation with spin–orbit coupling, and derived the linearized weak-proximity equations. SHJ performed the numerical calculations of the density of states. JAO performed the numerical calculations of the critical temperature. JL had the original idea and supervised the work process. All authors contributed to the discussion and writing of the manuscript.

Comments

This publication was technically not produced as part of my doctoral work, but rather during my master project [1, 2]. However, since it is closely linked to two papers produced during my doctoral work [III, IV], it is included here for completeness. This work has been presented as a talk at the March Meeting of the APS (Baltimore, United States, 2016).

Critical temperature and tunneling spectroscopy of superconductor-ferromagnet hybrids with intrinsic Rashba-Dresselhaus spin-orbit coupling

Sol H. Jacobsen,* Jabir Ali Ouassou,* and Jacob Linder

Department of Physics, Norwegian University of Science and Technology, N-7491 Trondheim, Norway

(Received 24 March 2015; revised manuscript received 17 June 2015; published 24 July 2015)

We investigate theoretically how the proximity effect in superconductor/ferromagnet hybrid structures with intrinsic spin-orbit coupling manifests in two measurable quantities, namely, the density of states and critical temperature. To describe a general scenario, we allow for both Rashba- and Dresselhaus-type spin-orbit coupling. Our results are obtained via the quasiclassical theory of superconductivity, extended to include spin-orbit coupling in the Usadel equation and in the Kupriyanov-Lukichev boundary conditions. Unlike previous works, we have derived a Riccati parametrization of the Usadel equation with spin-orbit coupling which allows us to address the full proximity regime and not only the linearized weak proximity regime. First, we consider the density of states in both SF bilayers and SFS trilayers, where the spectroscopic features in the latter case are sensitive to the phase difference between the two superconductors. We find that the presence of spin-orbit coupling leaves clear spectroscopic fingerprints in the density of states due to its role in creating spin-triplet Cooper pairs. Unlike SF and SFS structures without spin-orbit coupling, the density of states in the present case depends strongly on the direction of magnetization. Moreover, we show that the spin-orbit coupling can stabilize spin-singlet superconductivity even in the presence of a strong exchange field $h \gg \Delta$. This leads to the possibility of a magnetically tunable minigap: changing the direction of the exchange field opens and closes the minigap. We also determine how the critical temperature T_c of an SF bilayer is affected by spin-orbit coupling and, interestingly, demonstrate that one can achieve a spin-valve effect with a single ferromagnet. We find that T_c displays highly nonmonotonic behavior both as a function of the magnetization direction as well as the type and direction of the spin-orbit coupling, offering a new way to exert control over the superconductivity of proximity structures.

DOI: [10.1103/PhysRevB.92.024510](https://doi.org/10.1103/PhysRevB.92.024510)

PACS number(s): 74.50.+r, 74.45.+c, 74.78.-w, 75.70.Tj

I. INTRODUCTION

Material interfaces in hybrid structures give rise to proximity effects, whereby the properties of one material can “leak” into the adjacent material, creating a region with properties derived from both materials. In superconductor/ferromagnet (SF) hybrid structures [1], the proximity effect causes superconducting correlations to penetrate into the ferromagnetic region and vice versa. These correlations typically decay over short distances, which in diffusive systems is of the order $\sqrt{D/\hbar}$, where D is the diffusion coefficient of the ferromagnet and \hbar is the strength of the exchange field. However, for certain field configurations, the singlet correlations from the superconductor may be converted into so-called long-range triplets (LRTs) [2]. These triplet components have spin projection parallel to the exchange field, and decay over much longer distances. This results in physical quantities like supercurrents decaying over the length scale $\xi_N = \sqrt{D/T}$, which is usually much larger than the ferromagnetic coherence length $\xi_F = \sqrt{D/\hbar}$, where T is the temperature. This distance is independent of \hbar , and at low temperatures it becomes increasingly large, which allows the condensate to penetrate deep into the ferromagnet. The isolation and enhancement of this feature has attracted much attention in recent years as it gives rise to novel physics and possible low-temperature applications by merging spintronics and superconductivity [3].

It is by now well-known that the conversion from singlet to long-range triplet components of the superconducting state can happen in the presence of magnetic inhomogeneities [4,5],

i.e., a spatially varying exchange field, and until recently such inhomogeneities were believed to be the primary source of this conversion [6–15], although other proposals using, e.g., nonequilibrium distribution functions and intrinsic triplet superconductors also exist [16–19]. However, it has recently been established that another possible source of LRT correlations is the presence of a finite spin-orbit (SO) coupling, either in the superconducting region [20] or on the ferromagnetic side [21,22]. In fact, it can be shown that an SF structure where the magnetic inhomogeneity is due to a Bloch domain wall, as considered in, e.g., Refs. [23–25], is gauge equivalent to one where the ferromagnet has a homogeneous exchange field and intrinsic SO coupling [21]. It is known that SO scattering can be caused by impurities [26], but this type of scattering results in purely isotropic spin-relaxation, and so does not permit the desired singlet-LRT conversion. To achieve such a conversion, one needs a rotation of the spin pair into the direction of the exchange field [27]. This can be achieved by using materials with an intrinsic SO coupling, either due to the crystal structure in the case of noncentrosymmetric materials [28], or due to interfaces in thin-film hybrids [29], where the latter also modifies the fundamental process of Andreev reflection [30,31]. The role of SO coupling with respect to the supercurrent in ballistic hybrid structures has also been studied recently [32].

In this paper, we establish how the presence of spin-orbit coupling in SF structures manifests in two important experimental observables: the density of states $D(\epsilon)$ probed via tunneling spectroscopy (or conductance measurements), and the critical temperature T_c . A common consequence for both of these quantities is that neither becomes independent of the magnetization direction. This is in contrast to the case without

*These authors contributed equally to this work.

SO coupling in conventional monodomain ferromagnets, where the results are invariant with respect to rotations of the magnetic exchange field. This symmetry is now lifted due to SO coupling: depending on the magnetization direction, LRT Cooper pairs can be created, and this leaves clear fingerprints both spectroscopically and in terms of the T_c behavior. On the technical side, we will present in this work for the first time a Riccati parametrization of the Usadel equation and its corresponding boundary conditions that include SO coupling. This is an important advance in terms of exploring the full physics of triplet pairing due to SO coupling as it allows for a solution of the quasiclassical equations without any assumption of a weak proximity effect. We will also demonstrate that the SO coupling can actually protect the singlet superconducting correlations even in the presence of a strong exchange field, leading to the possibility of a minigap that is magnetically tunable via the orientation of the exchange field.

The remainder of the article will be organized as follows. In Sec. II, we introduce the relevant theory and notation, starting from the quasiclassical Usadel equation, which describes the diffusion of the superconducting condensate into the ferromagnet. We also motivate our choice of intrinsic SO coupling in this section, and propose a new notation for describing Rashba-Dresselhaus coupling. The section goes on to discuss key analytic features of the equations in the limit of weak proximity, symmetries of the density of states at zero energy, and analytical results needed to calculate the critical temperature of hybrid systems. We then present detailed numerical results in Sec. III: we analyze the density of states of an SF bilayer in Sec. III A [see Fig. 1(a)], with the case of pure Rashba coupling considered in Sec. III B, and we study the SFS Josephson junction in Sec. III C [see Fig. 1(b)]. We consider different orientations and strengths of the exchange field and SO coupling, and in the case of the

Josephson junction, the effect of altering the phase difference between the condensates. Then, in Sec. III D, we continue our treatment of the SF bilayer in the full proximity regime by including a self-consistent solution in the superconducting layer, and focus on how the presence of SO coupling affects the critical temperature of the system. We discover that the SO coupling allows for spin-valve functionality with a single ferromagnetic layer, meaning that rotating the magnetic field by $\pi/2$ induces a large change in T_c . Finally, we conclude in Sec. IV with a summary of the main results, a discussion of some additional consequences of the choices made in text, as well as possibilities for further work.

II. THEORY

A. Fundamental concepts

The diffusion of the superconducting condensate into the ferromagnet can be described by the Usadel equation, which is a second-order partial differential equation for the Green function of the system [33]. Together with appropriate boundary conditions, the Usadel equation establishes a system of coupled differential equations that can be solved in one dimension. We will consider the case of diffusive equilibrium, where the retarded component \hat{g}^R of the Green function is sufficient to describe the behavior of the system [34,35]. We start by examining the superconducting correlations in the ferromagnet, and use the standard Bardeen-Cooper-Schrieffer (BCS) bulk solution for the superconductors. In particular, we will clarify the spectroscopic consequences of having SO coupling in the ferromagnetic layer.

In the absence of SO coupling, the Usadel equation [33] in the ferromagnet reads

$$D_F \nabla (\hat{g}^R \nabla \hat{g}^R) + i[\epsilon \hat{\rho}_3 + \hat{M}, \hat{g}^R] = 0, \quad (1)$$

where the matrix $\hat{\rho}_3 = \text{diag}(1, -1)$, 1 represents the 2×2 unit matrix, and ϵ is the quasiparticle energy. The magnetization matrix \hat{M} in the above equation is

$$\hat{M} = \begin{pmatrix} \underline{h} \cdot \underline{\sigma} & 0 \\ 0 & (\underline{h} \cdot \underline{\sigma})^* \end{pmatrix},$$

where $\underline{h} = (h_x, h_y, h_z)$ is the ferromagnetic exchange field, (*) denotes complex conjugation, $\underline{\sigma} = (\sigma_x, \sigma_y, \sigma_z)$ is the Pauli vector, and σ_k are the usual Pauli matrices. Throughout, we will use the notation $\underline{\cdot}$ for 3-vectors and $\hat{\cdot}$ for 4×4 matrices in Nambu-spin space. The corresponding Kupriyanov-Lukichev boundary conditions are [36]

$$2L_j \zeta_j \hat{g}_j^R \nabla \hat{g}_j^R = [\hat{g}_1^R, \hat{g}_2^R], \quad (2)$$

where the subscripts refer to the different regions of the hybrid structure; in the case of an SF bilayer as depicted in Fig. 1(a), $j = 1$ denotes the superconductor, and $j = 2$ the ferromagnet, while ∇ denotes the derivative along the junction $1 \rightarrow 2$. The respective lengths of the materials are denoted L_j , and the interface parameters $\zeta_j = R_B/R_j$ describe the ratio of the barrier resistance R_B to the bulk resistance R_j of each material.

We will use the Riccati parametrization [37] for the quasiclassical Green function \hat{g}^R ,

$$\hat{g}^R = \begin{pmatrix} N(1 + \gamma \tilde{\gamma}) & 2N\gamma \\ -2\tilde{N}\tilde{\gamma} & -\tilde{N}(1 + \tilde{\gamma}\gamma) \end{pmatrix}, \quad (3)$$

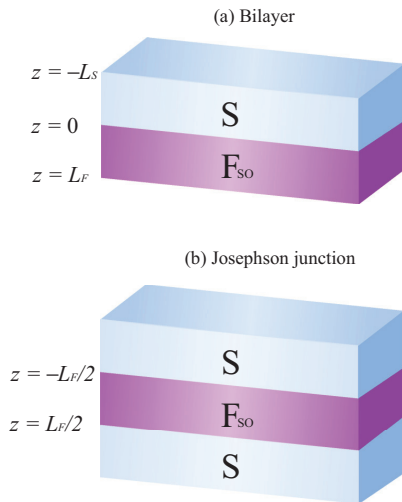


FIG. 1. (Color online) (a) The SF bilayer in Secs. III A, III B, and III D. (b) The SFS trilayer in Sec. III C. We take the thin-film layering direction along the z axis, and assume an xy plane Rashba-Dresselhaus coupling in the ferromagnetic layer.

where the normalization matrices are $N = (1 - \gamma\tilde{\gamma})^{-1}$ and $\tilde{N} = (1 - \tilde{\gamma}\gamma)^{-1}$. The tilde operation denotes a combination of complex conjugation $i \rightarrow -i$ and energy $\varepsilon \rightarrow -\varepsilon$, with $\gamma \rightarrow \tilde{\gamma}$, $N \rightarrow \tilde{N}$. The Riccati parametrization is particularly useful for numerical computation because the parameters are bounded $[0, 1]$, contrary to the multivalued θ parameterization [34]. In practice, this means that for certain parameter choices the numerical routines will only converge in the Riccati formulation. Appendix A contains some further details on this parametrization.

To include intrinsic SO coupling in the Usadel equation, we simply have to replace all the derivatives in Eq. (1) with their gauge covariant counterparts [21,38]:

$$\nabla(\cdot) \mapsto \tilde{\nabla}(\cdot) \equiv \nabla(\cdot) - i[\hat{A}, \cdot]. \quad (4)$$

This is valid for any SO coupling linear in momentum. We consider the leading contribution; higher-order terms, e.g., those responsible for the SU(2) Lorentz force, are neglected here. Such higher-order terms are required to produce so-called φ_0 junctions, which have lately attracted interest [39], and consequently we will see no signature of the φ_0 effect in the systems considered herein. The object \hat{A} has both a vector structure in geometric space and a 4×4 matrix structure in Spin-Nambu space, and can be written as $\hat{A} = \text{diag}(A, -A^*)$ in terms of the SO field $A = (A_x, A_y, A_z)$, which will be discussed in more detail in the next section. SO coupling in the context of quasiclassical theory has also been discussed in Refs. [38,40]. When we include the SO coupling as shown above, we derive the following form for the Usadel equation (see Appendix A):

$$\begin{aligned} D_F(\partial_k^2 \gamma + 2(\partial_k \gamma)\tilde{N}\tilde{\gamma}(\partial_k \gamma)) \\ = -2i\varepsilon\gamma - i\hbar \cdot (\underline{\sigma}\gamma - \gamma\underline{\sigma}^*) \\ + D_F[A\underline{A}\gamma - \gamma\underline{A}^*A^* + 2(\underline{A}\gamma + \gamma\underline{A}^*)\tilde{N}(A^* + \tilde{\gamma}\underline{A}\gamma) \\ + 2iD_F[(\partial_k \gamma)\tilde{N}(A_k^* + \tilde{\gamma}A_k\gamma) + (A_k + \gamma A_k^*)N(\partial_k \gamma)], \end{aligned} \quad (5)$$

where the index k indicates an arbitrary choice of direction in Cartesian coordinates. The corresponding equation for $\tilde{\gamma}$ is found by taking the tilde conjugate of Eq. (5). Similarly, the boundary conditions in Eq. (2) become

$$\begin{aligned} \partial_k \gamma_1 &= \frac{1}{L_1 \zeta_1} (1 - \gamma_1 \tilde{\gamma}_1) N_2 (\gamma_2 - \gamma_1) + i A_k \gamma_1 + i \gamma_1 A_k^*, \\ \partial_k \gamma_2 &= \frac{1}{L_2 \zeta_2} (1 - \gamma_2 \tilde{\gamma}_1) N_1 (\gamma_2 - \gamma_1) + i A_k \gamma_2 + i \gamma_2 A_k^*, \end{aligned} \quad (6)$$

and the $\tilde{\gamma}$ counterparts are found in the same way as before. For the details of these derivations, see Appendix A.

We will now discuss the definition of current in the presence of spin-orbit interactions. Since the Hamiltonian including SO coupling contains terms linear in momentum (see below), the velocity operator $v_j = \partial H / \partial k_j$ is affected. We stated above that the Kupriyanov-Lukichev boundary conditions are simply modified by replacing the derivative with its gauge covariant counterpart including the SO interaction. To make sure that current conservation is still satisfied, we must carefully examine the Usadel equation. In the absence of SO coupling, the quasiclassical expression for electric current is

given by

$$\underline{I}_e = I_0 \int_{-\infty}^{\infty} d\varepsilon \text{Tr}[\hat{\rho}_3(\check{g}\nabla\check{g})^K], \quad (7)$$

where \check{g} is the 8×8 Green function matrix in Keldysh space,

$$\check{g} = \begin{pmatrix} \hat{g}^R & \hat{g}^K \\ \hat{0} & \hat{g}^A \end{pmatrix}, \quad (8)$$

and I_0 is a constant that is not important for this discussion. Current conservation can now be proven from the Usadel equation itself. We show this for the case of equilibrium, which is relevant for the case of supercurrents in Josephson junctions. In this case, $\hat{g}^K = (\hat{g}^R - \hat{g}^A) \tanh(\varepsilon/2T)$ and we get

$$\underline{I}_e = I_0 \int_{-\infty}^{\infty} d\varepsilon \text{Tr}[\hat{\rho}_3(\hat{g}^R \nabla \hat{g}^R - \hat{g}^A \nabla \hat{g}^A)] \tanh(\varepsilon/2T). \quad (9)$$

Performing the operation $\text{Tr}[\hat{\rho}_3 \dots]$ on the Usadel equation, we obtain

$$D\nabla \cdot \text{Tr}[\hat{\rho}_3(\hat{g}^R \nabla \hat{g}^R)] + i \text{Tr}[\hat{\rho}_3[\varepsilon \hat{\rho}_3 + \hat{M}, \hat{g}^R]] = 0. \quad (10)$$

Now, inserting the most general definition of the Green function \hat{g}^R , one finds that the second term in the above equation is always zero. Thus we are left with

$$\nabla \cdot \text{Tr}[\hat{\rho}_3(\hat{g}^R \nabla \hat{g}^R)] = 0, \quad (11)$$

which expresses precisely current conservation since the same analysis can be done for \hat{g}^A . Now, let us include the SO coupling. The current should then be given by

$$\underline{I}_e = I_0 \int_{-\infty}^{\infty} d\varepsilon \text{Tr}[\hat{\rho}_3(\check{g}\tilde{\nabla}\check{g})^K], \quad (12)$$

so that the expression for the charge current is modified by the presence of SO coupling, as is known. The question is now if this current is conserved, as it has to be physically. We can prove that it is from the Usadel equation with SO coupling by rewriting it as

$$\begin{aligned} D\nabla \cdot (\hat{g}^R \tilde{\nabla} \hat{g}^R) \\ = D[\hat{A}, \hat{g}^R \nabla \hat{g}^R] + D[\hat{A}, [\hat{A}, \hat{g}^R]] - i[\varepsilon \hat{\rho}_3 + \hat{M}, \hat{g}^R], \end{aligned} \quad (13)$$

and then performing the operation $\text{Tr}[\hat{\rho}_3 \dots]$, one finds

$$D\nabla \cdot \text{Tr}[\hat{\rho}_3(\hat{g}^R \tilde{\nabla} \hat{g}^R)] = 0, \quad (14)$$

so we recover the current conservation law $\nabla \cdot \underline{I}_e = 0$.

B. Spin-orbit field

The precise form of the generic SO field \hat{A} is imposed by the experimental requirements and limitations. As the name suggests, spin-orbit coupling couples a particle's spin with its motion, and more specifically its momentum. As mentioned in the Introduction, the SO coupling in solids can originate from a lack of inversion symmetry in the crystal structure. Such spin-orbit coupling can be of both Rashba and Dresselhaus types and is determined by the point-group symmetry of the crystal [41,42]. It is also known that the lack of inversion symmetry due to surfaces, either in the form of interfaces to other materials or to vacuum, will give rise to antisymmetric

spin-orbit coupling of the Rashba type. For sufficiently thin structures, the SO coupling generated in this way can permeate the entire structure, but the question of precisely how far into adjacent materials such surface SO coupling may penetrate appears to be an open question in general. Intrinsic inversion asymmetry arises naturally due to interfaces between materials in thin-film hybrid structures such as the ones considered herein. Noncentrosymmetric crystalline structures provide an alternative source for intrinsic asymmetry, and are considered in Ref. [43]. In thin-film hybrids, the Rashba spin splitting derives from the cross product of the Pauli vector $\underline{\sigma}$ with the momentum \underline{k} ,

$$H_R = -\frac{\alpha}{m}(\underline{\sigma} \times \underline{k}) \cdot \hat{z}, \quad (15)$$

where α is called the Rashba coefficient, and we have chosen a coordinate system with \hat{z} as the layering direction. Another well-known type of SO coupling is the Dresselhaus spin splitting, which can occur when the crystal structure lacks an inversion center. For a two-dimensional electron gas (quantum well) confined in the \hat{z} direction, then to first order ($k_z = 0$), so the Dresselhaus splitting becomes

$$H_D = \frac{\beta}{m}(\sigma_y k_y - \sigma_x k_x), \quad (16)$$

where β is called the Dresselhaus coefficient. In our structure, we consider a thin-film geometry with the confinement being strongest in the z direction. Although there may certainly be other terms contributing to the Dresselhaus SO coupling in such a structure, since real thin-film structures will have three-dimensional quasiparticle diffusion and we use a 2D form of the SO coupling here, we consider the standard form (16) as an approximation that captures the main physics in the problem. This is a commonly used model in the literature to explore the effects originating from SO coupling in a system. When we combine both interactions, we obtain the Hamiltonian for a general Rashba-Dresselhaus SO coupling,

$$H_{RD} = \frac{k_x}{m}(\alpha\sigma_y - \beta\sigma_x) - \frac{k_y}{m}(\alpha\sigma_x - \beta\sigma_y). \quad (17)$$

In this work, we will restrict ourselves to this form of SO coupling. It should be noted that our setup may also be viewed as a simplified model for a scenario where the SO coupling and ferromagnetism exist in separate, thin layers, in which case we expect qualitatively similar results to the ones reported in this manuscript.

As explained in Ref. [21], the SO coupling acts as a background SU(2) field, i.e., an object with both a vector structure in geometric space and a 2×2 matrix structure in spin space. We can therefore identify the interaction above with an effective vector potential \underline{A} , which we will call the *SO field*,

$$H_{RD} \equiv -\underline{k} \cdot \underline{A}/m, \quad (18)$$

from which we derive that

$$\underline{A} = (\beta\sigma_x - \alpha\sigma_y, \alpha\sigma_x - \beta\sigma_y, 0). \quad (19)$$

At this point, it is convenient to introduce a new notation for describing Rashba-Dresselhaus coupling, which will let us distinguish between the physical effects that derive from

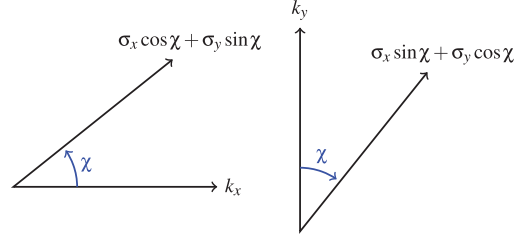


FIG. 2. (Color online) Geometric interpretation of the SO field (21) in polar coordinates: the Hamiltonian couples the momentum component k_x to the spin component $(\sigma_x \cos \chi + \sigma_y \sin \chi)$ with a coefficient $+a/m$, and the momentum component k_y to the spin component $(\sigma_x \sin \chi + \sigma_y \cos \chi)$ with a coefficient $-a/m$. Thus a determines the magnitude of the coupling, and χ the angle between the coupled momentum and spin components.

the strength of the coupling, and those that derive from the geometry. For this purpose, we employ polar notation defined by the relations

$$\alpha \equiv -a \sin \chi, \quad \beta \equiv a \cos \chi, \quad (20)$$

where we will refer to a as the *SO strength*, and χ as the *SO angle*. Rewritten in the polar notation, Eq. (19) takes the form:

$$\underline{A} = a(\sigma_x \cos \chi + \sigma_y \sin \chi)\hat{x} - a(\sigma_x \sin \chi + \sigma_y \cos \chi)\hat{y}. \quad (21)$$

From the definition, we can immediately conclude that $\chi = 0$ corresponds to a pure Dresselhaus coupling, while $\chi = \pm\pi/2$ results in a pure Rashba coupling, with the geometric interpretation of χ illustrated in Fig. 2. Note that $A_x^2 = A_y^2 = a^2$, which means that $\underline{A}^2 = 2a^2$. Another useful property is that we can switch the components $A_x \leftrightarrow A_y$ by letting $\chi \rightarrow 3\pi/2 - \chi$.

The appearance of LRTs in the system depends on the interplay between SO coupling and the direction of the exchange field. Recall that the LRT components are defined as having spin projections parallel to the exchange field, as opposed to the short-ranged triplet (SRT) component which appears as long as there is exchange splitting [44] but has spin projection perpendicular to the field and is therefore subject to the same pair-breaking effect as the singlets [3,27], penetrating only a very short distance into strong ferromagnets. If we have an SO field component along the layering direction, e.g., if we had $A_z \neq 0$ in Figs. 1(a) and 1(b), achievable with a noncentrosymmetric crystal or in a nanowire setup, then a nonvanishing commutator $[\underline{A}, \underline{h} \cdot \underline{\sigma}]$ creates the LRT. However, we will from now only consider systems where $A_z = 0$, in which case the criterion for LRT is [21] that $[\underline{A}, [\underline{A}, \underline{h} \cdot \underline{\sigma}]]$ must not be proportional to the exchange field $\underline{h} \cdot \underline{\sigma}$. Expanding, we have

$$[\underline{A}, [\underline{A}, \underline{h} \cdot \underline{\sigma}]] = 4a^2(\underline{h} \cdot \underline{\sigma} + h_z \sigma_z) - 4a^2(h_x \sigma_y + h_y \sigma_x) \sin 2\chi, \quad (22)$$

from which it is clear that no LRTs can be generated for a pure Dresselhaus coupling $\chi = 0$ or Rashba coupling $\chi = \pm\pi/2$ when the exchange field is in-plane. However, the effect of SO coupling becomes increasingly significant for angles

close to $\chi = \pm\pi/4$ (see Fig. 6 in Sec. III A). We also see that no LRTs can be generated for in-plane magnetization in the special case $h_x = h_y$ and $h_z = 0$, since $h_x\sigma_y + h_y\sigma_x$ can then be rewritten as $h_x\sigma_x + h_y\sigma_y$, which is proportional to $\underline{h} \cdot \underline{\sigma}$. There is no LRT generation for the case $h_x = h_y = 0$ and $h_z \neq 0$ for similar reasons. In general, however, the LRT will appear for an in-plane magnetization as long as $h_x \neq h_y$ and the SO coupling is not of pure Dresselhaus or pure Rashba type. It is also important to note that the LRT can be created even for pure Rashba type SO coupling if the magnetization has both in- and out-of-plane magnetization components. We will discuss precisely this situation in Sec. III B.

Once the condition for long-range triplet generation is satisfied, increasing the corresponding exchange field will also increase the proportion of long-range triplets compared with short-range triplets. Whether or not the presence of long-range triplets can be observed in the system, i.e., if they retain a clear signature in measurable quantities such as the density of states when the criteria for their existence is fulfilled, depends on other aspects such as the strength of the spin-orbit coupling and will be discussed later in this paper. Thus a main motivation for this work is to take a step further than discussing their existence [21] and instead make predictions for when long-ranged triplet Cooper pairs can actually be observed via spectroscopic or T_c measurements in SF structures with spin-orbit coupling. Moreover, we will demonstrate that the presence of SO coupling offers additional opportunities besides the creation of LRT Cooper pairs. We will show both analytically and numerically that the SO coupling can protect the singlet component even in the presence of an exchange field, which normally would suppress it. This provides the possibility of tuning the well-known minigap *magnetically*, both in bilayer and Josephson junctions, simply by altering the direction of the magnetization.

C. Weak proximity effect

In order to establish a better analytical understanding of the role played by SO coupling in the system before presenting the spectroscopy and T_c results, we will now consider the limit of weak proximity effect, which means that $|\gamma_{ij}| \ll 1$, $N \approx 1$ in the ferromagnet. The anomalous Green function in general is given by the upper-right block of Eq. (3), $f = 2N\gamma$, which we see reduces to $f = 2\gamma$ in this limit. It will also prove prudent to express the anomalous Green function using a singlet/triplet decomposition, where the singlet component is described by a scalar function f_s , and the triplet components encapsulated in the so-called d vector [45,46],

$$f = (f_s + \underline{d} \cdot \underline{\sigma})i\sigma_y. \quad (23)$$

Combining the above with the weak proximity identity $f = 2\gamma$, we see that the components of γ can be rewritten as

$$\gamma = \frac{1}{2} \begin{pmatrix} id_y - d_x & d_z + f_s \\ d_z - f_s & id_y + d_x \end{pmatrix}. \quad (24)$$

Under spin rotations, the singlet component f_s will then transform as a scalar, while the triplet component $\underline{d} = (d_x, d_y, d_z)$ transforms as an ordinary vector. Another useful feature of this notation is that it becomes almost trivial to distinguish

between short-range and long-range triplet components; the projection $d_{\parallel} = \underline{d} \cdot \hat{h}$ along the exchange field corresponds to the SRTs, while the perpendicular part $d_{\perp} = |\underline{d} \times \hat{h}|$ can be used to describe the LRTs, where \hat{h} here denotes the unit vector of the exchange field. For a concrete example, if the exchange field is oriented along the z axis, then d_z will be the short-range component, while both d_x and d_y are long-ranged components. In the coming sections, we will demonstrate that the LRT component can be identified from its density of states signature, as measurable by tunneling spectroscopy.

In the limit of weak proximity effect, we may linearize both the Usadel equation and Kupriyanov-Lukichev boundary conditions. Using the singlet/triplet decomposition in Eq. (24), and the Rashba-Dresselhaus coupling in Eq. (19), the linearized version of the Usadel equation can be written

$$\frac{i}{2} D_F \partial_z^2 f_s = \epsilon f_s + \underline{h} \cdot \underline{d}, \quad (25)$$

$$\frac{i}{2} D_F \partial_z^2 \underline{d} = \epsilon \underline{d} + \underline{h} f_s + 2i D_F a^2 \underline{\Omega}(\chi) \underline{d}, \quad (26)$$

where we for brevity have defined an SO interaction matrix

$$\underline{\Omega}(\chi) = \begin{pmatrix} 1 & -\sin 2\chi & 0 \\ -\sin 2\chi & 1 & 0 \\ 0 & 0 & 2 \end{pmatrix}. \quad (27)$$

We have now condensed the Usadel equation down to two coupled differential equations for f_s and \underline{d} , where the coupling is proportional to the exchange field and the SO interaction term. The latter has been written as a product of a factor $2i D_F a^2$, depending on the strength a , and a factor $\underline{\Omega}(\chi) \underline{d}$, depending on the angle χ in the polar notation. The matrix $\underline{\Omega}(\chi)$ becomes diagonal for a Dresselhaus coupling with $\chi = 0$ or a Rashba coupling with $\chi = \pm\pi/2$, which implies that there is no triplet mixing for such systems. In contrast, the off-diagonal terms are maximal for $\chi = \pm\pi/4$, which suggests that the triplet mixing is maximal when the Rashba and Dresselhaus coefficients have the same magnitude. In addition to the off-diagonal triplet mixing terms, we see that the diagonal terms of $\underline{\Omega}(\chi)$ essentially result in imaginary energy contributions $2i D_F a^2$. As we will see later, this can in some cases result in a suppression of all the triplet components in the ferromagnet.

We will now consider exchange fields in the xy plane,

$$\underline{h} = h \cos \theta \hat{x} + h \sin \theta \hat{y}. \quad (28)$$

Since the linearized Usadel equations show that the presence of a singlet component f_s only results in the generation of triplet components along \underline{h} , and the SO interaction term only mixes the triplet components in the xy plane, the only nonzero triplet components will in this case be d_x and d_y . The SRT amplitude d_{\parallel} and LRT amplitude d_{\perp} can therefore be written:

$$d_{\parallel} = d_x \cos \theta + d_y \sin \theta, \quad (29)$$

$$d_{\perp} = -d_x \sin \theta + d_y \cos \theta. \quad (30)$$

By projecting the linearized Usadel equation for \underline{d} along the unit vectors $(\cos \theta, \sin \theta, 0)$ and $(-\sin \theta, \cos \theta, 0)$, respectively,

then we obtain coupled equations for the SRTs and LRTs:

$$\frac{i}{2}D_F\partial_z^2 f_s = \varepsilon f_s + h d_{\parallel}, \quad (31)$$

$$\frac{i}{2}D_F\partial_z^2 d_{\parallel} = [\varepsilon + 2iD_F a^2(1 - \sin 2\theta \sin 2\chi)]d_{\parallel} - 2iD_F a^2 \cos 2\theta \sin 2\chi d_{\perp} + h f_s, \quad (32)$$

$$\frac{i}{2}D_F\partial_z^2 d_{\perp} = [\varepsilon + 2iD_F a^2(1 + \sin 2\theta \sin 2\chi)]d_{\perp} - 2iD_F a^2 \cos 2\theta \sin 2\chi d_{\parallel}. \quad (33)$$

These equations clearly show the interplay between the singlet component f_s , SRT component d_{\parallel} , and LRT component d_{\perp} . If we start with only a singlet component f_s , then the presence of an exchange field h results in the generation of the SRT component d_{\parallel} . The presence of an SO field can then result in the generation of the LRT component d_{\perp} , where the mixing term is proportional to $a^2 \cos 2\theta \sin 2\chi$. This implies that in the weak proximity limit, LRT mixing is absent for an exchange field direction $\theta = \pm\pi/4$, corresponding to $h_x = \pm h_y$, while it is maximized if $\theta = \{0, \pi/2, \pi\}$ and at the same time $\chi = \pm\pi/4$. In other words, the requirement for maximal LRT mixing is therefore that the exchange field is aligned along either the x or y axis, while the Rashba and Dresselhaus coefficients should have the same magnitude. It is important to note here that although the mixing between the triplet components is maximal at $\theta = \{0, \pi/2, \pi\}$, this does not necessarily mean that the signature of the triplets in physical quantities is most clearly seen for these angles, as we shall discuss in detail later.

Moreover, these equations show another interesting consequence of having an SO field in the ferromagnet, which is unrelated to the LRT generation. Note that the effective quasiparticle energies coupling to the SRTs and LRTs become

$$E_{\parallel} = \varepsilon + 2iD_F a^2(1 - \sin 2\theta \sin 2\chi), \quad (34)$$

$$E_{\perp} = \varepsilon + 2iD_F a^2(1 + \sin 2\theta \sin 2\chi). \quad (35)$$

When $\theta = \chi = \pm\pi/4$, then the SRTs are entirely unaffected by the presence of SO coupling; the triplet mixing term vanishes for these parameters, and E_{\parallel} is also clearly independent of a . However, when $\theta = -\chi = \pm\pi/4$, the situation is drastically different. There is still no possibility for LRT generation, however, the SRT energy $E_{\parallel} = \varepsilon + 4iD_F a^2$ will now obtain an imaginary energy contribution which destabilizes the SRTs. In fact, numerical simulations show that this energy shift destroys the SRT components as a increases. As we will see in Sec. III D, this effect results in an increase in the critical temperature of the bilayer. Thus switching between $\theta = \pm\pi/4$ in a system with $\chi \simeq \pm\pi/4$ may suggest a novel method for creating a triplet spin valve. The same thing should also occur even in the case of pure Rashba coupling when altering the ratio of in- and out-of-plane components of the exchange field.

When $\chi = \pm\pi/4$ but $\theta \neq \pm\pi/4$, the triplet mixing term proportional to $\cos 2\theta \sin 2\chi$ will no longer vanish, so we get LRT generation in the system. We can then see from the effective triplet energies that as $\theta \rightarrow \text{sgn}(\chi)\pi/4$, the imaginary part of E_{\parallel} vanishes, while the imaginary part

of E_{\perp} increases. This leads to a relative increase in the amount of SRTs compared to the amount of LRTs in the system. In contrast, as $\theta \rightarrow -\text{sgn}(\chi)\pi/4$, the imaginary part of E_{\perp} vanishes, and the imaginary part of E_{\parallel} increases. This means that we would expect a larger LRT generation for these parameters, up until the point where the triplet mixing term $\cos 2\theta \sin 2\chi$ becomes so small that almost no LRTs are generated at all. The ratio of effective energies coupling to the triplet component at the Fermi level $\varepsilon = 0$ can be written

$$\frac{E_{\perp}(0)}{E_{\parallel}(0)} = \frac{1 + \sin 2\theta \sin 2\chi}{1 - \sin 2\theta \sin 2\chi}. \quad (36)$$

D. Density of states

The density of states $D(\varepsilon)$ containing all spin components can be written in terms of the Riccati matrices as

$$D(\varepsilon) = \text{Tr}[N(1 + \gamma\tilde{\gamma})]/2, \quad (37)$$

which for the case of zero energy can be written concisely in terms of the singlet component f_s and triplet components \underline{d} ,

$$D(0) = 1 - |f_s(0)|^2/2 + |\underline{d}(0)|^2/2. \quad (38)$$

The singlet and triplet components are therefore directly competing to lower and raise the density of states [47]. Furthermore, since we are primarily interested in the proximity effect in the ferromagnetic film, we will begin by using the known BCS bulk solution in the superconductor,

$$\hat{g}_{\text{BCS}} = \begin{pmatrix} \cosh(\theta) & \sinh(\theta)i\sigma_y e^{i\phi} \\ \sinh(\theta)i\sigma_y e^{-i\phi} & -\cosh(\theta) \end{pmatrix}, \quad (39)$$

where $\theta = \text{atanh}(\Delta/\varepsilon)$, and ϕ is the superconducting phase. Using Eq. (24) and the definition of the tilde operation, and comparing \hat{g}^R in Eq. (3) with its standard expression in a bulk superconductor Eq. (39), we can see that at zero energy the singlet component $f_s(0)$ must be purely imaginary and the triplet $\underline{d}_z(0)$ must be purely real if the superconducting phase is $\phi = 0$.

By inspection of Eq. (26), we can see that a transformation $h_x \leftrightarrow h_y$ along with $d_x \leftrightarrow d_y$ leaves the equations invariant. The density of states will therefore be unaffected by such permutations,

$$D[\underline{h} = (a, b, 0)] = D[\underline{h} = (b, a, 0)], \quad (40)$$

while in general,

$$D[\underline{h} = (a, 0, b)] \neq D[\underline{h} = (b, 0, a)]. \quad (41)$$

However, whenever one component of the planar field is exactly twice the value of the other component, one can confirm that the linearized equations remain invariant under a rotation of the exchange field

$$\underline{h} = (a, 2a, 0) \rightarrow \underline{h} = (a, 0, 2a), \quad (42)$$

with associated invariance in the density of states.

E. Critical temperature

When superconducting correlations leak from a superconductor to a ferromagnet in a hybrid structure, there will also be an inverse effect, where the ferromagnet effectively drains

the superconductor of its superconducting properties due to tunneling of Cooper pairs. Physically, this effect is observable in the form of a reduction in the superconducting gap $\Delta(z)$ near the interface at all temperatures. Furthermore, if the temperature of the hybrid structure is close to the bulk critical temperature T_{cs} of the superconductor, this *inverse proximity effect* can be strong enough to make the superconducting correlations vanish entirely throughout the system. Thus proximity-coupled hybrid structures will in practice always have a critical temperature T_c that is lower than the critical temperature T_{cs} of a bulk superconductor. Depending on the exact parameters of the hybrid system, T_c can sometimes be significantly smaller than T_{cs} , and in some cases it may even vanish ($T_c \rightarrow 0$).

To quantify this effect, it is no longer sufficient to solve the Usadel equation in the ferromagnet only. We will now also have to solve the Usadel equation in the superconductor,

$$D_S \partial_z^2 \gamma = -2i\varepsilon\gamma - \Delta(\sigma_y - \gamma\sigma_y\gamma) - 2(\partial_z \gamma) \tilde{N} \tilde{\gamma}(\partial_z \gamma), \quad (43)$$

along with a self-consistency equation for the gap $\Delta(z)$,

$$\Delta(z) = N_0 \lambda \int_0^{\Delta_0 \cosh(1/N_0 \lambda)} d\varepsilon \operatorname{Re}[f_s(z, \varepsilon)] \times \tanh\left(\frac{\pi}{2e^\gamma} \frac{\varepsilon/\Delta_0}{T/T_{cs}}\right), \quad (44)$$

where N_0 is the density of states per spin at the Fermi level, and $\lambda > 0$ is the electron-electron coupling constant in the BCS theory of superconductivity. For a derivation of the gap equation, see Appendix B.

To study the effects of the SO coupling on the critical temperature of an SF structure, we therefore have to find a self-consistent solution to Eq. (5) in the ferromagnet, Eq. (6) at the interface, and Eqs. (43) and (44) in the superconductor. In practice, this is done by successively solving one of the equations at a time numerically, and continuing the procedure until the system converges towards a self-consistent solution. To obtain accurate results, we typically have to solve the Usadel equation for 100–150 positions in each material, around 500 energies in the range $(0, 2\Delta_0)$, and 100 more energies in the range $(2\Delta_0, \omega_c)$, where the Debye cutoff $\omega_c \approx 76\Delta_0$ for the superconductors considered herein. This procedure will then have to be repeated up to several hundred times before we obtain a self-consistent solution for any given temperature of the system. Furthermore, if we perform a conventional linear search for the critical temperature T_c/T_{cs} in the range $(0, 1)$ with a precision of 0.0001, it may require up to 10 000 such iterations to complete, which may take several days depending on the available hardware and efficiency of the implementation. The speed of this procedure may, however, be significantly increased by performing a binary search instead. Using this strategy, the critical temperature can be determined to a precision of $1/2^{12+1} \approx 0.0001$ after only 12 iterations, which is a significant improvement. The convergence can be further accelerated by exploiting the fact that $\Delta(z)$ from iteration to iteration should decrease monotonically to zero if $T > T_c$; however, the details will not be further discussed in this paper.

III. RESULTS

We consider the proximity effect in an SF bilayer in Sec. III A, using the BCS bulk solution for the superconductors. The case of pure Rashba coupling is discussed in Sec. III B, and the SFS Josephson junction is treated in Sec. III C. Results for the local density of states are given for the centre of the ferromagnetic layer, with the full spatial distribution discussed in Sec. III C. We take the thin-film layering direction to be oriented in the z direction and fix the spin-orbit coupling to Rashba-Dresselhaus type in the xy plane as given by Eq. (19). We set $L_F/\xi_S = 0.5$. The coherence length for a diffusive bulk superconductor typically lies in the range 10–30 nm. We solve the equations using MATLAB with the boundary value differential equation package BVP6C and examine the density of states $D(\varepsilon)$ for energies normalised to the superconducting gap Δ . For brevity of notation, we include the normalization factor in the coefficients α and β in these sections. This normalization is taken to be the length of the ferromagnetic region L_F , so that for instance $\alpha = 1$ in the figure legends means $\alpha L_F = 1$. Finally, in Sec. III D, we calculate the dependence of the critical temperature of an SF bilayer as a function of the different system parameters.

A. SF Bilayer

Consider the SF bilayer depicted in Fig. 1(a). In Sec. II B, we introduced the conditions for the LRT component to appear, and from Eq. (22) it is clear that no LRTs will be generated if the exchange field is aligned with the layering direction, i.e., $\underline{h} \parallel \hat{z}$, since Eq. (22) will be proportional to the exchange field. Conversely, the general condition for LRT generation with in-plane magnetization is both that $h_x \neq h_y$, and that the SO coupling is not of pure Rashba or pure Dresselhaus form. However, it became clear in Sec. II C that the triplet mixing was maximal for equal Rashba and Dresselhaus coupling strengths, and in fact the spectroscopic signature is quite sensitive to deviations from this. This changes when the ferromagnet also has an out-of-plane component, in which case pure Rashba coupling can generate the LRT.

In Ref. [50], the density of states for an SF bilayer was shown to display oscillatory behavior as a function of distance penetrated into the ferromagnet. The physical origin of this stems from the nonmonotonic dependence of the superconducting order parameter inside the F layer, which oscillates and leads to an alternation of dominant singlet and dominant triplet correlations as a function of distance from the interface. When the triplet ones dominate, the proximity-induced change in the density of states is inverted compared to SN structures, giving rise to an enhancement of the density of states at low energies in this so-called π phase where the proximity-induced superconducting order parameter is negative.

For SF bilayers without SO coupling and a homogeneous exchange field, one expects to see a spectroscopic minigap whenever the Thouless energy is much greater than the strength of the exchange field. The minigap in SF structures closes when the resonant condition $h \sim E_g$ is fulfilled, where E_g is the minigap occurring without an exchange field, and a zero-energy peak emerges instead [48]. The minigap E_g depends on both

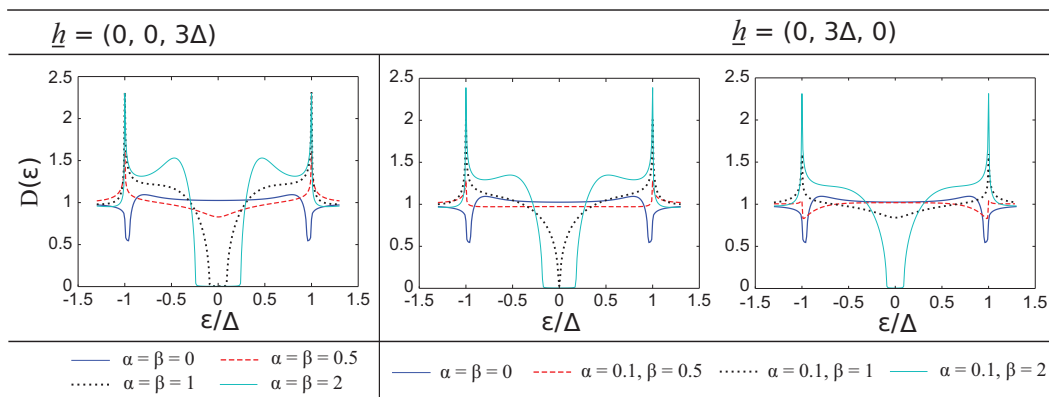


FIG. 3. (Color online) Density of states $D(\varepsilon)$ for the SF bilayer with energies normalized to the superconducting gap Δ and SO coupling normalised to the inverse ferromagnet length $1/L_F$. The table shows the spectroscopic effect of increasing SO coupling with $\alpha = \beta$ when the magnetization $\underline{h} = 3\Delta\hat{z}$, i.e., with the field perpendicular to the interface, and the effect of increasing difference between the Rashba and Dresselhaus coefficients for both $\underline{h} = 3\Delta\hat{z}$ and $\underline{h} = 3\Delta\hat{y}$. Although the conditions for LRT generation are fulfilled in the latter case, it is clear that no spectroscopic signature of this is present.

the Thouless energy and the resistance of the junction. For stronger fields, we will have an essentially featureless density of states (see e.g., Ref. [49] and references therein). This is, indeed, what we observe for $\alpha = \beta = 0$ in Fig. 3. With purely out-of-plane magnetization $\underline{h} \parallel \hat{z}$, the effect of SO coupling is irrespective of type: Rashba, Dresselhaus, or both will always create a minigap. With in-plane magnetization, however, the observation of a minigap above the SO-free resonant condition $h > E_g$ indicates that dominant Rashba or dominant Dresselhaus coupling is present. The same is true for SFS trilayers, and thus to observe a signature of long-range triplets in the case of a purely in-plane exchange field the Rashba and Dresselhaus coefficients must be similar in magnitude, and in the following we shall primarily focus on this regime. To clarify quantitatively how much the Rashba and Dresselhaus coefficients can deviate from each other before destroying the low-energy enhancement of the density of states, which is the signature of triplet Cooper pairs in this system, we have plotted in Fig. 4 the density of states at the Fermi level ($\varepsilon = 0$) as a function of the spin-orbit angle χ and the magnetization direction θ . For purely Rashba or Dresselhaus coupling ($\chi = \{0, \pm\pi/2\}$), the deviation from the normal-state value is small. However, as soon as both components are present a highly nonmonotonic behavior is observed. This is particularly pronounced for $\chi \rightarrow \pm\pi/4$, although the conversion from dominant triplets to dominant singlets as one rotates the field by changing θ is seen to occur even away from $\chi = \pm\pi/4$.

With either $\underline{h} = h\hat{x} \neq 0$, or equivalently $\underline{h} = h\hat{y} \neq 0$, LRTs are generated provided $\alpha\beta \neq 0$, and in Fig. 5, we can see that the addition of SO coupling introduces a peak in the density of states at zero energy, which saturates for a certain coupling strength. This peak manifests as sharper around $\varepsilon = 0$ than the zero-energy peak associated with weak field strengths of the order of the gap (i.e., as evident from $\alpha = \beta = 0$ in Fig. 5), which occurs regardless of magnetization direction or texture [48,49]. By analyzing the real components of the

triplets, for a gauge where the superconducting phase is zero, we can confirm that this zero-energy peak is due to the LRT component, in this case d_x , also depicted in Fig. 5, in agreement with the predictions for *textured magnetization without* SO coupling [49]. However, it is also evident from Fig. 5 that increasing the field strength rapidly suppresses the density of states towards that of the normal metal, making the effect more difficult to detect experimentally. The way to ameliorate this situation is to remember that the introduction of SO coupling means the *direction* of the exchange field is crucially important, as we see in Fig. 6, and this allows for a dramatic spectroscopic signature for fields without full alignment with the x or y axes.

Figure 6 shows how the density of states at zero energy varies with the angle θ between h_x and h_y at zero energy; with $\theta = 0$ the field is aligned with h_x , and with $\theta = \pi/2$

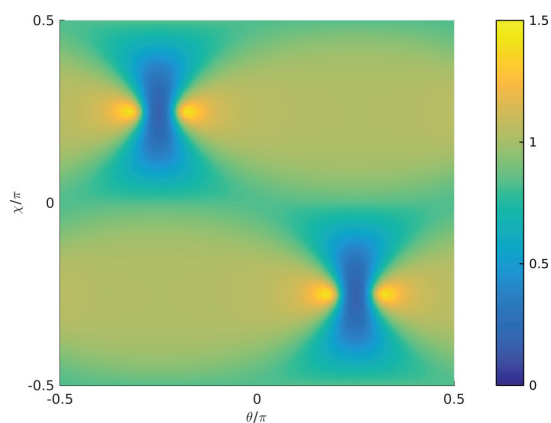


FIG. 4. (Color online) Zero-energy density of states $D(0)$ as a function of the spin-orbit angle χ and magnetization angle θ . We have used a ferromagnet of length $L_F/\xi_S = 0.5$ with an exchange field $h/\Delta = 3$ and a spin-orbit magnitude $a\xi_S = 2$.

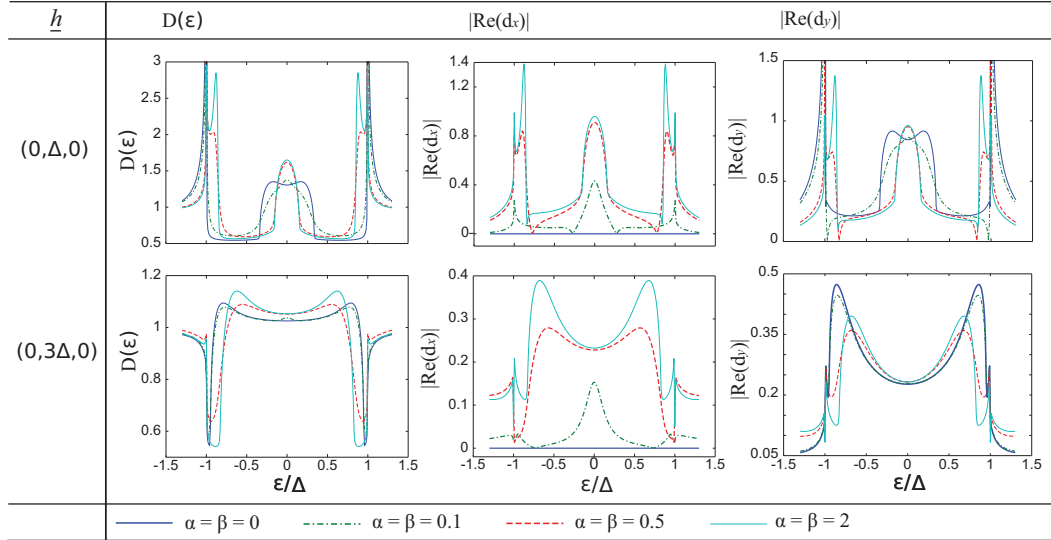


FIG. 5. (Color online) Density of states $D(\varepsilon)$ for the SF bilayer with energies normalized to the superconducting gap Δ and SO coupling normalized to the inverse ferromagnet length $1/L_F$. The table shows the spectroscopic effect of equal Rashba and Dresselhaus coefficients when the magnetization is oriented entirely in the y direction, and also the correlation between the SO-induced zero-energy peak with the long-range triplet component $|\text{Re}(d_x)| \equiv \text{Re}(d_\perp)$. It is clear that the predominant effect of the LRT component, which appears only when the SO coupling is included, is to increase the peak at zero energies. Increasing the field strength rapidly suppresses the density of states towards that of the normal metal.

it is aligned with h_y . We see that the inclusion of SO coupling introduces a nonmonotonic angular dependence in the density of states, with increasingly sharp features as the SO coupling strength increases, although the optimal angle at approximately $\theta = 7\pi/32$ and $\theta = 9\pi/32$ varies minimally with increasing SO coupling. Clearly, the ability to extract maximum LRT conversion from the inclusion of SO coupling is highly sensitive to the rotation angle, with near step-function behavior delineating the regions of optimal peak in the density of states and an energy gap for strong SO coupling. It is remarkable to see how $D(0)$ versus θ formally bears a strong resemblance to the evolution of a fully gapped BCS [64]

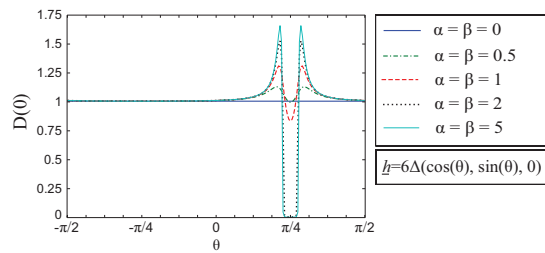


FIG. 6. (Color online) The dependence of the density of states of the SF bilayer at zero energy on the angle θ between the x and y components of the magnetization exchange field $\underline{h}/\Delta = 6(\cos(\theta), \sin(\theta), 0)$ for increasing SO coupling. As the strength of the SO coupling increases, we see increasingly sharp variations in the density of states from an optimal peak at around $\theta \approx 7\pi/32$ and $\theta \approx 9\pi/32$ to a gap around $\theta = \pi/4$.

density of states $D(\varepsilon)$ versus ε to a flat density of states as the SO coupling decreases.

These results can again be explained physically by the linearized equations (31)–(33). Since the case $\alpha = \beta$ corresponds to $\chi = -\pi/4$ in the notation developed in the preceding sections, Eq. (36) implies that $E_\perp(0) > E_\parallel(0)$ when $\theta < 0$, while $E_\perp(0) < E_\parallel(0)$ when $\theta > 0$. In other words, for negative θ , the SO coupling suppresses the LRT components, and the exchange field suppresses the other components. Since the singlet and SRT components have opposite sign in Eq. (38), this renders the density of states essentially featureless. However, for positive θ , both the SO coupling and the exchange field suppress the SRT components, meaning that LRT generation is energetically favoured. Note that $E_\perp/E_\parallel \rightarrow \infty$ as $\theta \rightarrow +\pi/4$, which explains why the LRT generation is maximized in this regime. Since the triplet mixing term in Eq. (33) is proportional to $(\cos 2\theta \sin 2\chi)$, the LRT component vanishes when the value of θ gets too close to $+\pi/4$. Furthermore, since E_\parallel has a large imaginary energy contribution in this case, the SRTs are also suppressed at $\theta = +\pi/4$. Thus, despite LRTs being most energetically favored at this exact point, we end up with a system dominated by singlets due to the SRT suppression and lack of LRT production pathway. Nevertheless, one would conventionally expect that exchange fields of a magnitude $h \gg \Delta$ as depicted in Fig. 6 would suppress any features in the density of states, while we observe an obvious minigap. Thus the singlet correlations become much more resilient against the pair-breaking effect of the exchange field when spin-orbit coupling is present. This effect persists even when the Rashba or Dresselhaus

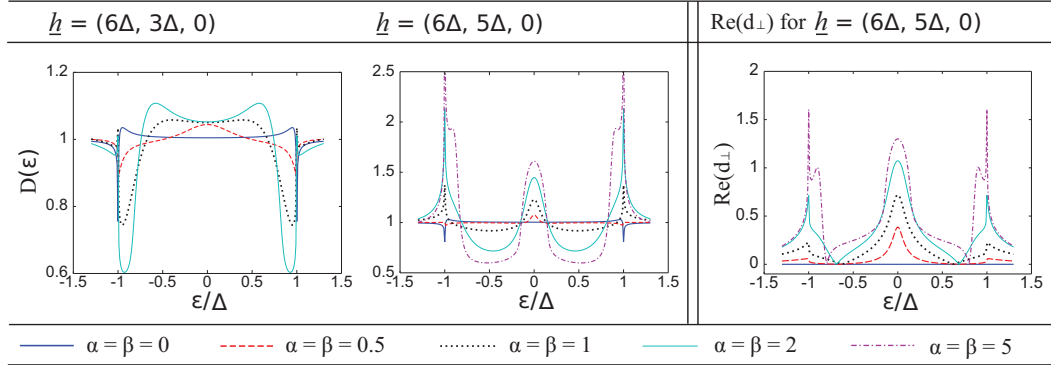


FIG. 7. (Color online) Density of states $D(\varepsilon)$ in the SF bilayer for energies normalized to the superconducting gap Δ and SO coupling normalized to the inverse ferromagnet length $1/L_F$. The table shows the spectroscopic features of the SF bilayer with rotated exchange field in the xy plane. Again we see a peak in the density of states at zero energy due to the LRT component, i.e., the component of \underline{d} perpendicular to \underline{h} , d_{\perp} . The height of this zero-energy peak is strongly dependent on the angle of the field vector in the plane, as shown in Fig. 6. For near-optimal field orientations, increasing the SO coupling leads to a dramatic increase in the peak of the density of states at zero energy.

component dominates the other one, i.e. α not close to β in magnitude.

To identify the physical origin of this effect, we solve the linearized equations (31)–(33) along with their corresponding boundary conditions for the specific case $\varepsilon = 0$, $\theta = -\chi = \pi/4$. We consider a bulk superconductor occupying the space $x < 0$, while the ferromagnet length L_F is so large that one in practice only needs to keep the decaying parts of the anomalous Green function. We then find the following expression for the singlet component at the SF interface in the absence of SO coupling:

$$f_s^0 = \frac{\sinh(\operatorname{arctanh}(\Delta/\varepsilon))}{2\zeta L_F} \sqrt{\frac{D_F}{h}}. \quad (45)$$

With increasing h , the singlet correlations are suppressed in the conventional manner. However, we now incorporate SO coupling in the problem. For more transparent analytical results, we focus on the case $2(a\xi)^2 \gg h/\Delta$. This condition can be rewritten as $2D_F a^2 \gg h$. In this case, a similar calculation gives the singlet component at the SF interface in the presence of SO coupling:

$$f_s = f_s^0 \sqrt{\frac{D_F a^2}{2h}}. \quad (46)$$

Clearly, the SO coupling enhances the singlet component in spite the presence of an exchange field since $\sqrt{D_F a^2/h} \gg 1$. This explains the presence of the conventional zero energy gap for large SO coupling even with a strong exchange field. A consequence of this observation is that SO coupling in fact provides a route to a *magnetically tunable minigap*. Figure 6 shows that when both an exchange field and SO coupling are present, the direction of the field determines when a minigap appears. This holds even for strong exchange fields $h \gg \Delta$ as long as the SO coupling is sufficiently large as well.

We recall that the LRT Cooper pairs, defined as the components of \underline{d} perpendicular to \underline{h} , may be characterized by a quantity d_{\perp} , which is defined by the cross product of the two vectors: $d_{\perp} = |\underline{d} \times \underline{h}|$. We saw above that the spectroscopic

signature of LRT generation is strongly dependent on the angle of the field, and this angle is a tunable parameter for sufficiently weak magnetic anisotropy. In Fig. 7, we see an example of the effect this rotation can have on the spectroscopic signature of LRT generation: when the exchange field is changed from $\underline{h} = (6\Delta, 3\Delta, 0) \rightarrow (6\Delta, 5\Delta, 0)$, i.e., changing the direction of the field, we see that a strong zero-energy peak emerges due to the presence of LRT in the system. This large peak emerges despite the stronger exchange field that would ordinarily reduce the density of states towards the normal state, i.e., as in Fig. 5 for $\underline{h} = \Delta\hat{y} \rightarrow 3\Delta\hat{y}$. If one were to remove the SO coupling, the low-energy density of states would thus have no trace of any superconducting proximity effect, which demonstrates the important role played by the SO interactions here. Finally, for completeness we include an example of the effect of rotating the field to have a component along the junction in Fig. 8. Comparing the case of $\underline{h} = (0, 3\Delta, 6\Delta)$ in Fig. 8 with $\underline{h} = (6\Delta, 3\Delta, 0)$ in Fig. 7, we see that the two cases are identical, as predicted in the limit of weak proximity effect, and increasing the magnitude of the out-of-plane z component of the field has no effect on the height of the zero-energy peak, which is instead governed by the in-plane y component.

B. SF bilayer with pure Rashba coupling

There exists another experimentally viable setup where the LRT can be created. In the case where pure Rashba SO coupling is present, originating, e.g., from interfacial asymmetry, the condition for the existence of LRT is that the exchange field has both the in-plane and out-of-plane components. Although the LRT formally is nonzero, it is desirable to clarify if and how it can be detected through spectroscopic signatures.

From an experimental point of view, it is known that PdNi and CuNi [11] can in general feature a canted magnetization orientation relative to the film-plane due to the competition between shape anisotropy and magnetocrystalline anisotropy. This is precisely the situation required in order to have an exchange field with both an in-plane (xy plane in our notation)

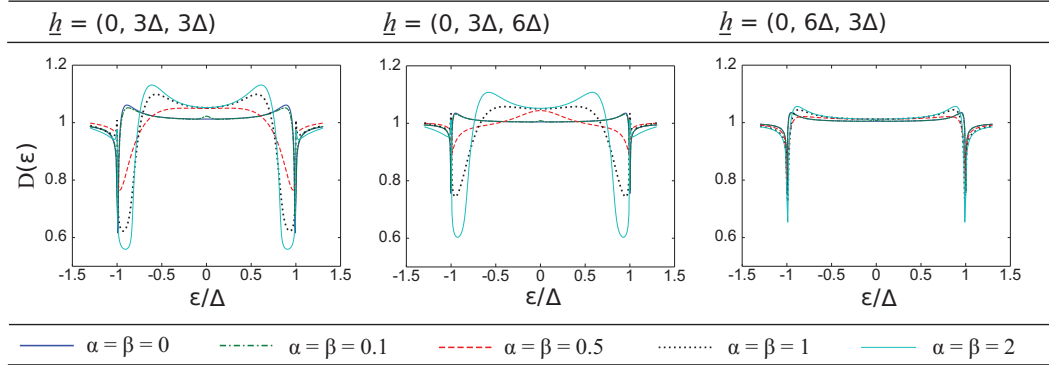


FIG. 8. (Color online) Density of states $D(\varepsilon)$ in the SF bilayer for energies normalized to the superconducting gap Δ and SO coupling normalized to the inverse ferromagnet length $1/L_F$. The table shows the spectroscopic features of the SF bilayer with a rotated exchange field in the $xz \equiv yz$ plane. Note that when the field component along the junction is twice the component in the y direction, here $\underline{h} = (0, 3\Delta, 6\Delta)$, the density of states is equivalent to the case $\underline{h} = (6\Delta, 3\Delta, 0)$ illustrated in Fig. 7, as predicted in the limit of weak proximity effect.

and out-of-plane (z direction) components. In our model, the ferromagnetism coexists with the Rashba SO coupling, which may be taken as a simplified model of two separate layers where the SO coupling is induced, e.g., by a very thin heavy metal and PdNi or CuNi is deposited on top of it.

To determine how the low-energy density of states is influenced by the triplet pairing, we plot in Fig. 9(a) $D(0)$ as a function of the misalignment angle φ between the film-plane and its perpendicular axis [see inset of Fig. 9(b) for junction geometry]. In order to correlate the spectroscopic features with the LRT, we plot in Fig. 9(b) the LRT Green function $|d_{\perp}|$.

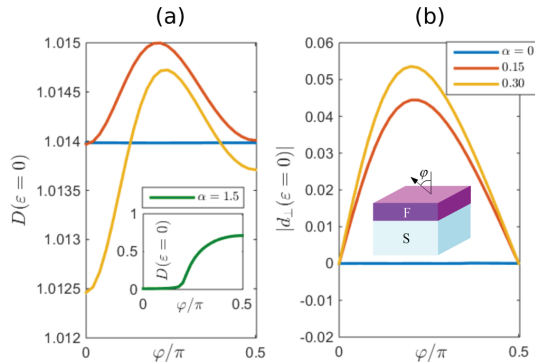


FIG. 9. (Color online) (a) Plot of the zero-energy density of states $D(0)$ in an S/F structure with pure Rashba spin-orbit coupling. We have set $h/\Delta = 4$ and $L/\xi_S = 0.5$. (Inset) Stronger SO coupling $\alpha = 1.5$, demonstrating that the angular variation of $D(0)$ remains, although the enhancement due to triplets is absent. (b) Plot of the magnitude of the LRT anomalous Green function $|d_{\perp}|$ at $\varepsilon = 0$. As seen, its enhancement correlates with an accompanying increase in the density of states for the same angle φ , and beyond an optimal SO coupling value there is anticorrelation between the density of states peak and $|d_{\perp}|$. The only angle of importance is the angle φ between the out-of-plane and in-plane components of the exchange field, shown in the inset.

It is clear that the LRT vanishes when $\varphi = 0$ or $\varphi = \pi/2$. This is consistent with the fact that for pure Rashba coupling, purely in-plane or out-of-plane direction of the exchange field gives $d_{\perp} = 0$ according to our previous analysis. However, for $\varphi \in (0, \pi/2)$ the LRT exists. Its influence on $D(0)$ is seen in Fig. 9(a): an enhancement of the zero-energy density of states. For any particular set of junction parameters there is an optimal value of the SO coupling, and in approaching this value the density of states is correlated with $\text{Re}(d_{\perp})$. Beyond this optimal value, they are anticorrelated, as evident from Fig. 9 as the SO coupling increases, but the angular correlation remains. We note that the magnitude of the enhancement of the density of states is substantially smaller than what we obtained with both Rashba and Dresselhaus coupling. At the same time, the magnitude of the enhancement is of the same order as previous experimental works that have measured the density of states in SF structures [50,51].

Note that it is only the angle between the plane and the tunneling direction, which is of importance: the density of states is invariant under a rotation in the film-plane of the exchange field. The SO-induced enhancement of the zero-energy density of states reaches an optimal peak before further increases in the magnitude of the Rashba coupling results in a suppression of both the short- and long-ranged triplet components, causing the low-energy density of states enhancement to vanish. The correlation with the LRT component $|d_{\perp}|$ correspondingly changes to anticorrelation, evident in Fig. 9. Nevertheless, the strong angular variation with $D(0)$ remains although $D(0) < 1$ for all φ [see inset of Fig. 9(a)]. Increasing the exchange field h further suppressed the proximity effect overall.

The main effect of the SO coupling is that $D(0)$ depends on the exchange-field direction. As seen for the case of $\alpha = 0$ in Fig. 9(a), there is no directional dependence without SO coupling. Thus, depending on the exchange-field angle between the in-plane and out-of plane direction, measuring an enhanced $D(0)$ at low-energies is a signature of the presence of LRT Cooper pairs in the ferromagnet. More generally, measuring a dependence on the exchange-field direction φ would be a direct consequence of the presence of SO coupling

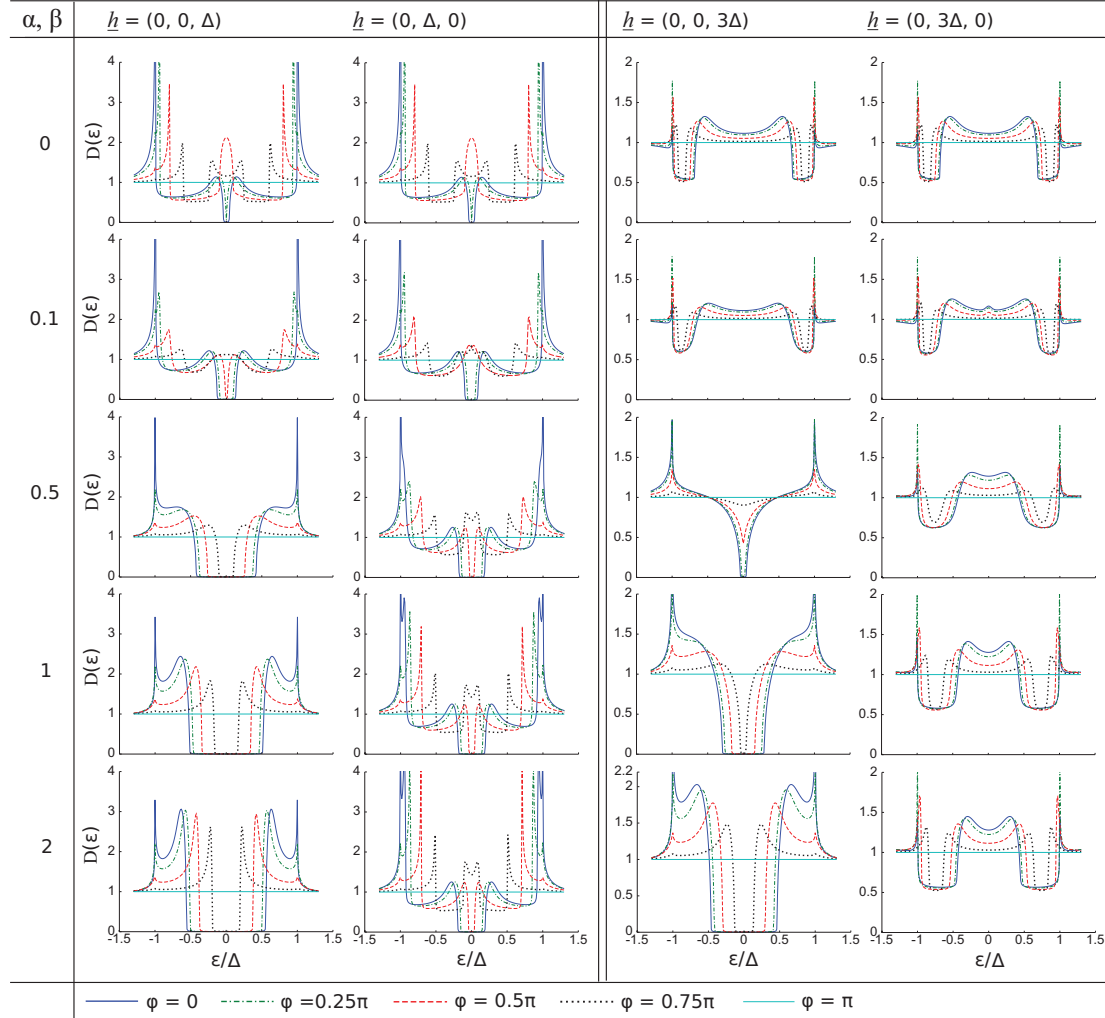


FIG. 10. (Color online) The table shows the density of states $D(\varepsilon)$ in the SFS junction with increasing SO coupling and exchange field in a single direction, with $D(\varepsilon)$ normalised to the superconducting gap Δ and SO coupling normalised to the inverse ferromagnet length $1/L_F$. With no SO coupling and very weak exchange field we see a phase-dictated gap-to-peak qualitative change in the density of states at zero energy. When the field is strong enough to destroy this gap, i.e., above the resonant condition, increasing the phase difference simply lowers the density of states towards that of the normal metal, which is achieved at a phase difference of $\phi = \pi$. With the addition of SO coupling we see a clear difference in the density of states due to the long range triplet component, which is present when the field is oriented in y but not in z . When LRTs are present with weak exchange fields, a phase-dictated gap-to-peak feature is retained and increased as the strength of SO coupling increases the gap, with the peak shown here at a phase difference of 0.75π . For stronger exchange fields, increasing the SO coupling produces the minigap when there is no LRT component, whereas the existence of an LRT component again introduces an increasing peak at zero energy when no minigap is present.

in the system, even in the regime of, e.g., moderate to strong Rashba coupling where the triplets are suppressed.

C. Josephson junction

By adding a superconducting region to the right interface of the SF bilayer, we form an SFS Josephson junction.

It is well known that the phase difference between the superconducting regions governs how much current can flow through the junction [52], and the density of states for a diffusive SNS junction has been measured experimentally with extremely high precision [53]. Here, we consider such a transversal junction structure as depicted in Fig. 1(b), again with intrinsic SO coupling in the xy plane [Eq. (19)]

in the ferromagnet and with BCS bulk values for each superconductor. In Sec. III C 1, we consider single orientations along the principal axes of the system (x, y, z) of the uniform exchange field, and in Sec. III C 2, we consider a rotated field. Experimentally, the density of states can be probed at the superconductor/ferromagnet interface if one of the superconductors is a superconducting island, and the scanning tunneling microscope approaches from the top, next to this superconductor island.

Let us first recapitulate some known results. We saw in Sec. II that the spin-singlet, SRT and LRT components compete to raise and lower the density of states at low energies. Their relative magnitude is affected by the magnitude and direction of both the exchange field and SO coupling and results in three distinctive qualitative profiles: the zero-energy peak from the LRTs, the singlet-dominated regime with a minigap, and the flat, featureless profile in the absence of superconducting correlations. In the Josephson junction, the spectroscopic features are in addition sensitive to the phase difference ϕ between the superconductors. In junctions with an interstitial normal metal, the gap decreases as $\phi = 0 \rightarrow \pi$, closing entirely at $\phi = \pi$ such that the density of states is that of the isolated normal metal; identically one [53,54]. Without an exchange field, the density of states is unaffected by the SO coupling. This is because without an exchange field the equations governing the singlet and triplet components are decoupled and thus no singlet-triplet conversion can occur. From a symmetry point of view, it is reasonable that the time-reversal invariant spin-orbit coupling does not alter the singlet correlations.

Without SO coupling and as long as the exchange field is not too large, changing the phase difference can qualitatively alter the density of states from minigap to peak at zero energy (see Fig. 10), a useful feature permitting external control of the quasiparticle current flowing through the junction. The underlying reason is that the phase difference controls the relative ratio of the singlet and triplet correlations: when the singlets dominate, a minigap is induced which mirrors their origin in the bulk superconductor. As in the bilayer case, there is a resonant condition [48,49] indicating an exchange-field strength beyond which the minigap can no longer be sustained and increasing the phase difference simply lowers the density of states towards that of the normal metal. Amongst the features we outline in the following sections, one of the effects of adding SO coupling is to make this useful gap-to-peak effect accessible with stronger exchange fields, i.e., for a greater range of materials. At the same time, the SO coupling cannot be *too strong* since the triplet correlations are suppressed in this regime leaving only the minigap and destroying the capability for qualitative change in the spectroscopic features.

1. Josephson junction with uniform exchange field in single direction

Consider first the case in which the exchange field is aligned in a single direction, meaning that we only consider an exchange field purely along the principal $\{x, y, z\}$ axes of the system. If we again restrict the form of the SO vector to (19), aligning \underline{h} in the z direction will not result in any LRTs. In this case, the spectroscopic effect of the SO coupling is dictated by

the singlet and short-range triplet features, much as in the SF bilayer case (Fig. 3). This is demonstrated in Fig. 10, where again we see a qualitative change in the density of states as the exchange field increases, with the regions of minigap and zero-energy-peak separated by the resonant condition $h \sim E_g$ without SO coupling.

We will now examine the effect of increasing the exchange field aligned in the x or, equivalently, the y direction. In this case, we have generation of LRT Cooper pairs. If \underline{h} is sufficiently weak to sustain a gap independently of SO coupling, introducing weak SO coupling will increase the gap at zero phase difference while maintaining a peak at zero energy for a phase difference of 0.75π (see Fig. 10). Increasing the SO coupling increases this peak at zero energy up to a saturation point. As the exchange field increases sufficiently beyond the resonant condition to keep the gap closed, increasing the SO coupling increases the zero-energy peak at all phases, again due to the LRT component, eventually also reaching a saturation point. As the phase difference $\phi = 0 \rightarrow \pi$, the density of states reduces towards that of the normal metal, closing entirely at $\phi = \pi$ as expected [43,54,55]. As the value of the density of states at zero energy saturates for increasing SO coupling, fixed phase differences yield the same drop at zero energy regardless of the strength of SO coupling.

We note in passing that when the SO coupling field has a component along the junction direction (z), it can qualitatively influence the nature of the superconducting proximity effect. As very recently shown in Ref. [43], a giant triplet proximity effect develops at $\phi = \pi$ in this case, in complete contrast to the standard scenario of a vanishing proximity effect in π -biased normal or magnetically homogeneous junctions without SO coupling.

2. Josephson junction with rotated exchange field

With two components of the field \underline{h} , e.g., from rotation, it is again useful to separate the cases with and without a component along the junction direction. When the exchange field lies in-plane (the xy plane), and provided we satisfy the conditions $h_x \neq h_y$ and $\alpha\beta \neq 0$, increasing the SO coupling drastically increases the zero energy peak as shown in Fig. 11, again due to the LRT component. This is consistent with the bilayer behavior, where the maximal generation of LRT Cooper pairs occurs at an angle $0 < \theta < \pi/4$. As the phase difference approaches π , the proximity-induced features are suppressed in the center of the junction. This can be understood intuitively as a consequence of the order parameter averaging to zero since it is positive in one superconductor and negative in the other.

The 2D plots in this paper of the local density of states are given for the center of the junction ($z = 0$), where one naturally expects the relative proportion of LRTs to be greatest. However, it is interesting to note that the large peak at zero energy—the signature of the LRTs—is maintained throughout the ferromagnet. This is shown in Fig. 12, for the case $\alpha = \beta = 1$ and $\underline{h} = (1.5\Delta, 3.5\Delta, 0)$, where the maximal peak for $\phi = 0$ is almost twice the normal-state value. In comparison, the depletion of this peak is surprisingly small at the superconductor interfaces.

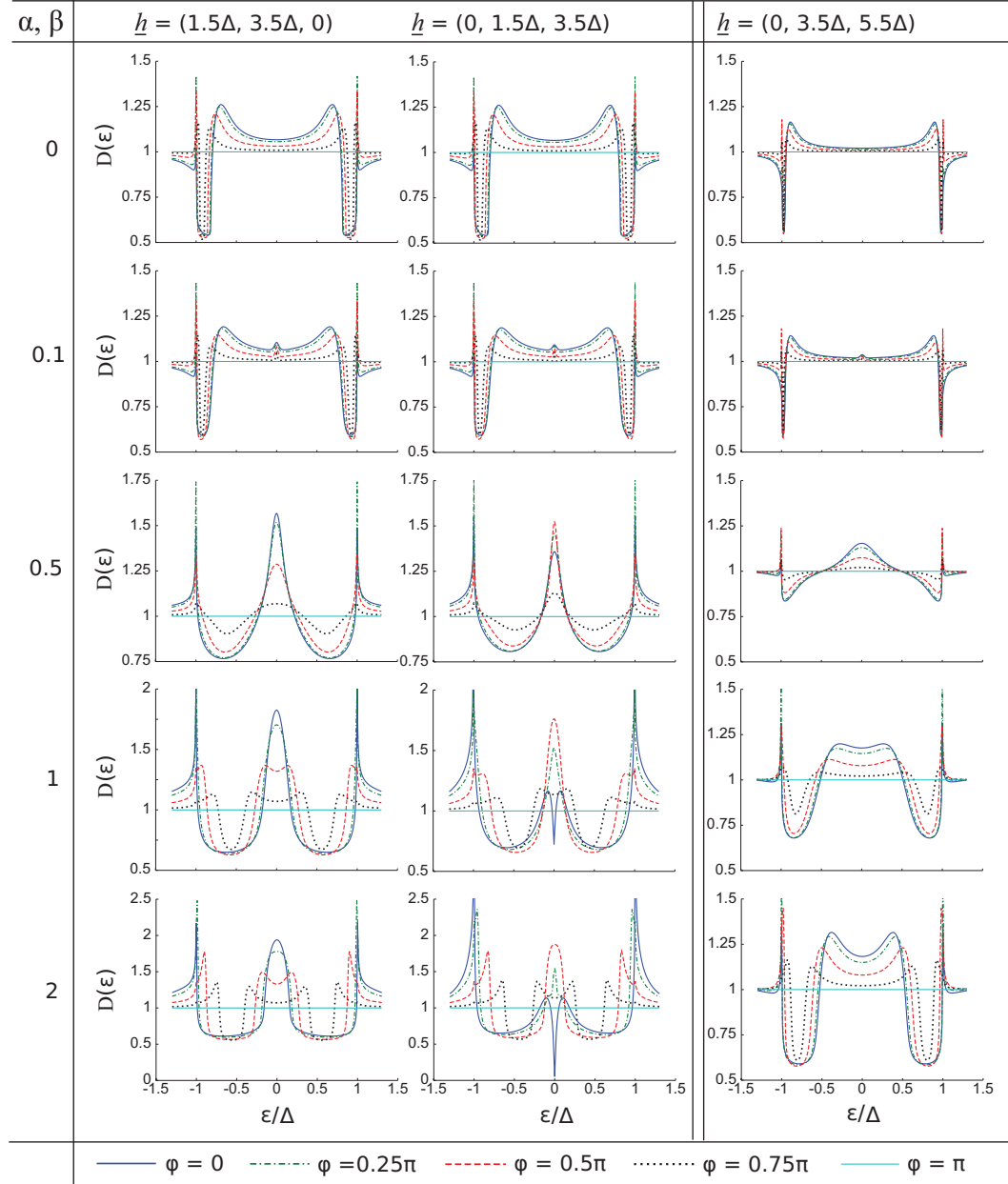


FIG. 11. (Color online) Density of states $D(\varepsilon)$ in the SFS junction for energies normalized to the superconducting gap Δ and SO coupling normalized to the inverse ferromagnet length $1/L_F$. The table shows the spectroscopic effects of increasing SO coupling in SFS with rotated exchange field. In the absence of SO coupling, the density of states is flat and featureless at low energies. Increasing the SO coupling again leads to a strong increase in the peak of the density of states at zero energy, while increasing the phase difference reduces the peak and shifts the density of states weight toward the gap edge for higher SO coupling strengths. With a component of the field in the junction direction a qualitative change in the density of states from strongly suppressed to enhanced at zero energy can be achieved by altering the phase difference between the superconductors. This change can occur in the presence of stronger exchange fields when SO coupling is included. Increasing the exchange field destroys the ability to maintain a gap in the density of states and the LRT component of the SO coupling increases the zero-energy peak as it did in the bilayer case.

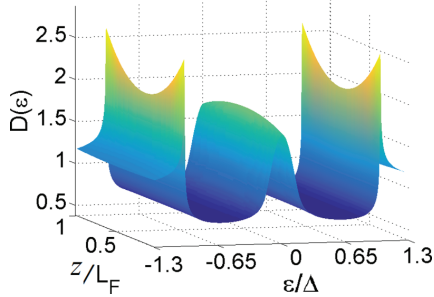


FIG. 12. (Color online) Spatial distribution of the density of states $D(\varepsilon)$ throughout the ferromagnet of an SFS junction with phase difference $\phi = 0$, spin-orbit coupling $\alpha = \beta = 1$, and magnetization $\underline{h} = (1.5\Delta, 3.5\Delta, 0)$.

With one component of the exchange field along the junction and another along either x or y , a phase-dictated gap-to-peak transition at zero energy is possible with stronger fields than with the field aligned in a single direction, as shown in Fig. 11. Notice that in this case increasing the phase difference $\phi = 0 \rightarrow 0.5\pi$ gives an increase in the peak at zero energy before reducing towards the normal metal state. For higher field strengths, we find once again that increasing the SO coupling increases the peak at zero energy, up to a system-specific threshold, and increasing phase difference reduces the density of states towards that of the normal metal.

It is also useful to consider how the zero-energy density of states depends simultaneously on the phase-difference and magnetization orientation. To this end, we show in Fig. 13 a contour plot of the density of states at the Fermi level ($\varepsilon = 0$) as a function of the superconducting phase difference ϕ across the junction and the magnetization direction θ . The proximity effect vanishes in the center of the junction at $\phi = \pi$ for any value of the exchange-field orientation, giving the normal-state value. Just as in the bilayer case (Fig. 4), we see that the proximity effect is strongly suppressed for the range of angles $\theta > 0$. When rotating the field in the opposite direction, $\theta < 0$, strongly nonmonotonic behavior emerges. For zero phase difference, the physics is qualitatively similar to the bilayer situation. In this case, we proved analytically that the LRT is not produced at all when $\theta = -\pi/4$. Accordingly, Fig. 13 shows a full minigap there.

Whether or not a clear zero-energy peak can be seen due to the LRT depends on the relative strength of the Rashba and Dresselhaus coupling. In the top panel, we have dominant Dresselhaus coupling in which case the low-energy density of states show either normal-state behavior or a minigap. Interestingly, we see that the same opportunity appears in the present case of a Josephson setup as in the bilayer case: a magnetically tunable minigap appears. This effect exists as long as the phase difference is not too close to π , in which case the minigap closes. In the bottom panel corresponding to equal magnitude of Rashba and Dresselhaus, however, a strong zero-energy enhancement due to long-range triplets emerges as one moves away from $\theta = -\pi/4$. With increasing phase difference, the singlets are seen to be more strongly suppressed than the triplet correlations since the minigap region (dark

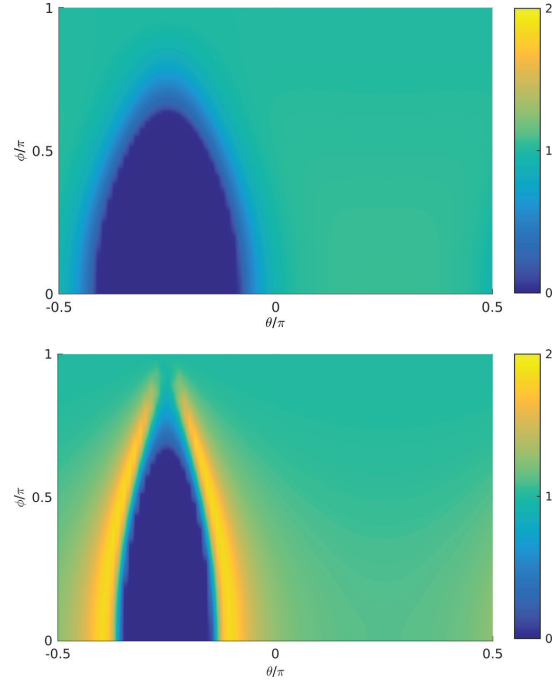


FIG. 13. (Color online) Zero-energy density of states $D(0)$ as a function of the phase-difference ϕ and magnetization angle θ , both tunable parameters experimentally. The other parameters used are $L_F/\xi_S = 0.5$, $h/\Delta_0 = 3$, $a\xi_S = 2$. In the top panel, we have dominant Dresselhaus coupling ($\chi = 0.15\pi$) while in the bottom panel we have equal magnitude of the Rashba and Dresselhaus coefficients ($\chi = \pi/4$).

blue) vanishes shortly after $\phi/\pi \simeq 0.6$ while the peaks due to triplets remain for larger phase differences.

D. Critical temperature

In this section, we present numerical results for the critical temperature T_c of an SF bilayer. The theory behind these investigations is summarized in Sec. II E, and discussed in more detail in Appendix B. An overview of the physical system is given in Fig. 1(a). In all of the simulations we performed, we used the material parameter $N_0\lambda = 0.2$ for the superconductor, the exchange field $h = 10\Delta_0$ for the ferromagnet, and the interface parameter $\zeta = 3$ for both materials. The other physical parameters are expressed in a dimensionless form, with lengths measured relative to the superconducting correlation length ξ_S , energies measured relative to the bulk zero-temperature gap Δ_0 , and temperatures measured relative to the bulk critical temperature T_{cs} . This includes the SO coupling strength a , which is expressed in the dimensionless form $a\xi_S$. The plots presented in this subsection were generated from 12–36 data points per curve, where each data point has a numerical precision of 0.0001 in T_c/T_{cs} . The results were smoothed with a LOESS algorithm.

Before we present the results with SO coupling, we will briefly investigate the effects of the ferromagnet length L_F

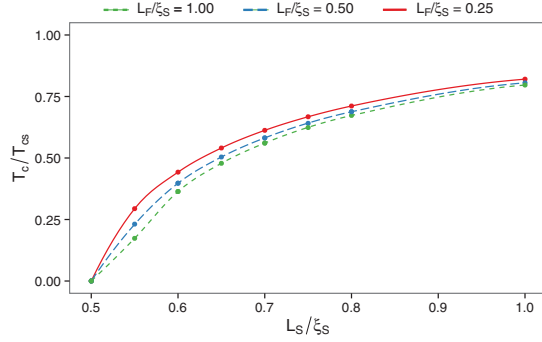


FIG. 14. (Color online) Plot of the critical temperature T_c/T_{cs} as a function of the length L_S/ξ_S of the superconductor for $a\xi_S = 0$. Below a critical length L_S , superconductivity can no longer be sustained and T_c becomes zero. For larger thicknesses of the superconducting layer, T_c reverts back to its bulk value.

and superconductor length L_S on the critical temperature, in order to identify the interesting parameter regimes. The critical temperature as a function of the size of the superconductor is shown in Fig. 14.

First of all, we see that the critical temperature drops to zero when $L_S/\xi_S \approx 0.5$. This observation is hardly surprising; since the superconducting correlation length is ξ_S , the critical temperature is rapidly suppressed once the length of the junction goes below ξ_S . After this, the critical temperature increases quickly, already reaching nearly 50% of the bulk value when $L_S/\xi_S = 0.6$, demonstrating that the superconductivity of the system is clearly very sensitive to small changes in parameters for this region.

The next step is then to observe how the behavior of the system varies with the size of the ferromagnet, and these results are presented in Fig. 15.

We again observe that the critical temperature increases with the size of the superconductor, and decreases with the size of the ferromagnet. The critical temperature for a supercon-

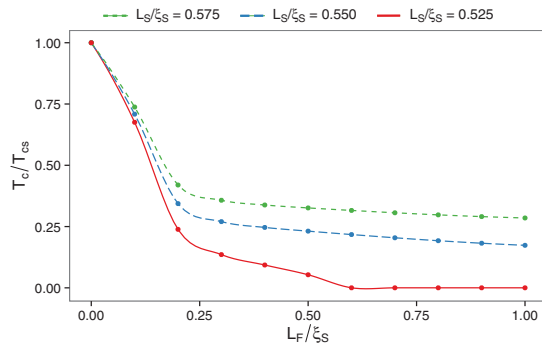


FIG. 15. (Color online) Plot of the critical temperature T_c/T_{cs} as a function of the ferromagnet length L_F/ξ_S for $a\xi_S = 0$. Increasing the thickness of the ferromagnet gradually suppresses the T_c of the superconductor, causing a stronger inverse proximity effect.

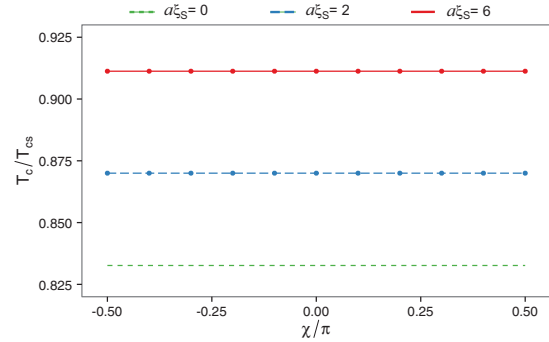


FIG. 16. (Color online) Plot of the critical temperature T_c/T_{cs} as a function of the SO angle χ , when $L_S/\xi_S = 1.00$, $L_F/\xi_S = 0.2$, and $\hbar \parallel \hat{z}$. Increasing the SO coupling causes T_c to move closer to its bulk value, since the triplet proximity effect channel becomes suppressed.

ductor with $L_S/\xi_S = 0.525$ drops to zero at $L_F/\xi_S \approx 0.6$, and stays that way as the size of the ferromagnet increases. Thus we do not observe any strongly nonmonotonic behavior, such as reentrant superconductivity, for our choice of parameters. This is consistent with the results of Fominov *et al.*, who only reported such behavior for systems where either the interface parameter or the exchange field is drastically smaller than for the bilayers considered herein [56].

We now turn to the effects of the antisymmetric SO coupling on the critical temperature, which has not been studied before. Figures 16 and 17 show plots of the critical temperature as a function of the SO angle χ for an exchange field in the z direction. The critical temperature is here independent of the SO angle χ . This result is reasonable, since the SO coupling is in the xy plane, which is perpendicular to the exchange field for this geometry. We also observe a noticeable increase in critical temperature for larger values of a . This behavior can be explained using the linearized Usadel equation. According to Eq. (26), the effective energy E_z coupling to the triplet component in the z direction becomes

$$E_z = \varepsilon + 4i D_F a^2; \quad (47)$$

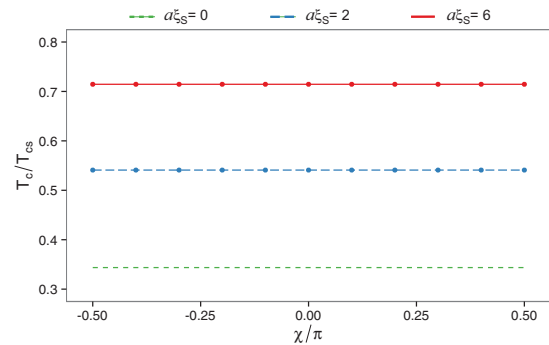


FIG. 17. (Color online) Plot of the critical temperature T_c/T_{cs} as a function of the SO angle χ , when $L_S/\xi_S = 0.55$, $L_F/\xi_S = 0.2$, and $\hbar \parallel \hat{z}$.

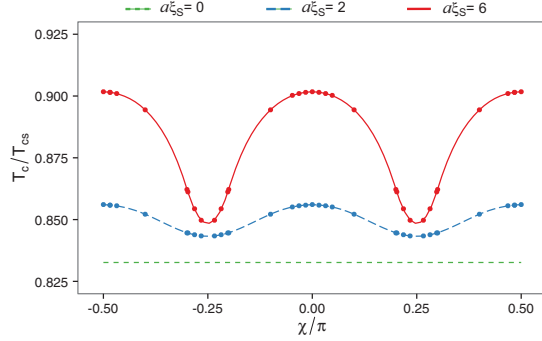


FIG. 18. (Color online) Plot of the critical temperature T_c/T_{cs} as a function of the SO angle χ , when $L_S/\xi_S = 1.00$, $L_F/\xi_S = 0.2$, and $\underline{h} \parallel \hat{x}$. The critical temperature depends on the relative magnitudes of the Rashba and Dresselhaus coefficients.

so in other words, the SRTs obtain an imaginary energy shift proportional to a^2 . However, as shown in Eq. (25), there is no corresponding shift in the energy of the singlet component. This effect reduces the triplet components relative to the singlet component in the ferromagnet, and as the triplet proximity channel is suppressed the critical temperature becomes restored to higher values.

The same situation for an exchange field along the x axis is shown in Figs. 18 and 19. For this geometry, we observe a somewhat smaller critical temperature for all $a > 0$ and all χ compared to Figs. 16 and 17. This can again be explained by considering the linearized Usadel equation in the ferromagnet, which suggests that the effective energy E_x coupling to the x component of the triplet vector should be

$$E_x = \varepsilon + 2iD_F a^2, \quad (48)$$

which has a smaller imaginary part than the corresponding equation for E_z . Furthermore, note the drop in critical temperature as $\chi \rightarrow \pm\pi/4$. Since the linearized equations contain a triplet mixing term proportional to $\sin 2\chi$, which is maximal precisely when $\chi = \pm\pi/4$, these are also the

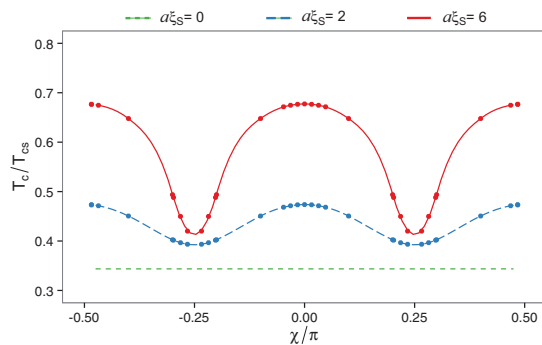


FIG. 19. (Color online) Plot of the critical temperature T_c/T_{cs} as a function of the SO angle χ , when $L_S/\xi_S = 0.55$, $L_F/\xi_S = 0.2$, and $\underline{h} \parallel \hat{x}$.

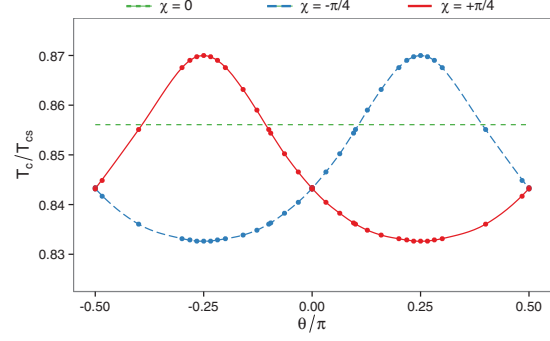


FIG. 20. (Color online) Plot of critical temperature T_c/T_{cs} as a function of the exchange-field angle θ , when $L_S/\xi_S = 1.00$, $L_F/\xi_S = 0.2$, and $a\xi_S = 2$. In contrast to ferromagnets without SO coupling, T_c now depends strongly on the magnetization direction. This gives rise to a spin-valve like functionality with a single ferromagnet featuring SO coupling.

geometries for which we expect a maximal LRT generation. Thus this decrease in critical temperature near $\chi = \pm\pi/4$ can be explained by a net conversion of singlet components to LRTs in the system, which has an adverse effect on the singlet amplitude in the superconductor, and therefore the critical temperature.

In Figs. 20 and 21, we present the results for a varying exchange field $\underline{h} \sim \cos\theta \hat{x} + \sin\theta \hat{y}$ in the xy plane. In this case, we observe particularly interesting behavior: the critical temperature has extrema at $|\chi| = |\theta| = \pi/4$, where the extremum is a maximum if θ and χ have the same sign, and a minimum if they have opposite signs. Since $\theta = \pm\pi/4$ is precisely the geometries for which we do not expect any LRT generation, triplet mixing cannot be the source of this behavior. For the choice of physical parameters chosen in Fig. 21, this effect results in a difference between the minimal and maximal critical temperature of nearly 60% as the magnetization direction is varied. As shown in Fig. 20, the

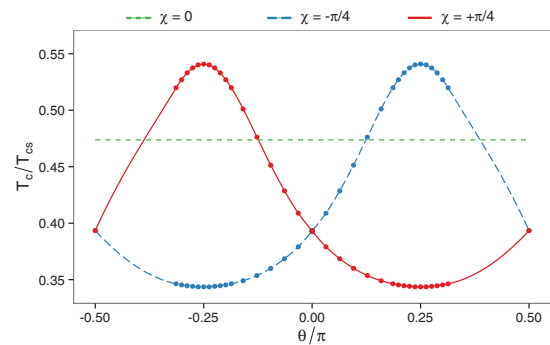


FIG. 21. (Color online) Plot of critical temperature T_c/T_{cs} as a function of the exchange-field angle θ , when $L_S/\xi_S = 0.55$, $L_F/\xi_S = 0.2$, and $a\xi_S = 2$.

effect persists qualitatively in larger structures as well, but is then weaker.

Instead, these observations may be explained using the theory developed in Sec. II. When we have a general exchange field and SO field in the xy plane, Eq. (34) reveals that the effective energy of the SRT component is

$$E_{\parallel} = \varepsilon + 2iD_F a^2(1 - \sin 2\theta \sin 2\chi). \quad (49)$$

Since the factor $(1 - \sin 2\theta \sin 2\chi)$ vanishes for $\theta = \chi = \pm\pi/4$, we get $E_{\parallel} = \varepsilon$ for this case. This geometry is also one where we do not expect any LRT generation, since the triplet mixing factor $\cos 2\theta \sin 2\chi = 0$, so the conclusion is that the SO coupling has no effect on the behavior of SRTs for these parameters—at least according to the linearized equations. However, since $1 - \sin 2\theta \sin 2\chi = 2$ for $\theta = -\chi = \pm\pi/4$, the situation is now dramatically different. The SRT effective energy is now $E_{\parallel} = \varepsilon + 4iD_F a^2$, with an imaginary contribution which again destabilizes the SRTs, and increases the critical temperature of the system. We emphasize that the variation of T_c with the magnetization direction is present when $\chi \neq \pi/4$ as well (unequal Rashba and Dresselhaus coefficients), albeit with a magnitude of the variation that gradually decreases as one approaches pure Rashba or pure Dresselhaus coupling.

E. Triplet spin-valve effect with a single ferromagnet

The results discussed in the previous section show that the critical temperature can be controlled via the magnetization direction of one single ferromagnetic layer. This is a new result originating from the presence of SO coupling. In conventional SF structures, T_c is independent of the magnetization orientation of the F layer. By using a spin-valve setup such as FSF [57–61], it has been shown that the relative magnetization configuration between the ferromagnetic layers will tune the T_c of the system. In contrast, in our case, such a spin-valve effect can be obtained with a single ferromagnet (see Figs. 20 and 21): by rotating the magnetization an angle $\pi/2$, T_c goes from a maximum to a minimum. The fact that only a single ferromagnet is required to achieve this effect is of practical importance since it can be challenging to control the relative magnetization orientation in magnetic multilayered structures.

IV. SUMMARY AND DISCUSSION

It was pointed out in Ref. [21] that for the case of transversal structures as depicted in Fig. 1(b), pure Rashba or pure Dresselhaus coupling and in-plane magnetization direction are insufficient for long range triplets to exist. However, although these layered structures are more restrictive in their conditions for LRT generation than lateral junctions, they are nevertheless one of the most relevant for current experimental setups [10,11,50], and herein we consider the corresponding experimentally accessible effects of SO coupling in this scenario. We have provided a detailed exposition of the density of states and critical temperature for both the SF bilayer and SFS junction with SO coupling, highlighting in particular the signature of long range triplets.

We saw that the spectroscopic signature depends nonmonotonically on the angle of the magnetic exchange field, and that

the LRT component can induce a strong peak in the density of states at zero energy for a range of magnetization directions. In addition to the large enhancement at zero energy, we see that by carefully choosing the SO coupling and exchange-field strengths in the Josephson junction it is again possible to control the qualitative features of the density of states by altering the phase difference between the two superconductors, e.g., with a loop geometry [53].

The intrinsic SO coupling present in the structures considered herein derives from their lack of inversion symmetry due to, e.g., the junction interfaces, so-called interfacial asymmetry, and we restricted the form of this coupling to the experimentally common and, in some cases, tunable Rashba-Dresselhaus form. A lack of inversion symmetry can also derive from intrinsic noncentrosymmetry of a crystal. This could in principle be utilised to provide a component of the SO field in the junction direction, but to date we are not aware of such materials having been explored in experiments with SF hybrid materials. However, analytic and numerical data suggest that such materials could have significant importance for spintronic applications making use of a large triplet Cooper pair population [43].

It is also worth considering the possibility of separating the spin-orbit coupling and the ferromagnetic layer, which would arguably be easier to fabricate, and we are currently pursuing this line of investigation. In this case, we would expect similar conclusions regarding when the long-range triplets leave clear spectroscopic signatures and also regarding the spin-valve effect with a single ferromagnet, as found when the SO coupling and exchange field coexist in the same material. One way to practically achieve such a setup would be to deposit a very thin layer of a heavy normal metal such as Au or Pt between a superconductor and a conventional homogeneous ferromagnet. The combination of the large atomic number Z and the broken structural inversion symmetry at the interface region would then provide the required SO coupling. With a very thin normal metal layer (of the order of a few nm), the proximity effect would be significantly stronger, and thus analysis of this regime is only possible with the full Usadel equations in the Riccati parametrization developed herein.

The current analysis pertains to thin film ferromagnets. Upon increasing the length of ferromagnetic film, one will increase the relative proportions of long-range to short-range triplets in the middle of the ferromagnet. For strong ferromagnets where the exchange field is a significant fraction of the Fermi energy, the quasiclassical Usadel formalism may no longer describe the system behavior appropriately, since it assumes that the impurity scattering rate is much larger than the other energy scales involved, and the Eilenberger equation should be used instead [62].

In the previous section, we also observed that the presence of SO coupling will in many cases *increase* the critical temperature of a hybrid structure compared to when SO coupling is absent. This effect is explained through an increase in the effective energy coupled to the triplet component in the Usadel equation, which destabilizes the triplet pairs and closes that proximity channel. However, for the special geometry $\theta = -\chi = \pm\pi/4$, the linearized equations suggest that the SRTs are unaffected by the presence of SO coupling, and

this is consistent with the numerical results. We also note that for the geometries with a large LRT generation, such as $\theta = 0$ and $\chi = \pm\pi/4$, the LRT generation reduces the critical temperature again. Thus, for the physical parameters considered herein, we see that there is only a slight net increase in critical temperature for these geometries, but not as large as for the geometries without LRT generation.

One particularly striking result from the critical temperature calculations is that when the Rashba and Dresselhaus contribution to the SO coupling is of similar magnitude, one observes that the critical temperature can change by as much as 60% upon changing $\theta = -\pi/4$ to $\theta = +\pi/4$, i.e., by a 90° rotation of the magnetic field. This implies that it is possible to create a novel kind of triplet spin valve using an SF bilayer, where the ferromagnet has a homogeneous exchange-field and Rashba-Dresselhaus coupling. This is in contrast to previous suggestions for triplet spin valves, such as the one described by Fominov *et al.*, which have required trilayers with different homogeneous ferromagnets [63]. The construction of such a device is likely to have possible applications in the emerging field of superconducting spintronics [3].

ACKNOWLEDGMENTS

The authors thank Angelo Di Bernardo, Matthias Eschrig, Camilla Espedal, and Iryna Kulagina for useful discussions and gratefully acknowledge support from the ‘‘Outstanding Academic Fellows’’ programme at NTNU and COST Action MP-1201 Novel Functionalities through Optimized Confinement of Condensate and Fields. J.L. was supported by the Research Council of Norway, Grant No. 205591 (FRINAT) and Grant No. 216700.

APPENDIX A: RICCATI PARAMETRIZATION OF THE USADEL EQUATION AND KUPRIYANOV-LUKICHEV BOUNDARY CONDITIONS

The 4×4 components of the retarded Green function \hat{g} are not entirely independent, but can be expressed as

$$\hat{g}(z, \varepsilon) = \begin{pmatrix} g(z, +\varepsilon) & f(z, +\varepsilon) \\ -f^*(z, -\varepsilon) & -g^*(z, -\varepsilon) \end{pmatrix}, \quad (\text{A1})$$

which suggests that the notation can be simplified by introducing the *tilde conjugation*

$$\tilde{g}(z, +\varepsilon) \equiv g^*(z, -\varepsilon). \quad (\text{A2})$$

Moreover, the normalization condition $\hat{g}^2 = 1$ further constrains the possible form of \hat{g} by relating the g components to the f components,

$$gg - f\tilde{f} = 1, \quad gf - f\tilde{g} = 0. \quad (\text{A3})$$

If we pick a suitable parametrization of \hat{g} , which automatically satisfies the symmetry and normalization requirements above, then both the Usadel equation and the Kupriyanov-Lukichev boundary conditions can be reduced from 4×4 to 2×2 matrix equations. In this paper, we employ the so-called *Riccati parametrization* for this purpose, which is defined by

$$\hat{g} = \begin{pmatrix} N & 0 \\ 0 & -\tilde{N} \end{pmatrix} \begin{pmatrix} 1 + \gamma\tilde{\gamma} & 2\gamma \\ 2\tilde{\gamma} & 1 + \tilde{\gamma}\gamma \end{pmatrix}, \quad (\text{A4})$$

where the normalization matrices are $N \equiv (1 - \gamma\tilde{\gamma})^{-1}$ and $\tilde{N} \equiv (1 - \tilde{\gamma}\gamma)^{-1}$. Solving the Riccati parametrized equations for the function $\gamma(z, \varepsilon)$ in spin space is then sufficient to uniquely construct the whole Green function $\hat{g}(z, \varepsilon)$. It is noteworthy that $\hat{g} \rightarrow 1$ when $\gamma \rightarrow 0$, while the elements of \hat{g} diverge to infinity when $\gamma \rightarrow 1$; so we see that a finite range of variation in γ parametrizes an infinite range of variation in \hat{g} .

We begin by deriving some basic identities, starting with the inverses of the two matrix products $N\gamma$ and $\gamma\tilde{N}$:

$$(N\gamma)^{-1} = \gamma^{-1}N^{-1} = \gamma^{-1}(1 - \gamma\tilde{\gamma}) = \gamma^{-1} - \tilde{\gamma}; \quad (\text{A5})$$

$$(\gamma\tilde{N})^{-1} = \tilde{N}^{-1}\gamma^{-1} = (1 - \tilde{\gamma}\gamma)\gamma^{-1} = \gamma^{-1} - \tilde{\gamma}. \quad (\text{A6})$$

By comparison of the results above, we see that $N\gamma = \gamma\tilde{N}$. Similar calculations for other combinations of the Riccati matrices reveal that we can always move normalization matrices past gamma matrices if we also perform a tilde conjugation in the process:

$$N\gamma = \gamma\tilde{N}, \quad \tilde{N}\gamma = \gamma N, \quad N\tilde{\gamma} = \tilde{\gamma}\tilde{N}, \quad \tilde{N}\tilde{\gamma} = \tilde{\gamma}N. \quad (\text{A7})$$

Since we intend to parametrize a differential equation, we should also try to relate the derivatives of the Riccati matrices. This can be done by differentiating the definition of N using the matrix version of the chain rule:

$$\begin{aligned} \partial_z N &= \partial_z (1 - \gamma\tilde{\gamma})^{-1} \\ &= -(1 - \gamma\tilde{\gamma})^{-1} [\partial_z (1 - \gamma\tilde{\gamma})] (1 - \gamma\tilde{\gamma})^{-1} \\ &= (1 - \gamma\tilde{\gamma})^{-1} [(\partial_z \gamma)\tilde{\gamma} + \gamma(\partial_z \tilde{\gamma})] (1 - \gamma\tilde{\gamma})^{-1} \\ &= N[(\partial_z \gamma)\tilde{\gamma} + \gamma(\partial_z \tilde{\gamma})]N. \end{aligned} \quad (\text{A8})$$

Performing a tilde conjugation of the equation above, we get a similar result for $\partial_z \tilde{N}$. Thus the derivatives of the normalization matrices satisfy the following identities:

$$\partial_z N = N[(\partial_z \gamma)\tilde{\gamma} + \gamma(\partial_z \tilde{\gamma})]N, \quad (\text{A9})$$

$$\partial_z \tilde{N} = \tilde{N}[(\partial_z \tilde{\gamma})\gamma + \tilde{\gamma}(\partial_z \gamma)]\tilde{N}. \quad (\text{A10})$$

In addition to the identities derived above, one should note that the definition of the normalization matrix $N = (1 - \gamma\tilde{\gamma})^{-1}$ can be rewritten in many forms which may be of use when simplifying Riccati parametrized expressions; examples of this include $\gamma\tilde{\gamma} = 1 - N^{-1}$ and $1 = N - N\gamma\tilde{\gamma}$.

Now that the basic identities are in place, it is time to parametrize the Usadel equation in the ferromagnet,

$$D_F \tilde{\nabla} \cdot (\hat{g} \tilde{\nabla} \hat{g}) + i[\varepsilon \hat{\rho}_3 + \hat{M}, \hat{g}] = 0, \quad (\text{A11})$$

where we for simplicity will let $D_F = 1$ in this Appendix. We begin by expanding the gauge covariant derivative $\tilde{\nabla} \cdot (\hat{g} \tilde{\nabla} \hat{g})$, and then simplify the result using the normalization condition $\hat{g}^2 = 1$ and its derivative $\{\hat{g}, \partial_z \hat{g}\} = 0$, which yields the result

$$\begin{aligned} \tilde{\nabla} \cdot (\hat{g} \tilde{\nabla} \hat{g}) &= \partial_z (\hat{g} \partial_z \hat{g}) - i \partial_z (\hat{g} \hat{A}_z \hat{g}) \\ &= -i[\hat{A}_z, \hat{g} \partial_z \hat{g}] - [\hat{A}, \hat{g} \hat{A} \hat{g}]. \end{aligned} \quad (\text{A12})$$

We then write \hat{g} in component form using Eq. (A1), and also write \hat{A} in the same form using $\hat{A} = \text{diag}(\underline{A}, -\underline{A}^*)$. In the rest of this Appendix, we will for simplicity assume that \underline{A} is real,

so that $\hat{A} = \text{diag}(\underline{A}, -\underline{A})$; in practice, this implies that \underline{A} can only depend on the spin projections σ_x and σ_z . The derivation

for the more general case of a complex \hat{A} is almost identical. The four terms in Eq. (A12) may then be written as follows:

$$\partial_z(\hat{g}\partial_z\hat{g}) = \begin{bmatrix} \partial_z(g\partial_zg - f\partial_z\tilde{f}) & \partial_z(g\partial_zf - f\partial_z\tilde{g}) \\ \partial_z(\tilde{g}\partial_z\tilde{f} - \tilde{f}\partial_zg) & \partial_z(\tilde{g}\partial_z\tilde{g} - \tilde{f}\partial_zf) \end{bmatrix}; \quad (\text{A13})$$

$$\partial_z(\hat{g}\hat{A}\hat{g}) = \begin{bmatrix} \partial_z(g\underline{A}g + f\underline{A}\tilde{f}) & \partial_z(g\underline{A}f + f\underline{A}\tilde{g}) \\ -\partial_z(\tilde{g}\underline{A}\tilde{f} + \tilde{f}\underline{A}g) & -\partial_z(\tilde{g}\underline{A}\tilde{g} + \tilde{f}\underline{A}f) \end{bmatrix}; \quad (\text{A14})$$

$$[\hat{A}, \hat{g}\partial_z\hat{g}] = \begin{bmatrix} [\underline{A}, g\partial_zg - f\partial_z\tilde{f}] & \{\underline{A}, g\partial_zf - f\partial_z\tilde{g}\} \\ -\{\underline{A}, \tilde{g}\partial_z\tilde{f} - \tilde{f}\partial_zg\} & -[\underline{A}, \tilde{g}\partial_z\tilde{g} - \tilde{f}\partial_zf] \end{bmatrix}; \quad (\text{A15})$$

$$[\hat{A}, \hat{g}\hat{A}\hat{g}] = \begin{bmatrix} [\underline{A}, g\underline{A}g + f\underline{A}\tilde{f}] & \{\underline{A}, g\underline{A}f + f\underline{A}\tilde{g}\} \\ [\underline{A}, \tilde{g}\underline{A}\tilde{f} + \tilde{f}\underline{A}g] & [\underline{A}, \tilde{g}\underline{A}\tilde{g} + \tilde{f}\underline{A}f] \end{bmatrix}. \quad (\text{A16})$$

Substituting these results back into Eq. (A12), we can find the upper blocks of the covariant derivative $\tilde{\nabla} \cdot (\hat{g}\tilde{\nabla}\hat{g})$,

$$[\tilde{\nabla} \cdot (\hat{g}\tilde{\nabla}\hat{g})]^{(1,1)} = \partial_z(g\partial_zg - f\partial_z\tilde{f}) - i\partial_z(gA_zg + fA_z\tilde{f}) - i[A_z, g\partial_zg - f\partial_z\tilde{f}] - [\underline{A}, g\underline{A}g + f\underline{A}\tilde{f}], \quad (\text{A17})$$

$$[\tilde{\nabla} \cdot (\hat{g}\tilde{\nabla}\hat{g})]^{(1,2)} = \partial_z(g\partial_zf - f\partial_z\tilde{g}) - i\partial_z(gA_zf + fA_z\tilde{g}) - i[A_z, g\partial_zf - f\partial_z\tilde{g}] - \{\underline{A}, g\underline{A}f + f\underline{A}\tilde{g}\}. \quad (\text{A18})$$

In this context, the notation $\hat{M}^{(n,m)}$ refers to the n th row and m th column in Nambu space. Since the Green function \hat{g} and background field \hat{A} also have a structure in spin space, the (1,1) element in Nambu space is the upper-left 2×2 block of the matrix, and the (1,2) element is the upper-right one.

There are two kinds of expressions that recur in the equations above, namely the components of $\hat{g}\partial_z\hat{g}$, and the components of $\hat{g}\hat{A}\hat{g}$. After we substitute in the Riccati parametrization $g = 2N - 1$ and $f = 2N\gamma$, these components take the form:

$$[\hat{g}\partial_z\hat{g}]^{(1,1)} = g\partial_zg - f\partial_z\tilde{f} = 2N[(\partial_z\gamma)\tilde{\gamma} - \gamma(\partial_z\tilde{\gamma})]N \quad (\text{A19})$$

$$[\hat{g}\partial_z\hat{g}]^{(1,2)} = g\partial_zf - f\partial_z\tilde{g} = 2N[(\partial_z\gamma) - \gamma(\partial_z\tilde{\gamma})\gamma]\tilde{N}; \quad (\text{A20})$$

$$[\hat{g}\hat{A}\hat{g}]^{(1,1)} = g\underline{A}g + f\underline{A}\tilde{f} = 4N(\underline{A} + \gamma\underline{A}\tilde{\gamma})N - 2\{\underline{A}, N\} + \underline{A}; \quad (\text{A21})$$

$$[\hat{g}\hat{A}\hat{g}]^{(1,2)} = g\underline{A}f + f\underline{A}\tilde{g} = 4N(\underline{A}\gamma + \gamma\underline{A})\tilde{N} - 2\{\underline{A}, N\gamma\}. \quad (\text{A22})$$

If we explicitly calculate the commutators of \hat{A} with the two matrices $\hat{g}\partial_z\hat{g}$ and $\hat{g}\hat{A}\hat{g}$, then we find

$$[\hat{A}, \hat{g}\partial_z\hat{g}]^{(1,1)} = [\underline{A}, g\partial_zg - f\partial_z\tilde{f}] = 2N(1 - \gamma\tilde{\gamma})\underline{A}N[(\partial_z\gamma)\tilde{\gamma} - \gamma(\partial_z\tilde{\gamma})]N - 2N[(\partial_z\gamma)\tilde{\gamma} - \gamma(\partial_z\tilde{\gamma})]N\underline{A}(1 - \gamma\tilde{\gamma})N; \quad (\text{A23})$$

$$[\hat{A}, \hat{g}\partial_z\hat{g}]^{(1,2)} = \{\underline{A}, g\partial_zf - f\partial_z\tilde{g}\} = 2N(1 - \gamma\tilde{\gamma})\underline{A}N[(\partial_z\gamma) - \gamma(\partial_z\tilde{\gamma})\gamma]\tilde{N} + 2N[(\partial_z\gamma) - \gamma(\partial_z\tilde{\gamma})\gamma]\tilde{N}\underline{A}(1 - \tilde{\gamma}\gamma)\tilde{N}; \quad (\text{A24})$$

$$[\hat{A}, \hat{g}\hat{A}\hat{g}]^{(1,1)} = [\underline{A}, g\underline{A}g + f\underline{A}\tilde{f}] = 4\underline{A}N(\underline{A} + \gamma\underline{A}\tilde{\gamma})N - 4N(\underline{A} + \gamma\underline{A}\tilde{\gamma})N\underline{A} - 2\{\underline{A}^2, N\}; \quad (\text{A25})$$

$$[\hat{A}, \hat{g}\hat{A}\hat{g}]^{(1,2)} = \{\underline{A}, g\underline{A}f + f\underline{A}\tilde{g}\} = 4\underline{A}N(\underline{A}\gamma + \gamma\underline{A})\tilde{N} + 4N(\underline{A}\gamma + \gamma\underline{A})\tilde{N}\underline{A} - 4\underline{A}N\gamma\underline{A} - 2\{\underline{A}^2, N\gamma\}. \quad (\text{A26})$$

If we instead differentiate the aforementioned matrices with respect to z , we obtain

$$[\partial_z(\hat{g}\partial_z\hat{g})]^{(1,1)} = \partial_z(g\partial_zg - f\partial_z\tilde{f}) = 2N[(\partial_z^2\gamma) + 2(\partial_z\gamma)\tilde{N}\tilde{\gamma}(\partial_z\gamma)]\tilde{\gamma}N - 2N\gamma[(\partial_z^2\tilde{\gamma}) + 2(\partial_z\tilde{\gamma})N\gamma(\partial_z\tilde{\gamma})]N; \quad (\text{A27})$$

$$[\partial_z(\hat{g}\partial_z\hat{g})]^{(1,2)} = \partial_z(g\partial_zf - f\partial_z\tilde{g}) = 2N[(\partial_z^2\gamma) + 2(\partial_z\gamma)\tilde{N}\tilde{\gamma}(\partial_z\gamma)]\tilde{N} - 2N\gamma[(\partial_z^2\tilde{\gamma}) + 2(\partial_z\tilde{\gamma})N\gamma(\partial_z\tilde{\gamma})]\tilde{\gamma}\tilde{N}; \quad (\text{A28})$$

$$\begin{aligned} [\partial_z(\hat{g}\hat{A}\hat{g})]^{(1,1)} &= \partial_z(g\underline{A}g + f\underline{A}\tilde{f}) = 2N(1 + \gamma\tilde{\gamma})\underline{A}N[\gamma(\partial_z\tilde{\gamma}) + (\partial_z\gamma)\tilde{\gamma}]N + 2N[\gamma(\partial_z\tilde{\gamma}) + (\partial_z\gamma)\tilde{\gamma}]N\underline{A}(1 + \gamma\tilde{\gamma})N \\ &\quad + 4N\gamma\underline{A}\tilde{N}[(\partial_z\tilde{\gamma}) + \tilde{\gamma}(\partial_z\gamma)\tilde{\gamma}]N + 4N[(\partial_z\gamma) + \gamma(\partial_z\tilde{\gamma})\gamma]\tilde{N}\underline{A}\tilde{\gamma}N; \end{aligned} \quad (\text{A29})$$

$$\begin{aligned} [\partial_z(\hat{g}\hat{A}\hat{g})]^{(1,2)} &= \partial_z(g\underline{A}f + f\underline{A}\tilde{g}) = 2N(1 + \gamma\tilde{\gamma})\underline{A}N[(\partial_z\gamma) + \gamma(\partial_z\tilde{\gamma})\gamma]\tilde{N} + 2N[(\partial_z\gamma) + \gamma(\partial_z\tilde{\gamma})\gamma]\tilde{N}\underline{A}(1 + \tilde{\gamma}\gamma)\tilde{N} \\ &\quad + 4N\gamma\underline{A}\tilde{N}[\tilde{\gamma}(\partial_z\gamma) + (\partial_z\tilde{\gamma})\gamma]\tilde{N} + 4N[\gamma(\partial_z\tilde{\gamma}) + (\partial_z\gamma)\tilde{\gamma}]N\underline{A}\tilde{\gamma}\tilde{N}. \end{aligned} \quad (\text{A30})$$

Combining all of the equations above, we can express Eqs. (A17) and (A18) using Riccati matrices. In order to isolate the second-order derivative $\partial_z^2 \gamma$ from these, the trick is to multiply Eq. (A17) by γ from the right, and subsequently subtract the result from Eq. (A18):

$$\frac{1}{2} N^{-1} \{ [\tilde{\nabla} \cdot (\hat{g} \tilde{\nabla} \hat{g})]^{(1,2)} - [\tilde{\nabla} \cdot (\hat{g} \tilde{\nabla} \hat{g})]^{(1,1)} \gamma \} = \partial_z^2 \gamma + 2(\partial_z \gamma) \tilde{N} \tilde{\gamma} (\partial_z \gamma) - 2i(A_z + \gamma A_z \tilde{\gamma}) N (\partial_z \gamma) - 2i(\partial_z \gamma) \tilde{N} (A_z + \tilde{\gamma} A_z \gamma) - 2(A\gamma + \gamma A) \tilde{N} (A + \tilde{\gamma} A \gamma) - A^2 \gamma + \gamma A^2. \quad (\text{A31})$$

If we finally rewrite $[\tilde{\nabla} \cdot (\hat{g} \tilde{\nabla} \hat{g})]^{(1,1)}$ and $[\tilde{\nabla} \cdot (\hat{g} \tilde{\nabla} \hat{g})]^{(1,2)}$ in the equation above by substituting in the Usadel equation (A11), then we obtain the following equation for the Riccati matrix γ :

$$\partial_z^2 \gamma = -2i\varepsilon\gamma - i\hbar \cdot (\underline{\alpha}\gamma - \gamma \underline{\alpha}^*) - 2(\partial_z \gamma) \tilde{N} \tilde{\gamma} (\partial_z \gamma) + 2i(A_z + \gamma A_z \tilde{\gamma}) N (\partial_z \gamma) + 2i(\partial_z \gamma) \tilde{N} (A_z + \tilde{\gamma} A_z \gamma) + 2(A\gamma + \gamma A) \tilde{N} (A + \tilde{\gamma} A \gamma) + A^2 \gamma - \gamma A^2. \quad (\text{A32})$$

The corresponding equation for $\tilde{\gamma}$ can be found by tilde conjugation of the above. After restoring the diffusion coefficient D_F , and generalizing the derivation to a complex SO field \underline{A} , the above result takes the form shown in Eq. (5).

After parametrizing the Usadel equation, the next step is to do the same to the Kupriyanov-Lukichev boundary conditions. The gauge covariant version of Eq. (2) may be written

$$2L_n \zeta_n \hat{g}_n \tilde{\nabla} \hat{g}_n = [\hat{g}_1, \hat{g}_2], \quad (\text{A33})$$

which upon expanding the covariant derivative $\hat{g} \tilde{\nabla} \hat{g}$ becomes

$$\hat{g}_n \partial_z \hat{g}_n = \frac{1}{2} \Omega_n [\hat{g}_1, \hat{g}_2] + i \hat{g}_n [\hat{A}_z, \hat{g}_n], \quad (\text{A34})$$

where we have introduced the notation $\Omega_n \equiv 1/L_n \zeta_n$ for the interface parameter. We will now restrict our attention to the (1,1) and (1,2) components of the above,

$$g_n \partial_z g_n - f_n \partial_z \tilde{f}_n = \frac{1}{2} \Omega_n (g_1 g_2 - g_2 g_1 - f_1 \tilde{f}_2 + f_2 \tilde{f}_1) + i g_n [A_z, g_n] + i f_n [A_z, \tilde{f}_n], \quad (\text{A35})$$

$$g_n \partial_z f_n - f_n \partial_z \tilde{g}_n = \frac{1}{2} \Omega_n (g_1 f_2 - g_2 f_1 - f_1 \tilde{g}_2 + f_2 \tilde{g}_1) + i g_n [A_z, f_n] + i f_n [A_z, \tilde{g}_n]. \quad (\text{A36})$$

Substituting the Riccati parametrizations $g_n = 2N_n - 1$ and $f_n = 2N_n \gamma_n$ in the above, we then obtain

$$N_n [(\partial_z \gamma_n) \tilde{\gamma}_n - \gamma_n (\partial_z \tilde{\gamma}_n)] N_n = \Omega_n N_1 (1 - \gamma_1 \tilde{\gamma}_2) N_2 - \Omega_n N_2 (1 - \gamma_2 \tilde{\gamma}_1) N_1 - i N_n (1 - \gamma_n \tilde{\gamma}_n) \underline{A} N_n - i N_n \underline{A} (1 - \gamma_n \tilde{\gamma}_n) N_n + 2i N_n (\underline{A} + \gamma_n \underline{A} \tilde{\gamma}_n) N_n, \quad (\text{A37})$$

$$N_n [(\partial_z \gamma_n) - \gamma_n (\partial_z \tilde{\gamma}_n) \gamma_n] \tilde{N}_n = \Omega_n N_1 (1 - \gamma_1 \tilde{\gamma}_2) \gamma_2 \tilde{N}_2 - \Omega_n N_2 (1 - \gamma_2 \tilde{\gamma}_1) \gamma_1 \tilde{N}_1 + i N_n (1 + \gamma_n \tilde{\gamma}_n) \underline{A} \gamma_n \tilde{N}_n + i N_n \gamma_n \underline{A} (1 + \tilde{\gamma}_n \gamma_n) \tilde{N}_n. \quad (\text{A38})$$

If we multiply Eq. (A37) by γ_n from the right, subtract this from Eq. (A38), and divide by N_n from the left, then we obtain the following boundary condition for γ_n :

$$\partial_z \gamma_n = \Omega_n (1 - \gamma_1 \tilde{\gamma}_2) N_2 (\gamma_2 - \gamma_n) + \Omega_n (1 - \gamma_2 \tilde{\gamma}_1) N_1 (\gamma_n - \gamma_1) + i \{A_z, \gamma_n\}. \quad (\text{A39})$$

When we evaluate the above for $n = 1$ and 2 , then it simplifies to the following:

$$\partial_z \gamma_1 = \Omega_1 (1 - \gamma_1 \tilde{\gamma}_2) N_2 (\gamma_2 - \gamma_1) + i \{A_z, \gamma_1\}, \quad (\text{A40})$$

$$\partial_z \gamma_2 = \Omega_2 (1 - \gamma_2 \tilde{\gamma}_1) N_1 (\gamma_2 - \gamma_1) + i \{A_z, \gamma_2\}. \quad (\text{A41})$$

The boundary conditions for $\partial_z \tilde{\gamma}_1$ and $\partial_z \tilde{\gamma}_2$ are found by tilde conjugating the above. If we generalize the derivation to a complex SO field \underline{A} , and substitute back $\Omega_n \equiv 1/L_n \zeta_n$ in the result, then we arrive at Eq. (6).

APPENDIX B: DERIVATION OF THE SELF-CONSISTENCY EQUATION FOR \underline{A}

For completeness, we present here a detailed derivation of the self-consistency equation for the BCS order parameter [64] in a quasiclassical framework. Similar derivations can also be found in Refs. [52,65–68]. In this paper, we follow the convention where the Keldysh component of the anomalous Green function is defined as

$$F_{\sigma\sigma'}^K(\underline{r}, t; \underline{r}', t') \equiv -i \langle [\psi_{\sigma}(\underline{r}, t), \psi_{\sigma'}(\underline{r}', t')] \rangle, \quad (\text{B1})$$

where $\psi_{\sigma}(\underline{r}, t)$ is the spin-dependent fermion annihilation operator, and the superconducting gap is defined as

$$\Delta(\underline{r}, t) \equiv \lambda \langle \psi_{\uparrow}(\underline{r}, t) \psi_{\downarrow}(\underline{r}, t) \rangle, \quad (\text{B2})$$

where $\lambda > 0$ is the electron-electron coupling constant in the BCS theory. For the rest of this appendix, we will also assume that we work in an electromagnetic gauge where Δ is a purely real quantity. Comparing Eqs. (B1) and (B2), and using the fermionic anticommutation relation

$$\psi_{\uparrow}(\underline{r}, t) \psi_{\downarrow}(\underline{r}, t) = -\psi_{\downarrow}(\underline{r}, t) \psi_{\uparrow}(\underline{r}, t), \quad (\text{B3})$$

we see that the superconducting gap $\Delta(\underline{r}, t)$ can be expressed in terms of the Green functions in two different ways:

$$\Delta(\underline{r}, t) = \frac{i\lambda}{2} F_{\uparrow\downarrow}^K(\underline{r}, t; \underline{r}, t), \quad (\text{B4})$$

$$\Delta(\underline{r}, t) = -\frac{i\lambda}{2} F_{\downarrow\uparrow}^K(\underline{r}, t; \underline{r}, t). \quad (\text{B5})$$

We may then perform a quasiclassical approximation by first switching to Wigner mixed coordinates, then Fourier transforming the relative coordinates, then integrating out the energy dependence, and finally averaging the result over the Fermi surface to obtain the isotropic part. The resulting equations for the superconducting gap are

$$\Delta(\underline{r}, t) = \frac{1}{4} N_0 \lambda \int d\varepsilon f_{\uparrow\downarrow}^K(\underline{r}, t, \varepsilon), \quad (\text{B6})$$

$$\Delta(\underline{r}, t) = -\frac{1}{4} N_0 \lambda \int d\varepsilon f_{\downarrow\uparrow}^K(\underline{r}, t, \varepsilon), \quad (\text{B7})$$

where $f_{\sigma\sigma'}^K$ is the quasiclassical counterpart to $F_{\sigma\sigma'}^K$, ε is the quasiparticle energy, and N_0 is the density of states per spin at the Fermi level.

In the equilibrium case, the Keldysh component \hat{g}^K can be expressed in terms of the retarded and advanced components of the Green function,

$$\hat{g}^K = (\hat{g}^R - \hat{g}^A) \tanh(\varepsilon/2T), \quad (\text{B8})$$

and the advanced Green function may again be expressed in terms of the retarded one,

$$\hat{g}^A = -\hat{\rho}_3 \hat{g}^{R\dagger} \hat{\rho}_3, \quad (\text{B9})$$

which implies that the Keldysh component can be expressed entirely in terms of the retarded component,

$$\hat{g}^K = (\hat{g}^R - \hat{\rho}_3 \hat{g}^{R\dagger} \hat{\rho}_3) \tanh(\varepsilon/2T). \quad (\text{B10})$$

If we extract the relevant anomalous components $f_{\uparrow\downarrow}^K$ and $f_{\downarrow\uparrow}^K$ from the above, we obtain the results

$$f_{\uparrow\downarrow}^K = [f_{\uparrow\downarrow}^R(\underline{r}, +\varepsilon) + f_{\downarrow\uparrow}^R(\underline{r}, -\varepsilon)] \tanh(\varepsilon/2T), \quad (\text{B11})$$

$$f_{\downarrow\uparrow}^K = [f_{\downarrow\uparrow}^R(\underline{r}, +\varepsilon) + f_{\uparrow\downarrow}^R(\underline{r}, -\varepsilon)] \tanh(\varepsilon/2T). \quad (\text{B12})$$

We then switch to a singlet/triplet-decomposition of the retarded component f^R , where the singlet component is described by a scalar function f_s , and the triplet component by the so-called d -vector (d_x, d_y, d_z) . This parametrization is defined by the matrix equation

$$f^R = (f_s + \underline{d} \cdot \underline{\sigma}) i\sigma_y, \quad (\text{B13})$$

or in component form,

$$\begin{pmatrix} f_{\uparrow\uparrow}^R & f_{\uparrow\downarrow}^R \\ f_{\downarrow\uparrow}^R & f_{\downarrow\downarrow}^R \end{pmatrix} = \begin{pmatrix} i d_y - d_x & d_z + f_s \\ d_z - f_s & i d_y + d_x \end{pmatrix}. \quad (\text{B14})$$

Parametrizing Eqs. (B11) and (B12) according to Eq. (B14), we obtain

$$f_{\uparrow\downarrow}^K(\underline{r}, \varepsilon) = [d_z(\underline{r}, +\varepsilon) + f_s(\underline{r}, +\varepsilon) + d_z(\underline{r}, -\varepsilon) - f_s(\underline{r}, -\varepsilon)] \tanh(\varepsilon/2T), \quad (\text{B15})$$

$$f_{\uparrow\downarrow}^K(\underline{r}, \varepsilon) = [d_z(\underline{r}, +\varepsilon) - f_s(\underline{r}, +\varepsilon) + d_z(\underline{r}, -\varepsilon) + f_s(\underline{r}, -\varepsilon)] \tanh(\varepsilon/2T). \quad (\text{B16})$$

The triplet component d_z can clearly be eliminated from the above equations by subtracting Eq. (B15) from Eq. (B16),

$$f_{\uparrow\downarrow}^K - f_{\downarrow\uparrow}^K = 2[f_s(\underline{r}, \varepsilon) - f_s(\underline{r}, -\varepsilon)] \tanh(\varepsilon/2T), \quad (\text{B17})$$

and a matching expression for the superconducting gap can be acquired by adding Eqs. (B6) and (B7),

$$2\Delta(\underline{r}) = \frac{1}{4} N_0 \lambda \int d\varepsilon [f_{\uparrow\downarrow}^K(\underline{r}, \varepsilon) - f_{\downarrow\uparrow}^K(\underline{r}, \varepsilon)] \tanh(\varepsilon/2T). \quad (\text{B18})$$

By comparing the two results above, we finally arrive at an equation for the superconducting gap which only depends on the singlet component of the quasiclassical Green function:

$$\Delta(\underline{r}) = \frac{1}{4} N_0 \lambda \int d\varepsilon [f_s(\underline{r}, \varepsilon) - f_s(\underline{r}, -\varepsilon)] \tanh(\varepsilon/2T). \quad (\text{B19})$$

If the integral above is performed for all real values of ε , it turns out to be logarithmically divergent, e.g., for a bulk superconductor. However, physically, the range of energies that should be integrated over is restricted by the energy spectra of the phonons that mediate the attractive electron-electron interactions in the superconductor. This issue may therefore be resolved by introducing a Debye cutoff ω_c , such that we only integrate over the region where $|\varepsilon| < \omega_c$. Including the integration range, the gap equation is therefore

$$\Delta(\underline{r}) = \frac{1}{4} N_0 \lambda \int_{-\omega_c}^{\omega_c} d\varepsilon [f_s(\underline{r}, \varepsilon) - f_s(\underline{r}, -\varepsilon)] \tanh(\varepsilon/2T). \quad (\text{B20})$$

The equation above can, however, be simplified even further. First of all, both $f_s(\varepsilon) - f_s(-\varepsilon)$ and $\tanh(\varepsilon/2T)$ are clearly antisymmetric functions of ε , which means that the product is a symmetric function, and so it is sufficient to perform an integral over positive values of ε ,

$$\Delta(\underline{r}) = \frac{1}{2} N_0 \lambda \int_0^{\omega_c} d\varepsilon [f_s(\underline{r}, \varepsilon) - f_s(\underline{r}, -\varepsilon)] \tanh(\varepsilon/2T). \quad (\text{B21})$$

However, because of the term $f_s(\underline{r}, -\varepsilon)$, we still need to know the Green function for negative values of ε before we can calculate the gap. On the other hand, the singlet component of the quasiclassical Green functions also has a symmetry when the superconducting gauge is chosen as real,

$$f_s(\underline{r}, \varepsilon) = -f_s^*(\underline{r}, -\varepsilon), \quad (\text{B22})$$

which implies that

$$f_s(\underline{r}, \varepsilon) - f_s(\underline{r}, -\varepsilon) = 2 \operatorname{Re}[f_s(\underline{r}, \varepsilon)]. \quad (\text{B23})$$

Substituting Eq. (B23) into Eq. (B21), the gap equation takes a particularly simple form, which only depends on the real part of the singlet component $f_s(\underline{r}, \varepsilon)$ for positive energies ε :

$$\Delta(\underline{r}) = N_0 \lambda \int_0^{\omega_c} d\varepsilon \operatorname{Re}[f_s(\underline{r}, \varepsilon)] \tanh(\varepsilon/2T). \quad (\text{B24})$$

Let us now consider the case of a BCS bulk superconductor, which has a singlet component given by the equation

$$f_s(\varepsilon) = \frac{\Delta}{\sqrt{\varepsilon^2 - \Delta^2}}, \quad (\text{B25})$$

so that the gap equation may be written as

$$\Delta = N_0 \lambda \int_0^{\omega_c} d\varepsilon \operatorname{Re} \left(\frac{\Delta}{\sqrt{\varepsilon^2 - \Delta^2}} \right) \tanh(\varepsilon/2T). \quad (\text{B26})$$

The part in the curly braces is only real when $|\varepsilon| \geq \Delta$, which means that the equation can be simplified by changing the lower integration limit to Δ . After also dividing the equation by $\Delta N_0 \lambda$, we then obtain the self-consistency equation

$$\frac{1}{N_0 \lambda} = \int_{\Delta}^{\omega_c} d\varepsilon \frac{\tanh(\varepsilon/2T)}{\sqrt{\varepsilon^2 - \Delta^2}}. \quad (\text{B27})$$

For the zero-temperature case, where $T \rightarrow 0$ and $\Delta \rightarrow \Delta_0$, performing the above integral and reordering the result yields

$$\omega_c = \Delta_0 \cosh(1/N_0 \lambda). \quad (\text{B28})$$

Using the above equation for ω_c , and the well-known result

$$\frac{\Delta_0}{T_c} = \frac{\pi}{e^\gamma}, \quad (\text{B29})$$

where $\gamma \approx 0.57722$ is the Euler-Mascheroni constant, we can finally rewrite Eq. (B24) as

$$\Delta(\underline{r}) = N_0 \lambda \int_0^{\Delta_0 \cosh(1/N_0 \lambda)} d\varepsilon \operatorname{Re}[f_s(\underline{r}, \varepsilon)] \times \tanh\left(\frac{\pi}{2e^\gamma} \frac{\varepsilon/\Delta_0}{T/T_c}\right). \quad (\text{B30})$$

This version of the gap equation is particularly well-suited for numerical simulations. One advantage is that we only need to know the Green function for positive energies, which halves the number of energies that we need to solve the Usadel equation for. The equation also takes a particularly simple form if we use energy units where $\Delta_0 = 1$ and temperature units where $T_c = 1$, which is common practice in such simulations.

-
- [1] A. I. Buzdin, *Rev. Mod. Phys.* **77**, 935 (2005).
[2] F. S. Bergeret, A. F. Volkov, and K. B. Efetov, *Rev. Mod. Phys.* **77**, 1321 (2005).
[3] J. Linder and J. W. A. Robinson, *Nat. Phys.* **11**, 307 (2015).
[4] F. S. Bergeret, A. F. Volkov, and K. B. Efetov, *Phys. Rev. Lett.* **86**, 4096 (2001).
[5] M. Eschrig, J. Kopu, J. C. Cuevas, and Gerd Schön, *Phys. Rev. Lett.* **90**, 137003 (2003).
[6] K. Halterman, P. H. Barsic, and O. T. Valls, *Phys. Rev. Lett.* **99**, 127002 (2007).
[7] A. Cottet, *Phys. Rev. Lett.* **107**, 177001 (2011).
[8] Y. Asano, Y. Sawa, Y. Tanaka, and A. A. Golubov, *Phys. Rev. B* **76**, 224525 (2007).
[9] Y. Kalcheim, I. Felner, O. Millo, T. Kirzhner, G. Koren, A. DiBernardo, M. Egilmez, M. G. Blamire, and J. W. A. Robinson, *Phys. Rev. B* **89**, 180506(R) (2014).
[10] J. W. A. Robinson, J. D. Witt, and M. Blamire, *Science* **329**, 59 (2010).
[11] T. S. Khaire, M. A. Khasawneh, W. P. Pratt, and N. O. Birge, *Phys. Rev. Lett.* **104**, 137002 (2010).
[12] M. Alidoust and J. Linder, *Phys. Rev. B* **82**, 224504 (2010); I. B. Sperstad, J. Linder, and A. Sudbø, *ibid.* **78**, 104509 (2008).
[13] L. Trifunovic and Z. Radović, *Phys. Rev. B* **82**, 020505(R) (2010).
[14] I. Sosnin, H. Cho, V. T. Petrashov, and A. F. Volkov, *Phys. Rev. Lett.* **96**, 157002 (2006).
[15] Z. Shomali, M. Zareyan, and W. Belzig, *New J. Phys.* **13**, 083033 (2012).
[16] G. Annunziata, M. Cuoco, C. Noce, A. Sudbø, and J. Linder, *Phys. Rev. B* **83**, 060508(R) (2011).
[17] I. V. Bobkova and A. M. Bobkov, *Phys. Rev. Lett.* **108**, 197002 (2012).
[18] F. Konschelle, J. Cayssol, and A. Buzdin, *Phys. Rev. B* **82**, 180509(R) (2010).
[19] M. Houzet, *Phys. Rev. Lett.* **101**, 057009 (2008).
[20] G. Annunziata, D. Manske, and J. Linder, *Phys. Rev. B* **86**, 174514 (2012).
[21] F. S. Bergeret and I. V. Tokatly, *Phys. Rev. B* **89**, 134517 (2014).
[22] F. S. Bergeret and I. V. Tokatly, *Phys. Rev. Lett.* **110**, 117003 (2013).
[23] M. Eschrig, J. Kopu, A. Konstantin, J. C. Cuevas, M. Fogelström, and G. Schön, *Adv. Solid State Phys.* **44**, 533 (2004).
[24] I. S. Burmistrov and N. M. Chitchev, *Phys. Rev. B* **72**, 144520 (2005).
[25] J. Linder and K. Halterman, *Phys. Rev. B* **90**, 104502 (2014).
[26] A. A. Abrikosov and L. P. Gor'kov, *Sov. Phys. JETP* **15**, 752 (1962).
[27] M. Eschrig, *Phys. Today* **64**, 43 (2011).
[28] K. V. Samokhin, *Ann. Phys.* **324**, 2385 (2009).
[29] V. M. Edelstein, *Phys. Rev. B* **67**, 020505 (2003).
[30] J. Linder and T. Yokoyama, *Phys. Rev. Lett.* **106**, 237201 (2011).
[31] K. Sun and N. Shah, *Phys. Rev. B* **91**, 144508 (2015).
[32] X. Liu, J. K. Jain, and C.-X. Liu, *Phys. Rev. Lett.* **113**, 227002 (2014).
[33] K. Usadel, *Phys. Rev. Lett.* **25**, 507 (1970).
[34] W. Belzig, F. K. Wilhelm, C. Bruder, G. Schön, A. D. Zaikin, *Superlattices and Microstructures* **25**, 1251 (1999).
[35] V. Chandrasekhar, *arXiv:cond-mat/0312507*.
[36] M. Y. Kupriyanov and V. F. Lukichev, *Sov. Phys. JETP* **67**, 1163 (1988).
[37] N. Schopohl and K. Maki, *Phys. Rev. B* **52**, 490 (1995); N. Schopohl, *arXiv:cond-mat/9804064*.
[38] C. Gorini, P. Schwab, R. Raimondi, and A. L. Shelankov, *Phys. Rev. B* **82**, 195316 (2010).
[39] A. I. Buzdin, *Phys. Rev. Lett.* **101**, 107005 (2008); A. A. Raynoso, G. Usaj, C. A. Balseiro, D. Feinberg, and M. Avignon,

- Phys. Rev. B **86**, 214519 (2012); I. Kulagina and J. Linder, *ibid.* **90**, 054504 (2014); F. S. Bergeret and I. V. Tokatly, arXiv:1409.4563.
- [40] F. Konschelle, Eur. Phys. J. B **87**, 119 (2014).
- [41] G. Dresselhaus, Phys. Rev. **100**, 580 (1955); E. Rashba, Fiz. Tverd. Tela (Leningrad) **2**, 1224 (1960) [Sov. Phys. Solid State **2**, 1109 (1960)].
- [42] E. Bauer and M. Sigrist (eds.), *Non-Centrosymmetric Superconductors: Introduction and Overview* (Springer-Verlag, Berlin, Heidelberg, 2012).
- [43] S. H. Jacobsen and J. Linder, Phys. Rev. B **92**, 024501 (2015).
- [44] P. Fulde and R. A. Ferrell, Phys. Rev. **135**, A550 (1964); A. I. Larkin and Y. N. Ovchinnikov, Sov. Phys. JETP **20**, 762 (1965).
- [45] R. Balian and N. R. Werthamer, Phys. Rev. **131**, 1553 (1963).
- [46] A. P. Mackenzie and Y. Maeno, Rev. Mod. Phys. **75**, 657 (2003).
- [47] Y. Tanaka and A. A. Golubov, Phys. Rev. Lett. **98**, 037003 (2007).
- [48] T. Yokoyama, Y. Tanaka, and A. A. Golubov, Phys. Rev. B **72**, 052512 (2005); **73**, 094501 (2006).
- [49] S. Kawabata, Y. Asano, Y. Tanaka, and A. A. Golubov, J. Phys. Soc. Jpn. **82**, 124702 (2013).
- [50] T. Kontos, M. Aprili, J. Lesueur, and X. Grison, Phys. Rev. Lett. **86**, 304 (2001); V. V. Ryazanov, V. A. Oboznov, A. Y. Rusanov, A. V. Veretennikov, A. A. Golubov, and J. Aarts, *ibid.* **86**, 2427 (2001).
- [51] P. SanGiorgio, S. Reymond, M. R. Beasley, J. H. Kwon, and K. Char, Phys. Rev. Lett. **100**, 237002 (2008).
- [52] M. Tinkham, *Introduction to Superconductivity*, 2nd ed. (McGraw-Hill, New York, 1996).
- [53] H. le Sueur, S. Reymond, M. R. Beasley, J. H. Kwon, and K. Char, Phys. Rev. Lett. **100**, 197002 (2008).
- [54] F. Zhou, P. Charlat, and B. Pannetier, J. Low Temp. Phys. **110**, 841 (1998).
- [55] J. C. Hammer, J. C. Cuevas, F. S. Bergeret, and W. Belzig, Phys. Rev. B **76**, 064514 (2007).
- [56] Y. Fominov, N. M. Chtchelkatchev, and A. A. Golubov, Phys. Rev. B. **66**, 014507 (2002).
- [57] J. Y. Gu, C. Y. You, J. S. Jiang, J. Pearson, Y. B. Bazaliy, and S. D. Bader, Phys. Rev. Lett. **89**, 267001 (2002).
- [58] I. C. Moraru, W. P. Pratt, Jr., and N. O. Birge, Phys. Rev. Lett. **96**, 037004 (2006).
- [59] J. Zhu, I. N. Krivorotov, K. Halterman, and O. T. Valls, Phys. Rev. Lett. **105**, 207002 (2010).
- [60] P. V. Leksin, N. N. Garifyanov, I. A. Garifullin, Y. V. Fominov, J. Schumann, Y. Krupskaya, V. Kataev, O. G. Schmidt, and B. Buchner, Phys. Rev. Lett. **109**, 057005 (2012).
- [61] N. Banerjee, J. W. A. Robinson, and M. G. Blamire, Nat. Commun. **5**, 4771 (2014).
- [62] G. Eilenberger, Z. Phys. **214**, 195 (1968).
- [63] Ya. V. Fominov, A. A. Golubov, T. Yu. Karminskaya, M. Yu. Kuproyanov, R. G. Deminov, and L. R. Tagirov, Pis'ma v ZhETF **91**, 329 (2010) [JETP Lett. **91**, 308 (2010)].
- [64] J. Bardeen, L. N. Cooper, and J. R. Schrieffer, Phys. Rev. **108**, 1175 (1957).
- [65] N. Kopnin, *Theory of Nonequilibrium Superconductivity* (Oxford, Clarendon, 2001).
- [66] A. A. Abrikosov, L. P. Gorkov, and I. E. Dzyaloshinski, *Quantum Field Theoretical Methods in Statistical Physics*, International Series of Monographs in Natural Philosophy Vol. 4 (Pergamon, Oxford, New York, 1965).
- [67] J. W. Serene and D. Rainer, Phys. Rep. **101**, 4 (1983).
- [68] P. G. deGennes, *Superconductivity Of Metals And Alloys* (Westview Press, Oxford, 1999).

III

Reference

J.A. Ouassou, A. Di Bernardo, J.W.A. Robinson, J. Linder.
Electric control of superconducting transition
through a spin–orbit coupled interface.
Scientific reports 6, 29312 (2016).
DOI: 10/GFGR9S

Contributions

JAO and ADB conceived the idea. JAO then performed the analytical and numerical calculations with support from JL. All authors contributed to the discussion and writing of the manuscript.

Comments

One of the results discovered in paper [II](#) was that in the presence of spin–orbit coupling, it is possible to achieve a superconducting spin-valve effect using only one homogeneous ferromagnet. In this paper, we extend this work by considering how one might *electrically* control the spin–orbit coupling, thus opening up for simultaneous electric and magnetic control over superconductivity in the same device. This was a theoretical project, but was done in collaboration with ADB and JWAR from an experimental research group at the University of Cambridge.

SCIENTIFIC REPORTS

OPEN

Electric control of superconducting transition through a spin-orbit coupled interface

Jabir Ali Ouassou¹, Angelo Di Bernardo², Jason W. A. Robinson² & Jacob Linder¹

Received: 28 April 2016

Accepted: 16 June 2016

Published: 18 July 2016

We demonstrate theoretically all-electric control of the superconducting transition temperature using a device comprised of a conventional superconductor, a ferromagnetic insulator, and semiconducting layers with intrinsic spin-orbit coupling. By using analytical calculations and numerical simulations, we show that the transition temperature of such a device can be controlled by electric gating which alters the ratio of Rashba to Dresselhaus spin-orbit coupling. The results offer a new pathway to control superconductivity in spintronic devices.

The dissipationless flow of electric charge and phase coherence are major driving forces for the research and development of superconducting electronics along with phase coherence. For example, superconducting logic circuits have already been implemented, including computer processors and memory chips that work at frequencies up to several gigahertz^{1–4}. For spintronics^{5–8} the main aim is to create logic and memory devices that exploit both the charge and spin degrees of freedom of electrons, and which offer high operating frequencies and low energy consumption⁹.

In recent years, there has been a surge of interest in the intersection of these fields, and new discoveries have enabled the new field of superconducting spintronics^{10,11}. At the interface between a conventional superconductor and a ferromagnet, the singlet electron pairs $|\uparrow\downarrow\rangle - |\downarrow\uparrow\rangle$ in the superconductor can be transformed into spin-polarized triplet pairs through a two-step process involving *spin-mixing* and *spin-rotation*¹⁰. Spin-mixing occurs at magnetic interfaces whereas magnetic inhomogeneities^{12,13} or spin-orbit coupling^{14–16} can rotate triplet Cooper pairs into each other, leading to long-ranged proximity effects in strong ferromagnets^{17–31}.

One important application of superconducting spintronics is to control the temperature T_c at which a material becomes superconducting using *spin-valves*^{32–44}. These systems consist of a superconductor proximity-coupled to two ferromagnetic layers. By changing the relative magnetization direction of two ferromagnets one can toggle superconductivity on and off. A key to achieving this effect lies in whether the magnetic configuration allows generation of spin-polarized Cooper pairs or not. When permitted, the generation of spin-polarized pairs which can penetrate deeper into adjacent ferromagnets opens an extra proximity “leakage channel”. This contributes to the draining of superconductivity from the superconductor and therefore further reduces T_c . Although much research has been dedicated to magnetic control of T_c , it would be beneficial to be able to *electrically* control T_c , as that would enable integration of superconducting nanostructures into electronic circuits without the requirement of applying magnetic fields, e.g. by changing the quasiparticle distribution^{45,46}.

Here we propose a device comprised of a ferromagnetic insulator (FI) and a semiconductor with a two-dimensional electron gas (2DEG) in contact with a conventional superconductor (S). Experimentally, it is known that the Rashba and Dresselhaus spin-orbit coupling in a 2DEG can be tuned via a gate voltage^{47–50}; this voltage can change the Rashba coefficient by a factor of 1.5–2.5 in thin-film structures based on GaAs or InAs^{47–49}, and up to a factor of ~6 in nanowires⁵⁰. These results were obtained for different gate voltage ranges; e.g., ref. 48 varied it from –6 V to +2 V, while ref. 42 used –1.0 V to +1.5 V. It has also been shown that a suitably doped 2DEG can have Rashba and Dresselhaus coefficients of the same order of magnitude, with a ratio of ~1.5 in GaAs/AlGaAs⁵¹. It should therefore be possible to engineer a thin-film semiconductor with approximately matching Rashba and Dresselhaus couplings, and dynamically modulate the ratio between them by a factor of ~2 via a gate voltage.

¹Department of Physics, NTNU, Norwegian University of Science and Technology, N-7491 Trondheim, Norway.

²Department of Materials Science and Metallurgy, University of Cambridge, 27 Charles Babbage Road, Cambridge CB3 0FS, United Kingdom. Correspondence and requests for materials should be addressed to J.A.O. (email: jabir.a.ouassou@ntnu.no)

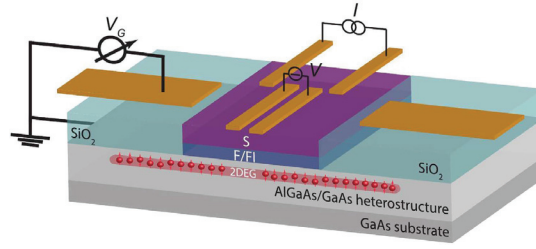


Figure 1. Schematic of the proposed superconducting device.

Recently, it was demonstrated that the superconductor proximity effect depends strongly on the amount of Rashba and Dresselhaus coupling that is present in the system⁵². Because of this, we set out to determine if T_c could be controlled purely electrically by tuning the ratio of Rashba to Dresselhaus interactions with an electric field when a 2DEG is in electrical contact to a superconductor via a FI, the latter one serving as a source of triplet pairs. In this work, we confirm this conjecture and predict that all-electric control of T_c is possible in a S/FI/2DEG device. In addition to a gate voltage control, T_c also responds to a change in the FI magnetization orientation, causing our proposed device to function as a combined superconducting transistor and magnetic spin-valve. By *superconducting transistor*, we mean a device where a gate voltage is used to switch on and off superconductivity in the structure, thus controlling to what extent a supercurrent can flow through the superconductor. This type of functionality is of interest since it corresponds to an electrically controlled transition from finite to zero resistance.

Here we investigate a setup where magnetism and spin-orbit coupling are split into two distinct layers rather than coexisting in the same material⁵², the former being experimentally more feasible to achieve. Furthermore, whereas previous works have modelled the superconductor/ferromagnet interface using spin-independent tunneling boundary conditions, we here use the recently derived boundary conditions for strongly spin-polarized interfaces⁵³. This means that spin-dependent tunneling, phase-shifts, and depairing effects for arbitrarily strong polarization are included in our new model whereas this has not been possible previously in the literature.

Results

Proposed experimental setup. Our proposed experimental setup is sketched in Fig. 1. The electrically controlled superconducting switch is based on an S/FI bilayer grown on an epitaxial GaAs-based (e.g. AlGaAs/GaAs) semiconductor thin-film multilayer. To enable electrical control over the Rashba spin-orbit interaction in the 2DEG, Au gate electrodes are fabricated by electron-beam lithography on a few-nanometer-thick insulating SiO₂ layer deposited after the growth and lithographic patterning of the S/FI stack. A four-point probe setup is used to measure changes in the superconducting critical temperature as a function of applied gate voltage V_g . Although the insulating SiO₂ layer should minimize possible modulations in the Curie temperature T_c of the FI driven by the applied gate voltage V_g , which can alone have an effect on the superconducting proximity effect, control samples without the FI layer should also be fabricated to exclude this possibility. We also note that the Rashba spin-orbit coupling is independent on the polarity of V_g ⁵⁰. In contrast, V_g usually has an opposite effect on T_c , meaning that a positive V_g normally enhances T_c , while a negative V_g decreases T_c ⁵⁴. Therefore, modulations in T_c due to V_g can also be excluded by investigating variations in the spin-orbit-driven superconducting proximity effect as a function of the V_g polarity.

Analytical results. To explain the mechanism of the electric control of T_c , we first approximate the multilayer structure as an effective monolayer structure where spin-orbit coupling and magnetic exchange fields coexist. This analogy is relevant because the spin-dependent phase-shifts induced by proximity to a FI are known to act as an effective exchange field in thin superconducting structures⁵⁵. Afterwards, we will confirm the analytical treatment by full numerical simulations performed without these approximations.

To the linear order in the superconducting pair amplitudes, the diffusion equations of the system are⁵²

$$(iD/2)\partial_z^2 f_s = \epsilon f_s + h f_{\parallel}, \quad (1)$$

$$(iD/2)\partial_z^2 f_{\parallel} = E_{\parallel}(\theta, \chi) f_{\parallel} - R(\theta, \chi) f_{\perp} + h f_s, \quad (2)$$

$$(iD/2)\partial_z^2 f_{\perp} = E_{\perp}(\theta, \chi) f_{\perp} - R(\theta, \chi) f_{\parallel}. \quad (3)$$

The symbols f_s , f_{\parallel} , f_{\perp} refer to the electron pair amplitudes with spin-singlet, short-range spin-triplet, and long-range spin-triplet projections, respectively. We have also defined the triplet mixing factor

$$R(\theta, \chi) = 2iDA^2 \cos 2\theta \sin 2\chi, \quad (4)$$

and the effective triplet energies

$$E_{\perp}(\theta, \chi) = \epsilon + 2iDA^2[1 + \sin 2\theta \sin 2\chi], \quad (5)$$

$$E_{\parallel}(\theta, \chi) = \epsilon + 2iDA^2[1 - \sin 2\theta \sin 2\chi]. \quad (6)$$

The ferromagnetism is described by an in-plane exchange splitting $\mathbf{h} = h(\cos \theta \mathbf{e}_x + \sin \theta \mathbf{e}_y)$, which is parametrized in terms of a magnitude h and direction θ . We also assume an in-plane spin-orbit coupling, which is described in polar coordinates by a magnitude $A \equiv \sqrt{\alpha^2 + \beta^2}$ and type $\chi \equiv \text{atan}(\alpha/\beta)$, where α and β are the Rashba and Dresselhaus coefficients. The spin-orbit coefficients are defined by the single-particle Hamiltonian $H = \frac{\alpha}{m^*}(p_y \sigma_x - p_x \sigma_y) + \frac{\beta}{m^*}(p_y \sigma_y - p_x \sigma_x)$, where m^* is the effective mass, \mathbf{p} the momentum, and σ the spin. Finally, D is the diffusion coefficient of the material, and ϵ is the quasiparticle energy.

The singlet component f_s is produced in all conventional superconductors. When these pairs leak into the adjoining ferromagnet, eqs (1–3) show that a magnetic exchange splitting h induces a nonzero short-ranged triplet component f_{\parallel} as is well-known¹³. When spin-orbit coupling is present ($A \neq 0$), with both Rashba and Dresselhaus contributions ($\sin 2\chi \neq 0$), one also generates the long-range¹⁵ triplet component f_{\perp} so long as the magnetization direction satisfies $\cos 2\theta \neq 0$. It is the latter observation which offers several ways to control the long-ranged triplet generation. Firstly, since the triplet mixing term is proportional to $\cos 2\theta$, we may enable this mechanism by letting $\theta \rightarrow 0$, or disable it by letting $\theta \rightarrow \pm\pi/4$. Secondly, since the same term is also proportional to $\sin 2\chi$, where we defined $\chi = \text{atan}(\alpha/\beta)$, the mechanism is enhanced for $\alpha \cong \beta$, but suppressed when $\alpha \ll \beta$ or $\alpha \gg \beta$. Since the magnetization direction θ can be changed using an external magnetic field, and the Rashba coefficient α can be changed using an external electric field, this means that the triplet mixing can be in principle be controlled using either a magnetic field by itself^{56–60}, an electric field by itself, or a combination thereof.

It is important to note that the spin-orbit coupling not only introduces a coupling between the different types of spin-polarized Cooper pairs, but that it also has a depairing effect. This is seen by how A modifies the diagonal terms in the equations above, resulting in an alteration of the effective energies in eqs (5) and (6) associated with the superconducting correlation functions f . Imaginary terms in the effective energy can be interpreted as a destabilization and suppression of the given correlations, so the spin-orbit coupling can suppress either $f_{\parallel}f_{\perp}$, or both, depending on the parameters χ and θ . It follows from eq. (5) that increasing the magnitude of A and $\sin 2\chi$ increases this pair-breaking effect, meaning that the same spin-orbit coupling that maximizes the triplet mixing also maximizes the depairing. However, while the mixing term is proportional to $\cos 2\theta$, the depairing terms are proportional to $\sin 2\theta$. A key observation which enables the purely electric control over T_c is that for a fixed magnetization orientation θ , the depairing energy is controlled by the ratio of Rashba and Dresselhaus spin-orbit coupling $\chi = \text{atan}(\alpha/\beta)$. This argument is of importance since we from the numerical simulations find that the dominant effect of the spin-orbit coupling on the critical temperature is not the long-range triplet generation, but rather the short-range triplet suppression. In fact, the most extreme results were obtained for $\theta = \pm\pi/4$, which are precisely the configurations where the linearized diffusion equations disallow triplet mixing.

Numerical results. We have calculated T_c numerically and the results are shown in Fig. 2. S is taken as conventional (e.g. Nb), the FI (e.g. GdN, EuO) is treated as a polarized spin-active interface, and the semiconducting layer (e.g. GaAs, InAs) is treated as a normal metal with a Rashba–Dresselhaus spin-orbit coupling. We used the Ricatti-parametrization⁶¹ including the case of spin-orbit coupling⁶² together with general magnetic boundary conditions⁵³ valid for arbitrary polarization of the interface region. We provide a detailed exposition of the computation of the critical temperature in the Methods section.

For all structures, we assumed a thickness of 0.65ξ for the superconductor and 0.15ξ for the 2DEG, where ξ is the zero-temperature coherence length of a bulk superconductor. Assuming $\xi = 30$ nm, this would imply a superconductor thickness of ~ 20 nm and thickness of ~ 4 nm for the spin-orbit coupled layer. As for the magnitude of the spin-orbit coupling, we normalized both α and β to \hbar^2/ξ . If the effective quasiparticle mass m^* is assumed equal to the bare electron mass, and we again set $\xi = 30$ nm, we find that $\alpha, \beta = 1$ in dimensionless units corresponds to a coupling $\alpha/m^*, \beta/m^* = 2.2 \times 10^{-12}$ eV m. The spin-active interface was taken to have an experimentally realistic spin-polarization of 50%, a tunneling conductance $G_T/G \in \{0.2, 0.3\}$, and a spin-mixing conductance $G_{\uparrow}/G_T = 1.25$, where G is the bulk normal-state conductance of both materials (taken as equal for simplicity). We have run extensive T_c calculations for other parameter values as well (not shown here), where we find qualitatively the same behavior as in Fig. 2, but quantitatively less variation if either the tunneling conductance G_T is reduced, the spin-mixing conductance G_{\uparrow} is reduced, or the spin-polarization is increased. In particular, depending on the quality of the contact between the 2DEG and the FI layer, the tunneling conductance could be very small compared to the normal-state conductance, $G_T \ll G$.

The results in Fig. 2 display the same basic dependence on the magnetic field direction: the critical temperature is maximal when $\theta \rightarrow -\pi/4$, and minimal when $\theta \rightarrow +\pi/4$. It is interesting to note how spin-valve functionality is obtained in the present structure with just one magnetic layer, tuning T_c from a maximum to minimum upon 90 degrees rotation of the magnetization. The magnitude of this variation depends strongly on the parameters. For strong spin-orbit coupling and moderate interface conductance, we see a variation of nearly $0.6T_{cs}$ in Fig. 2, where T_{cs} is the critical temperature of a bulk superconductor. This corresponds to 5.5 K for niobium; for comparison, the current experimental record for spin-valve effects is around 1 K⁶². Furthermore, in the region where $\theta > 0$, the critical temperature drops to zero, which means that such a device could in principle function as a spin-valve even at absolute zero. Increasing the interface polarization or weakening the spin-orbit coupling diminishes this effect.

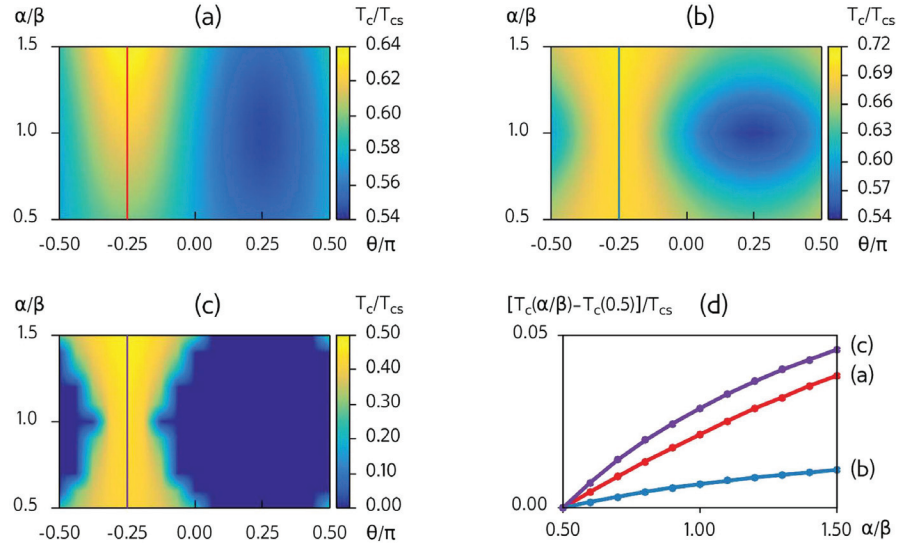


Figure 2. Critical temperature results. (a–c) Critical temperature normalized by the bulk value T_c/T_{cs} (colors) as a function of the in-plane magnetization angle θ/π (horizontal axis) and spin-orbit ratio α/β (vertical axis). We have used the parameters (a) $\beta=1, G_T/G=0.2$, (b) $\beta=5, G_T/G=0.2$, and (c) $\beta=5, G_T/G=0.3$. (d) Variation $[T_c(\alpha/\beta) - T_c(0.5)]/T_{cs}$ in the critical temperature as a function of α/β when $\theta/\pi = -0.25$. The different curves correspond to the systems used in (a–c). For other magnetization angles $|\theta/\pi| \neq 0.25$, the variation of T_c with α/β is non-monotonic since such orientations allow for long-range triplet generation.

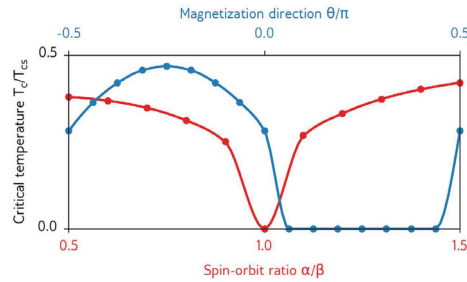


Figure 3. Critical temperature highlights. Normalized critical temperature T_c/T_{cs} as function of the spin-orbit coupling ratio α/β (blue line, $\theta/\pi = -0.125$), and as function of the in-plane magnetization θ (red line, $\alpha/\beta = 1.5$). The other parameters are the same as in Fig. 2.

The most interesting observation is nevertheless that we can achieve all-electric control over T_c for a fixed orientation θ of the FI magnetic moment. One particularly striking example is seen in Fig. 2: for a range of magnetization orientations θ , T_c increases from absolute zero at $\alpha/\beta=1$ to a substantial fraction of the bulk critical temperature T_{cs} as α/β is either increased or decreased. For instance, when $\theta/\pi = -0.125$, $T_c=0$ at $\alpha/\beta=1$ while $T_c=0.42T_{cs}$ at $\alpha/\beta=1.5$. For *e.g.* niobium, this yields a variation of 3.9 K by increasing the Rashba coefficient α by 50%. We highlight this behavior in Fig. 3, where T_c is plotted against the spin-orbit coupling ratio α/β for a fixed magnetization orientation. Moreover, we show in Fig. 3 the large change in T_c that occurs when altering the in-plane magnetization orientation θ for a fixed α/β .

Let us now interpret the numerical findings in terms of the previous analytical treatment. Although the 2DEG by itself has no intrinsic exchange field, rendering the distinction between short-ranged and long-ranged pairs more accurately described by the terminology “opposite and equal spin-pairing states relative to the FI orientation”, we will continue to refer to f_{\parallel} as short-ranged pairs for brevity and easy comparison with the analytical treatment. When $\alpha \rightarrow \beta$ and $\theta \rightarrow -\pi/4$, the short-ranged triplet energy $E_{\parallel} \rightarrow \epsilon + 4iDA^2$, resulting in a strong suppression of these triplet pairs. By closing the triplet proximity channel, this reduces the leakage of Cooper pairs from the superconductor, thus *increasing* the critical temperature of the structure. On the other hand, when $\alpha \rightarrow \beta$ and $\theta \rightarrow +\pi/4$, the energy $E_{\parallel} \rightarrow \epsilon$, resulting in a minimal suppression of short-ranged triplets. This causes a larger

leakage from the superconductor, and *decreases* the critical temperature. This leading-order analysis of the physics is in accordance with the numerical results in Fig. 2, as is reasonable since the weak proximity effect described by the linearized equations is expected to be a good approximation for $T \cong T_c$.

Discussion

In the quasiclassical theory used to compute the critical temperature, one assumes that the thickness of the layer exceeds the Fermi wavelength. This criterion is not satisfied in a 2DEG, which means that phenomena such as weak localization/antilocalization cannot be described by quasiclassical theory. However, the coupling mechanism governing the appearance of a superconducting triplet proximity channel in the system is not expected to change because of this and hence our results should remain qualitatively valid even in this scenario. Moreover, we have considered the diffusive limit of transport which is of relevance for the in-plane motion, whereas the 2DEG thickness is much smaller than the mean free path. There is nevertheless scattering at the multiple interfaces of our structure which is expected to enhance the effective diffusive character of quasiparticle motion considered in our model. 2DEGs can also feature a rather strong spin-orbit interaction, in which case corrections to the Usadel equation have been examined⁶³. It could also be of interest to go beyond quasiclassical theory to study T_c and other proximity effects in this kind of system⁶⁴, although this is beyond the scope of the present work.

Semiconductors such as GaAs and InAs are known to provide both an intrinsic Dresselhaus coupling and an electrically tunable Rashba coupling^{48–50}. By combining such 2DEG materials with a superconductor and a ferromagnetic insulator, we have shown both analytically and numerically that T_c responds to changes in both electric and magnetic fields, either individually or combined. It should therefore be possible to create a device that can function as a superconducting transistor, superconducting spin-valve, or both, depending on whether electric or magnetic stimuli are used as the input signal.

Methods

Diffusion equation. In the diffusive and quasiclassical limit, we can describe the structures discussed herein with the Usadel diffusion equation^{5,16,52}

$$iD \tilde{\nabla}(\hat{g} \tilde{\nabla} \hat{g}) = [\epsilon \hat{\tau}_z + \hat{\Delta} + \hat{h}, \hat{g}], \quad (7)$$

where \hat{g} is the retarded quasiclassical propagator in Nambu \otimes Spin space, $\hat{\tau}_z$ is the third Pauli matrix in Nambu space, ϵ is the quasiparticle energy of the electrons and holes, $\hat{\Delta} = \text{antidiag}(+\Delta, -\Delta, +\Delta^*, -\Delta^*)$, Δ is the superconducting gap, $\hat{h} = \mathbf{h} \cdot \text{diag}(\sigma, -\sigma^*)$, \mathbf{h} is the ferromagnetic exchange field, σ is the Pauli vector in spin space, and D is the diffusion coefficient. The notation $\tilde{\nabla}(\cdot) = \nabla(\cdot) - i[\hat{A}, \cdot]$ is used for the gauge covariant derivative, where $\hat{A} = \text{diag}(A, -A^*)$ is a background field that accounts for spin-orbit coupling. In this paper, we assume that we have a thin-film structure oriented along the z -axis so $\nabla \rightarrow \partial_z$. We assume the exchange field and Rashba–Dresselhaus coupling are both confined to the xy -plane, so they can be parametrized as

$$\mathbf{h} = h(\cos \theta \mathbf{e}_x + \sin \theta \mathbf{e}_y), \quad (8)$$

$$\mathbf{A} = (\beta \sigma_x - \alpha \sigma_y) \mathbf{e}_x + (\alpha \sigma_x - \beta \sigma_y) \mathbf{e}_y. \quad (9)$$

Note that it is the orientation of the spin-orbit field \mathbf{A} that defines the x - and y -axes of our coordinate system, since the Dresselhaus spin-orbit coupling is determined by the crystal structure. Thus, the magnetic orientation is measured relative to the crystal structure.

Numerically, solving directly for the propagator \hat{g} is impractical for two reasons. Firstly, the elements of \hat{g} are unbounded, and can be arbitrarily large complex numbers. Secondly, the propagator satisfies a normalization condition and particle-hole symmetry which reduces the number of degrees of freedoms, such that solving for each individual matrix element in \hat{g} would be redundant. Because of this, we have used the so-called Riccati parametrization of the propagators in the numerical simulations⁶¹:

$$\hat{g} = \begin{pmatrix} N & 0 \\ 0 & -\tilde{N} \end{pmatrix} \begin{pmatrix} 1 + \gamma \tilde{\gamma} & 2N\gamma \\ 2\tilde{N}\tilde{\gamma} & 1 + \tilde{\gamma}\gamma \end{pmatrix}, \quad (10)$$

where the Riccati parameters γ and $\tilde{\gamma}$ are 2×2 matrices in spin space which are related by tilde-conjugation $\tilde{\gamma}(+\varepsilon) = \gamma^*(-\varepsilon)$, and the normalization matrices are defined by $N \equiv (1 - \gamma\tilde{\gamma})^{-1}$. For an in-plane spin-orbit interaction, eq. (7) parametrizes as

$$iD[\partial_z^2 \gamma + 2(\partial_z \gamma) \tilde{N} \tilde{\gamma}(\partial_z \gamma)] = 2\epsilon\gamma - \Delta\sigma_y + \gamma\Delta^*\sigma_y\gamma + \mathbf{h} \cdot (\sigma\gamma - \gamma\sigma^*) + iD[\mathbf{A}\mathbf{A}\gamma - \gamma\mathbf{A}^*\mathbf{A}^* + 2(\mathbf{A}\gamma + \gamma\mathbf{A}^*)\tilde{N}(\mathbf{A}^* + \tilde{\gamma}\mathbf{A}\gamma)], \quad (11)$$

which is the form we use numerically. For more information about the derivation and interpretation of the above, see ref. 52.

Gap equation. Before we can calculate the critical temperature of a material, we require not only a way to calculate the propagator \hat{g} , but also a way to dynamically update the superconducting gap Δ based on the calculated propagators. This gap equation can be written⁵²

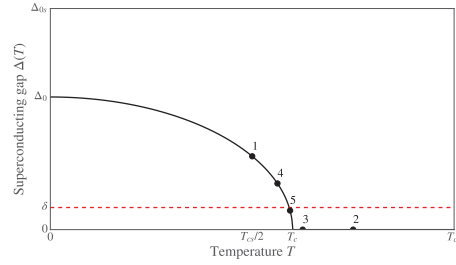


Figure 4. Sketch of the superconducting gap Δ as a function of temperature T for a superconducting hybrid structure. When performing a binary search for the critical temperature, we check whether $\Delta > \delta$ at a certain number of temperatures—in other words, whether the black solid line is above the red dashed line. The numbered markers show which points on the curve would be evaluated during the first five bisections of such a binary search, and in what order. Note that since the algorithm is actually looking for the intersection between the black solid curve and red dashed curve, we need $\delta \ll \Delta_0$ to obtain accurate results.

$$\Delta(z) = \lambda \int_0^{\Delta_0 \cosh(1/\lambda)} d\epsilon \operatorname{Re} [f_s(\epsilon, z)] \tanh \left(\frac{\pi \epsilon / \Delta_0}{2e^c T / T_{cs}} \right), \quad (12)$$

where λ is a dimensionless coupling constant, f_s the singlet component of the anomalous propagator, Δ_0 the zero-temperature gap of a bulk superconductor, T_{cs} the critical temperature of a bulk superconductor, and c the Euler–Mascheroni constant. In terms of the Riccati parametrization, $f_s = [N\gamma]_{12} - [N\gamma]_{21}$, where the subscript notation refers to individual matrix elements.

Boundary conditions. Since our purpose is to model a system where the superconductivity, ferromagnetism, and spin-orbit coupling originate from *different* thin-film layers, we need boundary conditions that connect the propagators of these materials at the interfaces. Numerically, we focused on S/FI/N structures, in which case the ferromagnetic insulator itself is modelled as a strongly polarized spin-active interface. We have used the low-transparency limit of the general spin-active boundary conditions derived in ref. 53,

$$2\hat{I}_L = G_T[\hat{g}_L, \hat{g}_R] + G_1[\hat{g}_L, \hat{m}\hat{g}_R\hat{m}] + G_{MR}[\hat{g}_L, \{\hat{g}_R, \hat{m}\}] - iG_\varphi[\hat{g}_L, \hat{m}], \quad (13)$$

where \hat{I}_L is the 4×4 matrix current on the left side of the interface, G_T is the tunneling conductance of the interface, G_1 describes the interfacial depairing, G_{MR} describes the magnetoresistance, G_φ describes the spin-mixing, $\hat{m} = \mathbf{m} \cdot \operatorname{diag}(\sigma, \sigma^*)$, \mathbf{m} is a unit vector that describes the interface magnetization, and \hat{g}_L and \hat{g}_R describes the propagators on the left and right side of the interface, respectively. An equivalent equation for the other side of the interface can be found by letting $\hat{I}_L \rightarrow -\hat{I}_R$ and $L \leftrightarrow R$ in the equation above. Assuming that all the interface scattering have the same polarization P , it can be shown that $G_{MR}/G_T = P/[1 + \sqrt{1 - P^2}]$ and $G_1/G_T = [1 - \sqrt{1 - P^2}]/[1 + \sqrt{1 - P^2}]$, so we can calculate G_1 and G_{MR} directly from the interface polarization.

The matrix current is related to the propagators at the interface by $\hat{I} = GL(\hat{g} \tilde{\nabla} \hat{g})$ where G is the normal-state conductance and L the length of the material. It can then be shown that the Riccati parameters must satisfy the boundary condition

$$\partial_z \gamma = (2GLN)^{-1}(I_{12} - I_{11}\gamma), \quad (14)$$

where I_{12} and I_{11} refers to the top-right and top-left 2×2 blocks of the 4×4 matrix current \hat{I} . In this equation, the matrix current \hat{I} should be interpreted as either \hat{I}_L or \hat{I}_R , depending on which side of the interface the boundary conditions should describe.

Critical temperature. The critical temperature can be defined as the temperature T_c such that the superconducting gap $\Delta = 0$ if and only if $T \geq T_c$. However, in practice, we cannot expect to obtain the exact result $\Delta = 0$ in simulations due to inexact numerical methods and random floating-point errors. For numerical simulations, we therefore use a more relaxed criterion $|\Delta| < \delta$ to define the critical temperature T_c , where we have set $\delta = 10^{-3}\Delta_0$, and Δ_0 is the zero-temperature gap of a bulk superconductor. See the solid black curve in Fig. 4 for a sketch of how $\Delta(T)$ typically behaves, and how this is related to the critical temperature T_c .

Conceptually, the simplest way to find this critical temperature is to explicitly calculate the superconducting gap Δ as a function of temperature T , and check directly at which temperature we first find $|\Delta| < \delta$. However, such a linear search can be very costly when a high accuracy is desired. For instance, to determine the critical temperature to a precision of $0.0001T_{cs}$, where T_{cs} is the critical temperature of a bulk superconductor, this would require that $\Delta(T)$ be calculated for 10,000 different values of T . For each of these temperatures, we need to solve a set of nonlinear diffusion equations for 150 positions and 800 energies, and repeat this procedure in one material

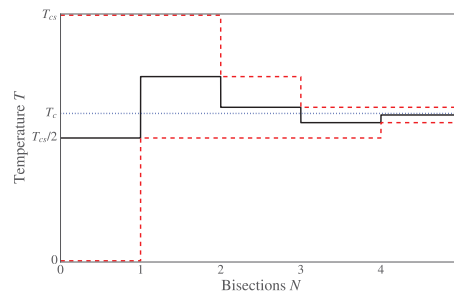


Figure 5. Sketch of how the binary search algorithm works. The blue dotted line at $T = T_c$ shows the critical temperature we wish to find, the solid black line shows the critical temperature estimate after N bisections, and the red dashed lines show the bounds for the critical temperature after N bisections. After N bisections, T_c has been determined with an accuracy $T_{cs}/2^{N+1}$.

of the hybrid structure at a time until a selfconsistent solution is found. Thus, the calculation at each of these 10,000 temperatures can in some cases take hours, making this method quite inefficient.

We have instead used a much more efficient binary search algorithm to determine the critical temperature numerically. The main benefit of this algorithm is that after calculating $\Delta(T)$ for N particular values of T , we can determine the critical temperature to a precision $T_{cs}/2^{N+1}$. So in contrast to the linear search algorithm, an accuracy of around $0.0001 T_{cs}$ would require calculations at 12 temperatures instead of 10,000. Furthermore, we do not actually need to calculate $\Delta(T)$ exactly at these temperatures—it is sufficient to check whether $|\Delta| < \delta$ or $|\Delta| > \delta$ to determine whether $T > T_c$ or $T < T_c$. Thus, at each of these 12 temperatures, we only have to initialize the entire system to a BCS superconducting state with $\Delta = \delta$, then solve the Usadel equation and gap equation a fixed number of times in each material, and finally check whether $|\Delta| < \delta$ or $|\Delta| > \delta$ to determine whether T is an upper or lower bound on T_c . How the binary search algorithm converges is illustrated in Figs 4 and 5.

References

- Dorojevets, M., Bunyk, P. & Zinoviev, D. FLUX chip: design of a 20-GHz 16-bit ultrapipelined RSFQ processor prototype based on 1.75- μm LTS technology. *IEEE T. Appl. Supercond.* **11**, 326 (2001).
- Likharev, K. K. & Semenov, V. K. RSFQ logic/memory family: a new Josephson-junction technology for sub-terahertz-clock-frequency digital systems. *IEEE T. Appl. Supercond.* **1**, 3 (1991).
- Nagasawa, S., Hashimoto, Y., Numata, H. & Tahara, S. A 380 ps, 9.5 mW Josephson 4-kbit RAM operated at a high bit yield. *IEEE T. Appl. Supercond.* **5**, 2447 (1995).
- Tanaka, M. *et al.* Demonstration of a single-flux-quantum microprocessor using passive transmission lines. *IEEE T. Appl. Supercond.* **15**, 400 (2005).
- Johnson, M. & Silsbee, R. H. Interfacial charge-spin coupling: injection and detection of spin magnetization in metals. *Phys. Rev. Lett.* **55**, 1790 (1985).
- Ralph, D. C. & Stiles, M. D. Spin transfer torques. *J. Magn. Magn. Mater.* **320**, 1190 (2008).
- Baibich, M. N. *et al.* Giant magnetoresistance of (001)Fe/(001)Cr magnetic superlattices. *Phys. Rev. Lett.* **61**, 2472 (1988).
- Binasch, G., Grunberg, P., Saurenbach, F. & Zinn, W. Enhanced magnetoresistance in layered magnetic structures with antiferromagnetic interlayer exchange. *Phys. Rev. B* **39**, 4828(R) (1989).
- Brataas, A., Kent, A. & Ohno, H. Current-induced torques in magnetic materials. *Nat. Mater.* **11**, 372 (2012).
- Eschrig, M. Spin-polarized supercurrents for spintronics. *Phys. Today* **64**, 43 (2011).
- Linder, J. & Robinson, J. W. A. Superconducting spintronics. *Nat. Phys.* **11**, 307 (2015).
- Bergeret, F. S., Volkov, A. F. & Efetov, K. B. Long-range proximity effects in superconductor-ferromagnet structures. *Phys. Rev. Lett.* **86**, 4096 (2001).
- Buzdin, A. I. Proximity effects in superconductor-ferromagnet heterostructures. *Rev. Mod. Phys.* **77**, 935 (2005).
- Annunziata, G., Manske, D. & Linder, J. Proximity effect with noncentrosymmetric superconductors. *Phys. Rev. B* **86**, 174514 (2012).
- Bergeret, F. S. & Tokatly, I. V. Singlet-triplet conversion and the long-range proximity effect in superconductor-ferromagnet structures with generic spin dependent fields. *Phys. Rev. Lett.* **110**, 117003 (2013).
- Bergeret, F. S. & Tokatly, I. V. Spin-orbit coupling as a source of long-range triplet proximity effect in superconductor-ferromagnet hybrid structures. *Phys. Rev. B* **89**, 134517 (2014).
- Robinson, J. W. A., Witt, J. D. S. & Blamire, M. G. Controlled injection of spin-triplet supercurrents into a strong ferromagnet. *Science* **329**, 59 (2010).
- Khaire, T. S., Khasawneh, M. A., Pratt, W. P. & Birge, N. O. Observation of spin-triplet superconductivity in co-based Josephson junctions. *Phys. Rev. Lett.* **104**, 137002 (2010).
- Klose, C. *et al.* Optimization of spin-triplet supercurrent in ferromagnetic Josephson junctions. *Phys. Rev. Lett.* **108**, 127002 (2012).
- Witt, J. D. S., Robinson, J. W. A. & Blamire, M. G. Josephson junctions incorporating a conical magnetic holmium interlayer. *Phys. Rev. B* **85**, 184526 (2012).
- Robinson, J. W. A., Chioldi, F., Halász, G. B., Egilmez, M. & Blamire, M. G. Supercurrent enhancement in Bloch domain walls. *Sci. Rep.* **2**, 699 (2012).
- Banerjee, N., Robinson, J. W. A. & Blamire, M. G. Reversible control of spin-polarized supercurrents in ferromagnetic Josephson junctions. *Nat. Commun.* **5**, 4771 (2014).
- Robinson, J. W. A., Banerjee, N. & Blamire, M. G. Triplet pair correlations and nonmonotonic supercurrent decay with Cr thickness in Nb/Cr/Fe/Nb Josephson devices. *Phys. Rev. B* **89**, 104505 (2014).
- Di Bernardo, A. *et al.* Signature of magnetic-dependent gapless odd frequency states at superconductor/ferromagnet interfaces. *Nat. Commun.* **6**, 8053 (2015).

25. Anwar, M. S., Czeschka, F., Hesselberth, M., Porcu, M. & Aarts, J. Long-range supercurrents through half-metallic ferromagnetic CrO_2 . *Phys. Rev. B* **82**, 100501(R) (2010).
26. Kalchauer, Y., Millo, O., Egilmez, M., Robinson, J. W. A. & Blamire, M. G. Evidence for anisotropic triplet superconductor order parameter in half-metallic ferromagnetic $\text{La}_{0.7}\text{Ca}_{0.3}\text{Mn}_2\text{O}$ proximity coupled to superconducting $\text{Pr}_{1.85}\text{Ce}_{0.15}\text{CuO}_4$. *Phys. Rev. B* **85**, 104504 (2012).
27. Egilmez, M. *et al.* Supercurrents in half-metallic ferromagnetic $\text{La}_{0.7}\text{Ca}_{0.3}\text{MnO}_3$. *Europhys. Lett.* **106**, 37003 (2014).
28. Kalchauer, Y. *et al.* Magnetic field dependence of the proximity-induced triplet superconductivity at ferromagnet/superconductor interfaces. *Phys. Rev. B* **89**, 180506(R) (2014).
29. Kalchauer, Y., Millo, O., Di Bernardo, A., Pal, A. & Robinson, J. W. A. Inverse proximity effect at superconductor-ferromagnet interfaces: evidence for induced triplet pairing in the superconductor. *Phys. Rev. B* **92**, 060501(R) (2015).
30. Di Bernardo, A., Salman, Z., Wang, X. L., Amado, M., Egilmez, M., Flokstra, M. G., Suter, A., Lee, S. L., Zhao, J. H., Prokscha, T., Morenzoni, E., Blamire, M. G., Linder, J. & Robinson, J. W. A. Intrinsic paramagnetic Meissner effect due to *s*-wave odd-frequency superconductivity. *Physical Review X* **5**, 041021 (2015).
31. Banerjee, N., Smiet, C. B., Smits, R. G. J., Ozaeta, A., Bergeret, F. S., Blamire, M. G. & Robinson, J. W. A. Evidence for spin-selectivity of triplet pairs in superconducting spin-valves. *Nature Communications* **5**, 3340 (2014).
32. Oh, S., Youm, D. & Beasley, M. R. A superconductive magnetoresistive memory element using controlled exchange interaction. *Appl. Phys. Lett.* **71**, 2376 (1997).
33. Tagirov, L. R. Low-field superconducting spin switch based on a superconductor ferromagnet multilayer. *Phys. Rev. Lett.* **83**, 02058 (1999).
34. Buzdin, A. & Vedyayev, A. Spin-orientation-dependent superconductivity in F/S/F structures. *Europhys. Lett.* **686** (1999).
35. Bobkov, A. M. & Bobkova, I. V. Enhancing of the critical temperature of an in-plane FFLO state in heterostructures by the orbital effect of the magnetic field. *JETP Lett.* **99**, 333 (2014).
36. Gu, J. Y. *et al.* Magnetization-orientation dependence of the superconducting transition temperature in the ferromagnet-superconductor-ferromagnet system: CuNi/Nb/CuNi . *Phys. Rev. Lett.* **89**, 267001 (2002).
37. Moraru, I. C., Pratt, W. P. & Birge, N. O. Magnetization-dependent T_c shift in ferromagnet/superconductor/ferromagnet trilayers with a strong ferromagnet. *Phys. Rev. Lett.* **96**, 037004 (2006).
38. Fominov, Y. V. *et al.* Superconducting triplet spin valve. *JETP Lett.* **91**, 308 (2010).
39. Zhu, J., Krivorotov, I. N., Halterman, K. & Valls, O. T. Angular dependence of the superconducting transition temperature in ferromagnet-superconductor-ferromagnet trilayers. *Phys. Rev. Lett.* **105**, 207002 (2010); Jara, A. A. *et al.* Angular dependence of superconductivity in superconductor/spin-valve heterostructures. *Phys. Rev. B* **89**, 184502 (2014).
40. Banerjee, N. *et al.* Evidence for spin selectivity of triplet pairs in superconducting spin valves. *Nat. Commun.* **5**, 3048 (2014); Wang, X. L. *et al.* Giant triplet proximity effect in superconducting pseudo spin valves with engineered anisotropy. *Phys. Rev. B* **89**, 140508(R) (2014).
41. Chioldi, F. *et al.* Supra-oscillatory critical temperature dependence of Nb-Ho bilayers. *Europhys. Lett.* **101**, 37002 (2013).
42. Gu, Y. *et al.* Magnetic state controllable critical temperature in epitaxial Ho/Nb bilayers. *APL Mat.* **2**, 46103 (2014).
43. Gu, Y., Halász, G. B., Robinson, J. W. A. & Blamire, M. G. Large superconducting spin valve effect and ultrasmall exchange splitting in epitaxial rare-earth-niobium trilayers. *Phys. Rev. Lett.* **115**, 067201 (2015).
44. Wang, X. L., Di Bernardo, A., Banerjee, N., Wells, A., Bergeret, F. S., Blamire, M. G. & Robinson, J. W. A. Giant triplet proximity effect in superconducting pseudo spin valves with engineered anisotropy. *Physical Review B* **89**, 140508(R) (2014).
45. Bobkova, I. V. & Bobkov, A. M. Recovering the superconducting state via spin accumulation above the pair-breaking magnetic field of superconductor/ferromagnet multilayers. *Phys. Rev. B* **84**, 140508(R) (2011).
46. Bobkova, I. V. & Bobkov, A. M. Recovering of superconductivity in S/F bilayers under spin-dependent nonequilibrium quasiparticle distribution. *Pis'ma v ZhETF* **101**, 442 (2015).
47. Nitta, J., Akazaki, T., Takayanagi, H. & Enoki, T. Gate control of spin-orbit interaction in an inverted $\text{In}_{0.53}\text{Ga}_{0.47}\text{As}/\text{In}_{0.52}\text{Al}_{0.48}\text{As}$ Heterostructure. *Phys. Rev. Lett.* **78**, 1335 (1997).
48. Engels, G., Lange, J., Schapers, T. & Luth, H. Experimental and theoretical approach to spin splitting in modulation-doped $\text{InGa}_{1-x}\text{As}/\text{InP}$ quantum wells for $B \rightarrow 0$. *Phys. Rev. B* **55**, 1958 (1997).
49. Grundler, D. Large Rashba splitting in InAs quantum wells due to electron wave function penetration into the barrier layers. *Phys. Rev. Lett.* **84**, 6074 (2000).
50. Liang, D. & Gao, X. P. A. Strong tuning of Rashba spin-orbit interaction in single InAs nanowires. *Nano Lett.* **12**, 3263 (2012).
51. Giglberger, S. *et al.* Rashba and Dresselhaus spin splittings in semiconductor quantum wells measured by spin photocurrents. *Phys. Rev. B* **75**, 035327 (2007).
52. Jacobsen, S. H., Ouassou, J. A. & Linder, J. Critical temperature and tunneling spectroscopy of superconductor-ferromagnet hybrids with intrinsic Rashba-Dresselhaus spin-orbit coupling. *Phys. Rev. B* **92**, 024510 (2015).
53. Eschrig, M., Cottet, A., Belzig, W. & Linder, J. General boundary conditions for quasiclassical theory of superconductivity in the diffusive limit: application to strongly spin-polarized systems. *New J. Phys.* **17**, 83037 (2015).
54. Chiba, D. *et al.* Electrical control of the ferromagnetic phase transition in cobalt at room temperature. *Nat. Mater.* **10**, 853 (2011).
55. Cottet, A. Spectroscopy and critical temperature of diffusive superconducting/ferromagnetic hybrid structures with spin-active interfaces. *Phys. Rev. B* **76**, 224505 (2007).
56. Jacobsen, S. H. & Linder, J. Giant triplet proximity effect in π -biased Josephson junctions with spin-orbit coupling. *Phys. Rev. B* **92**, 024501 (2015).
57. Arjoranta, J. & Heikkilä, T. Intrinsic spin-orbit interaction in diffusive normal wire Josephson weak links: supercurrent and density of states. *Phys. Rev. B* **93**, 024522 (2016).
58. Espedal, C., Yokoyama, T. & Linder, J. Anisotropic paramagnetic Meissner effect by spin-orbit coupling. *Phys. Rev. Lett.* **116**, 127002 (2016).
59. Mal'shukov, A. G. Nonlocal effect of a varying in-space Zeeman field on supercurrent and helix state in a spin-orbit-coupled *s*-wave superconductor. *Phys. Rev. B* **93**, 054511 (2016).
60. Jacobsen, S. H., Kulagina, I. & Linder, J. Controlling superconducting spin flow with spin-flip immunity using a single homogeneous ferromagnet. *Scientific Reports* **6**, 23926 (2016).
61. Schopohl, N. & Maki, K. Quasiparticle spectrum around a vortex line in a *d*-wave superconductor. *Phys. Rev. B* **52**, 490 (1995); Schopohl, N. Transformation of the Eilenberger equations of superconductivity to a scalar Riccati equation. arXiv:cond-mat/9804064; Konstandin, A., Kopu, J. & Eschrig, M. Superconducting proximity effect through a magnetic domain wall. *Phys. Rev. B* **72**, 140501(R) (2005).
62. Singh, A., Voltan, S., Lahabi, K. & Aarts, J. Colossal proximity effect in a superconducting triplet spin valve based on the half-metallic ferromagnet CrO_2 . *Phys. Rev. X* **5**, 21019 (2015).
63. Houzet, M. & Meyer, J. S. Quasiclassical theory of disordered Rashba superconductors. *Phys. Rev. B* **92**, 014509 (2015).
64. Reeg, C. R. & Maslov, D. L. Proximity-induced triplet superconductivity in Rashba materials. *Phys. Rev. B* **92**, 134512 (2015).

Acknowledgements

We wish to thank Niladri Banerjee for useful discussions. J.L. and J.A.O. acknowledge funding via the “Outstanding Academic Fellows” programme at NTNU, the COST Action MP-1201 and the Research Council of Norway Grant numbers 205591, 216700, and 240806. J.W.A.R. and A.D.B. acknowledge funding from the Leverhulme Trust (IN-2013-033), the Royal Society and the EPSRC through the Programme Grant “Superconducting Spintronics” (EP/N017242/1), and the Doctoral Training Grant (NanoDTC EP/G037221/1).

Author Contributions

J.A.O. and A.D.B. conceived the idea, and J.A.O. performed the analytical and numerical calculations with support from J.L., J.A.O., A.D.B., J.W.A.R. and J.L. contributed to the discussion and writing of the manuscript.

Additional Information

Competing financial interests: The authors declare no competing financial interests.

How to cite this article: Ouassou, J. A. *et al.* Electric control of superconducting transition through a spin-orbit coupled interface. *Sci. Rep.* **6**, 29312; doi: 10.1038/srep29312 (2016).



This work is licensed under a Creative Commons Attribution 4.0 International License. The images or other third party material in this article are included in the article’s Creative Commons license, unless indicated otherwise in the credit line; if the material is not included under the Creative Commons license, users will need to obtain permission from the license holder to reproduce the material. To view a copy of this license, visit <http://creativecommons.org/licenses/by/4.0/>

IV

Reference

N. Banerjee, J.A. Ouassou, Y. Zhu,
N.A. Stelmashenko, J. Linder, M.G. Blamire.
Controlling the superconducting transition by spin-orbit coupling.
Physical review B 97, 184521 (2018).
DOI: 10/GFGR9V

Contributions

NB, YZ, NAS and MGB designed and performed the experiment. JAO theoretically predicted the single-ferromagnet spin-valve effect that was observed, and performed numerical fits to the experimental results, with support and supervision from JL. All authors contributed to the discussion and writing of the manuscript.

Comments

In paper II, it was shown that a superconducting spin-valve effect can be realized using only a single homogeneous ferromagnet in the presence of Rashba-Dresselhaus spin-orbit coupling. In this paper, we demonstrate that this effect can be realized in junctions with only Rashba spin-orbit coupling if the magnetization direction is rotated between in-plane and out-of-plane. This prediction was confirmed experimentally by researchers at the University of Cambridge. This research has also been presented as a poster at the SPICE workshop *Exotic new states in superconducting devices* (Mainz, Germany, 2017).

Controlling the superconducting transition by spin-orbit couplingN. Banerjee,^{1,2,*} J. A. Ouassou,³ Y. Zhu,² N. A. Stelmashenko,² J. Linder,^{3,†} and M. G. Blamire²¹*Department of Physics, Loughborough University, Loughborough LE11 3TU, United Kingdom*²*Department of Materials Science and Metallurgy, University of Cambridge, 27 Charles Babbage Road, Cambridge CB3 0FS, United Kingdom*³*Center for Quantum Spintronics, Department of Physics, Norwegian University of Science and Technology, NO-7491 Trondheim, Norway*

(Received 16 May 2017; revised manuscript received 8 May 2018; published 31 May 2018)

Whereas considerable evidence exists for the conversion of singlet Cooper pairs into triplet Cooper pairs in the presence of inhomogeneous magnetic fields, recent theoretical proposals have suggested an alternative way to exert control over triplet generation: intrinsic spin-orbit coupling in a homogeneous ferromagnet coupled to a superconductor. Here, we proximity couple Nb to an asymmetric Pt/Co/Pt trilayer, which acts as an effective spin-orbit-coupled ferromagnet owing to structural inversion asymmetry. Unconventional modulation of the superconducting critical temperature as a function of in-plane and out-of-plane applied magnetic fields suggests the presence of triplets that can be controlled by the magnetic orientation of a single homogeneous ferromagnet. Our studies demonstrate an active role of spin-orbit coupling in controlling the triplets, an important step towards the realization of novel superconducting spintronic devices.

DOI: 10.1103/PhysRevB.97.184521

I. INTRODUCTION

Conventional superconductivity emerges from an attractive pairing of spin-up and spin-down electrons, whereas ferromagnetism arises due to an imbalance in the number of spin-up and spin-down electrons. In superconductor/ferromagnet (S/F) proximity structures, the competing nature of these two orders is the source of rich physics [1,2]. For example, the two electrons in a conventional Cooper pair enter different spin bands upon transmission into an adjacent F layer, resulting in a finite center-of-mass momentum. This causes a weak oscillatory dependence of the superconducting transition temperature T_c , which is superimposed on the monotonic T_c suppression due to increasing F layer thickness [3,4]. In more complex F/S/F trilayers, T_c is higher when the F moments are antiparallel than when they are parallel [1,5–7], arising from the higher net pair-breaking exchange field in the parallel state. This spin-switch effect allows an active control of T_c using magnetic states.

In contrast, S/F/F and F/S/F systems have recently shown an enhancement in the proximity effect between the S and F layers [8–11] for noncollinear F-moment alignments. This unusual proximity effect results from conventional spin-zero singlet Cooper pairs being transformed into spin-one triplet pairs. These long-range triplets (LRTs) consist of electrons from the same spin band and are therefore immune to a pair-breaking exchange field in F oriented along the spin polarization of the Cooper pairs, enhancing the coupling between the layers. The increased coupling makes superconductivity spread across the whole system, reducing T_c by up to 120–400 mK [8,10,12]. Although the control of superconductivity by modulating magnetic states is attractive for applications in superconducting spintronics [13–17], precisely controlling the

angle between the magnetic layers is difficult [8–10,17–19]. Practical applications require a simplified structure with fewer interfaces to minimize spin scattering, motivating the exploration of alternative mechanisms for triplet generation. Theoretical studies [20–27] predict that spin-orbit coupling (SOC) in S/F bilayers can produce an anisotropic depairing effect on triplets. The Cooper pair spin direction being determined by the F layer moment then implies that in an S/F bilayer with SOC, triplets can be controlled by the magnetization direction of a single homogeneous magnet [25]. In this paper, we report measurements on Nb/Pt(x)/Co/Pt proximity structures, where the structural inversion asymmetry gives rise to a Rashba coupling for $x > 0$ [28,29]. We compare the $T_c(H)$ behavior between samples with and without SOC to demonstrate the role of a triplet proximity effect in the former and confirm the prediction that T_c can be controlled by rotating a single homogeneous magnetic layer in SOC systems.

The structure of this paper is as follows. We start by giving a brief theoretical discussion of the proposed mechanism in Sec. II, which serves to motivate the experiment. In Sec. III, we then describe the experimental setup and measurements, demonstrating a spin-valve effect with only one homogeneous ferromagnet. These results are then compared to numerical simulations based on the Usadel equation in Sec. IV and further interpreted and discussed in Sec. V.

II. THEORY

In the quasiclassical and diffusive limits, superconductivity is well described by the so-called Usadel diffusion equation [30]. Near the critical temperature T_c , the superconducting pair amplitudes go to zero, meaning that the diffusion equation can be linearized with respect to pair amplitudes near this transition. In materials with superconductivity, ferromagnetism, and spin-orbit coupling, the linearized diffusion equations

*Corresponding author: N.Banerjee@lboro.ac.uk

†Corresponding author: jacob.linder@ntnu.no

are [25]

$$iD \nabla^2 f_s = \epsilon f_s + \mathbf{h} f_t - \Delta, \quad (1)$$

$$iD \nabla^2 f_t = \epsilon f_t + \mathbf{h} f_s + 2iD \mathbf{\Omega} f_t, \quad (2)$$

where f_s is the singlet pair amplitude, f_t is the triplet pair amplitude, D is the diffusion coefficient, ϵ is the quasiparticle energy, Δ is the superconducting gap, \mathbf{h} is the exchange field, and $\mathbf{\Omega}$ is a 3×3 matrix that describes the effects of the spin-orbit coupling.

From these equations alone, we can understand a lot about the system behavior. When the superconducting gap Δ is nonzero, Eq. (1) implies that there has to be singlet pairs f_s in the system as well. Indeed, it is precisely these singlet pairs that form the superconducting condensate of a conventional superconductor like Nb in the first place. Next, in the presence of an exchange field \mathbf{h} , some of these singlets f_s are converted into triplets f_t according to Eq. (2). Note that the direction of the triplet vector f_t parametrizes the spins of the pair, and f_t is proportional to the conventional \mathbf{d} vector [23]. The triplets generated here are oriented along the exchange field ($f_t \parallel \mathbf{h}$) and are known as *short-range triplets* (SRTs) in the literature since they are exposed to the pair-breaking effects of the exchange field. Finally, Eq. (2) shows that the triplet pairs are then affected by the spin-orbit matrix $\mathbf{\Omega}$. Depending on the structure of this matrix, the triplet pairs can either be rotated into LRTs or just be suppressed by the pair-breaking effect of the spin-orbit coupling.

For a Rashba coupling in the xy plane, i.e., broken inversion symmetry along the z axis, $\mathbf{\Omega}$ becomes diagonal [25],

$$\mathbf{\Omega} = \alpha^2 \begin{pmatrix} 1 & 0 & 0 \\ 0 & 1 & 0 \\ 0 & 0 & 2 \end{pmatrix}, \quad (3)$$

where α is the Rashba coefficient. The fact that this matrix is diagonal implies that the spin-orbit coupling does not facilitate any conversion between SRTs and LRTs. Note that this is different from the case of both Rashba and Dresselhaus couplings and also different from the nonlinear equations (required when $T \ll T_c$). The spin-orbit coupling shifts the effective energies of the in-plane (IP) triplets f_x, f_y by $2iD\alpha^2$ and of the out-of-plane (OOP) triplets f_z by $4iD\alpha^2$. This energy penalty is twice as large for OOP compared to IP triplets, and since the triplets are again oriented along the exchange field \mathbf{h} , we note that the triplet energy penalty can effectively be adjusted by rotating the exchange field.

To make this manifest, let us parametrize the exchange field

$$\mathbf{h} = h (\cos \theta \mathbf{e}_x + \sin \theta \mathbf{e}_z), \quad (4)$$

with θ being a parameter that rotates the field from IP to OOP. We can then project Eqs. (1) and (2) along the exchange field, obtaining the scalar diffusion equations

$$iD \nabla^2 f_s = \epsilon f_s + h f_t - \Delta, \quad (5)$$

$$iD \nabla^2 f_t = E_t f_t + h f_s, \quad (6)$$

where we have defined the effective triplet energy

$$E_t(\theta) = \epsilon + iD\alpha^2(3 - \cos 2\theta). \quad (7)$$

This effective energy rotates between $\epsilon + 2iD\alpha^2$ and $\epsilon + 4iD\alpha^2$ depending on the magnetization angle θ . But we again

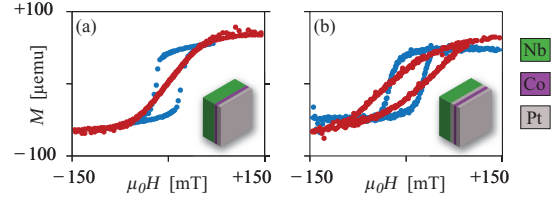


FIG. 1. Magnetization M as a function of the applied field H for (a) Nb(24)/Co(1.5)/Pt(1.5) and (b) Nb(24)/Pt(2.0)/Co(1.5)/Pt(1.5). The blue and red points show the results for IP and OOP applied fields, respectively. The insets show the stack sequence.

note that the origin of this magnetic field dependence is that the spin-orbit coupling suppresses triplets oriented OOP more than triplets oriented IP; the magnetic field dependence appears only because the magnetic field controls what triplets we generate.

This magnetically tunable energy penalty lies at the core of the T_c control discussed in this paper. By increasing the triplet energy E_t , we can directly suppress the triplet amplitude in the effective ferromagnet, thus closing the triplet proximity channel. Because this implies that fewer pairs will leak out of the superconductor, the singlet amplitude in the superconductor goes up, and this restores T_c to higher levels.

Note that the *spin-valve effect*, i.e., the variation of the critical temperature T_c with the magnetization direction θ , is not a monotonic function of the spin-orbit coupling α . If α is very low, then *neither* energy penalty, $2iD\alpha^2$ or $4iD\alpha^2$, is high enough to significantly suppress triplets, and T_c is low for all magnetic configurations. However, if α is very high, then *both* energy penalties are high enough to strongly suppress triplets, and T_c is high for all magnetic configurations. It is for intermediate values of α that the spin-valve effect is maximized.

III. EXPERIMENT

The thin-film stacks were deposited by dc magnetron sputtering in an ultrahigh vacuum chamber onto unheated oxidized Si(100) substrates placed on a rotating table. The substrates passed under magnetrons whose power and the rotation speed of the substrate table were adjusted to control the layer thicknesses (thicknesses are in nanometers in parentheses below). The Pt and Co layer thicknesses were adjusted to tune the IP and OOP magnetic anisotropy, allowing control over the angle between the magnetization and sample plane by applying moderate magnetic fields, and so control the effectiveness of the singlet/triplet conversion. During deposition, the chamber was cooled by a liquid-nitrogen jacket to achieve a pressure below 3×10^{-7} Pa. The layers were sputtered in 1.5-Pa Ar. Control samples of Nb/Pt and Nb/Co/Pt, as well as samples with varying Pt and Nb thickness, were also deposited. Figures 1(a) and 1(b) show magnetization M vs applied field H for Nb(24)/Co(1.5)/Pt(1.5) and Nb(24)/Pt(2.0)/Co(1.5)/Pt(1.5), which was measured at 10 K using a superconducting quantum interference device magnetometer. The blue and red points, respectively, represent the magnetic field applied in the IP and OOP directions. While for the Nb/Co/Pt stack the magnetization preferentially lies IP [Fig. 1(a)], insertion of a 2-nm

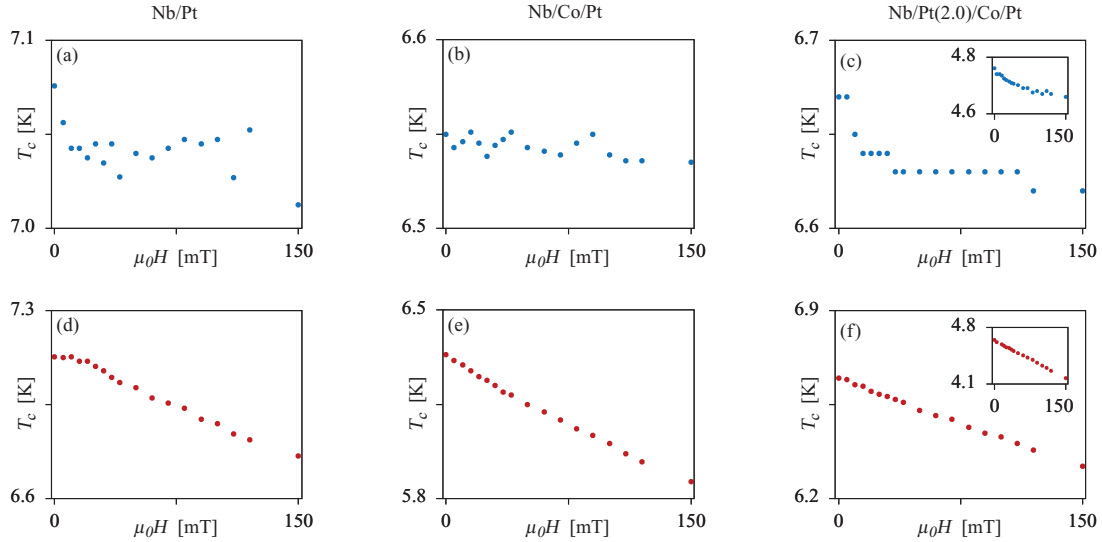


FIG. 2. Superconducting transition temperature T_c plotted against the applied field H for (a) and (d) Nb(24)/Pt(2), (b) and (e) Nb(24)/Co(1.5)/Pt(1.5), and (c) and (f) Nb(24)/Pt(2)/Co(1.5)/Pt(1.5). The rows correspond to (a)–(c) IP and (d)–(f) OOP applied fields. The insets in (c) and (f) show the T_c vs H plot for IP and OOP applied fields for Nb(18)/Pt(2)/Co(1.5)/Pt(1.5) with a thinner Nb layer, respectively.

Pt layer at the Nb/Co interface [Fig. 1(b)] results in a clear hysteretic switching for IP and OOP applied fields. This allows us to control the magnetization tilt with respect to the film plane using moderate magnetic fields. Perpendicular magnetic anisotropy in Pt/Co systems [31,32] is generally attributed to an enhancement in the perpendicular Co orbital moment resulting from a Pt(5d)-Co(3d) hybridization. The OOP anisotropy is inversely proportional to the Co layer thickness [33], and a 1.5-nm Co layer allows us to control the tilt using low magnetic fields. Transport measurements were performed on unpatterned samples in the range of 3–8 K using the four-point resistance measurement technique in a pulsed-tube cryocooler. The critical temperature T_c was defined as the temperature corresponding to 50% of the resistive transition. A constant bias current of 5 μA was used. The magnetic field was applied by starting at zero and ramping it up in 5–10-mT steps, and each T_c measurement was carried out in constant field. The maximum transition width was ~ 180 mK.

Figure 2 shows $T_c(H)$ for the three different samples. For most of the samples there is an apparent difference between $T_c(0)$ for IP and OOP measurements likely arising due to the different relative positions of the sample holders with respect to the temperature sensor. Several measurements from the same sample show that this difference in $T_c(0)$ is random and field independent and does not affect the overall trends of the $T_c(H)$ curve. This possibly arises due to minor differences in steady-state gas-flow conditions between each cooling cycle.

Figures 2(a) and 2(b) show $T_c(H)$ for a Nb(24)/Pt(2) bilayer and Nb(24)/Co(1.5)/Pt(1.5) trilayer in an IP field. Except for ~ 15 mK background noise, we find that T_c remains roughly constant up to $H = 120$ mT. Figure 2(c) shows corresponding measurements for the Nb(24)/Pt(2)/Co(1.5)/Pt(1.5) stack. Strikingly, we find a rapid 40 mK suppression of the critical

temperature between 0 and 100 mT. The full data range for all three samples shows that the T_c suppression below 100 mT for Nb(24)/Pt(2)/Co(1.5)/Pt(1.5) is comparable to the T_c suppression for the other two structures for the entire field range up to 500 mT (data not shown). While the net constant field-induced T_c suppression of ~ 60 mK until 500 mT for all the structures can be explained by a weak field-induced depairing for 24-nm-thick Nb films, the explanation for the T_c suppression by 40 mK at low fields for the structure with an additional Pt interlayer is not straightforward. From the systematic layer sequences, it is clear that the extra Pt layer between Nb and Co plays a role. For the OOP fields [Figs. 2(d)–2(f)], all samples show a pronounced T_c suppression due to the strong orbital depairing from the applied field.

Before attempting to explain our results in terms of SOC-induced control of triplets, we rule out two other possibilities. First, domain-wall-induced suppression of superconductivity can be ruled out since at higher fields elimination of domain walls should restore superconductivity. This is in sharp contrast to Fig. 2(c), where superconductivity is suppressed at larger IP fields. Second, we quantify the flux-induced T_c modulation which arises from the OOP magnetization of Co-containing samples [Figs. 2(e) and 2(f)]; for the Nb/Pt sample there is no magnetic moment, so the suppression shown in Fig. 2(d) must originate purely from the orbital depairing effect. The Co layer in the Nb/Co/Pt sample has an IP anisotropy with an OOP saturation field of ~ 120 mT [Fig. 1(a)]; the corresponding T_c plot [Fig. 2(e)] shows a rapid T_c suppression in the field range below this value, which can be partially explained by the magnetization-induced flux density being drawn OOP and added to the applied field. A similar effect would be expected for the Nb/Pt/Co/Pt sample, albeit with a lower saturation field reflecting the OOP anisotropy [Fig. 1(b)];

in fact, the low-field suppression of T_c is lower than that for the Nb/Co/Pt sample, implying that a different, partially compensating, T_c -modulating effect must be at work. This behavior is more pronounced for Nb/Pt/Co/Pt containing a thinner 18-nm Nb [Fig. 2(f), inset]. The OOP T_c suppression is expected to be significantly larger for the following reason: in superconducting thin films, we can use Ginzburg-Landau theory to understand the magnetic field dependence of the critical temperature T_c [34]. In a perpendicular field, the upper critical $H_c(T)$ is found from

$$\frac{dH_c}{dT} = -\frac{\Phi_0}{2\pi T_{c0}\xi_0^2}, \quad (8)$$

where ξ_0 is the zero-temperature Ginzburg-Landau coherence length and $\Phi_0 = h/2e$ is the flux quantum. Integrating this from zero critical field ($H_c = 0$, $T = T_{c0}$) to a finite field ($H_c = H_\perp$, $T = T_c < T_{c0}$), we find that the critical temperature reduction $\Delta T_c = T_c - T_{c0}$ due to orbital depairing follows

$$\frac{\Delta T_c}{T_{c0}} = -\frac{2\pi\xi_0^2}{\Phi_0} H_\perp. \quad (9)$$

Thus, the T_c variation with the field H_\perp should depend only on the coherence length ξ_0 . Fitting the observations for Nb(24)/Pt and Nb(20)/Pt and extrapolating linearly to Nb(18)/Pt, we get an estimated $\xi_0 \approx 15.5$ nm for 18-nm Nb. We therefore expect $\Delta T_c \approx 406$ mK for Nb(18)/Pt/Co/Pt with $H_\perp = 120$ mT.

Note that the equation above ignores the additional flux injection from Co due to the magnetization rotation. To estimate a lower bound for this flux, we can rewrite Eq. (9) with the effective magnetic field $H_\perp = H_{\text{ext}} + H_{\text{int}}$, where H_{ext} is the external applied field and H_{int} is the internal contribution from the Co layer. Solving the resulting equation for H_{int} , we get

$$H_{\text{int}} = H_{\text{ext}} - \frac{\Phi_0}{2\pi\xi_0^2} \frac{\Delta T_c}{T_{c0}}. \quad (10)$$

Using the experimental ΔT_c for the Nb(24)/Co/Pt sample and $H_{\text{ext}} = 120$ mT, we estimate $H_{\text{int}} \approx 52$ mT, yielding a total field $H_\perp \approx 172$ mT. Applying an effective field $H_\perp = 172$ mT to Nb(18)/Pt/Co/Pt, we then estimate $\Delta T_c \approx 581$ mK, while the measured value was 380 mK. We note that the estimated value here gives us only a lower bound since Nb(18)/Pt/Co/Pt is expected to have a larger flux injection from the Co layer than Nb/Co/Pt due to the increased OOP anisotropy of the sample. A similar calculation for Nb(24)/Pt/Co/Pt gives an estimated $\Delta T_c \approx 420$ mK, while the measured value was 270 mK.

Taking the difference between the estimated and measured values above, we can attribute a critical temperature change of 201 mK to proximity effects in Nb(18)/Pt/Co/Pt, compared to 150 mK for Nb(24)/Pt/Co/Pt. This shows that the spin-valve effect increases significantly for thinner Nb layers.

The role of an unconventional proximity effect in the Nb/Pt/Co/Pt sample is further strengthened by the IP T_c data in Figs. 2(a)–2(c). The data in Fig. 2(a) without a magnetic layer demonstrate small orbital depairing in the IP configuration, resulting in $\Delta T_c < 15$ mK for $H < 120$ mT. Similar behavior is observed for the Nb/Co/Pt sample [Fig. 2(b)], for which the IP anisotropy means that an IP field does not modify the magnetic moment. In contrast, the Nb/Pt/Co/Pt sample shows a decrease in T_c of 50 mK in the same range; if this

T_c modulation arose from field-induced changes to the flux injection from the Co layer, T_c should have increased as the OOP magnetization decreased. Similar behavior is observed for thinner Nb: T_c remains roughly constant at low IP fields for a Nb(20)/Pt(2) bilayer but is suppressed by 90 mK for Nb(18)/Pt(2)/Co(1.5)/Pt(1.5) [Fig. 2(c), inset]. Changes arising from anisotropic interface magnetoresistance in Pt/Co/Pt structures [35,36] can be ruled out as the resistance changes would be an order of magnitude smaller than here. To summarize, while the Nb/Pt and Nb/Co/Pt results can be qualitatively explained in terms of flux and field-induced orbital depairing, the Nb/Pt/Co/Pt behavior is distinctly different, and a rapid low-field T_c suppression is induced for the IP field which tends to align the Co magnetization parallel to the Nb plane.

The key to understanding our results is that the proximity effect in S/F systems with a single homogeneous F layer cannot be controlled by changing the magnetization angle with respect to the film plane (after subtracting the effect of flux injection from the F layer). In S/F/F' systems, noncollinear F and F' layer moments generate LRTs, which enhance the proximity coupling between S and F and so decrease T_c . However, in our inversion asymmetric Pt/Co/Pt trilayers, we have both a magnetic field \mathbf{h} and a Rashba coupling α in the system. As shown in Sec. II, this setup admits a spin-valve mechanism whereby superconductivity can be toggled on and off using the orientation of a single homogeneous magnetic layer.

IV. NUMERICS

We have modeled our results using the Usadel formalism, where we treat the Pt/Co/Pt trilayer as an effective diffusive ferromagnet with an intrinsic Rashba coupling. This approach has two advantages: first, scattering at Pt/Co interfaces allows us to use a diffusive model without knowing the microscopic details of the interface; second, the exchange splitting of the Co layer is now averaged out over a larger volume, allowing us to use a quasiclassical approach. Below, we first summarize the numerical results and then discuss the fitting procedure.

The results of the numerical simulations are shown in Fig. 3 along with a comparison with the experimental results. The difference ΔT_c is calculated between Nb(24)/Pt(2)/Co(1.5)/Pt(1.5) and Nb(24)/Co(1.5)/Pt(1.5) for IP and OOP fields. The experimental and numerically calculated ΔT_c are shown for IP [Figs. 3(a) and 3(b)] and the corresponding plots for OOP fields [Figs. 3(c) and 3(d)]. The overall numerical trend [Figs. 3(b) and 3(d)] is in excellent agreement with the experiments [Figs. 2(a) and 2(c)]. The magnitude of ΔT_c from the simulation (~ 22 mK) is 55% of that of the experimental value of 40 mK. The lower simulated values can arise due to a simplified model where we have assumed an ideal interface and a simplified magnetic model. In real systems, interdiffusion and interface roughness can affect the magnitude of ΔT_c . The shaded regions indicate the range of T_c variation in our model when the exchange field rotation range by an external field is varied. The significance of this range and the corresponding T_c variation is explained below under the discussion on magnetization modeling. But importantly, the difference ΔT_c has the right trend and order of magnitude for both IP and OOP fields. We discuss the underlying mechanism in detail in Sec. V.

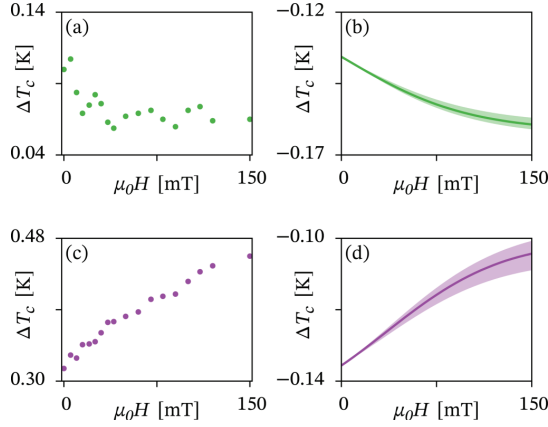


FIG. 3. Critical temperature difference ΔT_c calculated between Nb(24)/Pt(2)/Co(1.5)/Pt(1.5) and Nb(24)/Co(1.5)/Pt(1.5) as a function of the applied IP and OOP fields H . The top row shows the (a) experimental and (b) simulated ΔT_c for IP fields. The corresponding OOP (c) experimental and (d) simulated ΔT_c are shown in the bottom row. The solid curves in (b) and (d) show the exchange field components for a rotation angle $\delta\theta = 30^\circ$, while the shaded regions correspond to $\delta\theta \in [25^\circ, 35^\circ]$.

We have also compared the critical temperature difference ΔT_c between Nb/Pt/Co/Pt and Nb/Co/Pt for different Pt inter-layer thicknesses, which is discussed in more detail in Sec. V.

For the numerical calculations of the critical temperature, we solved the full nonlinear diffusion equations [25],

$$iD\tilde{\nabla}(\hat{g}\tilde{\nabla}\hat{g}) = [\epsilon\hat{\tau}_z + \hat{\Delta} + \hat{h} + \hat{\kappa}, \hat{g}], \quad (11)$$

where \hat{g} is the 4×4 retarded quasiclassical propagator and $\tilde{\nabla}(\cdot) = \nabla(\cdot) - i[\hat{A}, \cdot]$ is a gauge-covariant derivative that accounts for spin-orbit coupling. The other matrices are

$$\hat{\tau}_z = \text{diag}(+1, +1, -1, -1), \quad (12)$$

$$\hat{\Delta} = \text{antidiag}(+\Delta, -\Delta, +\Delta^*, -\Delta^*), \quad (13)$$

$$\hat{h} = \text{diag}(h\sigma, h\sigma^*), \quad (14)$$

$$\hat{A} = \text{diag}(A, -A^*), \quad (15)$$

$$\hat{\kappa} = i\kappa\hat{\tau}_z\hat{g}\hat{\tau}_z. \quad (16)$$

Here, Δ is the superconducting gap, h is the exchange field, σ is the Pauli vector, $A = \alpha(\sigma_x e_y - \sigma_y e_x)$ is the spin-orbit field [25], and κ is a parameter that accounts for the orbital depairing [37]. To get rid of the diffusion coefficient in Eq. (11), we used the diffusive coherence length $\xi \equiv \sqrt{D/\Delta_0} \approx 14$ nm. Using the relation $\xi \approx \sqrt{\xi_0 \ell}$ for the coherence length, where $\xi_0 \approx 38$ nm is the ballistic coherence length of Nb and ℓ is the mean free path of the sample, we find that this corresponds to a reasonable estimate for the mean free path, $\ell \approx 5$ nm [38,39]. The diffusion coefficient was assumed to be the same in all materials.

For the interface between the superconductor and effective ferromagnet, we used the tunneling boundary conditions [40],

$$2G_0 L_L \hat{g}_L \partial_z \hat{g}_L = 2G_0 L_R \hat{g}_R \partial_z \hat{g}_R = G_T [\hat{g}_L, \hat{g}_R], \quad (17)$$

where G_0 is the normal-state conductance of each material, G_T is the tunneling conductance of the interface, $\hat{g}_{L,R}$ are the propagators on the left and right sides of the interface, respectively, and $L_{L,R}$ are the corresponding material lengths. The tunnel conductance between the superconductor and effective ferromagnets was determined by calculating the critical temperature T_c/T_{cs} in the absence of an external field and selecting the best possible values for the conductance ratio G_T/G_0 . We simultaneously tried to make sure that the ratio between T_c for Nb/Co/Pt and Nb/Pt/Co/Pt was as close to the experimental values as possible. Unfortunately, we were unable to get a perfect quantitative fit using reasonable parameters here, but using $G_T/G_0 = 0.65$ for Nb/Co/Pt and $G_T/G_0 = 0.85$ for Nb/Pt/Co/Pt did provide a qualitative match. Note that we assume the normal-state conductance G_0 is the same in Nb and the [Pt]/Co/Pt heterostructure. In reality, these two are different, and estimating G_0 for the heterostructure from known parameters is not straightforward. However, a difference in the normal-state conductances of the materials simply decreases the proximity effect [2], and the same happens if the tunneling conductance is decreased. Thus, we may compensate for a conductance asymmetry by adjusting G_T accordingly, and since the tunneling conductance is already treated as a fitting parameter, this happens automatically.

In order to self-consistently determine the superconducting properties of a hybrid structure, we require not only equations for the propagator \hat{g} but also an accompanying equation for the superconducting gap Δ . This equation can be written as [25]

$$\Delta = \frac{1}{\ln(2\omega_c/\Delta_0)} \int_0^{\omega_c} d\epsilon \text{Re}[f_s] \tanh\left(\frac{\pi}{2e\gamma} \frac{\epsilon/\Delta_0}{T/T_{cs}}\right), \quad (18)$$

where ω_c is the Debye cutoff energy, Δ_0 is the zero-temperature gap of a bulk superconductor, T_{cs} is the critical temperature of a bulk superconductor, and γ is the Euler-Mascheroni constant. We used $\omega_c = 30\Delta_0$ in our simulations, and for Nb the relevant material constants are $\Delta_0 \approx 1.4$ meV and $T_{cs} \approx 9.2$ K. In the numerical implementation, we use a Riccati parametrization for the propagator \hat{g} and employ a kind of binary search algorithm for the calculation of the critical temperature T_c . For more details about this numerical procedure, see Ref. [41].

The magnetization was modeled as follows. The measured magnetization was found to roughly follow the profile

$$M = M_0 + \delta M \tanh(H/H_0), \quad (19)$$

where M is the magnetization component along the applied field H . This suggests that we model the exchange field as

$$h_x/h_0 = \cos(\theta_0) + [\cos(\theta_0 - \delta\theta) - \cos(\theta_0)] \tanh(H/H_0) \quad (20)$$

in the case of an IP applied field H and

$$h_z/h_0 = \sin(\theta_0) + [\sin(\theta_0 + \delta\theta) - \sin(\theta_0)] \tanh(H/H_0) \quad (21)$$

for an OOP applied field H . In both cases, we have assumed that the exchange field remains in the xz plane, so that the relation $h_x^2 + h_z^2 = h_0^2$ can be used to find the other component. Here, θ_0 is interpreted as the angle that the exchange field direction makes with the thin-film plane in the absence of external fields, while $\delta\theta$ parametrizes the maximum exchange field rotation that can be achieved using an external field. Based

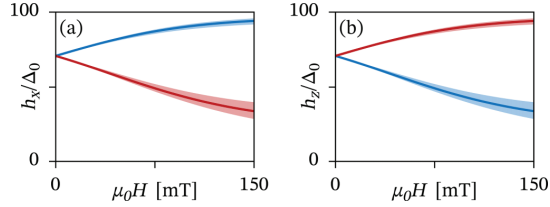


FIG. 4. Plot of the (a) IP and (b) OOP exchange field in our numerical model as functions of the applied field H . The blue curves correspond to an IP applied field, and the red curves correspond to an OOP applied field. The solid curves show the exchange field components for a rotation angle $\delta\theta = 30^\circ$, while the shaded regions correspond to $\delta\theta \in [25^\circ, 35^\circ]$.

on the experimental measurements, we found the saturation parameter $H_0 \approx 100$ mT to fit the data very well, but estimating θ_0 and $\delta\theta$ turned out to be difficult. We therefore fixed the first parameter to $\theta_0 = 45^\circ$ and varied $\delta\theta \in [25^\circ, 35^\circ]$ to see how the results change since the critical temperature T_c is more sensitive to variations in $\delta\theta$ than θ_0 . Finally, we assumed an average exchange field $h_0 = 100\Delta_0 \approx 140$ meV for the Pt/Co/Pt heterostructure based on previously reported values of 300 meV for Co [42]. Using the model above, we plot the resulting exchange field \mathbf{h} as a function of the applied field H in Fig. 4.

Next, we discuss the orbital depairing effect. For thin-film systems, the depairing effect usually causes the critical temperature to decrease linearly with the applied field when the external field is applied OOP and quadratically when the external field is applied IP [43]. These two cases correspond to the depairing parameters $\kappa = \Delta_0(H/H_c)$ and $\kappa = \Delta_0(H/H_c)^2$, respectively, where H_c is a critical field for which $T_c \rightarrow 0$ in the absence of proximity effects. From the experimental results, we see that for an OOP case we do get a linear decrease in T_c as expected. By fitting the critical temperature decay $T_c(H = 120 \text{ mT})/T_c(H = 0)$ that we get from the numerical simulations to that in the Nb/Co/Pt experiment, we get an estimate $H_c \approx 1.8$ T for the critical field. For the Nb/Pt/Co/Pt structure, we simply assumed that the orbital depairing effect was the same as for Nb/Co/Pt. For the case of an IP applied field, however, we see from the experiment that the orbital depairing is negligible for $H < 150$ mT, and it was therefore excluded from the IP models (i.e., $H_c = \infty$).

Finally, we estimated the Rashba coupling $\alpha \approx 12$ by fitting the ratio $T_c(H = 120 \text{ mT})/T_c(H = 0)$ for the Nb/Pt/Co/Pt structures and selecting the value of α that produces the best possible fits for both the IP and OOP cases. This is in units of $\hbar^2/m\xi$, where m is the electron mass and \hbar is Planck's reduced constant; restoring the units, we get $\alpha \approx 6.5 \times 10^{-11}$ eV m, which is very close to previous experimental estimates. This value is close to $\sim 5 \times 10^{-12}$ eV m for asymmetric Pt/Co/Pt structures estimated from Ref. [44]. The higher values in our system could arise due to different Pt and Co thicknesses and interfaces, which strongly influence the Rashba coupling [29].

V. DISCUSSION

In the previous section, a comparison of the experimental results with the numerical calculation shows that the T_c

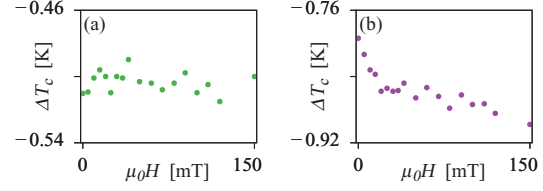


FIG. 5. Critical temperature difference ΔT_c calculated between Nb(24)/Co(1.5)/Pt(1.5) and Nb(24)/Pt(1.5) as a function of the applied (a) IP and (b) OOP fields H .

suppression for OOP fields for Nb(24)/Co(1.5)/Pt(1.5) is purely due to orbital effects. The Pt layer at the Nb/Co interface in Nb/Pt/Co/Pt therefore plays an important role. This is most strikingly evident in the ΔT_c between Nb/Co/Pt and Nb/Pt (Fig. 5). The IP ΔT_c [Fig. 5(a)] remains constant (~ 10 mK fluctuation), whereas the OOP ΔT_c [Fig. 5(b)] decreases with increasing applied field, in sharp contrast to Nb/Pt/Co/Pt structures. This can easily be explained by equal negligible orbital depairing for IP fields in both structures and increased flux injection in Nb/Co/Pt for OOP fields which suppresses T_c more rapidly for Nb/Co/Pt.

However, in Nb(24)/Pt(2)/Co(1.5)/Pt(1.5) there is a compensating effect due to suppression of the spin-zero triplet (SRT) generation resulting in an increasing ΔT_c with the applied field. For IP fields with negligible orbital depairing, ΔT_c decreases due to an enhancement of the proximity effect in Nb(24)/Pt(2)/Co(1.5)/Pt(1.5) arising from an increased SRT generation. To better understand the role of the Pt layer at the Nb/Co interface, we have examined T_c variation with the thickness of this layer. In Fig. 6, we plot ΔT_c between Nb(24)/Pt(x)/Co(1.5)/Pt(1.5) and Nb(24)/Co(1.5)/Pt(1.5) for $x = 0.3$ and $x = 1$ and the results of the numerical simulation for these structures. While for IP fields ΔT_c is ~ 15 mK for 0.3 nm [Fig. 6(a)], the 1-nm structure shows an ~ 25 mK drop superimposed on the noise [Fig. 6(b)]. The fitting process described in Sec. IV has been repeated for Pt interlayers with thicknesses of 0.3 and 1.0 nm, instead of the 2.0-nm interlayer discussed above. The simulated ΔT_c values [Figs. 6(e) and 6(f)] are in reasonable agreement with the experimental data. For the 0.3-nm case, we found a reduced Rashba coupling $\alpha \approx 9$, and the same tunneling conductance as for Nb/Co/Pt. For the 1.0-nm case, however, both these parameters were the same as for the 2.0-nm case.

The ΔT_c trend with Pt thickness becomes clear when it is compared with the $M(H)$ loops (Fig. 7) for these samples measured at 10 K. With increasing Pt layer thickness from 0.3 to 1 nm, the magnetization gradually changes from fully IP [Fig. 7(a)] with an OOP hard axis [Fig. 7(c)] to a clear hysteretic switching for both IP and OOP [Figs. 7(b) and 7(d)]. This develops further when the bottom Pt thickness is increased to 2 nm, as seen from Fig. 1. The corresponding IP field-dependent T_c for 2-nm Pt shows a large change of ~ 50 mK at low fields [Fig. 2(c)].

The large change in low-field T_c appears only in the region where the IP magnetization approaches saturation, beyond which the T_c suppression is comparable for all the structures. This indicates the active role played by the magnetization

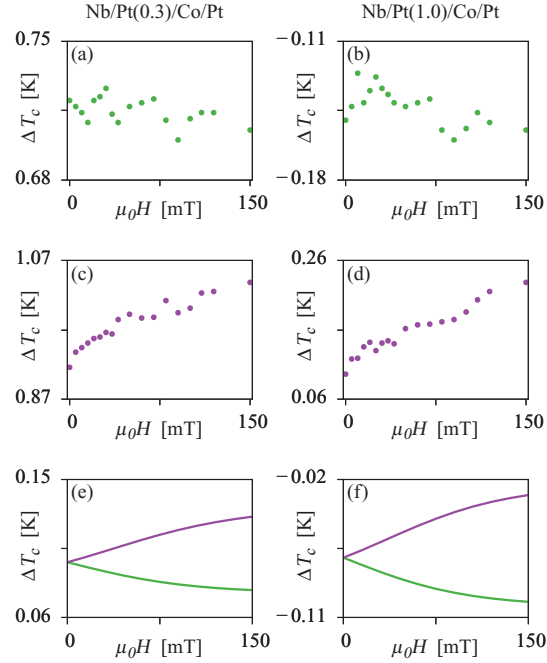


FIG. 6. Critical temperature difference ΔT_c between Nb(24)/Pt(x)/Co(1.5)/Pt(1.5) and Nb(24)/Co(1.5)/Pt(1.5) as a function of the applied field H . The columns correspond to $x = 0.3$ and $x = 1.0$. From top to bottom, the rows correspond to IP fields, OOP fields, and numerical simulations.

angle in modulating T_c for structures showing a comparable IP and OOP anisotropy in addition to the presence of a Pt layer at the Nb/Co interface. ΔT_c for the OOP field [Figs. 6(c) and 6(d)] increases with applied field, and similar to the IP ΔT_c [Figs. 6(a) and 6(b)], the magnitude of this change increases with thicker Pt layer at the Nb/Co interface. Our measurements possibly underestimate the magnitude of the SOC-induced change. This is because the increased OOP magnetization with increasing x in Nb/Pt(x)/Co/Pt results in more Co flux being directed into Nb. This reduces T_c as x is increased, which can counteract some of the T_c increase caused by the stronger SOC associated with increasing x . This implies that even though we see a finite nonzero T_c for OOP fields for $x = 0.3$ and $x = 1.0$, the actual SOC-induced changes get progressively higher with increasing Pt thickness to compensate for the increasing flux injection from OOP magnetization. SOC introduces two competing effects: triplet depairing due to imaginary terms in the effective energy and LRT generation due to triplet mixing terms [25]. Numerically, we found the energy penalty of the SRT is more important than the LRT generation for the T_c modulation. We reiterate an important point: SOC couples the magnetization with the SRT energy, which is different from spin-relaxation effects induced by SOC on superconductivity [38].

In S/F structures without SOC, the SRT energy is independent of the magnetization state, and T_c is independent of

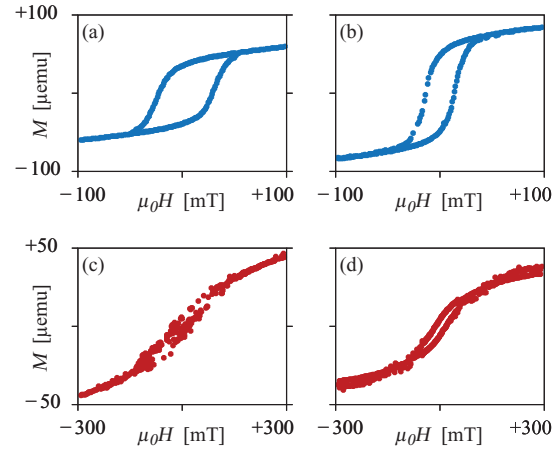


FIG. 7. Magnetization M as a function of the applied field H . The left column shows results for Nb/Pt(0.3)/Co/Pt, and the right column shows results for Nb/Pt(1.0)/Co/Pt. The top row corresponds to IP applied fields, and the bottom row corresponds to OOP applied fields.

the magnetization angle θ . However, in the presence of SOC the SRT energy depends on T_c ; with an increasing OOP field, the “leakage” of the Cooper pairs through the triplet channel is reduced, thereby increasing T_c (since the superconducting gap directly depends on the singlet pair amplitude). As the magnetization is made IP, the SRT generation is energetically more favorable, thereby “draining” the superconductor of Cooper pairs and reducing T_c . The triplet Cooper pairs are not confined to the ferromagnetic region and are also expected to exist in the Nb region near the interface. However, an explicit demonstration of this would require, e.g., local scanning tunnel microscope measurements, which is outside of the scope of the present work. There is thus a qualitative difference between the samples for which SOC is expected to be relevant and those which simply have a magnetic layer whose magnetic orientation controls the injected flux.

VI. CONCLUSION

The results reported here cannot be explained by conventional S/F proximity theory without considering SOC. While the superconducting spin valve with a single homogeneous ferromagnet demonstrated here drastically simplifies the control of superconductivity, a natural progression involves structures with combined Rashba and Dresselhaus coupling predicted to control LRT [25]. Incorporating such structures in Josephson junctions would allow the design of devices currently under intense focus in superspintronics.

ACKNOWLEDGMENTS

N.B. was supported by UKIERI Grant and funding from Loughborough University. J.L. and J.A.O. were supported by the Research Council of Norway through Grant No. 240806, and through its Centres of Excellence funding scheme Grant No. 262633, QuSpin. M.G.B. was supported by EPSRC Programme Grant No. EP/N017242/1.

- [1] A. I. Buzdin, *Rev. Mod. Phys.* **77**, 935 (2005).
- [2] F. S. Bergeret, A. F. Volkov, and K. B. Efetov, *Rev. Mod. Phys.* **77**, 1321 (2005).
- [3] L. Lazar, K. Westerholt, H. Zabel, L. R. Tagirov, Yu. V. Goryunov, N. N. Garif'yanov, and I. A. Garifullin, *Phys. Rev. B* **61**, 3711 (2000).
- [4] J. S. Jiang, D. Davidović, D. H. Reich, and C. L. Chien, *Phys. Rev. Lett.* **74**, 314 (1995).
- [5] L. R. Tagirov, *Phys. Rev. Lett.* **83**, 2058 (1999).
- [6] I. Baladić, A. Buzdin, N. Ryzhanova, and A. Vedyayev, *Phys. Rev. B* **63**, 054518 (2001).
- [7] A. I. Buzdin, A. Vedyayev, and N. V. Ryzhanova, *Europhys. Lett.* **48**, 686 (1999).
- [8] P. V. Leksin, N. N. Garif'yanov, I. A. Garifullin, Y. V. Fominov, J. Schumann, Y. Krupskaya, V. Kataev, O. G. Schmidt, and B. Büchner, *Phys. Rev. Lett.* **109**, 057005 (2012).
- [9] V. I. Zdravkov, J. Kehrlé, G. Obermeier, D. Lenk, H.-A. Krug von Nidda, C. Müller, M. Y. Kupriyanov, A. S. Sidorenko, S. Horn, R. Tidecks, and L. R. Tagirov, *Phys. Rev. B* **87**, 144507 (2013).
- [10] X. L. Wang, A. Di Bernardo, N. Banerjee, A. Wells, F. S. Bergeret, M. G. Blamire, and J. W. A. Robinson, *Phys. Rev. B* **89**, 140508(R) (2014).
- [11] A. Singh, S. Voltan, K. Lahabi, and J. Aarts, *Phys. Rev. X* **5**, 021019 (2015).
- [12] M. Houzet and A. I. Buzdin, *Phys. Rev. B* **76**, 060504(R) (2007).
- [13] J. Linder and J. W. A. Robinson, *Nat. Phys.* **11**, 307 (2015).
- [14] M. Eschrig, *Phys. Today* **64**(1), 43 (2011).
- [15] J. W. A. Robinson, J. D. S. Witt, and M. G. Blamire, *Science* **329**, 59 (2010).
- [16] T. S. Khaire, M. A. Khasawneh, W. P. Pratt, and N. O. Birge, *Phys. Rev. Lett.* **104**, 137002 (2010).
- [17] N. Banerjee, C. B. Smiet, R. G. J. Smits, A. Ozaeta, F. S. Bergeret, M. G. Blamire, and J. W. A. Robinson, *Nat. Commun.* **5**, 3048 (2014).
- [18] N. Banerjee, J. W. A. Robinson, and M. G. Blamire, *Nat. Commun.* **5**, 4771 (2014).
- [19] M. G. Blamire, C. B. Smiet, N. Banerjee, and J. W. A. Robinson, *Supercond. Sci. Technol.* **26**, 55017 (2013).
- [20] L. P. Gor'kov and E. I. Rashba, *Phys. Rev. Lett.* **87**, 037004 (2001).
- [21] G. Annunziata, D. Manske, and J. Linder, *Phys. Rev. B* **86**, 174514 (2012).
- [22] F. S. Bergeret and I. V. Tokatly, *Phys. Rev. Lett.* **110**, 117003 (2013).
- [23] A. P. MacKenzie and Y. Maeno, *Rev. Mod. Phys.* **75**, 657 (2003).
- [24] F. S. Bergeret and I. V. Tokatly, *Phys. Rev. B* **89**, 134517 (2014).
- [25] S. H. Jacobsen, J. A. Ouassou, and J. Linder, *Phys. Rev. B* **92**, 024510 (2015).
- [26] V. M. Edelstein, *Phys. Rev. B* **67**, 020505 (2003).
- [27] V. M. Edelstein, *Pis'ma Zh. Eksp. Teor. Fiz.* **77**, 212 (2003). [*JETP Lett.* **77**, 182 (2003)].
- [28] P. P. J. Haazen, E. Muré, J. H. Franken, R. Lavrijsen, H. J. M. Swagten, and B. Koopmans, *Nat. Mater.* **12**, 299 (2013).
- [29] R. Lavrijsen, D. M. F. Hartmann, A. van den Brink, Y. Yin, B. Barcones, R. A. Duine, M. A. Verheijen, H. J. M. Swagten, and B. Koopmans, *Phys. Rev. B* **91**, 104414 (2015).
- [30] K. D. Usadel, *Phys. Rev. Lett.* **25**, 507 (1970).
- [31] N. Nakajima, T. Koide, T. Shidara, H. Miyachi, H. Fukutani, A. Fujimori, K. Iio, T. Katayama, M. Nývlt, and Y. Suzuki, *Phys. Rev. Lett.* **81**, 5229 (1998).
- [32] S. Bandiera, R. C. Sousa, B. Rodmacq, and B. Dieny, *IEEE Magn. Lett.* **2**, 3000504 (2011).
- [33] T. Ueno, J. Sinha, N. Inami, Y. Takeichi, S. Mitani, K. Ono, and M. Hayashi, *Sci. Rep.* **5**, 14858 (2015).
- [34] S. I. Krasnovobodtsev, N. P. Shabanova, E. V. Ekimov, V. S. Nozdrin, and E. V. Pechen, *Sov. Phys. JETP* **81**, 534 (1995).
- [35] A. Kobs, S. Heße, W. Kreuzpaintner, G. Winkler, D. Lott, P. Weinberger, A. Schreyer, and H. P. Oepen, *Phys. Rev. Lett.* **106**, 217207 (2011).
- [36] Y. M. Lu, J. W. Cai, S. Y. Huang, D. Qu, B. F. Miao, and C. L. Chien, *Phys. Rev. B* **87**, 220409(R) (2013).
- [37] M. Silaev, P. Virtanen, F. S. Bergeret, and T. T. Heikkilä, *Phys. Rev. Lett.* **114**, 167002 (2015).
- [38] J. Draskovic, T. R. Lemberger, B. Peters, F. Yang, J. Ku, A. Bezryadin, and S. Wang, *Phys. Rev. B* **88**, 134516 (2013).
- [39] C. Delacour, L. Ortega, M. Faucher, T. Crozes, T. Fournier, B. Pannetier, and V. Bouchiat, *Phys. Rev. B* **83**, 144504 (2011).
- [40] M. Y. Kupriyanov and V. F. Lukichev, *Sov. Phys. JETP* **67**, 1163 (1988).
- [41] J. A. Ouassou, A. Di Bernardo, J. W. A. Robinson, and J. Linder, *Nat. Sci. Rep.* **6**, 29312 (2016).
- [42] J. W. A. Robinson, S. Piano, G. Burnell, C. Bell, and M. G. Blamire, *Phys. Rev. Lett.* **97**, 177003 (2006).
- [43] R. Meservey and P. M. Tedrow, *Phys. Rep.* **238**, 173 (1994).
- [44] S. T. Lo, S. W. Lin, Y. T. Wang, S. D. Lin, and C. T. Liang, *Sci. Rep.* **4**, 5438 (2014).

V

Reference

J. Linder, M. Amundsen, [J.A. Ouassou](#).
Microwave control of the superconducting proximity
effect and minigap in magnetic and normal metals.
Scientific reports 6, 38739 (2016).
DOI: 10/GFGR9T

Contributions

JL did the majority of the analytical and numerical calculations with support from MA and JAO. All authors contributed to the discussion of the results and the writing of the manuscript.

In particular, JAO had a minor supporting role in this collaboration: helping discuss how the equations could be evaluated numerically, and assisting in the discussion and writing of the final manuscript.

SCIENTIFIC REPORTS

OPEN

Microwave control of the superconducting proximity effect and minigap in magnetic and normal metals

Received: 21 September 2016

Accepted: 14 November 2016

Published: 16 December 2016

Jacob Linder, Morten Amundsen & Jabir Ali Ouassou

We demonstrate theoretically that microwave radiation applied to superconducting proximity structures controls the minigap and other spectral features in the density of states of normal and magnetic metals, respectively. Considering both a bilayer and Josephson junction geometry, we show that microwaves with frequency ω qualitatively alters the spectral properties of the system: inducing a series of resonances, controlling the minigap size E_{mg} , and even replacing the minigap with a strong peak of quasiparticle accumulation at zero energy when $\omega = E_{mg}$. The interaction between light and Cooper pairs may thus open a route to active control of quantum coherent phenomena in superconducting proximity structures.

Combining materials with different properties is a certain way to generate exciting physics at their interface. Superconducting hybrid structures are particularly interesting in this regard due to the coherent quantum correlations that give rise to dissipationless transport of both charge and, when combined with magnetic materials, spin. There is currently much interest in discovering ways to exert well-defined control the properties of such proximity structures, including the electronic density of states, the critical temperature at which superconductivity arises, and the appearance of supercurrents^{1–3}.

The influence of microwave radiation on superconductors has been studied in several works, and includes investigations of its effect on the critical superconducting current⁴, the dissipative conductivity⁵, the current-phase relation in Josephson junctions^{6,7}, the non-equilibrium distribution of quasiparticles⁸, the photoelectric effect⁹, microwave-assisted supercurrents¹⁰, and the temperature for the onset of superconductivity^{11,12}. The appearance of coherent excited states and the depairing effect of microwave radiation on dirty superconductors was very recently theoretically considered in ref. 13.

However, what remains virtually unexplored is how microwave radiation alters the superconducting proximity effect, which is the existence of superconducting correlations in an otherwise non-superconducting material when placed in contact with a superconductor, made possible due to electron tunneling between the layers. A concrete manifestation is the strong modification of the density of states, in both normal and magnetic metals proximity-coupled to a superconductor. The reason for why this is of importance is that proximity structures play a key part in creating non-conventional types of coherent electron pairing that are not present in ordinary superconductors. This includes both spin-polarized triplet superconductivity¹⁴ and odd-frequency superconducting order¹⁵, which recently have been experimentally demonstrated to provide diametrically opposite Meissner response¹⁶ and low-energy spectral properties^{17,18} compared to Bardeen-Cooper-Schrieffer theory¹⁹. From another perspective, the opportunity to manipulate low-energy excitations in superconducting proximity structures has clear practical implications for cryogenic technology since it controls the availability of spin- and charge-carriers. In fact, quasiparticles in superconductors can become nearly chargeless spin-1/2 carriers, leading to effects such as^{20–24} strongly enhanced spin lifetimes and spin relaxation lengths when compared to injection of spin-polarized currents into normal metals, especially when using Zeeman split superconductors (a thin superconducting film in the presence of an in-plane magnetic field)²⁵. This, in turn, allows one to envision various types of devices such as highly sensitive magneto- and thermometers as well as superconducting magnetoresistive elements.

Department of Physics, NTNU, Norwegian University of Science and Technology, N-7491 Trondheim, Norway. Correspondence and requests for materials should be addressed to J.L. (email: jacob.linder@ntnu.no)

In this work, we show that shining light on superconducting hybrid structures offers a way to control the proximity effect in both normal metals and magnetic materials. We discover that an oscillating electric field $\mathcal{E}(t)$ applied transversely to the junction induces a series of resonances in the density of states, and that it can be used to control the size of the minigap E_{mg} in both bilayer superconductor/normal-metal (SN) and Josephson (SNS) junctions. The light interaction even inverts the minigap, generating a peak of quasiparticle accumulation at $E = 0$ when the frequency of the light is tuned to $\omega = E_{\text{mg}}$. These findings give interesting prospects for transistor-like functionality via light-superconductor interactions since the density of states controls the availability of charge- and spin-carriers. Providing both analytical and numerical results, including the case of a magnetic exchange-field being present in the metal or in the superconductor, we show how the interaction between light and Cooper pairs controls the low-energy density of states, offering a new way to manipulate superconducting correlations. This may open a new pathway to active control of quantum coherent phenomena in superconducting proximity structures.

Theory

We use the time-dependent quasiclassical Keldysh-Usadel theory^{26–29} to describe the superconductivity of these systems in the diffusive limit. We begin with the SN bilayer, in which case superconducting correlations leak into the normal metal via the proximity effect. The electric field $\mathcal{E}(t) = \omega A_0 \sin(\omega t) = -\partial A/\partial t$ is accounted for by the gauge field $A = A_0 \cos(\omega t)$. The Usadel equation in N then reads:

$$D\partial_x(\hat{g}\partial_x\hat{g}) + i[E\hat{\rho}_3 + i\alpha\hat{\rho}_3(\hat{g}_+ + \hat{g}_-)\hat{\rho}_3, \hat{g}] = 0. \quad (1)$$

Here, D is the diffusion coefficient, $\hat{g} = \hat{g}(x, E)$ is the quasiclassical time-averaged Green function, E is the quasiparticle energy, $\alpha = DA_0^2/4$ is a measure of the strength of the interaction with light, ω is the driving frequency, $\hat{\rho}_3 = \text{diag}(+1, +1, -1, -1)$, while $\hat{g}_\pm \equiv \hat{g}(x, E \pm \omega/2)$. The derivation of this equation is shown in the Methods section and is valid when $\alpha \ll \omega$. We assume that the field is screened in the S region, which is taken to have a size and thickness far exceeding the superconducting coherence length ξ and penetration depth λ , allowing us to use the bulk superconducting Green function \hat{g}_{BCS} there. Practically, our proposed setup could be realized by depositing a thick superconductor to partially cover a thin normal metal layer, such that the microwave field penetrates the normal layer where it is not covered by a superconductor whereas it is shielded in the superconductor (see the inset of e.g. Fig. 1). Such a lateral geometry should be well described by an effective 1D model, as done in ref. 30. The thickness of the N layer should be much smaller than the skin depth and penetration depth λ , which is experimentally feasible (typical values for the skin depth of a normal metal such as Cu is of order μm at microwave frequencies, whereas $\lambda_{\text{Nb}} \sim 50 \text{ nm}$ and $\lambda_{\text{Al}} \sim 20 \text{ nm}$). From Eq. (1), we derive the following Riccati-parametrized^{31,32} Usadel equation:

$$D[\partial_x^2\gamma + 2(\partial_x\tilde{\gamma})\tilde{\mathcal{N}}(\partial_x\gamma)] + 2i(E + i\delta)\gamma + i(\mathbf{h} \cdot \boldsymbol{\sigma})\gamma - i\gamma(\mathbf{h} \cdot \boldsymbol{\sigma}^*) - \alpha G\gamma - \alpha\gamma\tilde{G} + \alpha(F + \gamma\tilde{F}\gamma) = 0. \quad (2)$$

The Green function \hat{g} can then be calculated from the 2×2 matrix γ in spin space, the normalization matrix $\mathcal{N} \equiv (1 - \gamma\tilde{\gamma})^{-1}$, and their tilde-conjugates defined by $\tilde{f}(x, E) \equiv f^*(x, -E)$. An equivalent equation for $\tilde{\gamma}$ can be found by tilde-conjugation of Eq. (2). In Eq. (2), we have also incorporated the possibility of a magnetic exchange field $\mathbf{h} = |\mathbf{h}|$ which allows us to later consider the case of a ferromagnetic metal. The other quantities in the equation are the inelastic scattering rate δ , and the short-hand notations

$$G \equiv \sum_{\pm} \mathcal{N}_{\pm}(1 + \gamma_{\pm}\tilde{\gamma}_{\pm}), \quad F \equiv -2\sum_{\pm} \mathcal{N}_{\pm}\gamma_{\pm}, \quad (3)$$

where $\gamma_{\pm} \equiv \gamma(x, E \pm \omega/2)$. From these equations, physical quantities of interest may be computed, such as the proximity-modified density of states

$$N/N_0 = \text{Re}\{\text{Tr}(\mathcal{N})\} - 1. \quad (4)$$

The Usadel equation is supplemented by the Kupriyanov-Lukichev boundary conditions³³, which are valid at low-transparency tunneling interfaces.

We now have at hand a coupled set of non-linear partial differential equations which are non-local in energy space. A numerical solution can be obtained via iteration. After discretizing the energy space, the equations are initially solved for $\alpha = 0$. The procedure is then repeated with $\alpha \neq 0$ until self-consistency is achieved, using the solutions γ and $\tilde{\gamma}$ from the previous iteration to approximate G and F . In this way, we are able to compute the quasiclassical Green function in the presence of microwave radiation, $\hat{g}(\alpha \neq 0)$, and access the density of states N/N_0 in the proximate metal.

Results and Discussion

The light-interaction with the proximity-induced condensate has a strong effect on the spectral properties of the quasiparticles. We show this in what follows, considering an SN bilayer in Fig. 1, an SNS junction in Fig. 2, and an SF bilayer in Fig. 3. In each case, we have provided results for different system parameters in order to demonstrate the robustness of the microwave radiation influence.

Starting with the SN bilayer, it is seen that by tuning the microwave frequency ω , the density of states takes on qualitatively different characteristics. At $\omega/\Delta_0 = 0.4$, there is a strong quasiparticle accumulation at $E = 0$, diametrically opposite to the hallmark minigap that usually is present in SN bilayers. Increasing ω gradually to $\omega/\Delta_0 = 1.0$ causes the density of states to revert to a minigap structure, albeit with a much reduced magnitude. We

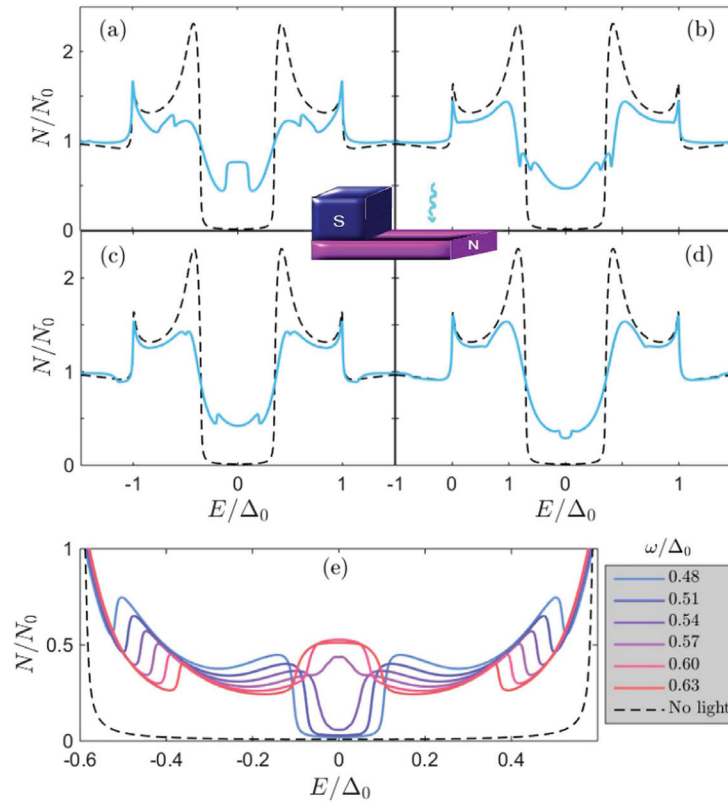


Figure 1. (a–d) Proximity-induced density of states at the vacuum edge ($x=L$) of an SN bilayer with length $L/\xi = 0.5$ of the N region, where ξ is the superconducting coherence length. We set the barrier strength $\zeta = 3$ and microwave field amplitude $\alpha/\Delta_0 = 0.1$ and (a) $\omega/\Delta_0 = 0.4$, (b) $\omega/\Delta_0 = 0.6$, (c) $\omega/\Delta_0 = 0.8$, (d) $\omega/\Delta_0 = 1.0$. (e) Zoom-in near $E=0$ illustrating the transition from minigap to quasiparticle accumulation peak as ω is tuned to E_{mg} . We set $L/\xi = 0.33$, yielding $E_{\text{mg}} \simeq 0.56\Delta_0$. The black dashed line corresponds to the absence of light, $A=0$.

will later in this manuscript describe the precise condition leading to the appearance of the quasiparticle accumulation peak and its physical origin, providing also analytical results which supports the underlying explanation. In the plots, we have set $\alpha/\Delta_0 = 0.1$, which gives a maximum ratio of $\alpha/\omega = 0.25$, so that α is always considerably smaller than ω . The criterion $\alpha \ll \omega$ is, however, more strictly satisfied at the higher frequency range considered in the figures.

The minigap itself is monotonically tuned with ω , as shown in Fig. 2 for the SNS case. At zero phase difference ϕ , the minigap is gradually reduced as ω increases, demonstrating that the driving frequency can be used to tailor the minigap size. At a finite phase difference, the light-interaction again inverts the minigap for certain frequencies, and generates a peak of quasiparticle accumulation at $E=0$, similarly to the bilayer case [see Fig. 1(e)]. This can be seen in Fig. 2(c) for $\phi/\pi = 0.5$. Finally, we show results for when an exchange field is present, i.e. a magnetic metal $h \neq 0$, in Fig. 3, in which case the microwave field also alters the modulation of the density of states. To facilitate comparison with experiments, we note that for a typical diffusion constant of e.g. $D = 7 \times 10^{-3} \text{ m}^2/\text{s}$ in Cu^{34} , the requirement $\omega \gg De^2A_0^2/4\hbar^2$ (having reinstated e and \hbar) corresponds to $\omega \gg 0.3 \text{ GHz}$ for a modest electric field magnitude of 0.1 V/m , which is feasible. Moreover, for a superconducting gap $\Delta_0 = 0.5 \text{ meV}$, the parameter choice $\hbar\omega/\Delta_0 = 0.4$ corresponds to a frequency $\omega \simeq 300 \text{ GHz}$.

Besides the control and inversion of the minigap, another particularly noteworthy feature that all the above-mentioned structures have in common is that the low-energy density of states features a series of spectral features resembling weak resonances, which vanish as soon as the microwave field is turned off ($\alpha = 0$). To gain insight into the physical origin of these features seen in the density of states, we provide an analytical solution which is permissible in the ferromagnetic case, but which also seems to account for the nature of the light interaction with the superconducting condensate in the normal case ($h = 0$). In the weak proximity effect regime, the linearized equation governing the behavior of the spinless f_s and spin-polarized f_i Cooper pairs reads

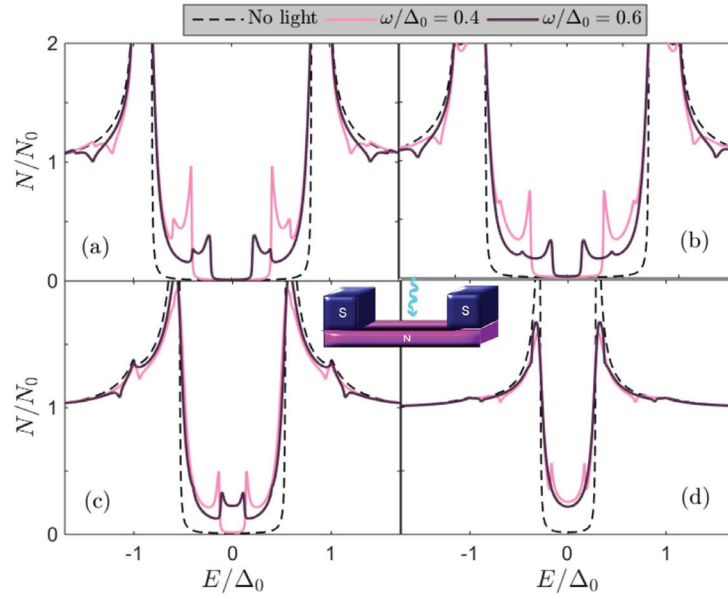


Figure 2. Proximity-induced density of states in the middle ($x=L/2$) of an SNS Josephson junction with $L/\xi = 0.33$, barrier strength $\zeta = 3$, microwave field amplitude $\alpha/\Delta_0 = 0.1$, and (a) $\phi/\pi = 0.0$, (b) $\phi/\pi = 0.25$, (c) $\phi/\pi = 0.5$, (d) $\phi/\pi = 0.75$.

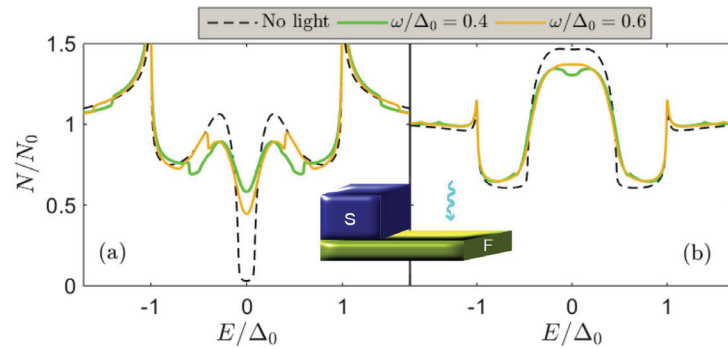


Figure 3. Proximity-induced density of states at the vacuum edge ($x=L$) of an SF bilayer with $L/\xi = 0.23$, barrier strength $\zeta = 3$, microwave field amplitude $\alpha/\Delta_0 = 0.1$, and (a) $h/\Delta_0 = 2$ and (b) $h/\Delta_0 = 4$.

$$D\partial_x^2 f_{\pm}(E) + 2i(E + 2i\alpha \pm h)f_{\pm}(E) - 2\alpha[f_{\pm}(E + \omega) + f_{\pm}(E - \omega)] = 0 \quad (5)$$

with $f_{\pm} = f_i \pm f_s$. In the regime where $h \gg \{E, \Delta_0\}$, as is usually the case for ferromagnets, one can solve the above equation via Fourier-transformation. Introducing $\mathcal{F}_{\pm}(t) = \int dE e^{iEt} f_{\pm}(E)$, one obtains

$$D\partial_x^2 \mathcal{F}_{\pm}(t) + 2i(2i\alpha \pm h)\mathcal{F}_{\pm}(t) - 4\alpha \cos(\omega t)\mathcal{F}_{\pm}(t) = 0.$$

The solution is $\mathcal{F}_{\pm}(t) = A_{\pm}(t)e^{ik_{\pm}x} + B_{\pm}(t)e^{-ik_{\pm}x}$, where

$$k_{\pm} = \sqrt{[2i(2i\alpha \pm h) - 4\alpha \cos(\omega t)]D^{-1}}, \quad (6)$$

while the coefficients $\{A_{\pm}, B_{\pm}\}$ are determined via the boundary conditions. For an SF bilayer, the boundary conditions read $\partial_x f_{\pm} = \pm f_{\text{BCS}}/C L$ at the superconducting interface ($x=0$), and $\partial_x f_{\pm} = 0$ at the vacuum border

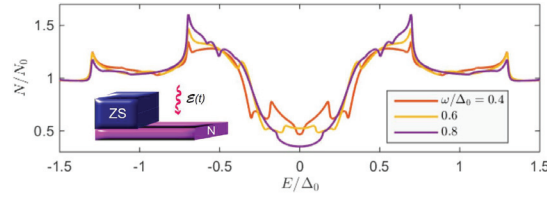


Figure 4. Proximity-induced density of states at the vacuum edge ($x=L$) of a Zeeman-split superconductor/normal-metal bilayer. We set $\zeta=3$, $\alpha/\Delta_0=0.1$, $L/\xi=0.5$, and $h_s/\Delta_0=0.3$, and considered several frequencies of the microwave radiation.

($x=L$), where $\zeta=R_B/R$ is the ratio between the interface barrier resistance and bulk resistance and $f_{\text{BCS}}(E)=\sinh\{\text{atanh}[1/(E+i\delta)]\}$.

Introducing the auxiliary quantity $D(t)=\int dE e^{iEt} f_{\text{BCS}}(E)$, a straight-forward calculation leads to

$$A_{\pm}(t)=\frac{\mp D(t)}{\zeta L i k_{\pm}(1-e^{2ik_{\pm}L})}, \quad B_{\pm}(t)=A_{\pm}(t)e^{2ik_{\pm}L}. \quad (7)$$

Inserting this into our expression for $\mathcal{F}_{\pm}(t)$ and performing an inverse Fourier-transformation, we end up with the final expression for $f_{\pm}(E)$:

$$f_{\pm}(E)=\mp \iint dt dE' e^{i(E'-E)t} f_{\text{BCS}}(E') p_{\pm}(t). \quad (8)$$

where we introduced

$$p_{\pm}(t)=\cos[k_{\pm}(x-L)][\zeta L k_{\pm} \sin(k_{\pm}L)]^{-1} \quad (9)$$

and $k_{\pm}=k_{\pm}(t)$. We note that $p_{\pm}(t)$ is a periodic function in t , while $f_{\text{BCS}} \rightarrow 0$ when $E \rightarrow \pm\infty$. In the absence of microwave radiation ($\alpha=0$), k_{\pm} becomes independent of t , and the above simplifies to the usual result $f_{\pm}(E)=\mp p_{\pm} \iint dt dE' e^{i(E'-E)t} f_{\text{BCS}}(E') = \mp p_{\pm} f_{\text{BCS}}(E)$. To solve the integral Eq. (8) in the general case, we make use of the periodicity of $p_{\pm}(t)$. The period is $T=2\pi/\omega$, so we can write the Fourier series $p_{\pm}(t)=\sum_n p_{n,\pm} e^{in\omega t}$, where $p_{n,\pm}=\frac{1}{T} \int_{-T/2}^{+T/2} dt p_{\pm} e^{-in\omega t}$. Performing the integral over t in Eq. (8) then leads to a sum over δ -functions, and one obtains:

$$f_{\pm}(E)=\mp \sum_{n=-\infty}^{n=+\infty} p_{n,\pm} f_{\text{BCS}}(E-n\omega). \quad (10)$$

Numerically, we find that it is usually sufficient with ~ 15 Fourier-coefficients $p_{n,\pm}$ to obtain a perfect representation of $p_{\pm}(t)$. Using the same procedure as above, one can also find an expression for the anomalous Green function in a Josephson geometry consisting of a superconductor/ferromagnet/superconductor trilayer. The only difference is the expression for $p_{\pm}(t)$, which takes the form

$$p_{\pm}(t)=\{\{\cos(k_{\pm}x)+e^{i\phi}\cos[k_{\pm}(x-L)]\}[\zeta L k_{\pm} \sin(k_{\pm}L)]^{-1}, \quad (11)$$

where ϕ is the phase difference between the superconductors.

From the analytical expression, it is clear that resonances should be expected whenever $E=\Delta_0 \pm n\omega$, $n=0, 1, 2, \dots$ since $f_{\text{BCS}}(E=\Delta_0)$ formally diverges, although this divergence is in practice diminished due to inelastic scattering. The weight of these resonances, i.e. the magnitude of their spectral peak, is in turn governed by the Fourier series coefficients p_n which depends on the other system parameters. We note that, very recently, similar features were reported for a narrow and thin dirty superconducting strip subject to microwave radiation in ref. 13. In the present proximity-system, there is an additional minigap E_{mg} in the system, and one might expect to have similar resonances at $E=E_{\text{mg}} \pm n\omega$. The density of states plots in Fig. 2 [see for instance (a) for $\omega/\Delta_0=0.4$] are consistent with this statement, demonstrating how additional spectral features, which are not present in the absence of light, occur at such excitation energies. It actually turns out that these resonances are the physical origin behind the transition from the minigap to the quasiparticle accumulation peak at $E=0$. To be exact, the transition from fully gapped DOS to a strong zero-energy peak occurs precisely when $\omega=E_{\text{mg}}$. We show an example of this behavior at the bottom of Fig. 1. It is intriguing that the light-interaction actually induces a second, inner minigap which upon closing generates this feature, whereas the outer minigap E_{mg} remains [see e.g. Fig. 2(a) showing a particularly clear example of the inner and outer minigaps].

The fact that the microwave radiation induces a series of weak resonances shifted with $\pm n\omega$ from the conventional spectral peaks ($E=\Delta$ and $E=E_{\text{mg}}$ in the normal metal case) has interesting consequences when a finite magnetic field splits the density of states in the superconductor³⁵, since the exchange field in the superconductor h_s itself produces a similar shift in the spectral peaks from Δ_0 to $\Delta_0 \pm h_s$. We show the corresponding proximity-induced density of states in Fig. 4, where the combined influence of the exchange field and the light

interaction produce a very rich subgap structure in the density of states. Since the superconductor in this particular case, unlike the previous systems considered in this work, has to be sufficiently thin to permit the homogeneous penetration of a magnetic field, the microwave field is not completely shielded by the superconductor and we thus here assumed that $\mathcal{E}(t)$ is applied only to the non-superconducting part.

The most remarkable feature is nevertheless the influence of the microwave field on the minigap in the SN case, controlling its magnitude and even transforming it into a quasiparticle accumulation peak at $E=0$. These results may represent the first step toward a different way to control the superconducting proximity effect, and thus the available spin- and charge-carriers, in normal and magnetic metals, by using microwave radiation. One advantage of this is the fact that the control is *in situ* and that the length of the system (setting the Thouless energy scale), which normally changes the minigap, does not have to be altered, which would inevitably require fabrication of multiple samples. The zero-energy peak induced by the light-interaction resembles the type of spectral feature that is characteristically seen in the density of states of conventional SF structures due to odd-frequency superconductivity^{36–38}, but in this case it occurs without any such pairing at all. It could also be of interest to examine the consequences of the predictions made herein with regard to conductivity experiments³⁹ and non-equilibrium Josephson contacts⁴⁰.

Concluding remarks

Building on these results, an interesting future direction to explore would be the influence of light on supercurrents and the critical temperature in magnetic proximity systems, to see if the microwave radiation may be used to manipulate these quantities as well, which we intend to explore in a future work. The interaction between light and Cooper pairs could in this way open a different route to active control of quantum coherent phenomena in superconducting proximity structures.

Methods

Derivation of the Usadel equation incorporating microwave radiation. The time-dependent Usadel equation may be written as

$$D \nabla \circ (\hat{g} \circ \nabla \circ \hat{g}) = -i [E \hat{\rho}_3, \hat{g}], \quad (12)$$

where we defined the gauge-covariant derivative

$$\nabla \circ \hat{g} \equiv \nabla \hat{g} - ie [A \hat{\rho}_3, \hat{g}], \quad (13)$$

the commutator $[a, b] \equiv a \circ b - b \circ a$, and the associated product

$$(a \circ b)(E, T) \equiv e^{i(\partial_{E_1} \partial_{T_2} - \partial_{E_2} \partial_{T_1})/2} a(E_1, T_1) \times b(E_2, T_2) \Big|_{E_1=E_2=E, T_1=T_2=T}. \quad (14)$$

Above, e is the electron charge, E is the quasiparticle energy, and A is the time-dependent vector potential which describes, in our case, an ac electric field $E = -\partial A / \partial t$. We note that a useful property of the \circ -product is that:

$$a(E, T) \circ e^{i\omega T} = e^{i\omega T} a(E - \omega/2, T), \quad e^{i\omega T} \circ a(E, T) = e^{i\omega T} a(E + \omega/2, T). \quad (15)$$

These relations are useful in the present context since we can write the gauge field as

$$A(T) = A_0 (e^{i\omega T} + e^{-i\omega T})/2. \quad (16)$$

We set $|e|=1$ in what follows for brevity of notation and also apply the electric field perpendicularly to the junction direction, so that

$$\nabla \cdot A = A \cdot \nabla = 0. \quad (17)$$

In this case, the left hand side of Eq. (12) becomes

$$D \nabla \cdot (\hat{g} \circ \nabla \hat{g}) - D [A \hat{\rho}_3, \hat{g} \circ A \hat{\rho}_3 \circ \hat{g} - A \hat{\rho}_3]. \quad (18)$$

Since $A = A(T)$ is independent on E we have

$$A \hat{\rho}_3 A \hat{\rho}_3 = A^2 \hat{1}. \quad (19)$$

Moreover, the Green function satisfies the normalization condition

$$\hat{g} \circ \hat{g} = \hat{1}. \quad (20)$$

This brings us to

$$D \nabla \cdot (\hat{g} \circ \nabla \hat{g}) - D [A \hat{\rho}_3 \circ \hat{g} \circ A \hat{\rho}_3, \hat{g}]. \quad (21)$$

At this stage, we see that the contribution from the gauge field can be included as a self-energy

$$\hat{\Sigma}_A = iDA\hat{\rho}_3 \circ \hat{g} \circ A\hat{\rho}_3 \quad (22)$$

in the Usadel equation, which in its complete form reads:

$$D\nabla \cdot (\hat{g} \circ \nabla \hat{g}) + i[E\hat{\rho}_3 + iDA\hat{\rho}_3 \circ \hat{g} \circ A\hat{\rho}_3, \hat{g}] = 0. \quad (23)$$

The next step is to obtain the Fourier-transformed version of the above equation in energy-space. To accomplish this, we make use of similar approximations as in ref. 13. In the presence of a driving field $A(T)$, we take into account A up to second order by deriving an equation for the harmonic Green function at zero frequency (see Appendix of ref. 13) which is essentially the time-averaged Green function. Higher order harmonic time-dependent terms in \hat{g} are induced by A and thus correspond to fourth order in A and higher. This approximation is valid when

$$DA_0^2/4 \ll \omega. \quad (24)$$

Computing the contribution from the self-energy term $\hat{\Sigma}_A$ in the Usadel equation gives

$$\begin{aligned} i[\hat{\Sigma}_A, \hat{g}] &= -\frac{DA_0^2}{4} [(e^{i\omega T} + e^{-i\omega T})\hat{\rho}_3 \circ \hat{g} \circ (e^{i\omega T} + e^{-i\omega T})\hat{\rho}_3 \circ \hat{g} \\ &\quad - \hat{g} \circ (e^{i\omega T} + e^{-i\omega T})\hat{\rho}_3 \circ \hat{g} \circ (e^{i\omega T} + e^{-i\omega T})\hat{\rho}_3]. \end{aligned} \quad (25)$$

We now average Eq. (25) over a period $2\pi/\omega$, which means that all terms that go like $e^{\pm 2i\omega T}$ are removed since \hat{g} is the time-averaged Green function. After laborious calculations, using for instance that

$$\begin{aligned} &e^{i\partial_{E_1}\partial_{T_2}/2} \left[1 - \frac{i}{2}\partial_{E_2}\partial_{T_1} + \frac{1}{2}\left(\frac{i}{2}\right)^2 (\partial_{E_2}\partial_{T_1})^2 - \dots \right] e^{\pm i\omega T_1} \hat{\rho}_3 \hat{g}(E_1 \pm \omega/2) e^{\mp i\omega T_2} \\ &\quad \times \hat{\rho}_3 \hat{g}(E_2 \mp \omega/2) \Big|_{E_1=E_2=E, T_1=T_2=T} \\ &= e^{i\partial_{E_1}\partial_{T_2}/2} \left[1 \mp \frac{i}{2}(i\omega)\partial_{E_2} + \frac{1}{2}\left(\frac{\omega}{2}\right)^2 (\partial_{E_2})^2 - \dots \right] e^{\pm i\omega T_1} \\ &\quad \times \hat{\rho}_3 \hat{g}(E_1 \pm \omega/2) e^{\mp i\omega T_2} \hat{\rho}_3 \hat{g}(E_2 \mp \omega/2) \Big|_{E_1=E_2=E, T_1=T_2=T} \\ &= e^{i\partial_{E_1}\partial_{T_2}/2} e^{\pm i\omega T_1} e^{\mp i\omega T_2} \hat{\rho}_3 \hat{g}(E_1 \pm \omega/2) \hat{\rho}_3 \hat{g}(E_2) \Big|_{E_1=E_2=E, T_1=T_2=T} \\ &= \hat{\rho}_3 \hat{g}(E \pm \omega) \hat{\rho}_3 \hat{g}(E) \end{aligned} \quad (26)$$

via Eq. (15), the remaining terms take the form

$$D\nabla \cdot (\hat{g} \nabla \hat{g}) + i[E\hat{\rho}_3 + i\alpha\hat{\rho}_3(\hat{g}_+ + \hat{g}_-)\hat{\rho}_3, \hat{g}] = 0, \quad (27)$$

where the \circ -commutators are now replaced with regular matrix commutators, $\alpha \equiv DA_0^2/4$, $\hat{g} = \hat{g}(x, E)$ is the quasiclassical Green function, while

$$\hat{g}_{\pm} \equiv \hat{g}(x, E \pm \omega/2). \quad (28)$$

Derivation of the linearized Usadel equation (weak proximity effect). Analytical progress can be made in the so-called weak proximity effect regime, where one assumes that the magnitude of the superconducting proximity effect is small in the sense that the anomalous Green function components f satisfy $|f| \ll 1$. Physically, such a situation is realized either in the case of a low interface transparency between the superconducting and normal part or if the temperature is close to the critical temperature of the superconductor. This allows for a linearization of the Usadel equation in the anomalous Green functions in the following manner³. The total Green function matrix in Nambu-spin space may be written as the normal-state matrix \hat{g}_0 and a small deviation \hat{f} :

$$\hat{g} \simeq \hat{g}_0 + \hat{f}, \quad (29)$$

where $\hat{g}_0 = \hat{\rho}_3$ and the anomalous Green function matrix can be written as

$$\hat{f} = \begin{pmatrix} \underline{0} & \underline{f} \\ -\underline{\tilde{f}} & \underline{0} \end{pmatrix}. \quad (30)$$

The 2×2 matrix \underline{f} in spin space describes the four types of anomalous Green functions that can be present in the system: one describing spin-singlet Cooper pairs (f_s) and three describing spin-triplet Cooper pairs ($f_{\uparrow\uparrow}, f_{\downarrow\downarrow}, f_t$). The f_t component corresponds to the $S=1, S_z=0$ component of the triplets with spin-symmetry $\uparrow\downarrow + \downarrow\uparrow$ and the $\tilde{\cdot}$ operation is defined in the main text. For the systems considered in our work, with homogene-

ous exchange fields, we find that $f_{\sigma\sigma} = 0$ whereas f_s and f_t can be non-zero. Inserting Eq. (29) into Eq. (2) in the main manuscript produces the linearized equation

$$D\partial_x^2 f_{\pm}(E) + 2i(E + 2i\alpha \pm h)f_{\pm}(E) - 2\alpha[f_{\pm}(E + \omega) + f_{\pm}(E - \omega)] = 0 \quad (31)$$

with $f_{\pm} = f_t \pm f_s$. This governs the behavior of the spinless f_s and spin-polarized f_t Cooper pairs induced in the normal metal.

References

1. J. Linder & J. W. A. Robinson. Superconducting spintronics. *Nat. Phys.* **11**, 307 (2015).
2. J. W. A. Robinson & M. G. Blamire. The interface between superconductivity and magnetism: understanding and device prospects. *J. Phys.: Cond. Mat.* **26**, 453201 (2014).
3. M. Eschrig. Spin-polarized supercurrents for spintronics: a review of current progress. *Rep. Prog. Phys.* **78**, 10 (2015).
4. I. O. Kulik. Nonlinear High-frequency Properties of Thin Superconducting Films. *Sov. Phys. JETP* **30**, 329 (1970).
5. A. Gurevich. Reduction of Dissipative Nonlinear Conductivity of Superconductors by Static and Microwave Magnetic Fields. *Phys. Rev. Lett.* **113**, 087001 (2014).
6. F. S. Bergeret, P. Virtanen, T. T. Heikkilä & J. C. Cuevas. Theory of Microwave-Assisted Supercurrent in Quantum Point Contacts. *Phys. Rev. Lett.* **105**, 117001 (2010).
7. F. Kos, S. E. Nigg & L. I. Glazman. Frequency-dependent admittance of a short superconducting weak link. *Phys. Rev. B* **87**, 174521 (2013).
8. P. Virtanen, T. T. Heikkilä & F. S. Bergeret. Stimulated quasiparticles in spin-split superconductors. *Phys. Rev. B* **93**, 014512 (2016).
9. M. S. Kalenkov & A. D. Zaikin. Diffusive superconductors beyond the Usadel approximation: Electron-hole asymmetry and large photoelectric effect. *Phys. Rev. B* **92**, 014507 (2015).
10. P. Virtanen *et al.* Theory of Microwave-Assisted Supercurrent in Diffusive SNS Junctions. *Phys. Rev. Lett.* **104**, 247003 (2010).
11. J. E. Mooji. In *Nonequilibrium Superconductivity, Phonons and Kapitza Boundaries*, edited by K. E. Gray (Plenum, New York, 1981).
12. V. M. Dmitriev, V. N. Gubankov & F. Y. Nad. In *Nonequilibrium Superconductivity*, edited by D. N. Langenberg & A. I. Larkin (North-Holland, Amsterdam 1986).
13. A. V. Semenov, I. A. Devyatov, P. J. de Visser & T. M. Klapwijk. Coherent Excited States in Superconductors due to a Microwave Field. *Phys. Rev. Lett.* **117**, 047002 (2016).
14. A. P. Mackenzie & Y. Maeno. The superconductivity of Sr_2RuO_4 and the physics of spin-triplet pairing. *Rev. Mod. Phys.* **75**, 657 (2003).
15. V. L. Berizinskii. New model of the anisotropic phase of superfluid He^3 . *JETP Lett.* **20**, 287 (1974).
16. A. Di Bernardo *et al.* Intrinsic Paramagnetic Meissner Effect Due to s-Wave Odd-Frequency Superconductivity. *Phys. Rev. X* **5**, 041021 (2015).
17. A. Di Bernardo *et al.* Signature of magnetic-dependent gapless odd frequency states at superconductor/ferromagnet interfaces. *Nat. Commun.* **6**, 8053 (2015).
18. Y. Kalcheim, O. Millo, A. Di Bernardo, A. Pal & J. W. A. Robinson. Inverse proximity effect at superconductor-ferromagnet interfaces: Evidence for induced triplet pairing in the superconductor. *Phys. Rev. B* **92**, 060501(R) (2015).
19. J. Bardeen, L. N. Cooper & J. R. Schrieffer. Theory of Superconductivity. *Phys. Rev.* **108**, 1175 (1957).
20. T. Yamashita, S. Takahashi, H. Imamura & S. Maekawa. Spin transport and relaxation in superconductors. *Phys. Rev. B* **65**, 172509 (2002).
21. H. Yang, S.-H. Yang, S. Takahashi, S. Maekawa & S. S. P. Parkin. Extremely long quasiparticle spin lifetimes in superconducting aluminium using MgO tunnel spin injectors. *Nature Mater.* **9**, 586 (2010).
22. C. H. L. Quay, D. Chevallier, C. Bena & M. Aprili. Spin imbalance and spin-charge separation in a mesoscopic superconductor. *Nature Phys.* **9**, 84 (2013).
23. F. Hübner, M. J. Wolf, D. Beckmann & H. v. Löhneysen. Long-range spin-polarized quasiparticle transport in mesoscopic Al superconductors with a Zeeman splitting. *Phys. Rev. Lett.* **109**, 207001 (2012).
24. T. Wakamura, N. Hasegawa, K. Ohnishi, Y. Niimi & Y. Otani. Spin injection into a superconductor with strong spin-orbit coupling. *Phys. Rev. Lett.* **112**, 036602 (2014).
25. D. Beckmann. Spin manipulation in nanoscale superconductors. *J. Phys. Cond. Mat.* **28**, 163001 (2016).
26. J. Rammer & H. Smith. Quantum field-theoretical methods in transport theory of metals. *Rev. Mod. Phys.* **58**, 323 (1986).
27. W. Belzig, F. K. Wilhelm, C. Bruder, G. Schön & A. D. Zaikin. Quasiclassical Green's function approach to mesoscopic superconductivity. *Superlattices Microstruct.* **25**, 1251 (1999).
28. V. Chandrasekhar. *An introduction to the quasiclassical theory of superconductivity for diffusive proximity-coupled systems*, Chapter published in, "The Physics of Superconductors", Vol II, edited by Bennemann & Ketterson, Springer-Verlag (2004).
29. K. Usadel. Generalized Diffusion Equation for Superconducting Alloys. *Phys. Rev. Lett.* **25**, 507 (1970).
30. H. le Sueur *et al.* Phase Controlled Superconducting Proximity Effect Probed by Tunneling Spectroscopy. *Phys. Rev. Lett.* **100**, 197002 (2008).
31. N. Schopohl & K. Maki. Quasiparticle spectrum around a vortex line in a d-wave superconductor. *Phys. Rev. B* **52**, 490 (1995).
32. N. Schopohl. Transformation of the Eilenberger Equations of Superconductivity to a Scalar Riccati Equation. arXiv:cond-mat/9804064.
33. M. Y. Kupriyanov & V. F. Lukichev. Influence of boundary transparency on the critical current of "dirty" S/S structures. *Sov. Phys. JETP* **67**, 1163 (1988).
34. S. Gueron *et al.* Superconducting Proximity Effect Probed on a Mesoscopic Length Scale. *Phys. Rev. Lett.* **77**, 3025 (1996).
35. R. Meservey, P. M. Tedrow & P. Fulde. Magnetic Field Splitting of the Quasiparticle States in Superconducting Aluminum Films. *Phys. Rev. Lett.* **25**, 1270 (1970).
36. T. Kontos, M. Aprili, J. Lesueur & X. Grison. Inhomogeneous Superconductivity Induced in a Ferromagnet by Proximity Effect. *Phys. Rev. Lett.* **86**, 304 (2001).
37. T. Yokoyama, Y. Tanaka & A. A. Golubov. Manifestation of the odd-frequency spin-triplet pairing state in diffusive ferromagnet/superconductor junctions. *Phys. Rev. B* **75**, 134510 (2007).
38. J. Linder, A. Sudbø, T. Yokoyama, R. Grein & M. Eschrig. Signature of odd-frequency pairing correlations induced by a magnetic interface. *Phys. Rev. B* **81**, 214504 (2010).
39. M. S. Pambianchi, S. N. Mao & S. M. Anlage. Microwave surface impedance of proximity-coupled Nb/Al bilayer films. *Phys. Rev. B* **52**, 4477 (1995).
40. J. J. A. Baselmans, A. F. Morpurgo, B. J. van Wees & T. M. Klapwijk. Reversing the direction of the supercurrent in a controllable Josephson junction. *Nature* **397**, 43 (1999).

Acknowledgements

Funding via the “Outstanding Academic Fellows” programme at NTNU, the COST Action MP-1201, the NT-Faculty, and the Research Council of Norway Grant numbers 216700 and 240806, is gratefully acknowledged.

Author Contributions

J.L. did the majority of the analytical and numerical calculations with support from M.A. and J.A.O. All authors contributed to the discussion of the results and the writing of the manuscript.

Additional Information

Competing financial interests: The authors declare no competing financial interests.

How to cite this article: Linder, J. *et al.* Microwave control of the superconducting proximity effect and minigap in magnetic and normal metals. *Sci. Rep.* **6**, 38739; doi: 10.1038/srep38739 (2016).

Publisher's note: Springer Nature remains neutral with regard to jurisdictional claims in published maps and institutional affiliations.



This work is licensed under a Creative Commons Attribution 4.0 International License. The images or other third party material in this article are included in the article's Creative Commons license, unless indicated otherwise in the credit line; if the material is not included under the Creative Commons license, users will need to obtain permission from the license holder to reproduce the material. To view a copy of this license, visit <http://creativecommons.org/licenses/by/4.0/>

© The Author(s) 2016

VI

Reference

M. Amundsen, [J.A. Ouassou](#), J. Linder.
Analytically determined topological phase diagram of the
proximity-induced gap in diffusive n -terminal Josephson junctions.
Scientific reports 7, 40578 (2017).
DOI: [10/F9K69K](#)

Contributions

JL conceived the idea of the project and performed the initial analytical and numerical calculations, with input from JAO and MA. The majority of the analytical results were obtained and refined by MA, with support from JL and JAO. All authors contributed to the discussion and writing. In particular, JAO had a minor supporting role in this collaboration: helping search for analytical solutions, joining the discussions of the results, and contributing to the writing of the final manuscript.

SCIENTIFIC REPORTS

OPEN

Analytically determined topological phase diagram of the proximity-induced gap in diffusive n -terminal Josephson junctions

Received: 26 October 2016
Accepted: 07 December 2016
Published: 17 January 2017

Morten Amundsen, Jabir Ali Ouassou & Jacob Linder

Multiterminal Josephson junctions have recently been proposed as a route to artificially mimic topological matter with the distinct advantage that its properties can be controlled via the superconducting phase difference, giving rise to Weyl points in 4-terminal geometries. A key goal is to accurately determine when the system makes a transition from a gapped to non-gapped state as a function of the phase differences in the system, the latter effectively playing the role of quasiparticle momenta in conventional topological matter. We here determine the proximity gap phase diagram of diffusive n -terminal Josephson junctions ($n \in \mathbb{N}$), both numerically and analytically, by identifying a class of solutions to the Usadel equation at zero energy in the full proximity effect regime. We present an analytical equation which provides the phase diagram for an arbitrary number of terminals n . After briefly demonstrating the validity of the analytical approach in the previously studied 2- and 3-terminal cases, we focus on the 4-terminal case and map out the regimes where the electronic excitations in the system are gapped and non-gapped, respectively, demonstrating also in this case full agreement between the analytical and numerical approach.

The interest in topological quantum phases of matter has grown steadily in recent years, and the fundamental importance of this topic in physics was recently recognized by Thouless, Haldane, and Kosterlitz being awarded the 2016 Nobel prize in physics for their contribution to this field. So far, specific material classes such as telluride-based quantum wells (HgTe, CdTe), bismuth antimony ($\text{Bi}_{1-x}\text{Sb}_x$) and bismuth selenide (Bi_2Se_3) have received the most attention in the pursuit of symmetry-protected topological phases and excitations^{1–4}. However, it was recently proposed⁵ that similar physics could be obtained using conventional superconducting materials. More specifically, by using multiterminal Josephson junctions, the authors of ref. 5 showed that it was possible to create an artificial topological material displaying Weyl singularities under appropriate conditions. In multiterminal Josephson junctions hosting well-defined Andreev bound states, the crossing of these states with the Fermi level has been shown to be analogous to Weyl points in 3D solids with the Andreev bound state taking on the role of energy bands and the superconducting phase differences corresponding to quasiparticle momenta. A considerable advantage in utilizing multiterminal Josephson junctions rather than 3D solids to study exotic phenomena such as Weyl singularities and topologically different phases is that the phase differences are much more easily controlled experimentally than the quasiparticle momenta.

In order to probe electronic excitations with topological properties, a key goal is to map out the phase diagram of the system in terms of when it is gapped or not. A gapped system here means that there are no available excitations in a finite interval around the Fermi level. The reason for why this is important is that transitions between topologically protected states can occur via gap closing, and so by identifying under which circumstances the system makes such a transition provides information about when the topological nature of the system's quantum state changes.

The arguably easiest way to probe such a phase transition is via the readily available density of states measurements, which pick up whether or not the system is gapped at a specific energy. The electronic density of states can be probed via conductance measurements, for instance in the form of tunneling between the system and a small metallic tip using so-called scanning tunneling microscopy. Recent previous works have considered the case of

Department of Physics, Norwegian University of Science and Technology, N-7491 Trondheim, Norway. Correspondence and requests for materials should be addressed to M.A. (email: morten.amundsen@ntnu.no)

3-terminal Josephson junctions, both in ballistic^{6,7} and diffusive systems⁸, and also the 4-terminal case in the case of chaotic cavities being connected to each other and the superconductors⁹. In particular the 4-terminal case is of interest due to the possibility of creating Weyl singularities⁵.

In terms of experimental realization, metallic diffusive systems are of high relevance as the conditions for realizing such systems are far less stringent than, for instance, the discrete Andreev bound states of quantum dots. However, the proximity-gap phase diagram has not yet been studied for the 4-terminal case involving diffusive normal metals.

Motivated by this, we here determine the proximity gap phase diagram of diffusive n -terminal Josephson junctions ($n \in \mathbb{N}$), both numerically and analytically, by identifying a class of solutions to the Usadel equation¹⁰ at zero energy in the full proximity effect regime. We present an analytical equation which provides the phase diagram for an arbitrary number of terminals n . After briefly demonstrating the validity of the analytical approach in the previously studied 2- and 3-terminal cases, we focus on the 4-terminal case and map out the regimes where the electronic excitations in the system are gapped and non-gapped, respectively, demonstrating also in this case full agreement between the analytical and numerical approach. Our results may serve as a guideline for exploring the interesting physics of multiterminal devices involving the experimentally prevalent and accessible scenario of diffusive metals connected to superconductors, which has a long history¹¹.

Theory

We will use the quasiclassical theory of superconductivity which is known to yield good agreement with experimental measurements on mesoscopic superconducting devices. As only non-magnetic structures will be considered here, only singlet Cooper pairs exist and it is possible to work in Nambu-space alone due to the spin degeneracy. Using a field operator basis $\psi = (\psi, \psi^\dagger)$, the 2×2 quasiclassical Green function matrix \underline{g} describing the existence of superconductivity in the system via the anomalous correlation function f reads:

$$\underline{g} = \begin{pmatrix} g & f \\ \tilde{f} & -\tilde{g} \end{pmatrix} \quad (1)$$

Here, $\{g, f\}$ are complex scalars that depend on position \mathbf{r} and quasiparticle energy E . In a bulk BCS superconductor with order parameter $\Delta = \Delta_0 e^{i\phi}$, \underline{g} takes the form:

$$\underline{g}_{\text{BCS}} = \begin{pmatrix} c & s e^{i\phi} \\ -s e^{-i\phi} & -c \end{pmatrix} \quad (2)$$

where $c \equiv \cosh(\theta)$, $s \equiv \sinh(\theta)$, and $\theta = \text{atanh}[\Delta_0/(E + i\delta)]$. Here, δ accounts for inelastic scattering processes and causes a smearing of the spectral density. In writing $\underline{g}_{\text{BCS}}$, we have used that $\tilde{c} = c$ and $\tilde{s} = -s$. The above matrix may be Ricatti-parametrized¹² in the same way as one would do in the case of non-degenerate spin (see e.g. ref. 13 for a general Ricatti-parametrization in this case) with two differences: (i) we have to let $\tilde{\gamma} \rightarrow -\tilde{\gamma}$, and (ii) treat $\{\gamma, \tilde{\gamma}\}$ as scalars rather than matrices. More specifically, we write the Green function in the form

$$\underline{g} = \begin{pmatrix} N(1 - \gamma\tilde{\gamma}) & 2N\gamma \\ 2\tilde{N}\tilde{\gamma} & -\tilde{N}(1 - \tilde{\gamma}\gamma) \end{pmatrix} \quad (3)$$

with $N = \tilde{N} = (1 + \gamma\tilde{\gamma})^{-1}$. The Usadel equation in the normal wires, which governs the behavior of the Green function \underline{g} , reads:

$$D\partial_x(\underline{g}\partial_x\underline{g}) + i[E\mathcal{I}_z, \underline{g}] = 0, \quad (4)$$

where D is the diffusion coefficient, \mathcal{I}_z is the third Pauli matrix, and E is the quasiparticle energy. Since we are interested in mapping out the regime where the system is gapped, it suffices to consider the behavior of \underline{g} at the Fermi level ($E=0$). In this case, we have $\tilde{\gamma} = \gamma^*$, and the Ricatti-parametrized Usadel equation [obtained by inserting Eq. (3) into Eq. (4)] determining γ takes the form

$$\partial_x^2 \gamma - \frac{2(\partial_x \gamma)^2 \gamma^*}{1 + |\gamma|^2} = 0. \quad (5)$$

This equation has the following general and exact solution if $\gamma \in \mathbb{R}$:

$$\gamma(x) = \tan(c_1 x + c_2). \quad (6)$$

Although a purely real γ might seem like a very particular case, this scenario in fact allows us to gain important information about the proximity-gap phase diagram. To see this, consider the expression for the normalized (against its normal-state value) density of states \mathcal{N} at zero energy:

$$\mathcal{N} = \frac{1 - |\gamma|^2}{1 + |\gamma|^2}. \quad (7)$$

The solution $\gamma = 0$ corresponds to the absence of superconducting correlations, i.e. completely closed gap, in which case the density of states resumes its normal-state value $\mathcal{N} = 1$. The solutions $\gamma = \pm 1$ correspond to the

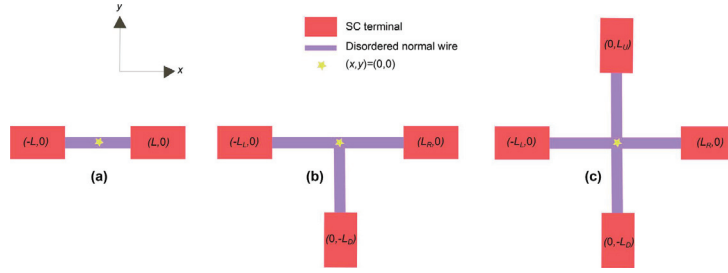


Figure 1. Multiterminal Josephson junctions. The density of states \mathcal{N} at zero energy (Fermi level) is measured at the point indicated by a star, i.e. at the intersection of the diffusive normal wires. **(a)** 2-terminal, **(b)** 3-terminal, and **(c)** 4-terminal setups. Since the wires are assumed to be diffusive, their precise geometrical orientation does not influence the topological properties of the system. For instance, the same 3-terminal topological phase diagram would have been obtained if the leads were connected in a Y-shape rather than a T-shape: only the physical properties of the wires (e.g. their Thouless energies) are of consequence.

fully gapped case $\mathcal{N} = 0$ where no available quasiparticle excitations exist at the Fermi level. The existence of such points can now be identified analytically by determining c_1 and c_2 in Eq. (6) via the boundary conditions in the N -terminal system. We later proceed to do so explicitly. It is also worth noting that Eq. (5) also has a general solution when γ is purely imaginary [$\gamma \in \mathbb{C}$, $\text{Re}(\gamma) = 0$]:

$$\gamma(x) = i \tan(c_1 x + c_2). \quad (8)$$

The solution Eq. (6) is of particular relevance in the case where the phase differences between the terminals is $n\pi$, with $n = 0, 1, 2, \dots$. The reason for this is that in such a scenario, one can choose a gauge where all superconducting order parameters are purely imaginary in the reservoirs (phases $\phi_j = \pi/2$ or $3\pi/2$), which renders the BCS anomalous correlation function $f = se^{i\phi_j}$ to be purely real at zero energy since $s(E=0) = -i$. If one assumes ideal boundary conditions at the superconducting interfaces, meaning that f is continuous, there are no imaginary terms in the boundary conditions or in the equation of motion for γ itself, meaning that the solution γ can be taken as real. From Eq. (7), it is clear that the maximum value of the Fermi-level density of states in the presence of a superconducting proximity effect is $\mathcal{N}_{\text{max}} = 1$. We can thus conclude that the analytical approach presented above is valid whenever the superconducting phase differences between the terminals are $n\pi$.

The above class of exact solutions are useful since they are valid at specific phase differences and provide information about whether or not the DOS is gapped there. However, we have identified an additional class of exact solutions which is useful because it is valid at *any phase-differences where $\mathcal{N} = 0$* , which is precisely the regime of interest. By noting that $\mathcal{N} = 0$ only when $|\gamma| = 1$, a reasonable ansatz is:

$$\gamma = -ie^{iS(x)}, S(x) \in \mathbb{R}. \quad (9)$$

The prefactor $-i$ is just a convention that simplifies the boundary conditions for S . Insertion into Eq. (5) gives immediately

$$S(x) = ax + b \quad (10)$$

where a and b are real constants determined by the boundary conditions. Besides allowing us to analytically determine the region in phase-space where the system is gapped, this solution also allows us to analytically compute the topological number associated with the gapped regime defined as¹⁴:

$$m = \oint \nabla S(\mathbf{r}) \cdot d\mathbf{r} \quad (11)$$

where $S(\mathbf{r})$ is interpreted as the phase of the superconducting correlations at $E=0$. There are several ways to relate the Riccati parameter γ to the physical properties of the system. First of all, it can be related to the physically observable density of states using Eq. (7). Moreover, when the system is fully gapped so that the zero-energy density of states $\mathcal{N} = 0$, γ is in fact just the anomalous Green function f , which quantifies the superconducting correlations in the system. This can be seen by comparing Eqs (1) and (3): in general, the anomalous Green function is given by $f = 2N\gamma$, but since $\gamma = -ie^{iS(\mathbf{r})}$ for a fully gapped system, we find that $N = [1 + e^{+iS(\mathbf{r})}e^{-iS(\mathbf{r})}]^{-1} = 1/2$ using the definition given above. It is assumed that the Green functions in the superconductors may be approximated by bulk expressions, and that the interfaces to the normal metals are transparent. This leads to the boundary conditions $S(\mathbf{r}_j) = \phi_j$, where \mathbf{r}_j are the locations of the terminals in Fig. 1, and ϕ_j are the corresponding phases. This can be deduced by comparing with the anomalous Green function in a bulk superconductor, $f_{\text{BCS}} = -ie^{i\phi}$.

Although Eq. (9) is exact whenever the system is gapped ($\mathcal{N} = 0$), it cannot be used carelessly because one still has to specify for which choices of the phases ϕ_j it is valid. It is clearly valid when all phases are equal in the system, so that the phase-difference between all terminals is zero. As we will later show, it is also valid in large regimes of phase-space, and one needs a criterion for when Eq. (9) can be used. Such a criterion can be obtained

in a convenient way by noting that as soon as $S(x)$ acquires a non-zero imaginary part, the consequence is that $\mathcal{N} \neq 0$. Identifying the condition for when a complex $S(x)$ becomes a possible solution is thus our strategy for describing analytically the topological phase diagram. By using Eq. (9) with $S(x) \in \mathbb{C}$ and writing $S(x) = S_r(x) + iS_i(x)$, Eq. (5) becomes

$$\partial_x^2 S + i(\partial_x S)^2 \left[1 - \frac{2}{1 + e^{2S_i}} \right] = 0 \quad (12)$$

It is observed that the solution of Eq. (12) reduces to Eq. (10) in the limit $S_i(x) \rightarrow 0$. This means that by allowing a small $S_i(x)$, it is possible to map out regions where Eq. (10) is not valid and the imaginary component begins to matter. To do so, we Taylor expand the square bracket of Eq. (12), and insert the perturbation expansion

$$S(x) = S_r(x) + i(\lambda S_{i1}(x) + \lambda^2 S_{i2}(x) + \dots) \quad (13)$$

where $S_{i1}(x) \ll S_r(x)$ and $S_{ik+1} \ll S_{ik}$. The expansion parameter λ is a helper variable used to collect different orders of the expansion. This gives

$$\lambda^0: \quad \partial_x^2 S_r = 0 \quad (14)$$

$$\lambda^1: \quad \partial_x^2 S_{i1} + (\partial_x S_r)^2 S_{i1} = 0 \quad (15)$$

and similarly for higher orders of λ . It is noticed in particular that Eq. (10) remains a solution for $S_i(x)$. The first order correction $S_{i1}(x)$ is easily solved, giving

$$S_{i1}(x) = C_1 \cos(ax) + C_2 \sin(ax) \quad (16)$$

In an n -terminal Josephson junction with transparent interface between superconductors and the normal metal, it is clear that $|\gamma| = 1$ at the interface regardless of the phase. The proper boundary conditions are therefore that $S_{ij}(x_j) = 0$, with x_j being the position of superconducting interface j . In addition, current conservation at the intersection between the arms of the multiterminal junction requires continuity of the Green function as well as the following relation between derivatives:

$$\sum_j \vec{e}_j \cdot \nabla \gamma_j = 0 \quad (17)$$

where γ_j is the solution of the Usadel equation in arm j , and \vec{e}_j is a unit vector pointing towards the intersection. Using these conditions, it is possible to formulate a criterion for when the purely real solution for $S(x)$ is valid, namely: Any combination of boundary conditions for which the only solution for $S_{ij}(x)$ possible is one where $C_1 = C_2 = 0$. The curves where this is *not* satisfied may be found from the boundary conditions for an n -terminal Josephson junction as

$$\sum_{j=1}^n \frac{\psi_j}{\tan \psi_j} = 0 \quad (18)$$

with ψ_j given as

$$\psi_j = \phi_j - \langle \phi \rangle = \phi_j - \frac{1}{n} \sum_{k=1}^n \phi_k \quad (19)$$

Equations (18) and (19) represent a key analytical result in this manuscript as they provide the phase diagram for the proximity-induced gap for an arbitrary number of terminals n . It is emphasized that the curves satisfying Eq. (18) only determine when a small imaginary contribution to $S(x)$ is possible and hence for which phases a transition between gapped and ungapped regimes in phase space occur. These curves are therefore referred to as transition curves. Higher order terms in the perturbation expansion are required in order to more accurately describe the ungapped regions. This is however not necessary when only interested in the gapped regions. It will be shown that it is possible to distinguish between the two regimes using only the first order correction.

To complement our analytical considerations, we also perform a fully numerical determination of the proximity-gap phase diagram by solving the Usadel equation numerically for any phase differences ϕ_j and without assuming ideal boundary conditions. In the following sections, we first provide a brief discussion of the already known 2-terminal and 3-terminal cases in order to prove the correctness of our novel analytical approach. Then, we proceed to discuss the less explored 4-terminal case in more detail.

We comment here that multiterminal geometries beyond effective 1D models can also be treated using the recently developed¹⁵ numerical solution of the full Usadel equation in 3D, allowing for the study of non-trivial geometrical effects. Moreover, previous works have considered analytical solutions of the Usadel equation using the so-called θ -parametrization in SN bilayers^{16–18} and also approximate solutions in the SNS case^{19–21}, whereas in our work the analytical solution is *exact* for the key cases of (i) $\mathcal{N} = 0$ and (ii) for phase differences $n\pi$ between the terminals.

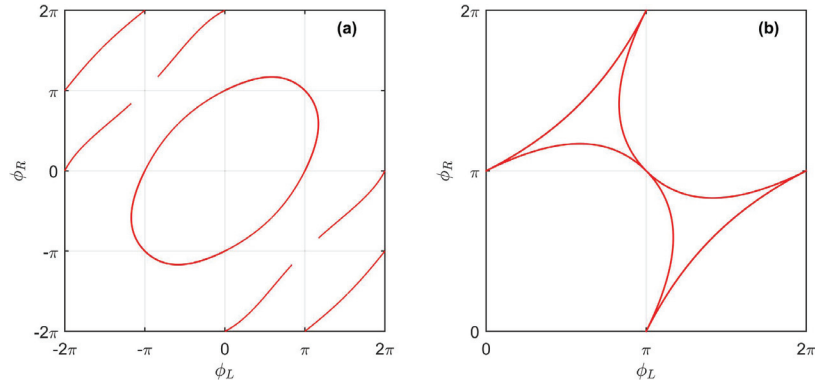


Figure 2. Analytically calculated transition curves between gapped and ungapped regions in the 3-terminal case. Plot of curves where the first order correction $S_{\pi}(x)$ can have non-zero solutions. (a) Structure of the condition in the extended phase space, showing metastable solutions. (b) Translation of physically relevant curves into $[0, 2\pi] \times [0, 2\pi]$.

Results: 2-terminal case

Assuming ideal boundary conditions at the superconducting interfaces $x = -L/2$ and $x = L/2$ see Fig. 1(a), real solutions of γ must satisfy $\gamma = \tan(c_1 x + c_2)$ where:

$$\tan(-c_1 L/2 + c_2) = -ie^{i\phi_L} \text{ and } \tan(c_1 L/2 + c_2) = -ie^{i\phi_R} \quad (20)$$

This restricts the superconducting phases to be $\phi_j = \{\pi/2, 3\pi/2\}$ in order to ensure $\gamma \in \mathbb{R}$. A number of solutions can be obtained from this. If $\phi_L = \pi/2$ and $\phi_R = 3\pi/2$ or vice versa, the solution is $c_2 = 0$ which gives a DOS in the center of the wire $\mathcal{N}(x = 0) = 1$. This is the expected result for a phase difference of π between the superconducting terminals. If instead the phase difference is zero, meaning $\phi_L = \phi_R = \{\pi/2, 3\pi/2\}$, then the solution is $c_2 = \pm\pi/4$, providing $\mathcal{N}(x = 0) = 0$. This is also consistent with the result that the DOS is allowed to be fully gapped when there is no phase difference. These results are in agreement with the condition given in Eq. (18), which identifies $\phi_L - \phi_R = n\pi$, $n = 1, 2, \dots$ as the only configurations for which a non-zero density of states is possible. The phase-dependent minigap in an SNS junction was originally considered in ref. 19.

Results: 3-terminal case

In the 3-terminal case, we consider the geometry of Fig. 1(b). The regions in phase space where $\mathcal{N}(x = 0, y = 0) = 0$ is mapped out using Eq. (18). Since only phase differences matter physically, we fix the phase of one superconducting terminal, $\phi_D = 0$, without loss of generality. Transition curves indicating the transition between gapped and ungapped regions are shown in Fig. 2(a) for the extended phase space $[-2\pi, 2\pi] \times [-2\pi, 2\pi]$. It can be seen that one such curve encircles the origin, with a near-elliptical shape, thereby splitting the plane into two regions. It is known that the origin resides in a gapped region, so that the outer region may be identified as ungapped. There also appears several open curves in the second and fourth quadrant. These curves are considered to be metastable solutions, corresponding to a higher phase-winding of the superconducting correlations in the normal wires, and are not investigated further. Due to the 2π -periodicity of the superconducting phases, the physically relevant transition curves must be translated into $[0, 2\pi] \times [0, 2\pi]$, as shown in Fig. 2(b).

The density of states may also be computed analytically in the select points where the boundary conditions are real. Using Eq. (6), the solutions in the left, down, and right arm are written as $\gamma_L = \tan(c_1 x + c_2)$, $\gamma_R = \tan(c_3 x + c_4)$, $\gamma_D = \tan(c_5 x + c_6)$. For this particular calculation, it is necessary to set $\phi_D = \pi/2$ in order to make $\gamma_{\text{BCS},D} = -ie^{i\phi_D} = 1$ real. At the intersection point $(x, y) = (0, 0)$ continuity of the Green function and its derivative ensure continuity of the current. We assume here for simplicity equal lengths and normal-state conductances of the three normal wires, although the analytical treatment does not require this in general. In this case, we obtain the boundary conditions

$$\begin{aligned} \tan(-c_1 L + c_2) &= -ie^{i\phi_L}, & \tan(-c_5 L + c_6) &= 1, \\ \tan(c_3 L + c_4) &= -ie^{i\phi_R}, & (1 + \tan^2 c_2)(c_1 + c_5 - c_3) &= 0. \end{aligned} \quad (21)$$

The values of $\{\phi_L, \phi_R\}$ are restricted to $\pi/2$ and $3\pi/2$ in order to ensure the validity of the solution for γ . Since $\tan c_2 \in \mathbb{R}$, the last boundary condition is equivalent to $c_1 + c_5 - c_3 = 0$. The above non-linear system of equations may be solved analytically, keeping the physically acceptable solution which gives $\mathcal{N} > 0$. For instance, for $(\phi_L, \phi_R) = (3\pi/2, 3\pi/2)$ one finds that $\tan(c_2) = -2 \pm \sqrt{3}$. The positive solution is the physically acceptable one since it provides $\mathcal{N} > 0$. The Fermi-level DOS in the center of the system $(x, y) = (0, 0)$ is given by

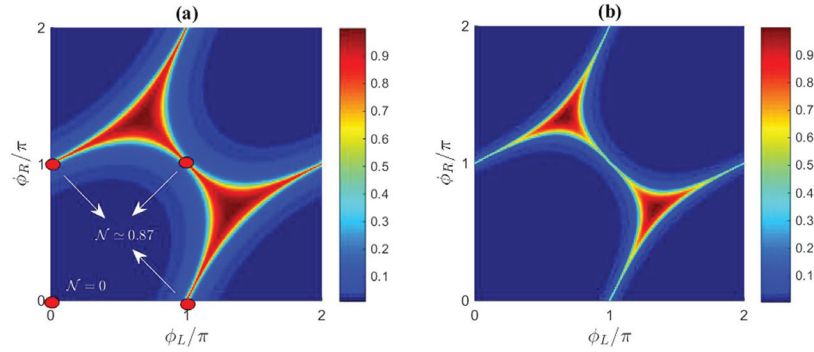


Figure 3. Numerically calculated proximity-gap phase diagram for 3-terminal Josephson junctions. Plot of the Fermi level density of states \mathcal{N} for a 3-terminal setup as a function of the phases ϕ_L and ϕ_R . For both plots, we set $L/\xi = 0.67$ and $\delta/\Delta_0 = 5 \times 10^{-3}$. The phase of the ‘down’ superconducting terminal has been set to $\phi_D = 0$. **(a)** Ideal boundary conditions. **(b)** Kupriyanov-Lukichev boundary conditions with finite interface resistance. We have set $\zeta_j = 2.5, j = \{L, R, D\}$.

$$\mathcal{N}(x = 0, y = 0) = \frac{1 - |\tan(c_2)|^2}{1 + |\tan(c_2)|^2}, \quad (22)$$

and we find from the solution of c_2 that:

$$\mathcal{N}(x = 0, y = 0) = \begin{cases} 0, & \text{if } (\phi_L, \phi_R) = (\pi/2, \pi/2) \\ 0.866, & \text{if } (\phi_L, \phi_R) = (\pi/2, 3\pi/2) \\ 0.866, & \text{if } (\phi_L, \phi_R) = (3\pi/2, \pi/2) \\ 0.866, & \text{if } (\phi_L, \phi_R) = (3\pi/2, 3\pi/2) \end{cases} \quad (23)$$

These solutions may be compared with the numerical solution of the full proximity-gap phase diagram in Fig. 3(a), where it can be seen that the analytically determined transition curves of Fig. 2(b) trace out exactly the regions where the density of states is non-zero. The excellent correspondance is explained by the rapid transition between the two regimes, as shown by the numerical solution. In addition, the four red circles are gauge-equivalent to the above phase-choices (note that in the figure we have set $\phi_D = 0$). As seen, the analytical expressions match the numerical result. In order to model a more realistic setting with finite interface transparencies, we provide the phase diagram using the Kupriyanov-Lukichev boundary conditions²² in Fig. 3(b). The interface transparency is quantified by the parameter $\zeta_j = R_{B,j}/R_{N,j}$ where $R_{B,j}$ is the barrier resistance and $R_{N,j}$ is the normal-state resistance of wire j . As seen, the gapped region extends compared to the fully transparent case, in agreement with ref. 8.

Results: 4-terminal case

We now focus on the 4-terminal case and demonstrate both the robustness of the analytical approach developed above in addition to providing comprehensive numerical results. The transition surface in the, now three dimensional, extended phase space is shown in Fig. 4(a), where ϕ_U has been fixed to zero and metastable solutions have been removed for clarity. It can be seen to have an ellipsoidal shape, which is an expected generalization of the 3-terminal case. Figure 4(b–d) show slices of the surface after translation into the first quadrant for $\phi_D = 0, \frac{\pi}{2}$ and π , respectively. The resulting phase diagram displays a more complicated behavior than in the 3-terminal case. At $\phi_D = 0$, the phase diagram is similar to the 3-terminal case, but as ϕ_D is increased toward $\pi/2$ one of the gapped regions expands greatly at the expense of the other gapped regions which are separated from each other by a ‘‘barrier’’ of finite DOS $\mathcal{N} \neq 0$. As ϕ_D is further increased toward π , the phase-diagram morphs into a qualitatively different shape than at $\phi_D = 0$, and at $\phi_D = \pi$ two of the gapped regions have been almost completely expelled from the phase diagram whereas two gapped ‘‘valleys’’ remain, the latter again separated by a non-gapped region.

With purely real boundary conditions, and $\phi_U = \frac{\pi}{2}$, the solutions in the left, down, right, and up arm are written as $\gamma_L = \tan(c_1x + c_2)$, $\gamma_D = \tan(c_3x + c_4)$, $\gamma_R = \tan(c_5x + c_6)$, $\gamma_U = \tan(c_7x + c_8)$. As in the previous section, we assume here for simplicity equal lengths and normal-state conductances of the four normal wires. The resulting boundary conditions take the form:

$$\begin{aligned} \tan(-c_1L_L + c_2) &= -ie^{i\phi_L}, \quad \tan(-c_5L_D + c_2) = -ie^{i\phi_D}, \quad \tan(c_3L_R + c_2) = -ie^{i\phi_R}, \\ \tan(c_7L_U + c_2) &= 1, \quad (c_1 + c_5 - c_3 - c_7) = 0. \end{aligned} \quad (24)$$

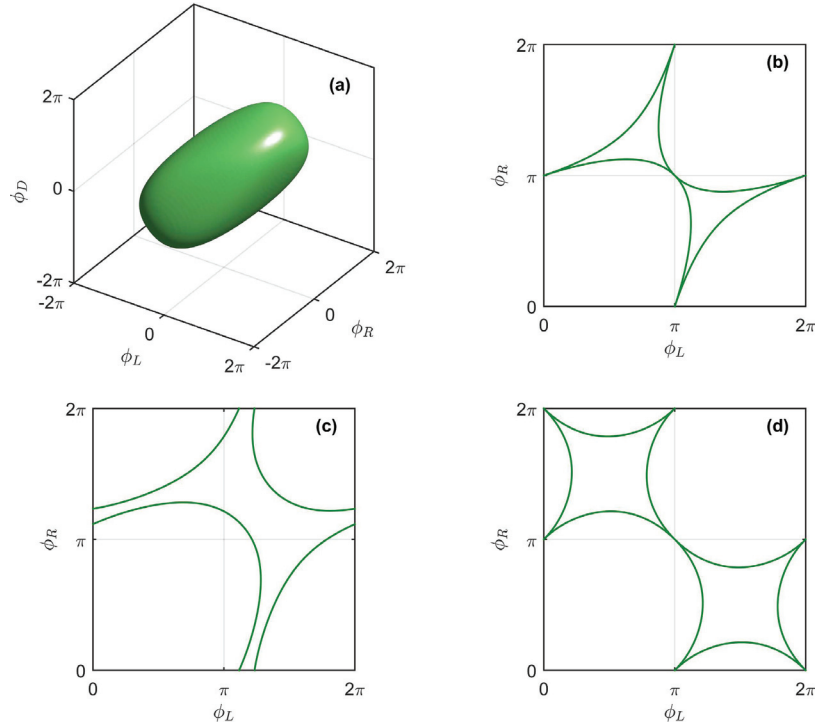


Figure 4. Analytically calculated transition curves between gapped and ungapped regions in the 4-terminal case. The mapping of three-dimensional phase space was performed using Eq. (18), with $\phi_U = 0$. (a) Transition surface in extended phase space. (b–d) Translation of physically relevant curves into the first quadrant for $\phi_D = 0, \frac{\pi}{2}$ and π , respectively.

	$(\phi_L, \phi_R) = (\pi/2, \pi/2)$	$(\phi_L, \phi_R) = (3\pi/2, \pi/2)$	$(\phi_L, \phi_R) = (\pi/2, 3\pi/2)$	$(\phi_L, \phi_R) = (3\pi/2, 3\pi/2)$
$\phi_D = \pi/2$	$\mathcal{N} = 0.00$	$\mathcal{N} = 0.71$	$\mathcal{N} = 0.71$	$\mathcal{N} = 1.00$
$\phi_D = 3\pi/2$	$\mathcal{N} = 0.71$	$\mathcal{N} = 1.00$	$\mathcal{N} = 1.00$	$\mathcal{N} = 0.71$

Table 1. Analytically obtained values of \mathcal{N} at special points in phase-space. The solution for the zero-energy DOS \mathcal{N} at the intersection point of the wires $(x, y) = (0, 0)$ obtained through analytically solving the non-linear equations for γ_j assuming transparent interfaces to the superconducting terminals (in contrast to Figs 5 and 6 where a finite interface resistance is used). We fixed $\phi_U = \pi/2$. At all points $(\phi_U, \phi_D, \phi_L, \phi_R)$ shown in the table, the analytically obtained value of \mathcal{N} matches the numerically obtained solution.

This non-linear system of equations may be solved analytically. Due to the requirement that $\gamma \in \mathbb{R}$, we restrict our attention to $\{\phi_L, \phi_R, \phi_U\}$ taking the values $\pi/2$ and $3\pi/2$. We provide the solutions in Table 1 which again match the values obtained from a fully numerical solution, thus indicating the correctness of our analytical approach.

We now proceed to present numerical results for the 4-terminal case when there exists a finite interface resistance between the superconducting terminals and the normal wires, which is experimentally more realistic. We fix $\phi_U = 0$ without loss of generality and plot the evolution of the proximity-gap phase diagram, quantified via the zero-energy DOS \mathcal{N} at the intersection point $(x, y) = (0, 0)$, as the remaining superconducting phases $\{\phi_U, \phi_D, \phi_L, \phi_R\}$ are varied in Fig. 5. Once again, the analytical transition curves correspond well with the regions where the numerically computed density of states differs from zero.

In an experimental setting, the phase-differences can be tuned by connecting the superconducting terminals and thus creating loops which a magnetic flux can pass through, the latter controlling ϕ_j . We consider in Fig. 6 the special case where the flux penetrating all loops is the same, meaning that the phase difference between each pair of terminals is equal to ϕ (except between the up and left terminal, see inset of Fig. 6). We set all wire lengths $L_j = L$ and interface resistances to be equal for simplicity, and consider different sizes L . Regardless of L , the superconducting correlations vanish completely at $\phi = \pi/2$ and $\phi = \pi$, as indicated by \mathcal{N} taking its normal state value

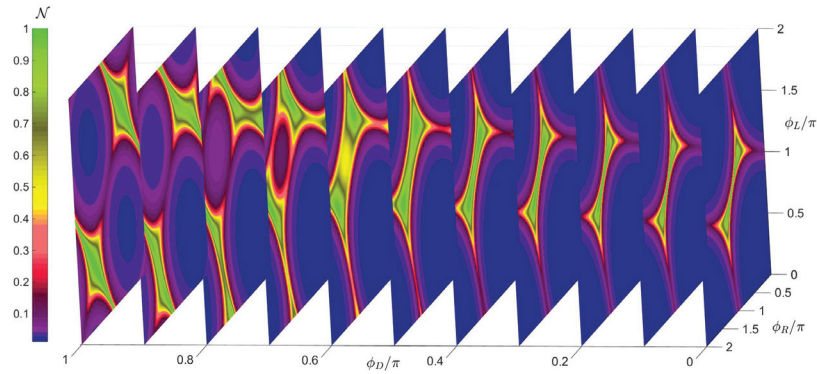


Figure 5. Numerically calculated density of states at $E=0$ for a 4-terminal Josephson junction for different phase-configurations. Setting the upper superconducting phase to zero without loss of generality, $\phi_U=0$, we plot the evolution of the proximity-gap phase diagram, quantified via the zero-energy density of states \mathcal{N} at the intersection between the wires, as the phases at the other superconducting terminals are varied. We have set the wire lengths equal to $L/\xi=0.67$ and the interface contact with the superconductors parametrized by a finite interface resistance ratio to the bulk resistance $\zeta=2.5$. The blue regions correspond to the gapped regime where $\mathcal{N}=0$.

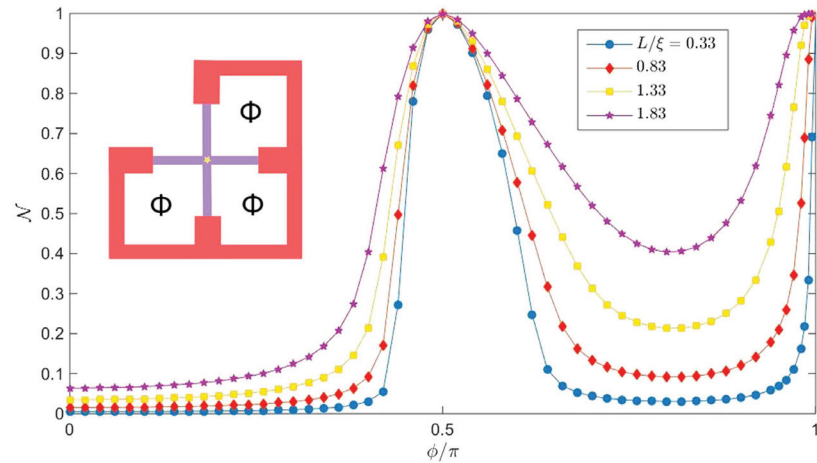


Figure 6. Numerically calculated density of states at $E=0$ for a 4-terminal Josephson junction for equal flux through the loops. Plot of the Fermi level density of states \mathcal{N} for a 4-terminal setup as a function of ϕ where $\phi_R=\phi$, $\phi_D=2\phi$, $\phi_L=3\phi$, which corresponds to a scenario where the same flux Φ penetrates loops that connects the superconducting terminals (see inset). We have set $\phi_U=0$ without loss of generality, $\delta/\Delta_0=3 \times 10^{-3}$, and $\zeta_j=2.5, j=\{L, R, D, U\}$.

($\mathcal{N}=1$). The gapped region at $0 < \phi < \pi/2$ for small lengths $L/\xi \ll 1$ starts to fill up with available electronic excitations as L increases.

Conclusion

The main new results in this work are the class of analytical solutions of the Riccati-parametrized Usadel equation at $E=0$ in the full proximity effect regime, the equations (18) and (19) providing the transition between the gapped and non-gapped regimes for an arbitrary number of terminals n , and the specific results for the 4-terminal case. An interesting expansion of the present work would be to explore how magnetic interfaces^{23–25} and spin-orbit coupling would influence the proximity-gap phase diagram and topological properties of multi-terminal Josephson junctions, as recent works have demonstrated that in particular the latter of these can induce several novel effects in both diffusive and ballistic superconducting hybrids^{13,26–34}.

References

- C.-K. Chiu, J. C. Y. Teo, A. P. Schnyder & S. Ryu. Classification of topological quantum matter with symmetries. *Rev. Mod. Phys.* **88**, 035005 (2016).
- M. Z. Hasan & C. L. Kane. Topological insulators. *Rev. Mod. Phys.* **82**, 3045 (2010).
- J. Alicea. New directions in the pursuit of Majorana fermions in solid state systems. *Rep. Prog. Phys.* **75**, 076501 (2012).
- X.-L. Qi & S.-C. Zhang. Topological insulators and superconductors. *Rev. Mod. Phys.* **83**, 1057 (2011).
- R.-P. Riwar, M. Houzet, J. S. Meyer & Y. V. Nazarov. Multi-terminal Josephson junctions as topological materials. *Nat. Commun.* **7**, 11167 (2016).
- B. van Heck, S. Mi & A. R. Akhmerov. Single fermion manipulation via superconducting phase differences in multiterminal Josephson junctions. *Phys. Rev. B* **90**, 155450 (2014).
- T. Yokoyama & Y. V. Nazarov. Singularities of Andreev spectrum in multi-terminal Josephson junction. *Phys. Rev. B* **92**, 155437 (2015).
- C. Padurariu *et al.* Closing the proximity gap in a metallic Josephson junction between three superconductors. *Phys. Rev. B* **92**, 205409 (2015).
- T. Yokoyama, J. Reutlinger, W. Belzig & Y. V. Nazarov. Order, disorder and tunable gaps in the spectrum of Andreev bound states in a multi-terminal superconducting device. *arXiv:1609.05455*.
- Usadel, K. D. Generalized diffusion equation for superconducting alloys. *Phys. Rev. Lett.* **25**(8), 507–509 (1970).
- W. Belzig *et al.* Quasiclassical Green's function approach to mesoscopic superconductivity. *Superlattices and Microstructures* **25**, 1251 (1999).
- N. Schopohl. Transformation of the Eilenberger equations of superconductivity to a scalar Riccati equation. *arxiv:cond-mat/9804064* (1998).
- S. H. Jacobsen, J. A. Ouassou & J. Linder. Critical temperature and tunneling spectroscopy of superconductor-ferromagnet hybrids with intrinsic Rashba-Dresselhaus spin-orbit coupling. *Phys. Rev. B* **92**, 024510 (2015). *arXiv:1603.00338*. *Nature Nanotechnology*. **11**, 1055–1059 (2016).
- M. Amundsen & J. Linder. General solution of 2D and 3D superconducting quasiclassical systems: coalescing vortices and nanoisland geometries. *Sci. Rep.* **6**, 22765 (2016).
- D. A. Ivanov & Ya. V. Fominov. Minigap in superconductor-ferromagnet junctions with inhomogeneous magnetization. *Phys. Rev. B* **73**, 214524 (2006).
- B. Crouzy, E. Bascones & D. A. Ivanov. Minigap in a superconductor-normal metal junction with paramagnetic impurities. *Phys. Rev. B* **72**, 092501 (2005).
- W. Belzig, C. Bruder & G. Schon. Local density of states in a dirty normal metal connected to a superconductor. *Phys. Rev. B* **54**, 9443 (1996).
- F. Zhou, P. Charlat, B. Spivak & B. Pannetier. Density of States in Superconductor-Normal Metal-Superconductor Junctions. *J. Low Temp. Phys.* **110**, 841 (1998).
- A. F. Volkov & V. V. Pavlovskii. Long-range thermoelectric effects in mesoscopic superconductor-normal metal structures. *Phys. Rev. B* **72**, 014529 (2005).
- A. F. Volkov, R. Seviour & V. V. Pavlovskii. Proximity-induced transport in hybrid mesoscopic normal-superconducting metal structures. *Superlattices and Microstructures* **25**, 647 (1999).
- Kuprianov, M. Y. & Lukichev, V. F. Influence of boundary transparency on the critical current of dirty SS'S structures. *Soviet Physics JETP*, **67**(6), 1163–1168 (1988).
- A. Cottet, D. Huertas-Hernando, W. Belzig & Y. V. Nazarov. Spin-dependent boundary conditions for isotropic superconducting Green's functions. *Phys. Rev. B* **80**, 184511 (2009).
- Eschrig, M., Cottet, A., Belzig, W. & Linder, J. General boundary conditions for quasiclassical theory of superconductivity in the diffusive limit: application to strongly spin-polarized systems. *New J. Phys.* **17**, 83037 (2015).
- Linder, J. & Robinson, J. W. A. Superconducting spintronics. *Nat. Phys.* **11**, 307 (2015).
- Bergeret, F. S. & Tokatly, I. V. Spin-orbit coupling as a source of long-range triplet proximity effect in superconductor-ferromagnet hybrid structures. *Phys. Rev. B* **89**, 134517 (2014).
- M. Houzet & J. S. Meyer. Quasiclassical theory of disordered Rashba superconductors. *Phys. Rev. B* **92**, 014509 (2015).
- Arjoranta, J. & Heikkilä, T. Intrinsic spin-orbit interaction in diffusive normal wire Josephson weak links: supercurrent and density of states. *Phys. Rev. B* **93**, 024522 (2016).
- C. Espedal, T. Yokoyama & J. Linder. Anisotropic paramagnetic Meissner effect by spin-orbit coupling. *Phys. Rev. Lett.* **116**, 127002 (2016).
- P. Högl, A. Matos-Abiague, I. Zutic & J. Fabian. Magnetoanisotropic Andreev Reflection in Ferromagnet-Superconductor Junctions. *Phys. Rev. Lett.* **115**, 116601 (2015).
- S. H. Jacobsen, I. Kulagina & J. Linder. Controlling superconducting spin flow with spin-flip immunity using a single homogeneous ferromagnet. *Sci. Rep.* **6**, 23926 (2016).
- F. Konschelle, I. V. Tokatly & F. S. Bergeret. Ballistic Josephson junctions in the presence of generic spin dependent fields. *Phys. Rev. B* **94**, 014515 (2016).
- J. A. Ouassou, A. Di Bernardo, J. W. A. Robinson & J. Linder. Electric control of superconducting transition through a spin-orbit coupled interface. *Sci. Rep.* **6**, 29312 (2016).
- K. Sun & N. Shah. General framework for transport in spin-orbit-coupled superconducting heterostructures: Nonuniform spin-orbit coupling and spin-orbit-active interfaces. *Phys. Rev. B* **91**, 144508 (2015).

Acknowledgements

J.L. was supported by the Research Council of Norway, Grant No. 216700 and the “Outstanding Academic Fellows” programme at NTNU. J.L. and J.A.O. were supported by the Research Council of Norway, Grant No. 240806.

Author Contributions

J.L. conceived the idea of the project and performed the initial analytical and numerical calculations with input from J.A.O. and M.A. The majority of the results for the analytical solution of the Riccati-equation and belonging phase-diagram were obtained and refined by M.A. with support from J.L. and J.A.O. All authors contributed to the discussion and writing of the manuscript.

Additional Information

Competing financial interests: The authors declare no competing financial interests.

How to cite this article: Amundsen, M. *et al.* Analytically determined topological phase diagram of the proximity-induced gap in diffusive n -terminal Josephson junctions. *Sci. Rep.* 7, 40578; doi: 10.1038/srep40578 (2017).

Publisher's note: Springer Nature remains neutral with regard to jurisdictional claims in published maps and institutional affiliations.



This work is licensed under a Creative Commons Attribution 4.0 International License. The images or other third party material in this article are included in the article's Creative Commons license, unless indicated otherwise in the credit line; if the material is not included under the Creative Commons license, users will need to obtain permission from the license holder to reproduce the material. To view a copy of this license, visit <http://creativecommons.org/licenses/by/4.0/>

© The Author(s) 2017

VII

Reference

A. Pal, [J.A. Ouassou](#), M. Eschrig, J. Linder, M.G. Blamire.
Spectroscopic evidence of odd frequency superconducting order.
Scientific reports 7, 40604 (2017).
DOI: 10/GFGR9X

Contributions

MGB and AP designed the experiment. AP grew the films, fabricated the devices, and performed the measurements. JAO, ME, and JL did the theoretical modelling. All authors contributed to writing the manuscript. In particular, JAO had a supporting role: fitting the experimental results to a theoretical model, and assisting with the writing of the manuscript.

Comments

The experiment was performed at the University of Cambridge.

SCIENTIFIC REPORTS

OPEN

Spectroscopic evidence of odd frequency superconducting order

Avradeep Pal¹, J. A. Ouassou², M. Eschrig³, J. Linder² & M. G. Blamire¹

Received: 11 October 2016
 Accepted: 30 November 2016
 Published: 20 January 2017

Spin filter superconducting S/I/N tunnel junctions (NbN/GdN/TiN) show a robust and pronounced Zero Bias Conductance Peak (ZBCP) at low temperatures, the magnitude of which is several times the normal state conductance of the junction. Such a conductance anomaly is representative of unconventional superconductivity and is interpreted as a direct signature of an odd frequency superconducting order.

In the context of paired electrons in superconductors (S), Pauli exclusion requires the electron pair to be odd in exchange in either spin, momentum, time (frequency) or across all three parameters. Spin singlet (odd spin) Cooper pairs are the standard carriers in conventional superconductors. Although much rarer, there is strong evidence for odd momentum (odd parity) superconductivity in Sr_2RuO_4 and in UPt^{1-3} and in artificially engineered hybrid structures⁴. So far, only indirect^{5,6} or weak⁷ signatures of odd frequency superconductivity has been obtained at S/F interfaces.

It is now widely accepted that odd frequency Cooper pairs can be generated at the interface of superconductors and ferromagnets. Where there is a region of inhomogeneous magnetization⁸⁻¹⁰, such pairs acquire a net spin and hence are immune to pair breaking due to the internal exchange field of the ferromagnet and can traverse distances much longer than the relevant singlet coherence length. Strong, but indirect evidence for the existence of such superconductivity has mainly been obtained through indirect measurements such as a long-ranged supercurrent^{5,6,11} or proximity effect¹².

Odd frequency Cooper-pairing should also give rise to an unconventional (non-BCS like) density of states (DOS) in the superconductor with an enhanced DOS at the Fermi level¹³⁻¹⁵. Evidence for such a DOS has recently been obtained via scanning tunnelling measurements of the local DOS of a Nb film proximity-coupled to a diffusive Ho layer⁷ but, because this has to be performed on an interface remote from that which is generating the odd-frequency pairing, only localized weak spectroscopic signatures of odd frequency pairing were detected.

In parallel with the work on diffusive ferromagnets, superconducting tunnel junctions with ferromagnetic insulator (FI) barriers have recently shown a range of intriguing effects, such as the appearance of a Josephson current with an unconventional pure second harmonic current-phase relation independent of a $0-\pi$ transition¹⁶, and an interfacial exchange field in the S layer¹⁷, which suggest that odd-frequency pairing is also being generated at the S/FI interface. Indeed, it has been very recently suggested in a theoretical study¹⁸ that strong odd-frequency pairing exists in Meservey-Tedrow type experiments with FIs¹⁹ that show Zeeman split DOS.

In this work, we present differential conductance measurements of NbN/GdN/TiN tunnel junctions, where GdN serves the purpose of both a spin active interface as well as a tunnel barrier - enabling direct measurement of the spatially averaged tunnelling DOS at the S/FI interface. The measured ZBCPs in such differential conductance measurements are larger by at least an order of magnitude than reported for diffusive systems, and hence provide definitive evidence for an odd frequency superconductivity at S/FI interfaces.

TiN was chosen as the metallic layer because an all nitride stack is required for the stability of GdN. Moreover, as stated later in this paper, one of the theoretical requirements for the observation of ZBCPs necessitates the choice of a metal, which has a Fermi vector largely different from superconducting NbN. Other possible metallic candidates like Au, Al and Cu have comparable Fermi vector as that of NbN.

Results and Discussion

Experimental. In Fig. 1, we show the temperature dependence of resistance of a 3 nm GdN junction. The spin-filter effect is clearly visible from the decrease in junction resistance below 33 K as exchange splitting of the conduction band lowers the transmission probability of one spin channel in comparison to the other²⁰. A sharp

¹Department of Materials Science, University of Cambridge, 27 Charles Babbage Road, Cambridge CB3 0FS, United Kingdom. ²Department of Physics, NTNU, Norwegian University, N-7491 Trondheim, Norway. ³SEPnet and Hubbard Theory Consortium, Department of Physics, Royal Holloway, University of London, Egham, Surrey TW20 0EX, United Kingdom. Correspondence and requests for materials should be addressed to A.P. (email: avradeep@gmail.com) or J.L. (email: jacob.linder@ntnu.no)

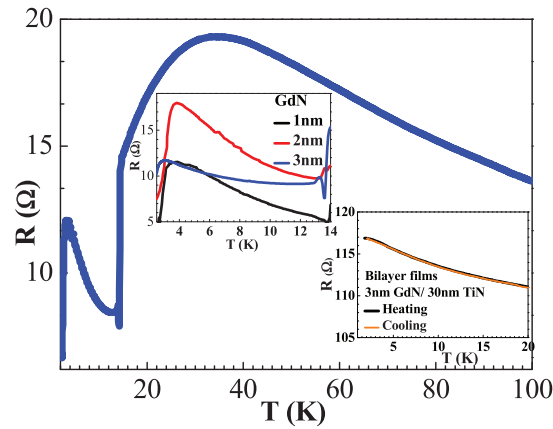


Figure 1. Temperature dependence of junction resistance. A 3 nm GdN junction measured at low bias. Top inset shows the Resistance vs Temperature (RT) dependence below superconducting transition of the NbN layer for junctions of 3 thicknesses – 1, 2, 3 nms. Bottom inset shows the RT dependence of a bilayer film of GdN and TiN to demonstrate the absence of superconducting transition in TiN films used in this work.

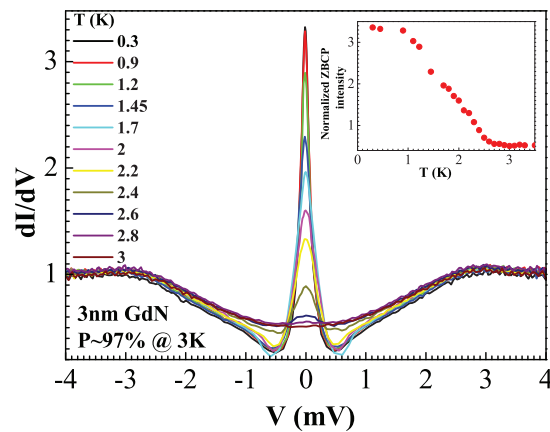


Figure 2. Evolution of Zero Bias Conductance Peak (ZBCP) with temperature. Differential conductance (dI/dV) measurements normalised to the normal state conductance of an 100 nm NbN/3 nm GdN/30 nm TiN tunnel junction showing evolution of a ZBCP with decreasing temperature. Inset to the figure shows the temperature dependence of the intensity of the ZBCP.

drop in resistance is observed below 14 K due to the superconducting transition of the NbN layer. Below 14 K, the observed rise in low bias resistance is due to the opening of the NbN gap and freezing out of sub-gap conductance. This rise of resistance below 14 K is reflective of a decreasing sub-gap resistance R_s to normal state resistance R_n ratio at low temperatures, and is therefore a signature of good quality junctions²¹. The drop in resistance below 4 K is due to the evolution of a zero bias conductance peak. To confirm the non-superconducting nature of the TiN used in these experiments, the temperature dependence of the resistance of un-patterned films of TiN/GdN grown in the same deposition run as that of the junctions, is shown in the bottom inset to Fig. 1. This shows no detectable superconducting transition above 1.6 K (the temperature limit of the cryostat used for Resistance vs Temperature (RT) measurements).

We observed that a wide range of properties can be obtained in TiN films by altering the nitrogen concentration. In order to obtain non-superconducting TiN, we have tuned the nitrogen concentration (8%) in the sputtering gas mixture.

In Fig. 2, we show the differential conductance curves of a junction with a 3 nm GdN barrier. The curves clearly show the emergence of a strong ZBCP as the junction is cooled to low temperatures. Identical characteristics have been found in all eight junctions on the same chip, and similar characteristics have also been found in all 8 junctions on the same chip of a thinner 2 nm GdN thickness tunnel junction which has spin-polarization

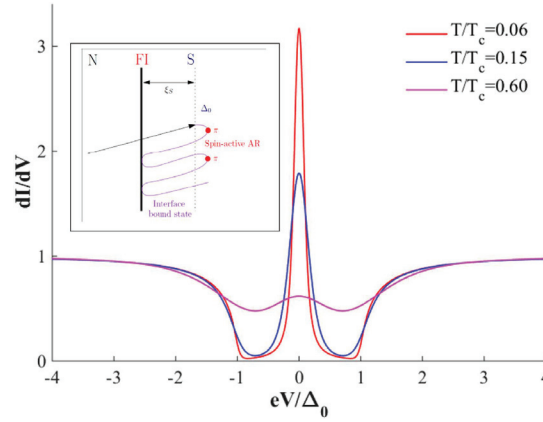


Figure 3. Theoretical dI/dV curves for an S/FI/N junction as a function of applied voltage eV . Following the framework of ref. 22, we have used transmission probabilities $D_{\uparrow} = 0.20$ and $D_{\downarrow} = 0.015$ for each spin species, a spin-mixing angle of 0.98π , and set the Dynes parameter to $0.05\Delta_0$. Inset: the formation of a zero-energy bound state at the interface due to spin-active Andreev reflection (AR) by the gap Δ_0 (indicated by red circles) where an additional phase-shift close to π is picked up by the quasiparticles.

(P)~65% at 4 K. The ZBCP in all junctions is extremely robust, reproducible, and independent of magnetic field history. The behaviour of these S/I/N junctions at temperatures above which the ZBCP disappears (>3 K), is well understood and has been addressed in detail in a previous publication¹⁷.

It has been theoretically predicted that for spin active interfaces, in the tunnelling limit, a subgap state appears due to spin-dependent phase-shifts²². This interface state is manifested via strong conductance peaks at a voltages $eV = \pm \Delta_0 \cos(\vartheta/2)$ where ϑ is the spin-dependent phase shift that is present due to the FI. For $\vartheta = \pi$ the state is pinned to the Fermi level (zero bias). The appearance of this interface state is intimately linked to odd-frequency pairing¹³.

ZBCPs are known to occur in several superconducting systems and for a variety of underlying physical mechanisms^{4,23–25}. A ZBCP analogous to our experiment observation is the case of d-wave superconductors²⁴, which occurs due to the sign change of the order parameter at regions in the a–b plane.

For s-wave superconductors, analogous phenomenon can be observed for sign change of the spin dependent phase shift due to the FI which translates to a phase shift of π . Such strong phase shifts^{26,27} can be obtained when (a) quasiparticles normal to the interface are the major contributors to the transport process, (b) when spin polarization by the barrier is high, (c) when the barrier profile is not sharp. All the above conditions are met by an NbN/GdN/TiN tunnel junction system, especially that of high spin polarization. An order of magnitude difference between Fermi vectors of NbN²⁸ and TiN²⁹ results in quasiparticles normal to the interface being the major contributors to the transport. A previous study has shown that NbN/GdN barrier is different from a conventional box type potential barrier, as a Schottky barrier forms at the NbN/GdN interface²⁰. The fact that all the conditions for obtaining a large spin-dependent phase-shift at the interface are met, taken in conjunction with the fact that the conductance spectra demonstrate a ZBCP is a clear indication that this phase-shift is likely to have a value very close to π .

Theoretical model. The experimental data in Fig. 2 can be modelled by the theoretical conductance of an S/FI/N structure with a spin-dependent phase-shift close to π , as shown in Fig. 3. The conductance for a ballistic S/FI/N structure has been studied previously²², and we have followed their analysis when fitting our experimental data. In the tunnelling limit, we neglect the suppression of the superconducting order parameter and use the following expression for the current density across the junction

$$J = J_N \int_{-\Delta}^{\Delta} \sum_{\pm} \frac{D_{\uparrow} D_{\downarrow} / D}{1 + R_{\uparrow} R_{\downarrow} - 2\sqrt{R_{\uparrow} R_{\downarrow}} \cos(2\delta \pm \vartheta)} T(E) dE + J_N \left(\int_{-\infty}^{-\Delta} + \int_{\Delta}^{\infty} \right) \frac{2 \cosh \delta [e^{-\delta} D_{\uparrow} D_{\downarrow} / D + \sinh \delta]}{e^{2\delta} + e^{-2\delta} R_{\uparrow} R_{\downarrow} - 2\sqrt{R_{\uparrow} R_{\downarrow}} \cos \vartheta} T(E) dE \quad (1)$$

where $T(E) = \tanh[\beta(E + eV)/2] - \tanh[\beta(E - eV)/2]$.

The following quantities have been defined in Eq. (1): $D = D_{\uparrow} + D_{\downarrow}$, J_N is the current density when the superconductor is in its normal state ($J_N \propto D$), D_{σ} and R_{σ} are the probability coefficients for transmission and reflection of spin σ carriers, respectively, $\beta = (k_B T)^{-1}$, V is the applied voltage, T is the temperature, E is the quasiparticle energy, Δ is the superconducting gap, ϑ is the spin-dependent phase-shift due to the magnetic barrier, and

$$\begin{aligned}\delta &= \arccos(E/\Delta) \text{ for } |E| < \Delta, \\ \delta &= \operatorname{acosh}(|E|/\Delta) \text{ for } |E| > \Delta.\end{aligned}\quad (2)$$

For the theoretically simulated conductance plots, we have differentiated Eq. (1) with respect to voltage and normalized the conductance against the normal-state conductance obtained at large voltages $eV \gg \Delta$. To model inelastic scattering, we have incorporated a Dynes parameter via the relation $E \rightarrow E + i\Gamma$ where Γ provides the quasiparticles with a finite lifetime. The model also accounts for the large difference in tunnelling probability for majority and minority carriers, as expected for a strongly polarized FI.

The temperature-evolution of the conductance spectra matches only qualitatively: the ZBCP vanishes experimentally more rapidly with temperature than in the theory, the reason for this is unclear. However, it must be noted that the temperature dependence of ZBCP is consistent with previous experimental observations of qualitatively similar origins of ZBCP. STM measurements of LDOS in Nb/Ho systems (due to odd frequency triplet superconductivity) observed the ZBCP disappearing at 660 mK⁷ – far below the superconducting transition of Nb used in the experiment ($T_{c,Nb} \sim 6.6$ K, please refer to supplementary information section of ref. 7), while ZBCPs in YBCO (originating due to sign change of order parameter in d-wave superconductors) were only observed until 40 K and 60 K ($T_{c,YBCO} \sim 90$ K) in refs 24 and 30 respectively. We therefore assume that the temperature dependence arises due to aspects of theory which have not been fully understood.

Conclusions

We have not seen oscillatory behaviour in the intensity of ZBCPs with the application of magnetic field, thus ruling out the possibility of attributing the observed ZBCP to possible Majorana bound states⁴. ZBCPs occurring due to Kondo effects, on application of an external magnetic field, should separate out to a double peak structures³¹. The strong intensity of the ZBCP (3.5 times the normal state conductance) rules out other possibilities like de Gennes-Saint-James resonances²³ or a pin hole mediated junction which in accordance to the BTK theory³² should give rise to a maximum ZBCP intensity of twice the normal state conductance. ZBCPs could also occur due to the TiN layer turning superconducting thus facilitating a critical current. However, the monotonic field-suppression and the observation of the ZBCP at high magnetic fields clearly indicate that Josephson effects do not cause the ZBCPs. Moreover, the top inset to Fig. 1 – shows that the ZBCPs start to evolve at 2.8 K, 3.8 K and 3.6 K for 3 nm, 2 nm and 1 nm barrier thicknesses respectively. Since the TiN layer for all these films were grown without breaking the vacuum and with the same plasma, this non-monotonic behaviour cannot be related to any possible superconductivity in TiN. However, such temperature dependence again points to an incomplete understanding of theoretical origins for ZBCPs for unconventional superconducting orders. For a more detailed analysis - which rules out superconductivity in TiN layer – please refer to the supplementary information section. Hence, none of the above possibilities are suitable in explaining the observed ZBCPs in our experiment.

The ZBCPs in NbN/GdN/TiN tunnel junctions therefore clearly establish an unconventional non-BCS type DOS indicating odd frequency superconductivity evolving at NbN/GdN interfaces. The current discovery of odd frequency pairing is not only relevant in understanding superconductivity beyond the conventional scope of BCS theory; but also firmly establishes FIs as important material systems for developing active devices for superconducting spintronics³³.

Methods

The trilayered films of NbN/GdN/TiN are grown without breaking the vacuum in an ultra high vacuum chamber, by means of reactive dc magnetron sputtering in an atmosphere of Argon and Nitrogen. TiN is here grown as a (non-superconducting) metallic layer. Mesa type tunnel junctions were fabricated from sputtered tri-layered films by means of a fabrication procedure described elsewhere²¹. The only difference was that instead of plasma etching, TiN had to be Ar ion milled controllably. Measurements were performed using a 3He dip probe in a closed cycle liquid helium cooled variable temperature insert capable of cooling down to 0.3 K. Spin polarization was calculated from resistance vs temperature measurements using a procedure described in a previous publication¹⁶.

References

- Ishida, K. *et al.* Spin-triplet superconductivity in Sr₂RuO₄ identified by 17O Knight shift. *Nature* **396**, 658–660 (1998).
- Luke, G. M. *et al.* Time-Reversal Symmetry Breaking Superconductivity in Sr₂RuO₄. *Nature* **394**, 558–561 (1998).
- Dalichaouch, Y. *et al.* Impurity scattering and triplet superconductivity in UPt₃. *Phys. Rev. Lett.* **75**, 3938–3941 (1995).
- Mourik, V. *et al.* Signatures of Majorana Fermions in Hybrid Superconductor-Semiconductor Nanowire Devices. *Science* (80). **336**, 1003–1007 (2012).
- Robinson, J. W. A., Witt, J. D. S. & Blamire, M. G. Controlled injection of spin-triplet supercurrents into a strong ferromagnet. *Science* **329**, 59–61 (2010).
- Khaire, T. S., Khasawneh, M. A., Pratt, W. P. & Birge, N. O. Observation of Spin-Triplet Superconductivity in Co-Based Josephson Junctions. *Phys. Rev. Lett.* **104**, 137002 (2010).
- Di Bernardo, A. *et al.* Signature of magnetic-dependent gapless odd frequency states at superconductor/ferromagnet interfaces. *Nat. Commun.* **6**, 8053 (2015).
- Bergeret, F. S., Volkov, A. F. & Efetov, K. B. Odd triplet superconductivity and related phenomena in superconductor-ferromagnet structures. *Rev. Mod. Phys.* **77**, 1321–1373 (2005).
- Buzdin, A. I., MeĤnikov, A. S. & Pugach, N. G. Domain walls and long-range triplet correlations in SFS Josephson junctions. *Phys. Rev. B* **83**, 144515 (2011).
- Eschrig, M. Spin-polarized supercurrents for spintronics: a review of current progress. *Reports Prog. Phys.* **78**, 104501 (2015).
- Keizer, R. S. *et al.* A spin triplet supercurrent through the half-metallic ferromagnet CrO₂. *Nature* **439**, 825–7 (2006).
- Singh, A., Voltan, S., Lahabi, K. & Aarts, J. Colossal Proximity Effect in a Superconducting Triplet Spin Valve Based on the Half-Metallic Ferromagnet CrO₂. *Phys. Rev. X* **5**, 21019 (2015).
- Tanaka, Y. & Golubov, A. A. Theory of the Proximity Effect in Junctions with Unconventional Superconductors. *Phys. Rev. Lett.* **98**, 37003 (2007).

14. Linder, J., Yokoyama, T., Sudbø, A. & Eschrig, M. Pairing Symmetry Conversion by Spin-Active Interfaces in Magnetic Normal-Metal-Superconductor Junctions. *Phys. Rev. Lett.* **102**, 107008 (2009).
15. Linder, J., Sudbø, A., Yokoyama, T., Grein, R. & Eschrig, M. Signature of odd-frequency pairing correlations induced by a magnetic interface. *Phys. Rev. B* **81**, 214504 (2010).
16. Pal, A., Barber, Z. H., Robinson, J. W. A. & Blamire, M. G. Pure second harmonic current-phase relation in spin-filter Josephson junctions. *Nat. Commun.* **5**, 3340 (2014).
17. Pal, A. & Blamire, M. G. Large interfacial exchange fields in a thick superconducting film coupled to a spin-filter tunnel barrier. *Phys. Rev. B* **92**, 180510(R) (2015).
18. Linder, J. & Robinson, J. W. A. Strong odd-frequency correlations in fully gapped Zeeman-split superconductors. *Sci. Rep.* **5**, 15483 (2015).
19. Tedrow, P. M., Tkaczyk, J. E. & Kumar, A. Spin-Polarized Electron Tunneling Study of an Artificially Layered Superconductor with Internal Magnetic Field: EuO-Al. *Phys. Rev. Lett.* **56**, 1746–1749 (1986).
20. Pal, A., Senapati, K., Barber, Z. H. & Blamire, M. G. Electric-Field-Dependent Spin Polarization in GdN Spin Filter Tunnel Junctions. *Adv. Mater.* **25**, 5581–5 (2013).
21. Blamire, M. G., Pal, A., Barber, Z. H. & Senapati, K. Spin filter superconducting tunnel junctions. In *Proc. SPIE* 8461, 84610J (2012).
22. Zhao, E., Löfwander, T. & Sauls, J. A. Nonequilibrium superconductivity near spin-active interfaces. *Phys. Rev. B* **70**, 134510 (2004).
23. Giazotto, F. *et al.* Resonant Transport in Nb/GaAs/AlGaAs Heterostructures: Realization of the de Gennes–Saint-James Model. *Phys. Rev. Lett.* **87**, 216808 (2001).
24. Lesueur, J., Greene, L. H., Feldmann, W. L. & Inam, A. Zero bias anomalies in YBa₂Cu₃O₇ tunnel junctions. *Phys. C Supercond.* **191**, 325–332 (1992).
25. Sasaki, S. *et al.* Topological Superconductivity in CuxBi₂Se₃. *Phys. Rev. Lett.* **107**, 217001 (2011).
26. Grein, R., Löfwander, T. & Eschrig, M. Inverse proximity effect and influence of disorder on triplet supercurrents in strongly spin-polarized ferromagnets. *Phys. Rev. B* **88**, 54502 (2013).
27. Grein, R., Löfwander, T., Metalidis, G. & Eschrig, M. Theory of superconductor-ferromagnet point-contact spectra: The case of strong spin polarization. *Phys. Rev. B* **81**, 94508 (2010).
28. Chockalingam, S. P., Chand, M., Jesudasan, J., Tripathi, V. & Raychaudhuri, P. Superconducting properties and Hall effect of epitaxial NbN thin films. *Phys. Rev. B* **77**, 214503 (2008).
29. Chawla, J. S., Zhang, X. Y. & Gall, D. Effective electron mean free path in TiN(001). *J. Appl. Phys.* **113**, (2013).
30. Greene, L. H. *et al.* Planar tunneling spectroscopy of high-temperature superconductors: Andreev bound states and broken symmetries. *Phys. C Supercond.* **387**, 162–168 (2003).
31. Goldhaber-Gordon, D. *et al.* Kondo effect in a single-electron transistor. *Nature* **391**, 156–159 (1998).
32. Blonder, G., Tinkham, M. & Klapwijk, T. Transition from metallic to tunneling regimes in superconducting microconstrictions: Excess current, charge imbalance, and supercurrent conversion. *Phys. Rev. B* **25**, 4515–4532 (1982).
33. Linder, J. & Robinson, J. W. A. Superconducting spintronics. *Nat. Phys.* **11**, 307–315 (2015).

Acknowledgements

This work of A.P. and M.G.B. was partially supported by an ERC Advanced Investigators Grant ‘Superspin’. M.E. and M.G.B. acknowledges financial support from the EPSRC grant EP/N017242/1. M.E. also acknowledges funding from the Lars Onsager committee during his stay as Lars Onsager Professor at NTNU. J.A.O. and J.L. acknowledge funding via the “Outstanding Academic Fellows” programme at NTNU, the COST Action MP-1201 and the Research Council of Norway Grant numbers 205591, 216700, and 240806. The authors acknowledge helpful discussions with Jason Robinson.

Author Contributions

M.G.B. and A.P. designed the experiment. A.P. grew the films, fabricated the devices and performed the measurements. J.A.O., M.E. and J.L. did the theoretical modelling. All authors contributed equally to writing the manuscript.

Additional Information

Supplementary information accompanies this paper at <http://www.nature.com/srep>

Competing financial interests: The authors declare no competing financial interests.

How to cite this article: Pal, A. *et al.* Spectroscopic evidence of odd frequency superconducting order. *Sci. Rep.* **7**, 40604; doi: 10.1038/srep40604 (2017).

Publisher's note: Springer Nature remains neutral with regard to jurisdictional claims in published maps and institutional affiliations.



This work is licensed under a Creative Commons Attribution 4.0 International License. The images or other third party material in this article are included in the article's Creative Commons license, unless indicated otherwise in the credit line; if the material is not included under the Creative Commons license, users will need to obtain permission from the license holder to reproduce the material. To view a copy of this license, visit <http://creativecommons.org/licenses/by/4.0/>

© The Author(s) 2017

Supplementary information

Spectroscopic evidence of odd frequency superconducting order

Avradeep Pal^{1*}, J. A. Ouassou², M. Eschrig³, J. Linder^{2*}, M. G. Blamire¹

¹*Department of Materials Science, University of Cambridge,
27 Charles Babbage Road, Cambridge CB3 0FS, United Kingdom*

²*Department of Physics, Norwegian University of Science and Technology, N-7491 Trondheim, Norway*

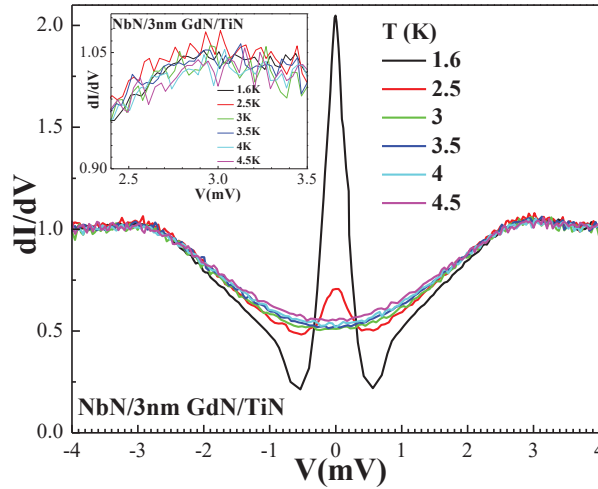
³*SEPnet and Hubbard Theory Consortium, Department of Physics, Royal Holloway,
University of London, Egham, Surrey TW20 0EX, United Kingdom*

We provide the following evidence to rule out superconductivity in the TiN layer and establish conclusively that the ZBCP is due to SIN junctions and therefore represents an enhancement in DOS around the Fermi level in NbN:

a) Variation of gap edge with temperature

If TiN turned superconducting at 3 K ($T_{cTiN} \sim 3K$), and assuming that TiN behaves like an ideal BCS superconductor, $\Delta_{TiN}(0) \sim 1.76 k_B T_{cTiN} = 0.455 mV$.

At 1.6 K: $\Delta_{TiN}(1.6K) \sim \Delta_{TiN}(0) * \tanh\left(1.74 * \sqrt{\left(\frac{T_{cTiN}}{1.6} - 1\right)}\right) = 0.42 mV$.



Supplementary Figure 1 – Differential conductance curves at temperatures from 4.5K to 1.6K demonstrating that there is no observation in enhancement of gap edge due to possible superconductivity of TiN layer.

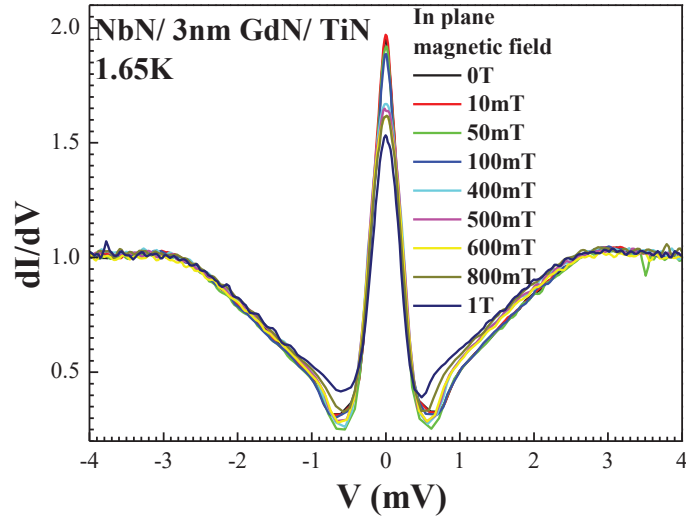
Hence, we would expect the gap edge in NbN/GdN/TiN junctions to increase by ~ 0.5 mV as the junction is cooled. The figure below and the inset to it, clearly indicates that no such increase is observed. In fact, no increase is observed even at 0.3 K (Refer to Fig. 2 of the main manuscript). This is a clear demonstration that NbN is the only superconducting layer in the tri-layer stack. Owing to high transition temperature of NbN ($T_{cNbN} \sim 13.5$ K), the magnitude of its gap edge feature saturates below approximately 7 K. Thus, these junctions are SIN junctions throughout the entire temperature range below 13.5 K.

b) Discussion on a potential Josephson effect

Josephson junctions with two superconducting NbN electrodes [1] with exactly identical junction dimensions to the devices reported here exhibit $I_c(H)$ Fraunhofer patterns with an oscillation period or lobe width of 1.5-3.5 mT. If we assume that, despite the arguments above, that the TiN is superconducting then we can take its penetration depth (λ_L) to be $\sim 700nm$, and therefore should have lobe width:

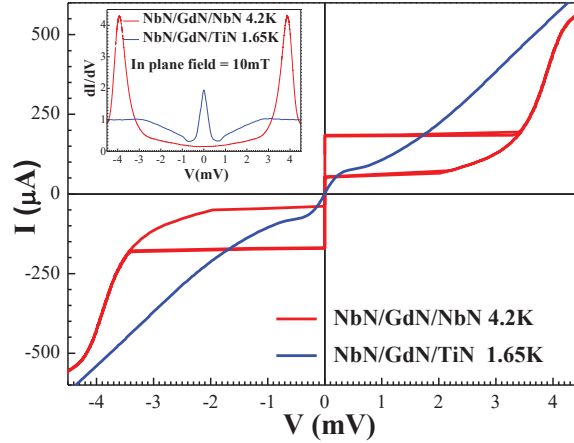
$$H_0 = \Phi_0 / (L \left(\lambda_{NbN} * \tanh \left(\frac{d_{NbN}}{\lambda_{NbN}} \right) + \lambda_{TiN} * \tanh \left(\frac{d_{TiN}}{\lambda_{TiN}} \right) + d_{GdN} \right))$$

where $d_{NbN} = 100nm$, $d_{TiN} = 30nm$, $d_{GdN} = 3nm$, $\lambda_{NbN} \sim 250nm$ and Φ_0 is the universal flux quantum. As per the above expression, the Fraunhofer patterns should have critical current oscillation periods as approximately 4.4mT. Taking the standard decay envelope of the Fraunhofer pattern, we can therefore say that any Josephson effects should die out at high fields ($>45mT$; i.e. beyond the supposed 10th Fraunhofer lobe). However, the ZBCPs in our samples are only suppressed slowly and monotonically and remain visible even till 1 T, thus ruling out ZBCPs due to critical currents (conductance maxima) at low bias due to Josephson effects.



Supplementary Figure 2 – Differential conductance measurements of the ZBCP at different values of externally applied in-plane magnetic fields.

c) Comparison of IV curves of SIS and SIN junctions



Supplementary Figure 3 – IV curves (including forward and backward traces) of two junctions, one with a superconducting NbN counter-electrode (red), while the other has non-superconducting TiN electrode (blue). IV curves are measured at zero field and well below the supposed superconducting T_c of NbN (13.5 K) and TiN (either 5.4 K or 3 K as suggested by referee). Inset to figure shows the comparison of respective differential conductance curves measured with an in-plane magnetic field of 10 mT.

The most noticeable features in Figure 3 are that for the (SIN) junction with the TiN counter-electrode (blue curve), the high conductance region around zero bias is not vertical and that switching away from this region (which occurs at roughly the same magnitude of current ($\sim \pm 65 \mu\text{A}$) as the critical current of the NbN/GdN/NbN SIS junction) shows no sign of hysteresis – a feature that is expected in underdamped SIS Josephson junctions and clearly present in the NbN/GdN/NbN device. However, for the junction with NbN counter-electrode, we see clear hysteresis (Switching current $\sim \pm 168 \mu\text{A}$, Re-trapping current $\sim \pm 37 \mu\text{A}$). We have reported in a prior publication [2] that our GdN junctions are in the underdamped regime, and hence the above IV traces clearly demonstrate that the high conductance region in TiN junctions is not a feature caused by critical currents, but rather, represents an enhancement in the DOS around the Fermi level of the NbN superconductor for the NbN/GdN/TiN device.

The inset shows the previously discussed effect of magnetic field on the supercurrent due to the Josephson effect (Fraunhofer pattern). While the critical current in NbN/GdN/NbN junction is completely suppressed due to the 10 mT in-plane magnetic field, an identical in-plane field has no effect on the magnitude of the ZBCP.

VIII

Reference

J.A. Ouassou, A. Pal, M. Blamire, M. Eschrig, J. Linder.
Triplet Cooper pairs induced in diffusive *s*-wave superconductors interfaced with strongly spin-polarized magnetic insulators or half-metallic ferromagnets.
Scientific reports 7, 1932 (2017).
DOI: 10/F99CHF

Contributions

JAO performed the analytical and numerical calculations with minor support from JL. The majority of the writing was done by JAO and JL. ME contributed to the discussion and understanding of the boundary conditions on which the manuscript is based. All authors contributed to the discussion of the results and the revision of the manuscript.

Comments

This project was initiated right after the recent publication of general boundary conditions for strongly polarized magnetic interfaces [115]. The motivation was to investigate the physical implications of these boundary conditions, by numerically modelling some experimentally relevant setups involving half-metallic and insulating ferromagnets. During this process, we also developed some new theoretical results: a model for strongly polarized metals, and a drastically simplified version of the second-order boundary conditions. The work on half-metallic ferromagnets was presented as a poster at the Heraeus seminar *Trends in mesoscopic superconductivity* (Bad Honnef, Germany, 2016).

SCIENTIFIC REPORTS

OPEN Triplet Cooper pairs induced in diffusive *s*-wave superconductors interfaced with strongly spin-polarized magnetic insulators or half-metallic ferromagnets

Received: 17 October 2016
Accepted: 28 March 2017
Published online: 16 May 2017

Jabir Ali Ouassou¹, Avradeep Pal², Mark Blamire², Matthias Eschrig³ & Jacob Linder¹

Interfacing superconductors with strongly spin-polarized magnetic materials opens the possibility to discover new spintronic devices in which spin-triplet Cooper pairs play a key role. Motivated by the recent derivation of spin-polarized quasiclassical boundary conditions capable of describing such a scenario in the diffusive limit, we consider the emergent physics in hybrid structures comprised of a conventional *s*-wave superconductor (e.g. Nb, Al) and either strongly spin-polarized ferromagnetic insulators (e.g. EuO, GdN) or halfmetallic ferromagnets (e.g. CrO₂, LCMO). In contrast to most previous works, we focus on how the superconductor itself is influenced by the proximity effect, and how the generated triplet Cooper pairs manifest themselves in the self-consistently computed density of states (DOS) and the superconducting critical temperature T_c . We provide a comprehensive treatment of how the superconductor and its properties are affected by the triplet pairs, demonstrating that our theory can reproduce the recent observation of an unusually large zero-energy peak in a superconductor interfaced with a half-metal, which even exceeds the normal-state DOS. We also discuss the recent observation of a large superconducting spin-valve effect with a T_c change ~ 1 K in superconductor/half-metal structures, in which case our results indicate that the experiment cannot be explained fully by a long-ranged triplet proximity effect.

Combining materials with different types of quantum order can result in new quantum phenomena at their interface. One example is the interaction between superconducting and magnetic materials^{1,2}, which besides its interesting fundamental physics has spawned the field of superconducting spintronics³, and could lead to novel cryogenic spin-based applications.

Recently, several experimental works have been carried out on superconductors interfaced to strongly spin-polarized magnetic materials. The latter include both ferromagnetic insulators such as EuO or GdN^{4,5}, with spin-polarizations ranging up to 90%, and half-metallic ferromagnets such as CrO₂ and La_{2/3}Ca_{1/3}MnO₃ (LCMO)^{6–8}. In ref. 8, STM-measurements were performed on the superconducting side of a NbN/LCMO bilayer, and revealed an unusually large zero-energy peak in the density of states (DOS) which, surprisingly, exceeded even the normal-state DOS. Such a peak, often taken as a hallmark signature of odd-frequency pairing^{9,10}, was also observed recently in Nb/Ho bilayers in ref. 11, albeit with a reduced magnitude. Moreover, resistance measurements probing the superconducting critical temperature T_c in MoGe/Ni/Cu/CrO₂ multilayers revealed a change in T_c of up to 1 K; this was attributed to the generation of long-ranged triplet pairs when the relative magnetization between ferromagnetic Ni and half-metallic CrO₂ was changed from parallel to perpendicular⁷. It would be of high interest to understand and model the findings in these experiments, yet such an endeavour is complicated by the fact that there up to recently has existed no convenient framework allowing for the study

¹Department of Physics, NTNU, Norwegian University of Science and Technology, N-7491, Trondheim, Norway. ²Department of Materials Science, University of Cambridge, Cambridge, CB3 0FS, United Kingdom. ³Department of Physics, Royal Holloway, University of London, Surrey, TW20 0EX, United Kingdom. Correspondence and requests for materials should be addressed to J.A.O. (email: jabir.a.ouassou@ntnu.no)

of strongly spin-polarized magnetic materials in contact with superconductors in the experimentally relevant diffusive regime of transport.

Motivated by this, we here present a solution of the quasiclassical Usadel equation¹² with arbitrarily strongly spin-polarized magnetic regions and obtain the DOS and T_c using the generally valid spin-dependent boundary conditions derived in ref. 13. We have applied this framework on superconductors interfaced to strongly spin-polarized ferromagnetic insulators and half-metallic ferromagnets, solving the equations selfconsistently in order to study the manifestation of triplet Cooper pairs induced in the superconductor. While previous works have considered the case of strong spin-polarization in the ballistic limit^{14–24}, we here present results valid for the diffusive regime of transport. We show that our theory is able to reproduce an unusually strong zero-energy peak, exceeding the normal-state value, induced in a superconductor as seen experimentally in ref. 8. Moreover, we compute the T_c shift when the magnetization in a spin-valve S/F/N/HM multilayer is rotated, and discuss the results in the context of the experiment described in ref. 7. Our results indicate that the experimental measurements cannot be fully explained by a long-ranged triplet proximity effect, suggesting that some different physical mechanism may also be at play. We clarify the difference in length-scale for the inverse proximity effect in a superconductor and the length-scale for which a spin-valve effect occurs.

Theory

Quasiclassical theory. In this paper, we employ the quasiclassical theory of superconductivity^{12, 25, 26} to describe diffusive hybrid structures in equilibrium. With this approach, the main objective is to calculate the quasiclassical retarded propagator \hat{g} as a function of quasiparticle energy ϵ and position z , where the z -axis is along the junction direction. The propagator may then be used to calculate various physical observables of interest, such as the density of states, tunneling currents, and superconducting critical temperature. We use a hat to denote that the propagator has a 2×2 matrix structure in Nambu space, an underline to indicate a 2×2 matrix structure in spin space, and that we use the normalization convention $\hat{g}^2 = 1$. The quasiclassical propagator can be calculated from the Usadel diffusion equation¹²,

$$iD \partial_z (\hat{g} \partial_z \hat{g}) = \hat{U}, \quad (1)$$

where D is the diffusion constant, and \hat{U} is a material-dependent matrix potential that incorporates the effects of various self-energies and scattering processes. We will later generalize eq. (1) to strong ferromagnets, where the diffusion constants become spin-dependent. In superconductor/normal-metal hybrid structures, the matrix potential takes the form^{12, 26}

$$\hat{U} = [(\epsilon + i\eta)\hat{\tau}_3 + \hat{\Delta}], \quad (2)$$

where ϵ is the quasiparticle energy, η mimics an inelastic scattering rate, $\hat{\tau}_3 = \text{diag}(+1, -1)$ is the third Pauli matrix in Nambu space, and the superconducting order parameter $\Delta(z)$ is embedded in the antidiagonal matrix $\hat{\Delta} = \text{antidiag}(+\Delta, -\Delta, +\Delta^*, -\Delta^*)$. Note that we follow the convention where sums and products of dimensionally incompatible matrices should be resolved by taking Kronecker products with identity matrices. For instance, in the above equation, $\hat{\tau}_3$ lacks an explicit structure in spin space, and should therefore implicitly be interpreted as $\hat{\tau}_3 \otimes \mathcal{I}_0$, where $\mathcal{I}_0 = \text{diag}(+1, +1)$ is the identity matrix in spin space.

The above equations must also be accompanied by the appropriate boundary conditions,

$$G_L L_L (\hat{g}_L \partial_z \hat{g}_L) = G_R L_R (\hat{g}_R \partial_z \hat{g}_R) = \hat{I}, \quad (3)$$

where the subscripts indicate whether the quantities correspond the left or right side of the interface, $G_j = \sigma_j A / L_j$ is the bulk conductance of material j , L_j is the material length, A is the cross-sectional area of the interface, σ_j is the intrinsic conductivity in the non-superconducting state, and \hat{I} is the matrix current^{27–29} at the interface. In general, the matrix current depends on the propagators at both sides of the interface, as well as the physical properties of the interface itself. The simplest case is when the interface has a relatively low transparency and no spin-active properties, in which case the matrix current is given by the Kuprianov–Lukichev tunneling equation³⁰

$$2\hat{I} = G_0 [\hat{g}_L, \hat{g}_R], \quad (4)$$

where \hat{g}_L and \hat{g}_R are the propagators at the left and right sides of the interface, respectively, and $G_0 \ll G$ is the conductance of the interface. How to calculate the matrix current at spin-active interfaces will be discussed in the following sections.

In practice, when solving the equations above, it is convenient to use the Riccati parametrization of the propagator^{14, 31–33},

$$\hat{g} = \begin{pmatrix} \underline{N} & \\ & -\underline{\tilde{N}} \end{pmatrix} \begin{pmatrix} 1 + \underline{\gamma} \underline{\tilde{\gamma}} & 2\underline{\gamma} \\ 2\underline{\tilde{\gamma}} & 1 + \underline{\tilde{\gamma}} \underline{\gamma} \end{pmatrix}, \quad (5)$$

where tilde conjugation $\underline{\tilde{\gamma}}(z, \epsilon) = \underline{\gamma}^*(z, -\epsilon)$ is defined as a combination of complex conjugation $i \mapsto -i$ and energy $\epsilon \mapsto -\epsilon$, and the normalization matrices are defined as $\underline{N} = (1 - \underline{\gamma} \underline{\tilde{\gamma}})^{-1}$ and $\underline{\tilde{N}} = (1 - \underline{\tilde{\gamma}} \underline{\gamma})^{-1}$. Mathematically, this parametrization automatically satisfies the normalization condition $\hat{g}^2 = 1$, and enforces the particle-hole symmetries of the propagator. The Riccati parameters $\underline{\gamma}$ and $\underline{\tilde{\gamma}}$ are also single-valued and bounded, and the parametrization is numerically stable relative to alternatives like *e.g.* the θ -parametrization. Using the

definitions of \underline{N} and $\tilde{\underline{N}}$ in terms of $\underline{\gamma}$ and $\tilde{\underline{\gamma}}$, as well as the easily derivable identities $\underline{N}\underline{\gamma} = \underline{\gamma}\tilde{\underline{N}}$ and $\tilde{\underline{N}}\tilde{\underline{\gamma}} = \tilde{\underline{\gamma}}\underline{N}$, it can be shown that eqs (1) and (3) can be Riccati parametrized as

$$\partial_z^2 \underline{\gamma} = (2iD\underline{N})^{-1}(\underline{U}_{12} - \underline{U}_{11}\underline{\gamma}) - 2(\partial_z \underline{\gamma})\tilde{\underline{N}}\tilde{\underline{\gamma}}(\partial_z \underline{\gamma}), \quad (6)$$

$$\partial_z \underline{\gamma} = (2GL\underline{N})^{-1}(\underline{I}_{12} - \underline{I}_{11}\underline{\gamma}), \quad (7)$$

where the notation $\underline{U}_{\tau\tau'}$ and $\underline{I}_{\tau\tau'}$ refer to the (τ, τ') components in Nambu space of the matrix potential \hat{U} and matrix current \hat{I} . The corresponding equations for $\tilde{\underline{\gamma}}$ can be found by tilde conjugation of the equations above. Together, the differential equations for $\underline{\gamma}$ and $\tilde{\underline{\gamma}}$ form a boundary value problem that can be solved numerically as long as we know the matrix potential and current.

While the equations above are sufficient to solve for the propagator of the system, these equations implicitly depend on the superconducting order parameter $\Delta(z)$ through eq. (2). We therefore need an equation which relates this order parameter to the propagator in order to find a selfconsistent solution. In equilibrium, the appropriate selfconsistency equation can be written³⁴

$$\Delta(z) = \frac{1}{2}N_0\lambda \int_0^{\Delta_0 \cosh(1/N_0\lambda)} d\epsilon [f_s(z, \epsilon) - f_s(z, -\epsilon)] \tanh(\epsilon/2T), \quad (8)$$

where $f_s = (f_{12} - f_{21})/2$ is the singlet component of the anomalous propagator $\underline{f} = [\hat{g}]_{12}$, N_0 is the density of states per spin at the Fermi level, λ is the BCS coupling constant, is the zero-temperature gap of a bulk superconductor, T is the temperature of the superconductor, and T_c is the critical temperature of a bulk superconductor. The above equation can be written in terms of the Riccati parameters using the equations $\underline{f} = 2\underline{N}\underline{\gamma}$ and $f_s(-\epsilon) = \tilde{f}_s^*(\epsilon)$. If we furthermore divide the equation by Δ_0 , and use the approximations $\cosh(1/N_0\lambda) \cong \exp(1/N_0\lambda)/2$ and $\Delta_0/T_c \cong \pi/e^c$ where c is the Euler–Mascheroni constant, we obtain

$$\begin{aligned} \Delta(z)/\Delta_0 &= \frac{1}{2}N_0\lambda \int_0^{\exp(1/N_0\lambda)/2} d(\epsilon/\Delta_0) [(\underline{N}\underline{\gamma})_{12} - (\underline{N}\underline{\gamma})_{21} - (\tilde{\underline{N}}\tilde{\underline{\gamma}})_{12}^* + (\tilde{\underline{N}}\tilde{\underline{\gamma}})_{21}^*] \\ &\times \tanh\left(\frac{\pi}{2e^c} \frac{\epsilon/\Delta_0}{T/T_c}\right), \end{aligned} \quad (9)$$

where all the Riccati matrices \underline{N} , $\tilde{\underline{N}}$, $\underline{\gamma}$, $\tilde{\underline{\gamma}}$ are functions of position z and quasiparticle energy ϵ . Note that the approximations above are only valid in the weak-coupling regime $N_0\lambda \ll 1$. In practice, $N_0\lambda \leq 1/4$ is sufficient to make the results insensitive to the cutoff, and we set $N_0\lambda = 1/5$. This result is expressed in terms of only the Riccati matrices \underline{N} , $\tilde{\underline{N}}$, $\underline{\gamma}$, $\tilde{\underline{\gamma}}$ and dimensionless quantities Δ/Δ_0 , ϵ/Δ_0 , T/T_c , $N_0\lambda$, making this version of the equation better suited for numerics than the equivalent eq. (8).

Spin-active tunneling interfaces (1st order in φ_n and T_n). In the case of low-transparency spin-active junctions where the spin-mixing is weak, the matrix current may be written^{13, 35, 36}

$$2\hat{I} = G_0[\hat{g}_L, \hat{g}_R] + G_1[\hat{g}_L, \hat{m}\hat{g}_R\hat{m}] + G_{MR}[\hat{g}_L, \{\hat{g}_R, \hat{m}\}] - iG_\varphi[\hat{g}_L, \hat{m}_L], \quad (10)$$

where the magnetization matrix $\hat{m} = \text{diag}(\mathbf{m} \cdot \underline{\sigma}, \mathbf{m} \cdot \underline{\sigma}^*)$, \mathbf{m} is a unit vector that describes the interface magnetization, $\underline{\sigma}$ is the Pauli vector, and \hat{g}_L and \hat{g}_R are the propagator at the left and right sides of the interface, respectively. Note this version of the matrix current equation is for the left side of the interface; a similar equation for the other side of the interface can be found by letting $\hat{I} \mapsto -\hat{I}$ and $L \leftrightarrow R$. Note that there are two different magnetization matrices \hat{m} , \hat{m}_L in the equation: \hat{m} refers to the average magnetization felt by a quasiparticle *transmitted* through the interface, while \hat{m}_L refers to the magnetization felt by a *reflected* quasiparticle. If there is an interfacial magnetic misalignment, these two magnetizations will in general be different, and this may cause long-range triplet generation. The interface conductances in the equation above can be written¹³

$$G_0 = G_Q \sum_{n=1}^N T_n \left(1 + \sqrt{1 - P_n^2}\right), G_1 = G_Q \sum_{n=1}^N T_n \left(1 - \sqrt{1 - P_n^2}\right), G_{MR} = G_Q \sum_{n=1}^N T_n P_n, G_\varphi = G_Q \sum_{n=1}^N 2\varphi_n, \quad (11)$$

where T_n , P_n , φ_n are respectively the transmission probability, spin-polarization, and spin-mixing angle associated with each scattering channel n . The quantity G_Q in the equations above is the conductance quantum e^2/π (in units with $\hbar = 1$), while we interpret G_0 as the tunneling conductance, G_1 as a depairing term, G_{MR} as a magnetoresistive term, and G_φ as the spin-mixing term. Note that in this context, the polarization is defined as $P_n \equiv [T_{n\uparrow} - T_{n\downarrow}]/[T_{n\uparrow} + T_{n\downarrow}]$, where $T_{n\sigma}$ are the spin-dependent transmission probabilities, and σ is the spin of a quasiparticle as measured along the quantization axis \mathbf{m} . In other words, the polarization determines how many spin-up vs. spin-down particles are transmitted through the spin-active interface for each transmissive conductance channel n . Note that these equations can be used with arbitrary interface polarizations $P \in [-1, +1]$, but only remain valid as long as the transmission probabilities T_n and spin-mixing angles φ_n are small. In general, the number of channels contributing to G_φ can be different from the number of channels contributing to $\{G_0, G_1, G_{MR}\}$ since channels that are purely reflecting can contribute to the former. If we assume that all

scattering channels have the same polarization P , then G_L and G_{MR} can be calculated straight from the polarization P and tunneling conductance G_0 ,

$$\frac{G_L}{G_0} = \frac{1 - \sqrt{1 - P^2}}{1 + \sqrt{1 - P^2}}, \quad \frac{G_{MR}}{G_0} = \frac{P}{1 + \sqrt{1 - P^2}}, \quad (12)$$

where the common prefactors $G_0 \sum_n T_n$ cancel. However, this cancellation does not occur for the ratio G_φ/G_0 , where we get a factor $[\sum_n \varphi_n]/[\sum_n T_n]$ that can become arbitrarily small or large depending on the spin-mixing angles and transmission probabilities. Thus, G_φ/G_0 can for the purpose of comparing with experimental data be regarded as a fitting parameter.

Spin-active tunneling interfaces (2nd order in φ_n and T_n). To 2nd order in the transmission probabilities and spin-mixing angles, the interfacial matrix current may be written:

$$2\hat{I} = G_0 \left[\hat{g}_L, \hat{F}(\hat{g}_R) \right] + \frac{1}{4} G_2 \hat{F}(\hat{g}_R) \hat{g}_L \hat{F}(\hat{g}_R) - i G_\varphi \left[\hat{g}_L, \hat{m}_L \right] + \frac{1}{4} G_{\varphi 2} \left[\hat{g}_L, \hat{m}_L \hat{g}_L \hat{m}_L \right] + \frac{i}{4} G_{\chi L} \left[\hat{g}_L, \hat{F}(\hat{g}_R) \hat{g}_L \hat{m}_L + \hat{m}_L \hat{g}_L \hat{F}(\hat{g}_R) \right] + \frac{i}{4} G_{\chi R} \left[\hat{g}_L, \hat{F}(\hat{g}_R) \hat{m}_R \hat{g}_R - \hat{m}_R \right], \quad (13)$$

where the matrix function $\hat{F}(\hat{g})$ is the contents of the commutator in the 1st order boundary conditions divided by G_0 :

$$\hat{F}(\hat{g}) = \hat{g} + \frac{P}{1 + \sqrt{1 - P^2}} \{ \hat{m}, \hat{g} \} + \frac{1 - \sqrt{1 - P^2}}{1 + \sqrt{1 - P^2}} \hat{m} \hat{g} \hat{m}. \quad (14)$$

In other words, the 2nd order boundary conditions may be written concisely as a function of the 1st order boundary conditions. This is a new result compared to ref. 13 where the 2nd order contribution was originally derived, substantially simplifying and speeding up the numerical implementation of these boundary conditions and the solution of the Usadel equation utilizing them. We use the notation \hat{m} for the magnetization experienced by transmitted particles, and \hat{m}_L and \hat{m}_R for particles reflected on the left and right sides of the interface, respectively. As for the new conductances that appear above, these are defined as¹³

$$G_2 = G_Q \sum_{n=1}^N T_n^2 \left(1 + \sqrt{1 - P^2} \right)^2, \quad G_\chi = G_Q \sum_{n=1}^N T_n \varphi_n \left(1 + \sqrt{1 - P^2} \right), \quad G_{\varphi 2} = G_Q \sum_{n=1}^N 2 \varphi_n^2, \quad (15)$$

These conductances can be connected through $G_\chi/G_0 \cong G_{\varphi 2}/G_\varphi \cong G_\varphi G_2/2G_0^2$ if we can assume that the mean spin-mixing angle and transmission probability (T) are much smaller than their standard deviations $\Delta\varphi$ and ΔT . Furthermore, it can be shown that $G_\chi/G_0 \cong \langle \varphi \rangle$; since we need less than approximately to be able to stop at a 2nd order expansion in φ , we should therefore assume that $G_\chi/G_0 < 0.3$. Finally, note that there are two different G_χ in the boundary condition: one $G_{\chi L}$ for the left side of the interface, and one $G_{\chi R}$ for the right side of the interface. For the rest of this paper, we will assume that these two conductances are equal. With all of these assumptions, we are left with a single new parameter G_χ to include in our model.

To derive the equations above, one may start with the 2nd order boundary conditions in ref. 13, and make the approximations of (i) channel-diagonal scattering $T_{nn'} = T_n$, and (ii) channel-independent polarization $P_n = P$. We will not show the derivation itself here, as the derivation is relatively straight-forward but quite lengthy.

Spin-active reflecting interfaces (all orders in φ_n). For a completely reflecting spin-active interface, the matrix current for arbitrarily large spin-mixing angles φ_n can be written¹³

$$\hat{I} = -G_Q \sum_{n=1}^N \left[1 - \frac{i}{4} \sin(\varphi_n) (\hat{g} \hat{m} \hat{g} - \hat{m}) + \frac{1}{2} \sin^2(\varphi_n/2) (\hat{g} \hat{m} \hat{g} \hat{m} - 1) \right]^{-1} \times [-i \sin(\varphi_n) (\hat{m} \hat{g} - \hat{g} \hat{m}) + \sin^2(\varphi_n/2) (\hat{m} \hat{g} \hat{m} \hat{g} - \hat{g} \hat{m} \hat{g} \hat{m})] \times \left[1 - \frac{i}{4} \sin(\varphi_n) (\hat{g} \hat{m} \hat{g} - \hat{m}) + \frac{1}{2} \sin^2(\varphi_n/2) (\hat{m} \hat{g} \hat{m} \hat{g} - 1) \right]^{-1} \quad (16)$$

where N is the number of scattering channels at the interface. To leading order in the spin-mixing angles φ_n , the second bracket $[-i \sin(\varphi_n) (\hat{m} \hat{g} - \hat{g} \hat{m}) + \dots] \rightarrow -i(\varphi_n) (\hat{m} \hat{g} - \hat{g} \hat{m})$, while the first and third brackets $[1 - \dots]^{-1} \rightarrow 1$, so the equation for the matrix current linearizes to $\hat{I} = i G_Q \sum_n \varphi_n [\hat{m}, \hat{g}]$. For comparison, the spin-mixing term in eq. (10) has the form $2\hat{I} = -i G_\varphi [\hat{g}, \hat{m}]$, and eq. (11) specifies that $G_\varphi = 2G_Q \sum_n \varphi_n$, so this can be written $\hat{I} = -i G_Q \sum_n \varphi_n [\hat{g}, \hat{m}]$. Thus, we see that the eqs (10) and (16) converge in the combined limit of zero transmission $T_n \rightarrow 0$ and weak spin-mixing $\varphi_n \ll 1$.

For simplicity, we will assume that all scattering channels have the same spin-mixing angle φ , so that $\sum_{n=1}^N \varphi_n \rightarrow N$ in the equation above. Such an approximation is e.g. justified when there is a strong Fermi vector mismatch between the superconductor and ferromagnetic insulator¹⁵. The above equation is formulated at the left side of an interface; the corresponding equation at the other side of the interface is found by dropping the initial

minus-sign. Using the normalization conditions $\hat{m}^2 = \hat{g}^2 = 1$, it is also possible to reformulate the equation above in the more economical form

$$\begin{aligned} \hat{I} = & -NG_Q \left[1 - \frac{i}{4} \sin(\varphi) \hat{a} + \frac{1}{2} \sin^2(\varphi/2) \hat{a} \hat{m} \right]^{-1} \\ & \times [-i \sin(\varphi) \hat{g} \hat{a} + \sin^2(\varphi/2) [\hat{m}, \hat{a}]] \\ & \times \left[1 - \frac{i}{4} \sin(\varphi) \hat{a} + \frac{1}{2} \sin^2(\varphi/2) \hat{m} \hat{a} \right]^{-1} \end{aligned} \quad (17)$$

where we have defined the auxiliary matrix $\hat{a} = \hat{g} \hat{m} \hat{g} - \hat{m}$. Using this form of the equation, it is possible to reduce the number of matrix multiplications from 18 to 5 by reusing matrix products, which results in a more efficient numerical implementation.

Strongly polarized ferromagnets. In general, the propagator \hat{g} has a 2×2 matrix structure in both Nambu space and spin space. For normal metals and singlet superconductors, the spin structure of the normal component is diagonal, while the spin structure of the anomalous component is antidiagonal. Explicitly written out in matrix form, this means that these materials have propagators with the 4×4 structure

$$\hat{g} = \begin{pmatrix} g_{\uparrow\uparrow} & 0 & 0 & f_{\uparrow\downarrow} \\ 0 & g_{\downarrow\downarrow} & f_{\downarrow\uparrow} & 0 \\ 0 & -\tilde{f}_{\downarrow\uparrow} & -\tilde{g}_{\uparrow\uparrow} & 0 \\ -\tilde{f}_{\uparrow\downarrow} & 0 & 0 & -\tilde{g}_{\downarrow\downarrow} \end{pmatrix}. \quad (18)$$

On the other hand, in the presence of magnetic elements and spin-dependent scattering, we also need to account for triplet superconductivity and spin-flip processes in materials, and this forces us to use the most general 4×4 form for the propagator,

$$\hat{g} = \begin{pmatrix} g_{\uparrow\uparrow} & g_{\uparrow\downarrow} & f_{\uparrow\uparrow} & f_{\uparrow\downarrow} \\ g_{\downarrow\uparrow} & g_{\downarrow\downarrow} & f_{\downarrow\uparrow} & f_{\downarrow\downarrow} \\ -\tilde{f}_{\uparrow\uparrow} & -\tilde{f}_{\uparrow\downarrow} & -\tilde{g}_{\uparrow\uparrow} & -\tilde{g}_{\uparrow\downarrow} \\ -\tilde{f}_{\downarrow\uparrow} & -\tilde{f}_{\downarrow\downarrow} & -\tilde{g}_{\downarrow\uparrow} & -\tilde{g}_{\downarrow\downarrow} \end{pmatrix}. \quad (19)$$

However, for the case of very strong ferromagnets, the spin-splitting of the energy bands can be so severe that there is effectively no interaction between quasiparticles from different spin bands. The spin structure of the propagator will then become diagonal,

$$\hat{g} = \begin{pmatrix} g_{\uparrow\uparrow} & 0 & f_{\uparrow\uparrow} & 0 \\ 0 & g_{\downarrow\downarrow} & 0 & f_{\downarrow\downarrow} \\ -\tilde{f}_{\uparrow\uparrow} & 0 & -\tilde{g}_{\uparrow\uparrow} & 0 \\ 0 & -\tilde{f}_{\downarrow\downarrow} & 0 & -\tilde{g}_{\downarrow\downarrow} \end{pmatrix}, \quad (20)$$

which means the only kind of superconductivity possible will be spin-triplet ($f_{\uparrow\uparrow}$ and $f_{\downarrow\downarrow}$). Since the propagator is diagonal in spin space for such materials, its components can also be represented as simply two decoupled propagators in Nambu space,

$$\hat{g}_{\uparrow\uparrow} = \begin{pmatrix} g_{\uparrow\uparrow} & f_{\uparrow\uparrow} \\ -\tilde{f}_{\uparrow\uparrow} & -\tilde{g}_{\uparrow\uparrow} \end{pmatrix}, \quad (21)$$

$$\hat{g}_{\downarrow\downarrow} = \begin{pmatrix} g_{\downarrow\downarrow} & f_{\downarrow\downarrow} \\ -\tilde{f}_{\downarrow\downarrow} & -\tilde{g}_{\downarrow\downarrow} \end{pmatrix}. \quad (22)$$

If we assume that the two spin-bands in the ferromagnet individually behave as normal metals, it should be reasonable to assume that the two sets of quasiparticles follow two separate metallic diffusion equations. Introducing the spin-dependent diffusion constants D_\uparrow and D_\downarrow , these diffusion equations may be written

$$iD_\uparrow \partial_z (\hat{g}_{\uparrow\uparrow} \partial_z \hat{g}_{\uparrow\uparrow}) = [(\epsilon + i\eta) \hat{\tau}_3, \hat{g}_{\uparrow\uparrow}], \quad (23)$$

$$iD_{\uparrow}\partial_z(\hat{g}_{\uparrow\downarrow}\partial_z\hat{g}_{\uparrow\downarrow}) = [(\epsilon + i\eta)\hat{\tau}_3, \hat{g}_{\uparrow\downarrow}], \quad (24)$$

We will also define the spin-independent diffusion constant $D = D_{\uparrow} + D_{\downarrow}$ and spin-polarization $\Pi = (D_{\uparrow} - D_{\downarrow})/(D_{\uparrow} + D_{\downarrow})$, where we note that $D_{\sigma} = D(1 + \Pi\sigma)/2$. By dividing each of the above equations by its polarization factor $(1 \pm \Pi)/2$, we get

$$iD\partial_z(\hat{g}_{\uparrow\uparrow}\partial_z\hat{g}_{\uparrow\uparrow}) = [2(1 + \Pi)^{-1}(\epsilon + i\eta)\hat{\tau}_3, \hat{g}_{\uparrow\uparrow}], \quad (25)$$

$$iD\partial_z(\hat{g}_{\uparrow\downarrow}\partial_z\hat{g}_{\uparrow\downarrow}) = [2(1 - \Pi)^{-1}(\epsilon + i\eta)\hat{\tau}_3, \hat{g}_{\uparrow\downarrow}], \quad (26)$$

or if we restore the matrix notation for the spin structure,

$$iD\partial_z(\hat{g}\partial_z\hat{g}) = [(\epsilon + i\eta)\underline{\Pi}\hat{\tau}_3, \hat{g}], \quad (27)$$

where we have defined the polarization matrix

$$\underline{\Pi} = \begin{pmatrix} 2/(1 + \Pi) & 0 \\ 0 & 2/(1 - \Pi) \end{pmatrix}. \quad (28)$$

This equation follows the pattern in eq. (1) if we define the matrix potential $\hat{U} = [(\epsilon + i\eta)\underline{\Pi}\hat{\tau}_3, \hat{g}]$, which written out becomes

$$\hat{U} = \begin{pmatrix} 0 & 4(\epsilon + i\eta)\underline{\Pi}\underline{N}\underline{\gamma} \\ 4(\epsilon + i\eta)\underline{\Pi}\underline{N}\underline{\tilde{\gamma}} & 0 \end{pmatrix}. \quad (29)$$

We then extract the components $\underline{U}_{11} = 0$ and $\underline{U}_{12} = 4(\epsilon + i\eta)\underline{\Pi}\underline{N}\underline{\gamma}$, and invoke eq. (6) to find an equation for $\partial_z^2\underline{\gamma}$, which reads

$$iD[\partial_z^2\underline{\gamma} + 2(\partial_z\underline{\gamma})\underline{N}\underline{\tilde{\gamma}}(\partial_z\underline{\gamma})] = 2(\epsilon + i\eta)\underline{\Pi}\underline{\gamma}. \quad (30)$$

Thus, the only difference between Riccati parametrized diffusion equation for a normal metal and a strong ferromagnet is the occurrence of the polarization matrix $\underline{\Pi}$. However, it should be stressed that the above equation was derived under the assumption that the propagator \hat{g} has a diagonal structure in spin space, which implies that the Riccati parameters $\underline{\gamma}$ and $\underline{\tilde{\gamma}}$ must be diagonal as well. Thus, when implementing the equation above numerically, one must ensure that the off-diagonal terms of $\underline{\gamma}$ and $\underline{\tilde{\gamma}}$ are treated as constants and not variables; deviations from this procedure could produce numerical artifacts that violate these initial assumptions. The main motivation for writing the equation for $\underline{\gamma}$ in matrix form, is that it can now be used in a boundary condition like eq. (7) at both sides of the interface, without requiring modification. Note that the interface to a strong ferromagnet is bound to be strongly magnetized, which means that we should use eqs (10) or (17) as boundary conditions. In the limit of full polarization $\Pi \rightarrow 1$, the matrix $\underline{\Pi} \rightarrow \text{diag}(1, \infty)$. The infinite element will essentially just force the condition $\gamma_{\downarrow\downarrow} = 0$ for the spin-down component, while we get a normal metallic diffusion equation for the spin-up component,

$$iD[\partial_z^2\gamma_{\uparrow\uparrow} + 2(\partial_z\gamma_{\uparrow\uparrow})\tilde{N}_{\uparrow\uparrow}\tilde{\gamma}_{\uparrow\uparrow}(\partial_z\gamma_{\uparrow\uparrow})] = 2(\epsilon + i\eta)\gamma_{\uparrow\uparrow}. \quad (31)$$

Physically, what happens in this limit is that the spin-splitting of the energy bands is strong enough to make the spin-up band metallic and the spin-down band insulating, which results in a so-called half-metal. Thus, we are left with two different ways to model a half-metallic ferromagnet: we can either use eq. (30), and implement a strong ferromagnet with *e.g.* $\Pi = \pm 0.999$, thus taking the limit $\Pi \rightarrow 1$ numerically; or we can take the limit $\Pi \rightarrow 1$ analytically, and implement a scalar diffusion equation for $\gamma_{\uparrow\uparrow}$ like eq. (31). We chose the first approach, since the resulting code may then be reused to model strong ferromagnets as well.

Results and Discussion

Density of states in S/FI/N multilayers. To begin with, we consider the DOS in a normal metal (N) connected to a superconductor (S) via a ferromagnetic insulator (FI), which becomes modified by the existence of triplet Cooper pairs. The FI in this setup is modelled as a spin-active interface with zero spatial extent, but a finite tunneling conductance G_0 , spin-mixing conductance G_{φ} , and spin-polarization P . Assuming no spatial extent means that the FI must have a thickness comparable to atomic length scales, which is much smaller than all the superconducting length scales in the problem. In reality, the properties of the FI would of course scale with its length, which in our model would be described by choosing a smaller tunneling conductance and larger spin-polarization at the interface. The special case of $P=0$ was considered in refs 37 and 38 where it was shown that for a critical value of G_{φ} , pure odd-frequency pairing was induced at the Fermi level $\epsilon = 0$. This is manifested as a large zero-energy peak in the DOS. In Fig. 1, we now show how this effect is modified when taking into account an interface polarization P .

For these simulations, we set the tunneling conductance to $G_0/G=0.3$, where G is the normal-state conductance of each material. If we increase G_0 while keeping G_{φ}/G_0 and P fixed, we increase the magnitude of the

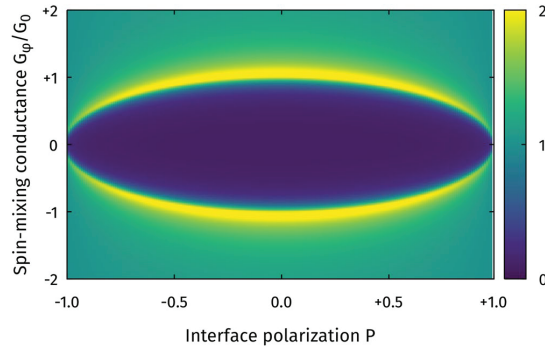


Figure 1. Plot of the zero-energy DOS $D(0)$ as function of interface polarization P and spin-mixing conductance G_ϕ . The DOS was calculated in the center of the normal metal in an S/FI/N structure, where we used the BCS solution for the superconductor, treated the ferromagnetic insulator as a spin-active interface, and the normal metal was taken to have the length ξ_S .

proximity effect, but we do not change whether it is dominated by singlets or triplets. In other words, increasing G_0 makes the blue regions darker and the yellow regions brighter, but does not alter the shape of the plot. Note that for zero polarization, this reproduces the well-known result that a peak suddenly appears for $G_\phi/G_0 = 1$ ³⁷, while the value of G_ϕ necessary to get a zero-energy peak gradually decreases to zero as the polarization tends to one. These results suggest that the spin-dependent transmission probabilities facilitate the conversion from singlet to triplet superconducting correlations in such a fashion that smaller spin-dependent mixing angles are required for this purpose. However, spin-dependent transmissions by themselves only weaken the singlet proximity effect: if $G_\phi = 0$, there is no generation of triplet Cooper pairs as seen in Fig. 1 (fully gapped DOS for $G_\phi = 0$).

In the above example, the superconductor was treated as a reservoir, meaning that the bulk propagator was used in that region. The main purpose of this paper is to determine how the superconducting region is influenced by the magnetic proximity effect, which generates triplet Cooper pairs in the superconductor. In what follows, we therefore only present self-consistent results where the superconducting order parameter and propagator are both obtained in an iterative manner. This allows us to explore how triplet Cooper pairs manifest in the superconducting region, as recently experimentally seen in refs 8 and 11.

We thus show results for a self-consistently solved DOS in both the superconducting and normal region of an S/FI/N system in Figs 2 and 3, setting the length of the superconducting region to $L_S = 3\xi_S$ and $L_S = \xi_S$ in the figures, respectively, where ξ_S is the diffusive coherence length of a bulk superconductor at zero temperature. In all cases, we use the value $G_0/G = 0.3$ for the tunneling conductance. In both cases, we keep the length of the normal layer fixed at $L_N = \xi_S$. The DOS in the N region is very similar in both cases, illustrating the zero-bias peak characteristic of odd-frequency triplet pairs. It is worth to underline that although such a peak is often taken to be a signature of odd-frequency pairing, recent work has demonstrated that a system with fully gapped DOS can still exhibit strong odd-frequency pairing³⁹. The DOS in the superconductor, on the other hand, changes substantially when going from $L_S = 3\xi_S$ to $L_S = \xi_S$. In the former case, the DOS only weakly deviates from the gapped bulk behavior of an *s*-wave superconductor. In the latter case, however, the gap is not only strongly smeared out, but a noticeable zero-energy peak emerges in the superconductor as well due to the appearance of odd-frequency triplet pairs there.

Note that in Figs 1–3, we use the definition $G_\phi/G_0 = [\sum_n \varphi_n]/[\sum_n T_n]$, which differs by a factor $[1 + \sqrt{1 - P^2}]/2$ from the definitions used in the rest of this paper. This does not change any conclusions, as this affects G_ϕ/G_0 by a factor 2 at most, while Fig. 1 shows that G_ϕ/G_0 needs to change by more than a factor 10 in order to produce a zero-energy peak at high polarizations.

It is interesting to note that one can obtain a very large zero-energy enhancement of the DOS in the superconductor, even exceeding its normal-state value, if the FI barrier itself is magnetically inhomogeneous. This is included in our model using the interfacial magnetic misalignment in the boundary conditions described previously. For a very high polarization P , we show how the DOS depends on the spin-mixing conductance G_ϕ in the left panel of Fig. 4. For large G_ϕ , the combination of a strongly suppressed superconducting gap Δ near the interface and the generation of triplet Cooper pairs with all spin projections (due to the interfacial magnetic misalignment) permits the DOS to completely shed its gapped character and instead develop a large zero-energy peak typical of odd-frequency pairing⁴⁰. In the right panel, we show how the DOS develops for a fixed G_ϕ when P is increased, from which one infers that while a broad enhancement takes place even for $P = 0$, a sharp peak is only obtained when the spin-filtering effect of the interface is incorporated.

Density of states in S/FI bilayers. If the normal metal is removed, so that the superconductor is terminated by vacuum on one side and a fully reflecting magnetic insulator on the other, we have an S/FI bilayer with zero transmission of quasiparticles from S and into the FI. This can be modelled as a superconductor with boundary conditions given by eq. (17). We then find that the proximity-induced DOS in the superconductor

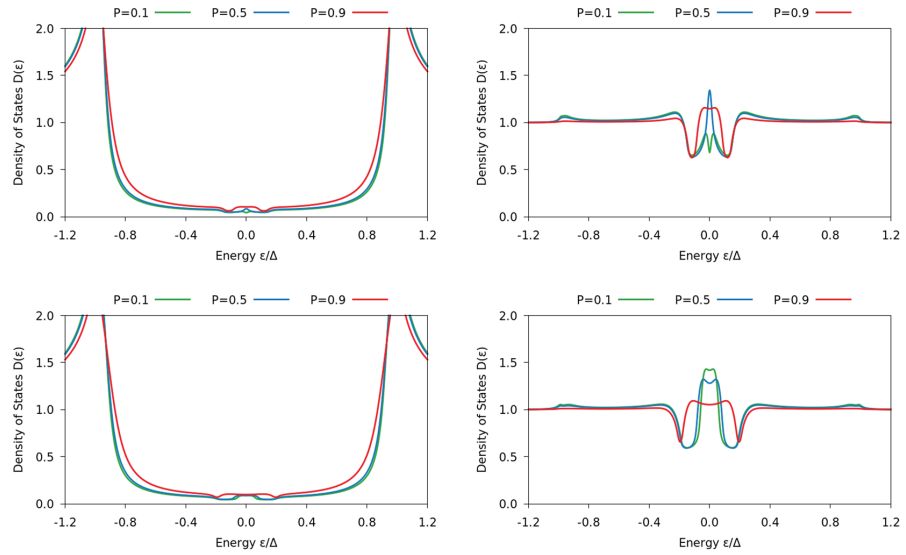


Figure 2. Plots of the DOS for an S/FI/N junction with $L_S = 3\xi_S$ and $L_N = \xi_S$ as function of energy. The left column shows the results on the superconducting side of the interface, and the right column on the normal-metal side. The spin-mixing conductance G_φ/G_0 is 0.75 in the top row and 1.25 in the bottom row, while the interface polarization P is written in the legend.

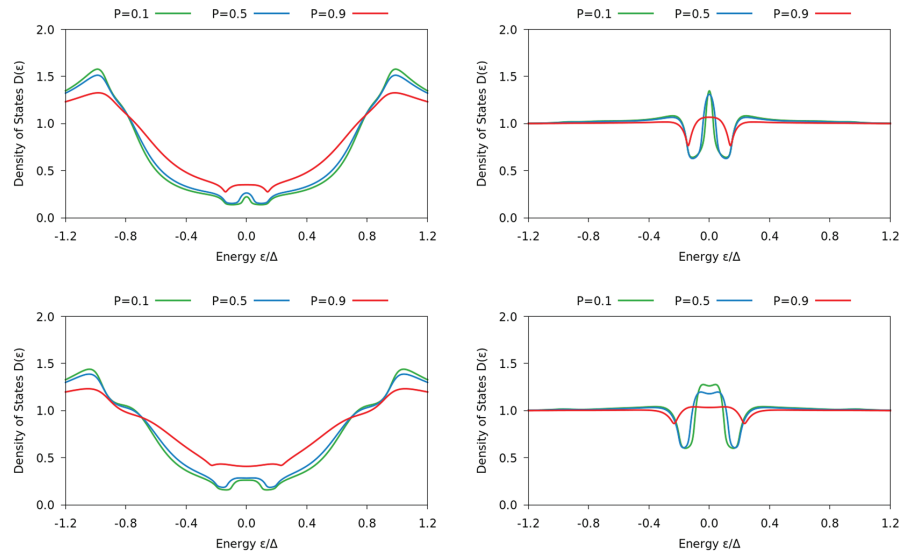


Figure 3. Plots of the DOS for an S/FI/N junction with $L_S = L_N = \xi_S$ as function of energy. The left column shows the results on the superconducting side of the interface, and the right column on the normal-metal side. The spin-mixing conductance G_φ/G_0 is 0.75 in the top row and 1.25 in the bottom row, while the interface polarization P is written in the legend.

depends strongly on both the spin-mixing angle φ and the conductivity of the superconductor relative the number of reflective channels, parametrized by G/NG_Q . This is shown in Fig. 5. Moreover, the spin-mixing angle φ strongly influences the size of the superconducting gap, as demonstrated in Fig. 6. For a thin superconductor $L_S = \xi_S$, the gap is suppressed to around 20% of its bulk value for a FI with a spin-mixing angle $\varphi/\pi = 0.9$. A larger superconductor $L_S = 3\xi_S$ is able to recover the bulk value of the order parameter at its vacuum interface, but the

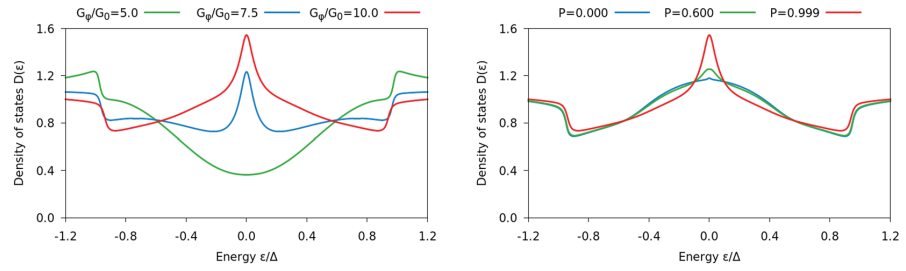


Figure 4. Plots of the DOS at the superconducting side of the interface in an S/FI/N junction with $L_S = 3 \xi_S$ and $L_N = 10 \xi_S$ as function of energy. The ferromagnetic insulator was modelled as a spin-active interface with very strong spin-mixing and polarization: in the left plot, we set the polarization $P = 0.999$ and vary G_φ , in the right plot we set $G_\varphi/G_0 = 10$ and vary P . In contrast to Figs 2 and 3, we also included a magnetic inhomogeneity in the model, which was incorporated by using two different magnetizations $\mathbf{m}_L = \mathbf{e}_x$ and $\mathbf{m} = \mathbf{m}_R = \mathbf{e}_z$ in the spin-active boundary conditions.

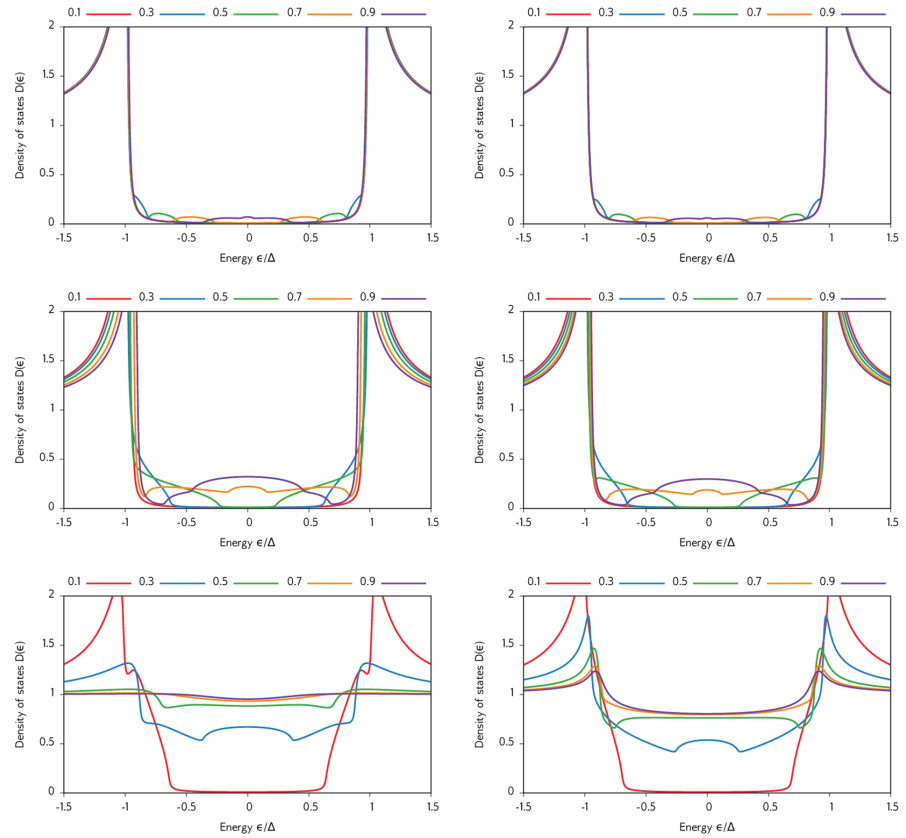


Figure 5. Plots of the DOS of an S/FI bilayer, measured at the superconducting side of the interface. The ferromagnetic insulator is modelled as a fully reflecting spin-active interface, and the superconductor has length $L_S = \xi_S$ in the left column and $L_S = 3 \xi_S$ in the right one. The junction has $GL_S/NG_Q \xi_S \in \{300, 30, 3\}$, decreasing downward. The different curves correspond to different values for the spin-dependent interfacial phase shifts φ/π , as shown in the legends above the plots.

suppression of Δ is nevertheless substantial near the FI interface for large spin-mixing angles. The reduced gap edge is manifested in Fig. 5.

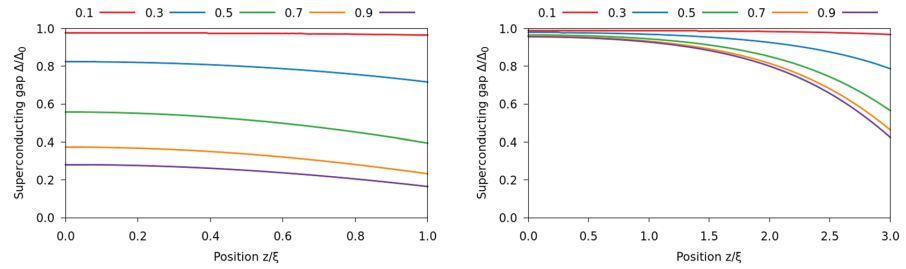


Figure 6. Plots of the superconducting gap in an S/FI bilayer. The superconductor has length $L_S = \xi_S$ in the left plot and $L_S = 3 \xi_S$ in the right one. In both cases, we chose $GL_S/NG_Q\xi_S = 3$, and the spin-mixing angle φ/π is shown in the legend.

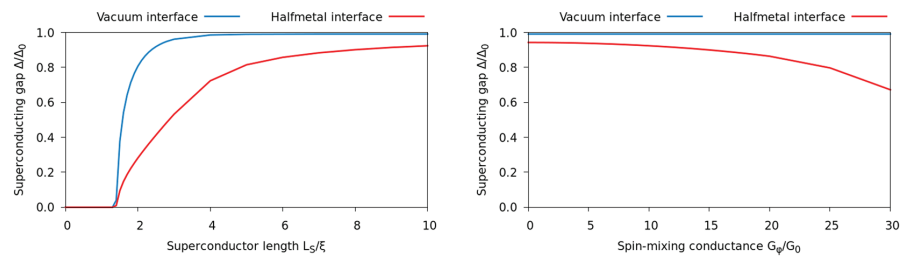


Figure 7. Plots of the superconducting gap at the interfaces of an S/HM bilayer. Both the plots are for a long halfmetal $L_H = 10 \xi_S$; the difference is that we fix $G_\varphi/G_0 = 10$ but vary L_S in the left plot, while we fix $L_S = 10 \xi_S$ and vary G_φ in the right.

We emphasize that, as shown in the Theory section, the S/FI results would be identical to the S/FI/N results in the limit of zero tunneling conductance and weak spin-mixing. However, we used a finite tunneling conductance in the previous subsection, and spin-mixing angles all the way up to 0.9π in this subsection, which is why the results are quite different.

Density of states in S/HM bilayers. A recent experiment by Kalcheim *et al.*⁸ reported an unexpected result for STM-measurements on the superconducting side of a NbN/LCMO bilayer, which is precisely a S/HM structure. They found that the DOS in the superconductor could be so strongly modified by the proximity to the half-metal that all signs of gapped behavior would vanish and be replaced by a zero-energy peak that exceeded even the normal-state value. This is in stark contrast to the results we showed above for a ferromagnetic insulator, where the zero-energy peak in the superconductor always appeared inside a gapped region and whose magnitude did not exceed the normal-state value. Such a remarkably strong inverse proximity effect as seen in the experiment⁸ can in fact be modelled by our theory, as we now demonstrate. For the plots below (Figs 7 and 8), we consider a S/HM bilayer and assume a $\pi/2$ magnetic misalignment at the interface. The $L_S = 3 \xi_S$ case shown in the top left figure of Fig. 8 shows good agreement with the experimental data: a zero-bias peak which exceeds even the normal-state DOS. With increasing thickness L_S , a usual gapped structure is recovered. The results do, however, depend on the misalignment angle: when it is reduced to zero, the distinct zero-energy peak morphs into a weaker and more diffuse subgap plateau. This enhancement can still be larger than the normal-state DOS in some cases; e.g. when $L_S = 2 \xi_S$, $L_H = 10 \xi_S$, and $G_\varphi/G_0 = 10$, $D(0)$ is reduced from 1.30 with $\pi/2$ misalignment to 1.10 with no misalignment. Note also the similarity between the results in Figs 4 and 8 on the superconducting side of the interface: for similar interface parameters, we obtain nearly identical results in the S/HM and S/FI/N structures.

The generation of triplet Cooper pairs on the superconducting side has an interesting non-monotonic dependence on the length L_S of the superconductor (see bottom left panel of Fig. 8), unlike the triplet proximity effect on the half-metal which decays monotonically with increasing L_H (see bottom right panel of Fig. 8). For thin superconducting layers $L_S \cong \xi_S$, the superconducting gap is fully suppressed at the interface, as shown in Fig. 7. As a result, the normal-state DOS $D(0) = 1$ is obtained in the superconductor near the interface as the superconducting correlations are fully suppressed there. As L_S increases, a finite value of the order parameter Δ is permitted, and around $L_S \cong 3 \xi_S$ the largest triplet proximity effect is obtained. This is the regime where the unusually strong zero-energy peak is observed. Increasing L_S even further, $D(0)$ starts to fall off rapidly and one recovers the standard BCS behavior of the superconducting DOS with a gap at low energies. We also note that as one moves away from the superconducting interface, the zero-energy peak shown in the top left figure of Fig. 8 also decreases and drops below the normal-state value $D(0) = 1$. Our theory is thus able to partially explain the experimental result

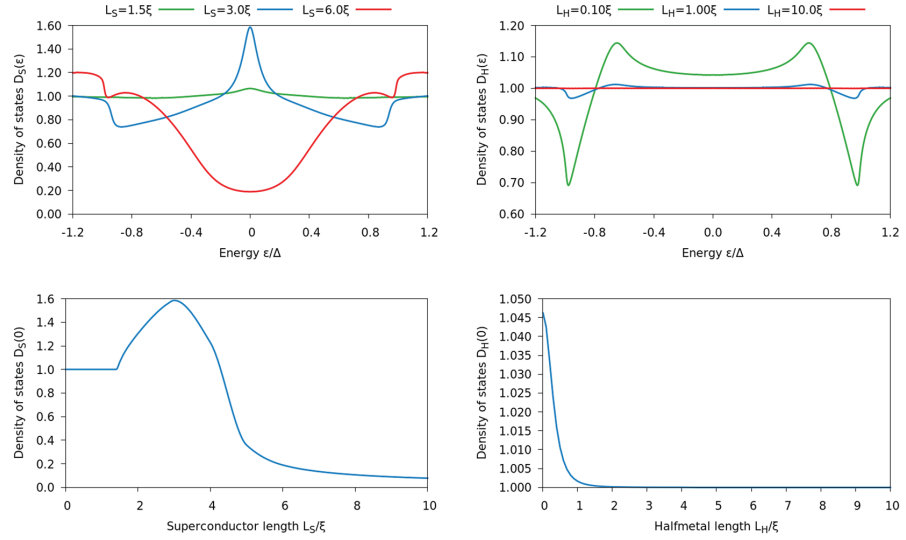


Figure 8. Plots of the DOS at an S/HM interface with $G_{\uparrow}/G_0 = 10$. The left plots show how the DOS D_S on the superconducting side changes with the length L_S of the superconductor, when we fix the halfmetal length $L_H = 10 \xi_S$. Conversely, the right plots show how the DOS D_H on the halfmetallic side changes with L_H when we set $L_H = 10 \xi_S$. The top plots display the energy dependence of the DOS, while the bottom plots highlight the zero-energy peak.

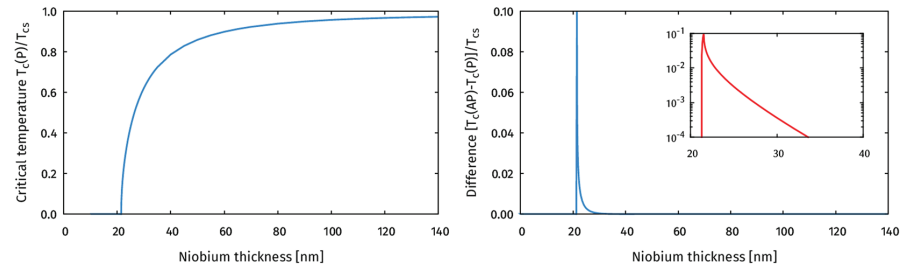


Figure 9. The left plot shows how the critical temperature in the parallel configuration $T_c(P)$ varies with the thickness of the superconductor. The right plot shows the critical temperature difference between the parallel and antiparallel configurations. The inset shows how this spin-valve effect decays on a logarithmic scale.

of ref. 8, where the peak was observed even at the vacuum interface of the superconductor. Finally, we note that we have also solved for the DOS selfconsistently when taking into account the 2nd order boundary conditions, finding no qualitative difference and only a very weakly suppressed magnitude of the spectral features, thus justifying the usage of the 1st order boundary conditions.

Critical temperature in F/S/F trilayers. Before presenting new results for the critical temperature in half-metal/superconductor hybrids, we assess how well our theory agrees with known previous spin-valve experiments. We will first consider the critical temperature of a Py/Nb/Py spin-valve structure as investigated in ref. 41. The permalloy layers were treated as homogeneous ferromagnets with an exchange field $h = 100\Delta_0$, in line with the estimate $h \cong 135$ meV for permalloy⁴¹ and $\Delta_0 \cong 1.4$ meV for niobium. The S/F interfaces were modelled using spin-active boundary conditions with a high interface conductance $G_0/G = 1$ and spin-mixing conductance $G_{\uparrow}/G_0 = 12$, and an experimentally realistic polarization $P = 0.38$ ⁴². As in the experiment, we fixed the thickness of each permalloy layer to 8 nm, varied the thickness d of the niobium layer, and used a superconducting coherence length $\xi_S = 6$ nm. For each thickness of the niobium layer, we then calculated the critical temperatures $T_c(P)$ and $T_c(AP)$ for parallel and antiparallel orientations of the permalloy magnetization directions, respectively. The results are shown in Fig. 9 below.

First of all, the results show that the proximity effect in such a trilayer can be significant even for a several coherence lengths long superconductor. Superconductivity is entirely suppressed until the superconductor

thickness $d \geq 21.5 \text{ nm} \cong 3.6 \xi_S$. After that, the critical temperature converges towards the bulk value T_{cs} , but is reduced by more than 1% compared to this value even for $d = 140 \text{ nm} \cong 23 \xi_S$. Both these results are quantitatively consistent with the results reported by Moraru *et al.* in ref. 41, where they found no superconductivity for $d < 20.5 \text{ nm}$, and the critical temperature curve closely matches Fig. 9.

The right panel of Fig. 9 shows how the spin-valve effect $T_c(\text{AP}) - T_c(\text{P})$ in the system varies with the superconductor thickness. Using a critical temperature $T_{cs} = 9.2 \text{ K}$ for niobium, we see that the spin-valve effect abruptly rises from 0 to 0.9 K when $d = 21.3 \text{ nm}$, *i.e.* the thickness at which $T_c(\text{AP})$ becomes nonzero. However, the spin-valve effect decays exponentially fast as d is increased; it drops to about 0.1 K for $d = 22.7 \text{ nm}$, and decreases below 1 mK for $d = 33.5 \text{ nm}$. For comparison, Moraru *et al.* observed a lower spin-valve effect of about 20 mK for their best sample⁴¹. However, combining observations in their Figs 1 and 3, they find that the spin-valve effect drops below 1 mK for $d \geq 33 \text{ nm}$, which fits very well with our results. The discrepancy in the spin-valve amplitude could *e.g.* be explained by wrong estimates for the interface parameters, or by the experimental difficulty manufacturing an ideal sample given the sensitivity of the spin-valve effect to the niobium thickness. The key observation here is nevertheless that the *spin-valve effect is completely absent for a large range of thicknesses where an inverse proximity effect exists, i.e.* the regime $d \geq 33 \text{ nm}$ in the plot.

The results for the proximity effect are remarkably robust: even if we use extreme values such as $G_\varphi/G_0 = 500$ for the spin-mixing (while keeping the other parameters as above), or a giant tunneling conductance $G_0/G = 100$ (with non-magnetic boundary conditions), the critical superconductor thickness required for $T_c \geq 0$ remains in the region 20–24 nm. This can be explained as follows. Once the properties of the interfaces become sufficiently extreme that they force the gap $\Delta \rightarrow 0$ there, then making the interface properties even more extreme cannot further suppress the gap at the interface. The strength of the spin-valve effect, on the other hand, remains more sensitive to the values of G_φ and G_0 .

The most notable conclusion one can draw from these results, is the extreme discrepancy that can exist between having a significant proximity effect and spin-valve effect. While the former remains visible for superconductors that are longer than 20 coherence lengths, the latter becomes negligible after just 6 coherence lengths. This is for an F/S/F spin-valve setup; for an S/F/F setup one would expect both these length scales to be reduced by at least a factor two, due to the reduced coupling between the superconductor and the second ferromagnet in the structure.

Critical temperature in S/HM bilayers. Inspired by the experiment by Keizer *et al.*⁴³, we wanted to check how an interfacial magnetic misalignment affects the critical temperature of an S/HM bilayer. This was modelled by setting $\mathbf{m} = \mathbf{e}_z$ and $\mathbf{m}_1 = \cos \alpha \mathbf{e}_z + \sin \alpha \mathbf{e}_x$ in eq. (10); *i.e.* \mathbf{m} was oriented along the magnetization of the half-metal, while \mathbf{m}_1 differs from it by an angle α . First, we assumed that the superconductor was $0.7\text{--}1.5 \xi_S$ long, that the half-metal was $12 \xi_S$ long, that the conductance ratio was $G_0/G = 0.4$, and varied the spin-mixing conductance G_φ/G_0 in the range 0–12. Then, we fixed the length of the superconductor to ξ_S , and investigated the effect of varying the length of the half-metal, and the effect of including the 2nd order contributions in the boundary conditions. For each set of parameters described above, we computed the critical temperature T_c for the interfacial magnetic misalignments $\alpha = 0$ and $\alpha = \pi/2$, and calculated the difference $T_c(0) - T_c(\pi/2)$ between these results as a measure of the critical temperature shift due to magnetic misalignments. The results are shown in Fig. 10.

Several noteworthy features appear. Consider first the difference between T_c in the parallel and perpendicular alignment shown in the top left panel. The perpendicular configuration $T_c(\pi/2)$ is always smaller than $T_c(0)$. This can be explained physically by the fact that in the perpendicular configuration, the long-ranged proximity effect channel is opened up, allowing Cooper pairs to be converted into triplets with spin-polarization along the magnetization of the halfmetallic region and thus leak out of the superconductor. The panel also shows that for a given length L_S of the superconductor, the range of spin-mixing conductance G_φ where the device can work as a superconducting switch [$T_c(0)$ finite while $T_c(\pi/2) = 0$] is quite narrow. This is shown explicitly for a fixed length L_S in the top right panel of Fig. 10. Thicker superconducting layers L_S require larger spin-mixing conductance G_φ in order to obtain the switching effect. This is physically reasonable since a larger inverse proximity effect, and thus G_φ , is required to alter the T_c as the superconductor becomes bigger and acts more as a reservoir.

It is also interesting to determine how the difference in T_c between the parallel and perpendicular configurations of the interface and bulk moments depend on the length L_H of the half-metallic region. This is shown in the bottom left panel, where we have plotted $[T_c(0) - T_c(\pi/2)]/T_{cs}$ vs. both L_H and the spin-mixing conductance G_φ . The first thing to notice is that upper horizontal line, denoting the value of G_φ where $T_c(0) \rightarrow 0$, is completely independent on L_H . This is understood physically by the fact that in the parallel alignment, there is no superconducting proximity effect in the half-metal. Thus, the critical temperature of the superconductor is determined uniquely by the inverse proximity effect generated by the full reflection taking place at the interface which naturally does not depend on L_H .

A more surprising feature is the fact that as L_H is reduced, a smaller and smaller spin-mixing conductance G_φ is required to suppress superconductivity in the perpendicular configuration, *i.e.* $T_c(\pi/2) \rightarrow 0$. For a fixed value of G_φ , one might expect that T_c is suppressed more the larger the half-metal thickness L_H is. The fact that this does not occur can be explained physically as follows. For large L_H , the half-metal behaves essentially as a normal metal with a very weak superconducting proximity effect. This fact is corroborated by *e.g.* the behavior of the DOS in the upper right panel of Fig. 8. As L_H is reduced, however, the half-metal starts to act more and more like a triplet superconductor since the only types of Cooper pairs that can exist in the half-metal are odd-frequency triplets. In other words, there is no singlet proximity effect at all in the half-metal, unlike the case in *e.g.* S/N bilayers. The key point is that the triplet superconductivity behavior is more harmful toward the host superconductor than the normal metal behavior, because in the former case there is not only a suppression of Cooper pairs but additionally a conversion from singlets to triplets. This reduces T_c even further compared to when the half-metal acts as an

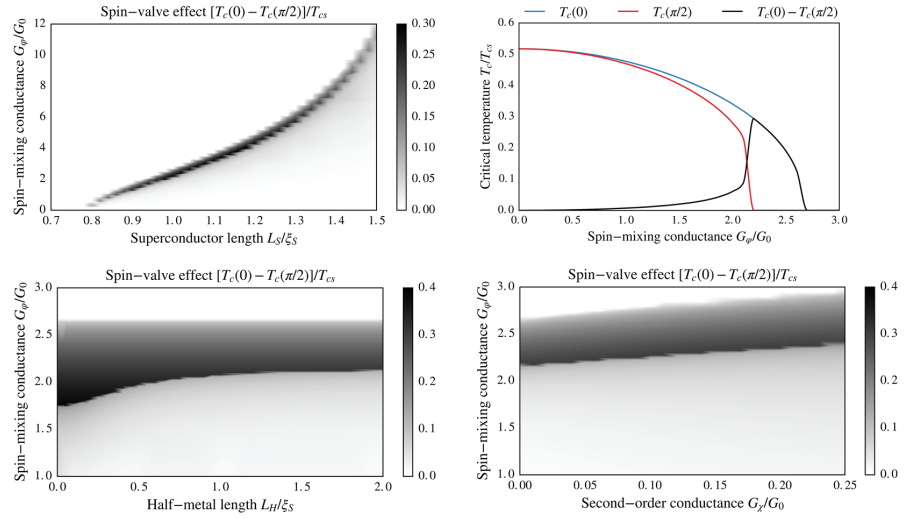


Figure 10. Plots of $[T_c(0) - T_c(\pi/2)]/T_{cs}$, where $T_c(\alpha)$ is the critical temperature of an S/HM bilayer with an interfacial magnetic misalignment α , and T_{cs} is the critical temperature of a bulk superconductor. Top left: We fixed the halfmetal length to $12\xi_S$, and varied the superconductor length and spin-mixing conductance. Above the black region, *i.e.* for small superconductors or strong spin-mixing, we see both $T_c(\pi/2)$ and $T_c(0)$ go to zero. Below the black region, *i.e.* for large superconductors and weak spin-mixing, both $T_c(\pi/2)$ and $T_c(0)$ converge to the same finite value. The black curve delineates a critical region where $T_c(\pi/2)$ drops to zero while $T_c(0)$ remains finite, leading to a very large difference. Top right: We fixed the halfmetal length to $12\xi_S$ and the superconductor length to $1\xi_S$, and highlight how $T_c(0)$ and $T_c(\pi/2)$ behave. This illustrates why the top-left curve looks like it does. Bottom left: We fixed the superconductor length to $1\xi_S$, and varied the halfmetal length and spin-mixing conductance. We also checked lengths L_H up to $12\xi_S$ and find that the halfmetal length is essentially irrelevant for $L_H > 2\xi_S$. Bottom right: We fixed the superconductor length to $1\xi_S$ and halfmetal length to $12\xi_S$, and varied the 2nd order conductance G_χ and spin-mixing conductance G_φ . We see that the 2nd order terms basically produce a quantitative shift of the transition region towards higher values of G_φ , but does not appear to qualitatively change anything.

effective one spin-band normal metal in the limit $L_H \gg \xi_S$. As a result, steadily smaller are G_φ required to suppress $T_c(\pi/2)$ as L_H is reduced.

Finally, we have also determined the influence of including the 2nd order boundary conditions in the calculation of T_c . This is shown in the lower right panel of Fig. 10, revealing that there is only a small quantitative correction to the value of G_φ providing the superconducting transition by including these additional terms parametrized by G_χ . The conclusion that 2nd order terms have the same effect as a quantitative shift in G_φ was also corroborated by DOS calculations for this setup (not shown).

Critical temperature in S/F/N/HM multilayers. Motivated by the recent experiment by Singh *et al.*⁷, we have calculated T_c for a superconductor/ferromagnet/normal-metal/half-metal multilayer. In accordance with the experiment, we set the superconductor thickness to $10\xi_S$, the half-metal thickness to $20\xi_S$, set the ferromagnet thickness to $0.3\xi_S$, and set the normal metal thickness to $1.0\xi_S$. For the ferromagnet, we used an exchange field of magnitude $h = 50\Delta$ in the bulk (essentially as large as quasiclassical theory permits to model the relatively strong exchange field of Ni), and set the polarization $P = 0.20$ and spin-mixing $G_\varphi/G_0 = 0.5$ at its interfaces. The superconductor used in the experiment (MoGe) had an extremely short mean free path $\ell \ll \xi_S$, firmly placing it in the diffusive limit of transport as modelled here. For the halfmetallic interfaces, we used a polarization $P = 0.999$ and spin-mixing G_φ/G_0 in the range 0–10. At all interfaces, we chose a relatively large ratio between the barrier and bulk conductances $G_0/G = 0.4$. We then calculated the critical temperature $T_c(\alpha)$, where α is the angle between the magnetizations of the ferromagnet and the half-metal, and used this to calculate the critical temperature shift $T_c(0) - T_c(\pi/2)$.

The result was zero critical temperature shift (with a precision of 0.0002 in T_c/T_{cs}). In fact, we find that both the critical temperature $T_c(0)$ with no magnetic inhomogeneity, and $T_c(\pi/2)$ with maximum magnetic noncollinearity, are essentially equal to the bulk critical temperature T_{cs} for a $10\xi_S$ long superconductor. We therefore tried to reduce the superconductor size to below $1.0\xi_S$ in order to check whether that would help. In this case, both $T_c(0)$ and $T_c(\pi/2)$ were significantly reduced compared to the bulk critical temperature, with the result $T_c/T_{cs} \cong 0.7$. However, the values of $T_c(0)$ and $T_c(\pi/2)$ still ended up being equal, so that we could not find any appreciable spin-valve effect $T_c(0) - T_c(\pi/2)$. The lack of spin-valve effect indicates that the only proximity effect we find numerically is caused by the regular ferromagnet, with the halfmetallic layer being inconsequential. We therefore tried to remove the halfmetal from the system entirely, and redo the calculations for a similar superconductor/

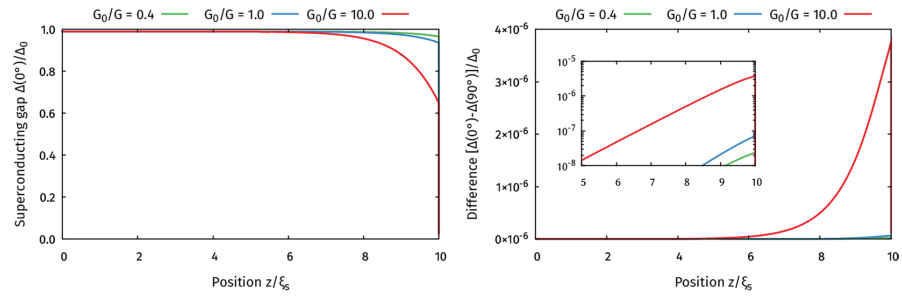


Figure 11. Plot of the superconducting gap Δ as a function of position inside the superconductor in the S/F/N/HM setup. The left plot shows the result for a 0° misalignment between the magnetizations of the F and HM, which is a measure of the proximity effect in the system. The right plot shows the difference between the results for 0° and 90° misalignment, which is a measure of the spin-valve effect. The inset shows how this spin-valve effect decays on a logarithmic scale. As indicated in the legends, we repeated the calculations for various interface conductances G_0 .

ferromagnet/normal-metal multilayer, and got precisely the same critical temperature results. This indicates that the inverse proximity effect on the superconductor was dominated by the ferromagnet and not the half-metal, and that the Cooper pairs leaking from the superconductor and into the ferromagnet likely substantially decay before even reaching the normal metal. We tried checking some different lengths for the superconductor and ferromagnet, and different strengths for the spin-mixing. The highest critical temperature shift we found was for a superconductor length $L_S = 0.7 \xi_S$ and ferromagnet length $L_F = 0.1 \xi_S$, using $G_0/G_0 = 10$ for the halfmetal interface. But even in that case, the critical temperature shift was only $[T_c(0) - T_c(\pi/2)]/T_{cs} = 0.001$. In other words, the largest simulation result we managed to achieve is two orders of magnitude smaller than the experimental result by Singh *et al.*, even after reducing the superconductor length by a factor 14 relative to the experiment, and tweaking the ferromagnet length as much as possible while remaining within the quasiclassical limits. It should however be noted that the present theory does not permit inclusion of highly transparent interfaces, in contrast to *e.g.* Nazarov's boundary conditions for non-magnetic interfaces²⁸, but is restricted to the limit of tunneling interfaces. For further details about our modelling of the experiment by Singh *et al.*, as well as a quantitative comparison of $T_c(0)$ and $T_c(\pi/2)$ for both S/F/N/HM and S/F/N systems with various parameters, the reader may consult the Supplementary Information.

Our results for the S/HM bilayer also show that even if the superconducting gap is strongly suppressed at the interface, it still recovers a few coherence lengths away from the interface. To investigate whether the same happens in the S/F/N/HM setup, we also performed zero-temperature calculations of the superconducting gap in this structure, as shown in Fig. 11. In all cases, we found that the proximity effect remains significant only for the first 2–3 coherence lengths away from the magnetic interface, while the spin-valve effect is insignificant for all positions and conductances. These results further support our hypothesis that the standard long-ranged proximity effect interpretation cannot fully explain the results of Singh *et al.*⁷.

Previous works have considered the critical temperature of S/HM layers in the diffusive⁴⁴ and ballistic²⁴ limit, but cannot be compared to the measurements by Singh *et al.*⁷ since these works considered a thin superconducting layer with size L_S comparable to or smaller than the superconducting coherence length ξ_S rather than $L_S = 10 \xi_S \gg \xi_S$ as in the experiment. Note that in contrast to ref. 44, where it was assumed that all interfaces in the junction were transparent, we used a finite interface transparency at each interface of the S/F/N/HM junction, as this should be experimentally more realistic, and we also chose a larger magnitude of the exchange field. Since there are three such interfaces between S and HM in the junction, our structure has a much lower net transparency than in ref. 44, so that the T_c variation in our case is small even for very thin superconductors $L_S < T_c$. This may explain why the T_c results herein were much weaker than the one found in ref. 44 when $L_S < \xi_S$.

Conclusion

Summarizing, we have developed a framework for studying the interaction between diffusive superconducting and strongly polarized magnetic materials and half-metals using quasiclassical theory. We have applied this framework on superconductors interfaced to strongly polarized ferromagnetic insulators and half-metallic ferromagnets, solving the equations selfconsistently in order to study the manifestation of triplet Cooper pairs induced in the superconductor. We have computed the density of states and critical temperature in the abovementioned systems. Recent experimental work have measured precisely these quantities in via STM in S/HM bilayers (DOS)⁸ and resistance measurements in S/F/N/HM layers (T_c)⁷. We have shown that our theory is able to reproduce an unusually strong zero-energy peak in the S/HM bilayer, exceeding the normal-state value, induced in a superconductor as seen experimentally in ref. 8. We also predicted a strong spin-valve effect in such bilayers, as shown in Fig. 10. Moreover, we computed the T_c shift upon 90° rotation of the magnetization in a spin-valve S/F/N/HM multilayer and discussed this result in the context of the experiment of ref. 7 and clarified the difference in length-scale for the inverse proximity effect in a superconductor and the length-scale for which a spin-valve effect occurs.

References

- Robinson, J. W. A. & Blamire, M. G. The interface between superconductivity and magnetism: understanding and device prospects. *J. Phys. Condens. Matter* **26**, 453201, doi:10.1088/0953-8984/26/45/453201 (2014).
- Eschrig, M. Spin-polarized supercurrents for spintronics: a review of current progress. *Rep. Prog. Phys.* **78**, 10, doi:10.1088/0034-4885/78/10/104501 (2015).
- Linder, J. & Robinson, J. W. A. Superconducting spintronics. *Nat. Phys.* **11**, 307–315, doi:10.1038/nphys3242 (2015).
- Pal, A., Barber, Z. H., Robinson, J. W. A. & Blamire, M. G. Pure second harmonic current-phase relation in spin-filter Josephson junctions. *Nat. Commun.* **5**, 3340, doi:10.1038/ncomms4340 (2014).
- Pal, A. & Blamire, M. B. Large interfacial exchange fields in a thick superconducting film coupled to a spin-filter tunnel barrier. *Phys. Rev. B* **92**, 180510(R), doi:10.1103/PhysRevB.92.180510 (2015).
- Kalchauer, Y., Millo, O., Egilmez, M., Robinson, J. W. A. & Blamire, M. G. Evidence for anisotropic triplet superconductor order parameter in half-metallic ferromagnetic $\text{La}_{0.7}\text{Ca}_{0.3}\text{Mn}_2\text{O}$ proximity coupled to superconducting $\text{Pr}_{1.85}\text{Ce}_{0.15}\text{CuO}_4$. *Phys. Rev. B* **85**, 104504, doi:10.1103/PhysRevB.85.104504 (2012).
- Singh, A., Voltan, S., Lahabi, K. & Aarts, J. Colossal proximity effect in a superconducting triplet spin valve based on the half-metallic ferromagnet CrO_2 . *Physical Review X* **5**, 021019, doi:10.1103/PhysRevX.5.021019 (2015).
- Kalchauer, Y., Millo, O., Di Bernardo, A., Pal, A. & Robinson, J. W. A. Inverse proximity effect at superconductor-ferromagnet interfaces; Evidence for induced triplet pairing in the superconductor. *Phys. Rev. B* **92**, 060501(R), doi:10.1103/PhysRevB.92.060501 (2015).
- Berezinskii, V. L. New model of the anisotropic phase of superfluid ^3He . *JETP Letters* **20**, 287 (1974).
- Bergeret, F. S., Volkov, A. F. & Efetov, K. B. Long-Range proximity effects in superconductor-ferromagnet structures. *Phys. Rev. Lett.* **86**, 4096–9, doi:10.1103/PhysRevLett.86.4096 (2001).
- Di Bernardo, A. *et al.* Signature of magnetic-dependent gapless odd frequency states at superconductor/ferromagnet interfaces. *Nat. Commun.* **6**, 8053, doi:10.1038/ncomms9053 (2015).
- Usadel, K. D. Generalized diffusion equation for superconducting alloys. *Phys. Rev. Lett.* **25**, 507–509, doi:10.1103/PhysRevLett.25.507 (1970).
- Eschrig, M., Cottet, A., Belzig, W. & Linder, J. General boundary conditions for quasiclassical theory of superconductivity in the diffusive limit: application to strongly spin-polarized systems. *New J. Phys.* **17**, 083037, doi:10.1088/1367-2630/17/8/083037 (2015).
- Eschrig, M., Kopu, J., Konstandin, A., Fogelström, M. & Schön, G. Singlet-triplet mixing in superconductor-ferromagnet hybrid devices. *Advances in Solid State Physics* **44**, 533–546, doi:10.1007/b95888 (2004).
- Grein, R., Löfwander, T., Metalidis, G. & Eschrig, M. Theory of superconductor-ferromagnet point-contact spectra: the case of strong spin polarization. *Phys. Rev. B* **81**, 094508, doi:10.1103/PhysRevB.81.094508 (2010).
- Eschrig, M., Kopu, J., Cuevas, J. C. & Schön, G. Theory of half-metal/superconductor heterostructures. *Phys. Rev. Lett.* **90**, 137003, doi:10.1103/PhysRevLett.90.137003 (2003).
- Kopu, J., Eschrig, M., Cuevas, J. C. & Fogelström, M. Transfer-matrix description of heterostructures involving superconductors and ferromagnets. *Phys. Rev. B* **69**, 094501, doi:10.1103/PhysRevLett.90.137003 (2004).
- Eschrig, M. & Löfwander, T. Triplet supercurrents in clean and disordered half-metallic ferromagnets. *Nature Physics* **4**, 138–143, doi:10.1038/nphys831 (2008).
- Grein, R., Eschrig, M., Metalidis, G. & Schön, G. Spin-Dependent Cooper pair phase and pure spin supercurrents in strongly polarized ferromagnets. *Phys. Rev. Lett.* **102**, 227005, doi:10.1103/PhysRevLett.102.227005 (2009).
- Eschrig, M. Scattering problem in nonequilibrium quasiclassical theory of metals and superconductors: general boundary conditions and applications. *Phys. Rev. B* **80**, 134511, doi:10.1103/PhysRevB.80.134511 (2009).
- Löfwander, T., Grein, R. & Eschrig, M. Is CrO_2 fully spin polarized? Analysis of Andreev spectra and excess current. *Phys. Rev. Lett.* **105**, 207001, doi:10.1103/PhysRevLett.105.207001 (2010).
- Halterman, K., Barsic, P. H. & Valls, O. T. Odd triplet pairing in clean superconductor/ferromagnet heterostructures. *Phys. Rev. Lett.* **99**, 127002, doi:10.1103/PhysRevLett.99.127002 (2007).
- Grein, R., Löfwander, T. & Eschrig, M. Inverse proximity effect and influence of disorder on triplet supercurrents in strongly spin-polarized ferromagnets. *Phys. Rev. B* **88**, 054502, doi:10.1103/PhysRevB.88.054502 (2013).
- Halterman, K. & Alidoust, M. Half-metallic superconducting triplet spin valve. *Phys. Rev. B* **94**, 064503, doi:10.1103/PhysRevB.94.064503 (2016).
- Rammer, J. & Smith, H. Quantum field-theoretical methods in transport theory of metals. *Rev. Mod. Phys.* **58**, 323–359, doi:10.1103/RevModPhys.58.323 (1986).
- Chandrasekhar, V. Introduction to the quasiclassical theory of superconductivity for diffusive proximity-coupled systems. In: *The Physics of Superconductors* (Springer-Verlag, 2004).
- Nazarov, Y. V. Circuit theory of Andreev conductance. *Phys. Rev. Lett.* **73**, 1420–1423, doi:10.1103/PhysRevLett.73.1420 (1994).
- Nazarov, Y. V. Novel circuit theory of Andreev reflection. *Superlattices and Microstructures* **25**, 1221–1231, doi:10.1006/spmi.1999.0738 (1999).
- Nazarov, Y. V. & Blanter, Y. M. Quantum transport: introduction to nanoscience (Cambridge University Press, 2009).
- Kuprianov, M. Y. & Lukichev, V. F. Influence of boundary transparency on the critical current of dirty SS structures. *Soviet Physics JETP* **67**, 1163 (1988).
- Schopohl, N. Transformation of the Eilenberger equations of superconductivity to a scalar Riccati equation arxiv:cond-mat/9804064 (1998).
- Eschrig, M. Distribution functions in nonequilibrium theory of superconductivity and Andreev spectroscopy in unconventional superconductors. *Phys. Rev. B* **61**, 9061–9076, doi:10.1103/PhysRevB.61.9061 (2000).
- Konstandin, A., Kopu, J. & Eschrig, M. Superconducting proximity effect through a magnetic domain wall. *Phys. Rev. B* **72**, 140501, doi:10.1103/PhysRevB.72.140501 (2005).
- Jacobsen, S. H., Ouassou, J. A. & Linder, J. Critical temperature and tunneling spectroscopy of superconductor-ferromagnet hybrids with intrinsic Rashba-Dresselhaus spin-orbit coupling. *Phys. Rev. B* **92**, 024510, doi:10.1103/PhysRevB.92.024510 (2015).
- Machon, P., Eschrig, M. & Belzig, W. Nonlocal thermoelectric effects and nonlocal onsager relations in a three-terminal proximity-coupled superconductor-ferromagnet device. *Phys. Rev. Lett.* **110**, 047002, doi:10.1103/PhysRevLett.110.047002 (2013).
- Bergeret, F. S., Verso, A. & Volkov, A. F. Electronic transport through ferromagnetic and superconducting junctions with spin-filter tunneling barriers. *Phys. Rev. B* **86**, 214516, doi:10.1103/PhysRevB.86.214516 (2012).
- Linder, J., Yokoyama, T., Sudbo, A. & Eschrig, M. Pairing symmetry conversion by spin-active interfaces in magnetic normal-metal-superconductor junctions. *Phys. Rev. Lett.* **102**, 107008, doi:10.1103/PhysRevLett.102.107008 (2009).
- Linder, J., Sudbo, A., Yokoyama, T., Grein, R. & Eschrig, M. Signature of odd-frequency pairing correlations induced by a magnetic interface. *Phys. Rev. B* **81**, 214504, doi:10.1103/PhysRevB.81.214504 (2010).
- Linder, J. & Robinson, J. W. A. Strong odd-frequency correlations in fully gapped Zeeman-split superconductors. *Sci. Rep.* **5**, 15483, doi:10.1038/srep15483 (2015).
- Yokoyama, T., Tanaka, Y. & Golubov, A. A. Manifestation of the odd-frequency spin-triplet pairing state in diffusive ferromagnet/superconductor junctions. *Phys. Rev. B* **75**, 134510, doi:10.1103/PhysRevB.75.134510 (2007).
- Moraru, I. C., Pratt, W. P. Jr. & Birge, N. O. Observation of standard spin-switch effects in ferromagnet/superconductor/ferromagnet trilayers with a strong ferromagnet. *Phys. Rev. B* **74**, 220507(R), doi:10.1103/PhysRevLett.96.037004 (2006).

42. Villamor, E., Isasa, M., Hueso, L. E. & Casanova, F. Temperature dependence of spin polarization in ferromagnetic metals using lateral spin valves. *Phys. Rev. B* **88**, 184411, doi:10.1103/PhysRevB.88.184411 (2013).
43. Keizer, R. S., Goennenwein, S. T. B., Klapwijk, T. M., Miao, G., Xiao, G. & Gupta, A. A spin triplet supercurrent through the half-metallic ferromagnet CrO₂. *Nature* **439**, 825–827, doi:10.1038/nature04499 (2006).
44. Mironov, S. & Buzdin, A. Triplet proximity effect in superconducting heterostructures with a half-metallic layer. *Phys. Rev. B* **92**, 184506, doi:10.1103/PhysRevB.92.184506 (2015).

Acknowledgements

J. Aarts, A. Singh, J. W. A. Robinson, A. Di Bernardo, and N. Banerjee are thanked for useful discussions. J.L. was supported by the Research Council of Norway, Grant No. 216700 and the *Outstanding Academic Fellows* programme at NTNU. J.L. and J.A.O. were supported by the Research Council of Norway, Grant No. 240806. M.E. and M.G.B. was supported by EPSRC grant EP/N017242/1.

Author Contributions

J.A.O. performed the analytical and numerical calculations with minor support from J.L. The majority of the writing of the manuscript was done by J.A.O. and J.L. M.E. contributed to discussion and understanding of the boundary conditions for strongly spin-polarized diffusive systems on which the manuscript is based. All authors (J.A.O., A.P., M.B., M.E., and J.L.) contributed to the discussion of the results and revisions of the manuscript.

Additional Information

Supplementary information accompanies this paper at doi:10.1038/s41598-017-01330-1

Competing Interests: The authors declare that they have no competing interests.

Publisher's note: Springer Nature remains neutral with regard to jurisdictional claims in published maps and institutional affiliations.



Open Access This article is licensed under a Creative Commons Attribution 4.0 International License, which permits use, sharing, adaptation, distribution and reproduction in any medium or format, as long as you give appropriate credit to the original author(s) and the source, provide a link to the Creative Commons license, and indicate if changes were made. The images or other third party material in this article are included in the article's Creative Commons license, unless indicated otherwise in a credit line to the material. If material is not included in the article's Creative Commons license and your intended use is not permitted by statutory regulation or exceeds the permitted use, you will need to obtain permission directly from the copyright holder. To view a copy of this license, visit <http://creativecommons.org/licenses/by/4.0/>.

© The Author(s) 2017

Supplementary information for: Triplet Cooper pairs induced in diffusive *s*-wave superconductors interfaced with strongly spin-polarized magnetic insulators or half-metallic ferromagnets

Jabir Ali Ouassou, Avradeep Pal, Mark Blamire, Matthias Eschrig, & Jacob Linder

Modelling the Singh experiment

As discussed in the main article, we modelled the experiment by Singh *et al.* as a diffusive S/F/N/HM multilayer with spin-dependent tunneling boundary conditions. We set the tunneling conductance at each interface to $G_0/G = 0.4$, where G is the normal-state conductance of each material. At the S/F and F/N interfaces, we chose the modest spin-mixing conductance $G_\varphi/G_0 = 0.5$ and polarization $P = 0.2$. At the N/HM interface, however, we chose the much larger values $G_\varphi/G_0 = 10$ and $P = 0.999$. As for the magnetization directions, we assume that the magnetization of the HM is oriented along the z -axis, while the magnetization of F is along the direction $\sin\alpha e_x + \cos\alpha e_z$ in the xz -plane, so that α is the magnetic misalignment in the structure. In accordance with the experiment, we set the length of S to $10\xi_S$, F to $0.3\xi_S$, N to $1.0\xi_S$, and HM to $20\xi_S$, where $\xi_S = 5$ nm is the coherence length of the superconductor MoGe. However, we found no spin-valve effect $T_c(0) - T_c(\pi/2)$ for this set of parameters, where $T_c(\alpha)$ is the critical temperature for a structure with a misalignment α as defined above.

In figs. 1 to 4 below, we show that this conclusion is very robust to changes in model parameters. All plots show the critical temperature T_c measured relative to the bulk superconductor critical temperature T_{cs} . The four subfigures in each figure show the critical temperatures $T_c(0)$ and $T_c(\pi/2)$ for different magnetic configurations, as well as results for both an S/F/N/HM and S/F/N junction with the same parameters. In fact, not only do we find that $T_c(\pi/2)$ is nearly identical to $T_c(0)$ for a very wide parameter span, but we also see that the results for an S/F/N/HM and S/F/N junction look the same as well. From this, we draw the conclusion that although there is a large proximity effect in these structures – as evidenced by $T_c(0)$ and $T_c(\pi/2)$ being much smaller than T_{cs} – there is only a negligible spin-valve effect $T_c(0) - T_c(\pi/2)$. The comparison between the S/F/N/HM and S/F/N junctions show that in all cases, the observed proximity effect can be attributed solely to the F layer and not the HM layer.

The reason for this lack of spin-valve effect, seems to be that there are too many interfaces inbetween the S and HM in the S/F/N/HM junction. Since we assume that each interface in this junction is a tunneling barrier, this leads to a very low effective transparency between the S and HM layers. In other words, if all the Cooper pairs leaking out of S are either reflected at one of these interfaces, or decay inside the F, then they do not reach the HM. This, of course, means that the properties of the HM become irrelevant for the physical state of S. Thus, we end up with an effective S/F bilayer and not a spin-valve.

We therefore conclude that the the experiment by Singh *et al.* is likely to have a different mechanism than a triplet spin-valve.

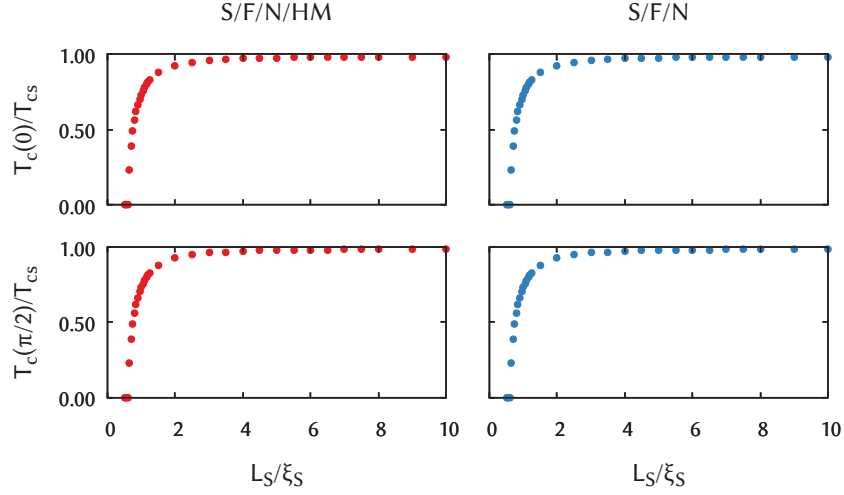


Figure 1. Critical temperature as a function of the superconductor length L_S . The other parameters were set to the experimental estimates described in the text. To see a significant proximity effect, we need the superconductor to be shorter than $\sim 2\xi_S$, which is much smaller than the $\sim 10\xi_S$ used in the experiment. This result is consistent with the conventional wisdom that the coherence length is the “healing length” of a superconductor, over which the superconducting gap is restored to nearly its bulk value: even if $\Delta \rightarrow 0$ at one end, $\Delta \rightarrow \Delta_0$ at the other end if $L_S \gg \xi_S$, resulting in a high T_c . Note that even for a superconductor as short as $1\xi_S$, we see no evidence of a spin-valve effect since the curves for $T_c(0)$ and $T_c(\pi/2)$ behave in the same way. We also see no evidence of the HM having any effect on the superconductor, since removing it produces the same T_c curves.

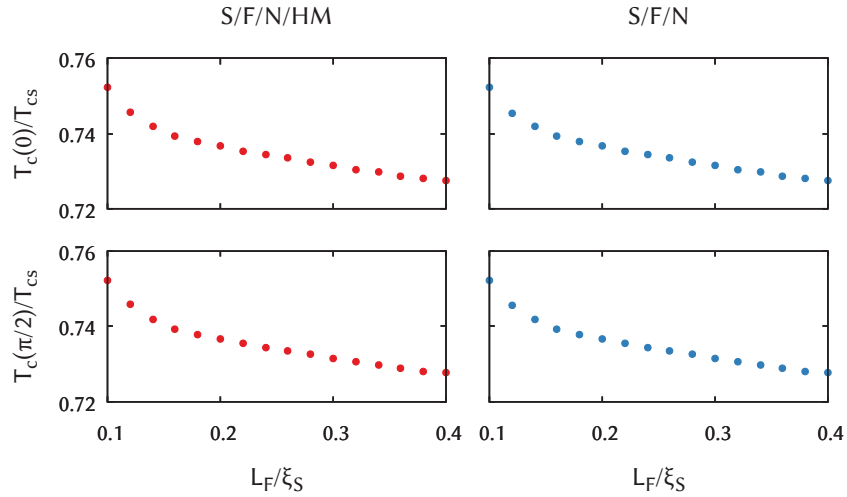


Figure 2. Critical temperature as a function of the ferromagnet length L_F . In order to see any proximity effect at all, we have chosen a superconductor length $L_S = \xi_S$ for this simulation, which is much smaller than the experimental value $10\xi_S$. The other parameters are as close to the experimental estimates as possible, as described in the text. Even with these changes, we see no evidence of a spin-valve effect even with an F length significantly different from the experimental value $0.3\xi_S$.

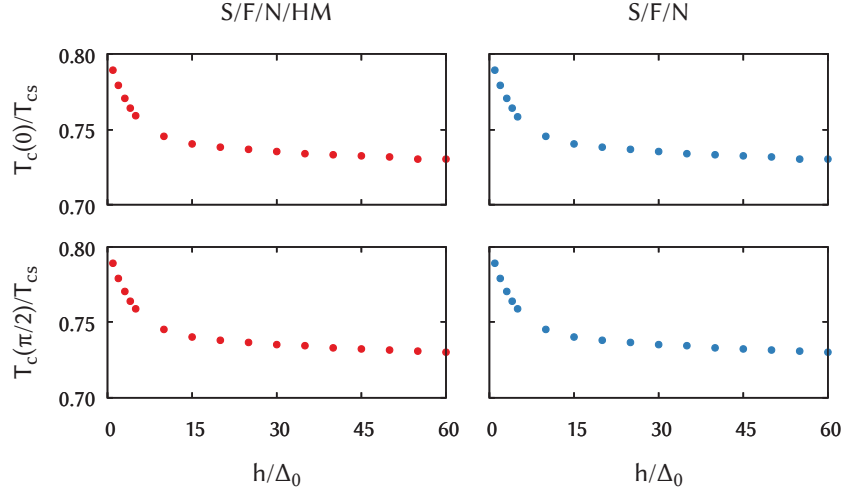


Figure 3. Critical temperature as a function of the exchange field h . In order to see any proximity effect at all, we have chosen a superconductor length $L_S = \xi_S$. The other parameters are as close to the experimental estimates as possible, as described in the text. Even if we decrease the exchange field with more than an order of magnitude compared to the value $h = 50\Delta_0$, which is already low compared to the experiment, we do not find any spin-valve effect. Increasing the exchange field would not help either, since that would cause even more Cooper pairs to decay inside the F, further reducing the number that reaches the HM.

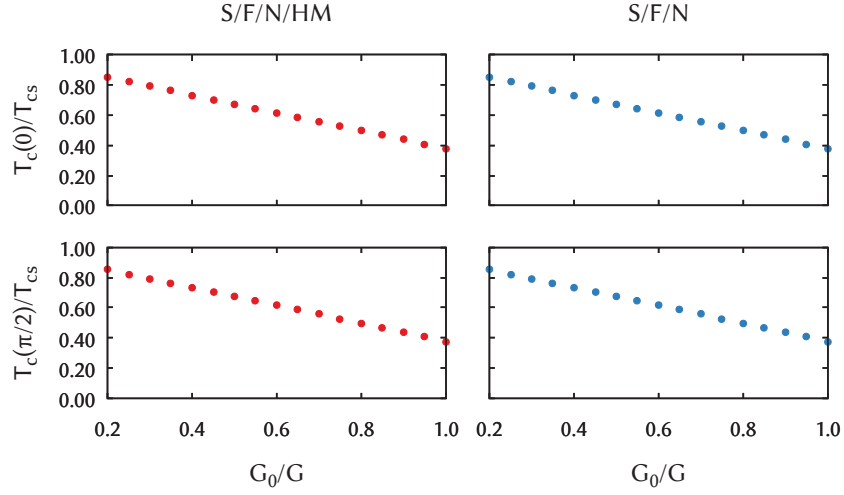


Figure 4. Critical temperature as a function of the tunneling conductance G_0/G at each interface in the junction. We chose a superconductor length $L_S = \xi_S$ for this simulation to obtain a reasonable proximity effect, but kept the other parameters as close to the experimental estimates as possible, as described in the text. Even using a relatively high tunneling conductance $G_0 = G$ does not produce any evidence of a spin-valve effect in our numerical simulations.

IX

Reference

J.A. Ouassou, S.H. Jacobsen, J. Linder.
Conservation of spin supercurrents in superconductors.
Physical review B 96, 094505 (2017).
DOI: 10/GC4M2N

Contributions

JAO suggested the geometry, performed all the numerical simulations, and analyzed the results. SHJ had the original idea behind the project, and analytically showed that spin supercurrents have to be conserved in conventional superconductors. JL provided support and supervision. All authors contributed to the discussion and writing of the manuscript.

Comments

This project was based on reference 181. In that paper, it was pointed out that spin supercurrents are conserved in nonmagnetic metals, even in the presence of spin-flip and spin-orbit impurities. It turned out to be a widespread idea that the picture should be different inside conventional superconductors, and that spin supercurrents ought to decay there. In this paper, we demonstrate analytically and numerically that spin supercurrents are in fact conserved also in superconductors. Notably, the magnitude of the spin supercurrent does decline with the size of the superconductor—but it does so throughout the superconductor, without violating the conservation of spin supercurrents. In the process, we also stumbled over some other interesting effects, e.g. that the supercurrents vary nonmonotonically with impurity concentration.

This project was presented in a talk at the COST workshop *Coherent superconducting hybrids and related materials* (Les Arcs, France, 2018).

Conservation of spin supercurrents in superconductors

Jabir Ali Ouassou, Sol H. Jacobsen, and Jacob Linder

Center for Quantum Spintronics, Department of Physics, Norwegian University of Science and Technology, N-7491 Trondheim, Norway

(Received 16 June 2017; published 7 September 2017)

We demonstrate that spin supercurrents are conserved upon transmission through a conventional superconductor, even in the presence of spin-dependent scattering by impurities with magnetic moments or spin-orbit coupling. This is fundamentally different from conventional spin currents, which decay in the presence of such scattering, and has important implications for the usage of superconducting materials in spintronics.

DOI: 10.1103/PhysRevB.96.094505

I. INTRODUCTION

Superconducting spintronics marries the dissipationless currents of superconductors with nanoscopic hardware in which both charge and spin degrees of freedom are manipulated [1–4]. Recent experiments have demonstrated that such devices offer significant improvements over their non-superconducting counterparts, showcasing, e.g., enhanced spin lifetimes [5], relaxation lengths [6], spin Hall effects [7], and infinite magnetoresistance [8].

Magnetic and spin-orbit impurities usually act as antagonists to spintronics as they cause a rapid spatial decay of conventional spin currents, which remain polarized only up to the spin relaxation length [9,10]. Realistic superconductors also contain magnetic and spin-orbit impurities that randomize the electron spins. Taken in combination with the fact that Cooper pairs in the bulk of a conventional superconductor are spinless, one might expect such impurities to also cause a decay of spin supercurrents in a superconductor. However, it has recently been shown that spin supercurrents do not decay in homogeneous magnets with spin-dependent scattering [11]. Here, we find the surprising result that the spin supercurrent is also conserved in superconductors, and we analyze the underlying physical mechanism. The result has significant implications for the use of superconductors in spintronic architectures, the experimental implementation of which is just starting to flourish [1–8].

II. PHYSICAL SYSTEM

We consider theoretically the spin supercurrents in a Sn/Ho/Co/Sn/Co/Ho/Sn multilayer stack, as shown in Fig. 1. This structure is inspired by the Nb/Ho/Co/Ho/Nb system investigated experimentally in Ref. [12]; however, we insert a superconductor within the central magnetic layer to investigate how spin currents behave in superconductors. A related model was considered in Ref. [13], which however focused on the behavior of the charge and not spin supercurrents. In contrast to their model, we also treat the central superconductor self-consistently in order to ensure charge conservation.

Tin (Sn) is a conventional superconductor with a zero-temperature gap $\Delta_0 \approx 1.15$ meV, coherence length $\xi \approx 30$ nm, and density of states $N_0 \approx 66$ eV⁻¹ nm⁻³ at the Fermi level [14]. Note that the value for the density of states corresponds to white tin at room temperature, but we will use it as an order-of-magnitude estimate also at cryogenic temperatures. The source and drain are bulk superconductors

with gaps $\Delta_0 e^{\pm i\varphi/2}$, where φ is their phase-difference, while the gap is determined self-consistently in the central Sn [15]. Holmium (Ho) is a conical antiferromagnet below ~ 20 K [16], having a spatially rotating in-plane magnetization with a constant out-of-plane component. We therefore model the exchange field in the Ho layer as

$$\mathbf{h} = 5\Delta_0[\sin(\gamma)\cos(z/\zeta), \sin(\gamma)\sin(z/\zeta), \cos(\gamma)], \quad (1)$$

where the cone angle $\gamma = 0.45\pi$ [16], and the spiral length $\zeta = 3.34$ nm [17]. We set the Ho layer lengths to $1.5\zeta = 5$ nm, since the spin current in the central layer is maximal for nonintegral numbers of Ho spirals [12]. Lastly, we model the relatively strong exchange fields of both Cobalt (Co) layers as $\mathbf{h} = 50\Delta_0\mathbf{e}_y$, assuming that their magnetizations are homogeneous, parallel, and in-plane. The lengths of each Co layer was set to $0.1\xi = 3$ nm. Note, however, that the results are qualitatively unaffected by these specific parameter choices.

The outer Sn layers in Fig. 1 are superconducting reservoirs, and act as sources for singlet Cooper pairs $|\uparrow\downarrow\rangle - |\downarrow\uparrow\rangle$. These singlet pairs leak into the neighboring Ho layers, where the inhomogeneous magnetic order converts them into a mixture of all possible triplet pairs: $|\uparrow\downarrow\rangle + |\downarrow\uparrow\rangle$, $|\uparrow\uparrow\rangle$, and $|\downarrow\downarrow\rangle$, with spin projections measured relative to the Co magnetization. The $|\uparrow\downarrow\rangle + |\downarrow\uparrow\rangle$ contributions rapidly decay inside Co, because the constituent electrons belong to different spin bands. Furthermore, the interfacial spin polarization leads to a slight increase in the number of $|\uparrow\uparrow\rangle$ pairs compared to $|\downarrow\downarrow\rangle$ pairs. Thus the central Sn layer obtains a proximity-induced repository of triplet pairs, which is dominated by the $|\uparrow\uparrow\rangle$ component, but also contains traces of other triplet components. In addition, this Sn layer has its own condensate of singlet pairs, which may be converted into $|\uparrow\downarrow\rangle + |\downarrow\uparrow\rangle$ triplets at the Co interfaces. This leads to a complex mixture of Cooper pairs throughout the junction, which may partake in the transmission of a completely general spin supercurrent. In the rest of the manuscript, we analyze the properties and behavior of this current.

III. THEORY

For the numerical analysis, we employ the quasiclassical theory of superconductivity, taking the whole junction to be diffusive and in equilibrium. Specifically, we solve simultaneously the Usadel diffusion equation in each layer [18–22],

$$i\hbar D\partial_z(\hat{g}\partial_z\hat{g}) = [\hat{\Sigma}, \hat{g}], \quad (2)$$

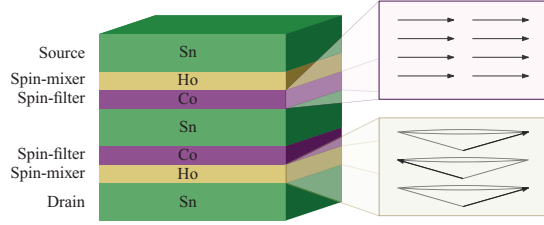


FIG. 1. The thin-film stack considered in this paper. The insets on the right show the magnetization textures in the Co and Ho layers.

and the gap equation in the central superconductor [15],

$$\Delta(z) = \frac{1}{2} N_0 \lambda \int_{-\Theta}^{+\Theta} d\epsilon f_s(z, \epsilon) \tanh(\epsilon/2T), \quad (3)$$

yielding self-consistent results. Equation (2) is solved for the 4×4 matrix $\hat{g}(z, \epsilon)$, which contains the spin-resolved normal and anomalous retarded propagators as functions of the quasiparticle energy ϵ and position z . The other matrices are

$$\hat{\Sigma} = \epsilon \hat{\tau}_3 + \hat{\Delta} + \mathbf{h} \hat{\sigma} + \alpha_{sf} \hat{\sigma} \hat{\sigma} + \alpha_{so} \hat{\tau}_3 \hat{\sigma} \hat{\sigma} \hat{\tau}_3, \quad (4)$$

$$\hat{\tau}_3 = \text{diag}(+1, +1, -1, -1), \quad (5)$$

$$\hat{\Delta} = \text{antidiag}(+\Delta, -\Delta, +\Delta^*, -\Delta^*), \quad (6)$$

$$\hat{\sigma} = \text{diag}(\boldsymbol{\sigma}, \boldsymbol{\sigma}^*), \quad (7)$$

where $\boldsymbol{\sigma}$ is the Pauli vector. In addition, the equations involve the local superconducting gap Δ , exchange field \mathbf{h} , spin-flip scattering rate α_{sf} , spin-orbit scattering rate α_{so} , normal-state density of states at the Fermi level N_0 , BCS coupling constant λ , diffusion coefficient $D = \Delta_0 \xi^2 / \hbar$, temperature T , Debye cutoff $\Theta = \Delta_0 \cosh(1/N_0 \lambda)$, and Planck's reduced constant \hbar . Inelastic scattering is approximated by a complex quasiparticle energy, i.e., $\epsilon \rightarrow \epsilon + 0.01 \Delta_0 i$. Only the singlet component f_s of the propagator matrix \hat{g} enters Eq. (3). For more details about the numerical solution of these equations, see Ref. [23].

We use Kupriyanov–Lukichev boundary conditions for Sn/Ho interfaces [24], and general spin-active boundary conditions for Ho/Co and Co/Sn interfaces [25–29]. To model experimentally realistic interfaces with low to moderate transparency, we set the ratio of tunneling to bulk conductance to be $G_T/G_0 = 0.3$ at each interface. We set $G_\varphi/G_T = 0.3$ at each Co interface, where G_φ is the spin-mixing conductance. The interfacial spin polarization of Co was set to $P = 0.12$, based on estimates for the polarization of the conductivity [30].

Once the equations above are solved, the charge current J_e and spin current J_s are found via

$$J_e(z) = 2J_{e0} \int_{-\infty}^{+\infty} d\epsilon \text{Re Tr}[\hat{\tau}_3 \hat{g}(z, \epsilon) \partial_z \hat{g}(z, \epsilon)] \tanh(\epsilon/2T), \quad (8)$$

$$J_s(z) = 2J_{s0} \int_{-\infty}^{+\infty} d\epsilon \text{Re Tr}[\hat{\sigma} \hat{\tau}_3 \hat{g}(z, \epsilon) \partial_z \hat{g}(z, \epsilon)] \tanh(\epsilon/2T), \quad (9)$$

where $J_{e0} = eN_0 \Delta_0^2 \xi^2 A / 4\hbar L$, $J_{s0} = \hbar J_{e0} / 2e$, e is the electron charge, L is the length of the central superconductor, and A is the cross-sectional area of the junction. Using the previously specified material parameters for Sn, and assuming a superconductor length $L \approx \xi$, the current density unit can be estimated as $J_{e0}/A \approx 16 \text{ MA/cm}^2$. The charge and spin currents are measured relative to this unit throughout the manuscript, and are typically 1–4 orders of magnitude smaller.

The spin current above may be decomposed into an exchange current J_{s+} and polarization current J_{s-} :

$$\mathbf{J}_{s\pm}(\varphi) \equiv [\mathbf{J}_s(+\varphi) \pm \mathbf{J}_s(-\varphi)]/2. \quad (10)$$

By construction, these currents $J_{s\pm}$ are symmetric and antisymmetric under $\varphi \rightarrow -\varphi$, respectively. The polarization current is just the spin-polarized component of the charge current, and vanishes at $\varphi = 0$ as expected. Note that a polarization current can only be obtained if one includes the interfacial polarization of Co in the model, to act as a spin filter by providing different tunneling amplitudes for $|\uparrow\uparrow\rangle$ and $|\downarrow\downarrow\rangle$ Cooper pairs, where the spin-directions are measured relative to the Co magnetization. Otherwise, the electric current will be transported by an equal number of $|\uparrow\uparrow\rangle$ and $|\downarrow\downarrow\rangle$ pairs, resulting in no net spin transfer. On the other hand, the exchange current mediates the exchange interaction between ferromagnetic layers [31], and can be finite even for $\varphi = 0$, i.e., without any charge current. These quantities behave quite differently as functions of the superconducting phase-difference [11]. Herein, we focus on the magnitudes $J_{s\pm} = |\mathbf{J}_{s\pm}|$ of these spin currents, and not their polarization directions.

In Josephson junctions [32], the supercurrent depends on the phase-difference φ between the superconductors as well as the properties of the barrier [33]. Whereas it takes a $\sin(\varphi)$ form for normal tunneling barriers, it can take a $\sin(\varphi + \pi)$ form when the barrier is magnetic [33–35], and an even more exotic $\sin(\varphi + \varphi_0)$ form in the presence of spin-orbit coupling [36–40]. Herein, we are interested in studying supercurrents *inside* a superconductor, which is why we focus on double-barrier junctions with a superconductor sandwiched in the middle. Depending on the system parameters, the supercurrent can also take a more complex $\sin(\varphi/2) \text{sgn}[\cos(\varphi/2)]$ form in such junctions [41–46]. This $\sin(\varphi/2)$ behavior can intuitively be understood if one thinks of the double-barrier junction as a concatenation of two regular Josephson junctions, where a total phase-difference φ over the double-barrier junction is distributed evenly between the subjunctions. In this manuscript, we will briefly discuss the charge supercurrent for completeness, but the main focus will however be the *spin supercurrents*.

IV. ANALYTICAL ARGUMENT

We will now prove analytically that the spin supercurrent is conserved in superconductors with spin-flip and spin-orbit scattering within a self-consistent Born approximation framework, where conventional spin currents typically decay [47,48]. First, let us rewrite the spin current in Eq. (9) as

$$J_s(z) = 2J_{s0} \int_{-\infty}^{+\infty} d\epsilon \text{Re}[j_s(z, \epsilon)] \tanh(\epsilon/2T), \quad (11)$$

where we define a spectral spin current

$$\mathbf{j}_s \equiv \text{Tr}[\hat{\sigma} \hat{\tau}_3 \hat{g} \partial_z \hat{g}]. \quad (12)$$

The easiest way to satisfy the conservation of spin current \mathbf{J}_s would be if the spectral spin current \mathbf{j}_s is conserved as well. Mathematically, this can be checked by differentiating Eq. (12), and investigating whether the resulting expression vanishes:

$$\partial_z \mathbf{j}_s = \text{Tr}[\hat{\sigma} \hat{\tau}_3 \partial_z (\hat{g} \partial_z \hat{g})] = 0. \quad (13)$$

Note that $\partial_z (\hat{g} \partial_z \hat{g})$ is just the left-hand side of the Usadel equation [Eq. (2)], such that the condition simplifies to

$$\text{Tr}\{\hat{\sigma} \hat{\tau}_3 [\hat{\Sigma}, \hat{g}]\} = 0. \quad (14)$$

This condition can be checked by inserting the most general form for \hat{g} , containing all allowed symmetry components of the normal and anomalous propagators, and explicitly evaluating the trace [11]. The process is straightforward but tedious, and therefore omitted here. The result is that the condition holds in the presence of a superconducting gap Δ , spin-flip scattering α_{sf} , and spin-orbit scattering α_{so} . This constitutes an analytical proof that spin currents are conserved in superconductors with spin-flip and spin-orbit scattering.

However, the quasiclassical approach also allows one to go further, permitting a self-consistent numerical investigation to expose the underlying physical mechanisms behind this conservation of the spin supercurrent in superconductors. We focus on this topic in the remainder of the paper.

V. NUMERICAL RESULTS

In Fig. 2, we see how the charge and spin currents vary as functions of position in a junction with scattering rates $\alpha_{sf} = \alpha_{so} = 0.01\Delta_0$ and a phase-difference $\varphi = \pi/2$. For comparison, these scattering rates α are related to the scattering lengths ℓ by $\alpha = \Delta_0 \xi^2 / 8\ell^2$. Using the spin-flip lengths reported in Ref. [9], we find that α_{sf}/Δ_0 varies in the range 10^{-4} – 10^{-1} for typical nonmagnetic metals at

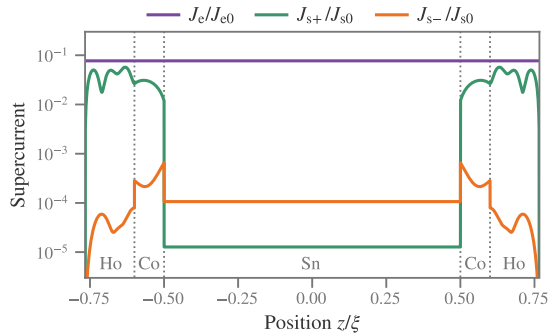


FIG. 2. Charge current J_e and spin currents $J_{s\pm}$ as functions of position z . The dotted vertical lines indicate interfaces between materials in the junction. In this case, the phase-difference between the outer superconductors is $\varphi = \pi/2$, the central superconductor has length $L = \xi$, and the scattering rates are $\alpha_{sf} = \alpha_{so} = 0.01\Delta_0$. Note that the charge current is conserved throughout the junction, while the spin current is only conserved inside the central superconductor.

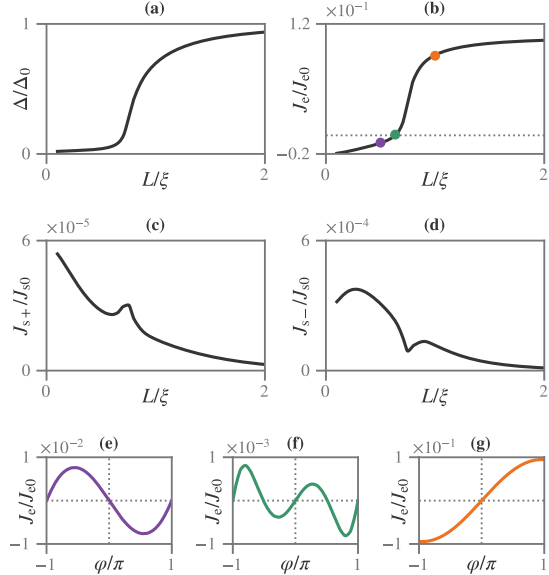


FIG. 3. Plots of the (a) superconducting gap, (b) charge current, (c) exchange current, and (d) polarization current as functions of the superconductor length L . The shape of the charge current-phase relation is shown below for a superconductor length (e) $L/\xi = 0.500$, (f) $L/\xi = 0.635$, and (g) $L/\xi = 1.000$. The currents were calculated for $\alpha_{sf} = \alpha_{so} = 0$, and a phase-difference $\varphi = \pi/2$ between source and drain. The lengths in (e)–(g) are indicated by coloured markers in (b).

cryogenic temperatures, but it can be further increased by doping with magnetic atoms. We see that the charge current is preserved as expected, and since J_{s-} is interpreted as the spin-polarization of the charge current, this must necessarily also be dissipationless. To consider the exchange current, we note that the spin current is carried by triplet pairs, and randomization by scattering merely alters the number of singlet/triplet states available, via the introduction of an imaginary energy term. Since the impurities provide no means of conversion from triplet to singlet states, or rotation to another triplet state, the magnitude of the conserved current is governed by the size of the junction (Fig. 3) and the scattering strength (Fig. 4), as discussed below.

The effect of the superconductor length is investigated in Fig. 3 for the ideal case without spin-dependent scattering. From Fig. 3(a), we see that as the length is increased, the superconducting gap Δ increases from zero to the bulk gap Δ_0 . During this transition from a normal to superconducting state, the charge current (b) switches sign, indicating that we have a 0 – π transition in the junction. We also note that the charge current is significantly increased when the central layer is in a superconducting rather than normal state, as one should expect. Investigating the current-phase relation around the 0 – π transition [between (e) and (g) as indicated in (b)], reveals that the junction simultaneously switches from a $\sin(\varphi)$ to $\sin(\varphi/2) \text{sgn}[\cos(\varphi/2)]$ current-phase relation during the transition [41–46]. Exactly at the 0 – π transition (f), the

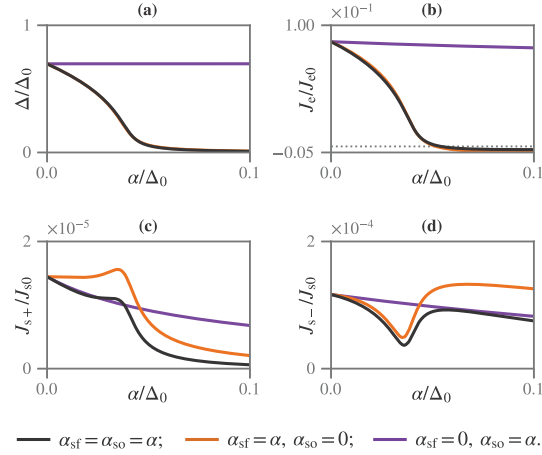


FIG. 4. Plots of the (a) superconducting gap, (b) charge current, (c) exchange current and (d) polarization current as functions of the scattering rate α . The black curves include both spin-flip and spin-orbit scattering; the orange curves show pure spin-flip scattering; the purple curves show pure spin-orbit scattering. Note that in (a) and (b), the black and orange curves overlap almost completely.

current-phase relation is dominated by a higher-order $\sin(2\varphi)$ contribution.

As the superconductor length increases, the exchange (c) and polarization (d) currents decay. This can be explained as follows. The concentration of triplet pairs decays exponentially away from the interfaces, meaning that the triplet concentration at the center of the junction decreases exponentially with the superconductor length. Since the spin currents are conserved, the triplet concentration at the center acts as a “bottleneck” for the spin currents. Thus, the spin currents also decay exponentially with the system length. One notable exception to this monotonic decay occurs precisely at the $0-\pi$ transition point, where the spin currents suddenly fluctuate. This happens because the charge current drops abruptly near the transition point, which causes the polarization current to decrease while the exchange current increases.

In Fig. 4(a), we see how the scattering rates affect the gap. Since singlet pairs are resistant to spin-orbit scattering but destroyed by spin-flip scattering, the gap is only significantly suppressed by the spin-flip impurities. The majority of the charge current in a superconductor is of course transported by the condensate of singlet pairs, so the charge current (b) is also hindered by spin-flip but not spin-orbit scattering. Just like we found in Fig. 3, the system undergoes a $0-\pi$ transition when the superconducting gap becomes nonzero, and the charge current-phase relation (not shown) changes from a $\sin(\varphi)$ to $\sin(\varphi/2) \text{sgn}[\cos(\varphi/2)]$ shape during this phase-transition.

Looking at the spin currents [(c) and (d)], we note that an increasing spin-orbit scattering causes a weak monotonic decrease. This is because the scattering suppresses the triplet population throughout the junction, limiting the size of the spin currents. In the case of spin-flip scattering, however, the picture becomes more complex. Small increases in the scattering rate decrease the polarization current—but further increasing it

leads to a resurgence. In fact, it reaches a value that is even higher than for zero spin-flip scattering, leading to the counter-intuitive conclusion that a moderate spin-flip scattering can actually *increase* the spin current. For the exchange current, we see the opposite trend: it initially increases with the spin-flip scattering, but then decays rapidly afterwards.

The reason for this behavior is as follows. There are two triplet sources for the central superconductor: (i) singlet pairs from the central superconductor that are converted to triplets at the Co-interface; (ii) singlet pairs from the outer superconductors that are converted to triplets as they diffuse through the Ho and Co layers. The first kind of triplet dominates the transport when the central gap is strong ($\Delta \rightarrow \Delta_0$), but only the second kind contributes when it is weak ($\Delta \rightarrow 0$). It can be shown that for our junction parameters, the first kind results in a positive contribution to the charge current and the second a negative, explaining the $0-\pi$ transition as a function of any parameter that modulates the gap. The $0-\pi$ transition in the triplet current occurs slightly earlier than the corresponding transition in the total charge current, but the transition regime matches the nonmonotonic regimes in Figs. 4(c) and 4(d) very well. Furthermore, the first kind of triplet is less spin-polarized than the second kind since it did not have to pass *through* the Co spin filters, explaining the increase of the polarization current in Fig. 4(d) as the dominant triplet source changes.

VI. DISCUSSION

We have shown analytically and numerically that spin supercurrents are conserved in superconductors, even when we include spin-flip and spin-orbit scattering processes. We proceeded to analyze how the results varied with sample size and scattering rates in Figs. 3 and 4, and identified a combination of a $0-\pi$ transition, $\sin(\varphi) \rightarrow \sin(\varphi/2) \text{sgn}[\cos(\varphi/2)]$ transition, and a complex modulation of the spin current. Increasing the interface transparencies would have increased all currents in the junction, and choosing a material with higher polarization than Co should enhance the polarization current.

The conservation of spin currents can intuitively be understood as follows. The polarization current physically corresponds to the spin-polarized part of the charge current. Since Cooper pairs that participate in charge transport are protected against resistive scattering, the same protection applies to the polarization current as well, resulting in it being conserved. The exchange current, on the other hand, can be shown to be conserved even in non-superconducting F/N/F systems [31]. If both the polarization and exchange currents are conserved separately, the total spin current is conserved as well.

It was noted in Ref. [49] that an equilibrium spin current is conserved in a superconductor free from magnetic impurities. The conservation of the spin current is consistent with the angular momentum conservation law since spatial variations in the current must generate a torque on a magnetic order parameter, and no such torque is present in a superconductor. However, this argument breaks down in the presence of magnetic impurities: in this case, the spatial variations in the current could generate a torque on the impurity spin orientations. Since we still find that the spin supercurrent is conserved in the presence of such impurities, the spin

supercurrents must behave in a fundamentally different way from their dissipative counterparts.

As shown in Figs. 3(c) and 3(d), the spin supercurrents are small if the central superconductor becomes much larger than the coherence length, which in our proposed junction is $\xi \approx 30$ nm. Since the spin-relaxation length can exceed $0.5 \mu\text{m}$ in e.g. Al, the conservation of spin supercurrents over ~ 30 nm may not seem that significant. However, we expect the spin supercurrent to have a conserved component also in ballistic junctions. Since the superconducting coherence length in e.g. Al can reach $1.6 \mu\text{m}$ in the ballistic case, this entails a conservation over remarkable length scales. Moreover, spin supercurrents are fundamentally different from conventional spin currents since they may be manipulated using phase-coherent circuits in equilibrium, which may lead to entirely new kinds of spintronic device design. While we do not propose any device that supersedes its conventional equivalents here, a thorough understanding of the properties of spin supercurrents will be vital for the future development of such devices.

Our numerical results show that the charge currents are typically below $10^{-1} J_{c0} \approx 1 \text{ MA/cm}^2$, which is reasonable for a supercurrent inside a superconductor. However, the spin currents are typically of order $10^{-4} J_{s0} \approx (\hbar/2e) \times 1 \text{ kA/cm}^2$, which is small compared to what is routinely produced in nonsuperconducting spintronics circuits.¹ The purpose of the junction studied in this paper was however not to maximize the spin currents, but to investigate the fundamental physics and demonstrate that spin currents are conserved for a completely general structure with both exchange and polarization currents. It would, however, be straightforward to enhance the spin currents by a few orders of magnitude. For instance, one could increase the tunneling conductance towards G_0 , reduce the thickness of the Ho layers to $\zeta/2$, and remove the Co spin filters. The spin current is conserved also in these more optimized junctions, which may be of more interest for applications. Moreover, in our structure we used

magnetically inhomogeneous Ho layers to generate the $|\uparrow\uparrow\rangle$ and $|\downarrow\downarrow\rangle$ triplet components, which are long-ranged in the Co spin filters. However, intrinsic spin-orbit coupling can also perform this function [15,51,52]. In that case, homogeneous ferromagnets would be sufficient [11], and it could be instructive to include such systems in further investigations of current maximization.

A numerical treatment of a ballistic S/F/S/F/S system in equilibrium was considered in Ref. [53]. In such a system, the current magnitude decreases with layer length because it decreases the ferromagnetic coupling. In our case, we have demonstrated the surprising result that spin currents are immune to magnetic and spin-orbit impurities, inevitably present in real materials, which rapidly destroy spin currents in nonsuperconducting systems. Furthermore, we have shown the counterintuitive result that the magnitude of the spin currents can actually increase with impurity concentration.

VII. CONCLUSION

Using a combination of both analytical arguments and numerical simulations, we have shown that spin supercurrents are conserved in superconductors, even in the presence of spin-dependent scattering processes. Furthermore, we have shown that the charge and spin supercurrents have a nonmonotonic dependence on the various junction parameters, and that the current-phase relation also changes its shape as these are varied. The result that spin supercurrents do not decay in superconductors has profound consequences with regard to potential applications based on spintronics, since it implies that information carried by the spin degree of freedom can be transmitted without loss or decoherence through a superconductor.

ACKNOWLEDGMENTS

We thank Morten Amundsen and Vette Risinggård for useful discussions, and acknowledge support from the Research Council of Norway Grants No. 216700 and No. 240806 and the Outstanding Academic Fellows programme at NTNU. We also acknowledge support from NTNU and the Research Council of Norway for funding via the Center for Quantum Spintronics.

¹For instance, charge current densities up to 120 MA/cm^2 have been achieved in permalloy [50], which has a spin polarization of 0.38 [30], thus yielding spin current densities of $(\hbar/2e) \times 46 \text{ MA/cm}^2$.

-
- [1] J. Linder and J. W. A. Robinson, *Nat. Phys.* **11**, 307 (2015).
 - [2] M. Eschrig, *Phys. Today* **64**, 43 (2011).
 - [3] M. Eschrig, *Rep. Prog. Phys.* **78**, 104501 (2015).
 - [4] M. G. Blamire and J. W. A. Robinson, *J. Phys. Condens. Matter* **26**, 453201 (2014).
 - [5] H. Yang *et al.*, *Nat. Mater.* **9**, 586 (2010).
 - [6] C. H. L. Quay *et al.*, *Nat. Phys.* **9**, 84 (2013).
 - [7] T. Wakamura *et al.*, *Nat. Mater.* **14**, 675 (2015).
 - [8] B. Li, N. Roschewsky, B. A. Assaf, M. Eich, M. Epstein-Martin, D. Heiman, M. Müntenberg, and J. S. Moodera, *Phys. Rev. Lett.* **110**, 097001 (2013).
 - [9] J. Bass and W. P. Pratt, Jr., *J. Phys.: Condens. Matter* **19**, 183201 (2007).
 - [10] Y. Otani and T. Kimura, *Phil. Trans. R. Soc. A* **369**, 3136 (2011).
 - [11] S. H. Jacobsen, I. Kulagina, and J. Linder, *Sci. Rep.* **6**, 23926 (2016).
 - [12] J. W. A. Robinson, J. D. S. Witt, and M. G. Blamire, *Science* **329**, 59 (2010).
 - [13] M. Alidoust and K. Halterman, *Phys. Rev. B* **89**, 195111 (2014).
 - [14] C. Yu, J. Liu, H. Lu, and J. Chen, *Solid State Commun.* **140**, 538 (2006).
 - [15] S. H. Jacobsen, J. A. Ouassou, and J. Linder, *Phys. Rev. B* **92**, 024510 (2015).
 - [16] W. Koehler, J. Cable, M. Wilkinson, and E. Wollan, *Phys. Rev.* **151**, 414 (1966).

- [17] F. Chiodi *et al.*, *Europhys. Lett.* **101**, 37002 (2013).
- [18] K. Usadel, *Phys. Rev. Lett.* **25**, 507 (1970).
- [19] J. Rammer, *Rev. Mod. Phys.* **58**, 323 (1986).
- [20] V. Chandrasekhar, *Phys. Supercond.* **2**, 55 (2004).
- [21] W. Belzig *et al.*, *Superlattices Microstruct.* **25**, 1251 (1999).
- [22] M. Silaev, P. Virtanen, F. S. Bergeret, and T. T. Heikkilä, *Phys. Rev. Lett.* **114**, 167002 (2015).
- [23] J. A. Ouassou, A. Di Bernardo, J. W. A. Robinson, and J. Linder, *Sci. Rep.* **6**, 29312 (2016).
- [24] M. Y. Kupriyanov and V. F. Lukichev, *Zh. Eksp. Teor. Fiz.* **94**, 139 (1988) [*Sov. Phys. JETP* **67**, 1163 (1988)].
- [25] M. Eschrig, A. Cottet, W. Belzig, and J. Linder, *New J. Phys.* **17**, 083037 (2015).
- [26] P. Machon, M. Eschrig, and W. Belzig, *Phys. Rev. Lett.* **110**, 047002 (2013).
- [27] A. Cottet, *Phys. Rev. B* **76**, 224505 (2007).
- [28] A. Cottet, D. Huertas-Hernando, W. Belzig, and Y. V. Nazarov, *Phys. Rev. B* **80**, 184511 (2009).
- [29] M. Lababidi and E. Zhao, *Phys. Rev. B* **83**, 184511 (2011).
- [30] E. Villamor, M. Isasa, L. E. Hueso, and F. Casanova, *Phys. Rev. B* **88**, 184411 (2013).
- [31] W. Chen, P. Horsch, and D. Manske, *Phys. Rev. B* **89**, 064427 (2014).
- [32] B. Josephson, *Phys. Lett.* **1**, 251 (1962).
- [33] A. A. Golubov, M. Yu. Kupriyanov, and E. Il'ichev, *Rev. Mod. Phys.* **76**, 411 (2004).
- [34] A. I. Buzdin, *Rev. Mod. Phys.* **77**, 935 (2005).
- [35] V. V. Ryazanov, V. A. Oboznov, A. Y. Rusanov, A. V. Veretennikov, A. A. Golubov, and J. Aarts, *Phys. Rev. Lett.* **86**, 2427 (2001).
- [36] D. B. Szombati *et al.*, *Nat. Phys.* **12**, 568 (2016).
- [37] A. I. Buzdin, *Phys. Rev. Lett.* **101**, 107005 (2008).
- [38] A. A. Reynoso, G. Usaj, C. A. Balseiro, D. Feinberg, and M. Avignon, *Phys. Rev. Lett.* **101**, 107001 (2008).
- [39] A. Zazunov, R. Egger, T. Jonckheere, and T. Martin, *Phys. Rev. Lett.* **103**, 147004 (2009).
- [40] Y. Tanaka, T. Yokoyama, and N. Nagaosa, *Phys. Rev. Lett.* **103**, 107002 (2009).
- [41] J. A. Ouassou and J. Linder, *Phys. Rev. B* **96**, 064516 (2017).
- [42] I. Zapata and F. Sols, *Phys. Rev. B* **53**, 6693 (1996).
- [43] H. Ishikawa, S. Kurihara, and Y. Enomoto, *Physica C* **350**, 62 (2001).
- [44] M. Yu. Kupriyanov *et al.*, *Physica C* **326**, 16 (1999).
- [45] R. De Luca and F. Romeo, *Phys. Rev. B* **79**, 094516 (2009).
- [46] C. W. J. Beenakker, *Annu. Rev. Condens. Matter Phys.* **4**, 113 (2013).
- [47] J. P. Morten, A. Brataas, and W. Belzig, *Phys. Rev. B* **70**, 212508 (2004).
- [48] J. P. Morten, A. Brataas, and W. Belzig, *Phys. Rev. B* **72**, 014510 (2005).
- [49] J. Linder, T. Yokoyama, and A. Sudbø, *Phys. Rev. B* **79**, 224504 (2009).
- [50] A. Yamaguchi, T. Ono, S. Nasu, K. Miyake, K. Mibu, and T. Shinjo, *Phys. Rev. Lett.* **92**, 077205 (2004).
- [51] F. S. Bergeret and I. V. Tokatly, *Phys. Rev. Lett.* **110**, 117003 (2013).
- [52] F. S. Bergeret and I. V. Tokatly, *Phys. Rev. B* **89**, 134517 (2014).
- [53] K. Halterman and M. Alidoust, *Supercond. Sci. Technol.* **29**, 055007 (2016).

X

Reference

J.A. Ouassou, J. Linder.
Spin-switch Josephson junctions with magnetically tunable $\sin(\delta\varphi/n)$ current–phase relation.
Physical review B 96, 064516 (2017).
DOI: 10/CMN8

Contributions

JAO came up with the idea, performed the analytical and numerical calculations, and wrote the initial draft. JL supervised the entire process, and helped with the discussion and writing of the manuscript.

Comments

This project was presented in a talk at the COST workshop *Coherent superconducting hybrids and related materials* (Les Arcs, France, 2018).

Spin-switch Josephson junctions with magnetically tunable $\sin(\delta\varphi/n)$ current-phase relation

Jabir Ali Ouassou* and Jacob Linder

QuSpin Center of Excellence, Department of Physics, Norwegian University of Science and Technology, N-7491 Trondheim, Norway

(Received 9 December 2016; revised manuscript received 27 July 2017; published 16 August 2017)

With a combination of simple analytical arguments and extensive numerical simulations, we theoretically propose a Josephson junction with $n + 1$ superconductors where the current-phase relation can be toggled *in situ* between a $\sin(\delta\varphi)$ and $\sin(\delta\varphi/n)$ shape using an applied magnetic field. Focusing in particular on the case $n = 2$, we show that by using realistic system parameters such as unequal interface transparencies, the $\sin(\delta\varphi/2)$ -shaped solution retains its 2π periodicity due to discontinuities at $\delta\varphi = \pm\pi$. Moreover, we demonstrate that as one toggles between the $\sin(\delta\varphi)$ - and $\sin(\delta\varphi/2)$ -shaped solutions, the system acts as an on-off switch, and can achieve more than two orders of magnitude difference between the supercurrent in the on and off states. Finally, we argue that the same approach can be generalized to switchable $\sin(\delta\varphi/n)$ junctions for arbitrary integers n , which we motivate by analytically solving the Josephson equations for double- and triple-barrier junctions.

DOI: 10.1103/PhysRevB.96.064516

I. INTRODUCTION

In a Josephson junction, two superconductors are proximity coupled through a nonsuperconducting region, such as a normal metal or insulator. In conventional Josephson junctions, it can be shown that the current flowing between the superconductors in the tunneling limit is proportional to $\sin(\delta\varphi)$, where $\delta\varphi$ is the phase difference between the superconductors [1]. These are also known as 0 junctions, as the ground state is $\delta\varphi = 0$. In recent years, there has been a lot of interest in developing Josephson junctions with unconventional current-phase relations. One of the first was the experimental realization of π junctions using magnetic elements between the superconductors [2,3], where the current is proportional to $\sin(\delta\varphi + \pi)$, i.e., it flows in the opposite direction to a 0 junction for the same phase difference $\delta\varphi$. This work was then extended to φ junctions with two ground states $\delta\varphi = \pm\varphi$ by combining 0 and π junctions [4,5]. Another important development was the very recent construction [6] of a φ_0 junction using spin-orbit interactions [7–11], where the current was found to be proportional to $\sin(\delta\varphi + \varphi_0)$, with an electrically controllable phase bias φ_0 .

In this paper, we focus on a different scenario, namely, a $\sin(\delta\varphi/n)$ junction. The special case of $\sin(\delta\varphi/2)$ has previously been discussed in Refs. [12–15], and has recently been subject of rekindled interest as a possible signature for a Majorana-mediated supercurrent [16–19]. Here, we demonstrate theoretically a Josephson junction where the current-phase relation can be toggled *in situ* between a $\sin(\delta\varphi)$ and $\sin(\delta\varphi/2)$ shape by changing the configuration of a spin valve via a magnetic field. The current-phase relation nevertheless retains its 2π periodicity due to discontinuities at $\delta\varphi = \pm\pi$. Moreover, we show that when toggling between the two current-phase relations, the system acts as an on-off switch; the supercurrent magnitude can differ by more than two orders of magnitude in the two states. We further argue that the same approach can be used to construct more general junctions with $\sin(\delta\varphi/n)$ shapes, where n is an arbitrary and magnetically tunable integer. In addition to being interesting

from a fundamental physics point of view, discovering novel kinds of Josephson junctions may also find applications in both digital and quantum computing [20].

II. ANALYTICAL ARGUMENT

A. Double-barrier junction

From here on, we use the notation S for superconductors and X for nonsuperconductors, where X can be any combination of ferromagnets (F), insulators (I), and normal metals (N). It is well known that in the tunneling limit, the current-phase relation for a single-barrier S/X/S Josephson junction is [1]

$$J = J_c \sin(\delta\varphi), \quad (1)$$

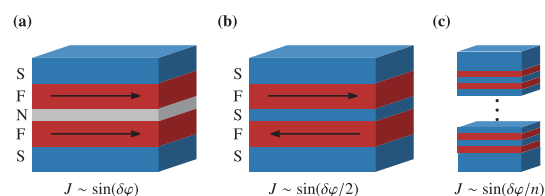


FIG. 1. Schematic of the proposed device. (a) If the ferromagnets are aligned in parallel, the effective exchange fields experienced by the conduction electrons add up inside the superconductor, resulting in a strong net field there. This net exchange field suppresses superconductivity, making the central layer act as a normal metal. We therefore get an effective S/X/S junction with a conventional $\sin(\delta\varphi)$ current-phase relation. (b) If the ferromagnets have an antiparallel alignment, their fields cancel near the center of the superconductor. The central layer thus acts as a superconductor, and we get an S/X/S/X/S junction with a more exotic $\sin(\delta\varphi/2)$ shape for the current-phase relation instead. (c) In principle, the same idea can be extended to a junction that consists of m superconductors sandwiched in-between ferromagnets. This should result in a junction with a general $\sin(\delta\varphi/n)$ shape for the current-phase relation, where $n \in [1, m + 1]$ is magnetically tunable. For instance, an S/X/S/X/S/X/S system could support $n = 1$ for an $\uparrow\uparrow\uparrow$ configuration of the magnetic layers, $n = 2$ for $\uparrow\uparrow\downarrow$, and $n = 3$ for $\uparrow\downarrow\uparrow$.

*jabir.a.ouassou@ntnu.no

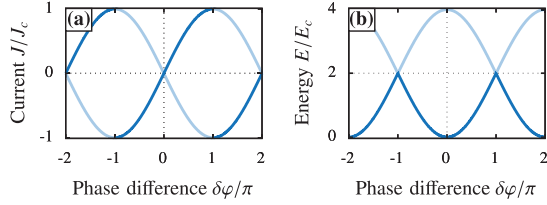


FIG. 2. Analytical plot of (a) the supercurrent and (b) the free energy as functions of the phase difference in a $\sin(\delta\varphi/2)$ junction. For every value of the phase difference $\delta\varphi$, there are two solutions: the low-energy state (dark blue line) and high-energy state (transparent).

where J_c is the critical charge current, and $\delta\varphi$ is the net phase difference across the junction. Under certain conditions, this result can be generalized to junctions with multiple superconducting elements. Let us first assume that the superconducting phase changes slowly as function of position inside each superconducting layer, i.e., that the supercurrent is relatively small. In this limit, we can treat an S/X/S/X/S junction (see Fig. 1) as a concatenation of two S/X/S subjunctions, where the subjunctions are described by the current-phase relations

$$J_{12} = J_c \sin(\varphi_2 - \varphi_1), \quad J_{23} = J_c \sin(\varphi_3 - \varphi_2), \quad (2)$$

where J_{ij} is the current from superconductor number i to j , φ_i is the phase of superconductor number i , and we have assumed that the critical current of each subjunction is equal. In any real physical system, these critical currents will not be identical, and we later discuss in detail how this influences the result. We have some freedom when choosing these phases φ_i since only *phase differences* affect the physics of the system. We may therefore define $\varphi_1 \equiv -\delta\varphi/2$ and $\varphi_3 \equiv +\delta\varphi/2$, such that the net phase difference across the junction is $\varphi_3 - \varphi_1 = \delta\varphi$:

$$J_{12} = J_c \sin(\delta\varphi/2 + \varphi_2), \quad J_{23} = J_c \sin(\delta\varphi/2 - \varphi_2). \quad (3)$$

Since the current has to be conserved through the junction, we have the constraint $J_{12} = J_{23} = J$. The resulting equations have two distinct solutions $\varphi_2 = 0$ and π , yielding the currents

$$J = \pm J_c \sin(\delta\varphi/2). \quad (4)$$

Adding up the energies $E_{ij} = E_c[1 - \cos(\varphi_j - \varphi_i)]$ of each subjunction, where $E_c = \hbar J_c/2e$ is the Josephson energy, we also find the corresponding junction energies

$$E = E_c[2 \mp 2 \cos(\delta\varphi/2)]. \quad (5)$$

Similarly, one can show that an S/X/S/X/S/X/S junction results in a $\sin(\delta\varphi/3)$ current-phase relation shape (see Sec. II B), and that adding more superconductors and barriers in this way may lead to more general $\sin(\delta\varphi/n)$ shapes (see Sec. II C).

For each external phase difference $\delta\varphi$, there is a low-energy and a high-energy solution, as illustrated in Fig. 2. Each of these branches are 2π periodic. From here on, we will focus on the low-energy branch, which can be written succinctly [15]

$$J = J_c \sin(\delta\varphi/2) \operatorname{sgn}[\cos(\delta\varphi/2)]. \quad (6)$$

Throughout this paper, we will for brevity refer to this current-phase relation as having a $\sin(\delta\varphi/2)$ shape, even though it is 2π periodic due to discontinuities at $\delta\varphi = \pm\pi$.

With this in mind, let us consider S/F/S/F/S double-barrier junctions, where the central F/S/F acts as a superconducting spin valve (see Fig. 1). Switching the orientation of only one F in such a structure can, e.g., be achieved using materials with intrinsically different coercivities [21], or using different thicknesses for the ferromagnets, where the latter affects both coercivities and anisotropies. Depending on whether the two F layers have a parallel (P) or antiparallel (AP) orientation, their effective magnetic exchange fields induced in the central S will either add or cancel. The stability of the superconducting condensate depends on the net exchange field felt by the Cooper pairs there, which means that one can toggle superconductivity on and off in the central region [22,23], effectively switching between an S/X/S and S/X/S/X/S junction. Since the S/X/S junction always has a $\sin(\delta\varphi)$ -shaped current-phase relation, while an S/X/S/X/S junction also supports $\sin(\delta\varphi/2)$ -shaped solutions, the result is that one should be able to magnetically switch between these current-phase relations. In Sec. III, we show the results of extensive self-consistent numerical simulations which confirm this prediction.

B. Triple-barrier junction

Let us now move on to a slightly more complicated case, namely, S/X/S/X/S/X/S junctions. In other words, we now have three concatenated S/X/S junctions, which we can describe using three currents J_{12}, \dots, J_{34} and four phases $\varphi_1, \dots, \varphi_4$:

$$J_{12} = J_c \sin(\varphi_2 - \varphi_1), \quad (7)$$

$$J_{23} = J_c \sin(\varphi_3 - \varphi_2), \quad (8)$$

$$J_{34} = J_c \sin(\varphi_4 - \varphi_3). \quad (9)$$

To simplify the derivations, we parametrize the superconductor phases $\varphi_1, \dots, \varphi_4$ in terms of their averages and differences:

$$\varphi_1 \equiv a - d/2, \quad \varphi_2 \equiv b - c/2, \quad (10)$$

$$\varphi_4 \equiv a + d/2, \quad \varphi_3 \equiv b + c/2. \quad (11)$$

In other words, the outer superconductors are described by their average a and difference d , while the inner ones are described by the corresponding parameters b and c . Since the overall phase of the system has no physical significance, we can set $a = 0$ without loss of generality. Thus, we obtain

$$J_{12} = J_c \sin(+b - c/2 + d/2), \quad (12)$$

$$J_{23} = J_c \sin(c), \quad (13)$$

$$J_{34} = J_c \sin(-b - c/2 + d/2). \quad (14)$$

To determine the current-phase relation of the junction, we need to solve the current conservation equation $J_{12} = J_{23} = J_{34}$ for a fixed external phase difference $\delta\varphi \equiv d \equiv \varphi_4 - \varphi_1$. Let us first consider the part $J_{12} = J_{34}$. Invoking the trigonometric identity $\sin(u \pm v) = \sin(u)\cos(v) \pm \cos(u)\sin(v)$ on both sides of the equation, this can be rewritten as $\sin(b)\cos(d/2 - c/2) = 0$. This has three distinct solutions: $b = 0$, $b = \pi$, and $c = d + \pi$. We will first address the solution branches $b = 0$ and π . If we substitute these solutions

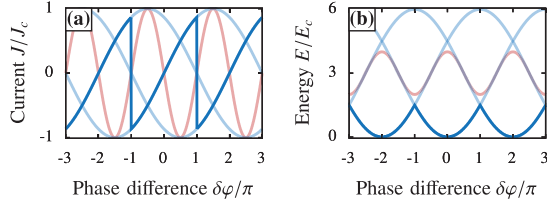


FIG. 3. Analytical plot of (a) the supercurrent and (b) the free energy as functions of the phase difference in a $\sin(\delta\varphi/3)$ junction. There are multiple solutions: the $\sin(\delta\varphi/3)$ -shaped low-energy state (dark blue), $\sin(\delta\varphi/3)$ -shaped excited states (transparent blue), and $\sin(\delta\varphi)$ -shaped excited state (transparent red). Note that the low-energy state is 2π periodic due to discontinuities at $\delta\varphi = \pm\pi, \pm 3\pi$.

into $J_{12} = J_{23}$, we obtain

$$\sin(c) = \pm \sin(d/2 - c/2). \quad (15)$$

This equation admits four distinct solutions: $b = 0, c = d/3$; $b = \pi, c = (d - 2\pi)/3$; $b = \pi, c = (d + 2\pi)/3$; $b = \pi, c = -d$. Let us first consider the first three solutions. Substituting these into the currents and energies of each subjunction, restoring the notation $\delta\varphi \equiv d$, and defining $k \in \{-1, 0, +1\}$, we find the current-phase and energy-phase relations

$$\begin{aligned} J &= J_c \sin[(\delta\varphi + 2\pi k)/3], \\ E &= E_c \{3 - 3 \cos[(\delta\varphi + 2\pi k)/3]\}. \end{aligned} \quad (16)$$

In other words, we do indeed find three solutions where the current-phase relation has the shape $\sin(\delta\varphi/3)$, as expected.

During the derivation above, we pointed out two alternative ways to satisfy the equations. Substituting these into the current conservation equation, we identify three additional solutions: $b = \pi, c = -d$; $b = d + \pi/2, c = d + \pi$; $b = d - \pi/2, c = d + \pi$. The currents and energies of these solutions are:

$$J = -J_c \sin(\delta\varphi), \quad E = E_c [3 + \cos(\delta\varphi)]. \quad (17)$$

In other words, the alternative solutions correspond to $\sin(\delta\varphi)$ -shaped current-phase relations in the π phase. However, as shown in Fig. 3, these are all excited states. The reason is that these alternative solution branches have two subjunctions with the energy-phase relation $E = E_c [1 + \cos(\delta\varphi)]$ and one with $E = E_c [1 - \cos(\delta\varphi)]$, meaning that minimizing the energy of one subjunction will simultaneously maximize the energy of another. This is different from the $\sin(\delta\varphi/3)$ -shaped solutions above, where the energy minima of each subjunction coincide.

C. Generalization

Let us now consider a general n -barrier junction, i.e., a system of $n + 1$ identical superconductors separated by n identical low-transparency barriers. As in the previous subsections, we can associate one phase $\varphi_0, \dots, \varphi_n$ with each superconductor, and write the currents and energies of the n subjunctions as

$$J_{m,m+1} = J_c \sin(\varphi_{m+1} - \varphi_m), \quad (18)$$

$$E_{m,m+1} = E_c [1 - \cos(\varphi_{m+1} - \varphi_m)]. \quad (19)$$

We fix the phase of the first superconductor $\varphi_0 = 0$, and the last one $\varphi_n = \delta\varphi$, so that $\delta\varphi$ is the phase difference between the outer superconductors. It is then straightforward to verify that the following phase distribution satisfies these requirements (modulo 2π), while also ensuring current conservation:

$$\varphi_m = (m/n)(\delta\varphi + 2\pi k), \quad (20)$$

where $m \in \{0, 1, \dots, n\}$ identifies each superconductor, and $k \in \{0, 1, \dots, n-1\}$ identifies each solution branch. Substituted into the current-phase and energy-phase relations, we get the following equations for the entire junction:

$$J = J_c \sin[(\delta\varphi + 2\pi k)/n], \quad (21)$$

$$E = E_c \{n - n \cos[(\delta\varphi + 2\pi k)/n]\}. \quad (22)$$

Each of these solutions has to contribute to the lowest-energy branch of the current-phase relation, as each of them provides a global energy minimum $E = 0$ for some phase difference $\delta\varphi$. The lowest-energy branch is again manifestly 2π periodic.

III. NUMERICAL RESULTS

To investigate the ideas outlined in the previous sections, we numerically investigated the simplest possible structure of this kind, namely, an S/F/S/F/S structure where the ferromagnetic layers are atomically thin insulators. The superconductors at the ends of the junction are assumed to be much larger than the superconducting coherence length ξ , so that we can treat them as bulk superconductors with order parameters $\Delta_0 e^{\pm i\delta\varphi/2}$, where Δ_0 and $\delta\varphi$ are real numbers. The central superconductor is assumed to have the length $L = \xi/2$. To describe the superconducting correlations there properly, we had to simultaneously solve the Usadel diffusion equation [24]

$$i\hbar D \partial_z (\hat{g} \partial_z \hat{g}) = [(\epsilon + i\delta)\hat{\tau}_3 + \hat{\Delta}, \hat{g}], \quad (23)$$

and the gap equation

$$\Delta(z) = \frac{1}{2} N_0 \lambda \int_{-\Theta}^{+\Theta} d\epsilon f_s(z, \epsilon) \tanh(\epsilon/2T), \quad (24)$$

yielding self-consistent results. Above, $\Theta = \Delta_0 \cosh(1/N_0 \lambda)$ is the Debye cutoff, ϵ the quasiparticle energy, δ the inelastic scattering rate, N_0 the normal-state density of states at the Fermi level, λ the BCS coupling constant, $D = \Delta_0 \xi^2 / \hbar$ the diffusion coefficient, T the temperature of the system, and \hbar Planck's reduced constant. The 4×4 matrix $\hat{g}(z, \epsilon)$ contains the spin-resolved normal and anomalous retarded Green functions in the system, $\hat{\Delta} = \text{antidiag}(+\Delta, -\Delta, +\Delta^*, -\Delta^*)$ contains the superconducting order parameter $\Delta(z)$, and $\hat{\tau}_3 = \text{diag}(+1, +1, -1, -1)$. Only the spin-singlet part f_s of the anomalous Green function enters the gap equation above. For more details about the numerical solution of these equations, see Refs. [25,26].

The ferromagnetic insulators are approximated as spin-active interfaces between the superconducting layers, which we describe using the recently derived spin-dependent boundary conditions for strongly polarized interfaces [27]. The boundary conditions can be written in terms of the *tunneling conductance* G_T , which depends on the number of transmission channels and their transparencies: a *spin-mixing conductance* G_φ , which describes the difference in phase shift between spin-up and spin-down electrons reflected off the interface; and a spin-polarization P , which describes the

different interface transparencies perceived by spin-up and spin-down electrons. See Refs. [26,27] for more details about these parameters. We assumed a strong interface polarization $P = 0.90$, a small tunneling conductance $G_T = 0.02G_0$, and a spin-mixing conductance $G_\varphi = 0.3G_0$, where G_0 is the normal-state conductance of the central superconductor. Such a parameter choice is likely suitable for strongly polarized ferromagnetic insulators such as GdN or EuS, where polarizations of 90% and upward have been experimentally reported [28,29]. Finally, we calculated the supercurrent throughout the junction via the equation

$$J(z) = 2J_0 \int_{-\Theta}^{+\Theta} d\epsilon \operatorname{Re} \operatorname{Tr} [\hat{\tau}_3 \hat{g}(z, \epsilon) \partial_z \hat{g}(z, \epsilon)] \tanh(\epsilon/2T), \quad (25)$$

where $J_0 = eN_0\Delta_0^2\xi^2A/4\hbar L$, e is the electron charge, and A is the cross-sectional area of the central superconductor.

A. Ideal case: Symmetric junction

We will start by considering the lowest-energy current-phase relation of a perfectly symmetric S/F/S/F/S structure, where the symmetry implies that the critical currents of the constituent S/F/S subjunctions are equal. In this section, we restrict our attention to the regime $-\pi < \delta\varphi < +\pi$ since the lowest-energy state is known to be 2π periodic. The numerical results are shown in Figs. 4 and 5. In Fig. 4, we see that it is indeed possible to magnetically switch between a very clean $\sin(\delta\varphi)$ - and $\sin(\delta\varphi/2)$ -shaped current-phase relation. The transition between a conventional and unconventional Josephson effect obtained in this manner is sensitive to the parameters of the junction. In a regular spin valve, achieving an absolute spin-valve effect in the junction requires that the superconductor length is short enough and the ferromagnetic properties strong enough to vanquish the superconducting condensate in the P configuration. In the system under consideration here, an additional complication is that one simultaneously requires a

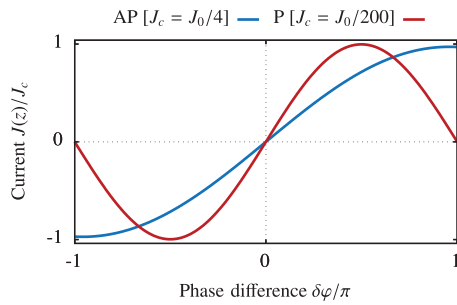


FIG. 4. Numerical results for the current-phase relation of an S/F/S/F/S junction. When we flip the magnetization direction of one magnet, we clearly switch between a $J = J_c \sin(\delta\varphi/2)$ and $J = J_c \sin(\delta\varphi)$ current-phase relation. Note that the magnitude of the critical current J_c is roughly 50 times larger in the AP orientation compared to the P orientation, as indicated in the figure legend. Since the current-phase relation is 2π periodic, while $J \rightarrow \pm J_c$ as $\delta\varphi \rightarrow \pm\pi$, the $\sin(\delta\varphi/2)$ -shaped solution is discontinuous at $\delta\varphi \rightarrow \pm\pi$.

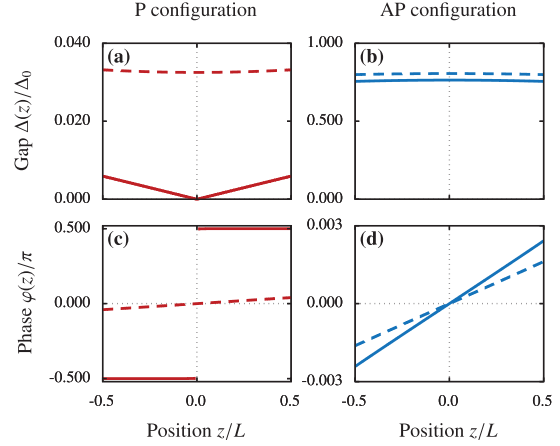


FIG. 5. Numerical results for the superconducting order parameter $\Delta(z) e^{i\varphi(z)}$, where Δ and φ are real-valued functions of the position z in the central superconductor. The dashed lines correspond to a phase difference $\delta\varphi = \pi/2$, and the solid lines to $\delta\varphi \rightarrow \pi$. In the AP case, the gap $\Delta(z)$ is close to the bulk gap Δ_0 . We have a finite phase winding for both $\delta\varphi = \pi/2$ and $\delta\varphi \rightarrow \pi$, but it is larger in the latter case. In the P case, however, the gap is one to two orders of magnitude smaller, and even drops to zero at the center for $\delta\varphi \rightarrow \pi$. Note the discontinuity in the phase for $\delta\varphi \rightarrow \pi$ and $z = 0$, which is where the order parameter $\Delta e^{i\varphi}$ changes sign. The gap plots are consistent with a spin-valve effect since Δ is suppressed in the P but not AP configuration. The phase plots are consistent with Fig. 4 since the current J is proportional to the phase winding $\partial_z \varphi$ at every point.

sufficiently low conductance through the ferromagnetic insulators to turn superconductivity off in the central superconductor. Otherwise, the bulk superconductors are able to supply enough Cooper pairs via the proximity effect to keep the central layer superconducting regardless of the magnetic configuration. However, making the conductance too low would limit the supercurrents that we are interested in. Therefore, in an experiment, some trial and error might be required to obtain ideal thicknesses for the material layers.

We proceed to discuss the physics underlying the transition between the conventional and unconventional Josephson effects. From Fig. 5, we see that the gap is close to the bulk value Δ_0 in the AP configuration, while it drops below $0.04\Delta_0$ in the P configuration. In other words, we have the desired spin-valve effect, where the magnetic configuration of the junction alone is enough to change the self-consistently calculated gap in the central superconductor by orders of magnitude. Note that in all cases where a current is flowing, the phase winding in the central superconductor is relatively small, which means that a large part of the phase winding must be happening in the ferromagnetic insulators in-between the superconductors. In the P configuration with $\delta\varphi = \pi$, the order parameter $\Delta(z) e^{i\varphi(z)}$ changes linearly through the junction, and drops to zero at the center. This is the same result as one would obtain for the proximity-induced minigap in a short π -biased S/N/S junction, meaning that this system indeed does act as such a junction.

B. Realistic case: Asymmetric junction

It is impossible to construct a perfectly symmetric S/X/S/X/S junction in reality, and it is therefore prudent to check how sensitive the proposed setup is to asymmetries. We have done so by setting the tunneling conductance to $G_T = 0.02G_0(1 \pm a)$ at the left and right interface, respectively. Here, a parametrizes the asymmetry in the junction. It is easy to see that in the limit $a \rightarrow 0$ we regain the symmetric case, while $a \rightarrow 1$ would decouple the central superconductor entirely from one of the electrodes. As we see from the results in Fig. 6, the main effect of the asymmetry is to soften the discontinuities at $\delta\varphi = \pm\pi$.

For perfectly symmetric junctions $a = 0$ with a high phase difference $|\delta\varphi| > \pi$, the numerics converged to the high-energy branch $J = -J_c \sin(\delta\varphi/2) \operatorname{sgn}[\cos(\delta\varphi/2)]$ instead of the low-energy $J = +J_c \sin(\delta\varphi/2) \operatorname{sgn}[\cos(\delta\varphi/2)]$, apparently producing a 4π -periodic current-phase relation. However, introducing even a tiny asymmetry $a = 0.0005$ results in the numerics correctly converging towards the 2π -periodic low-energy state regardless of the external phase difference. This state is characterized by abrupt discontinuities for $\delta\varphi = \pm\pi$ [Fig. 6(a)], accompanied by equally abrupt changes in the phase of the central superconductor from $\varphi_2 = 0$ to $\pm\pi$ [Fig. 6(b)]. As the asymmetry a increases, the discontinuities become smoother.

If we take the superconductors in the junction to be Nb, then the density of states at the Fermi level $N_0 \approx 80 \text{ eV}^{-1} \text{ nm}^{-3}$ [30], the zero-temperature gap $\Delta_0 \approx 1.4 \text{ meV}$, and a typical value for the coherence length $\xi \approx 15 \text{ nm}$. We assumed that the junction is at a temperature much lower than the critical temperature $T/T_c = 0.01$, and has an inelastic scattering rate $\delta/\Delta_0 = 0.01$. The Debye cutoff was set to $\Theta = 30\Delta_0$, which is high enough for the results to be independent of the cutoff. Furthermore, we assumed that the length of the central superconductor was $L = \xi/2 \approx 7.5 \text{ nm}$. Putting these values together, and dividing by the cross-sectional area A of the junction, we find that the current density unit $J_0/A \approx 3 \times 10^7 \text{ A/cm}^2$. Since we in Fig. 4 found critical currents between $J_0/4$ (AP) and $J_0/200$ (P), this translates to current densities of $\sim 10^7 \text{ A/cm}^2$ and $\sim 10^5 \text{ A/cm}^2$, respectively. Note that this likely overestimates the current densities one would observe experimentally since we treat the superconductors at

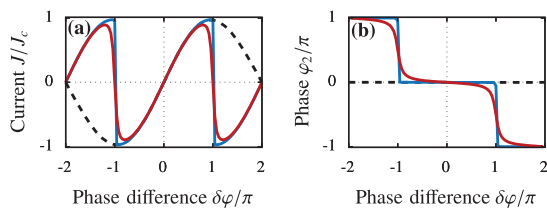


FIG. 6. Numerical results for (a) the current-phase relation and (b) the central phase φ_2 as functions of the external phase difference $\delta\varphi$. Both plots are for asymmetric junctions with interface conductances $G_T = 0.02G_0(1 \pm a)$, with a set to 0 (dashed), 0.0005 (blue), 0.1 (red). The physical current-phase relation in the lowest-energy state is always 2π periodic due to discontinuities at $\delta\varphi = \pm\pi$, but asymmetries in realistic junctions smooth these discontinuities.

the end of the junction as bulk superconductors. In reality, one might expect the order parameter to be suppressed near the interface to a strongly polarized magnetic insulator [26], which would throttle the current.

Using the the Fermi wavelength $\lambda \approx 0.533 \text{ nm}$ of Nb [31] and the parameters above, one may also estimate the interface transparency (average quasiparticle transmission probability):

$$\langle T \rangle \approx \frac{N_0 \Delta_0 \xi^2 \lambda^2}{1 + \sqrt{1 - P^2}} \frac{G_T}{LG_0}. \quad (26)$$

This gives the result $\langle T \rangle \approx 2G_T/3G_0$, which means that our parameter choice $G_T/G_0 = 0.02$ corresponds to an interface transparency of about 1.3%. This should be a reasonable value for the case of quasiparticles tunneling through an insulator.

C. Application: Spin-switch junction

A possible application of the proposed device, which works well in both the ideal and realistic regimes discussed in the previous sections, is as a junction with a magnetically controlled on-off switch for the supercurrent. Figure 4 shows that using the interface conductance $G_T = 0.02G_0$, spin-mixing conductance $G_\varphi = 0.3G_0$, and superconductor length $L = \xi/2$, one can already obtain a factor ~ 50 difference between the critical current in the P and AP configurations. To further investigate this prospect, we varied one of these parameters at a time while keeping the others fixed. For each parameter set, we calculated the ratio $J^{\text{AP}}/J^{\text{P}}$ between the charge current in the AP and P configurations, and the results are shown in Fig. 7. These calculations were done for a phase difference $\delta\varphi = \pi/2$, which means that $J^{\text{AP}}/J^{\text{P}}$ is not strictly equal to the critical current ratio $J_c^{\text{AP}}/J_c^{\text{P}}$, but they should be the same order of magnitude.

In Fig. 7(a), we see that for large interface conductances, the current ratio tends to one and, conversely, for very small interface conductances, the ratio diverges. Thus, with respect to the on-off ratio, low-interface conductances are the ideal choice. On the other hand, a low-interface conductance also means that the current is throttled even when the junction is turned on. In practice, there will therefore be a tradeoff between having a large on-off ratio (small conductance) and having a large current magnitude in the on state (large conductance).

In Fig. 7(b), we see that for small spin-mixing conductances G_φ , the on-off ratio tends to one. This is because in this limit, the spin-active properties are too weak to suppress superconductivity in either the P or AP states, leading to a large supercurrent in both the P and AP configurations. After $G_\varphi \approx 0.15G_0$, the gap in the central superconductor is strongly suppressed in the P configuration but not the AP configuration, resulting in very high on-off ratios. For very high spin-mixing conductances $G_\varphi \approx 0.9G_0$ (not shown), we also found a $0-\pi$ transition with a $\sin(2\delta\varphi)$ current-phase relation in the AP configuration, resulting in an even higher on-off ratio.

In Fig. 7(c), we see that for superconductors larger than about 0.7ξ , the on-off ratio tends to one. This is because in this limit, the superconductor is large enough to sustain a significant gap in both the P and AP configurations, enabling large supercurrents to in both configurations. On the other hand, for thin superconductors, the gap is strongly suppressed in the P but not AP configuration, yielding high on-off ratios.

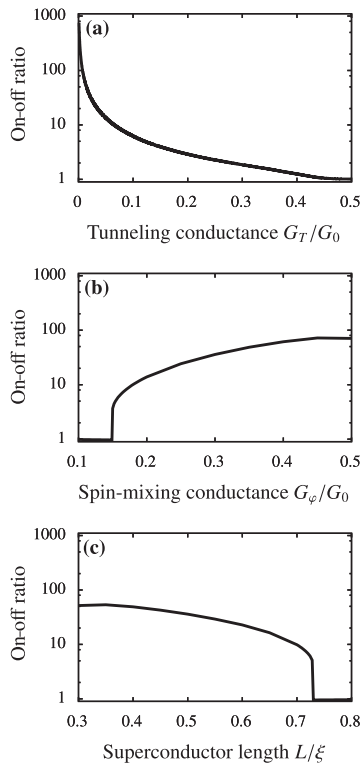


FIG. 7. Numerical results for the on-off ratio $J^{\text{AP}}/J^{\text{P}}$ as function of (a) the tunneling conductance G_T , (b) the spin-mixing conductance G_ϕ , and (c) the length of the central superconductor L .

IV. DISCUSSION

The results in Fig. 4 confirm that it should be possible to toggle between current-phase relations with clear $\sin(\delta\varphi)$ and $\sin(\delta\varphi/2)$ shapes magnetically using experimentally realistic parameters. The current-phase relation remains 2π periodic in the low-energy state due to discontinuities at $\delta\varphi = \pm\pi$, which are smoothed out as the junctions become more asymmetric.

Note that there is a factor 50 difference between the critical current in the P and AP states of Fig. 4. For potential applications where it is mainly the shape and not size of the current-phase relation that matters, this is of course not an obstacle. For applications where the size of the supercurrent is important as well, the setup we propose may instead be considered as a $\sin(\delta\varphi/2)$ junction with a magnetic on-off switch, similar to the ideas in Refs. [32–34]. As shown in Fig. 7, we find that this kind of setup can produce very high on-off ratios of 100–1000, as long as the superconductor is short enough and the spin mixing high enough, in line with conventional wisdom regarding optimal spin-valve design. The tunneling conductance was found to be the limiting ingredient, with lower conductances consistently resulting in

higher on-off ratios. However, at the same time, lower interface conductances mean lower currents in both the on and off states. Thus, there is a tradeoff between achieving high on-off ratios and high current densities in the on state.

In principle, it might be possible to create a similar device using magnetic metals instead of insulators since it has been experimentally demonstrated that superconducting spin valves can be constructed out of metals too [35]. However, it is then critical that the net tunneling conductance between each superconducting layer is small enough. If the tunneling conductance is too high, then one would end up with both $\sin(\delta\varphi)$ - and $\sin(\delta\varphi/2)$ -shaped contributions in the AP configuration instead of a pure $\sin(\delta\varphi/2)$ -shaped current-phase relation.

Although we have focused on using a magnetic field to toggle between a $\sin(\delta\varphi)$ - and $\sin(\delta\varphi/2)$ -shaped current-phase relation so far, the same basic idea can be extended to other physical setups as well. For instance, consider an S/I/S'/I/S structure, where S is a superconductor with a particular critical temperature (e.g., Nb with $T_c \approx 9.2$ K), S' a superconductor with a lower critical temperature (e.g., Al with $T'_c \approx 1.2$ K), and the I are thin layers of nonmagnetic insulators. This junction should act as an S/X/S system with a $\sin(\delta\varphi)$ relation above T'_c , but as an S/X/S'/X/S system with a $\sin(\delta\varphi/2)$ relation below T'_c when the interface conductance is low enough to permit most of the phase winding to occur at the interfaces (as in Fig. 5). In other words, it should also be possible to thermally toggle between these $\sin(\delta\varphi/n)$ -shaped current-phase relations [14].

V. CONCLUSION

We have demonstrated theoretically that by changing the magnetic configuration from a P to AP alignment in a spin-valve Josephson junction (S/F/S'/S), it is possible to toggle between a $\sin(\delta\varphi)$ - and $\sin(\delta\varphi/2)$ -shaped current-phase relation, which retains a 2π periodicity due to discontinuities at $\delta\varphi = \pm\pi$. The same mechanism may be used to construct a Josephson junction with an on-off switch, achieving two to three orders of magnitude difference between the on and off states. We have also argued that the same procedure can be generalized to create arbitrary $\sin(\delta\varphi/n)$ junctions where n is a magnetically tunable integer. This way to exert control over superconductivity in nanoscale structures may spur new fundamental research in superconducting spintronics [36] and find practical applications in future cryogenic technology.

ACKNOWLEDGMENTS

We thank M. Amundsen and M. Yu. Kupriyanov for useful discussions. J.L. and J.A.O. were supported by the Research Council of Norway (Grant No. 240806). J.L. was also supported by the Research Council of Norway (Grant No. 216700), and the *Outstanding Academic Fellows* programme at NTNU. The Research Council of Norway and NTNU are acknowledged for funding the Center of Excellence *QuSpin*.

- [1] A. A. Golubov, M. Y. Kupriyanov, and E. Il'ichev, *Rev. Mod. Phys.* **76**, 411 (2004).
- [2] A. I. Buzdin, *Rev. Mod. Phys.* **77**, 935 (2005).
- [3] V. V. Ryazanov, V. A. Oboznov, A. Y. Rusanov, A. V. Veretennikov, A. A. Golubov, and J. Aarts, *Phys. Rev. Lett.* **86**, 2427 (2001).
- [4] N. G. Pugach, E. Goldobin, R. Kleiner, and D. Koelle, *Phys. Rev. B* **81**, 104513 (2010).
- [5] H. Sickinger, A. Lipman, M. Weides, R. G. Mints, H. Kohlstedt, D. Koelle, R. Kleiner, and E. Goldobin, *Phys. Rev. Lett.* **109**, 107002 (2012).
- [6] D. B. Szombati, S. Nadj-Perge, D. Car, S. R. Plissard, E. P. A. M. Bakkers, and L. P. Kouwenhoven, *Nat. Phys.* **12**, 568 (2016).
- [7] A. I. Buzdin, *Phys. Rev. Lett.* **101**, 107005 (2008).
- [8] A. A. Reynoso, G. Usaj, C. A. Balseiro, D. Feinberg, and M. Avignon, *Phys. Rev. Lett.* **101**, 107001 (2008).
- [9] A. Zazunov, R. Egger, T. Jonckheere, and T. Martin, *Phys. Rev. Lett.* **103**, 147004 (2009).
- [10] Y. Tanaka, T. Yokoyama, and N. Nagaosa, *Phys. Rev. Lett.* **103**, 107002 (2009).
- [11] J. Linder, Y. Tanaka, T. Yokoyama, A. Sudbø, and N. Nagaosa, *Phys. Rev. B* **81**, 184525 (2010).
- [12] I. Zapata and F. Sols, *Phys. Rev. B* **53**, 6693 (1996).
- [13] H. Ishikawa, S. Kurihara, and Y. Enomoto, *Phys. C (Amsterdam)* **350**, 62 (2001).
- [14] M. Yu. Kupriyanov, A. Brinkman, A. A. Golubov, M. Siegel, and H. Rogalla, *Phys. C (Amsterdam)* **326-327**, 16 (1999).
- [15] R. De Luca and F. Romeo, *Phys. Rev. B* **79**, 094516 (2009).
- [16] C. W. J. Beenakker, *Annu. Rev. Condens. Matter Phys.* **4**, 113 (2013).
- [17] A. Kitaev, *Phys. Usp.* **44**, 131 (2001).
- [18] F. Zhang and C. L. Kane, *Phys. Rev. B* **90**, 020501 (2014).
- [19] J. Wiedenmann *et al.*, *Nat. Commun.* **7**, 10303 (2016).
- [20] A. K. Feofanov, V. A. Oboznov, V. V. Bol'ginov, J. Lisenfeld, S. Poletto *et al.*, *Nat. Phys.* **6**, 593 (2010).
- [21] E. C. Gingrich, B. M. Niedzielski, J. A. Glick, Y. Wang, D. L. Miller, R. Loloee, W. P. Pratt, Jr., and N. Birge, *Nat. Phys.* **12**, 564 (2016).
- [22] P. G. de Gennes, *Phys. Lett.* **23**, 10 (1966).
- [23] J. J. Hauser, *Phys. Rev. Lett.* **23**, 374 (1969).
- [24] K. D. Usadel, *Phys. Rev. Lett.* **25**, 507 (1970).
- [25] J. A. Ouassou, A. Di Bernardo, J. W. A. Robinson, and J. Linder, *Sci. Rep.* **6**, 29312 (2016).
- [26] J. A. Ouassou, A. Pal, M. Blamire, M. Eschrig, and J. Linder, *Sci. Rep.* **7**, 1932 (2017).
- [27] M. Eschrig, A. Cottet, W. Belzig, and J. Linder, *New J. Phys.* **17**, 083037 (2015).
- [28] B. Li, N. Roschewsky, B. A. Assaf, M. Eich, M. Epstein-Martin, D. Heiman, M. Munzenberg, and J. S. Moodera, *Phys. Rev. Lett.* **110**, 097001 (2013).
- [29] A. Pal and M. G. Blamire, *Phys. Rev. B* **92**, 180510(R) (2015).
- [30] A. R. Jani, N. E. Brener, and J. Callaway, *Phys. Rev. B* **38**, 9425 (1988).
- [31] N. W. Ashcroft and N. D. Mermin, *Solid State Physics* (Holt, Rinehart, and Winston, New York, 1976).
- [32] W. M. Martinez, W. P. Pratt, and N. O. Birge, *Phys. Rev. Lett.* **116**, 077001 (2016).
- [33] B. Baek, W. H. Rippard, S. P. Benz, S. E. Russek, and P. D. Dresselhaus, *Nat. Commun.* **5**, 3888 (2014).
- [34] V. V. Bol'ginov, V. S. Stolyarov, D. S. Sobanin, A. L. Karpovich, and V. V. Ryazanov, *JETP Lett.* **95**, 366 (2012).
- [35] J. Y. Gu, C.-Y. You, J. S. Jiang, J. Pearson, Y. B. Bazaliy, and S. D. Bader, *Phys. Rev. Lett.* **89**, 267001 (2002).
- [36] J. Linder and J. W. A. Robinson, *Nat. Phys.* **11**, 307 (2015).

XI

Reference

K. Lahabi, M. Amundsen, [J.A. Ouassou](#), E. Beukers, M. Pleijster, J. Linder, P. Alkemade, J. Aarts. Controlling supercurrents and their spatial distribution in ferromagnets. *Nature communications* 8, 2056 (2017). DOI: 10/GCRHMZ

Contributions

KL and JA conceived the disk geometry. KL and EB performed the micro-magnetic simulations. MA, JAO and JL performed the supercurrent simulations, and assisted in the Fourier analysis of the critical current measurements. KL, MP and PA fabricated the devices. KL and MP performed the measurements. All authors contributed to discussions.

In particular, JAO had a supporting role: performing a Fourier analysis with the Dynes–Fulton method [182] and contributing to discussions.

Comments

The experiment was performed by a research group at Leiden University.

ARTICLE

DOI: 10.1038/s41467-017-02236-2

OPEN

Controlling supercurrents and their spatial distribution in ferromagnets

Kaveh Lahabi¹, Morten Amundsen², Jabir Ali Ouassou¹, Ewout Beukers¹, Menno Pleijster¹, Jacob Linder², Paul Alkemade³ & Jan Aarts¹

Spin-triplet Cooper pairs induced in ferromagnets form the centrepiece of the emerging field of superconducting spintronics. Usually the focus is on the spin-polarization of the triplets, potentially enabling low-dissipation magnetization switching. However, the magnetic texture which provides the fundamental mechanism for generating triplets also permits control over the spatial distribution of supercurrent. Here we demonstrate the tailoring of distinct supercurrent pathways in the ferromagnetic barrier of a Josephson junction. We combine micromagnetic simulations with three-dimensional supercurrent calculations to design a disk-shaped structure with a ferromagnetic vortex which induces two transport channels across the junction. By using superconducting quantum interferometry, we show the existence of two channels. Moreover, we show how the supercurrent can be controlled by moving the vortex with a magnetic field. This approach paves the way for supercurrent paths to be dynamically reconfigured in order to switch between different functionalities in the same device.

¹Huygens—Kamerlingh Onnes Laboratory, Leiden Institute of Physics, University Leiden, P.O. Box 9504, 2300 RA Leiden, The Netherlands. ²Department of Physics, Center of Excellence QuSpin, Norwegian University of Science and Technology, NO-7491 Trondheim, Norway. ³Kavli Institute of Nanoscience, Delft University of Technology, Lorentzweg 1, 2628 CJ Delft, The Netherlands. Correspondence and requests for materials should be addressed to J.A. (email: aarts@physics.leidenuniv.nl)

The conversion of spin-singlet Cooper pairs to the equal-spin triplets which are needed in superconducting spintronics^{1,2} requires carefully designed interfaces between a conventional superconductor (S) and a ferromagnet (F). The process entails both spin-mixing and spin-rotation, and can be brought about by magnetic inhomogeneities at the interface³. One method to realize this is to place a thin ferromagnet F' at the S/F interface, and make the magnetization of F and F' non-collinear⁴. This technique was recently implemented in Josephson junctions described by 1D geometries, where the supercurrent amplitude was controlled by varying degrees of magnetic non-collinearity (MNC)^{5–7}. The present letter establishes a different direction. Here, the central goal is to exert dynamic control over the triplet generator and thereby to determine where the supercurrent spatially flows.

We demonstrate how distinct supercurrent paths in a device can be tailored entirely by spin texture, and altered in a dynamic fashion. Such behavior is intrinsically higher-dimensional and can pave the way for novel hybrid devices in superconducting electronics.

Results

Micromagnetic simulations. The device consists of a disk-shaped planar Josephson junction involving a multilayer of Co/Cu/Ni/Nb, as shown in Fig. 1a. A central trench cuts the top superconducting Cu/Ni/Nb layers in two halves, here connected via a Co weak link. The disk design combines two crucial elements. First, the magnetic moments in Co are arranged in plane and orthogonal to the trench between the superconducting

electrodes, while the moments in Ni lie also in plane but parallel to the trench. Micromagnetic simulations show that this geometry results in a well-defined magnetic ground state with a high degree of MNC, a condition optimal for generating triplets (Fig. 1c–e). An equally important element is that the disk shape creates a magnetic vortex state in the Co. This vortex produces a distinct suppression of MNC at the centre of the disk (Fig. 1e), which will be used to distribute the supercurrent in Co over two channels. The MNC suppression is due to the local out-of-plane magnetization at the vortex core, which turns the magnetic moments in the Ni also out-of-plane and, hence, collinear to the Co moments. Incidentally, the in-plane exchange field gradient of a magnetic vortex, without a second ferromagnet, has also been proposed to generate long-ranged triplets^{8,9}.

Supercurrent calculations. To investigate whether a supercurrent can be expected, we numerically simulate the critical current density passing through the Josephson junction by solving the quasiclassical Usadel equation¹⁰ in 3D using the magnetization texture obtained from the micromagnetic simulations. We do this by means of the finite element method, using the finite element library libMesh¹¹ in a similar fashion as in ref. 12 (for details, see Supplementary Note 1, Supplementary Fig. 3). The superconductors are modeled as bulk, with a phase difference of $\Delta\phi = \frac{\pi}{2}$. In Fig. 2a the discretized model is shown. To reduce the calculation time we truncated the otherwise circular geometry to a width of 40% of the disk diameter, as the currents farther away from the trench are negligible. The results are shown in Fig. 2b, c, where it can be seen that the critical current is suppressed at the

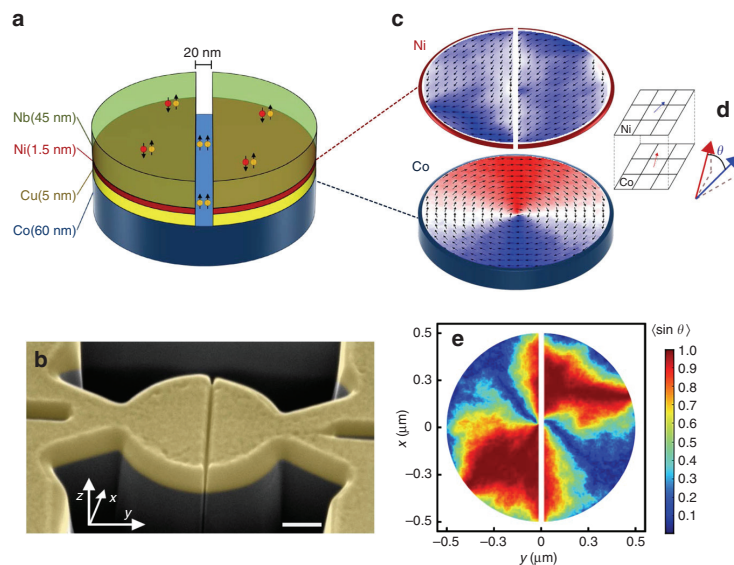


Fig. 1 Micromagnetic simulations and device layout. **a** Schematic of the device layout. **b** False-color scanning electron microscope image of a device. The scale bar corresponds to 250 nm. The disk is structured with Ga^+ focused ion beam (FIB) milling. The junction is formed by opening up a gap in the top Nb/Ni/Cu layers, leaving only Co in the weak link (see Methods section for more details). **c** Plane view of the magnetic states of Co and Ni layers in the disk (from 3D OOMMF simulations). The pixel color scheme, red-white-blue, scales with the magnetization along y . Magnetic moments in Ni tend to align with the gap which defines the junction, while the vortex configuration in Co arranges the magnetic moments perpendicular to it. This provides a high degree of magnetic non-collinearity (MNC) for triplet generation. The curled magnetic structure of the vortex is also highly effective in minimizing the stray fields from Co, which otherwise would dominate the Ni magnetization, hence compromising our control of MNC. **d** Representation of our method to obtain the MNC profile. For each cell at the top of the Co layer, we determine the angle θ between its magnetization vector and that of the Ni cell above. **e** Spatially resolved MNC profile calculated from the simulation results shown in **c**. The observed suppression of MNC (the blue region) at the centre of the junction is a result of interlayer dipole coupling at the vortex core

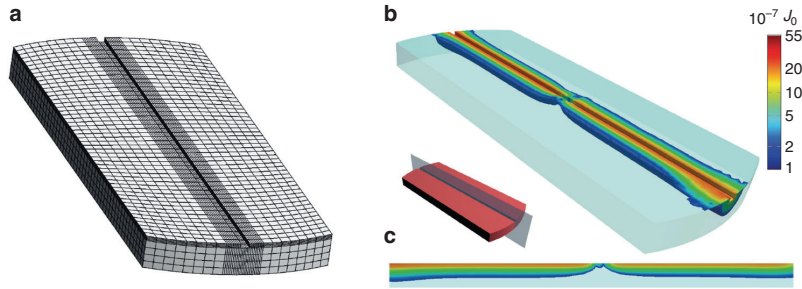


Fig. 2 Numerical simulation of the critical current. **a** The discretized model (or mesh) used in the numerical simulation of the critical current. Since the triplet current is mostly concentrated in the immediate vicinity of the trench, the mesh density (and hence the accuracy) is set to be higher for this region. For the same reason, the regions farthest away from the trench have been removed to reduce the calculation time. **b** The critical current density divided by a factor $J_0 = \frac{N_0 e D \Delta}{2 \xi}$, where N_0 is the density of states at the Fermi level, D is the diffusion constant, Δ is the superconducting gap and ξ is the superconducting coherence length. For clarity, currents lower than $10^{-7} J_0$ are not shown. **c** A slice through the centre of the trench, showing how the current passes across the Co barrier in two separate channels, on either side of the vortex core

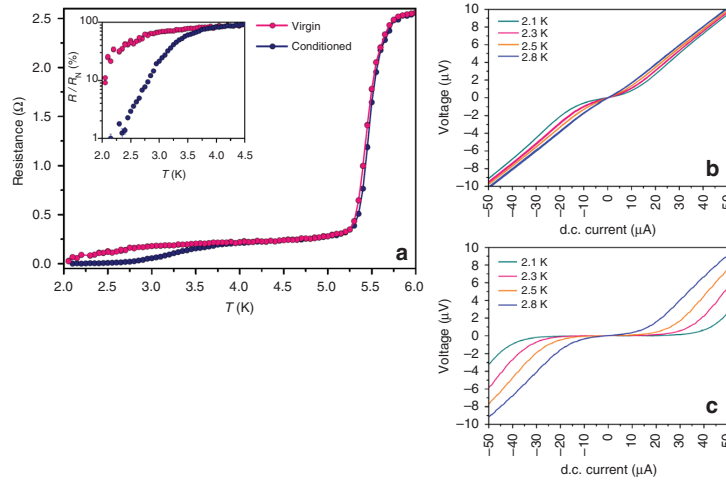


Fig. 3 Junction transport in the virgin and conditioned states. **a** Resistance as a function of temperature, measured using $10 \mu\text{A}$, before (pink) and after (navy) conditioning the sample. Each set shows two distinct transitions. At $T = 5.5 \text{ K}$, the Nb electrodes become superconducting, while the junction is still in the normal state ($R_N \approx 240 \text{ m}\Omega$). Upon cooling further, resistance undergoes a second transition as the barrier begins to proximize by triplet correlations—eventually reaching zero resistance. For clarity, the $R-T$ dependence at lower temperatures is plotted on a logarithmic scale in the inset. While the superconducting electrodes are unaffected by conditioning the ferromagnets, we observe substantial enhancement of superconductivity in the barrier. **b, c** $I-V$ traces taken at several temperatures before and after conditioning the sample, respectively. The pronounced contrast between the two sets indicates that transport depends strongly on the magnetic configuration of the junction

centre of the disk, thereby effectively creating two separate current channels.

Basic transport properties. As shown in Fig. 3, our junctions show zero resistance and finite critical currents I_c below 3 K. The magnetic state of the sample was conditioned by applying a 2.5 T out-of-plane field at 10 K. This is to reduce the stochastic magnetization introduced by FIB milling when structuring the junction. Figure 3 shows there is a strong difference with data taken before and after conditioning the sample, which is a first indication that MNC and a triplet supercurrent are involved (also see Supplementary Note 2). For instance, conditioning allows the magnetic moments in Ni to rearrange more freely, and align with the gap opened by the FIB. This process increases the MNC in the vicinity of the barrier which, in turn, results in an enhancement of triplet supercurrent at zero field. A consequence of this can be

found in the pronounced contrast between the $I-V$ traces measured before and after conditioning the magnetization, as shown in Fig. 3b, c.

Superconducting quantum interferometry. To examine the spatial distribution of current density across our junctions, we apply an out-of-plane magnetic field B_z , and analyze the resulting supercurrent interference pattern. As demonstrated by Dynes and Fulton¹³, the shape of such a superconducting quantum interference (SQI) pattern is given by the Fourier transform of the position-dependent critical current density across a junction $J_c(x)$ through

$$I_c(B_z) = \left| \int_{-R}^R dx J_c(x) e^{2\pi i L B_z x \Phi_0} \right|, \quad (1)$$

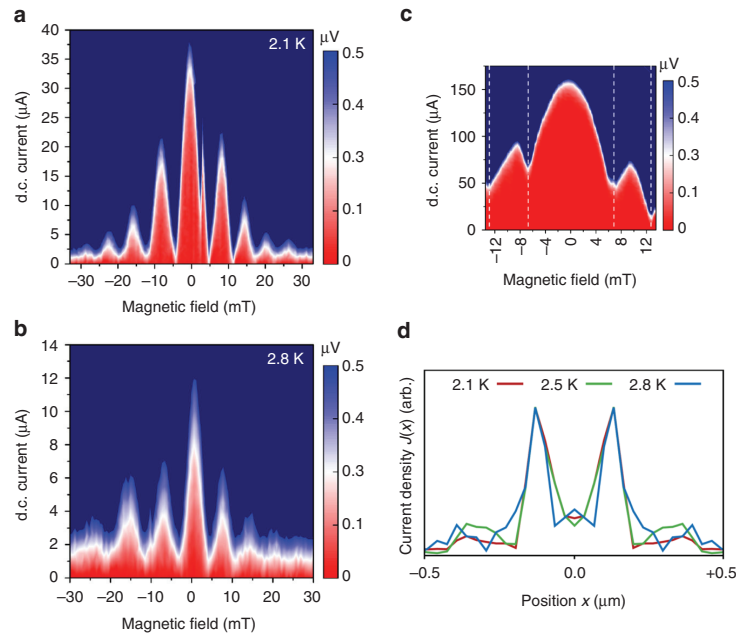


Fig. 4 Interference patterns and the corresponding current density profiles. **a, b** the result of superconducting quantum interference (SQI) measurements taken at 2.1 and 2.8 K, respectively. The patterns show clear double-slit interference, with all lobes having the same width. **c** Single-slit interference pattern from a disk junction where transport is dominated by singlet correlations via a non-magnetic barrier. **d** The current density profiles constructed from the Fourier analysis of SQI patterns taken at 2.1, 2.5, and 2.8 K. The presence of two transport channels, responsible for the SQUID-like interference patterns, is evident

where L is the effective length of the junction, $2R$ is its lateral width (here the disk diameter), and $\Phi_0 = h/2e$ is the superconducting flux quantum. In a typical junction, the uniform distribution of supercurrent density ($J_c(x) = \text{constant}$) leads to the well-known Fraunhofer interference pattern with a sinusoidal current-phase relation given by $I_c(B_z)/I_c(0) \sim |\sin(\pi\Phi/\Phi_0)/(\pi\Phi/\Phi_0)|$. Characteristic for the Fraunhofer pattern is a central lobe that is twice as wide as the side lobes (as in Fig. 4c). These oscillations decay with a $1/B$ dependence. Different device configurations may introduce deviations from the standard pattern, but the described relative widths of the lobes persist as a common feature in all Josephson junctions, since it represents a single-slit interference pattern. In contrast, we expect our disk to exhibit a double-slit interference pattern. This is characterized by slowly decaying sinusoidal oscillations with Φ_0 -periodicity, where all lobes have the same width. These patterns are typical for superconducting quantum interference devices (SQUIDs) which, contrary to our device, consist of two individual junctions operated in parallel.

As shown in Fig. 4a, b, the period of the oscillations in our disk device is 7.8 mT (i.e., fluxoid quantization over an effective area of $2.65 \times 10^{-13} \text{ m}^2$), and appears to be temperature-independent. Qualitatively, the SQI patterns in Fig. 4a, b already foretell the presence of two supercurrent channels: the width of the central lobe is comparable to that of the side lobes, and the oscillations decay far more gradually in field than as $1/B$. Two-channel interference patterns were recently observed in junctions with topological weak links^{14–16}, where the two-slit interference is a result of edge-dominated transport caused by band bending. In our junction however, this is due to the suppression of triplet supercurrent by the (controllable) magnetic vortex core.

To illustrate the contrast with single-slit interference in a similar device configuration, we prepared a disk junction without the Ni layer, and retaining a thin layer of Cu/Nb at the bottom of the trench. This provides a non-magnetic path in the barrier, allowing singlet correlations to contribute to junction transport. Indeed, we observe a typical Fraunhofer-like interference pattern with a two times wider central lobe, shown in Fig. 4c. Provided that singlet current can dominate the transport, similar results can also be produced in presence of the Ni layer (Supplementary Fig. 5).

Figure 4d shows the supercurrent density profiles extracted from Fourier analysis of the measured interference patterns. A description of this method can be found in the Supplementary Note 3, Supplementary Fig. 4 but it should be mentioned that there is some arbitrariness in choosing the position of the sample edge if the effective junction length L is not known. We put the edge at the position where the current density goes to zero, which leads to a value for L of 170 nm. This is a reasonable number. For a homogeneous junction where $L = 2\lambda_L + d$, with d the gap between the electrodes and λ_L the London penetration depth, taking 100 nm for λ_L of the Nb, would yield L to be of the order of 200 nm. There is no reason however to expect very close agreement as discussed in Supplementary Note 3. Important is that for any choice of the edge position, two distinct transport channels are clearly visible in the extracted profiles. Comparing these results with the simulations, the supercurrents appear to follow narrower paths, located near the centre of the disk. We attribute this to current crowding effects, in which the neck-shaped contacts and their sharp corners lead to a forward orientation of the currents.

It is important to note that the origin of the two-channel transport in our junction cannot be explained by singlet

supercurrents in a doubly connected path. Direct evidence for this can be found in the SQI measurements taken before conditioning the sample (the virgin state). If two separate current paths had formed unintentionally during fabrication, and allowed singlet

correlations to bypass the Co layer via two symmetric channels, then those channels would have already been present before the magnetic state conditioning, and the device would have behaved as a SQUID from the beginning. In contrast, despite several

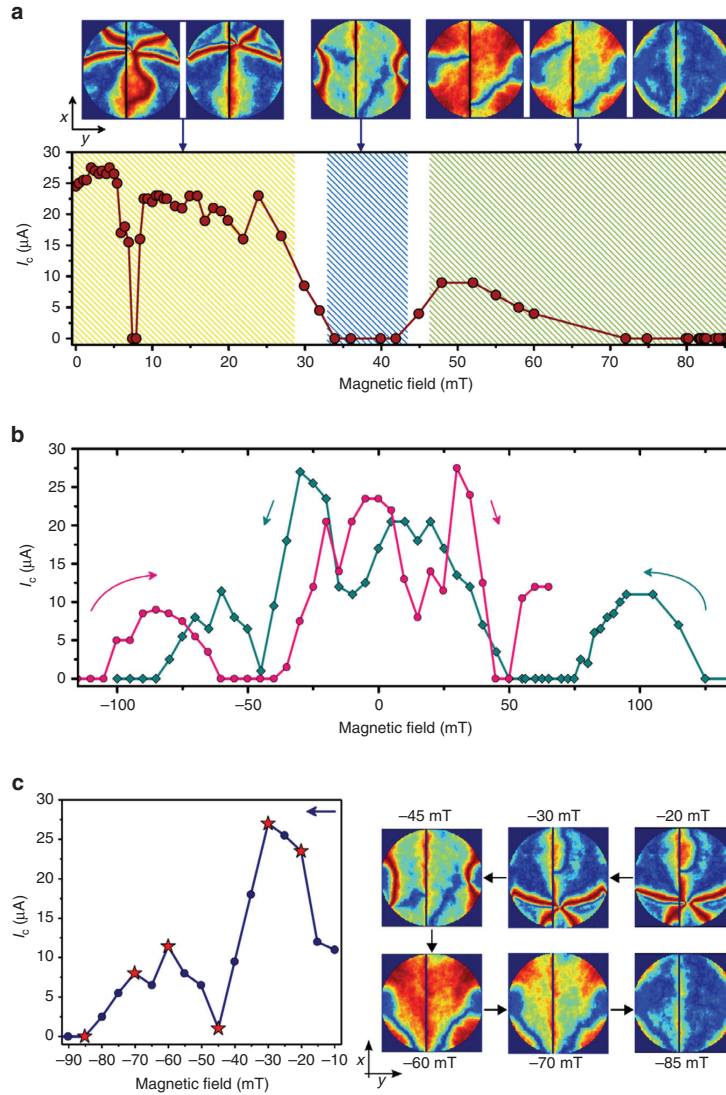


Fig. 5 Critical current variation and MNC simulations with in-plane field. **a** Measured I_c values and the corresponding magnetic non-collinearity (MNC) profiles, as the system is magnetized by sweeping the field in +y direction. For small fields the vortex core moves along the junction (perpendicular to field direction) to the side of the disk. In this range (shaded yellow), highly non-collinear regions are continuously present and appear to follow the position of the vortex core. The vortex state in Co, which has been effective in suppressing the stray fields, is subsequently removed as the field approaches 30 mT. This leads to a negative dipole field from Co which dominates the effective field acting on Ni. As a result, Ni gets magnetized antiparallel to Co (along -y), hence the suppression of MNC and I_c (shaded blue). As the applied field is raised above 45 mT, it begins to compensate for the local stray fields from the Co layer, ultimately reversing the Ni magnetization along +y. The change in the magnetic orientation associated with this reversal leads to a distinct (re-)emergence of MNC that gradually fades away above 60 mT—as Ni magnetization aligns with Co (shaded green). **b** I_c measured while reversing the field in both directions along y. A clear hysteresis is observed, with individual features are mirrored with respect to field sweep direction. This complex pattern is a result of a changing MNC as the multilayer reverses its magnetization. **c** Positive to negative branch of experimentally measured $I_c(B_y)$ shown together with simulated MNC profiles. Each MNC snapshot is obtained at the specified field, and corresponds to a measurement labeled by the star symbol. Taking steps of 5 mT, simulation shows the vortex enters at -20 mT, moves along -x, and exits the system at -45 mT. The MNC is once again is enhanced at -60 mT, and gradually fades away as the field magnetizes all layers along -y

attempts, no sign of a double-slit interference was found in the virgin state (Supplementary Fig. 1). The SQUID pattern only appeared when the magnetic state was properly conditioned to produce the intended MNC, designed specifically to generate two symmetric triplet channels. More details about the SQI measurements from the virgin state can be found in Supplementary Note 2.

Magnetotransport measurements with an in-plane field. Having established the principal role of MNC in shaping the supercurrent, we also examine the possibility of controlling them by altering the MNC profiles using an in-plane field B_y , which moves the vortex along the trench. Figure 5a shows the measured currents $I_c(B_y)$ together with the micromagnetic MNC calculations for various stages during the (zero to positive) field sweep. In the first regime (below 28 mT, shaded yellow), we modify the MNC profile by moving the vortex core along $+x$ toward the side of the disk. As the field is raised beyond 30 mT, we remove the vortex, thereby suppressing the supercurrent. The suppression of I_c in this regime (above 34 mT, shaded blue) is caused by the anti-parallel configuration of the ferromagnets, which occurs through the increase of stray fields from Co (now magnetized along $+y$) when the vortex leaves the disk. In the third regime (above 46 mT, shaded green), Ni magnetization begins to reverse from negative to positive y direction, while Co remains magnetized along $+y$. At first, this process recovers I_c as a MNC re-emerges over the entire disk. As we increase the field however, the MNC begins to fade away as both layers magnetize along $+y$, resulting in a gradual suppression of I_c . Figure 5b shows the variations in $I_c(B_y)$ when sweeping the field from a high positive to negative value, and back. We observe a complex pattern accompanied with a peculiar hysteresis, where individual features are mirrored (and not just shifted) with respect to the direction of field sweep.

The observed field dependence is fundamentally different from the usual hysteresis in SFS junctions, where the self-field of the ferromagnets can distort or introduce a shift in the interference pattern^{7,17,18}. This is rather a distinct characteristic of triplet supercurrents produced by a varying degree of MNC, as the multilayer reverses its magnetization. The measured hysteresis is of a similar nature as the ones reported in refs. 6,7 for multilayer vertical stacks. The most notable difference here is arguably the relatively large field range where I_c is zero, and the pronounced reentrant superconductivity that follows. Figure 5c compares one branch (positive to negative) of the measured $I_c(B_y)$ with the simulated MNC snapshots taken at various stages of the vortex reversal. Even though the experiment and the simulation both sweep the field in steps of 5 mT, the simulated fields for vortex entry and exit translate to direct enhancement and suppression of the measured I_c , respectively. For the fields below -45 mT, the behavior is similar to the one described for the third regime (green shade) in Fig. 5a.

As a final point, it should be noted that in the present letter we have assumed the channels have an equal phase. This assumption is reasonable for a symmetric MNC (hence spin-mixing) on each side⁴. Whether both channels are 0 or π , as long as they are symmetric, the SQI results will be indistinguishable. This would not strictly apply to systems with asymmetric spin texture (e.g., caused by vortex displacement), which can result in different phases for the triplet channels⁹.

Discussion

Spin-triplet supercurrents in ferromagnets have been bearing the promise of dissipationless use of spin-polarized currents. This study opens up a completely different direction, in which the focus is not the homogeneous amplitude of the supercurrent, but

rather the dynamical control over its spatial distribution. This can lead to novel hybrid devices for superconducting electronics. Moreover, our extensive use of simulations, both of the micro-magnetic configurations and of the supercurrents themselves, allow for detailed design and understanding before the actual fabrication of the hybrid device. The next step will be to introduce magnetization dynamics. Magnetic vortices or domain walls can be moved with pulses in the GHz regime, and this can also be simulated. Directing supercurrents then becomes possible on nanosecond timescales, opening the way for high-speed superconducting electronics.

Methods

Device fabrication. Multilayers of Co (60 nm)/Cu (5 nm)/Ni (1.5 nm)/Nb (45 nm) were deposited on unheated SiO₂-coated Si substrates by Ar sputtering in an ultra-high vacuum chamber (base pressure below 10^{-8} Pa). The thickness of Co and the diameter of the disk (1 μ m) are chosen to ensure stabilization of a magnetic vortex^{19,20}. The 5 nm Cu layer is used to avoid exchange coupling between the layers. The thickness of the Ni layer was tuned for optimal triplet generation in similar systems^{21,22}. The samples were subsequently coated with Pt (7 nm) to protect them from oxidation and to reduce the damage introduced by Ga⁺ ions during focused ion beam (FIB) processing.

A combination of electron-beam lithography and FIB milling (50 pA Ga⁺ beam current) was used to structure the disks. Next, FIB with 1 pA current was applied to open the sub-20 nm gap that forms the junction. The trench depth is controlled by the duration of milling. The 1 pA beam current provided sufficient timespan (several seconds) to vary the depth in a controlled manner. The device used for investigating single-slit transport was subject to the same processing steps, with the following exceptions. First, the multilayer was deposited without Ni to minimize triplet generation. Second, when creating the weak link, the duration of FIB milling was reduced by 20% to retain a layer of Cu/Nb at the bottom of the trench. This provides a non-magnetic path for singlet supercurrent in the weak link (on top of Co).

The trench is presumably deeper near the sides of the disks (where sputtered atoms can escape more easily) than at the centre. Hence, in contrast to triplets, singlet correlations would favor the centre of the disk where a non-magnetic channel may be still present on top of the Co.

Magnetotransport measurements. The magnetic properties of Co and Ni films used in our devices were characterized by ferromagnetic resonance experiments and SQUID magnetometry. Transport measurements were performed in a Quantum Design Physical Properties Measurement System where samples could be cooled down to 2.1 K. For both in-plane and out-of-plane measurements, the field was aligned within 2° of the sample plane. Resistance versus temperature was measured with a current of 10 μ A. The current-voltage characteristics were taken in a four-probe configuration using a current-biased circuit and a nanovoltmeter. The critical current was determined using a voltage criterion: $V > 0.3 \mu$ V for SQI and $V > 0.1 \mu$ V for the measurements with an in-plane field.

The virgin state was measured directly after fabrication (Supplementary Note 2). Prior to the $I_c(B_y)$ measurements presented in the letter, the magnetic state of the sample was conditioned by applying a 2.5 T out-of-plane field at 10 K. The sample was stored in a UHV chamber for 106 days and re-wired to a different puck, and the same measurements were repeated using a different magnet. We were able to reproduce the same I_c patterns, and no discernable changes in transport characteristics (e.g., $R(T)$ or I_c) were observed.

Micromagnetic simulations. Micromagnetic modeling of the behavior of magnetic Josephson junctions was reported before²³. Here, finite element micromagnetic calculations were carried out using the Object Oriented Micromagnetic Framework (OOMMF)²⁴. The multilayer is divided into a three-dimensional mesh of 5 nm cubic cells. The exchange coefficient and saturation magnetization of Co were set to 30×10^{-12} Jm⁻¹ and 1.40×10^6 Am⁻¹, respectively, while for Ni these values were 9.0×10^{-12} Jm⁻¹ and 4.90×10^5 Am⁻¹. The Gilbert damping constant α was set to 0.5 to allow for rapid convergence. The direction of anisotropy was defined by a random vector field to represent the polycrystalline nature of the sputtered films. The Usadel calculations are based on static micromagnetic simulations of a multilayer disk with a diameter of 1 μ m. For simulations with an applied in-plane field (shown in Fig. 5), the disk design was extended to include the leads used for transport measurements in the actual device (Supplementary Fig. 2). In the absence of in-plane fields, the overall magnetic configuration remains relatively unaffected by the leads: the vortex core continues to suppress the MNC, resulting in two main channels for long-ranged triplet correlations. However, the influence of the leads on shape anisotropy becomes relevant when sweeping the field along y . This allows for an accurate estimate of the MNC, and the resulting variation in I_c during the magnetization reversal.

Control experiment. In addition to the device used for investigating the triplet currents, a control sample was prepared in parallel, on the same substrate. This was deposited together with the main device, and received the same treatment, with only one exception: the Ga⁺ dose used for opening the gap that forms the weak link was lowered by 50%. Reducing the dose stops the milling before it reaches the Co layer in the trench. This leaves a non-magnetic path in the weak link for singlet correlations. The contribution of singlet supercurrent results in a critical current that is around 20 times higher than its neighboring junction (the main device) where the Co weak link can effectively suppress singlet correlations, hence allowing long-ranged triplet supercurrents to dominate the transport. Unlike triplets, the singlet current is not sensitive to the spin texture (i.e., MNC) of the system. This is evident from the single-slit (Fraunhofer-like) interference pattern, shown in Supplementary Fig. 5.

Data availability. The data that support the findings of this study are available from the corresponding author upon request.

Received: 30 May 2017 Accepted: 14 November 2017

Published online: 12 December 2017

References

- Eschrig, M. Spin-polarized supercurrents for spintronics: a review of current progress. *Rep. Prog. Phys.* **78**, 104501 (2015).
- Linder, J. & Robinson, J. W. A. Superconducting spintronics. *Nat. Phys.* **11**, 307–315 (2015).
- Bergeret, F. S., Volkov, A. F. & Efetov, K. B. Long-range proximity effects in superconductor-ferromagnet structures. *Phys. Rev. Lett.* **86**, 4096–4099 (2001).
- Houzet, M. & Buzdin, A. I. Long range triplet Josephson effect through a ferromagnetic trilayer. *Phys. Rev. B* **76**, 060504 (2007).
- Robinson, J. W. A., Blamire, M. G. & Banerjee, N. Reversible control of spin-polarized supercurrents in ferromagnetic Josephson junctions. *Nat. Commun.* **5**, 4771 (2014).
- Iovan, A., Golod, T. & Krasnov, V. M. Controllable generation of a spin-triplet supercurrent in a Josephson spin valve. *Phys. Rev. B* **90**, 134514 (2014).
- Silaev, M. A. Possibility of a long-range proximity effect in a ferromagnetic nanoparticle. *Phys. Rev. B* **79**, 184505 (2009).
- Kalenkov, M. S., Zaikin, A. D. & Petrashov, V. T. Triplet superconductivity in a ferromagnetic vortex. *Phys. Rev. Lett.* **107**, 087003 (2011).
- Usadel, K. D. Generalized diffusion equation for superconducting alloys. *Phys. Rev. Lett.* **25**, 507–509 (1970).
- Martinez, W. M., Pratt, W. P. Jr. & Birge, N. O. Amplitude control of the spin-triplet supercurrent in S/F/S Josephson junctions. *Phys. Rev. Lett.* **116**, 077001 (2016).
- Kirk, B. S., Peterson, J. W., Stogner, R. H. & Carey, G. F. libMesh: a C++ Library for parallel adaptive mesh refinement/coarsening simulations. *Eng. Comput.* **22**, 237–254 (2006).
- Amundsen, M. & Linder, J. General solution of 2D and 3D superconducting quasiclassical systems: coalescing vortices and nanoisland geometries. *Sci. Rep.* **6**, 22765 (2015).
- Dynes, R. C. & Fulton, T. A. Supercurrent density distribution in Josephson Junctions. *Phys. Rev.* **B3**, 3015–3023 (1971).
- Hart, S. et al. Induced superconductivity in the quantum spin Hall edge. *Nat. Phys.* **10**, 638–643 (2014).
- Pribiag, V. S. et al. Edge-mode superconductivity in a two-dimensional topological insulator. *Nat. Nanotechnol.* **10**, 593–597 (2015).
- Allen, M. T. et al. Spatially resolved edge currents and guided-wave electronic states in graphene. *Nat. Phys.* **12**, 128–133 (2016).
- Bol'ginov, V. V., Stolyarov, V. S., Sobanin, D. S., Karpovich, A. L. & Ryazanov, V. V. Magnetic switches based on Nb–PdFe–Nb Josephson junctions with a magnetically soft ferromagnetic interlayer. *JETP Lett.* **95**, 366–371 (2012).
- Gingrich, E. C. et al. Spin-triplet supercurrent in Co/Ni multilayer Josephson junctions with perpendicular anisotropy. *Phys. Rev. B* **86**, 224506 (2012).
- d'Albuquerque e Castro, J., Altbir, D., Retamal, J. C. & Vargas, P. Scaling approach to the magnetic phase diagram of nanosized systems. *Phys. Rev. Lett.* **88**, 237202 (2002).
- Dao, N., Whittenburg, S. L. & Cowburn, R. P. Micromagnetics simulation of deep-submicron supermalloy disks. *J. Appl. Phys.* **90**, 5235–5237 (2001).
- Khasawneh, M. A., Khaire, T. S., Klose, C., Pratt, W. P. Jr. & Birge, N. O. Spin-triplet supercurrent in Co-based Josephson junctions. *Supercond. Sci. Technol.* **24**, 024005 (2011).
- Voltan, S., Singh, A. & Aarts, J. Triplet generation and upper critical field in superconducting spin valves based on CrO₂. *Phys. Rev. B* **94**, 054503 (2016).
- Golovchanskiy, I. A. et al. Micromagnetic modeling of critical current oscillations in magnetic Josephson junctions. *Phys. Rev. B* **94**, 214514 (2016).
- Donahue, M. J. & Porter, D. G. *OOMMF User's Guide, Version 1.0*, Interagency Report NISTIR 6376, National Institute of Standards and Technology, Gaithersburg, MD, (1999).

Acknowledgements

The authors would like to thank S. Goswami, A. Singh, M. Kupryianov, S. Bakurskiy and J. Jobst for valuable discussions and comments. This work was supported by The Netherlands Organisation for Scientific Research (NWO/OCW), as part of the Frontiers of Nanoscience program. The work was partly supported by the Research Council of Norway through its Centres of Excellence funding scheme, project number 262633, QuSpin. Support was also received from COST actions MP1201 and CA16218.

Author contributions

K.L. and J.A. conceived the disk geometry, K.L. and E.B. performed the micromagnetic simulations, M.A., J.A.O. and J.L. performed the supercurrent simulations and assisted in the Fourier analysis, K.L., M.P. and P.A. fabricated the devices, K.L. and M.P. performed the measurements. All authors contributed to discussions.

Additional information

Supplementary Information accompanies this paper at <https://doi.org/10.1038/s41467-017-02236-2>.

Competing interests: The authors declare no competing financial interests.

Reprints and permission information is available online at <http://npg.nature.com/reprintsandpermissions/>

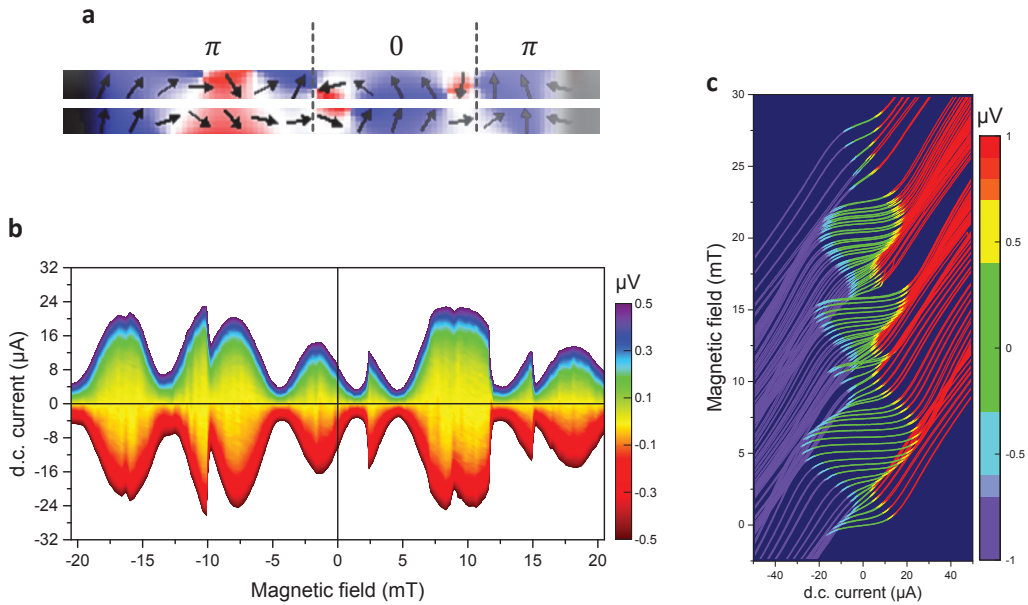
Publisher's note: Springer Nature remains neutral with regard to jurisdictional claims in published maps and institutional affiliations.



Open Access This article is licensed under a Creative Commons Attribution 4.0 International License, which permits use, sharing, adaptation, distribution and reproduction in any medium or format, as long as you give appropriate credit to the original author(s) and the source, provide a link to the Creative Commons license, and indicate if changes were made. The images or other third party material in this article are included in the article's Creative Commons license, unless indicated otherwise in a credit line to the material. If material is not included in the article's Creative Commons license and your intended use is not permitted by statutory regulation or exceeds the permitted use, you will need to obtain permission directly from the copyright holder. To view a copy of this license, visit <http://creativecommons.org/licenses/by/4.0/>.

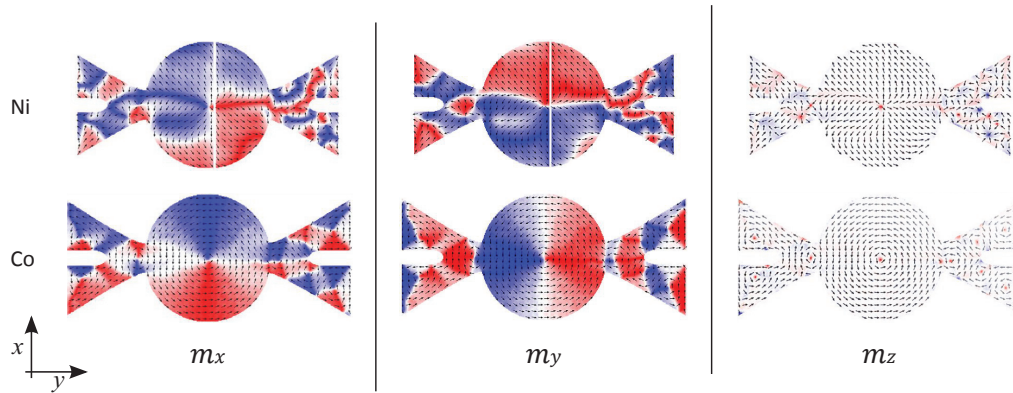
© The Author(s) 2017

Supplementary Figures

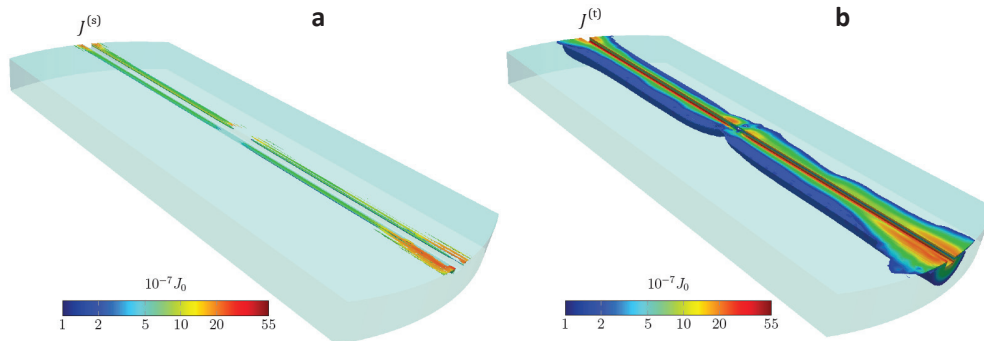


Supplementary Figure 1 | Interference patterns from the virgin magnetic state.

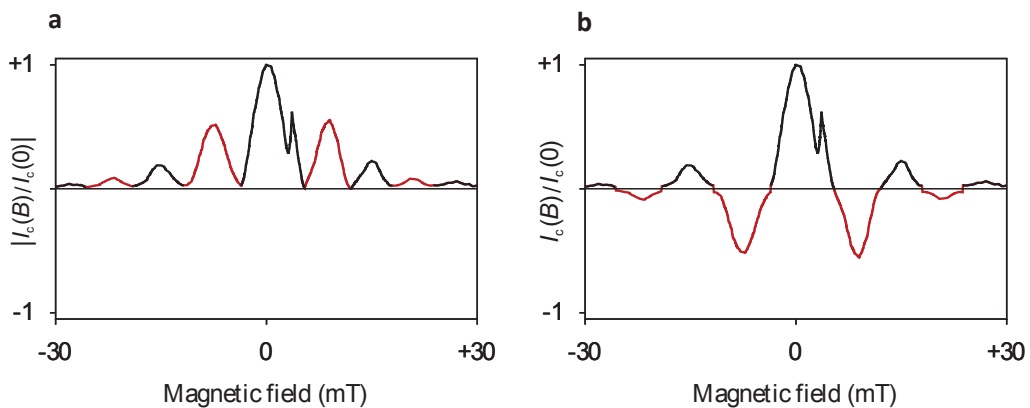
(a) Disordered magnetic state of Ni before conditioning (schematic). The stochastic magnetic orientation of Ni on each side of the trench can lead to the formation of multiple 0 and π segments across the junction. (b) Supercurrent interference pattern of the virgin magnetic state, measured while sweeping the out-of-plane field from negative to positive 30 mT in steps of 0.3 mT. On average, the supercurrent is suppressed for small fields (below 5 mT) in both field directions. The interference pattern is characterized by random discontinuities. These irregularities are shown more clearly in (c) which shows individual $I - V$ curves taken while scanning the field from 28 mT back to zero. The curves are given an offset to represent the field they were measured at. All measurements are taken at $T = 2.1$ K.



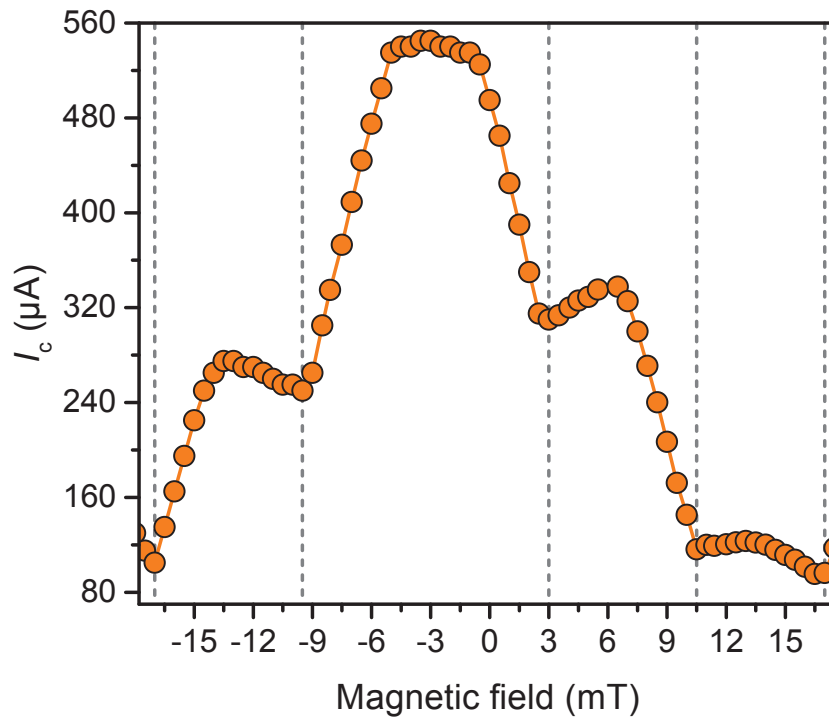
Supplementary Figure 2 | Micromagnetic simulations with an in-plane field. Top views of the magnetic states of Co and Ni layers obtained from OOMMF simulations. The leads are included in the design to produce a more realistic shape anisotropy, needed to accurately describe the system under an in-plane field. Individual components of the magnetization vector \mathbf{m} are plotted separately for clarity. The pixel colour scheme, red-white-blue, scales with the magnitude of each component. The red and blue pixels represent positive and negative values respectively. Out of plane magnetization (m_z) is generally suppressed, except at the vortex core where both layers have a highly localized out of plane component. In the actual device, the trench that forms the junction is slightly off-centred. This feature is accounted for in the simulations by placing the gap in Ni 40 nm away from the centre of the disk.



Supplementary Figure 3 | Simulated contributions of singlet and triplet supercurrents (a) Magnitude of the current density generated by singlet Cooper pairs, $J^{(s)} = \mathbf{J}^{(s)}$, which is greatly suppressed except for in the immediate vicinity of the superconductors. (b) Magnitude of the current density generated by triplet Cooper pairs, $J^{(t)} = \mathbf{J}^{(t)}$. For clarity, currents lower than $10^{-7}J_0$ have been removed, which explains why no singlet current is observed in the trench. It is noted that while the total current $\mathbf{J} = \mathbf{J}^{(s)} + \mathbf{J}^{(t)}$ is conserved, $\mathbf{J}^{(s)}$ and $\mathbf{J}^{(t)}$ are generally not. This is due to the magnetization, which causes oscillations between the singlet and triplet states.



Supplementary Figure 4 | Recovering the complex critical current. (a) The (unsigned) $|I(B)|$ pattern extracted from $I - V$ measurements. (b) The signed $I_c(B)$ interference pattern reconstructed by flipping the signs of alternate lobes as in ref. 1. The data were taken at 2.1 K.



Supplementary Figure 5 | Control experiment. Supercurrent interference pattern measured at $T = 2.1$ K from a control device that was processed in parallel with the one presented in the main text. Deposited together on one substrate, the same multilayer of Pt(7 nm)/Nb(45 nm)/Ni(1.5 nm)/Cu(5 nm)/Co(60 nm) was used in both devices. The Ga^+ dose applied in milling the weak link for the control device was reduced by 50%. This provides a nonmagnetic pathway in the weak link, where singlet current is not suppressed, and can therefore dominate the transport. The result is a junction with a substantially higher critical current, showing single-slit interference pattern.

Supplementary Notes

Supplementary Note 1 | Numerical simulations of the critical current.

To calculate the critical current we use the quasiclassical approximation in the diffusive limit, which yields the Usadel equation⁵

$$D \nabla \hat{\mathbf{g}} \nabla \hat{\mathbf{g}} + i[\varepsilon \hat{\rho}_3 + \hat{\boldsymbol{\sigma}} \cdot \mathbf{h}, \hat{\mathbf{g}}] = 0 \quad (1)$$

where D is the diffusion constant and ε is the quasiparticle energy. The magnetization texture from the micromagnetic simulations are represented as an exchange field $\mathbf{h} = \mathbf{h}(\mathbf{r})$. Furthermore we have defined $\hat{\boldsymbol{\sigma}} = \text{diag}(\boldsymbol{\sigma}, \boldsymbol{\sigma}^*)$, where $\boldsymbol{\sigma}$ is a vector of Pauli matrices, and $\hat{\rho}_3 = \text{diag}(1, 1, -1, -1)$. From $\hat{\mathbf{g}} = \hat{\mathbf{g}}(\mathbf{r}, \varepsilon)$, the 4×4 retarded Green function matrix in Nambu \otimes spin space, the equilibrium current density may be computed as

$$\mathbf{J} = \frac{N_0 e D}{2} \int d\varepsilon \text{Re Tr}\{\hat{\rho}_3 \hat{\mathbf{g}} \nabla \hat{\mathbf{g}}\} \tanh\left[\frac{\beta \varepsilon}{2}\right] \quad (2)$$

where N_0 is the density of states at the Fermi level, and $\beta = 1/k_B T$. We neglect the inverse proximity effect, and assume that the superconductors on each side of the trench are large enough to be approximated as bulk. In the calculations, we have used that the critical current is approximately found for a phase difference between the superconductors of $\Delta\phi = \frac{\pi}{2}$. For simplicity, we use transparent boundary conditions between the Ni and the Co layer, whereas we use the low-transparency Kupriyanov-Lukichev boundary conditions⁶ at the Ni-Nb interface.

In the modeling of the geometry, we have assumed an effective superconducting coherence length of $\xi = 10$ nm, so that the radius of the circular disk becomes $R = 50\xi$. In the direction crossing the trench, the model has been truncated to a width of $W = 40\xi$ to reduce the model size. This has been done under the assumption that

any contribution to the current from the removed regions is negligible due to the vast distance to the opposite superconductor. The thickness of the Ni and the Co layers have been set to ξ and 6ξ , respectively, and the width of the trench is 2ξ . The Ni thickness is set larger than in the actual experiment to avoid unnecessarily small elements in the Ni-region, which would substantially increase the calculation time. Although this yields lower values for the triplet current, the purpose of our calculation here is to identify the origin of this current; and not its absolute magnitude.

The spatial distribution of the magnetization in both the Ni and the Co layer are accurately mapped onto the 3D mesh via the exchange field \mathbf{h} , where an amplitude of $|\mathbf{h}| = 30 \Delta \simeq 46 \text{ meV}$ was used. While this is significantly lower than typical exchange fields in Co, it is still sufficient to quench the contribution of singlet Cooper pairs to the current density. To verify this, we make use of the fact that the supercurrent density generated by the singlet $\mathbf{J}^{(s)}$ and triplet $\mathbf{J}^{(t)}$ Cooper pairs contribute additively $\mathbf{J} = \mathbf{J}^{(s)} + \mathbf{J}^{(t)}$. The two components are presented in Supplementary Figure 3. It is clear that the current density of singlet pairs rapidly vanishes away from the superconductors. In contrast, the triplet current density maintains an appreciable value over a substantially larger region, indicating that triplet Cooper pairs are the primary means of transport. The results will therefore be qualitatively the same for a more realistic strength of the exchange field. The advantage of using the reduced value is that the current densities become larger, which in turn make the numerical calculations less resource intensive.

The finite element analysis was carried out using 27-node hexagonal volume elements, and the Green function is interpolated within each element by means of

second order Lagrange polynomials. This means that the current density within each element is interpolated by linear polynomials. To ensure that the spatial distribution of the current density is accurately resolved, we use a refined mesh in a region surrounding the trench, as is shown in Fig. 2a in the main text. For more details regarding the finite element analysis of three-dimensional superconducting heterostructures, please consult ref. 7.

Supplementary Note 2 | Interference patterns from the virgin magnetic state. Prior to conditioning the magnetization, supercurrent interference patterns were measured using small out-of-plane fields. These are presented in Supplementary Figure 1. In contrast to the conditioned sample, $I_c(B_z)$ is generally suppressed around zero field. We observe two maxima, which always occur at fields higher than 5 mT. Note that this offset cannot be attributed to remnant fields from the ferromagnet. The applied field for the interferometry measurements is not sufficient to have an appreciable influence on the magnetization of either layer. This is verified by SQUID magnetometry and ferromagnetic resonance experiments.

It has been proposed that the phase of triplet correlations in a S/F'/F/F'/S junction such as ours, is determined by the relative magnetic orientation of the F and F' layers on each side². On the other hand, this unusual interference pattern, with two maxima and suppressed I_c at zero field, is the characteristic of a junction with multiple parallel 0 and π channels^{3,4}. This condition could be fulfilled in the virgin state, where the arbitrary orientation of Ni and Co magnetization can lead to random formation of multiple 0 and π segments across the junction. These interference patterns are also characterized by irregular discontinuities, which could be attributed to the arbitrary arrangement of the 0 and π segments.

Remarkably, we find these features to disappear altogether after conditioning the sample: $I_c(B_z)$ turns into a highly regular and reproducible SQUID pattern, with maximum I_c consistently appearing at $B_z = 0$. This pronounced dependence on magnetic conditioning was absent for junctions where singlet correlations dominated the transport: no significant changes in the interference pattern or the maximum value of I_c were observed.

Supplementary Note 3 | Fourier analysis of supercurrent density profiles.

As shown by Dynes and Fulton¹, the supercurrent density profile $J(x)$ can be determined from the superconducting interference pattern $I_c(B)$ using a Fourier transform:

$$J(x) \sim \int_{-\infty}^{+\infty} dB I_c(B) e^{\frac{2\pi i L B x}{\Phi_0}} \quad (3)$$

Here, the coordinate system is defined such that the magnetic field B is applied along the z -axis, the critical current I_c is measured along the y -axis, and the current distribution $J(x)$ can then be determined along the x -axis. The equation also depends on the effective length L of the junction and the flux quantum $\Phi_0 = h/2e$. Note that $I_c(B)$ is the signed critical current, where the sign is determined from the experimentally measured $|I_c(B)|$ by assuming that it consists of alternating positive and negative lobes, as described in more detail in ref. 1. This procedure is justified when the interference pattern consists of well-defined maxima separated by deep minima, as is the case for our measurements.

The original method by Dynes and Fulton was derived for a rectangular junction where the dimensions of each superconductor are much larger than the London penetration depth λ . In that case, the effective junction length $L = 2\lambda + d$, where d is

the thickness of the barrier between the superconducting leads. In our case, however, the junction is cylindrical and the current distribution not uniform, so the length (which determines the amount of flux to be screened) is not well defined. We therefore performed the Fourier analysis without making any assumptions regarding the value of L , but instead assumed that the position along the x -axis where we obtained $J(x) \rightarrow 0$ likely corresponded to the junction ends $x \approx \pm R$, where R is the cylinder radius. From this, we obtained an estimate $L \approx 180$ nm for the effective junction length. This value is somewhat lower than expected for a uniform rectangular junction: in that case the effective area is $2RL$ while the first minimum in $I_c(B_z)$ is at 7.8 mT, yielding $L \approx 270$ nm. Both numbers are of correct order of magnitude: the value of λ for a 50 nm Nb film is about 110 nm⁸ so $2\lambda + d$ is 240 nm. If we were to take the sharp drop in the current density profile as the sample edge, L would become less than 100 nm, which appears to be too low in view of the value of λ .

The SQI experiments are carried out by measuring the voltage as a function of current for a given applied magnetic field, i.e. $V(I, B)$. The critical current $|I_c(B)|$, used for the Fourier analysis, is obtained by extracting a contour for a small but finite voltage threshold $V(I_c, B) > 0.3 \mu\text{V}$. Experimentally we find this criterion to be optimal for reducing noise effects that distort the shape of $I_c(B)$. The result is then adjusted to the y -axis so that $|I_c(B)| = 0$ at the nodes between the lobes of the interference pattern. This is to account for the artificial offset introduced by the 0.3 μV threshold voltage. We then recover the complex critical current $I_c(B)$, by switching the sign of every other lobe of the measured $|I_c(B)|$. The original $|I_c(B)|$ and the signed $I_c(B)$ curves are shown side-by-side in Supplementary Figure 4.

Note that the measured $I_c(B)$ may slightly deviate from a perfectly symmetric pattern, and yield a complex supercurrent distribution $J(x)$ after Fourier transformation. This apparent asymmetry however is predominantly caused by experimental noise. We therefore discard the complex phase $J(x)$ to approximate the supercurrent distribution profile by $|J(x)|$, shown in Fig. 3f of the main text.

Supplementary References

1. Dynes, R. C. & Fulton, T. A. Supercurrent density distribution in Josephson junctions. *Phys. Rev. B* **3**, 3015-3023 (1971).
2. Houzet, M. & Buzdin, A. I. Long range triplet Josephson effect through a ferromagnetic trilayer. *Phys. Rev. B* **76**, 060504 (2007).
3. Smilde, H. J. H., Ariando, D. H. A., Blank, G. J., Gerritsma, H., Hilgenkamp, H. & Rogalla, H. *d*-Wave-Induced Josephson current counterflow in YBa₂Cu₃O₇/Nb zigzag junctions. *Phys. Rev. Lett.* **88**, 057004 (2002).
4. Gürlich, C. *et al.* Visualizing supercurrents in ferromagnetic Josephson junctions with various arrangements of 0 and π segments. *Phys. Rev. B* **81**, 094502 (2010).
5. Usadel, K. D. Generalized diffusion equation for superconducting alloys. *Phys. Rev. Lett.* **25**, 507–509 (1970).
6. Kuprianov, M. Y. & Lukichev, V. F. Influence of boundary transparency on the critical current of ‘dirty’ SS’S structures. *Sov. Phys. JETP* **67**, 1163 (1988).
7. Amundsen, M. & Linder, J. General solution of 2D and 3D superconducting quasiclassical systems: coalescing vortices and nanoisland geometries. *Sci. Rep* **6**, 22765; doi: 10.1038/srep22765 (2016).
8. Gubin, A. I., Il’in, K. S., Vitusevich, S. A., Siegel, M. & Klein, N. Dependence of magnetic penetration depth on the thickness of superconducting Nb thin films. *Phys. Rev. B* **72**, 064503 (2005).

XII

Reference

M. Amundsen, [J.A. Ouassou](#), J. Linder.
Field-free nucleation of antivortices and
giant vortices in nonsuperconducting materials.
Physical review letters 120, 207001 (2018).
DOI: 10/GDG3KD

Contributions

MA performed the 2D numerical simulations of vortex patterns, and came up with the explanation of the results in terms of symmetries, energies, and winding numbers. JAO contributed to the idea behind the project, analytically derived the radial profile and energy of a giant vortex (by solving the Ginzburg–Landau equations), and derived the boundary conditions used for the numerical simulations (by analytically solving the Usadel equation in a current-carrying superconductor). JL supervised the entire process and provided support. All authors contributed to the discussion and writing of the manuscript.

Comments

This research was inspired by reference 160, where the idea of current-induced proximity vortices was originally suggested. In our research, we extend this idea by considering geometries that are completely enveloped by current-biased superconducting wires. Moreover, we use a more rigorous numerical model in our paper, which we show can lead to qualitatively different results for e.g. the density of states.

Field-Free Nucleation of Antivortices and Giant Vortices in Nonsuperconducting Materials

Morten Amundsen,^{*} Jabir Ali Ouassou, and Jacob Linder

Center for Quantum Spintronics, Department of Physics, Norwegian University of Science and Technology, NO-7491 Trondheim, Norway

(Received 12 December 2017; revised manuscript received 24 February 2018; published 14 May 2018)

Giant vortices with higher phase winding than 2π are usually energetically unfavorable, but geometric symmetry constraints on a superconductor in a magnetic field are known to stabilize such objects. Here, we show via microscopic calculations that giant vortices can appear in intrinsically nonsuperconducting materials, even without any applied magnetic field. The enabling mechanism is the proximity effect to a host superconductor where a current flows, and we also demonstrate that antivortices can appear in this setup. Our results open the possibility to study electrically controllable topological defects in unusual environments, which do not have to be exposed to magnetic fields or intrinsically superconducting, but instead display other types of order.

DOI: 10.1103/PhysRevLett.120.207001

Introduction.—It is well known that applying a magnetic field to a type-II superconductor can lead to the formation of Abrikosov vortices [1]. A gradient in the phase φ of the superconducting order parameter $\Delta = |\Delta|e^{i\varphi}$ causes a circulating supercurrent around such vortices, whereas $|\Delta| \rightarrow 0$ at their centers. Vortex excitations in superconductors [2,3] remains a vibrant research topic, not least because it lies at the intersection of two major research fields: superconductivity and topology in physics.

It was recently pointed out in Ref. [4] that it is also possible to generate Josephson vortices without applying magnetic fields. Such vortices are also characterized by a quantized phase winding and a suppressed order parameter at their core [5]. Motivated by this, we have performed microscopic calculations using the quasiclassical theory of superconductivity [6] on a normal metal enveloped by a current-biased superconducting wire (Fig. 1). The idea behind the device is simple: an external current source forces a supercurrent through the wire, and this circulation whirls the condensate in a proximitized normal metal as well. Our objective has been to determine what type of electrically controllable vortex physics then emerges. We demonstrate here that both giant vortices and antivortices appear in the nonsuperconducting region even in the absence of any applied magnetic field. This provides an alternative method of creating complex vortex patterns by applying electric currents. Since these patterns are generated in a proximitized nonsuperconductor, this opens up the intriguing prospect of studying unusual topological vortex excitations in materials with other types of quantum order, which do not have to be compatible with bulk superconductivity. One example is a magnetic metal, where the generation of odd-frequency triplet superconducting order could reverse the chirality of some vortices, similarly

to the paramagnetic Meissner effect [7,8]. More fundamentally, it raises the intriguing question: what characterizes a vortex in an odd-frequency order parameter?

Geometric effect and winding number.—Since a circulating supercurrent requires a finite phase-gradient $\nabla\varphi$, and the analyticity of the superconducting wave function implies integral winding numbers $n = \Delta\varphi/2\pi$ around any point, the system is topologically coerced into nucleating vortices in the normal metal region of Fig. 1. Assuming a thin-film structure, the total charge current associated with this circulation is small, and the magnetic field generated by the circulation can safely be neglected. Note that in contrast to the setup proposed in Ref. [4], our normal metal is surrounded by a continuous superconducting wire on all sides, instead of having two separate wires on the top and bottom, which we will show fundamentally alters the vortex physics in the system. Another important difference is that we model the superconducting wire using an exact solution

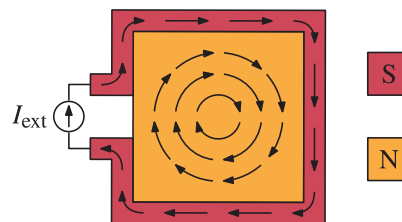


FIG. 1. Conceptual sketch of the physical system. An external current source is used to inject a current into a superconductor (red). The circulating current also affects a proximitized normal metal (yellow), causing an electrically controlled vortex to emerge there.

of the Usadel equation in the current-biased superconductor and tunneling boundary conditions. As we will demonstrate, this is necessary to correctly describe qualitative changes that the phase winding induces in, e.g., the density of states (DOS).

When the current in the superconducting wire makes a total winding number $N > 1$, there are multiple ways to satisfy the boundary conditions. Among other possibilities, we can get (i) N vortices with a winding 1 each, (ii) $N + M$ vortices with a winding +1 and M antivortices with winding -1, or (iii) just one giant vortex with a winding N . The kinetic energy of an n -winding vortex scales with n^2 , so the most energetically favorable is configuration (i). Hence, giant vortices and antivortices are seldom seen. However, since the superconducting order parameter respects the symmetries of the underlying geometry, vortices only nucleate along the symmetry axes of the system. For highly symmetric geometries, these additional constraints may force the appearance of giant vortices or antivortices. The resulting interplay between topological defects, geometric symmetries, and energy minimization was previously studied in Refs. [9–12] using the phenomenological Ginzburg-Landau formalism for type-II superconductors in a magnetic field. Here, we show that this effect also arises in proximitized normal metals without magnetic fields. This generalization is particularly important as it opens the possibility to study novel vortex physics in materials featuring completely different order than superconductors, e.g., ferromagnets or topological insulators.

2D diffusive metal with phase-winding.—As shown in Fig. 1, we consider a normal metal with a superconducting loop grown on top. We describe the properties of the metal in terms of quasiclassical propagators \hat{g} in Nambu and spin space,

$$\hat{g}(\mathbf{r}, \epsilon) = \begin{pmatrix} g(\mathbf{r}, +\epsilon)\sigma_0 & f(\mathbf{r}, +\epsilon)i\sigma_2 \\ -f^*(\mathbf{r}, -\epsilon)i\sigma_2 & -g^*(\mathbf{r}, -\epsilon)\sigma_0 \end{pmatrix}, \quad (1)$$

where the normal part g and anomalous part f are complex scalar functions, subject to the normalization constraint $\hat{g}^2 = 1$. Here, σ_0 is the 2×2 identity matrix, and σ_2 is the second Pauli matrix. We assume that all length scales in the problem are large compared to the Fermi wavelength and mean free path; i.e., we take the quasiclassical diffusive limit. The propagators \hat{g} are then governed by the Usadel equation [6,13,14],

$$D\nabla(\hat{g}\nabla\hat{g}) + i[\epsilon\hat{\tau}_3, \hat{g}] = 0, \quad (2)$$

where D is the diffusion constant, ϵ the quasiparticle energy, and $\hat{\tau}_3 = \text{diag}(+\sigma_0, -\sigma_0)$. Furthermore, we assume that the normal region is connected to the superconducting wire by a low-transparency interface. We may then use the Kupriyanov-Lukichev boundary condition $\zeta\mathbf{e}_\perp \cdot \nabla\hat{g}_n = [\hat{g}_n, \hat{g}_s]/\xi$ [15], where ζ parametrizes interface resistance,

\mathbf{e}_\perp is the outwards-pointing interface normal vector, \hat{g}_n and \hat{g}_s are propagators on the normal and superconducting sides, and ξ the superconducting coherence length. The propagators \hat{g}_s in the current-biased superconductors were evaluated analytically. The applied current also creates a magnetic field which penetrates the proximitized material. Its strength depends on the total applied current, which in turn depends on the pair density and dimensions of the superconductor. However, since the field is perpendicular to and roughly constant within the current loop, its only effect is to slightly perturb the applied current for which a given vortex pattern appears. We have neglected the quantitative correction from the magnetic field herein.

In practice, the differential equations above are Riccati-parametrized for stability [16], and then solved numerically using a finite-element method on a two-dimensional mesh. This lets us handle arbitrary sample geometries, such as the regular polygons considered herein. For more information about the numerical solution procedure itself, see Ref. [17].

Superconducting wire with a uniform current.—As shown in Sec. II of the Supplemental Material [18], the propagator \hat{g} in a current-biased bulk superconductor can be written [23,24]

$$\hat{g} = \frac{1}{\sqrt{\epsilon^2 - \Theta^2}} \begin{pmatrix} +\epsilon\sigma_0 & \Theta e^{+i\varphi}i\sigma_2 \\ \Theta e^{-i\varphi}i\sigma_2 & -\epsilon\sigma_0 \end{pmatrix}, \quad (3)$$

where $\Theta(\epsilon)$ parametrizes the strength of the superconductivity, and φ is the superconducting phase. The phase varies linearly with the distance ℓ along the wire. Defining $\varphi(0) \equiv 0$, and parametrizing the variation using a winding rate $u \equiv \xi|\nabla\varphi|$, we therefore get $\varphi(\ell) = u\ell/\xi$. The function $\Theta(\epsilon)$ is determined by

$$\Theta = \frac{|\Delta|}{1 + u^2/2\sqrt{\Theta^2 - \epsilon^2}}, \quad (4)$$

$$|\Delta| = \frac{1}{\text{acosh}\omega_c} \int_0^{\omega_c} d\epsilon \text{Re} \left(\frac{\Theta}{\sqrt{\epsilon^2 - \Theta^2}} \right) \tanh \left(\frac{\pi \epsilon}{2e^\gamma T} \right). \quad (5)$$

These equations have been written in a form where Θ , Δ , ϵ , ω_c are all normalized to the zero-current gap Δ_0 , while the temperature T is normalized to the critical temperature T_c . Here, ω_c refers to the Debye cutoff, and γ is the Euler-Mascheroni constant. The first of these equations is a fixpoint iteration equation. This is easily solved by guessing $\Theta(\epsilon) = 1$ and $|\Delta| = 1$, and applying Newton's method to the equation for a discretized set of energies from the Debye cutoff $\epsilon = \omega_c$ to zero energy $\epsilon = 0$. The second is a self-consistency equation for the gap Δ , which is evaluated by numerical integration of the results for $\Theta(\epsilon)$. We then alternate between solving the fixpoint equation and self-consistency equation until satisfactory convergence. The solutions to the equations above are visualized in Fig. 2.

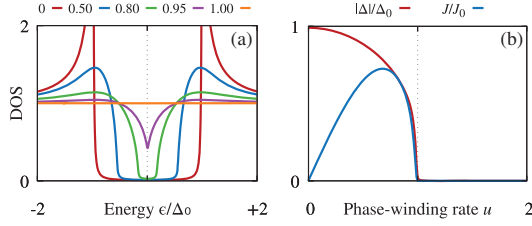


FIG. 2. Visualization of a bulk superconductor with a uniform current at zero temperature. (a) DOS for varying winding rates u , as shown in the legends above. Note how the coherence peaks are smoothed out for $u > 0$ and the gap closes as $u \rightarrow 1$, illustrating a qualitatively different behavior for $u > 0$. (b) Gap Δ and current density J as functions of u , where the unit $J_0 = eDN_0\Delta_0/4\xi$. As long as $u < 1/2$, we see that $\Delta \approx \Delta_0$ and $J \sim u$, and a non-self-consistent solution is reasonably accurate. However, the current becomes nonmonotonic for $u > 2/3$, so this regime is inaccessible in our proposed setup.

When approaching the setup in Fig. 1 numerically, we assumed that the superconducting wire suffers a negligible inverse proximity effect from the normal metal. In this case, we can use the analytical equation above for the superconducting wire, and reduce the superconductor to effective boundary conditions for the normal metal. Furthermore, we numerically only considered phase-winding rates $u \leq 0.5$, in which case Eq. (5) can be replaced by the approximation $|\Delta| \approx 1$. Note that since the phase-winding rate u cannot be arbitrarily large, we need a system much larger than the coherence length to obtain high winding numbers using a current bias.

Quantifying vortices.—We can study the proximity-induced superconductivity in a normal metal via the pair correlation

$$\Psi(\mathbf{r}) \sim \int_0^{\omega_c} d\epsilon [f(\mathbf{r}, +\epsilon) - f(\mathbf{r}, -\epsilon)] \tanh(\epsilon/2T), \quad (6)$$

which behaves like a complex order parameter. This pair correlation can be decomposed as $\Psi \equiv |\Psi| \exp(i\varphi)$, and the phase φ can then be extracted using $\varphi = \arctan(\text{Im}\Psi/\text{Re}\Psi)$.

As discussed in the introduction, the circulating current in the enclosing superconductor creates a phase-winding $\nabla\varphi$ along the interface. However, the phase φ is uniquely defined modulo 2π , which means that it is only possible for the phase to vary continuously around the edges of the normal metal if it increases by $\Phi_I = 2\pi N$ after having traversed the entire circumference. In other words, we must have a total vorticity

$$N = \frac{\Phi_I}{2\pi} \equiv \frac{1}{2\pi} \oint_{\partial\Omega} (\nabla\varphi) \cdot d\ell, \quad (7)$$

where $\partial\Omega$ is the boundary of the normal metal. When we have a finite vorticity N , the currents inside the normal

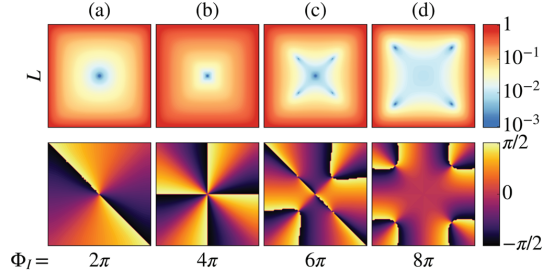


FIG. 3. Vortex nucleation patterns for various applied current windings Φ_I , for a quadratic normal metal with side lengths $L = 12\xi$. The top row shows the magnitude $|\Psi|$ of the pair correlation, where the minima indicate the vortices. The bottom row shows the phase φ of the pair correlation, from which the winding of individual vortices can be determined. The total windings Φ_I are listed below.

metal will form closed loops, leading to the appearance of vortices. More precisely, the total vorticity N will be equal to the sum of the winding numbers n of all the induced vortices. The vortices manifest as nodes in the pair correlation Ψ .

Numerical results.—In the upper row of Fig. 3, the vortex pattern for increasing applied current winding Φ_I is shown. The winding of the individual vortices may be determined graphically from the phase of the pair correlation function φ , which is plotted in the bottom row of Fig. 3. By using Eq. (7) with the replacements $N \rightarrow n$ and $\partial\Omega \rightarrow \mathcal{C}$, where \mathcal{C} is any contour encircling a single vortex, one sees that $n \neq 0$ only if the integration path crosses discontinuities. Furthermore, each discontinuity contributes a value to the integral equal to the size of the jump. For $\Phi_I = 2\pi$, shown in Fig. 3(a), there is a single vortex in the center of the normal metal, and any closed contour around this point must traverse two jumps $\Delta\varphi = \pi$, thus showing that the vortex has a winding $n = +1$. We note that the precise locations of these discontinuities depend on the reference point for the phase of the superconductors, and are hence not physically significant. The number of times a closed loop crosses a discontinuity, however, is. In Fig. 3(b), where $\Phi_I = 4\pi$, there is still only a single vortex in the system, but now the plot of φ shows four discontinuities, from which it is inferred that this is a giant vortex with $n = +2$.

For $\Phi_I = 6\pi$, shown in Fig. 3(c), five vortices are found. As the sum of the individual topological numbers should add up to $N = +3$, in accordance with Eq. (7), one of these vortices must be an antivortex. The phase plot shows that this is indeed the case: the central vortex winds in the opposite direction of other vortices. Hence, this configuration consists of one central $n = -1$ antivortex with four surrounding $n = +1$ vortices. For $\Phi_I = 8\pi$, there are four regular $n = +1$ vortices along the diagonals, as shown in Fig. 3(d). Since these vortex patterns arise from symmetry constraints, they are naturally sensitive to asymmetries in

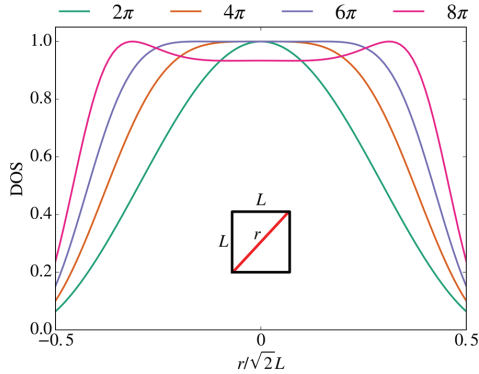


FIG. 4. DOS along the diagonal of the normal metal for various applied current windings Φ_I . Superconductivity is suppressed in the vortex cores, and the normal-state DOS = 1 is recovered.

the geometry. The giant vortex in Fig. 3(b) splits into two $n = +1$ vortices as the geometry becomes rectangular. However, the vortices continue to overlap strongly for sufficiently small deviations, as shown in Sec. III of the Supplemental Material [18]. This means that the giant vortex could in practice be stabilized against deviations from perfect symmetry by creating a pinning potential at this location [25]. Since the vortex positions are also influenced by the applied currents, another option is to fine-tune the currents to experimentally realize the giant vortex. The pattern in Fig. 3(c) is, on the other hand, stable against small deviations in aspect ratio. The reason is that when the geometry becomes increasingly rectangular, it eventually becomes energetically favorable to satisfy $N = +3$ as three $n = +1$ vortices along the longest axis. The transition to such a pattern can only occur in a way which respects the symmetries of the rectangle, and hence the central antivortex turns into a vortex, and additional antivortices must appear so that the off-center vortices can annihilate symmetrically [26].

The vortices also create a spatial modulation of the DOS: at the vortex cores, superconductivity vanishes, and the minigap disappears. This means that the vortices we predict can be directly inferred via local STM measurements. In Fig. 4, the DOS for $\epsilon = 0$ is plotted along the diagonal of the normal metal (i.e., between two opposite corners). This confirms that the normal-state result DOS = 1 is recovered at the vortex cores. For the $n = +2$ vortex produced by $\Phi_I = 4\pi$, the minigap is suppressed in a larger region around the vortex than for $\Phi_I = 2\pi$. For $\Phi_I = 6\pi$, the normal region is larger still, but this is likely due to the close proximity of three vortices. For $\Phi_I = 8\pi$, the vortices are sufficiently far apart for a dip in the DOS to appear in between, providing an observable signature.

The above can be understood by analyzing the pair correlation. In Sec. I of the Supplemental Material [18], it is shown that for small distances r from the vortex center,

$\Psi \sim (r/2\xi_0)^n/n!$, where ξ_0 is the Ginzburg-Landau coherence length. For $r < 2\xi_0(n!)^{1/n} \approx 2[1 + (n-1)/e]\xi_0$, these correlations recover more slowly with increasing winding n , and hence the minigap is increasingly suppressed. The fact that the vortex size increases linearly with n also in the diffusive limit can be motivated from Fig. 2. There, we see that superconductivity vanishes entirely as the phase-winding rate $u \equiv \xi|\nabla\varphi| \rightarrow 1$. Assuming that this remains approximately valid in nonbulk materials, and using that $|\nabla\varphi| = |n|/r$ around an n -winding vortex, we find that superconductivity vanishes for $r < n\xi$. In other words, we find that the core size of a giant vortex scales linearly with its winding number n , providing an observational signature of giant vortices that can be seen via STM measurements.

The vortex patterns of Fig. 3 may be deduced from energy considerations. In general, the kinetic energy of a vortex with a winding number n scales as n^2 . This is because kinetic energy $E_k \sim v^2$, where $v \sim \nabla\varphi \sim n$ is the velocity of the superconducting condensate. In Sec. I of the Supplemental Material [18], we solve the linearized Ginzburg-Landau equation near a vortex with winding number n , and use this to confirm that the kinetic energy is indeed proportional to n^2 . Similar n^2 dependencies have previously been noted for magnetic vortices in type-II superconductors [27], and these properties are shared by vortices in proximitized nonsuperconductors [5,28].

The above provides a simple prescription for predicting the vortex nucleation pattern. When a total vorticity N is introduced to the system, it splits into vortices with individual windings n_i in a way that satisfies $N = \sum_i n_i$. Among all patterns permitted by the symmetries of the geometry, the energetically favored is the one that minimizes $E = \sum_i n_i^2$. Note that n_i can be either positive or negative, allowing for antivortex nucleation.

In the geometry considered so far, off-center vortices can only appear in a square formation without breaking the symmetry of the system, as is seen in Fig. 3. This symmetry constraint explains why it is possible to produce a vortex with winding $n = +2$. A higher winding is, however, not possible because it will always be energetically favorable to introduce four new vortices away from the center, and, potentially, an antivortex in the center. Similar results were found for a mesoscopic superconductor in an applied magnetic field [10–12]. The present analysis differs in that the vortex patterns are generated in an intrinsically non-superconducting material solely by an applying an electric current. A regular polygon with a higher symmetry (larger number of sides), will by the same reasoning as above allow for a higher winding at the center, as any alternative will require a larger number of $n = +1$ vortices to be distributed in a symmetrical fashion. Figure 5 shows the pair correlation function for a hexagonal normal metal surrounded by a superconductor with an applied current equivalent to $\Phi_I = 6\pi$. Here, we find a single vortex of

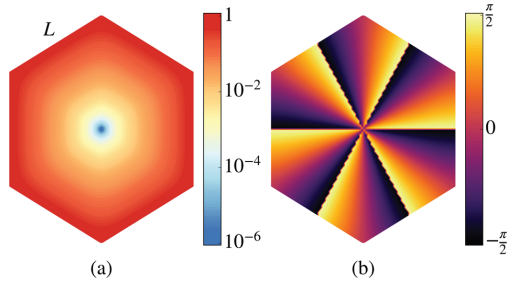


FIG. 5. Hexagonal geometry with side lengths $L = 6\xi$, and an applied current winding $\Phi_I = 6\pi$. (a) The pair correlation Ψ , showing a single vortex at the center. (b) The phase φ of the pair correlation, demonstrating that it is a giant vortex with winding number $n = +3$.

winding $n = +3$. Generally, a regular polygon with m sides allows for a giant vortex with winding up to $n = \lfloor m/2 \rfloor$.

Conclusion.—We have used microscopic calculations to show that one can induce giant vortices and antivortices in nonsuperconducting materials in the absence of magnetic fields. We also analyzed the vortex nucleation pattern using arguments of symmetry and energy minimization. Our results open the possibility to study novel topological defects in unusual environments, which do not have to be intrinsically superconducting or exposed to magnetic fields.

The authors thank Vetle Kjær Risinggård for useful discussions. This work was partly supported by the Research Council of Norway through its Centres of Excellence funding scheme, Project No. 262633, “QuSpin.” J.L. and J.A.O. also acknowledge funding from the Research Council of Norway Grant No. 240806.

*morten.amundsen@ntnu.no

- [1] A. A. Abrikosov, *J. Phys. Chem. Solids* **2**, 199 (1957).
- [2] G. Blatter, M. V. Feigel'man, V. B. Geshkenbein, A. I. Larkin, and V. M. Vinokur, *Rev. Mod. Phys.* **66**, 1125 (1994).
- [3] H. Suderow, I. Guillamon, J. G. Rodrigo, and S. Vieira, *Supercond. Sci. Technol.* **27**, 063001 (2014).
- [4] D. Roditchev, C. Brun, L. Serrier-Garcia, J. C. Cuevas, V. H. L. Bessa, M. V. Milošević, F. Debontridder, V. Stolyarov, and T. Cren, *Nat. Phys.* **11**, 332 (2015).
- [5] J. C. Cuevas and F. S. Bergeret, *Phys. Rev. Lett.* **99**, 217002 (2007).
- [6] K. Usadel, *Phys. Rev. Lett.* **25**, 507 (1970).
- [7] A. Di Bernardo *et al.*, *Phys. Rev. X* **5**, 041021 (2015).
- [8] S. Mironov, A. Mel'nikov, and A. Buzdin, *Phys. Rev. Lett.* **109**, 237002 (2012).
- [9] H. J. Fink and A. G. Presson, *Phys. Rev.* **151**, 219 (1966).
- [10] L. F. Chibotaru, A. Ceulemans, V. Bruyndoncx, and V. V. Moshchalkov, *Nature (London)* **408**, 833 (2000).
- [11] L. F. Chibotaru, A. Ceulemans, V. Bruyndoncx, and V. V. Moshchalkov, *Phys. Rev. Lett.* **86**, 1323 (2001).
- [12] L. F. Chibotaru, A. Ceulemans, G. Teniers, and V. V. Moshchalkov, *Physica (Amsterdam)* **369C**, 149 (2002).
- [13] J. Rammer and H. Smith, *Rev. Mod. Phys.* **58**, 323 (1986).
- [14] W. Belzig, F. K. Wilhelm, C. Bruder, G. Schön, and A. D. Zaikin, *Superlattices Microstruct.* **25**, 1251 (1999).
- [15] M. Y. Kupriyanov and V. F. Lukichev, *Zh. Eksp. Teor. Fiz.* **94**, 139 (1988) [*Sov. Phys. JETP* **67**, 1163 (1988)].
- [16] N. Schopohl, [arXiv:cond-mat/9804064](https://arxiv.org/abs/cond-mat/9804064).
- [17] M. Amundsen and J. Linder, *Sci. Rep.* **6**, 22765 (2016).
- [18] See the Supplemental Material at <http://link.aps.org/supplemental/10.1103/PhysRevLett.120.207001> for a calculation of the giant vortex energies, an analytical solution of the Usadel equation in a current-carrying superconductor, and numerical results for asymmetric geometries. The Supplemental Material includes Refs. [19–22].
- [19] K. Fosshem and A. Sudbø, *Superconductivity: Physics and Applications* (John Wiley & Sons, Chichester, 2004), Sec. 4.7.
- [20] J. P. Morten, Master's thesis, Norwegian University of Science and Technology, Trondheim, Norway, 2003.
- [21] S. H. Jacobsen, J. A. Ouassou, and J. Linder, *Phys. Rev. B* **92**, 024510 (2015).
- [22] W. Hu, K. Sarveswaran, M. Lieberman, and G. H. Bernstein, *J. Vac. Sci. Technol. B* **22**, 1711 (2004).
- [23] S. V. Bakurskiy, N. V. Klenov, I. I. Soloviev, M. Y. Kupriyanov, and A. A. Golubov, *Phys. Rev. B* **88**, 144519 (2013).
- [24] J. Romijn, T. M. Klapwijk, M. J. Renne, and J. E. Mooij, *Phys. Rev. B* **26**, 3648 (1982).
- [25] I. V. Grigorieva, W. Escoffier, V. R. Misko, B. J. Baelus, F. M. Peeters, L. Y. Vinnikov, and S. V. Dubonos, *Phys. Rev. Lett.* **99**, 147003 (2007).
- [26] G. Teniers, L. F. Chibotaru, A. Ceulemans, and V. V. Moshchalkov, *Europhys. Lett.* **63**, 296 (2003).
- [27] P. G. de Gennes, *Superconductivity of Metals and Alloys* (W.A. Benjamin, New York, 1966).
- [28] F. S. Bergeret and J. C. Cuevas, *J. Low Temp. Phys.* **153**, 304 (2008).

Supplemental information

Morten Amundsen,¹ Jabir Ali Ouassou,¹ and Jacob Linder¹

¹*Center for Quantum Spintronics, Department of Physics, Norwegian University of Science and Technology, NO-7491 Trondheim, Norway*

(Dated: February 24, 2018)

In this supplemental, we derive two sets of equations that are applied in the main manuscript. In Section I, we find an exact solution to the linearized Ginzburg-Landau equation near a vortex with an arbitrary winding number n , and show that the kinetic energy is proportional to n^2 . This is used to explain the vortex configurations in the main manuscript. In Section II, we find a selfconsistent solution to the Usadel equation in a bulk superconductor with a uniform charge current. This is used as a boundary condition in the main manuscript.

I. ANALYTICAL SOLUTION AROUND A VORTEX CORE

Let us consider a superconducting vortex with a winding number n . This means that as we move one counter-clockwise turn around the vortex core, the phase of the superconducting condensate changes by $\Delta\varphi = 2\pi n$. We will here calculate the energy of such a vortex, which in the main manuscript is used to understand what nucleation patterns are energetically favored. To keep the calculations simple and intuitive, we approach the problem using the Ginzburg-Landau formalism. Furthermore, we will assume that the energy of a vortex is dominated by the region close to the vortex core, and that this region exhibits a cylindrical symmetry. Since the energy of a vortex ($n > 0$) and antivortex ($n < 0$) are exactly the same, we focus on $n > 0$.

A. Linearized Ginzburg-Landau theory

The starting point of the Ginzburg-Landau framework is the free energy density in a superconducting material,¹

$$E = \alpha|\Psi|^2 + \frac{\beta}{2}|\Psi|^4 + \frac{1}{2m}|(-i\hbar\nabla - 2e\mathbf{A})\Psi|^2 + \frac{\mathbf{B}^2}{2\mu_0}, \quad (1)$$

where Ψ is the superconducting wavefunction, \mathbf{A} is the magnetic potential, $\mathbf{B} = \nabla \times \mathbf{A}$ is the magnetic field, and we choose $E \equiv 0$ in the normal state. Minimizing the free energy of the system, one arrives at the Ginzburg-Landau equation,¹

$$\alpha\Psi + \beta|\Psi|^2\Psi + \frac{1}{2m}(-i\hbar\nabla - 2e\mathbf{A})^2\Psi = 0. \quad (2)$$

We now introduce some approximations. Firstly, as in the main manuscript, we are interested in current-induced vortices in thin-films, for which there is a negligible magnetic potential $\mathbf{A} \approx 0$ in the system. Secondly, we are interested in the behaviour near a vortex core, where the superconducting wavefunction is suppressed $|\Psi| \ll 1$, so that we can linearize the equation. We then obtain an effective Helmholtz equation,

$$\nabla^2\Psi \approx \Psi/\xi_0^2, \quad (3)$$

where $\xi_0 \equiv \sqrt{\hbar^2/2m|\alpha|}$ is the Ginzburg-Landau coherence length. We can parametrize the wavefunction as $\Psi \equiv \psi e^{i\varphi}$, where the amplitude ψ and phase φ are real. Substituting this parametrization into the Helmholtz equation, we obtain

$$\nabla^2\psi + 2i(\nabla\psi)(\nabla\varphi) + i\psi(\nabla^2\varphi) - \psi(\nabla\varphi)^2 = \psi/\xi_0^2. \quad (4)$$

This equation can be significantly simplified using the law of charge conservation. The charge current density in a system governed by the Ginzburg-Landau equation is in general:¹

$$\mathbf{J} = \frac{e}{m}[\Psi^*(-i\hbar\nabla - 2e\mathbf{A})\Psi + \Psi(+i\hbar\nabla - 2e\mathbf{A})\Psi^*]. \quad (5)$$

If we again set $\mathbf{A} \approx 0$ and substitute in $\Psi = \psi e^{i\varphi}$,

$$\mathbf{J} = \frac{2\hbar e}{m}\psi^2\nabla\varphi. \quad (6)$$

From this equation for the charge current, combined with the fact that charge current is conserved $\nabla \cdot \mathbf{J} = 0$, we conclude:

$$2\psi(\nabla\psi)(\nabla\varphi) + \psi^2\nabla^2\varphi = 0. \quad (7)$$

At any point with a finite wavefunction $\psi \neq 0$, this means that two of the terms on the left-hand side of Eq. (4) have to cancel. This lets us write Eq. (4) as simply:

$$\nabla^2\psi - \psi(\nabla\varphi)^2 = \psi/\xi_0^2. \quad (8)$$

B. Exact vortex profile

We now focus on the specific case of a vortex with winding n , meaning that the total phase-difference around the core is $\Delta\varphi = 2\pi n$. At a distance r from the core, this phase-difference occurs over a length $2\pi r$, yielding an average phase-gradient $|\nabla\varphi| = \Delta\varphi/2\pi r = n/r$. Assuming cylindrical symmetry, we expect the amplitude ψ to only depend on the radius r from the vortex core, so that $\nabla^2\psi \rightarrow r^{-1}\partial_r(r\partial_r\psi)$. Together, these observations let us reduce Eq. (8) to an ordinary differential equation for the radial profile $\psi(r)$, which can be written as:

$$r^2\frac{d^2\psi}{dr^2} + r\frac{d\psi}{dr} - \left(n^2 + \frac{r^2}{\xi_0^2}\right)\psi = 0. \quad (9)$$

This is the defining equation for the *modified* or *hyperbolic* Bessel functions $I_n(r/\xi_0)$ and $K_n(r/\xi_0)$. However, whereas the first kind $I_n(r/\xi_0)$ always converges to a finite value as $r \rightarrow 0$, the second kind diverges there, and is therefore an unphysical solution. The radial profile of a vortex is therefore:

$$\psi(r) = \psi_0 I_n(r/\xi_0). \quad (10)$$

C. Asymptotic kinetic energy

In the previous subsection, we found exact solutions of the linearized Ginzburg-Landau equation in the vicinity of a vortex. These are however not straight-forward to use for analytically comparing vortex energies. Physically, we expect the dominant contributions to the kinetic energy to come from the region close to the vortex. This means that we can do a Taylor expansion around the vortex core $r = 0$,

$$I_n(r/\xi_0) = \sum_{m=0}^{\infty} \frac{1}{m!(m+n)!} \left(\frac{r}{2\xi_0} \right)^{2m+n} \quad (11)$$

and focus on the region near the vortex core $r \ll \xi_0$ where the $m = 0$ term becomes the dominant contribution. This gives us the following asymptotic profile for a vortex with winding n :

$$\psi(r) \approx \frac{\psi_0}{n!} \left(\frac{r}{2\xi_0} \right)^n. \quad (12)$$

We can now go back to the free energy, and use these solutions to determine the energy associated with each vortex. Let us consider the kinetic energy density E_k . In the absence of magnetism, this is just the gradient term in Eq. (1):

$$E_k = \frac{\hbar^2}{2m} |\nabla \Psi|^2. \quad (13)$$

We then switch to polar coordinates $\nabla = \partial_r \mathbf{e}_r + r^{-1} \partial_\theta \mathbf{e}_\theta$:

$$E_k = \frac{\hbar^2}{2m} \left(|\partial_r \Psi|^2 + r^{-2} |\partial_\theta \Psi|^2 \right). \quad (14)$$

Substituting in the asymptotic solutions $\Psi \sim r^n e^{in\theta}$:

$$E_k = \frac{\hbar^2 |\Psi|^2}{mr^2} n^2. \quad (15)$$

Thus, the kinetic energy of a giant vortex is proportional to n^2 .

II. SUPERCONDUCTOR WITH A UNIFORM CURRENT

In the main manuscript, we considered a system consisting of a superconducting wire encircling a normal metal. Although the superconductor was assumed to be thick enough to act as a bulk material, the fact that it also carries a supercurrent means that the propagators are no longer given by the standard BCS solution. In order to use as realistic boundary conditions as possible for that setup, we here solve the Usadel equation analytically for a current-carrying superconductor.

A. Background theory

In a superconductor, the Usadel equation can be written²⁻⁴

$$iD\nabla(\hat{g}\nabla\hat{g}) = [\epsilon\hat{\tau}_3 + \hat{\Delta}, \hat{g}], \quad (16)$$

where $\hat{\tau}_3 = \text{diag}(+1, +1, -1, -1)$, and the gap matrix is defined as $\hat{\Delta} = \text{antidiag}(+\Delta, -\Delta, +\Delta^*, -\Delta^*)$. The superconducting gap can in turn be parametrized as $\Delta = |\Delta|e^{i\varphi}$ where $\varphi \in \mathbb{R}$. The matrices on the left-hand side of the commutator are then:

$$\epsilon\hat{\tau}_3 = \epsilon \begin{pmatrix} +\sigma_0 & 0 \\ 0 & -\sigma_0 \end{pmatrix}, \quad \hat{\Delta} = |\Delta| \begin{pmatrix} 0 & e^{+i\varphi} i\sigma_2 \\ e^{-i\varphi} i\sigma_2 & 0 \end{pmatrix}. \quad (17)$$

The propagator \hat{g} can be written using the θ -parametrization:^{4,5}

$$\hat{g} = \begin{pmatrix} +\cosh \theta \sigma_0 & e^{+i\chi} \sinh \theta i\sigma_2 \\ e^{-i\chi} \sinh \theta i\sigma_2 & -\cosh \theta \sigma_0 \end{pmatrix}. \quad (18)$$

The parameters θ and χ satisfy the particle-hole symmetries $\theta^*(+\epsilon) = -\theta(-\epsilon)$ and $\chi^*(+\epsilon) = \chi(-\epsilon)$.⁵ For brevity, we also use the abbreviations $s \equiv \sinh \theta$ and $c \equiv \cosh \theta$. Finally, the self-consistency equation for the gap is:⁸

$$\Delta = N_0 \lambda e^{i\chi} \int_0^{\omega_c} d\epsilon \text{Re}[\sinh \theta] \tanh(\epsilon/2T). \quad (19)$$

Comparing this to the parametrization of the gap $\Delta = |\Delta|e^{i\varphi}$, we immediately note that the phases $\varphi = \chi$ must be equal.

B. Zero current

In the absence of charge currents, we must have a homogeneous solution $\nabla\hat{g} = 0$. Thus, the Usadel equation has to reduce to:

$$[\epsilon\hat{\tau}_3 + \hat{\Delta}, \hat{g}] = 0. \quad (20)$$

Writing the terms in the commutator explicitly, we get:

$$[\epsilon\hat{\tau}_3, \hat{g}] = +2\epsilon \begin{pmatrix} 0 & +s e^{+i\varphi} i\sigma_2 \\ -s e^{-i\varphi} i\sigma_2 & 0 \end{pmatrix}, \quad (21)$$

$$[\hat{\Delta}, \hat{g}] = -2|\Delta| \begin{pmatrix} 0 & +c e^{+i\varphi} i\sigma_2 \\ -c e^{-i\varphi} i\sigma_2 & 0 \end{pmatrix}. \quad (22)$$

From this, we can extract the scalar equation $\epsilon s - |\Delta|c = 0$, which yields the standard BCS solution $\theta = \text{atanh}(|\Delta|/\epsilon)$.

C. Uniform current

Before we attempt to solve the Usadel equation in a current-carrying superconductor with $\partial_z \hat{g} \neq 0$, let us try to constrain the allowed position-dependence of our parameters θ and φ . One such condition can be found from the density of states,

$$N = \frac{1}{2} N_0 \text{Re Tr}[g] = N_0 \text{Re}[\cosh \theta]. \quad (23)$$

For a bulk superconductor carrying a uniform current, we insist that the density of states is uniform as well, i.e. that $\partial_z N = 0$. Using the chain rule, we can rewrite this condition as follows:

$$(\partial_z \theta)(\partial_\theta \text{Re}[\cosh \theta]) = 0. \quad (24)$$

Thus, we may either have $\partial_z \theta = 0$ or $\partial_\theta \text{Re}[\cosh \theta] = 0$. Since θ is a direct function of energy, the latter is equivalent to the

density of states being energy-independent, which we know is false for a superconductor. Thus, we conclude that $\partial_z \theta = 0$.

Now that we know $\partial_z \theta = 0$, differentiating \hat{g} is quite easy:

$$\partial_z \hat{g} = i \partial_z \varphi \begin{pmatrix} 0 & +e^{+i\varphi} s i \sigma_2 \\ -e^{-i\varphi} s i \sigma_2 & 0 \end{pmatrix}. \quad (25)$$

Multiplying by \hat{g} from the left, we then obtain:

$$\hat{g} \partial_z \hat{g} = i \partial_z \varphi \begin{pmatrix} s^2 \sigma_0 & e^{+i\varphi} c s i \sigma_2 \\ e^{-i\varphi} c s i \sigma_2 & -s^2 \sigma_0 \end{pmatrix}. \quad (26)$$

Another constraint can then be found from the spectral current,

$$j_z = \frac{1}{4} j_0 \text{Tr}[\hat{\tau}_3 \hat{g} \partial_z \hat{g}]. \quad (27)$$

Substituting in the expression for $\hat{g} \partial_z \hat{g}$ above, we find that $j_z / j_0 = i s^2 \partial_z \varphi$. But insisting that the divergence $\partial_z j_z = 0$, and keeping in mind that $\partial_z s = 0$ because we determined that $\partial_z \theta = 0$ above, this gives us the constraint $\partial_z^2 \varphi = 0$. One might however argue that perhaps the spectral current does not have to be conserved, since charge conservation only requires that the *integral* of the spectral current above is position-independent. However, for a *uniform current-carrying superconductor*, we can safely insist that the spectral current be constant as well.

Now that we have the additional constraint $\partial_z^2 \varphi = 0$, it is straight-forward to differentiate $\hat{g} \partial_z \hat{g}$:

$$\partial_z (\hat{g} \partial_z \hat{g}) = (i \partial_z \varphi)^2 \begin{pmatrix} 0 & +e^{+i\varphi} c s i \sigma_2 \\ -e^{-i\varphi} c s i \sigma_2 & 0 \end{pmatrix}. \quad (28)$$

This defines the left-hand side of the Usadel equation. Combining the above with the rest of the Usadel equation, we find the following equation from the off-diagonal parts:

$$iD(i\partial_z \varphi)^2 c s = 2\epsilon s - 2|\Delta|c. \quad (29)$$

We will now normalize everything with respect to the zero-current gap Δ_0 , so that $|\Delta| \equiv \delta \Delta_0$ and $\epsilon \equiv E \Delta_0$. Furthermore, we define a phase-winding rate $u^2 \equiv D(\partial_z \varphi)^2 / \Delta_0$. Thus:

$$E s - \delta c + i(u^2/2) c s = 0. \quad (30)$$

Note that since the diffusion constant can be written $D = \Delta_0 \xi^2$, we could also write $u = \xi \partial_z \varphi$, which means that this parameter basically measures the phase-winding per coherence length. By substituting the hyperbolic identity $c = \sqrt{1 + s^2}$ into Eq. (30), the resulting 4th-order algebraic equation in s can easily be solved to provide the analytical solution. However, for practical reasons we here pursue a numerical approach.

D. Non-selfconsistent solution

In order to solve Eq. (30), it is convenient to reparametrize the equation using the following mapping, where $\Theta(E)$ is an unknown function of energy:^{6,7}

$$c = \frac{E}{\sqrt{E^2 - \Theta^2}}, \quad s = \frac{\Theta}{\sqrt{E^2 - \Theta^2}}. \quad (31)$$

Note that this parametrization manifestly satisfies the identity $c^2 - s^2 = 1$. Substituting the above into Eq. (30) and rearranging, we find that the Usadel equation can be rewritten as:

$$\Theta = \frac{\delta}{1 + u^2 / 2 \sqrt{\Theta^2 - E^2}}. \quad (32)$$

In the absence of currents $u = 0$, we get a trivial solution $\Theta = \delta$. For a finite phase-winding rate u , it takes the form of a fixpoint iteration equation, and can be solved using Newton's method.

In addition to the above equation for Θ , we need to determine the superconducting phase φ . However, in the previous subsection, we discovered that $\partial_z^2 \varphi = 0$. This means that the phase φ has to be a linear function of position. Furthermore, since the reference-point for the superconducting phase is arbitrary, we can define $\varphi(0) \equiv 0$. Thus, the phase φ can be expressed as:

$$\varphi(z) = uz / \xi. \quad (33)$$

For small currents, one can safely assume that the gap is nearly the same as for zero current, meaning that $\delta \approx 1$. However, in general, this fixpoint equation has to be accompanied by a selfconsistency equation for the current-dependent gap factor δ .

E. Selfconsistent solution

Let us now revisit the selfconsistency equation for the gap, using the Θ -parametrization from the previous subsection. We normalize the energy $E \equiv \epsilon / \Delta_0$, gap $\delta \equiv |\Delta| / \Delta_0$, Debye cutoff $\Omega_c \equiv \omega_c / \Delta_0$, and temperature $\tau \equiv T / T_c$. Furthermore, the cutoff is in general related to the BCS coupling strength by $\Omega_c = \cosh(1/N_0 \lambda)$, while the gap and critical temperature are related by the BCS ratio $\Delta_0 / T_c = \pi / e^\gamma$, where γ is the Euler-Mascheroni constant.⁸ Combining all of these remarks, Eq. (19) for the current-dependent gap may be written as:

$$\delta = \frac{1}{\text{acosh } \Omega_c} \int_0^{\Omega_c} dE \text{Re} \left(\frac{\Theta}{\sqrt{E^2 - \Theta^2}} \right) \tanh \left(\frac{\pi E}{2e^\gamma \tau} \right). \quad (34)$$

In general, the selfconsistent problem is solved in two steps. First, we guess that the solution is $\Theta(E) = 1$ and $\delta = 1$. For each energy in a discretized range from $E = \Omega_c$ to $E = 0$, one solves Eq. (32) for $\Theta(E)$ using Newton's method. The solutions are substituted into Eq. (34), which is integrated to find a new estimate for δ . This procedure is repeated until convergence.

III. GIANT VORTICES IN ASYMMETRIC GEOMETRIES

Giant vortices are inherently unstable and will seek to split into single vortices unless hindered from doing so. For the systems under consideration, the giant vortices are maintained due to symmetry constraints. It is therefore interesting to investigate how, for instance, Fig. 3(b) in the manuscript reacts to a small deviation from perfect symmetry. We do so by introducing a small perturbation ε of the aspect ratio α by defining $\alpha = 1 + \varepsilon$, thereby making the system rectangular. The results are shown in Fig. 1, from which it is seen that vortices

do indeed split as ε is increased, but this splitting occurs in a continuous way, and the resulting vortex pair remains within close proximity to the location of the original giant vortex for a deviation of up to $\varepsilon = 1\%$. This means that the giant vortex can be stabilized against small deviations in the geometry by placing a pinning potential at this position,⁹ or by forcing the split vortices together by fine tuning the applied currents. To reduce the influence of unintended asymmetry, it is recommended to use a superconductor with as large a coherence length as possible. Choosing for instance aluminium, one gets an estimated diffusive coherence length of $\xi \simeq 100$ nm. For a square geometry with side lengths $L = 12\xi$, a deviation of $\varepsilon = 1\%$ then corresponds to $\Delta L \simeq 12$ nm, which is an experimentally achievable level of accuracy.¹⁰

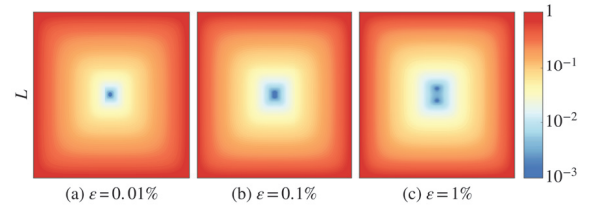


FIG. 1: Vortex patterns for an applied current winding of $\Phi_I = 4\pi$, with increasing aspect ratio deviation ε .

-
- ¹ K. Fosshem and A. Sudbø, *Superconductivity: Physics and Applications* (John Wiley & Sons, Chichester, 2004), Sec. 4.7.
² K. Usadel. *Phys. Rev. Lett.* **25**, 507 (1970).
³ J. Rammer and H. Smith. *Rev. Mod. Phys.* **58**, 323 (1986).
⁴ W. Belzig, F. K. Wilhelm, C. Bruder, G. Schön, and A. D. Zaikin. *Superlattices and Microstructures* **25**, 1251 (1999).
⁵ J.P. Morten, Master thesis, NTNU, 2003.
⁶ S.V. Bakurskiy, N.V. Klenov, I.I. Soloviev, M.Yu. Kupriyanov, and A.A. Golubov. *Phys. Rev. B* **88**, 144519 (2013).
⁷ J. Romijn, T.M. Klapwijk, M.J. Renne, and J.E. Mooij.

Phys. Rev. B **26**, 3648 (1982).

- ⁸ S.H. Jacobsen, J.A. Ouassou, and J. Linder. *Phys. Rev. B* **92**, 024510 (2015).

- ⁹ I. V. Grigorieva, W. Escoffier, V. R. Misko, B. J. Baelus, F. M. Peeters, L. Y. Vinnikov, and S. V. Dubonos. *Phys. Rev. Lett.* **99**, 147003 (2007).

- ¹⁰ W. Hu, K. Sarveswaran, M. Lieberman, and G. H. Bernstein. *J. Vac. Sci. Technol. B* **22**, 1711 (2004).

XIII

Reference

J.A. Ouassou, T.D. Vethaak, J. Linder.
Voltage-induced thin-film superconductivity in high magnetic fields.
Physical review B 98, 144509 (2018).
DOI: 10/GFGR9W

Contributions

JAO came up with the idea, performed all calculations, and wrote the initial draft. TDV contributed to the ideas behind the formalism presented in appendices B and C. JL supervised the entire work process. All authors contributed to the discussion and writing of the manuscript.

Comments


This project was directly inspired by reference 173, where it was shown analytically that the effects of a voltage bias and magnetic field on a superconductor are identical. However, what had not been previously investigated, was what happens when *both* are present. In this paper, we show that their effects partially cancel, resulting in the theoretical prediction of voltage-induced superconductivity in high magnetic fields. This provides a loophole in the Chandrasekhar–Clogston limit from 1962, which previously placed a theoretical upper limit for the magnetic field that can coexist with conventional superconductivity.

This is perhaps the most important paper enclosed in this thesis with regards to potential for further research and applications. It has been featured in the newsletter *Superconductor Week* (October 31, 2018); in a contributed talk at the COST workshop *Coherent superconducting hybrids and related materials* (Les Arcs, France, 2018); in an invited talk at the *QuSpin Workshop* (Trondheim, Norway, 2018); and in an invited talk at the University of Konstanz (Konstanz, Germany, 2018).

Voltage-induced thin-film superconductivity in high magnetic fields

Jabir Ali Ouassou,^{*} Tom Doekle Vethaak, and Jacob Linder

Center for Quantum Spintronics, Department of Physics, Norwegian University of Science and Technology, NO-7491 Trondheim, Norway

 (Received 18 March 2018; revised manuscript received 5 September 2018; published 11 October 2018; corrected 13 November 2018)

We predict that superconductivity in mesoscopic thin films can be stabilized in high magnetic fields if the superconductor is driven out of equilibrium by a DC voltage bias. For realistic material parameters and temperatures, we show that superconductivity is restored in fields many times larger than the Chandrasekhar-Clogston limit. After motivating the effect analytically, we perform rigorous numerical calculations to corroborate these findings and present concrete experimental signatures. On the technical side, we also introduce a formulation of the nonequilibrium kinetic equations that both generalizes and simplifies previous results.

DOI: 10.1103/PhysRevB.98.144509

I. INTRODUCTION

It is well known that magnetism is harmful to conventional superconductivity; the mechanisms responsible are a diamagnetic orbital effect and paramagnetic spin effect. The orbital effect refers to the Lorentz force felt by electrons moving in a magnetic field, which forces the electronic condensate to rotate. That requires kinetic energy and eventually makes condensation unfavorable. This can be neglected in thin films with in-plane fields, since currents perpendicular to the plane are suppressed [1]. The spin effect refers to the magnetic spin splitting of the electronic dispersion relation. Since a conventional Cooper pair consists of two electrons with opposite spins, this results in a momentum mismatch between the electrons in the pair. In clean systems, this may lead to an inhomogeneous superconducting state [2–4]. However, in dirty thin films, impurity and surface scattering prevent such an FFLO state from forming [2], and the spin effect just causes depairing instead. Superconductivity can therefore survive only up to the Chandrasekhar-Clogston limit $m = \Delta_0/\sqrt{2}$ [5,6], where m is the Zeeman splitting of the magnetic field and Δ_0 the zero-temperature gap of a bulk superconductor. In this paper, we show that this fundamental limit can be circumvented using a surprisingly simple trick: voltage biasing the superconductor. The results are directly applicable to the dawning field of superconducting spintronics, where stabilizing superconductivity in proximity to magnetic elements is paramount [7–10].

Figure 1 illustrates relevant experiments. The centerpiece is a thin-film superconductor exposed to an in-plane magnetic field. In theory, it does not matter whether this field is provided by a proximity effect or external source. However, a proximity effect provides a fixed field strength, limiting the parameter space one can explore with a single sample. On the other hand, externally inducing a Zeeman field $m \sim \Delta_0$ requires tens of teslas. Thus, the ideal solution is a combination: A ferromagnet produces a large offset $m = m_0 \sim \Delta_0$, while an external field tunes it to $m = m_0 + \mu_B H_{\text{ext}}$, where μ_B is

the Bohr magneton. Finally, the superconductor is voltage biased via tunneling contacts, providing an additional control parameter.

In Fig. 1(a), the voltage is applied across the superconductor. This both induces a nonequilibrium distribution there and injects a current that can be used as an observable. In Fig. 1(b), transverse wires are used to manipulate the distribution without any charge accumulation or current injection [11–13]. Herein, we focus on Fig. 1(a) and assume $\ell_e < \xi < L < \ell_{\text{in}}$ for an elastic mean free path ℓ_e , diffusive coherence length ξ , system length L , and inelastic scattering length ℓ_{in} .

While both spin-split and voltage-biased superconductors have been investigated for a long time, a number of interesting discoveries have been made in recent years [14–27]. For instance, Bobkova and Bobkov [14] pointed out that there is a regime around the Chandrasekhar-Clogston limit where both a superconducting and normal state are allowed. This *bistability* means that if the field is varied adiabatically, and the metastable states relax slowly, one might observe a superconducting hysteresis effect. Snyman and Nazarov [15]

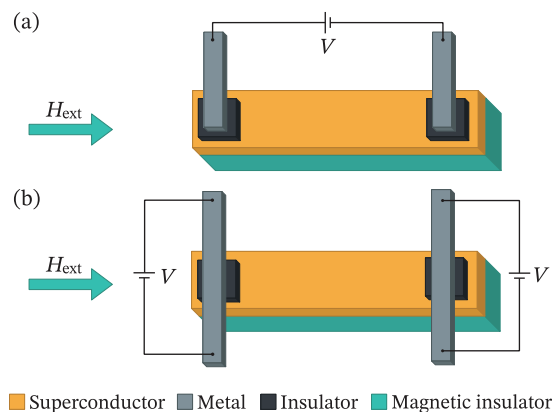


FIG. 1. Suggested experiments. A magnet induces a field $m = m_0$ in the superconductor, while an external field H_{ext} shifts it to $m = m_0 + \mu_B H_{\text{ext}}$. The spin-split superconductor is then subjected to a voltage bias V , which stabilizes the superconducting state.

^{*}Corresponding author: jabir.a.ouassou@ntnu.no

had previously predicted the same kind of bistability in voltage-biased superconductors. Moreover, their results for the gap were similar to previous results for spin-split superconductors as discussed by Moor *et al.* [16], who showed that the gap equations for spin-split and voltage-biased superconductors are equivalent. Given the close analogy between these phenomena, a natural question is: What happens when both are present?

II. ANALYTICAL MOTIVATION

Let us first consider a conventional superconductor in equilibrium, without any fields or voltages. The order parameter then satisfies a self-consistency equation $\Delta = N_0 \lambda F(\Delta)$, where the gap function $F(\Delta)$ is given by [28–30]

$$F(\Delta) = \frac{1}{2} \int_{-\omega_c}^{+\omega_c} d\epsilon \operatorname{Re}[f(\epsilon)] h(\epsilon). \quad (1)$$

Here, N_0 is the density of states (DOS) at the Fermi level, λ the BCS coupling constant, $f(\epsilon) = \Delta/\sqrt{\epsilon^2 - \Delta^2}$ the pair amplitude, $h(\epsilon) = \tanh(\epsilon/2T)$ the distribution function, ϵ the quasiparticle energy, ω_c the Debye cutoff, and T the temperature. We measure energies relative to the zero-temperature gap Δ_0 , temperatures relative to the critical temperature T_c , and set the cutoff $\omega_c = 30\Delta_0$. Finally, in the weak-coupling limit the above are related by $N_0 \lambda \approx 1/\log(2\omega_c/\Delta_0)$ and $\Delta_0 \approx \pi e^{-\gamma} T_c$, where $\gamma \approx 0.57722$ is the Euler-Mascheroni constant [28].

In response to a Zeeman-splitting field m , the quasiparticle energies become spin split according to $\epsilon \rightarrow \epsilon \pm m$, and the pair amplitude in Eq. (1) therefore ends up taking the form $[f(\epsilon + m) + f(\epsilon - m)]/2$. On the other hand, when a voltage V is applied over the superconductor, the electronic distribution functions of the contacts are shifted to $h(\epsilon \pm eV/2)$. By linear combination of the electron and hole distributions, this can be decomposed into a charge mode $[h(\epsilon \pm eV/2) - h(\epsilon \mp eV/2)]/2$ and energy mode $[h(\epsilon \pm eV/2) + h(\epsilon \mp eV/2)]/2$ [13,29,31]. The charge mode, which is related to charge accumulation, relaxes quickly inside the superconductor [17]. The energy mode, on the other hand, remains constant throughout the superconductor and couples to the order parameter in Eq. (1) instead of $h(\epsilon)$. For further discussion of the relevant modes, see Sec. V. In reality, voltage biasing the superconductor also induces a supercurrent, which manifests as a phase winding of the pair amplitude $f(\epsilon)$ and a suppression of the gap. In the tunneling limit, this phase winding is small enough to be neglected in the self-consistency equation. However, when we later in this paper study the system fully numerically, we also take phase-winding and nonequilibrium spin modes into account. Making the above modifications to Eq. (1), we find that for a field m and voltage V the gap function becomes

$$\begin{aligned} F(\Delta, m, eV/2) &= \frac{1}{8} \int_{-\omega_c}^{+\omega_c} d\epsilon \operatorname{Re}[f(\epsilon - m) + f(\epsilon + m)] h(\epsilon + eV/2) \\ &+ \frac{1}{8} \int_{-\omega_c}^{+\omega_c} d\epsilon \operatorname{Re}[f(\epsilon - m) + f(\epsilon + m)] h(\epsilon - eV/2). \end{aligned} \quad (2)$$

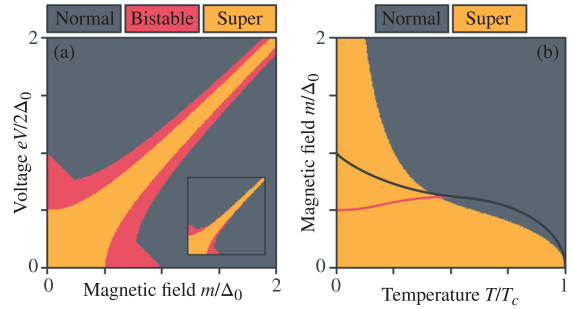


FIG. 2. Analytically calculated phase diagrams for a voltage-biased spin-split superconductor at (a) $T = 0$ and (b) $eV/2 = m$. The inset shows numerical results, which qualitatively match the analytical ones. For comparison, we overlaid phase transition lines for $V = 0$ in (b), where red marks the onset of bistability and black where superconductivity vanishes entirely.

Following the same approach as Moor *et al.* [16], we substitute $\epsilon' \equiv \epsilon \pm eV/2$ into the above to express the voltages as equivalent magnetic fields. Formally, the integration limits have to be shifted accordingly—but since $\omega_c \gg \Delta, m, eV/2$, this is inconsequential. After some reordering, the result becomes

$$F(\Delta, m, eV/2) = F(\Delta, m - eV/2, 0)/2 + F(\Delta, m + eV/2, 0)/2. \quad (3)$$

At this point, we find three properties worth remarking. Firstly, the right-hand side is invariant under $eV/2 \leftrightarrow m$. In other words, the gap responds in precisely the same way to an applied voltage and magnetic field. Moreover, plotted as a function of these two control parameters, the superconducting gap should be symmetric around the diagonals $eV/2 = \pm m$. Secondly, in spin-split superconductors without any voltage, it is known that a superconducting solution $\Delta = \Delta_0$ exists as long as the magnetic field $m < \Delta_0$. Applied to Eq. (3) above, $\Delta = \Delta_0$ should remain a valid solution for $|m| + |eV/2| < \Delta_0$. Part of this regime is bistable and admits a normal-metal solution as well. Finally, we note that the effects of a voltage and magnetic field cancel in the first term but act constructively in the second. This becomes especially clear if we tune the voltage to $eV/2 = m$, where we find the peculiar result:

$$F(\Delta, m, m) = [F(\Delta, 0, 0) + F(\Delta, 2m, 0)]/2. \quad (4)$$

The first term is just the gap function in the absence of fields and voltages, which by itself always results in superconductivity at low temperatures. The second is the gap function for a superconductor with a magnetic field $2m$, which only contributes to superconductivity until $m = \Delta_0/2$. We therefore expect the combination to yield a bulk gap until $m = \Delta_0/2$, but also produce a weaker superconducting solution for much higher fields, since half the gap function is independent of m .

In Fig. 2, we show phase diagrams for the voltage-biased spin-split superconductor, which were calculated using Eq. (2). For more details on how the phases were classified, and in particular how bistability was checked, see Appendix A. Figure 2(a) demonstrates all the qualitative

features motivated above: Superconducting solutions exist for $eV/2 \approx m$ and $|eV/2| + |m| < \Delta_0$, and are symmetric around $eV/2 = m$. For $eV/2 \approx m$, the system is not even bistable but *only* admits superconducting solutions. In other words, no stable normal-state solution exists along $eV/2 \approx m$ at low temperatures, even for fields much larger than the Chandrasekhar-Clogston limit. For high magnetic fields $m > \Delta_0$, the effect is particularly striking: There is no superconductivity in the system *until* a voltage $eV/2 \approx m$ is applied. *In other words, a voltage bias can be used to allow coexistence of superconductivity and a Zeeman-splitting magnetic field that is much larger than both the Chandrasekhar-Clogston limit and the bulk gap.*

Figure 2(b) shows the temperature dependence for $eV/2 = m$. This is clearly a low-temperature effect: The limiting magnetic field seems to diverge as $T \rightarrow 0$, while a comparison with the overlays indicate that the cancellation becomes insignificant after $\sim 0.4T_c$. However, the plot also shows that superconductivity is stabilized in high fields $m > \Delta_0$ at temperatures up to $T \approx 0.25T_c$, which for niobium corresponds to reasonable value ~ 2.3 K. Going down to ~ 1 K, one can even expect superconductivity for $m > 2\Delta_0$.

Note that the stabilization of superconductivity for $eV/2 = m$ is similar to an effect previously reported by Bobkova and Bobkov [26,27]. They found that if one applies a spin-dependent voltage $eV_\uparrow/2 = -eV_\downarrow/2 = m$, which can be achieved using voltage-biased half-metallic contacts, superconductivity is recovered. Our effect is, however, qualitatively different, since it arises for a spin-independent quasi-particle distribution and purely electric voltage bias using normal metal contacts. Related effects were demonstrated in Refs. [32–35], which found that the critical current in Josephson junctions behaved symmetrically with respect to voltages and magnetic fields.

III. NUMERICAL APPROACH

We use the quasiclassical formalism [13,22,29,36,37], where observables are described via an 8×8 propagator in Keldysh \otimes Nambu \otimes spin space,

$$\check{g} = \begin{pmatrix} \hat{g}^R & \hat{g}^A \\ 0 & \hat{g}^K \end{pmatrix}. \quad (5)$$

The components are related by $\hat{g}^K = \hat{g}^R \hat{h} - \hat{h} \hat{g}^A$ and $\hat{g}^A = -\hat{\tau}_3 \hat{g}^{R\dagger} \hat{\tau}_3$, where \hat{h} is the distribution matrix, and $\hat{\tau}_3 = \text{diag}(+1, +1, -1, -1)$ is a Pauli matrix in Nambu space. It is therefore sufficient to determine the retarded propagator \hat{g}^R and distribution matrix \hat{h} . It is commonly stated that \hat{g}^R describes the equilibrium state, while \hat{h} describes the nonequilibrium one. However, this is actually incorrect for a superconductor, since \hat{g}^R implicitly depends on \hat{h} via the self-consistently determined gap Δ . In practice, one therefore has to alternate between solving a diffusion equation for \hat{g}^R , a kinetic equation for \hat{h} , and a self-consistency equation for Δ , until all three converge.

The propagator is governed by the Usadel equation [37],

$$i\xi^2 \nabla(\check{g} \nabla \check{g}) = [\hat{\Delta} + \epsilon \hat{\tau}_3 + m \hat{\sigma}_3, \check{g}]/\Delta_0, \quad (6)$$

where $\hat{\Delta} = \text{antidiag}(+\Delta, -\Delta, +\Delta^*, -\Delta^*)$ is the gap matrix, $\hat{\sigma}_3 = \text{diag}(+1, -1, +1, -1)$ a Pauli matrix in spin space.

The film is voltage biased via tunneling contacts, which we model with Kupriyanov-Lukichev boundary conditions [38] to normal reservoirs with chemical potentials $\mu = \pm eV/2$ relative to the superconductor. The interfaces are characterized by the ratio of tunneling to bulk conductance, which we set to a moderate value $G_T/G_0 = 0.3$. For an 8ξ thick Nb superconductor, this corresponds to an average channel transparency of $\sim 1\%$. Finally, we set the superconductor length $L = 8\xi$; in general, we found a stronger recovery of superconductivity for longer junctions, but at $L = 8\xi$ the gap had nearly saturated. We also performed a number of tests using transparent interfaces and found similar results as long as the superconductor was made sufficiently long; this indicates that the results are not very sensitive to the specific material parameters used. The retarded propagator \hat{g}^R was Riccati parametrized for stability [39] and solved for in the same way as usual [40]. The gap function can be written as an integral of the singlet anomalous component of the Keldysh propagator \hat{g}^K [28]. Physical observables, such as the current and DOS, were calculated from the quasiclassical propagators using standard formulas [9,13,22,29,36].

We modeled inelastic scattering using the Dynes approximation $\epsilon \rightarrow \epsilon + 0.01i\Delta_0$ [41,42]. While this is a very good approximation for the spectral features, it does not produce the expected decay of the energy mode due to inelastic scattering. We note that in the most relevant temperature range for experiments (below ~ 1 K), electron-electron interactions are the dominant contribution to the inelastic scattering length [43], which appears to diverge at lower temperatures [44]. A more rigorous modeling of the electron-electron interaction is beyond the scope of this paper and left for future work.

As for the kinetic equations, we have derived a form which generalizes and simplifies previous results. Our approach is similar to the treatment of nonequilibrium S/N systems in Refs. [13,29] and especially the treatment of S/F systems with spin-flip and spin-orbit scattering in Refs. [19–22]. However, we extend their results to a Usadel equation with a completely general second-order self-energy $\nabla(\check{g} \nabla \check{g}) \sim [\hat{\Sigma}^{(1)} + \hat{\Sigma}^{(2)} \check{g} \hat{\Sigma}^{(2)}, \check{g}]$ and derive accompanying boundary conditions for strongly polarized magnetic interfaces based on Ref. [45]. We do not make any simplifying assumptions, so the results can be used for systems with voltages, spin voltages, temperature gradients, spin-temperature gradients, and any combination of spin projections. The final result is an *explicit linear second-order differential equation* with a simple form,

$$M_{nm} \nabla^2 h_m = -(\nabla M_{nm} + \mathcal{Q}_{nm}) \cdot \nabla h_m - (\nabla \cdot \mathcal{Q}_{nm} + V_{nm} + W_{nm}) h_m, \quad (7)$$

where we sum over repeated indices. The distribution is parametrized as an 8-element vector h , which describes all charge, spin, heat, and spin-heat degrees of freedom. The coefficients M , \mathcal{Q} , V , W are 8×8 matrices that depend on the retarded propagator \hat{g}^R and self-energy factors $\hat{\Sigma}^{(1)}$, $\hat{\Sigma}^{(2)}$ but not the distribution h . In addition to being simple and general, this formulation is very efficient numerically since all coefficients are independent of h ; in fact, it takes less time to solve than the Riccati-parametrized equations for \hat{g}^R . For

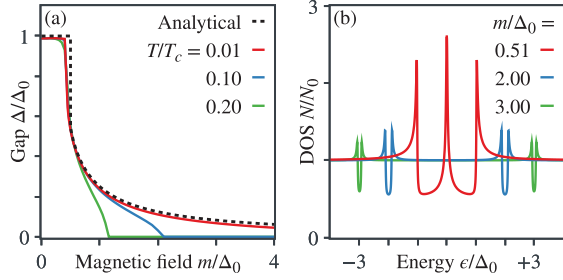


FIG. 3. We set $eV/2 = m$ and investigate how m affects (a) the order parameter and (b) the DOS at $T = 0.01T_c$. The dashed line was calculated analytically using Eq. (2) at $T = 0$, while the colored lines were calculated numerically at $T > 0$.

more details about the kinetic equations, see Appendices B and C.

IV. PHYSICAL OBSERVABLES

Figure 3 highlights some properties of the configuration $eV/2 = m$ that stabilizes superconductivity. Figure 3(a) compares the analytical and numerical approaches: Even though the former neglects both inelastic scattering and spatial variations, we find an impeccable agreement at low temperatures. Beyond the point $m = \Delta_0/2$, the gap suddenly starts to decrease with m . At finite temperatures, we find that superconductivity remains until $m \approx 2\Delta_0$ at $T = 0.1T_c$ and $m \approx \Delta_0$ at $T = 0.2T_c$, in agreement with Fig. 2(b).

Figure 3(b) shows the DOS in the center of the superconductor, which can be observed by scanning tunneling microscopy (STM). These predictions are interesting: At $m \approx \Delta_0/2$, a gigantic zero-energy peak develops throughout the superconductor without destroying the singlet condensate. For $m \gg \Delta_0$, another unusual state develops, manifesting as two half-filled BCS gaps far from the Fermi level $\epsilon = 0$. However, these are not unreasonable results: It is exactly what one would expect from a BCS DOS $N(\epsilon) = N_0 \text{Re}[\epsilon/\sqrt{\epsilon^2 - \Delta^2}]$, if one uses the gaps Δ in Fig. 3(a) and introduces spin splitting $\epsilon \rightarrow \epsilon \pm m$. For $m \approx \Delta_0/2 \approx \Delta(m = \Delta_0/2)$, this results in two BCS shapes that are shifted so that their coherence peaks overlap at $\epsilon = 0$, causing a zero-energy peak to manifest. At higher fields $m \gg \Delta_0$, we instead see two disjoint BCS shapes. The spin-resolved DOS (not shown) confirms that there is actually a full spectral gap in the spin-down DOS at $\epsilon = +m$ and spin-up DOS at $\epsilon = -m$, causing the spin-independent DOS in Fig. 3(b) to exhibit two apparently half-filled spectral gaps.

In Fig. 4, we present another experimental signature. Figure 4(a) shows that for a fixed field $m = \Delta_0$, no superconductivity exists without a voltage bias. At $eV/2 \approx \Delta_0$, superconductivity is suddenly stabilized; taking the superconductor to be, e.g., niobium, the gap is then restored to $\Delta \approx 0.36$ meV at $T \approx 1$ K and $\Delta \approx 0.22$ meV at $T \approx 2$ K. This manifests as a spike in the otherwise ohmic current flowing through the junction, causing an excess current of $\sim 5\%$ at 1 K and $\sim 1\%$

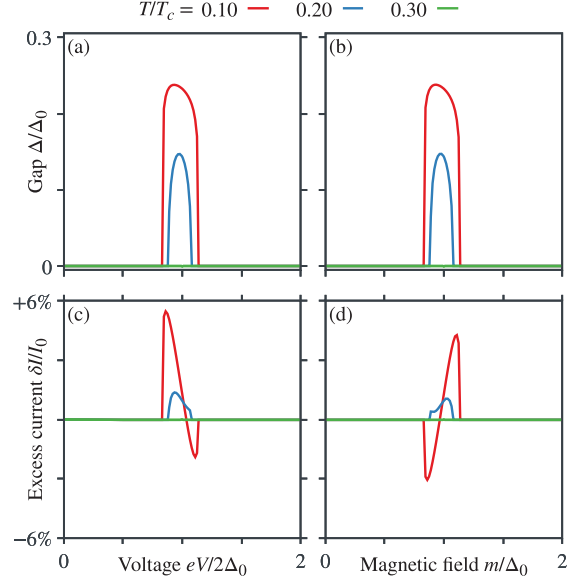


FIG. 4. Numerically calculated gap Δ for (a) fixed field $m = \Delta_0$ and varying voltage, and (b) fixed voltage $eV/2 = \Delta_0$ and varying field. The temperatures T are given in the legends above. Panels (c) and (d) show the corresponding deviations δI from the normal-state current $I = GV$ due to superconductivity, which have been normalized to the current I_0 at $eV/2 = \Delta_0$.

at 2 K. Figure 4(b) demonstrates that the same qualitative behavior is expected for a fixed voltage $eV/2 = \Delta_0$ and varying magnetic field. This shows that there is similarly a regime where an applied magnetic field is required to induce superconductivity. Although Fig. 2 shows that the stable superconducting regime $eV/2 \approx m$ should be padded by a bistable regime, this bistable regime shrinks considerably at finite inelastic scattering and temperature. So while we do find bistability numerically for low temperatures $T = 0.01T_c$, the bistable regime is almost nonexistent for the parameters in Fig. 4.

V. DISTRIBUTION FUNCTION

In this section, we show how the numerically calculated distribution function \hat{h} varies as a function of position x and energy ϵ . Since a full decomposition and exposition of the distribution function takes a lot of space to visualize, we focus on the parameters $m = eV/2 = \Delta_0$ at a low temperature $T = 0.01T_c$. We note that the results for other magnetic fields and voltages are qualitatively similar to the ones shown here, and the results at higher temperatures are basically just thermally smeared.

Following the notation of Appendix B, we parametrize the distribution function in terms of the modes $h_n = \text{Tr}[\hat{\rho}_n \hat{h}]/4$. For a system with a homogeneous magnetic field along the z axis, only four components may be nonzero: the energy mode h_0 , spin-energy mode h_3 , charge mode h_4 , and pure spin mode h_7 . Numerically, these have only been calculated

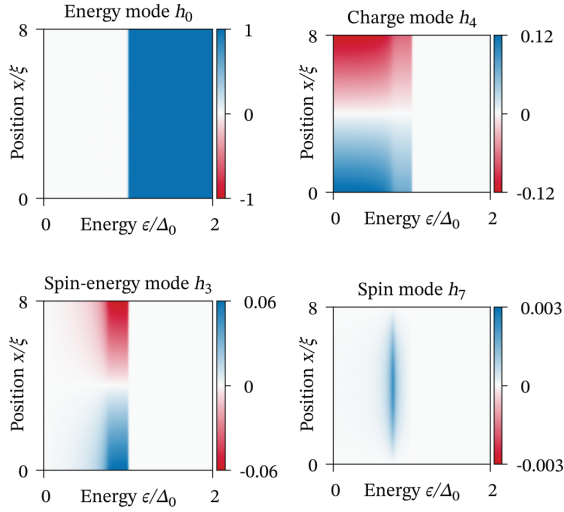


FIG. 5. Nonequilibrium modes h_n of the distribution function \hat{h} as a function of position and energy. Note that the color bars used for the different panels differ by several orders of magnitude.

for positive energies $\epsilon > 0$. However, the energy and spin-energy modes are by definition odd functions of ϵ , while the charge and spin modes are even functions of ϵ ; these energy symmetries can be used to obtain the distribution at $\epsilon < 0$.

The results are shown in Fig. 5. We see that the energy mode h_0 agrees perfectly with the analytically expected result

$$h_0 = \frac{1}{2} \{ \tanh[(\epsilon + eV/2)/2T] + \tanh[(\epsilon - eV/2)/2T] \}, \quad (8)$$

which at low temperatures gives $h_0 = 0$ for $0 < \epsilon < eV/2$ and $h_0 = 1$ for $\epsilon > eV/2$, where $eV/2 = \Delta_0$ here. In general, an energy-mode excitation relaxes over the inelastic scattering length, which we take to be long compared to the system size. However, the Dynes model used for the inelastic scattering herein does not describe the energy-mode decay properly.

The charge mode is an order of magnitude smaller than the energy mode at the interfaces. Since the voltages $\pm V/2$ at the interfaces are opposite, the charge mode is also forced to be an antisymmetric function of position. In total, the charge mode is therefore much smaller than the energy mode even at the interfaces and vanishes completely deeper inside the superconductor. This helps to explain the remarkably accurate agreement between the analytical and numerical calculations and legitimizes the approximation $\hat{h} \approx h_0 \hat{\rho}_0$.

In addition to the energy and charge modes, which were explained in previous sections, we see that there is also a small spin-energy and pure spin mode in the system. However, these are roughly two orders of magnitude smaller than the energy mode, which explains why these are not essential for the analytical understanding presented earlier.

The origin of the spin-energy mode is actually straightforward. As can be read out from Fig. 3(a), the self-consistent order parameter $\Delta \approx \Delta_0/4$ for $m = eV/2 = \Delta_0$. Figure 3(b) and related discussion shows that this causes two gaps in

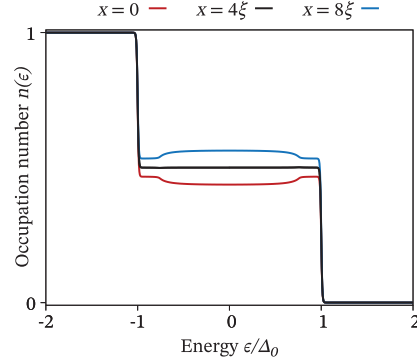


FIG. 6. Occupation number $n(\epsilon)$ at different positions. The distribution has a two-step shape throughout the superconductor, but a local charge accumulation distorts it slightly near the interfaces.

the DOS: a hard gap in the spin-down DOS centered at $\epsilon = +m = +\Delta_0$ and a hard gap in the spin-up DOS centered at $\epsilon = -m = -\Delta_0$. This spin-split superconducting state is then coupled to a reservoir at a voltage $eV/2 = +\Delta_0$ at the left end $x = 0$. There is therefore a region $(3/4)\Delta_0 < \epsilon < \Delta_0$ where spin-up quasiparticles are injected while the spin-down band has a hard gap. At the right end $x = 8\xi$, the material similarly couples to a reservoir at a voltage $-eV/2 = -\Delta_0$. This causes spin-down quasiparticles to be drained from the region $-\Delta_0 < \epsilon < -(3/4)\Delta_0$, while the spin-up band has a hard gap. Thus, one has effectively injected spin-up electrons for $(3/4)\Delta_0 < \epsilon < \Delta_0$ and injected spin-down holes for $-\Delta_0 < \epsilon < -(3/4)\Delta_0$, which is an excitation of the spin-energy mode. Note that this energy region where the charge mode of the voltage-biased reservoirs couple to a spin-energy mode in the superconductor is the same region where the charge mode in the superconductor is slightly weakened.

Finally, in Fig. 6, we show how the spin-independent occupation number $n(\epsilon) = [1 - h_0(\epsilon) - h_4(\epsilon)]/2$ depends on position. This has a two-step Fermi-Dirac-like shape throughout the superconductor but has some variation through the superconductor due to the varying charge mode.

VI. CONCLUSION

We have shown that superconductivity can coexist with a Zeeman-splitting magnetic field far beyond the Chandrasekhar-Clogston limit $m = \Delta_0/\sqrt{2}$ if the superconductor is exposed to a voltage bias $eV/2 = m$. We present concrete setups for observing this effect in Fig. 1 and provide two experimental signatures: the peculiar spin-split DOS in Fig. 3, which can be measured using an STM, and the excess current in Fig. 4, which produces a significant deviation from the otherwise ohmic behavior. If we take the superconductor to be niobium, the signals should be very strong at 1 K, and should be observable at $m = \Delta_0$ for temperatures up to 2 K.

Possibilities for future work include investigating how robust this superconducting state is with respect to spin-flip scattering, spin-orbit scattering, and orbital depairing. It would also be interesting to check if a similar effect exists for unconventional high-temperature superconductors. Finally, our

setup might be used as a circuit element for superconducting spintronic junctions. For instance, the $m \approx \Delta_0/2$ curve in Fig. 3(b) shows a gigantic zero-energy peak inside the superconductor, which is reminiscent of an intrinsic odd-frequency superconductor. An even more peculiar behavior might arise for $m \gg \Delta_0$, when the spectral gaps of the spin bands do not overlap.

ACKNOWLEDGMENTS

We thank A. Golubov, W. Belzig, and M. Aprili for helpful discussions. The numerics was performed on resources provided by UNINETT Sigma2—the national infrastructure for high performance computing and data storage in Norway. This work was supported by the Research Council of Norway through Grant No. 240806 and through its Centres of Excellence funding scheme Grant No. 262633 “*QuSpin*.”

APPENDIX A: PHASE DIAGRAMS

The self-consistency relation for the superconducting gap can be written $\Delta \sim F(\Delta, m, eV/2)$ in the presence of a magnetic field m and voltage bias V , as discussed in the main paper. The simplest way to solve such equations is by fixpoint iteration: For each field m and voltage V , one chooses an initial guess $\Delta = \Delta_1$ and calculates successive values using $\Delta_{n+1} \sim F(\Delta_n, m, eV/2)$. This is repeated until the difference $|\Delta_{n+1} - \Delta_n|$ between iterations drops below some acceptance threshold, at which point the system is said to have converged to a fixed point for the gap. These fixed points that the system converges toward correspond to minima in the free energy; this is not straightforward to verify within the Usadel formalism but can be found by comparison to the Ginzburg-Landau [14] and Bogoliubov-de Gennes [46] formalisms. Alternatively, it can be argued more heuristically that the Usadel equation should be possible to derive by minimizing some free energy—and its self-consistent solution should converge towards these minima.

In many cases, the magnitude of the gap converges towards the same fixed point for any finite initial guess $\Delta \neq 0$. This fixed point is then called a *stable solution*, since the system converges back to the same point after perturbations. Some care must be taken with the normal-state solution $\Delta = 0$: Mathematically, this is *always* a solution to the self-consistency equation. However, below the critical temperature of the superconductor, it actually corresponds to a *local maximum* in the free energy. In this case, one finds that even infinitesimal perturbations of the initial state results in a divergence away from this point, which is why it is called an *unstable solution*. These solutions are not very interesting from a physical point of view and can be discarded.

However, in some systems, the situation is more complicated. In a spin-split superconductor, there is a parameter regime $\Delta_0/2 < m < \Delta_0$ where the gap converges to a superconducting solution $\Delta = \Delta_0$ for large initial guesses but a normal-state solution $\Delta = 0$ for small guesses. Both solutions are *locally stable* in the sense that they are robust to small perturbations and correspond to different *local minima* of the free energy [14]. These two minima are separated by an energy barrier, which manifests as an unstable solution

$\Delta = \Delta_0 \sqrt{2m/\Delta_0 - 1}$ where the free energy of the system is maximized [47]. In a voltage-biased superconductor, the exact same situation occurs for $\Delta_0/2 < eV/2 < \Delta_0$ [15]. Other situations where multiple locally stable solutions can exist include optically pumped systems [48], complex Josephson junctions [49], and supercooled type-I superconductors in a magnetic field [30].

Originally, this *bistability* was resolved by comparing the energies of the two minima, since the system should eventually relax to the global minimum. In the magnetic case, this yields the Chandrasekhar-Clogston limit $m = \Delta_0/\sqrt{2}$ as the exact transition point in the interval $\Delta_0/2 < m < \Delta_0$, where a first-order phase transition takes place [5,6]. However, if the magnetic field is varied adiabatically beyond this point, the superconductor can in principle remain in a local minimum for some time before collapsing to the global minimum. Thus, one might observe a kind of superconducting hysteresis effect in this regime, and a more accurate characterization might be to call it bistable or hysteretic [14,15]. In this paper, we take this view and therefore classify the phase diagram of the junction into *superconducting*, *bistable*, and *normal* regions, where the bistable one might exhibit either a superconducting hysteresis or first-order phase transition depending on the relaxation times of the metastable states. Since it is not straightforward to accurately calculate the free energy itself within the Usadel formalism, we do not calculate the thermodynamic transition lines, but these can be assumed to lie in the bistable regime.

After introducing the terminology, we now demonstrate how the phase diagram itself was calculated. In Figs. 7(a)–7(c), we visualize how the superconducting gap Δ changes depending on the initial guess. Figure 7(a) in particular visualizes the spin-split superconductor discussed above. For $m < \Delta_0/2$, the gap increases for $\Delta < \Delta_0$, decreases for $\Delta > \Delta_0$, and always converges to $\Delta = \Delta_0$. This is a stable superconducting regime. Conversely, for $m > \Delta_0$, the gap decreases to $\Delta = 0$ regardless of our initial guess. This is a stable normal-state solution. But for the intermediate regime $\Delta_0/2 < m < \Delta_0$, there are three distinct solutions for the gap [47]: a superconducting one $\Delta = \Delta_0$, a normal one $\Delta = 0$, and an unstable one in between. This is an example of the bistability discussed above. Figure 7(b) shows the corresponding case for a voltage-biased superconductor, which behaves identically [15,16]. Note that in Fig. 7(c), we also find a brief bistability between two superconducting solutions at $m = eV/2 \approx \Delta_0/2$; such regions were classified as *superconducting* and not *bistable* in this paper.

Figures 7(d)–7(f) display how the superconducting states were classified, using similar colors to Fig. 2. In practice, two different initial guesses $\Delta = 10^{-4}\Delta_0$ and $\Delta = 1.01\Delta_0$ are sufficient to identify both solutions in bistable regimes; this was done for 400×400 values of m and $eV/2$ to construct Fig. 2. We note that our Fig. 7(d) is in agreement with Ref. [47], and Fig. 7(e) is in agreement with Ref. [15], while Fig. 7(f) is a result obtained in this paper.

APPENDIX B: KINETIC EQUATIONS

Here, we derive an *explicit linear ordinary differential equation* for the distribution function \hat{h} . The result is a

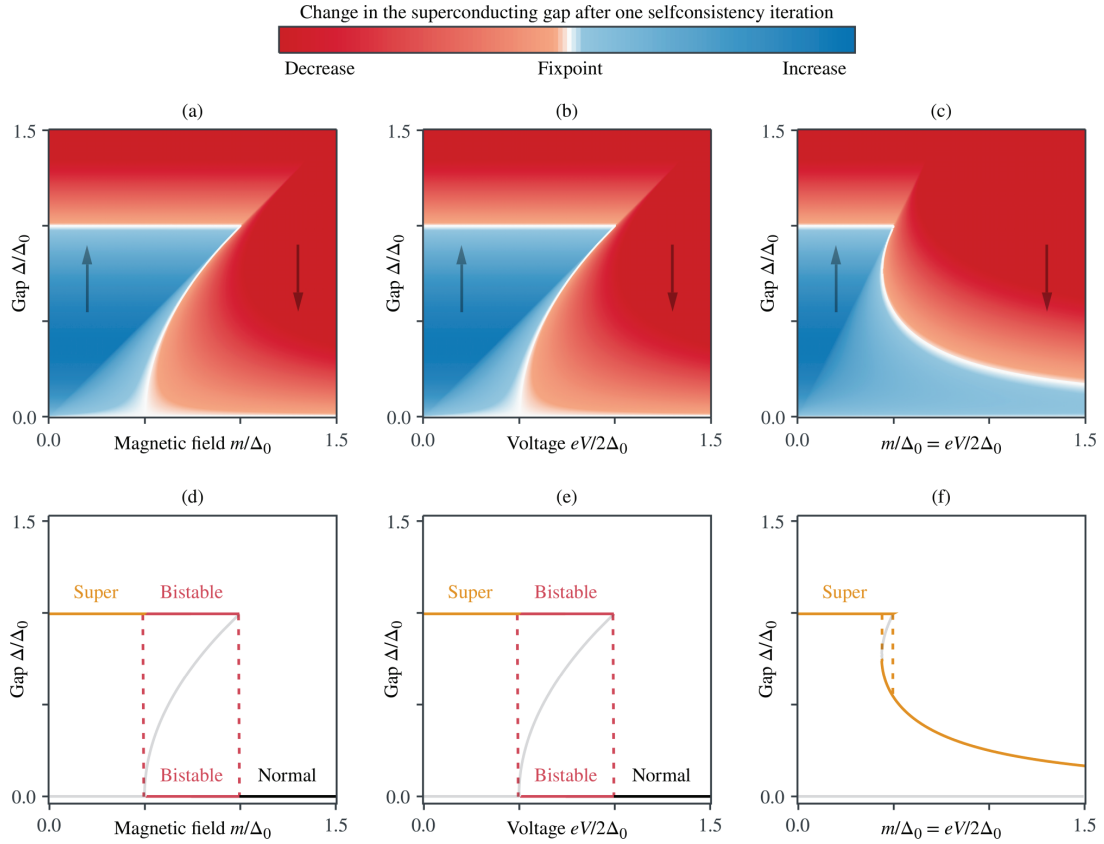


FIG. 7. Flow of the superconducting gap Δ between self-consistency iterations for (a) varying magnetic field m but zero voltage $V = 0$, (b) varying voltage V but zero magnetic field $m = 0$, and (c) matched magnetic field and voltage $m = eV/2$. The gap spontaneously *increases* in blue regions, *decreases* in red regions, and comes to a standstill in white regions. Panels (d) and (f) show the inferred solutions for the gap, classified as superconducting (yellow), bistable (red), normal (black), and unstable (gray), i.e., using a color scheme similar to Fig. 2.

highly computationally efficient form of the kinetic equations, which is also relatively straightforward to implement numerically.

The starting point is the Usadel equation [37,50], which describes diffusive materials in the quasiclassical limit. In terms of the matrix current $\check{\mathbf{I}} \equiv D(\check{g}\nabla\check{g})$ and self-energy $\check{\Sigma}$, the Usadel equation can be written $\nabla \cdot \check{\mathbf{I}} = -i[\check{\Sigma}, \check{g}]$ [51,52]. However, for our purposes, we only require the Keldysh component:

$$\nabla \cdot \check{\mathbf{I}}^K = -i[\check{\Sigma}, \check{g}]^K. \quad (\text{B1})$$

As we will see later, it will prove prudent to introduce a set of basis matrices $\hat{\rho}_n$ that span block-diagonal spin-Nambu space,

$$\hat{\rho}_0 \equiv \hat{\tau}_0\hat{\sigma}_0, \quad \hat{\rho}_1 \equiv \hat{\tau}_0\hat{\sigma}_1, \quad \hat{\rho}_2 \equiv \hat{\tau}_0\hat{\sigma}_2, \quad \hat{\rho}_3 \equiv \hat{\tau}_0\hat{\sigma}_3; \quad (\text{B2})$$

$$\hat{\rho}_4 \equiv \hat{\tau}_3\hat{\sigma}_0, \quad \hat{\rho}_5 \equiv \hat{\tau}_3\hat{\sigma}_1, \quad \hat{\rho}_6 \equiv \hat{\tau}_3\hat{\sigma}_2, \quad \hat{\rho}_7 \equiv \hat{\tau}_3\hat{\sigma}_3. \quad (\text{B3})$$

Here, $\hat{\tau}_0 \equiv \text{diag}(+\sigma_0, +\sigma_0)$ and $\hat{\tau}_3 \equiv \text{diag}(+\sigma_0, -\sigma_0)$ are the diagonal basis matrices in Nambu space, while $\hat{\sigma}_i \equiv \text{diag}(\sigma_i, \sigma_i^*)$ forms a complete basis for the spin structure, where σ_i are the Pauli matrices. This lets us rewrite the distribution matrix \hat{h} as

$$\hat{h} = h_n \hat{\rho}_n, \quad (\text{B4})$$

where we use the summation convention on the right-hand side and define the coefficients h_n as traces with the basis matrices,

$$h_n \equiv \frac{1}{4} \text{Tr}[\hat{\rho}_n \hat{h}]. \quad (\text{B5})$$

The kinetic equations take a simple form when written in terms of h_n instead of \hat{h} , while Eq. (B4) makes it trivial to reconstruct the matrix structure afterwards. When implementing our results numerically, h_n is treated as a real-valued 8-vector, while the kinetic equations will involve 8×8 -matrices operating on it.

1. Decomposition of the current

Combining $\check{\mathbf{I}} = D(\check{g}\nabla\check{g})$ and $\hat{g}^K = \hat{g}^R\hat{h} - \hat{h}\hat{g}^A$, we find that the Keldysh component of the matrix current is

$$\hat{\mathbf{I}}^K = D[(\hat{g}^R\nabla\hat{g}^R)\hat{h} - \hat{h}(\hat{g}^A\nabla\hat{g}^A)] + D[(\nabla\hat{h}) - \hat{g}^R(\nabla\hat{h})\hat{g}^A]. \quad (\text{B6})$$

Substituting in the parametrization $\hat{h} = h_m\hat{\rho}_m$, we see that the coefficients h_m and ∇h_m can be factored out of the brackets,

$$\hat{\mathbf{I}}^K = D[(\hat{g}^R\nabla\hat{g}^R)\hat{\rho}_m - \hat{\rho}_m(\hat{g}^A\nabla\hat{g}^A)]h_m + D[\hat{\rho}_m - \hat{g}^R\hat{\rho}_m\hat{g}^A]\nabla h_m. \quad (\text{B7})$$

If we then multiply the entire equation by $\hat{\rho}_n/4$ from the left and take the trace, the resulting equation can be written

$$\mathbf{I}_n = \mathbf{Q}_{nm}h_m + M_{nm}\nabla h_m, \quad (\text{B8})$$

where we have defined the quantities

$$\mathbf{I}_n \equiv \frac{1}{4}\text{Tr}[\hat{\rho}_n\hat{\mathbf{I}}^K], \quad (\text{B9})$$

$$\mathbf{Q}_{nm} \equiv \frac{D}{4}\text{Tr}[\hat{\rho}_m\hat{\rho}_n(\hat{g}^R\nabla\hat{g}^R) - \hat{\rho}_n\hat{\rho}_m(\hat{g}^A\nabla\hat{g}^A)], \quad (\text{B10})$$

$$M_{nm} \equiv \frac{D}{4}\text{Tr}[\hat{\rho}_n\hat{\rho}_m - \hat{\rho}_n\hat{g}^R\hat{\rho}_m\hat{g}^A]. \quad (\text{B11})$$

This has a straightforward interpretation [13,20,22,29]. The traces of $\hat{\rho}_n\hat{\mathbf{I}}^K$ are proportional to the spectral charge, spin, heat, and spin-heat currents, meaning that \mathbf{I}_n describes the physically observable currents in the system. The right-hand side of Eq. (B8) then relates this to the distribution function h_m and its derivative ∇h_m . The term proportional to h_m can be nonzero even in equilibrium, which means that \mathbf{Q}_{nm} can be identified as the supercurrent contribution. On the other hand, the term proportional to ∇h_m requires an inhomogeneous distribution function, so M_{nm} is a resistive contribution.

If we now go back to the Usadel equation, and multiply that by $\hat{\rho}_n/4$ from the left and take the trace, we find the equation:

$$\nabla \cdot \mathbf{I}_n = -\frac{i}{4}\text{Tr}\{\hat{\rho}_n[\check{\Sigma}, \check{g}]^K\}. \quad (\text{B12})$$

This will later be combined with Eq. (B8) to derive the kinetic equations. First, however, we need to express the right-hand side of the equation in terms of the distribution function h_m .

2. First-order self-energy terms

When describing phenomena such as superconductivity and ferromagnetism, the self-energy matrix $\check{\Sigma} = \hat{\Sigma}$ is diagonal in Keldysh space and independent of the propagator \check{g} . This simplifies the commutator in Eq. (B12):

$$[\check{\Sigma}, \check{g}]^K = [\hat{\Sigma}, \hat{g}^K]. \quad (\text{B13})$$

Substituting in $\hat{g}^K = \hat{g}^R\hat{h} - \hat{h}\hat{g}^A$ and $\hat{h} = h_m\hat{\rho}_m$, we find:

$$[\hat{\Sigma}, \hat{g}]^K = [\hat{\Sigma}, \hat{g}^R\hat{\rho}_m - \hat{\rho}_m\hat{g}^A]h_m. \quad (\text{B14})$$

Going back to Eq. (B12), we therefore find that

$$\nabla \cdot \mathbf{I}_n = -V_{nm}h_m, \quad (\text{B15})$$

where we have defined the quantity

$$V_{nm} \equiv \frac{i}{4}\text{Tr}\{\hat{\rho}_n[\hat{\Sigma}, \hat{g}^R\hat{\rho}_m - \hat{\rho}_m\hat{g}^A]\}. \quad (\text{B16})$$

Finally, we note that using the cyclic property of the trace, the above can be rewritten in the alternative form

$$V_{nm} = \frac{i}{4}\text{Tr}\{[\hat{\rho}_n, \hat{\Sigma}](\hat{g}^R\hat{\rho}_m - \hat{\rho}_m\hat{g}^A)\}. \quad (\text{B17})$$

Since all our basis matrices $\hat{\rho}_n$ commute with both $\hat{\tau}_0$ and $\hat{\tau}_3$, we see that $V_{nm} = 0$ for a normal metal where $\hat{\Sigma} = \epsilon\hat{\tau}_3$. This implies that in the absence of other self-energy terms, all currents \mathbf{I}_n must be conserved in normal metals.

3. Second-order self-energy terms

When describing phenomena such as spin-dependent scattering and orbital depairing [20], each self-energy contribution takes the form $\check{\Sigma} = \check{\Sigma}\check{g}\hat{\Sigma}$. Substituting this into the right-hand side of Eq. (B12), an explicit calculation yields

$$[\check{\Sigma}, \check{g}]^K = \hat{\Sigma}\hat{g}^R\hat{\Sigma}\hat{g}^K + \hat{\Sigma}\hat{g}^K\hat{\Sigma}\hat{g}^A - \hat{g}^R\hat{\Sigma}\hat{g}^K\hat{\Sigma} - \hat{g}^K\hat{\Sigma}\hat{g}^A\hat{\Sigma}. \quad (\text{B18})$$

We recognize the right-hand side as a commutator with $\hat{\Sigma}$,

$$[\check{\Sigma}, \check{g}]^K = [\hat{\Sigma}, \hat{g}^R\hat{\Sigma}\hat{g}^K + \hat{g}^K\hat{\Sigma}\hat{g}^A]. \quad (\text{B19})$$

We then multiply by $\hat{\rho}_n$ from the left and take the trace,

$$\text{Tr}\{\hat{\rho}_n[\check{\Sigma}, \check{g}]^K\} = \text{Tr}\{\hat{\rho}_n[\hat{\Sigma}, \hat{g}^R\hat{\Sigma}\hat{g}^K + \hat{g}^K\hat{\Sigma}\hat{g}^A]\}. \quad (\text{B20})$$

Using the cyclic property of the trace, this can be rewritten as

$$\text{Tr}\{\hat{\rho}_n[\check{\Sigma}, \check{g}]^K\} = \text{Tr}\{[\hat{\rho}_n, \hat{\Sigma}](\hat{g}^R\hat{\Sigma}\hat{g}^K + \hat{g}^K\hat{\Sigma}\hat{g}^A)\}. \quad (\text{B21})$$

Substituting in $\hat{g}^K = \hat{g}^R\hat{h} - \hat{h}\hat{g}^A$, the right side becomes

$$\text{Tr}\{[\hat{\rho}_n, \hat{\Sigma}](\hat{g}^R\hat{\Sigma}\hat{g}^R\hat{h} - \hat{h}\hat{g}^A\hat{\Sigma}\hat{g}^A + \hat{g}^R[\hat{h}, \hat{\Sigma}]\hat{g}^A)\}. \quad (\text{B22})$$

Substituting the parametrization $\hat{h} = h_m\hat{\rho}_m$ into the above, and substituting the result back into Eq. (B12), we find that

$$\nabla \cdot \mathbf{I}_n = -W_{nm}h_m, \quad (\text{B23})$$

where we have defined the quantity

$$W_{nm} \equiv \frac{i}{4}\text{Tr}\{[\hat{\rho}_n, \hat{\Sigma}] \times (\hat{g}^R\hat{\Sigma}\hat{g}^R\hat{\rho}_m - \hat{\rho}_m\hat{g}^A\hat{\Sigma}\hat{g}^A + \hat{g}^R[\hat{\rho}_m, \hat{\Sigma}]\hat{g}^A)\}. \quad (\text{B24})$$

4. Deriving the kinetic equation

In the previous subsections, we have shown that for a system described by a general second-order self-energy matrix $\check{\Sigma}$, which has contributions of the types $\check{\Sigma} = \hat{\Sigma}^{(1)}$ and $\check{\Sigma} = \hat{\Sigma}^{(2)}\check{g}\hat{\Sigma}^{(2)}$, the nonequilibrium distribution function

satisfies the equations

$$\nabla \cdot \mathbf{I}_n = -(V_{nm} + W_{nm})h_m, \quad (\text{B25})$$

$$\mathbf{I}_n = \mathbf{Q}_{nm}h_m + M_{nm}\nabla h_m. \quad (\text{B26})$$

Combining these equations, we find a differential equation for the distribution function components h_m :

$$M_{nm}\nabla^2 h_m = -(\nabla M_{nm} + \mathbf{Q}_{nm}) \cdot \nabla h_m - (\nabla \cdot \mathbf{Q}_{nm} + V_{nm} + W_{nm})h_m. \quad (\text{B27})$$

This is an *explicit linear differential equation* for the distribution h_m . This can be made manifest by first multiplying by the 8×8 matrix M^{-1} from the left and then rewriting the equation in terms of a 16-element state vector $(h, \nabla h)$.

Note that all coefficient matrices depend only on the equilibrium solution and can be precalculated *before* solving the kinetic equation. The coefficients do, however, depend on position, since the equilibrium propagators and self-energy terms may do so. In practice, one might therefore wish to precalculate the Jacobian of the differential equation at the discrete positions where the equilibrium problem was solved and then interpolate between these when solving the kinetic equation. In our experience, linear interpolation may lead to convergence issues, while, e.g., Catmull-Rom cubic splines work very well [53].

APPENDIX C: BOUNDARY CONDITIONS

In order to solve Eq. (B27), we also need boundary conditions. In some cases, a satisfactory approximation can be obtained using transparent boundary conditions for the propagator \check{g} . The corresponding boundary conditions for the distribution are then trivial to obtain: h_n is equal on both sides of the interface.

For more realistic interfaces, the boundary conditions are often written in terms of the matrix current \hat{I} that is flowing *outwards* from the interface. This directionality means that one typically has to flip the sign of the boundary condition at one end of a material, where the current is directed opposite from the coordinate axis. Furthermore, let us assume that this matrix current is a linear function of the distribution \hat{h} ; we will later prove that this is the case for spin-active tunneling or reflecting interfaces. Denoting the distribution on “this” side of the interface as h_m , and on the “other” side as \underline{h}_m , we get

$$\mathbf{I}_n = \underline{C}_{nm}\underline{h}_m - C_{nm}h_m. \quad (\text{C1})$$

Extracting the component I_n flowing out of the interface from Eq. (B8), and denoting the normal derivatives by $\nabla \rightarrow \partial$,

$$M_{nm}\partial h_m + (Q_{nm} + C_{nm})h_m = \underline{C}_{nm}\underline{h}_m. \quad (\text{C2})$$

If one uses a numerical solver that minimizes interface residuals, this is a very suitable form of the equation; but if one requires an explicit form, the derivative ∂h_m is also easy to

isolate. Note that the coefficients only depend on the equilibrium properties of the system and can therefore be precalculated. In the following derivations, we will use the notations

$$C_{nm} \equiv T_{nm} + R_{nm}, \quad (\text{C3})$$

$$\underline{C}_{nm} \equiv \underline{T}_{nm}, \quad (\text{C4})$$

where T and R refer to the boundary condition contributions from tunneling and reflection terms, respectively.

1. Spin-dependent tunneling contributions

We will now derive boundary conditions for magnetic interfaces with spin-dependent tunneling. To leading order in the tunneling probability, and all orders in the polarization, the matrix current at such an interface can be written [40,45,54,55]:

$$2L\hat{I} = Dt[F(\check{g}), \check{g}]. \quad (\text{C5})$$

Here, \check{g} refers to the propagator on “this” side of the interface, $\underline{\check{g}}$ to the “other” side, and the matrix function F is defined as

$$F(\check{g}) = \check{g} + \frac{P}{1 + \sqrt{1 - P^2}}\{\check{g}, \hat{m}\} + \frac{1 - \sqrt{1 - P^2}}{1 + \sqrt{1 - P^2}}\hat{m}\check{g}\hat{m}. \quad (\text{C6})$$

The remaining parameters are the ratio $t \equiv G_T/G_0$ between tunneling conductance and bulk conductance, material length L , interface polarization P , and magnetization matrix $\hat{m} \equiv \mathbf{m} \cdot \hat{\sigma}$, where \mathbf{m} is a unit vector pointing along the average interface magnetization. Note that for unpolarized interfaces, we get $F(\check{g}) = \check{g}$, which simplifies the boundary condition above and the results below. For vacuum interfaces, we can also set $\check{g} = 0$.

We start our derivation by noting that since \hat{m} is diagonal in Keldysh space, the function F has the following property:

$$F(\check{g})^{R,K,A} = F(\hat{g}^{R,K,A}). \quad (\text{C7})$$

Applied to the commutator in Eq. (C5), we then get

$$\hat{I}^K = \frac{Dt}{2L}[F(\hat{g}^R)\hat{g}^K + F(\hat{g}^K)\hat{g}^A - \hat{g}^R F(\hat{g}^K) - \hat{g}^K F(\hat{g}^A)]. \quad (\text{C8})$$

Substituting in $\hat{g}^K = \hat{g}^R \hat{h} - \hat{h} \hat{g}^A$, and grouping similar terms,

$$\begin{aligned} \hat{I}^K = & \frac{Dt}{2L}[F(\hat{g}^R)(\hat{g}^R \hat{h} - \hat{h} \hat{g}^A) - (\hat{g}^R \hat{h} - \hat{h} \hat{g}^A)F(\hat{g}^A)] \\ & + \frac{Dt}{2L}[F(\hat{g}^R \hat{h} - \hat{h} \hat{g}^A)\hat{g}^A - \hat{g}^R F(\hat{g}^R \hat{h} - \hat{h} \hat{g}^A)]. \end{aligned} \quad (\text{C9})$$

We then substitute in $\hat{h} = h_m \hat{\rho}_m$ and $\underline{\hat{h}} = \underline{h}_m \hat{\rho}_m$, multiply by $\hat{\rho}_n/4$ from the left, and take the trace. This results in a linear

boundary condition $I_n = \underline{T}_{nm} \underline{h}_m - T_{nm} h_m$, where we identify

$$T_{nm} \equiv \frac{Dt}{8L} \text{Tr}\{\hat{\rho}_n[(\hat{g}^R \hat{\rho}_m - \hat{\rho}_m \hat{g}^A)F(\hat{g}^A) - F(\hat{g}^R)(\hat{g}^R \hat{\rho}_m - \hat{\rho}_m \hat{g}^A)]\}, \quad (\text{C10})$$

$$\underline{T}_{nm} \equiv \frac{Dt}{8L} \text{Tr}\{\hat{\rho}_n[F(\hat{g}^R \hat{\rho}_m - \hat{\rho}_m \hat{g}^A)\hat{g}^A - \hat{g}^R F(\hat{g}^R \hat{\rho}_m - \hat{\rho}_m \hat{g}^A)]\}. \quad (\text{C11})$$

Finally, using the cyclic trace rule, these results simplify to:

$$T_{nm} = \frac{Dt}{8L} \text{Tr}\{[F(\hat{g}^A)\hat{\rho}_n - \hat{\rho}_n F(\hat{g}^R)](\hat{g}^R \hat{\rho}_m - \hat{\rho}_m \hat{g}^A)\}, \quad (\text{C12})$$

$$\underline{T}_{nm} = \frac{Dt}{8L} \text{Tr}\{(\hat{g}^A \hat{\rho}_n - \hat{\rho}_n \hat{g}^R)[F(\hat{g}^R \hat{\rho}_m - \hat{\rho}_m \hat{g}^A)]\}. \quad (\text{C13})$$

2. Spin-dependent reflection contributions

We will now derive the boundary coefficients for a spin-mixing interface. These boundary conditions can either be used alone, in the case of completely opaque interfaces to ferromagnetic insulators, or together with the tunneling boundary conditions from the previous subsection. The spin-mixing contribution to the matrix current is [40,45,55–57]:

$$2L\check{I} = -iDr[\hat{m}', \check{g}], \quad (\text{C14})$$

where $r \equiv G_\varphi/G_0$ is the ratio between the spin-mixing and bulk conductances, and $\hat{m}' \equiv \mathbf{m}' \cdot \hat{\sigma}$ is the interface magnetization matrix. In the case of inhomogeneous magnetic interfaces, \mathbf{m}' may be different from \mathbf{m} , due to reflected and transmitted quasiparticles experiencing different average magnetizations.

Extracting the Keldysh component of the boundary condition, and substituting in $\hat{g}^K = \hat{g}^R \hat{h} - \hat{h} \hat{g}^A$ on the right side,

$$\hat{I}^K = -\frac{iDr}{2L}[\hat{m}', \hat{g}^R \hat{h} - \hat{h} \hat{g}^A]. \quad (\text{C15})$$

Substituting in $\hat{h} = h_m \hat{\rho}_m$, multiplying by $\hat{\rho}_n/4$ from the left, and taking the trace, we find the current components

$$I_n = -\frac{iDr}{8L} \text{Tr}\{\hat{\rho}_n[\hat{m}', \hat{g}^R \hat{\rho}_m - \hat{\rho}_m \hat{g}^A]\}h_m. \quad (\text{C16})$$

Rewriting the commutator with the cyclic trace rule, and identifying the trace as a boundary coefficient, we conclude that this follows the pattern $I_n = -R_{nm}h_m$, where

$$R_{nm} \equiv -\frac{iDr}{8L} \text{Tr}\{[\hat{m}', \hat{\rho}_n](\hat{g}^R \hat{\rho}_m - \hat{\rho}_m \hat{g}^A)\}. \quad (\text{C17})$$

3. Nonequilibrium reservoirs

The boundary conditions above require knowledge of the distributions \underline{h} in any reservoirs that couple to the system. By a *reservoir*, we mean a bulk material with a homogeneous quasiparticle distribution, which may be either in or out of equilibrium. In equilibrium, the electron density $n_e = \langle \Psi^\dagger \Psi \rangle$ should be described by Fermi-Dirac statistics $f(\epsilon) = 1/[1 + \exp(\epsilon/T)]$, and the holes $n_h = \langle \Psi \Psi^\dagger \rangle$ by the remaining probability $1 - f(\epsilon)$, where the quasiparticle energy ϵ is measured relative to the Fermi level. This can be used to derive that the distribution is simply given by $\hat{h} = [1 - 2f(\epsilon)]\hat{\rho}_0$ in equilibrium, which reproduces the conventional expression $\hat{h} = \tanh(\epsilon/2T)\hat{\rho}_0$ [29,58].

Upon applying a voltage V , the chemical potential of the reservoir is shifted by eV . This increases the electron density but decreases the hole density and thus shifts the electron and hole blocks of the distribution above in opposite directions [29,59]:

$$\hat{h} = \begin{pmatrix} \tanh[(\epsilon + eV)/2T]\sigma_0 & 0 \\ 0 & \tanh[(\epsilon - eV)/2T]\sigma_0 \end{pmatrix}. \quad (\text{C18})$$

Substituted into Eq. (B5), one finds an energy mode h_0 and charge mode h_4 , while the spin-energy modes h_1, h_2, h_3 and spin modes h_5, h_6, h_7 remain zero.

In a more general spin-dependent reservoir, the distribution matrix \hat{h} should contain components proportional to $\sigma_1, \sigma_2, \sigma_3$ as well. One way to describe such a spin dependence is that spin-up and spin-down particles experience different voltages V_\uparrow and V_\downarrow and possibly different temperatures T_\uparrow and T_\downarrow [22,60]. Physically, the most extreme realization of this situation is given by half-metallic reservoirs, which only have one metallic spin band that can couple to regular conductors [26,40]. If we for simplicity take the spin-quantization axis to be the z axis, introducing spin-dependent voltages and temperatures yields

$$\hat{h} = \begin{pmatrix} \tanh[(\epsilon + eV_\uparrow)/2T_\uparrow] & 0 & 0 & 0 \\ 0 & \tanh[(\epsilon + eV_\downarrow)/2T_\downarrow] & 0 & 0 \\ 0 & 0 & \tanh[(\epsilon - eV_\uparrow)/2T_\uparrow] & 0 \\ 0 & 0 & 0 & \tanh[(\epsilon - eV_\downarrow)/2T_\downarrow] \end{pmatrix}.$$

This can also be parametrized in terms of an average voltage $V \equiv (V_\uparrow + V_\downarrow)/2$ and spin-voltage $V_s \equiv (V_\uparrow - V_\downarrow)/2$; in nonmagnetic materials, a gradient in the former gives rise to a pure electric current and in the latter a pure spin current. Similarly, one can define an average temperature $T \equiv (T_\uparrow + T_\downarrow)/2$ and spin-temperature $T_s \equiv (T_\uparrow - T_\downarrow)/2$, whose gradients cause energy and spin-

energy currents. Finally, the physics of the system should not depend on our arbitrary choice of coordinate axes, so a corresponding expression for a general spin quantization axis $\mathbf{u} = (u_1, u_2, u_3)$ can be obtained using spin rotation matrices.

Introducing spin voltages and spin temperatures as discussed above, performing a spin rotation to an arbitrary spin

axis u , and again applying Eq. (B5), we find the general result:

$$\begin{aligned}
h_0 &= [h_{++} + h_{+-} + h_{-+} + h_{--}], \\
h_1 &= [h_{++} - h_{+-} + h_{-+} - h_{--}]u_1, \\
h_2 &= [h_{++} - h_{+-} + h_{-+} - h_{--}]u_2, \\
h_3 &= [h_{++} - h_{+-} + h_{-+} - h_{--}]u_3, \\
h_4 &= [h_{++} + h_{+-} - h_{-+} - h_{--}], \\
h_5 &= [h_{++} - h_{+-} - h_{-+} + h_{--}]u_1, \\
h_6 &= [h_{++} - h_{+-} - h_{-+} + h_{--}]u_2, \\
h_7 &= [h_{++} - h_{+-} - h_{-+} + h_{--}]u_3.
\end{aligned} \tag{C19}$$

For brevity, the above is written in terms of the distributions

$$h_{cs} = \tanh[(\epsilon + cV + csV_s)/(T + sT_s)]/4, \tag{C20}$$

which describe quasiparticles with a charge index c and spin index s . For instance, h_{+-} corresponds to $c = +1$ (electrons) and $s = -1$ (spin-down), and so on. This describes a quite general reservoir that can have a voltage, spin voltage, temperature, and spin temperature, with an arbitrary spin-quantization axis. The main possibility not accounted for is that the spin splitting of the voltage and temperature could in principle be in different directions. Also, it might be possible to excite some even more exotic distributions via, e.g., optical methods, which might be unnatural to describe in terms of voltages and temperatures.

APPENDIX D: CONVERSION TO SUPERCURRENTS

For the numerical calculations presented in the main paper, the interfaces between the superconductor and voltage-biased reservoirs were assumed to be relatively opaque. However, we also performed numerical tests for other parameter sets, including voltage-biased N/S/N junctions with completely transparent interfaces. These showed that superconductivity remained stable in high magnetic fields m for a voltage bias $eV/2 = m$, provided that the superconductor is sufficiently long compared with the coherence length ξ . The fact that a voltage drop can exist across a “superconductor” even in the absence of interface resistance may seem a bit surprising. The answer has previously been derived in, e.g., Refs. [13, 17]. When a resistive current is injected into a superconductor via ideal interfaces, there is actually a layer of thickness $\sim \xi$ where the resistive current is converted into a supercurrent. In other words, there is still a “superconducting contact resistance” in the transparent limit, and the associated voltage drop occurs near the interfaces. For more details, see the numerical results in Ref. [17].

In a superconductor with a spin splitting that exceeds the order parameter, an even more peculiar situation arises. Since the DOS is no longer gapped at the Fermi level, and resistive currents are only converted into supercurrents in the gapped regions of the energy spectrum, a long-ranged resistive current can exist in the superconductor in this limit. On the following pages, we derive an approximate analytical result for the length scale over which resistive currents decay inside strongly spin-split superconductors to explain this observation. The derivation itself makes a number of approximations, some more reasonable than others, but the final analytical

equation is simple and agrees quite well with our numerical observations.

We should stress that even though the superconductor can harbor a long-ranged resistive current in this exotic state, the name “superconductor” is still fitting. The most fundamental way to justify it is that the material still exhibits a singlet order parameter Δ and a spontaneously broken $U(1)$ symmetry, which are the hallmarks of a superconducting state. Another perspective is that the material also supports dissipationless currents when the order parameter has a phase winding. This would perhaps be even clearer if we used the experimental setup sketched in Fig. 1(b). There, no resistive current is injected into the superconductor, and yet the same stabilization effect at $m = eV/2$ occurs. If a supercurrent is then generated using, e.g., a weak out-of-plane magnetic field, where the flux couples directly to the phase, we would generate a pure supercurrent in the system. The conclusion is that the abilities of a material to host resistive or dissipationless currents over long distances are not always mutually exclusive.

The starting point for our analytical derivation is Eq. (B27). Let us assume that the system under consideration is roughly homogeneous, so that $\nabla g^R \approx \nabla g^A \approx 0$, in which case $Q \approx 0$ and $\nabla M \approx 0$. Furthermore, let us assume that no spin-flip scattering, spin-orbit scattering, or orbital depairing effects are important in the system, so that the term $W = 0$ as well. The kinetic equation then reduces to the much simpler form

$$M_{nm} \nabla^2 h_m = -V_{nm} h_m. \tag{D1}$$

In the most general case, M and V are 8×8 matrices while h is an 8-vector. If one considers a system where only one spin axis is relevant, such as a bulk superconductor with a spin splitting along the z axis, this can be reduced to a system of 4×4 matrices in the equation for a 4-vector h . This gives us a system of coupled equations for the charge, energy, spin, and spin-energy modes of the nonequilibrium distribution function, which can in principle be solved explicitly.

We will now assume that the dominant relaxation process of the charge mode inside a superconductor occurs via the diagonal terms. The charge mode is given by h_4 in our notation, so neglecting the coupling to other modes, we then get

$$\nabla^2 h_4 \approx -(V_{44}/M_{44})h_4. \tag{D2}$$

Comparing this to the equation $\nabla^2 h_4 = h_4/\lambda^2$ that would define an exponential decay, we can describe such a decay via an energy-dependent *charge relaxation length* $\lambda \equiv \sqrt{-M_{44}/V_{44}}$.

The source term V_{44} can be calculated using Eq. (B17),

$$V_{nm} = \frac{i}{4} \text{Tr}\{[\hat{\rho}_n, \hat{\Sigma}](\hat{g}^R \hat{\rho}_m - \hat{\rho}_m \hat{g}^A)\}. \tag{D3}$$

We are interested in the case $n = m = 4$, and since the basis matrix $\hat{\rho}_4 = \hat{\tau}_3 \sigma_0$, the commutator $[\hat{\rho}_4, \hat{\Sigma}]$ vanishes for the self-energy terms corresponding to a regular magnet $\hat{\Sigma} = \epsilon \hat{\tau}_3 + m \hat{\sigma}_3$. The charge mode is therefore controlled by the superconducting contributions $\hat{\Sigma} = \hat{\Delta} = \text{antidiag}(+\Delta, -\Delta, +\Delta^*, -\Delta^*)$. If we choose a real gauge, which is possible since we already assumed that any supercurrents are negligible $Q \approx 0$, this reduces to

$\hat{\Sigma} = \Delta i \hat{\tau}_1 \sigma_2$. Substituted into the equation above, we find that

$$V_{44} = -\frac{\Delta}{4} \text{Tr}\{[\hat{\tau}_3, \hat{\tau}_1 \sigma_2](\hat{g}^R \hat{\tau}_3 - \hat{\tau}_3 \hat{g}^A)\}. \quad (\text{D4})$$

Using $[\hat{\tau}_3, \hat{\tau}_1] = 2i \hat{\tau}_2$ and $\hat{g}^A = -\hat{\tau}_3 \hat{g}^{R\dagger} \hat{\tau}_3$, this becomes

$$V_{44} = -\frac{i\Delta}{2} \text{Tr}\{\hat{\tau}_2 \sigma_2 (\hat{g}^R \hat{\tau}_3 + \hat{g}^{R\dagger} \hat{\tau}_3)\}. \quad (\text{D5})$$

We then use the cyclic rule to move the $\hat{\tau}_3$ matrices to the other end of the trace, and use the Pauli identity $\hat{\tau}_3 \hat{\tau}_2 = -i \hat{\tau}_1$, and finally apply $\text{Tr}[A + A^\dagger] = 2 \text{Re Tr}[A]$ to simplify the result:

$$V_{44} = -\Delta \text{Re Tr}\{\hat{\tau}_1 \sigma_2 \hat{g}^R\}. \quad (\text{D6})$$

This is essentially the same result as was used in Ref. [13] to show that resistive currents decay over a length $\sim \xi$ inside a superconductor, except that we will attempt to use it for the more general case of a spin-split superconductor.

In general, we can write the retarded propagator as

$$\hat{g}^R = \begin{pmatrix} +g & +f \\ -\tilde{f} & -\tilde{g} \end{pmatrix}. \quad (\text{D7})$$

Multiplying this by $\hat{\tau}_1 \sigma_2$ and taking the trace, we find that

$$\text{Tr}\{\hat{\tau}_1 \sigma_2 \hat{g}^R\} = \text{Tr}\{\sigma_2 (f - \tilde{f})\}. \quad (\text{D8})$$

Firstly, we can split the anomalous propagators into singlets and triplets using the decomposition $f = (f_s + \mathbf{f}_t \cdot \boldsymbol{\sigma}) i \sigma_2$.

Secondly, when the superconducting gap Δ is purely real, the singlet component satisfies $\tilde{f}_s = -f_s$. This leads us to the conclusion that the only contribution to the trace of $\sigma_2 (f - \tilde{f})$ comes from the singlet part $\sigma_2 (f_s + f_s) i \sigma_2 = 2i f_s \sigma_0$:

$$\text{Tr}\{\sigma_2 (f - \tilde{f})\} = 4i f_s. \quad (\text{D9})$$

Thus, the final form of the source term V_{44} derived above is

$$V_{44} = 4\Delta \text{Im}(f_s), \quad (\text{D10})$$

where as usual the singlet component $f_s \equiv (f_{\uparrow\downarrow} - f_{\downarrow\uparrow})/2$.

We now turn to the matrix M , which can be interpreted as an energy-dependent renormalized diffusion coefficient [29]. In previous sections, this quantity was defined as

$$M_{nm} = \frac{D}{4} \text{Tr}\{\hat{\rho}_n \hat{\rho}_m - \hat{\rho}_n \hat{g}^R \hat{\rho}_m \hat{g}^A\}. \quad (\text{D11})$$

We again set $n = m = 4$, and use $\hat{\rho}_4 = \hat{\tau}_3 \sigma_0$, $\hat{g}^A = -\hat{\tau}_3 \hat{g}^{R\dagger} \hat{\tau}_3$,

$$M_{44} = \frac{D}{4} \text{Tr}\{\hat{\tau}_3 \hat{\tau}_3 + \hat{\tau}_3 \hat{g}^R \hat{g}^{R\dagger} \hat{\tau}_3\}. \quad (\text{D12})$$

Applying the cyclic trace rule, and the identity $\hat{\tau}_3^2 = 1$, we get

$$M_{44} = \frac{D}{4} \text{Tr}\{1 + \hat{g}^R \hat{g}^{R\dagger}\}. \quad (\text{D13})$$

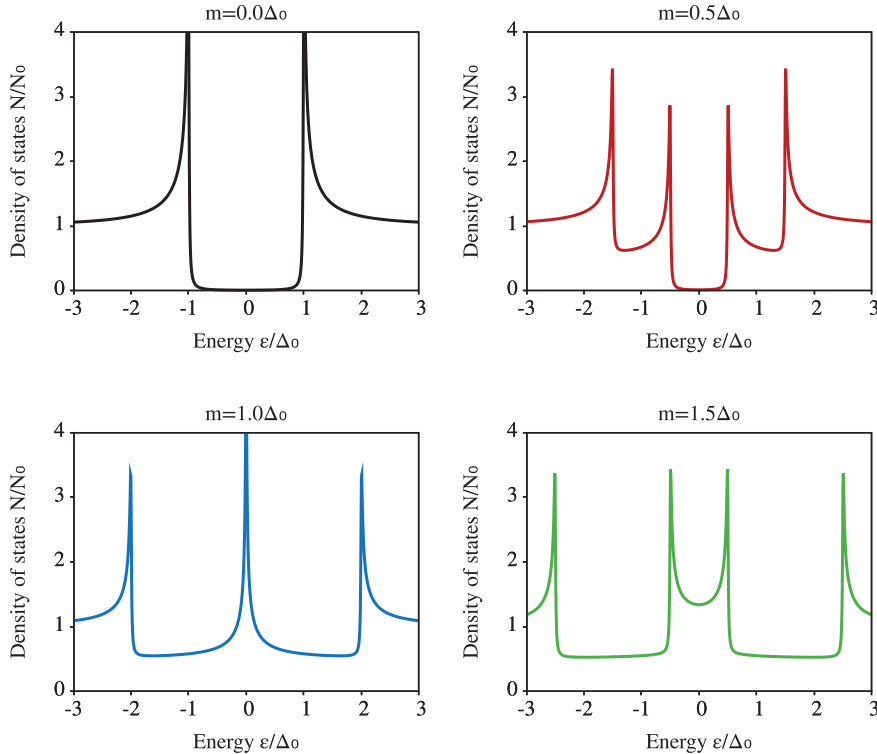


FIG. 8. DOS for a Zeeman-split superconductor with a magnetic field m . For simplicity, this was calculated using a non-self-consistent analytical solution for a bulk superconductor with an exchange field, using an inelastic scattering parameter $\epsilon \rightarrow \epsilon + 0.01i \Delta_0$.

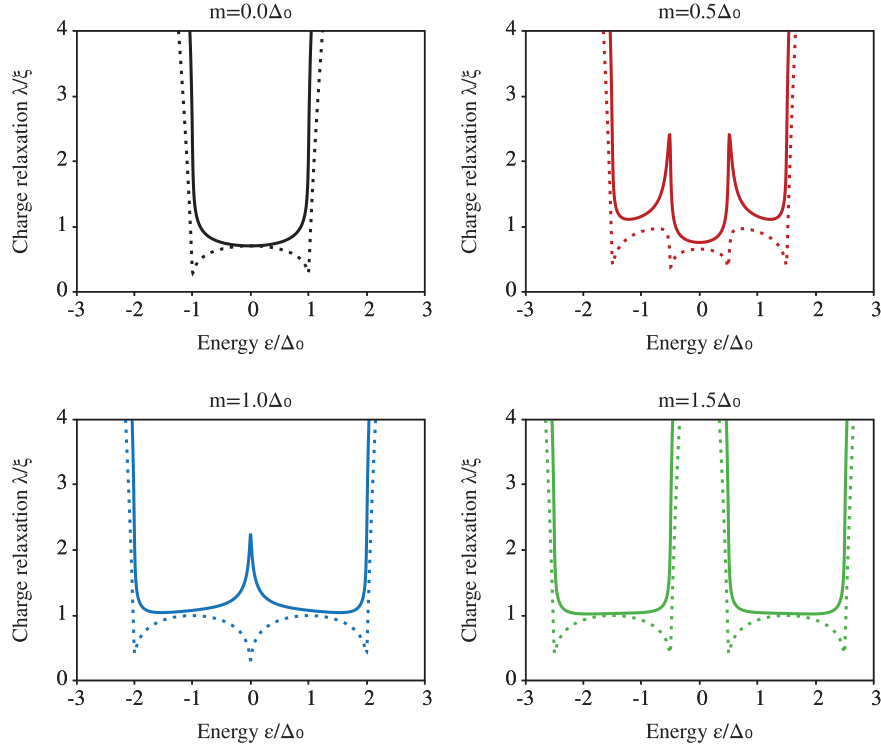


FIG. 9. Charge relaxation length for a Zeeman-split superconductor with a magnetic field m . The solid lines show the exact results from Eq. (D20), which we see align very well with how the DOS looks in Fig. 8. The dotted lines show the approximation in Eq. (D21), which manages to predict where the charge relaxation length is finite and infinite but does not replicate its precise shape.

One way to parametrize the retarded propagator \hat{g}^R is [9]

$$\hat{g}^R = \begin{pmatrix} (g_s + \mathbf{g}_t \cdot \boldsymbol{\sigma}) & (f_s + \mathbf{f}_t \cdot \boldsymbol{\sigma})i\sigma_2 \\ -i\sigma_2(\tilde{f}_s - \tilde{\mathbf{f}}_t \cdot \boldsymbol{\sigma}) & -\sigma_2(\tilde{g}_s - \tilde{\mathbf{g}}_t \cdot \boldsymbol{\sigma})\sigma_2 \end{pmatrix}. \quad (\text{D14})$$

Explicitly taking the complex transpose of this matrix, and using that σ_n are Hermitian while i is anti-Hermitian, we find

$$\hat{g}^{R\dagger} = \begin{pmatrix} (g_s^* + \mathbf{g}_t^* \cdot \boldsymbol{\sigma}) & (\tilde{f}_s^* - \tilde{\mathbf{f}}_t^* \cdot \boldsymbol{\sigma})i\sigma_2 \\ -i\sigma_2(f_s^* + \mathbf{f}_t^* \cdot \boldsymbol{\sigma}) & -\sigma_2(\tilde{g}_s^* - \tilde{\mathbf{g}}_t^* \cdot \boldsymbol{\sigma})\sigma_2 \end{pmatrix}. \quad (\text{D15})$$

We now calculate the product $\hat{g}^R \hat{g}^{R\dagger}$, keeping only diagonal terms proportional to an even power of Pauli matrices, since terms proportional to $\boldsymbol{\sigma}$ disappear when we later take the trace:

$$\hat{g}^R \hat{g}^{R\dagger} = \begin{pmatrix} |g_s|^2 + |\mathbf{g}_t|^2 + |f_s|^2 + |\mathbf{f}_t|^2 & \dots \\ \dots & |\tilde{f}_s|^2 + |\tilde{\mathbf{f}}_t|^2 + |\tilde{g}_s|^2 + |\tilde{\mathbf{g}}_t|^2 \end{pmatrix}. \quad (\text{D16})$$

Due to the electron-hole symmetry of quasiclassical theory, it is reasonable to expect all *magnitudes* $|g_s|^2$, $|\mathbf{g}_t|^2$, $|f_s|^2$, $|\mathbf{f}_t|^2$ to be invariant under tilde conjugation, even though the signs of the quantities themselves might change. Using this, we find

$$\text{Tr}\{1 + \hat{g}^R \hat{g}^{R\dagger}\} = 4 + 4|g_s|^2 + 4|\mathbf{g}_t|^2 + 4|f_s|^2 + 4|\mathbf{f}_t|^2. \quad (\text{D17})$$

Going back to our result for M_{44} , we find the final result:

$$M_{44} = D(1 + |g_s|^2 + |\mathbf{g}_t|^2 + |f_s|^2 + |\mathbf{f}_t|^2). \quad (\text{D18})$$

Putting together the pieces we have calculated so far, we find that the charge relaxation length $\lambda = \sqrt{-M_{44}/V_{44}}$ is:

$$\lambda = \sqrt{\frac{D(1 + |g_s|^2 + |\mathbf{g}_t|^2 + |f_s|^2 + |\mathbf{f}_t|^2)}{-4\Delta \text{Im} f_s}}. \quad (\text{D19})$$

Defining the coherence length $\xi' \equiv \sqrt{D/\Delta}$, which depends on temperature via the self-consistent gap Δ , this becomes

$$\lambda = \frac{\xi'}{2} \sqrt{\frac{1 + |g_s|^2 + |g_t|^2 + |f_s|^2 + |f_t|^2}{-\text{Im } f_s}}. \quad (\text{D20})$$

This is a somewhat general result, as it is valid regardless what mixture of singlets and triplets is present in the system, and we have not made any assumptions of weak proximity or weak inverse proximity effect. The result does, however, rest on two crucial assumptions. The first is that the charge mode couples only weakly to the other nonequilibrium modes of the distribution function, so that it was sufficient to consider the diagonal parts of Eq. (D1). This should be a reasonable approximation as long as either (i) the charge mode relaxes over a shorter length scale than the other modes or (ii) the coupling to the other modes is weak. The second assumption is that the system is roughly homogeneous, so that we can neglect variations in the propagator and the presence of any supercurrents. In practice, this should be a fair approximation if we consider a large superconductor with tunneling contacts.

Let us first consider the numerator of Eq. (D20). We see that the numerator is always larger than 1. Furthermore, for a normal metal $|g_s|^2 = 1$ while the other quantities are zero, making the numerator simply equal to 2. On the other hand, for a BCS superconductor, we get $|g_s|^2 = |\epsilon^2/(\epsilon^2 - \Delta^2)|$ while $|f_s|^2 = |\Delta^2/(\epsilon^2 - \Delta^2)|$. From this, we find that

$|g_s|^2 + |f_s|^2 \approx 1$ in the limits $|\epsilon| \ll \Delta$ and $|\epsilon| \gg \Delta$ but diverges as $\epsilon \rightarrow \pm\Delta$. Thus, except near the coherence peaks of a superconductor, the charge relaxation length should mainly be controlled by the denominator in Eq. (D20), yielding the approximation

$$\lambda \approx \frac{\xi}{\sqrt{-2 \text{Im } f_s}}. \quad (\text{D21})$$

If we again focus on a BCS superconductor, for $e = 0$ we find $f_s = \Delta/\sqrt{\epsilon^2 - \Delta^2}$ for $\epsilon > 0$. For energies outside the gap $\epsilon > \Delta$, we see that $\text{Im } f_s = 0$, yielding a charge relaxation length $\lambda \rightarrow \infty$. On the other hand, for energies inside the gap $\epsilon \ll \Delta$, we find that $\text{Im } f_s = -1$, yielding $\lambda \approx \xi/\sqrt{2}$. Thus, we found exactly the kind of behavior we were expecting: The charge mode is screened over a characteristic length $\sim \xi$ inside the gap but is not screened for energies that reside outside the gap.

In Figs. 8 and 9, we show how the DOS $N(\epsilon)$ and approximate charge relaxation length $\lambda(\epsilon)$ vary with the spin splitting m in a superconductor. The results confirm that resistive currents decay over a length $\sim \xi$ in gapped parts of the spectrum, while a long-ranged resistive current can exist in ungapped parts of the spectrum. This result agrees quite well with our numerical results, where we observe that for $m = eV/2 > \Delta$, a resistive current contribution can persist throughout the superconductor for the energy range between the two spectral gaps.

-
- [1] R. Meserve and P. M. Tedrow, *Phys. Rep.* **238**, 173 (1994).
[2] Y. Matsuda and H. Shimahara, *J. Phys. Soc. Jpn.* **76**, 051005 (2007).
[3] P. Fulde and R. A. Ferrell, *Phys. Rev.* **135**, A550 (1964).
[4] A. I. Larkin and Y. N. Ovchinnikov, *Sov. Phys. JETP* **20**, 762 (1965).
[5] B. S. Chandrasekhar, *Appl. Phys. Lett.* **1**, 7 (1962).
[6] A. M. Clogston, *Phys. Rev. Lett.* **9**, 266 (1962).
[7] M. Eschrig, *Phys. Today* **64**, 43 (2010).
[8] J. Linder and J. W. A. Robinson, *Nat. Phys.* **11**, 307 (2015).
[9] M. Eschrig, *Rep. Prog. Phys.* **78**, 104501 (2015).
[10] M. G. Blamire and J. W. A. Robinson, in *The Oxford Handbook of Small Superconductors* (Oxford University Press, Oxford, 2017), pp. 416–427.
[11] H. Pothier, S. Guéron, N. O. Birge, D. Esteve, and M. H. Devoret, *Phys. Rev. Lett.* **79**, 3490 (1997).
[12] F. K. Wilhelm, G. Schön, and A. D. Zaikin, *Phys. Rev. Lett.* **81**, 1682 (1998).
[13] W. Belzig, F. K. Wilhelm, C. Bruder, G. Schön, and A. D. Zaikin, *Superlattices Microstruct.* **25**, 1251 (1999).
[14] I. V. Bobkova and A. M. Bobkov, *Phys. Rev. B* **89**, 224501 (2014).
[15] I. Snyman and Y. V. Nazarov, *Phys. Rev. B* **79**, 014510 (2009).
[16] A. Moor, A. F. Volkov, and K. B. Efetov, *Phys. Rev. B* **80**, 054516 (2009).
[17] R. S. Keizer, M. G. Flokstra, J. Aarts, and T. M. Klapwijk, *Phys. Rev. Lett.* **96**, 147002 (2006).
[18] F. Giazotto, F. Taddei, P. D’Amico, R. Fazio, and F. Beltram, *Phys. Rev. B* **76**, 184518 (2007).
[19] I. V. Bobkova and A. M. Bobkov, *JETP Lett.* **101**, 118 (2015).
[20] M. Silaev, P. Virtanen, F. S. Bergeret, and T. T. Heikkilä, *Phys. Rev. Lett.* **114**, 167002 (2015).
[21] F. Aikebaier, M. A. Silaev, and T. T. Heikkilä, *Phys. Rev. B* **98**, 024516 (2018).
[22] F. S. Bergeret, M. Silaev, P. Virtanen, and T. T. Heikkilä, [arXiv:1706.08245](https://arxiv.org/abs/1706.08245) [Rev. Mod. Phys. (to be published)].
[23] T. Krishtop, M. Houzet, and J. S. Meyer, *Phys. Rev. B* **91**, 121407 (2015).
[24] D. Chevallier, M. Trif, C. Dutreix, M. Guigou, C. H. L. Quay, M. Aprili, and C. Bena, *New J. Phys.* **20**, 013014 (2018).
[25] I. V. Bobkova and A. M. Bobkov, *Phys. Rev. B* **93**, 024513 (2016).
[26] I. V. Bobkova and A. M. Bobkov, *Phys. Rev. B* **84**, 140508 (2011).
[27] I. V. Bobkova and A. M. Bobkov, *JETP Lett.* **101**, 407 (2015).
[28] S. H. Jacobsen, J. A. Ouassou, and J. Linder, *Phys. Rev. B* **92**, 024510 (2015).
[29] V. Chandrasekhar, in *Superconductivity* (Springer, Berlin, Heidelberg, 2008), pp. 279–313.
[30] M. Tinkham, *Introduction to Superconductivity*, 2nd ed. (Dover Publications, Mineola, 2004).
[31] A. Schmid and G. Schön, *J. Low Temp. Phys.* **20**, 207 (1975).
[32] I. V. Bobkova and A. M. Bobkov, *Phys. Rev. Lett.* **108**, 197002 (2012).
[33] T. T. Heikkilä, F. K. Wilhelm, and G. Schön, *Europhys. Lett.* **51**, 434 (2000).
[34] N. M. Chtchelkatchev, W. Belzig, and C. Bruder, *JETP Lett.* **75**, 646 (2002).

- [35] S.-K. Yip, *Phys. Rev. B* **62**, R6127(R) (2000).
- [36] J. Rammer and H. Smith, *Rev. Mod. Phys.* **58**, 323 (1986).
- [37] K. D. Usadel, *Phys. Rev. Lett.* **25**, 507 (1970).
- [38] M. Y. Kuprianov and V. F. Lukichev, *Sov. Phys. JETP* **67**, 1163 (1988).
- [39] N. Schopohl, [arXiv:cond-mat/9804064](https://arxiv.org/abs/cond-mat/9804064).
- [40] J. A. Ouassou, A. Pal, M. Blamire, M. Eschrig, and J. Linder, *Sci. Rep.* **7**, 1932 (2017).
- [41] F. Herman and R. Hlubina, *Phys. Rev. B* **97**, 014517 (2018).
- [42] R. C. Dynes, V. Narayanamurti, and J. P. Garno, *Phys. Rev. Lett.* **41**, 1509 (1978).
- [43] F. Pierre, A. B. Gougam, A. Anthore, H. Pothier, D. Esteve, and N. O. Birge, *Phys. Rev. B* **68**, 085413 (2003).
- [44] M. J. Black and V. Chandrasekhar, *Europhys. Lett.* **50**, 257 (2000).
- [45] M. Eschrig, A. Cottet, W. Belzig, and J. Linder, *New J. Phys.* **17**, 083037 (2015).
- [46] X. Li, Z. Zheng, D. Y. Xing, G. Sun, and Z. Dong, *Phys. Rev. B* **65**, 134507 (2002).
- [47] G. Sarma, *J. Phys. Chem. Solids* **24**, 1029 (1963).
- [48] V. F. Elisin, *Sov. Phys. JETP* **46**, 185 (1977).
- [49] S. V. Bakurskiy, V. I. Filippov, V. I. Ruzhickiy, N. V. Klenov, I. I. Soloviev, M. Y. Kupriyanov, and A. A. Golubov, *Phys. Rev. B* **95**, 094522 (2017).
- [50] N. B. Kopnin, *Theory of Nonequilibrium Superconductivity* (Clarendon Press, Oxford, 2001).
- [51] Y. V. Nazarov, *Superlattices Microstruct.* **25**, 1221 (1999).
- [52] Y. V. Nazarov and Y. M. Blanter, *Quantum Transport: Introduction to Nanoscience* (Cambridge University Press, New York, 2009).
- [53] C. Yuksel, S. Schaefer, and J. Keyser, *Comput.-Aided Des.* **43**, 747 (2011).
- [54] F. S. Bergeret, A. Verso, and A. F. Volkov, *Phys. Rev. B* **86**, 214516 (2012).
- [55] P. Machon, M. Eschrig, and W. Belzig, *Phys. Rev. Lett.* **110**, 047002 (2013).
- [56] A. Cottet, D. Huertas-Hernando, W. Belzig, and Y. V. Nazarov, *Phys. Rev. B* **80**, 184511 (2009).
- [57] A. Cottet, *Phys. Rev. B* **76**, 224505 (2007).
- [58] J. P. Morten, *Spin and Charge Transport in Dirty Superconductors*, Master thesis, NTNU, Norway (2005).
- [59] N. Chtchelkatchev, T. Baturina, A. Glatz, and V. Vinokur, in *Physical Properties of Nanosystems* (Springer, Netherlands, 2010), pp. 87–107.
- [60] G. E. W. Bauer, E. Saitoh, and B. J. van Wees, *Nat. Mater.* **11**, 391 (2012).

Correction: The previously published verso running head contained an error and has been replaced.

XIV

Reference

J.A. Ouassou, J. Linder.

Voltage control of superconducting exchange interaction and anomalous Josephson effect.

ARXIV: 1810.02820

Contributions

Both authors contributed to the ideas behind the project. JAO did the calculations. Both authors contributed to the writing of this manuscript.

Comments

This project was inspired by theoretical [175] and experimental [174] work which showed that the charge supercurrent in $S/N/S$ junctions can be reversed by applying a transverse voltage bias to the interlayer. We investigate related effects in Josephson junctions with magnetic interlayers, and find that the spontaneous spin current in $S/F/N/F/S$ junctions and spontaneous charge current in $S/F/F/S$ junctions can be controlled via such a voltage bias. The first result implies that one can electrically control the magnetic ground state of a heterostructure with superconducting elements, while the second result could be used to create voltage-controlled phase batteries for superconducting circuits.

This project has also been presented in an invited talk at the *QuSpin Workshop* (Trondheim, Norway, 2018), and in an invited talk at the University of Konstanz (Konstanz, Germany, 2018).

Voltage control of superconducting exchange interaction and anomalous Josephson effect

Jabir Ali Ouassou¹ and Jacob Linder¹

¹*Center for Quantum Spintronics, Department of Physics, Norwegian University of Science and Technology, NO-7491 Trondheim, Norway*

(Dated: November 30, 2018)

Exerting control of the magnetic exchange interaction in heterostructures is of both basic interest and has potential for use in spin-based applications relying on quantum effects. We here show that the sign of the exchange interaction in a spin-valve, determining whether a parallel (P) or antiparallel (AP) magnetic configuration is favored, can be controlled via an electric voltage. This occurs due to an interplay between a nonequilibrium quasiparticle distribution and the presence of spin-polarized Cooper pairs. Additionally, we show that a voltage-induced distribution controls the anomalous supercurrent that occurs in magnetic Josephson junctions, obviating the challenging task to manipulate the magnetic texture of the system. This demonstrates that two key phenomena in superconducting spintronics, the magnetic exchange interaction and the phase shift generating the anomalous Josephson effect, can be controlled electrically. Our findings are of relevance for spin-based superconducting devices which in practice most likely have to be operated precisely by nonequilibrium effects.

Introduction.—Driving a condensed matter system out of equilibrium via a control parameter such as electric voltage is a fundamentally interesting scenario. It offers a way to alter the physical properties of the system in a controllable manner and can give rise to new types of quantum effects. In recent years, it has been realized that rich physics ensues when considering magnetic-superconducting heterostructures that are out of equilibrium [1–3]. This includes very large thermoelectric effects [4–6], large quasiparticle spin Hall effects [7], raising the paramagnetic limit of superconducting films [8, 9], and supercurrent-induced magnetization dynamics [10, 13–17]. The study of such effects is associated with the field of superconducting spintronics [18], where the aim is to create a synergy between spin-polarized order and superconductivity.

Historically, creating a nonequilibrium distribution of quasiparticle states in superconducting structures has been shown to give rise to interesting effects. A prominent example is the supercurrent transistor demonstrated in Ref. [19], where the direction of a Josephson effect (charge supercurrent) was tuned via a voltage-induced nonequilibrium distribution in a superconductor/normal-metal/superconductor junction [20, 21]. In this Letter, we explore a spin-analogue of this effect. More precisely, we pose the question: can a *spin supercurrent* be controlled via the nonequilibrium mode induced by an electric voltage? Such a spin supercurrent exists when magnetic layers are added to the Josephson junction above and physically represents the exchange interaction between these layers [22, 23]. If the spin supercurrent—and in particular its sign—is controlled by a nonequilibrium distribution function, it allows the preferred magnetic configuration to be switched by an electric voltage. We show that this is indeed possible, and that it only requires small voltages below the superconducting gap Δ .

Additionally, we show that the recently experimentally observed anomalous phase shift in Josephson junctions [24] can be tuned via a nonequilibrium distribution of quasiparticles. This is induced via an electric current and permits a nonmagnetic way to control the anomalous Josephson effect, which removes the challenging requirement to manipulate the intricate noncollinear magnetic texture of structures that exhibit an anomalous supercurrent [25]. We predict large phase shifts that can be tuned by more than $\pi/2$ for voltages smaller than

the superconducting gap (~ 1 meV). This is two orders of magnitude smaller than the electric gate voltage that was used in Ref. [24] to observe the anomalous phase shift.

Methodology.—To determine the influence of nonequilibrium quasiparticle occupation in the system induced by an electric voltage, we use the quasiclassical theory of superconductivity. This framework is well-suited to address a range of physical phenomena occurring in mesoscopic heterostructures, including charge and spin supercurrents. We propose experimental setups for observing our predictions in Fig. 1. These setups should be experimentally feasible as they are similar to the setup used by Baselmans *et al.* [19], but with the addition of magnetic layers. In Fig. 1(a), an electric voltage injects a resistive charge current into a normal-metal wire. At the center of each wire, there is no net charge accumulation, but a surplus of *both* electrons and holes compared to the equilibrium situation. The superconducting and normal regions are interfaced by magnetic insulators, which influence each other via an exchange interaction. The quasiparticle injection described above alters the occupation of not only charge supercurrent-carrying states, as discussed in Refs. [19, 20, 26], but also the spin supercurrent-carrying states, which determine the exchange interaction between the magnetic insulators.

In Fig. 1(b), the weak link is made from a ferromagnetic metal, but except for that, the setup is identical. When the magnetizations of the ferromagnetic insulators, \mathbf{m}_L and \mathbf{m}_R , form a nonzero spin chirality χ together with the magnetization of the metallic ferromagnet according to $\chi = \mathbf{m} \cdot (\mathbf{m}_L \times \mathbf{m}_R)$, an anomalous Josephson effect appears at zero phase difference between the superconductors. This phenomenon can be understood from the fact that the broken spin-degeneracy combined with the broken chirality symmetry of the system allows the Cooper pairs to gain a net additional phase φ_0 as they tunnel through the system. By using quasiparticle injection to change the occupation of charge supercurrent-carrying states, we show below that this anomalous Josephson current can be altered.

Both systems in Fig. 1 can be described by the Usadel equation for diffusive systems [3, 27–29, 31],

$$\nabla \cdot \tilde{\mathbf{I}} = i[\hat{\Delta} + \mathbf{m} \cdot \hat{\sigma} + \varepsilon \hat{\tau}_3, \tilde{\mathbf{g}}], \quad \tilde{\mathbf{I}} = -D\tilde{g}\nabla\tilde{g}, \quad (1)$$

which determines the 8×8 quasiclassical Green functions

$$\check{g} = \begin{pmatrix} \check{g}^R & \check{g}^K \\ 0 & \check{g}^A \end{pmatrix}, \quad \check{I} = \begin{pmatrix} \hat{I}^R & \hat{I}^K \\ 0 & \hat{I}^A \end{pmatrix}. \quad (2)$$

Above, $\hat{\Delta} = \text{antidiag}(+\Delta, -\Delta, +\Delta^*, -\Delta^*)$, $\hat{\sigma} = (\hat{\sigma}_1, \hat{\sigma}_2, \hat{\sigma}_3)$, $\hat{\sigma}_n = \text{diag}(\sigma_n, \sigma_n^*)$, σ_n are Pauli matrices in spin space, and $\hat{\tau}_n$ are Pauli matrices in Nambu space. The parameter Δ is the superconducting gap, which we take to be $\Delta_0 e^{\pm i\varphi/2}$ for the superconductors in Fig. 1, where Δ_0 is the zero-temperature bulk gap, and φ is the phase difference between them. The parameter m is the exchange field of a magnetic metal, which we take to be homogeneous. We consider weakly polarized ferromagnetic alloys such as PdNi with a low content of Ni, where the exchange field is of order 10 meV [32]. Finally, D is the diffusion coefficient and ε the quasiparticle energy. We also define the coherence length $\xi = \sqrt{D/\Delta_0}$ and material length L .

The components of the Usadel equation are related by the identities $\check{g}^K = \hat{g}^R \hat{h} - \hat{h} \hat{g}^A$ and $\hat{g}^A = -\hat{\tau}_3 \hat{g}^{R\dagger} \hat{\tau}_3$, which means that it is in general sufficient to solve for the retarded component \hat{g}^R and a distribution function \hat{h} . We numerically solved the equations for the retarded component using a Riccati-parametrization [33, 34]. The magnetic insulators in Fig. 1(a–b) were treated as spin-active tunneling boundary conditions to superconducting reservoirs [5, 35–38],

$$(2L/D) \check{I} \cdot \mathbf{n} = (G_T/G_N) [\check{g}, F(\check{g}_{\text{BCS}})] - i(G_\varphi/G_N) [\check{g}, \hat{m}], \quad (3)$$

where the spin-filtering function [35]

$$F(\check{v}) = \check{v} + \frac{P}{1 + \sqrt{1 - P^2}} \{\check{v}, \hat{m}\} + \frac{1 - \sqrt{1 - P^2}}{1 + \sqrt{1 - P^2}} \hat{m} \check{v} \hat{m}. \quad (4)$$

Here, \check{g}_{BCS} is the standard solution for a bulk superconductor [34], since we treat the superconductors as reservoirs. Numerical values for the Drude conductance G_N , tunneling conductance G_T , spin-mixing conductance G_φ , and polarization P are given in the captions of Figs. 2 and 3. Finally, \mathbf{n} is the interface normal, and $\hat{m} = \hat{\sigma} \cdot \mathbf{m}_{\text{L,R}}$ is related to the interface magnetization. We use the notations \mathbf{m}_L and \mathbf{m}_R for the magnetizations of the “left” and “right” interfaces, respectively. The misalignment θ between the directions of \mathbf{m}_L and \mathbf{m}_R controls the magnitude of the spin supercurrent according to $J_s \sim \mathbf{m}_L \times \mathbf{m}_R \sim \sin \theta$. In our calculations, we have set $\mathbf{m}_L = \hat{x}$ and $\mathbf{m}_R = \hat{y}$ so that the polarization $J_s \sim \hat{z}$. As for the distribution function \hat{h} , we did not need to explicitly solve the kinetic equations [3, 8, 27, 28, 39–41], since an analytical solution is already known [20, 26, 42]:

$$\hat{h} = \frac{1}{2} [\tanh(\varepsilon + eV/2) + \tanh(\varepsilon - eV/2)] \hat{\tau}_0 \hat{\sigma}_0. \quad (5)$$

This result is valid near the centers of voltage-biased normal metals, including the weak links shown in Fig. 1. The charge and spin currents were determined from the numerically calculated Green functions using standard formulas [1, 3, 27–30]. More precisely, the charge current $J_e = eJ_0$ and spin current $J_s = (\hbar/2)(J_1, J_2, J_3)$ along the junction axis \mathbf{n} follow from

$$J_n = -\frac{G_N \Delta_0}{8De^2} \int_0^\infty d\varepsilon \text{Re Tr}[\hat{\tau}_3 \hat{\sigma}_n (\hat{I}^K \cdot \mathbf{n})], \quad (6)$$

and are normalized to $J_{e0} = G_N \Delta_0 / e$ and $J_{s0} = (\hbar/2e) J_{e0}$.

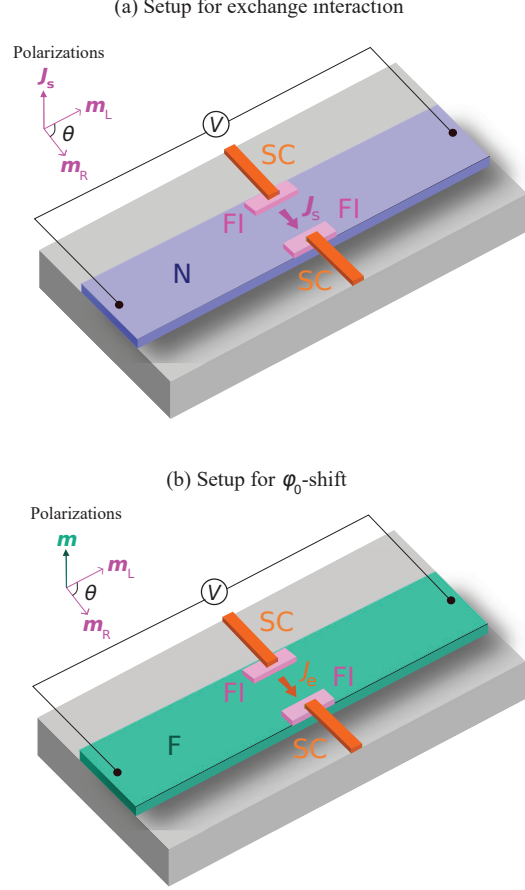


FIG. 1: (Color online) Suggested experimental setups. External voltage sources inject resistive charge currents into normal-metal regions. Near the centers of these wires, there is no net charge accumulation, but an excess of *both* electrons and holes compared to the equilibrium situation. These regions of the normal metals are then used as the weak links of magnetic Josephson junctions. (a) If the weak link is a normal metal, a spontaneous spin supercurrent $J_s \sim \mathbf{m}_L \times \mathbf{m}_R$ flows between the magnetic insulators (black arrow), where \mathbf{m}_L and \mathbf{m}_R refer to their magnetization directions. We show that this spin supercurrent can be reversed as a function of voltage, resulting in a voltage-controllable switching from anti- to ferromagnetic interactions between the magnets. (b) If the weak link is a ferromagnet, there will in addition be a spontaneous charge supercurrent $J_e \sim \mathbf{m} \cdot (\mathbf{m}_L \times \mathbf{m}_R)$ flowing between the superconductors (black arrow), where \mathbf{m} is the exchange field in the weak link. We show that this charge supercurrent can be tuned as a function of voltage, resulting in a voltage-controllable ground-state phase shift between the two superconductors.

Results.—The exchange interaction between two magnetic layers is a consequence of an equilibrium spin current \mathbf{J}_s flowing from one to the other and exerting a torque $\boldsymbol{\tau}$ by depositing spin angular momentum to the ferromagnet. The direction of the torque $\boldsymbol{\tau}$ is determined by the polarization of the spin supercurrent. This means that reversing the spin supercurrent, one can control the magnetization configuration of the spin-valve to favor either a parallel or antiparallel alignment. A comparison between the properties of the exchange interaction in normal and superconducting system was provided in Ref. [10]. We note that in equilibrium, the supercurrent-mediated exchange interaction acts antiferromagnetically [11, 12].

In Fig. 2(a), we show that the nonequilibrium distribution function in the Josephson weak link determines the sign of the superconducting spin current that mediates the exchange interaction. The plot shows the spin supercurrent polarized in the $\mathbf{m}_l \times \mathbf{m}_r = z$ direction. The spin supercurrent drops approximately linearly from its maximum at zero to its minimum occurring at $eV/2 \approx 0.35\Delta_0$ and changes sign in between. As a result, the favored configuration of the magnetic insulators is changed from anti- to ferromagnetic by modifying the distribution of quasiparticles in the weak link with a voltage that is smaller than the superconducting gap. This corresponds to a voltage less than ~ 1 meV. We expect that the same sign reversal of the spin supercurrent should be possible when using thin ferromagnetic metals rather than ferromagnetic insulators. The stability of a given magnetic configuration at a fixed voltage is determined by the sign of the spin supercurrent, because the sign determines the direction of the torque acting on the magnetic order parameter in the ferromagnetic insulators. If the torque favors an AP configuration for one particular sign, it favors the P configuration for the opposite sign.

Moreover, we have numerically confirmed that the sign change of the spin supercurrent as a function of applied voltage occurs for a wide parameter range, as shown in Fig. 2(c–f). In general, a high tunneling conductance G_T and short junction length L enhances the proximity effect; this increases the spin supercurrent at all voltages, but also increases the switching voltage required. The polarization P has a relatively small effect on our results. However, in the limit $P \rightarrow 1$, it suppresses tunneling of opposite-spin Cooper pairs from the superconducting reservoirs, which is detrimental to the spin supercurrent. Interestingly, the voltages where the strongest ferromagnetic and antiferromagnetic interactions occur are found to increase nearly linearly with the spin-mixing conductance G_φ . We note that for most parameter combinations explored here, a switching between P and AP ground-state configurations can be achieved using reasonable applied voltages $eV \lesssim \Delta_0$.

Recently, the superconducting exchange coupling between ferromagnets was experimentally reported in Ref. [43]. By lowering the temperature below the superconducting critical temperature T_c , an antiferromagnetic effective exchange interaction was induced by the transition to the superconducting state. Here, we have shown that the superconducting exchange interaction can be toggled between anti- and ferromagnetic via electric voltage, providing a new mechanism compatible with devices operating out-of-equilibrium for actively controlling the magnetic state. Physically, the sign change of the exchange

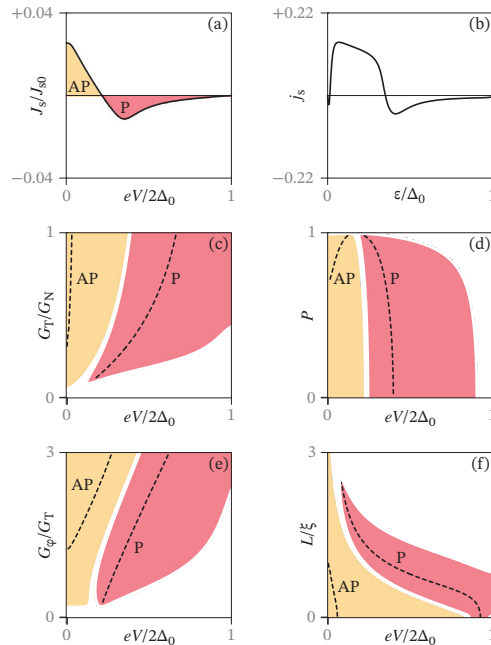


FIG. 2: (Color online) Numerical results for the setup in Fig. 1(a). (a) Spin supercurrent J_s as a function of applied voltage. The voltage shifts the distribution function in the weak link of the Josephson junction, and causes the spin supercurrent to change sign at $eV/2$ well below Δ_0 . Since the spin supercurrent mediates the exchange interaction between the magnets, the sign reversal implies a switch from anti- to ferromagnetic interactions, thus switching from an antiparallel (AP) to parallel (P) configuration as the magnetic ground state. The magnetic insulators were modeled as spin-active interfaces with polarization $P = 70\%$, tunneling conductance $G_T = 0.3G_N$, and spin-mixing conductance $G_\varphi = 1.25G_T$. The normal-metal weak link has a length $L_N = \xi$ and conductance G_N . (b) Spectral spin supercurrent J_s as a function of energy. Note that J_s changes its sign at higher energies, which explains why manipulating the distribution function can reverse the spin supercurrent J_s . The remaining panels show phase diagrams as functions of the voltage and (c) tunneling conductance, (d) polarization, (e) spin-mixing conductance, and (f) normal-metal length. The remaining parameters are the same as in panel (a). Yellow regions correspond to significant antiferromagnetic interactions ($J_s > +0.001J_{s0}$), and red to significant ferromagnetic interactions ($J_s < -0.001J_{s0}$). The dashed lines indicate the voltages required to maximize these interactions.

interaction can be understood from the fact that the voltage alters the occupation of not only states carrying the spectral (energy-resolved) charge supercurrent through the junction, but also the spin supercurrent.

For a more thorough explanation of the effect, we have to consider the spectral spin supercurrents. The total spin

supercurrent J_s can be expressed as an integral

$$J_s = J_{s0} \int_0^{\infty} d\varepsilon j_s(\varepsilon) h(\varepsilon), \quad (7)$$

where the spectral spin supercurrent j_s describes the spin supercurrent-carrying states available, and the distribution function $h(\varepsilon)$ describes which of these are occupied. According to Eq. (5) in the limit $T \rightarrow 0$, the distribution function at $\varepsilon > 0$ can be summarized as a step function $\Theta(\varepsilon - eV/2)$, where we assume a positive voltage V . Putting these equations together, we see that the spin supercurrent is basically just an integral of j_s from $\varepsilon = eV/2$ and up. In Fig. 2(b), we have plotted the numerically calculated spectral spin supercurrent as a function of energy. The result is primarily positive for $\varepsilon < 0.35\Delta_0$, and primarily negative for $\varepsilon > 0.35\Delta_0$. Since the equation above shows that the voltage $eV/2$ plays the role of a cutoff that determines which of these energy regions contribute to the total spin supercurrent, it becomes clear why the spin supercurrent can be switched via an electric voltage. The mechanism is thus similar to the charge supercurrent switching [20] in an S/N/S transistor setup with phase-biased superconductors.

Our second main result is that the voltage-controlled nonequilibrium quasiparticle distribution can be used to control the anomalous Josephson effect. We have for concreteness considered a fixed spin chirality χ corresponding to perpendicularly oriented magnetization vectors m_L, m_R , and m . Fig. 3(a) shows the phase shift as a function of applied voltage. As the phase increases from its minimum value $\varphi_0 \approx \pi/4$ at $eV/2 = 0.2\Delta_0$ to a maximum $\varphi_0 \approx \pi$ near $eV/2 = \Delta_0$, the phase shift is seen to be tuned by more than 120° within a voltage regime of ~ 1 meV. It is worth emphasizing that the voltage required here to change the φ_0 -shift is two orders of magnitude smaller than the gate voltage ~ 200 meV used in the recent experiment Ref. [24]. This suggests that the anomalous phase shift proposed in this manuscript can be tuned with much less power dissipation than by using gated quantum dots.

The physical mechanism behind the voltage-controlled phase shift can be understood as follows. The total supercurrent flowing in a Josephson junction with a finite spin-chirality χ has two contributions according to $J_e = J_{c1} \sin \varphi + J_{c2} \cos \varphi$ where $J_{c2} \sim \chi$ [44–50]. The latter term is responsible for the anomalous supercurrent at zero phase difference, as can be seen by rewriting the current-phase relation to the form $J_e = J_c \sin(\varphi - \varphi_0)$ where φ_0 depends on the relative magnitude of J_{c1} and J_{c2} . From previous works considering S/N/S transistors [19–21], it is known that the conventional term J_{c1} can be forced to change sign by inducing a nonequilibrium energy distribution, corresponding to a $0-\pi$ transition. Precisely at this transition point, only the anomalous part $\cos \varphi$ remains which is seen in the red curve ($eV/2 = 0.5\Delta_0$) of Fig. 3(b). As one moves away from the $0-\pi$ transition point, the critical supercurrent may increase since now both J_{c1} and J_{c2} contribute to J_e . This matches well with the $eV/2 = 0.3\Delta_0$ and $eV/2 = 0.6\Delta_0$ curves in Fig. 3. Additionally, since the ratio J_{c1}/J_{c2} changes rapidly around the $0-\pi$ transition point corresponding to $eV/2 = 0.5\Delta_0$, we would expect the anomalous phase shift to also vary rapidly near this voltage. This is

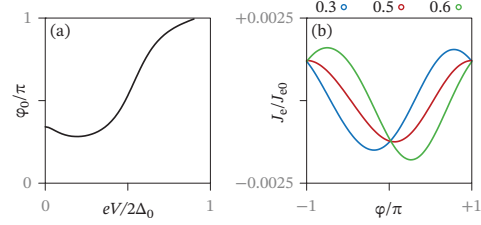


FIG. 3: (Color online) Phase shift causing the anomalous Josephson effect in the system depicted in Fig. 1(b). We have used the same interfacial parameter set as in Fig. 2 and set the length $L_F = 0.5\xi$ and exchange field $m = 5\Delta_0$ for the ferromagnetic metal weak link.

confirmed by the results in Fig. 3(a).

The electrically tunable anomalous phase shift could be of interest for the purpose of designing a phase battery. Similarly to how conventional batteries store a potential difference which can drive resistive currents, an anomalous Josephson junction provides a built-in phase difference which could be used to drive supercurrents. Recent works on magnetic Josephson junctions have taken steps toward realizing such a phase control [25]. Unless the magnetic anisotropies of the system are such that a finite spin chirality χ exists in the ground-state, the misoriented magnetization configuration producing $\chi \neq 0$ has to be fixed by external conditions such as an applied magnetic field.

Conclusion.—We have investigated the influence of nonequilibrium quasiparticle modes on a superconducting spin-valve and discovered two effects. First, the voltage-controlled distribution function controls the magnitude and sign of the superconducting exchange interaction, toggling the preferred configuration of the spin-valve from anti- to ferromagnetic. Moreover, we show that the same basic setup controls the anomalous Josephson effect in a junction with finite spin-chirality, obviating the requirement to manipulate the magnetic texture of the system. We believe this two phenomena may be of interest for the design of nonequilibrium superconducting devices that exploit spin-dependent quantum effects.

Acknowledgments

We thank O. Bolme and V. Risinggård for discussions. The numerics was performed on resources provided by UNINETT Sigma2—the national infrastructure for high performance computing and data storage in Norway. This work was supported by the Research Council of Norway through grant 240806, and its Centres of Excellence funding scheme grant 262633 “*QuSpin*”.

-
- [1] M. Eschrig. Rep. Prog. Phys. **78**, 104501 (2015).
- [2] D. Beckmann. J. Phys.: Condens. Matter **28**, 163001 (2016).
- [3] F.S. Bergeret, M. Silaev, P. Virtanen, and T.T. Heikkilä. arXiv:1706.08245.
- [4] M.S. Kalenkov, A.D. Zaikin, and L.S. Kuzmin. Phys. Rev. Lett. **109**, 147004 (2012).
- [5] P. Machon, M. Eschrig, and W. Belzig. Phys. Rev. Lett. **110**, 047002 (2013).
- [6] S. Kolenda, M.J. Wolf, and D. Beckmann. Phys. Rev. Lett. **116**, 097001 (2016).
- [7] T. Wakamura, H. Akaïke, Y. Omori, Y. Niimi, S. Takahashi, A. Fujimaki, S. Maekawa, and Y. Otani. Nature Materials **14**, 675–678 (2015).
- [8] J.A. Ouassou, T.D. Vethaak, and J. Linder. Phys. Rev. B **98**, 144509 (2018).
- [9] I. V. Bobkova and A. M. Bobkov. Phys. Rev. B. **84**, 140508(R) (2011).
- [10] X. Waintal and P.W. Brouwer. Phys. Rev. B **65**, 054407 (2002).
- [11] P.G. de Gennes. Physics Letters **23**, 10 (1966)
- [12] W. Chen, P. Horsch, and D. Manske. Phys. Rev. B **89**, 064427 (2014).
- [13] E. Zhao and J.A. Sauls. Phys. Rev. B **78**, 174511 (2008).
- [14] J. Linder and T. Yokoyama. Phys. Rev. B **83**, 012501 (2011).
- [15] C. Holmqvist, W. Belzig, and M. Fogelström. Phys. Rev. B **86**, 054519 (2012).
- [16] R. Takashima, S. Fujimoto, and T. Yokoyama. Phys. Rev. B **96**, 121203(R) (2017).
- [17] I.V. Bobkova, A.M. Bobkov, and M.A. Silaev. Phys. Rev. B **98**, 014521 (2018).
- [18] J. Linder and J.W.A. Robinson. Nature Physics **11**, 307 (2015).
- [19] J.J.A. Baselmans, A.F. Morpurgo, B.J. van Wees, and T.M. Klapwijk. Nature **397**, 43 (1999).
- [20] F.K. Wilhelm, G. Schön, and A.D. Zaikin. Phys. Rev. Lett. **81**, 1682 (1998).
- [21] A.F. Volkov. Phys. Rev. Lett. **74**, 4730 (1995).
- [22] J.C. Slonczewski. Phys. Rev. B **39**, 6995 (1989).
- [23] F.S. Nogueira and K.-H. Bennemann. EPL **67**, 620 (2004).
- [24] D.B. Szombati, S. Nadj-Perge, D. Car, S.R. Plissard, E.P.A.M. Bakkers, L.P. Kouwenhoven. Nat. Phys. **12**, 568 (2016).
- [25] J.A. Glick *et al.*. Sci. Adv. **27**, 7 (2018).
- [26] T.T. Heikkilä, W.K. Wilhelm, and G. Schön. EPL **51**, 434 (2000).
- [27] V. Chandrasekhar. In *Superconductivity* (Springer, Berlin, Heidelberg, 2008) pp. 279.
- [28] W. Belzig, F.K. Wilhelm, C. Bruder, G. Schön, and A.D. Zaikin. Superlattices and Microstructures **25**, 1251 (1999).
- [29] J. Rammer and H. Smith. Rev. Mod. Phys. **58**, 323 (1986).
- [30] J.A. Ouassou, J.W.A. Robinson, J. Linder. arXiv:1810.08623.
- [31] K.D. Usadel. Phys. Rev. Lett. **25**, 507 (1970).
- [32] T. Kontos, M. Aprili, J. Lesueur, and X. Grison. Phys. Rev. Lett. **86**, 304 (2001).
- [33] N. Schopohl. arXiv:cond-mat/9804064.
- [34] S.H. Jacobsen, J.A. Ouassou, and J. Linder. Phys. Rev. B **92**, 024510 (2015).
- [35] J.A. Ouassou, A. Pal, M. Blamire, M. Eschrig, J. Linder. Sci. Rep. **7**, 1932 (2017).
- [36] M. Eschrig, A. Cottet, W. Belzig, and J. Linder. New J. Phys. **17**, 083037 (2015).
- [37] A. Cottet, D. Huertas-Hernando, W. Belzig, and Y.V. Nazarov. Phys. Rev. B **80**, 184511 (2009).
- [38] A. Cottet. Phys. Rev. B **76**, 224505 (2007).
- [39] I.V. Bobkova and A.M. Bobkov. JETP Lett. **101**, 118 (2015).
- [40] M. Silaev, P. Virtanen, F.S. Bergeret, and T.T. Heikkilä. Phys. Rev. Lett. **114**, 167002 (2015).
- [41] F. Aikebaier, M.A. Silaev, and T.T. Heikkilä. arXiv:1712.08653.
- [42] H. Pothier, S. Guéron, N.O. Birge, D. Esteve, and M.H. Devoret. Phys. Rev. Lett. **79**, 3490 (1997).
- [43] Y. Zhu, A. Pal, M. Blamire, and Z.H. Barber. Nature Materials **16**, 195 (2017).
- [44] I. Kulagina and J. Linder. Phys. Rev. B **90**, 054504 (2014).
- [45] Y. Asano, Y. Sawa, Y. Tanaka, and A. Golubov. Phys. Rev. B **76**, 224525 (2007).
- [46] R. Grein, M. Eschrig, G. Metalidis, and G. Schön. Phys. Rev. Lett. **102**, 227005 (2009).
- [47] M. Eschrig and T. Löfwander. Nat. Phys. **4**, 138 (2008).
- [48] J.-F. Liu and K.S. Chan. Phys. Rev. B **82**, 184533 (2010).
- [49] S. Mironov and A. Buzdin. Phys. Rev. B **92**, 184506 (2015).
- [50] M.A. Silaev, I.V. Tokatly, and F.S. Bergeret. Phys. Rev. B **95**, 184508 (2017).

XV

Reference

J.A. Ouassou, J.W.A. Robinson, J. Linder.
Controlling spin supercurrents via nonequilibrium spin injection.
ARXIV: 1810.08623

Contributions

JAO performed all the analytical and numerical calculations, and wrote the initial draft for the manuscript. All authors contributed to the ideas behind the project, and to discussions and revisions of the manuscript.

Comments

This project was inspired by recent experiments on spin pumping into superconductors [75]. This prompted questions about how a nonequilibrium spin population couples to the triplet-pair population, and what experimental signatures one might expect in such setups. These questions were the motivation behind our theoretical investigation.

This project has also been presented in an invited talk at the *QuSpin Workshop* (Trondheim, Norway, 2018), and in an invited talk at the University of Konstanz (Konstanz, Germany, 2018).

Controlling spin supercurrents via nonequilibrium spin injection

Jabir Ali Ouassou,¹ Jason W. A. Robinson,² and Jacob Linder¹

¹Center for Quantum Spintronics, Department of Physics, Norwegian University of Science and Technology, NO-7491 Trondheim, Norway

²Department of Materials Science and Metallurgy, University of Cambridge, 27 Charles Babbage Road, Cambridge CB3 0FS, United Kingdom

We propose a mechanism whereby spin supercurrents can be manipulated in superconductor/ferromagnet proximity systems via nonequilibrium spin injection. More precisely, we find that if a spin supercurrent exists in equilibrium, a nonequilibrium spin accumulation will exert a torque on the spins transported by this current. This interaction causes a new spin supercurrent contribution to manifest out of equilibrium, which is proportional to and polarized perpendicularly to both the injected spins and equilibrium spin current. This is interesting for several reasons: as a fundamental physical effect; due to possible applications as a way to control spin supercurrents; and timeliness in light of recent experiments on spin injection in proximitized superconductors.

Introduction.—In the emerging field of superconducting spintronics, a key objective is to study the interactions between superconductors (S) and ferromagnets (F) [1–4]. These interactions can produce new types of Cooper pairs $|\uparrow\uparrow\rangle$ and $|\downarrow\downarrow\rangle$ with a net spin polarization, which enables the use of S/F systems for dissipationless spin transport. There has been a lot of research on generating spin supercurrents in equilibrium, either via inhomogeneous magnetism [5–10] or spin-orbit coupling [11–13]. In the magnetic case, it has been shown that two layers with noncollinear magnetic moments \mathbf{m}_1 and \mathbf{m}_2 give rise to an equilibrium spin supercurrent $\mathbf{J}_s^{\text{eq}} \sim \mathbf{m}_1 \times \mathbf{m}_2$, which transports spins polarized perpendicularly to both magnetic moments [14]. One challenge with these suggestions is, however, that it would be difficult to manipulate the polarization of the spin supercurrent *in situ*. To produce all spin projections, one would need to carefully control the magnetic orientations \mathbf{m}_1 and \mathbf{m}_2 independently. In addition, this would likely lead to high switching times for prospective device applications. It would therefore be interesting to investigate whether a spin supercurrent can be controlled via electronic spin injection instead. This would have the added benefit of enabling the coupling of superconducting and nonsuperconducting spintronics devices. Note that this is different from many previous works on spin injection in superconductors, which were largely explained in terms of quasiparticles and not a spin-triplet condensate [15–19].

Recently, there has been a renewed interest in using nonequilibrium spin injection as a means to manipulate spin supercurrents. This is largely due to a recent spin-pumping experiment [20], where microwaves were used to excite spins in the ferromagnetic layer of a N/S/F/S/N junction. Depending on the spin-orbit coupling in the normal metal N, the spin current leaving F could increase below the critical temperature T_c of the S layers. The main interpretation proposed in that paper was that the increased spin transmission for temperatures $T < T_c$ was due to a spin-triplet supercurrent, although alternative explanations have been proposed [21]. We will not consider that specific geometry here, but focus on the more general problem of how spin injection might affect spin supercurrents. One approach was explored in Ref. [13], where they considered Fermi-liquid interactions. In their model, a spin accumulation ρ_s induces an effective magnetic exchange field $\mathbf{m}_{\text{eff}} \sim \rho_s$. Since inhomogeneous exchange fields are well-known to pro-

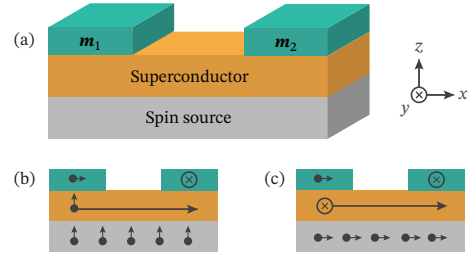


FIG. 1: (a) Magnetic insulators with magnetizations \mathbf{m}_1 and \mathbf{m}_2 on a superconductor. In equilibrium, this yields a spin supercurrent $\mathbf{J}_s^{\text{eq}} \sim \mathbf{m}_1 \times \mathbf{m}_2$. A spin source injects a spin accumulation ρ_s , which exerts a torque on the spins transported by the equilibrium current, resulting in a new contribution $\mathbf{J}_s^{\text{neq}} \sim \rho_s \times (\mathbf{m}_1 \times \mathbf{m}_2)$. (b) If the magnets are magnetized in the x - and y -directions, an equilibrium spin- z supercurrent arises. Injection of spin- z particles does not affect its polarization. (c) If spin- x particles are injected, however, a new spin- y supercurrent component is generated. Similarly, spin- y injection would produce a spin- x component.

duce spin supercurrents, this provides one mechanism for the generation of spin supercurrents.

In this manuscript, we introduce a different mechanism, as illustrated in Fig. 1. We show that a nonequilibrium spin accumulation actually produces new terms in the equations for the spin supercurrent itself. These terms have a natural interpretation in the form of the injected spin accumulation ρ_s exerting a torque on an equilibrium spin supercurrent \mathbf{J}_s^{eq} , thus giving rise to a new component $\mathbf{J}_s^{\text{neq}} \sim \rho_s \times \mathbf{J}_s^{\text{eq}}$ perpendicular to both. Although this term occurs out-of-equilibrium, it shares the property of an equilibrium spin supercurrent that it does not require a gradient in the total or spin-resolved chemical potential. Therefore, it is legitimate to refer to the new term $\mathbf{J}_s^{\text{neq}}$ as a supercurrent flowing without dissipation as there is no energy loss associated with a spatially varying chemical potential. We note that our mechanism differs from the one in Ref. [13] in three important ways. Our mechanism cannot cause a spin supercurrent to appear in a system without an equilibrium spin supercurrent since $\mathbf{J}_s^{\text{eq}} \rightarrow 0 \Rightarrow \mathbf{J}_s^{\text{neq}} \rightarrow 0$. It is also more universal as it does not require materials with specific Fermi-

liquid parameters (*i.e.*, metals near the Stoner criterion), and the effect is relevant for spin injection in any superconducting system with equilibrium spin transport. Finally, the spin supercurrent in Ref. [13] is manipulated via an *equilibrium* spin accumulation, while our result is inherently nonequilibrium.

Analytical results.—Let us first consider a material with a spin-independent density of states $N(\epsilon)$, where ϵ is the quasiparticle energy. The nonequilibrium spin accumulation ρ_s can then be related to a spin distribution function \mathbf{h}_s ,

$$\rho_s = -\frac{\hbar}{2} \int_0^\infty d\epsilon N(\epsilon) \mathbf{h}_s(\epsilon), \quad (1)$$

where \mathbf{h}_s describes the imbalance between spin-up and spin-down occupation numbers. We define \mathbf{h}_s as a vector that points in the polarization direction of the spins, while its magnitude can be described in terms of a *spin voltage* V_s ,

$$h_s(\epsilon) = \left\{ \tanh[(\epsilon + eV_s)/2T] - \tanh[(\epsilon - eV_s)/2T] \right\} / 2, \quad (2)$$

where $e < 0$ is the electron charge and T is the temperature. The spin voltage is defined as $V_s := (V_\uparrow - V_\downarrow)/2$, where V_σ are the effective potentials seen by spin- σ quasiparticles [22–24] where \mathbf{h}_s defines the direction of the spin quantization axis.

For a normal metal at $T = 0$, the density of states $N(\epsilon) = N_0$ is flat, while the spin distribution $|h_s| = 1$ for $|\epsilon| < eV_s$. This results in a spin accumulation $|\rho_s| = (\hbar/2)N_0eV_s$ that increases linearly with V_s . This gives a simple interpretation of V_s as a control parameter: if the spin source in Fig. 1 is a nonsuperconducting reservoir, the spin voltage V_s is directly proportional to the spin accumulation in the reservoir.

Similarly to the above, the excitation of quasiparticles from the Fermi level is described by an energy distribution $h_0(\epsilon)$,

$$h_0(\epsilon) = \left\{ \tanh[(\epsilon + eV_s)/2T] + \tanh[(\epsilon - eV_s)/2T] \right\} / 2. \quad (3)$$

At low temperatures, this shows that a spin voltage V_s also excites quasiparticles in a region of width $2eV_s$ around the Fermi level $\epsilon = 0$. For a more in-depth discussion of the nonequilibrium distribution function, see Refs. [19, 22, 23].

Spin supercurrents can in general be expressed as an energy integral over a spectral spin supercurrent,

$$\mathbf{J}_s = -\frac{\hbar}{2} N_0 \int_0^\infty d\epsilon \operatorname{Im}[\mathbf{j}_s]. \quad (4)$$

In equilibrium, the spectral current \mathbf{j}_s^{eq} is given by [3, 10]

$$\mathbf{j}_s^{\text{eq}} = (\mathbf{g}_t \times \nabla \mathbf{g}_t - \mathbf{f}_t \times \nabla \tilde{\mathbf{f}}_t) h_0. \quad (5)$$

Here, \mathbf{g}_t describes the spin-polarization of the density of states, while \mathbf{f}_t describes spin-triplet correlations [3]. The cross products should be taken between the orientations of \mathbf{g}_t and \mathbf{f}_t . In effectively 1D systems like Fig. 1, we can let the position derivative $\nabla \rightarrow \partial_x$. Note that the result depends only on the energy distribution h_0 , which is the only part of the electronic distribution function which remains finite in equilibrium.

Outside equilibrium, the spin distribution \mathbf{h}_s can become finite, and the spectral current gains an additional contribution:

$$\mathbf{j}_s^{\text{neq}} = (\mathbf{g}_t \times \nabla \mathbf{g}_t - \mathbf{f}_t \times \nabla \tilde{\mathbf{f}}_t) \times i\mathbf{h}_s. \quad (6)$$

The full derivation of this result is included in the Supplemental information. The structure of Eq. (6) is very reminiscent of Eq. (5), since both depend on $\mathbf{g}_t \times \nabla \mathbf{g}_t - \mathbf{f}_t \times \nabla \tilde{\mathbf{f}}_t$. However, its cross product structure generates a spin current *perpendicular* to the one in Eq. (5). We also see that it contains an extra factor i ; since the distribution functions h_0 and \mathbf{h}_s are both real, this causes Eq. (4) to extract the real and not imaginary part of $\mathbf{g}_t \times \nabla \mathbf{g}_t - \mathbf{f}_t \times \nabla \tilde{\mathbf{f}}_t$. This comparison shows that the nonequilibrium contribution can be summarized as

$$\mathbf{j}_s^{\text{neq}} = \mathbf{j}_s^{\text{eq}} \times (i\mathbf{h}_s/h_0). \quad (7)$$

So long as $\mathbf{g}_t \times \nabla \mathbf{g}_t - \mathbf{f}_t \times \nabla \tilde{\mathbf{f}}_t$ is a complex number—which it in general is—it produces an equilibrium spin supercurrent \mathbf{j}_s^{eq} according to Eqs. (4) and (5), which combined with a finite spin distribution \mathbf{h}_s immediately produces the new supercurrent term $\mathbf{j}_s^{\text{neq}}$ according to Eq. (7). This suggests an intuitive interpretation of the effect: injected spins described by \mathbf{h}_s exert a torque on the spins transported by the equilibrium component \mathbf{j}_s^{eq} , producing a nonequilibrium component $\mathbf{j}_s^{\text{neq}}$ perpendicular to both. This result also proposes that this nonequilibrium spin supercurrent should increase linearly with the equilibrium spin supercurrent and the injected spin accumulation. Thus, an equilibrium spin supercurrent gains a new component when propagating through a region with spin accumulation ρ_s . All these predictions that arise from Eq. (7) are confirmed numerically later in this paper.

Let us now consider the setup in Fig. 1. In equilibrium, the x - and y -polarized magnets give rise to a z -polarized spin supercurrent $\mathbf{j}_s^{\text{eq}} \sim \hat{z}$. A generic spin source then introduces a spin imbalance in the superconductor, which we describe via a nonzero spin distribution \mathbf{h}_s . If these spins are polarized in the z -direction, meaning that $\mathbf{h}_s \parallel \hat{z}$, then the nonequilibrium contribution $\mathbf{j}_s^{\text{neq}} = 0$. On the other hand, if these spins are polarized in the x -direction, so that $\mathbf{h}_s \perp \hat{z}$, then the nonequilibrium contribution $\mathbf{j}_s^{\text{neq}} \sim \mathbf{j}_s^{\text{eq}} \times \mathbf{h}_s$ obtains a y -polarized component proportional to the spin imbalance. Similarly, if one had injected spin- y particles instead, a spin- x supercurrent would appear in the superconductor.

To summarize, for the geometry in Fig. 1, the analytical results suggest that we should expect a spin- y supercurrent proportional to the spin- x voltage, while the spin supercurrent should remain unchanged for a spin- z voltage. In the following sections, we compare these expectations to numerical results.

Technical details.—We perform the numerical calculations using the Usadel equation [23, 25–28], which describes superconducting systems in the quasiclassical and diffusive limits. Within this formalism, observables are described via 8×8 quasiclassical propagators in Keldysh \otimes Nambu \otimes spin space,

$$\check{g} := \begin{pmatrix} \hat{g}^R & \hat{g}^K \\ 0 & \hat{g}^A \end{pmatrix}. \quad (8)$$

These components are related by the identities $\hat{g}^K = \hat{g}^R \hat{h} - \hat{h} \hat{g}^A$ and $\hat{g}^A = \hat{\tau}_3 \hat{g}^{R\dagger} \hat{\tau}_3$. Here, \hat{h} is a 4×4 distribution function, which in systems with spin accumulation can be written

$$\hat{h} = h_0 \hat{\sigma}_0 \hat{\tau}_0 + \mathbf{h}_s \cdot \hat{\sigma} \hat{\tau}_3, \quad (9)$$

where h_0 and \mathbf{h}_s were introduced earlier. The $\hat{\tau}_n$ are $\hat{\sigma}_n$ are Pauli matrices in Nambu and spin space. As for the retarded component \hat{g}^R , we analytically use the parametrization [3]

$$\hat{g}^R = \begin{pmatrix} (g_s + \mathbf{g}_t \cdot \boldsymbol{\sigma}) & (f_s + \mathbf{f}_t \cdot \boldsymbol{\sigma})i\sigma_2 \\ -i\sigma_2(\tilde{f}_s - \tilde{\mathbf{f}}_t \cdot \boldsymbol{\sigma}) & -\sigma_2(\tilde{g}_s - \tilde{\mathbf{g}}_t \cdot \boldsymbol{\sigma})\sigma_2 \end{pmatrix}, \quad (10)$$

while we numerically use the Riccati parametrization [29]. General equations for calculating spin supercurrents and spin accumulations from these quasiclassical propagators are derived and presented in the Supplemental Information.

To determine the propagators above for Fig. 1, we have to simultaneously solve the Usadel equation,

$$i\xi^2 \nabla(\tilde{g} \nabla \tilde{g}) = [\hat{\Delta} + \epsilon \hat{\tau}_3, \tilde{g}]/\Delta_0, \quad (11)$$

and a selfconsistency equation for the gap Δ which depends on \tilde{g}^K [30]. The other quantities are the coherence length ξ and bulk gap Δ_0 . The magnetic insulators in Fig. 1 are modelled as spin-active interfaces [31–34]. Note that we assume a fixed distribution function \hat{h} , and do not solve any kinetic equation [19, 22, 23, 25, 26, 35, 36]. Thus, there is no resistive spin current flowing in the superconductor, as $\nabla \mathbf{h}_s = 0$ ensures that there is no gradient in the spin accumulation.

Finally, we briefly summarize our parameter choices. The superconductor was taken to have a length $L = 1.5\xi$, where ξ is the superconducting coherence length in the dirty limit. The magnetic insulators were described using an interfacial spin-mixing conductance $G_\varphi/G_N = 0.6$, where G_N is the bulk normal-state conductance of the superconductor. Finally, we assumed a constant spin voltage V_s throughout the entire superconductor, instead of explicitly modelling the details of the spin source in Fig. 1. Thus, the junction is treated as a 1D superconductor with magnetic boundary conditions. Our results are not qualitatively sensitive to these parameter choices. The main constraints are that superconductivity collapses in short superconductors with high spin-mixing conductances, while the spin supercurrents become vanishingly small for long superconductors with low spin-mixing conductances.

Numerical results.—The spin supercurrent in the model considered here is conserved throughout the superconductor. We have also checked both analytically and numerically that it remains conserved even in the presence of spin-flip and spin-orbit impurities, thus extending the equilibrium considerations in Ref. [37] to this particular nonequilibrium situation. In fact, the analytical proof of this is straight-forward: the argument in Ref. [37] shows that $\nabla \cdot \mathbf{j}_s^{\text{eq}} = 0$ as long as h_0 is position-independent. Since the new contribution proposed in this paper $\mathbf{j}_s^{\text{neq}} = \mathbf{j}_s^{\text{eq}} \times (i\mathbf{h}_s/h_0)$, we conclude that $\nabla \cdot \mathbf{j}_s^{\text{neq}} = 0$ for the same physical setups if \mathbf{h}_s is position-independent. However, if either h_0 or \mathbf{h}_s becomes inhomogeneous, this argument breaks down, and the spin supercurrent is no longer conserved.

In Fig. 2, we show the spin supercurrent in the superconductor as a function of spin voltage at a low temperature $T = 0.01T_c$. Up until $eV_s \approx \Delta_0/2$, these results are in perfect agreement with the analytical predictions. More precisely, we see that a spin- z injection [Fig. 2(a)] has no effect on the spin supercurrent, while a spin- x injection [Fig. 2(b)] leads to a spin- y supercurrent. The spin- y supercurrent increases linearly with the spin voltage,

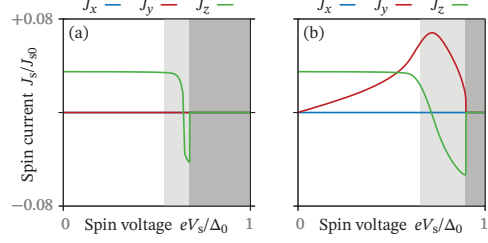


FIG. 2: Spin supercurrent \mathbf{J}_s as a function of spin voltage V_s . This spin voltage corresponds to injected (a) spin- z or (b) spin- x accumulation. The light shaded region shows where the system is bistable, and the dark region where superconductivity vanishes.

again in agreement with the predictions. Remarkably, the spin- z supercurrent does not decrease as the spin- y supercurrent increases, in contrast to what one might intuitively expect.

At low temperatures, we also see that there is a bistable regime at high spin voltages $eV_s > \Delta_0/2$. This means that both a superconducting and normal-state solution exist, which both correspond to local minima in the free energy. Depending on the dynamics of the system, this can either lead to hysteretic behaviour, or a first-order phase transition. Precisely where in the bistable region the thermodynamic transition point occurs is however difficult to predict within the Usadel formalism, as it is not straight-forward to explicitly evaluate the free energy of each solution. For more information on bistability in superconducting systems, see Refs. [22, 38, 39].

Within the bistable regime, there is a point where the spin- z supercurrent reverses direction as a function of the spin voltage. This behaviour can be understood [40] as a spin equivalent of the S/N/S transistor effect [41, 42] where, according to Eq. (3), the energy distribution h_0 is also modulated by a spin voltage, and may therefore tune the equilibrium contribution in Eq. (5).

Since the spin- y supercurrent remains positive for all spin voltages, there exists a point where we get a pure spin- y supercurrent. In other words, there is a particular spin voltage that causes a 90° rotation of the spin supercurrent polarization compared to equilibrium. The fact that the spin- y supercurrent can remain finite while the spin- z supercurrent goes to zero might at first seem contradictory to our previous explanation $\mathbf{j}_s^{\text{neq}} \sim \mathbf{j}_s^{\text{eq}} \times (i\mathbf{h}_s/h_0)$. However, it is the *energy-integrated* spin currents $\mathbf{J}_s \sim \int d\epsilon \text{Im}[\mathbf{j}_s]$ that are plotted in Fig. 2. The spin- y current is generated from the *spectral* spin- z current, which remains finite even though the *total* spin- z current is zero.

In Fig. 3, we show how the spin supercurrent varies as a function of temperature for a fixed spin voltage $eV_s = \Delta_0/4$. Curiously, we find that the spin current increases *linearly* with decreasing temperature in a relatively large parameter regime. That the spin- y current decreases at the same rate as the spin- z current seems reasonable in light of the equation $\mathbf{j}_s^{\text{neq}} \sim \mathbf{j}_s^{\text{eq}} \times \mathbf{h}_s$: if \mathbf{j}_s^{eq} decreases linearly, then $\mathbf{j}_s^{\text{neq}}$ should do so as well. The most important message from Fig. 3 is perhaps that the nonequilibrium contribution $\mathbf{j}_s^{\text{neq}}$ to the spin supercurrent remains significant all the way up to the critical temperature of the junction. This means that relevant experiments can be

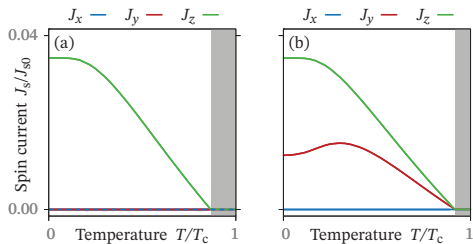


FIG. 3: Spin supercurrent J_s as a function of temperature T for a fixed spin voltage $eV_s = \Delta_0/4$ in the superconductor. This spin voltage corresponds to injected (a) spin- z or (b) spin- x accumulation. The shaded region shows where superconductivity vanishes.

performed at any temperature where superconductivity exists.

Discussion.—In the previous sections, we have shown that injection of a nonequilibrium spin accumulation can be used to generate new spin supercurrent components. The results are especially encouraging since the nonequilibrium contribution to the spin supercurrent can even be made larger than the equilibrium contribution, and we found that it persists all the way up to the critical temperature of the junction. Both these features should make it a particularly interesting effect for experimental detection and future device design. However, there are some questions that we have not addressed yet.

The first question is how the spin source in Fig. 1 works. So far, we have simply treated it as a generic device that manipulates the spin distribution \mathbf{h}_s inside the superconductor directly. One alternative is to use a normal metal coupled to a voltage-biased ferromagnet [17] or half-metallic ferromagnet [43]. In that case, the polarization of the magnets enable a charge-spin conversion, thus translating an electric voltage into a spin voltage. Another possibility would be spin-pumping experiments, where it is a microwave signal that is translated to a spin voltage [20].

In all these cases, the spin source necessarily contains magnetic elements, and one challenge would be how to prevent the spin source from affecting the *equilibrium* spin current. One solution might be to embrace the existing magnets in Fig. 1: one could use the same magnets to generate the equilibrium spin supercurrent and for spin injection. This spin injection may then be performed either using spin pumping—or if the magnets are sufficiently thin for electron tunneling—by placing voltage-biased contacts on top of the magnets. One complication with this strategy is that since the resulting spin

accumulation will necessarily be inhomogeneous, both spin supercurrents and resistive spin currents have to coexist.

Another question relates to how one might measure these spin supercurrents. How to perform a direct measurement of a spin supercurrent is an open question, although suggestions have been proposed very recently [44]. Indirect measurements of spin supercurrents, on the other hand, have already been performed experimentally. Most of these rely on measuring dissipationless charge currents through strongly polarized materials [45–52]. Since only $|\uparrow\uparrow\rangle$ and $|\downarrow\downarrow\rangle$ pairs can penetrate over longer distances, and the polarization breaks the degeneracy between them, one can infer the existence of spin supercurrents from the measured charge supercurrents.

One solution to the measurement problem might be to look for an *inverse* effect. We have shown that spin injection into a superconductor results in a torque on the spins transported by the equilibrium spin supercurrent. However, this interaction should cause a reaction torque on the spin source, which might be possible to detect. For instance, in a setup similar to Ref. [17], this reaction torque might directly affect the nonlocal spin conductance. Similarly, in a spin pumping setup, this might affect the FMR linewidths. In both cases, this reaction torque should only exist when there is an equilibrium spin supercurrent $\mathbf{j}_s^{\text{eq}} \sim \mathbf{m}_1 \times \mathbf{m}_2$ to interact with, so it should depend on the magnetic configuration of the device.

Conclusion.—We have shown analytically and numerically that if a system harbors a spin supercurrent \mathbf{j}_s^{eq} in equilibrium, then a spin injection \mathbf{h}_s creates a new component $\mathbf{j}_s^{\text{neq}} \sim \mathbf{j}_s^{\text{eq}} \times \mathbf{h}_s$. This effect can be intuitively understood as the injected spins exerting a torque on the spins transported by the equilibrium spin supercurrent, generating a component that is perpendicular to both. These results have implications for the control of spin supercurrents in novel superconducting spintronics devices.

Acknowledgments

We thank M. Amundsen and V. Risinggård for useful discussions. The numerics were performed on resources provided by UNINETT Sigma2—the National infrastructure for high performance computing and data storage in Norway. J.A.O. and J.L. were supported by the Research Council of Norway through grant 240806, and through its Centres of Excellence funding scheme grant 262633 “*QuSpin*”. J.W.A.R. acknowledges the EPSRC–JSPS “*OSS SuperSpin*” International Network Grant (EP/P026311/1) and Programme Grant (EP/N017242/1).

[1] J. Linder and J. W. A. Robinson, *Nat. Phys.* **11**, 307 (2015).
 [2] M. Eschrig, *Physics Today* **64**, 43 (2010).
 [3] M. Eschrig, *Rep. Prog. Phys.* **78**, 104501 (2015).
 [4] M. G. Blamire and J. W. A. Robinson, *J. Phys. Condens. Matter* **26**, 453201 (2014).
 [5] R. Grein, M. Eschrig, G. Metalidis, and G. Schön, *Phys. Rev. Lett.* **102**, 227005 (2009).
 [6] M. Alidoust, J. Linder, G. Rashedi, T. Yokoyama, and A. Sudbø, *Phys. Rev. B* **81**, 014512 (2010).

[7] Z. Shomali, M. Zareyan, and W. Belzig, *New J. Phys.* **13**, 083033 (2011).
 [8] P. M. R. Brydon, Y. Asano, and C. Timm, *Phys. Rev. B* **83**, 180504 (2011).
 [9] A. Moor, A. F. Volkov, and K. B. Efetov, *Phys. Rev. B* **92**, 180506 (2015).
 [10] I. Gommerud and J. Linder, *Phys. Rev. B* **92**, 035416 (2015).
 [11] F. Konschelle, I. V. Tokatly, and F. S. Bergeret, *Phys. Rev. B* **92**, 125443 (2015).

- [12] S. H. Jacobsen, I. Kulagina, and J. Linder, *Sci. Rep.* **6**, 23926 (2016).
- [13] X. Montiel and M. Eschrig, *Phys. Rev. B* **98**, 104513 (2018).
- [14] J. C. Slonczewski, *Phys. Rev. B* **39**, 6995 (1989).
- [15] D. Beckmann, *J. Phys. Condens. Matter* **28**, 163001 (2016).
- [16] C. H. L. Quay, D. Chevallier, C. Bena, and M. Aprili, *Nat. Phys.* **9**, 84 (2013).
- [17] T. Wakamura, N. Hasegawa, K. Ohnishi, Y. Niimi, and Y. Otani, *Phys. Rev. Lett.* **112**, 036602 (2014).
- [18] F. Hübler, M. J. Wolf, D. Beckmann, and H. v. Löhneysen, *Phys. Rev. Lett.* **109**, 207001 (2012).
- [19] M. Silaev, P. Virtanen, F. S. Bergeret, and T. T. Heikkilä, *Phys. Rev. Lett.* **114**, 167002 (2015).
- [20] K.-R. Jeon, C. Ciccarelli, A. J. Ferguson, H. Kurebayashi, L. F. Cohen, X. Montiel, M. Eschrig, J. W. A. Robinson, and M. G. Blamire, *Nat. Mater.* **17**, 499 (2018).
- [21] T. Taira, M. Ichioka, S. Takei, and H. Adachi, [arXiv:1808.02973](https://arxiv.org/abs/1808.02973).
- [22] J. A. Ouassou, T. D. Vethaak, and J. Linder, [arXiv:1803.07076](https://arxiv.org/abs/1803.07076).
- [23] F. S. Bergeret, M. Silaev, P. Virtanen, and T. T. Heikkilä, [arXiv:1706.08245](https://arxiv.org/abs/1706.08245).
- [24] G. E. W. Bauer, E. Saitoh, and B. J. van Wees, *Nat. Mater.* **11**, 391 (2012).
- [25] V. Chandrasekhar, in *Superconductivity* (Springer, Berlin, Heidelberg, 2008) pp. 279–313.
- [26] W. Belzig, F. K. Wilhelm, C. Bruder, G. Schön, and A. D. Zaikin, *Superlattices and Microstructures* **25**, 1251 (1999).
- [27] J. Rammer and H. Smith, *Rev. Mod. Phys.* **58**, 323 (1986).
- [28] K. D. Usadel, *Phys. Rev. Lett.* **25**, 507 (1970).
- [29] N. Schopohl, [arXiv:cond-mat/9804064](https://arxiv.org/abs/cond-mat/9804064).
- [30] S. H. Jacobsen, J. A. Ouassou, and J. Linder, *Phys. Rev. B* **92**, 024510 (2015).
- [31] M. Eschrig, A. Cottet, W. Belzig, and J. Linder, *New J. Phys.* **17**, 083037 (2015).
- [32] P. Machon, M. Eschrig, and W. Belzig, *Phys. Rev. Lett.* **110**, 047002 (2013).
- [33] A. Cottet, D. Huertas-Hernando, W. Belzig, and Y. V. Nazarov, *Phys. Rev. B* **80**, 184511 (2009).
- [34] A. Cottet, *Phys. Rev. B* **76**, 224505 (2007).
- [35] I. V. Bobkova and A. M. Bobkov, *JETP Lett.* **101**, 118 (2015).
- [36] F. Aikebaier, M. A. Silaev, and T. T. Heikkilä, *Phys. Rev. B* **98**, 024516 (2018).
- [37] J. A. Ouassou, S. H. Jacobsen, and J. Linder, *Phys. Rev. B* **96**, 094505 (2017).
- [38] I. V. Bobkova and A. M. Bobkov, *Phys. Rev. B* **89**, 224501 (2014).
- [39] I. Snyman and Y. V. Nazarov, *Phys. Rev. B* **79**, 014510 (2009).
- [40] J. A. Ouassou and J. Linder, [arXiv:1810.02820](https://arxiv.org/abs/1810.02820).
- [41] F. K. Wilhelm, G. Schön, and A. D. Zaikin, *Phys. Rev. Lett.* **81**, 1682 (1998).
- [42] J. J. A. Baselmans, A. F. Morpurgo, B. J. van Wees, and T. M. Klapwijk, *Nature* **397**, 43 (1999).
- [43] I. V. Bobkova and A. M. Bobkov, *Phys. Rev. Lett.* **108**, 197002 (2012).
- [44] V. Risinggård and J. Linder, Under preparation (2018).
- [45] R. S. Keizer, S. T. B. Goennenwein, T. M. Klapwijk, G. Miao, G. Xiao, and A. Gupta, *Nature* **439**, 825 (2006).
- [46] M. S. Anwar, F. Czeschka, M. Hesselberth, M. Porcu, and J. Aarts, *Phys. Rev. B* **82**, 100501 (2010).
- [47] J. W. A. Robinson, J. D. S. Witt, and M. G. Blamire, *Science* **329**, 59 (2010).
- [48] J. W. A. Robinson, G. B. Halász, A. I. Buzdin, and M. G. Blamire, *Phys. Rev. Lett.* **104**, 207001 (2010).
- [49] T. S. Khaire, M. A. Khasawneh, W. P. Pratt, and N. O. Birge, *Phys. Rev. Lett.* **104**, 137002 (2010).
- [50] J. D. S. Witt, J. W. A. Robinson, and M. G. Blamire, *Phys. Rev. B* **85**, 184526 (2012).
- [51] J. W. A. Robinson, N. Banerjee, and M. G. Blamire, *Phys. Rev. B* **89**, 104505 (2014).
- [52] M. Egilmez, J. W. A. Robinson, J. L. MacManus-Driscoll, L. Chen, H. Wang, and M. G. Blamire, *Europhys. Lett.* **106**, 37003 (2014).

Supplemental information

Jabir Ali Ouassou,¹ Jason W. A. Robinson,² and Jacob Linder¹

¹Center for Quantum Spintronics, Department of Physics, Norwegian University of Science and Technology, NO-7491 Trondheim, Norway

²Department of Materials Science and Metallurgy, University of Cambridge, 27 Charles Babbage Road, Cambridge CB3 0FS, United Kingdom

Section I provides a self-contained derivation of the charge and spin transport equations. Specifically, we start with the definitions of particle densities from quantum field theory, and derive quasiparticle continuity equations. The results are used to derive quasiclassical results for the charge accumulation, spin accumulation, charge current, and spin current. Section II then uses these results to derive an analytical expression for the spin supercurrent in materials with spin accumulation. The result is used to explain the predictions in the main manuscript.

I. CHARGE AND SPIN TRANSPORT

A. Quasiparticle accumulations

There are four relevant species of quasiparticles in the systems that we will consider: namely electrons and holes, which each have two distinct spin projections. These have the densities

$$n_{e\uparrow}(\mathbf{r}, t) := \langle \Psi_{\uparrow}^{\dagger}(\mathbf{r}, t) \Psi_{\uparrow}(\mathbf{r}, t) \rangle, \quad (\text{S1})$$

$$n_{e\downarrow}(\mathbf{r}, t) := \langle \Psi_{\downarrow}^{\dagger}(\mathbf{r}, t) \Psi_{\downarrow}(\mathbf{r}, t) \rangle, \quad (\text{S2})$$

$$n_{h\uparrow}(\mathbf{r}, t) := \langle \Psi_{\uparrow}(\mathbf{r}, t) \Psi_{\uparrow}^{\dagger}(\mathbf{r}, t) \rangle, \quad (\text{S3})$$

$$n_{h\downarrow}(\mathbf{r}, t) := \langle \Psi_{\downarrow}(\mathbf{r}, t) \Psi_{\downarrow}^{\dagger}(\mathbf{r}, t) \rangle, \quad (\text{S4})$$

where Ψ_{σ}^{\dagger} and Ψ_{σ} are standard creation and annihilation operators. For comparison, the propagators are defined as [S1–S3]:

$$G_{\sigma\sigma'}^{\text{R}}(\mathbf{r}, t; \mathbf{r}', t') := -i \langle \{ \Psi_{\sigma}(\mathbf{r}, t), \Psi_{\sigma'}^{\dagger}(\mathbf{r}', t') \} \rangle \theta(t - t'), \quad (\text{S5})$$

$$G_{\sigma\sigma'}^{\text{A}}(\mathbf{r}, t; \mathbf{r}', t') := +i \langle \{ \Psi_{\sigma}(\mathbf{r}, t), \Psi_{\sigma'}^{\dagger}(\mathbf{r}', t') \} \rangle \theta(t' - t), \quad (\text{S6})$$

$$G_{\sigma\sigma'}^{\text{K}}(\mathbf{r}, t; \mathbf{r}', t') := -i \langle [\Psi_{\sigma}(\mathbf{r}, t), \Psi_{\sigma'}^{\dagger}(\mathbf{r}', t')] \rangle, \quad (\text{S7})$$

where the subscripts σ and σ' denote possible spin projections. Combining these definitions, we see that the quasiparticle densities are directly related to the equal-coordinate propagators:

$$n_{e\sigma} = \frac{i}{2} [G_{\sigma\sigma}^{\text{R}} - G_{\sigma\sigma}^{\text{A}} - G_{\sigma\sigma}^{\text{K}}], \quad (\text{S8})$$

$$n_{h\sigma} = \frac{i}{2} [G_{\sigma\sigma}^{\text{R}} - G_{\sigma\sigma}^{\text{A}} + G_{\sigma\sigma}^{\text{K}}]. \quad (\text{S9})$$

These expressions can be used to calculate the spin-resolved density of electrons and holes, respectively. Note that holes carry both opposite charge and opposite spin compared to electrons [S16]. The charge and spin accumulations are then found by multiplying each quasiparticle density with their respective charges or spins, and summing up their contributions:

$$\rho_e := e \frac{1}{2} [+n_{e\uparrow} + n_{e\downarrow} - n_{h\uparrow} - n_{h\downarrow}], \quad (\text{S10})$$

$$\rho_z := \frac{\hbar}{2} \frac{1}{2} [+n_{e\uparrow} - n_{e\downarrow} - n_{h\uparrow} + n_{h\downarrow}], \quad (\text{S11})$$

where we use the convention that e is the *electron charge* ($e < 0$). The prefactors $1/2$ are required to prevent double-counting, and

can be explained as follows. If we add one physical electron to the system, then the charge of the system increases by e . However, the number of electrons increases by one, and the number of holes decreases by one, meaning that the difference between electrons and holes increases by *two*. Thus, when the charge density ρ_e is described in terms of *both* electrons and holes, we need an extra factor $1/2$ to get the right physical charge. The same logic applies to the spin density ρ_z . We can rewrite the results in terms of the propagators above, and recognize the remaining sum as a trace over spins:

$$\rho_e = -\frac{i}{2} e \text{Tr}[\sigma_0 G^{\text{K}}], \quad (\text{S12})$$

$$\rho_z = -\frac{i}{2} \frac{\hbar}{2} \text{Tr}[\sigma_3 G^{\text{K}}]. \quad (\text{S13})$$

There is nothing special about the spin- z axis, so it is straightforward to generalize this result to arbitrary spin-projections:

$$\rho_e = -\frac{i}{2} e \text{Tr}[\sigma G^{\text{K}}], \quad (\text{S14})$$

$$\rho_s = -\frac{i}{2} \frac{\hbar}{2} \text{Tr}[\sigma G^{\text{K}}], \quad (\text{S15})$$

where $\sigma = (\sigma_1, \sigma_2, \sigma_3)$ is the Pauli vector. From the definition of the Keldysh propagator above, we can also use the identity $\langle AB \rangle^* = \langle B^{\dagger} A^{\dagger} \rangle$ to show that $G_{\sigma\sigma}^{\text{K}*} = -G_{\sigma\sigma}^{\text{K}}$. This means that $G_{\sigma\sigma}^{\text{K}}$ is imaginary, which makes $\rho_e, \rho_s \sim iG^{\text{K}}$ manifestly real. For later convenience, we will therefore write this out explicitly:

$$\rho_e = -\frac{1}{2} e \text{Re} \text{Tr}[i\sigma_0 G^{\text{K}}], \quad (\text{S16})$$

$$\rho_s = -\frac{1}{2} \frac{\hbar}{2} \text{Re} \text{Tr}[i\sigma G^{\text{K}}]. \quad (\text{S17})$$

B. Quasiparticle currents

Now that we know the charge and spin accumulations, the next step is to find the corresponding currents. To derive these, we go back to the quasiparticle densities defined in Eq. (S1):

$$n_{e\sigma}(\mathbf{r}, t) := \langle \Psi_{\sigma}^{\dagger}(\mathbf{r}, t) \Psi_{\sigma}(\mathbf{r}, t) \rangle, \quad (\text{S18})$$

$$n_{h\sigma}(\mathbf{r}, t) := \langle \Psi_{\sigma}(\mathbf{r}, t) \Psi_{\sigma}^{\dagger}(\mathbf{r}, t) \rangle. \quad (\text{S19})$$

To rigorously derive expressions for the charge and spin currents, we will use the definitions above to look for quasiparticle continuity equations on the form

$$\partial_t n_{\tau\sigma} + \nabla \cdot \mathbf{j}_{\tau\sigma} = q_{\tau\sigma}, \quad (\text{S20})$$

where $\mathbf{j}_{\tau\sigma}$ is the particle- and spin-resolved current density we are interested in, while $q_{\tau\sigma}$ represents possible source terms.

We start by differentiating the densities with respect to time:

$$\partial_t n_{e\sigma} = \langle (\partial_t \Psi_\sigma^\dagger) \Psi_\sigma + \Psi_\sigma^\dagger (\partial_t \Psi_\sigma) \rangle, \quad (\text{S21})$$

$$\partial_t n_{h\sigma} = \langle (\partial_t \Psi_\sigma) \Psi_\sigma^\dagger + \Psi_\sigma (\partial_t \Psi_\sigma^\dagger) \rangle. \quad (\text{S22})$$

We can rewrite the above using the Heisenberg equation of motion for the field operators. Note that any contributions to the continuity equation arising from non-derivative terms in the Hamiltonian—such as a superconducting gap or an exchange field—can be incorporated into the source term q . Thus, for the purposes of deriving current equations, it is sufficient to consider only derivative terms. Whether or not the currents we derive are *conserved* currents can be checked at the end of the derivation, by substituting the Usadel equation into the final quasiclassical current equations [S4, S5]. If we for simplicity disregard gauge fields for now, the equations reduce to:

$$\partial_t \Psi_\sigma = +\frac{i}{2m} \nabla^2 \Psi_\sigma, \quad (\text{S23})$$

$$\partial_t \Psi_\sigma^\dagger = -\frac{i}{2m} \nabla^2 \Psi_\sigma^\dagger. \quad (\text{S24})$$

We then substitute these back into the equations for $\partial_t n_{\tau\sigma}$:

$$\partial_t n_{e\sigma} = -\frac{i}{2m} \langle (\nabla^2 \Psi_\sigma^\dagger) \Psi_\sigma - \Psi_\sigma^\dagger (\nabla^2 \Psi_\sigma) \rangle, \quad (\text{S25})$$

$$\partial_t n_{h\sigma} = +\frac{i}{2m} \langle (\nabla^2 \Psi_\sigma) \Psi_\sigma^\dagger - \Psi_\sigma (\nabla^2 \Psi_\sigma^\dagger) \rangle. \quad (\text{S26})$$

Thanks to cancellation of cross-terms, these can be factorized:

$$\partial_t n_{e\sigma} = -\frac{i}{2m} \nabla \cdot \langle (\nabla \Psi_\sigma^\dagger) \Psi_\sigma - \Psi_\sigma^\dagger (\nabla \Psi_\sigma) \rangle, \quad (\text{S27})$$

$$\partial_t n_{h\sigma} = +\frac{i}{2m} \nabla \cdot \langle (\nabla \Psi_\sigma) \Psi_\sigma^\dagger - \Psi_\sigma (\nabla \Psi_\sigma^\dagger) \rangle. \quad (\text{S28})$$

Comparing this to Eq. (S20), we conclude that:

$$\mathbf{j}_{e\sigma} = -\frac{i}{2m} \langle (\nabla \Psi_\sigma^\dagger) \Psi_\sigma - \Psi_\sigma^\dagger (\nabla \Psi_\sigma) \rangle, \quad (\text{S29})$$

$$\mathbf{j}_{h\sigma} = +\frac{i}{2m} \langle (\nabla \Psi_\sigma) \Psi_\sigma^\dagger - \Psi_\sigma (\nabla \Psi_\sigma^\dagger) \rangle. \quad (\text{S30})$$

As a mathematical trick, let us now use different coordinates $\Psi_\sigma = \Psi_\sigma(\mathbf{r}, t)$ and $\Psi_\sigma^\dagger = \Psi_\sigma^\dagger(\mathbf{r}', t')$ for the field operators, where we let $\mathbf{r}' \rightarrow \mathbf{r}$ and $t' \rightarrow t$ in the end. In this case, the differential operators acting on the field operators can be factored out of the expectation value without ambiguity:

$$\mathbf{j}_{e\sigma} = -\frac{i}{2m} (\nabla' - \nabla) \langle \Psi_\sigma^\dagger(\mathbf{r}', t') \Psi_\sigma(\mathbf{r}, t) \rangle, \quad (\text{S31})$$

$$\mathbf{j}_{h\sigma} = -\frac{i}{2m} (\nabla' - \nabla) \langle \Psi_\sigma(\mathbf{r}, t) \Psi_\sigma^\dagger(\mathbf{r}', t') \rangle. \quad (\text{S32})$$

We are now ready to define the charge and spin current densities. In correspondence with Eq. (S10), we define these as:

$$\mathbf{J}_e := e \frac{1}{2} [+j_{e\uparrow} + j_{e\downarrow} - j_{h\uparrow} - j_{h\downarrow}], \quad (\text{S33})$$

$$\mathbf{J}_z := \frac{\hbar}{2} \frac{1}{2} [+j_{e\uparrow} - j_{e\downarrow} - j_{h\uparrow} + j_{h\downarrow}]. \quad (\text{S34})$$

Substituting Eq. (S31) into Eqs. (S33) and (S34), comparing the results to the Keldysh propagator in Eq. (S7), and recognizing the results as traces in spin space, we conclude:

$$\mathbf{J}_e = -e \frac{1}{4m} (\nabla' - \nabla) \text{Tr}[\sigma_0 G^K], \quad (\text{S35})$$

$$\mathbf{J}_z = -\frac{\hbar}{2} \frac{1}{4m} (\nabla' - \nabla) \text{Tr}[\sigma_3 G^K]. \quad (\text{S36})$$

Generalizing to all spin projections, we obtain the final results:

$$\mathbf{J}_e = -e \frac{1}{4m} (\nabla' - \nabla) \text{Tr}[\sigma_0 G^K], \quad (\text{S37})$$

$$\mathbf{J}_s = -\frac{\hbar}{2} \frac{1}{4m} (\nabla' - \nabla) \text{Tr}[\sigma G^K]. \quad (\text{S38})$$

We wish to point out that these currents are manifestly real. From the definition of the Keldysh propagator, we see that:

$$(\nabla' - \nabla)[G^{K*}(\mathbf{r}, t; \mathbf{r}', t')] = (\nabla' - \nabla)[-G^K(\mathbf{r}', t'; \mathbf{r}, t)]. \quad (\text{S39})$$

But which set of coordinates we chose to call (\mathbf{r}, t) and (\mathbf{r}', t') was arbitrary, and should not affect the physical results, since we are considering the limit $\mathbf{r}', t' \rightarrow \mathbf{r}, t$ anyway. This means that we can interchange the coordinates (\mathbf{r}, t) and (\mathbf{r}', t') on the right-hand side of the equation, *as long as we do this consistently for every factor simultaneously*. The coordinate interchange leads to a sign flip in $(\nabla' - \nabla)$ which cancels the minus sign inside the brackets, and makes the two sides of the equation equal. This lets us conclude that $(\nabla' - \nabla)G^{K*} = (\nabla' - \nabla)G^K$, which in turn implies that the charge and spin currents are real. For later convenience, we can therefore rewrite the above as

$$\mathbf{J}_e = -e \frac{1}{4m} \text{Re} \text{Tr}[\sigma_0 (\nabla' - \nabla) G^K], \quad (\text{S40})$$

$$\mathbf{J}_s = -\frac{\hbar}{2} \frac{1}{4m} \text{Re} \text{Tr}[\sigma (\nabla' - \nabla) G^K]. \quad (\text{S41})$$

C. Quasiclassical and diffusive limits

To derive equations we can use together with the Usadel equation, we now follow the standard prescription for taking the quasiclassical and diffusive limits [S1–S3, S6]. The net change to the Keldysh propagator and its derivative are then:

$$iG^K \rightarrow \frac{1}{4} N_0 \int_{-\infty}^{+\infty} d\epsilon \langle g^K \rangle_{\text{F}}, \quad (\text{S42})$$

$$\frac{1}{2m} (\nabla' - \nabla) G^K \rightarrow \frac{1}{4} N_0 \int_{-\infty}^{+\infty} d\epsilon \langle \mathbf{v} g^K \rangle_{\text{F}}, \quad (\text{S43})$$

where $\mathbf{v} := \mathbf{p}/m$ is interpreted as the quasiparticle velocity, N_0 is the density of states at the Fermi level, and $\langle \cdots \rangle_F$ refers to the average over the Fermi surface. From the derivation of the Usadel equation, we also know that in the diffusive limit the Fermi-surface averages can be written [S6, S7]

$$\langle \check{g} \rangle_F := \check{g}_s, \quad \langle \mathbf{v} \check{g} \rangle_F \approx -D(\check{g}_s \tilde{\nabla} \check{g}_s), \quad (\text{S44})$$

where $\tilde{\nabla}$ is a gauge-covariant derivative including the electromagnetic vector potential and spin-orbit interactions [S6–S8], \check{g}_s is the isotropic propagator, and D is the diffusion constant. We drop the subscripts on the isotropic propagators \check{g}_s , and substitute the above into the accumulations and currents:

$$\rho_e = -e \frac{1}{8} N_0 \int_{-\infty}^{+\infty} d\epsilon \operatorname{Re} \operatorname{Tr}[\sigma_0 g^K], \quad (\text{S45})$$

$$\rho_s = -\frac{\hbar}{2} \frac{1}{8} N_0 \int_{-\infty}^{+\infty} d\epsilon \operatorname{Re} \operatorname{Tr}[\sigma g^K], \quad (\text{S46})$$

$$J_e = +e \frac{1}{8} N_0 \int_{-\infty}^{+\infty} d\epsilon \operatorname{Re} \operatorname{Tr}[\sigma_0 \mathbf{I}^K], \quad (\text{S47})$$

$$\mathbf{J}_s = +\frac{\hbar}{2} \frac{1}{8} N_0 \int_{-\infty}^{+\infty} d\epsilon \operatorname{Re} \operatorname{Tr}[\sigma \mathbf{I}^K], \quad (\text{S48})$$

where we have reintroduced the matrix current $\check{\mathbf{I}} := D(\check{g} \tilde{\nabla} \check{g})$. Note that these equations only depend on the “electronic” part of the propagators in Nambu space, which in reality contains information about both the electrons and holes in the system.

All these results can be written as integrals over only positive energies using the symmetries of the Nambu-space matrices

$$\hat{\sigma}_n \hat{g}^K(\epsilon) = \begin{pmatrix} +\sigma_n g^K(+\epsilon) & +\sigma_n f^K(+\epsilon) \\ +\sigma_n^* f^{K*}(-\epsilon) & +\sigma_n^* g^{K*}(-\epsilon) \end{pmatrix}, \quad (\text{S49})$$

$$\hat{\sigma}_n \hat{\mathbf{I}}^K(\epsilon) = \begin{pmatrix} +\sigma_n \mathbf{I}^K(+\epsilon) & +\sigma_n \mathbf{J}^K(+\epsilon) \\ -\sigma_n^* \mathbf{J}^{K*}(-\epsilon) & -\sigma_n^* \mathbf{I}^{K*}(-\epsilon) \end{pmatrix}. \quad (\text{S50})$$

In other words, the negative-energy contributions can be recast in terms of the lower-right blocks; and since take the real part of the results, the complex conjugations are irrelevant. The remaining structure can be recognized as a trace over Nambu space, yielding the final quasiclassical transport equations

$$\rho_e = -e \frac{1}{8} N_0 \int_0^{\infty} d\epsilon \operatorname{Re} \operatorname{Tr}[\hat{\tau}_0 \hat{\sigma}_0 \hat{g}^K], \quad (\text{S51})$$

$$\rho_s = -\frac{\hbar}{2} \frac{1}{8} N_0 \int_0^{\infty} d\epsilon \operatorname{Re} \operatorname{Tr}[\hat{\tau}_0 \hat{\sigma} \hat{g}^K], \quad (\text{S52})$$

$$J_e = +e \frac{1}{8} N_0 \int_0^{\infty} d\epsilon \operatorname{Re} \operatorname{Tr}[\hat{\tau}_3 \hat{\sigma}_0 \hat{\mathbf{I}}^K], \quad (\text{S53})$$

$$\mathbf{J}_s = +\frac{\hbar}{2} \frac{1}{8} N_0 \int_0^{\infty} d\epsilon \operatorname{Re} \operatorname{Tr}[\hat{\tau}_3 \hat{\sigma} \hat{\mathbf{I}}^K]. \quad (\text{S54})$$

Note that $\hat{\sigma} \hat{\mathbf{I}}^K$ should be interpreted as an outer product between two vectors, which results in a rank-2 tensor. This is because a general description of spin transport requires both a direction of transport $\sim \hat{\mathbf{I}}^K$ and a spin orientation $\sim \hat{\sigma}$.

D. Higher-order gauge contributions

The equations of motion for the field operators also include first-order derivative terms in systems with electromagnetic [S6, S9] or spin-orbit [S7, S8, S10, S11] gauge fields. If we ignore all other terms in the Hamiltonian, these derivative terms give the following Heisenberg equations:

$$\partial_t \Psi_\sigma = \frac{1}{m} \mathbf{A}_{\sigma\sigma'} \cdot (\nabla \Psi_{\sigma'}), \quad (\text{S55})$$

$$\partial_t \Psi_\sigma^\dagger = \frac{1}{m} (\nabla \Psi_{\sigma'}^\dagger) \cdot \mathbf{A}_{\sigma'\sigma}, \quad (\text{S56})$$

where we implicitly sum over the spin index σ' . Going through the same kind of derivations as without the gauge fields, we find that we basically just have to make the following replacement in the results right before taking the quasiclassical limit:

$$\mathbf{p} G^K \rightarrow \frac{1}{2} \{G^K, \mathbf{p} - \mathbf{A}\}. \quad (\text{S57})$$

Note that the gauge fields also affects charge and spin transport in a different way, since they also appear as covariant derivatives $\tilde{\nabla}(\cdot) = \nabla(\cdot) - i[\mathbf{A}, \cdot]$ in the matrix current $\check{\mathbf{I}} = D\check{g}\tilde{\nabla}\check{g}$.

II. NONEQUILIBRIUM SUPERCURRENTS

A. Supercurrents vs. resistive currents

As shown in previous sections, the total spin current \mathbf{J}_s can in the quasiclassical limit be calculated as an energy integral,

$$\mathbf{J}_s = \frac{\hbar}{2} N_0 \int_0^{\infty} d\epsilon \mathbf{j}_s, \quad (\text{S58})$$

where the spectral spin current $\mathbf{j}_s := \operatorname{Re} \operatorname{Tr}[\hat{\tau}_3 \hat{\sigma} \hat{\mathbf{I}}^K]/8$ and the matrix current $\hat{\mathbf{I}} := D\hat{g}\tilde{\nabla}\hat{g}$. If we substitute the parametrization $\hat{g}^K = \hat{g}^R \hat{h} - \hat{h} \hat{g}^A$ into the definition of the matrix current, we find that its Keldysh component can be expanded as

$$\hat{\mathbf{I}}^K = D[(\hat{g}^R \nabla \hat{g}^R) \hat{h} - \hat{h} (\hat{g}^A \nabla \hat{g}^A)] + D[(\nabla \hat{h}) - \hat{g}^R (\nabla \hat{h}) \hat{g}^A]. \quad (\text{S59})$$

The terms on the first line may be finite even for a homogeneous distribution function \hat{h} , and produces spin currents even in equilibrium. Furthermore, they are sensitive to the phase-winding of the superconducting condensate via $\hat{g}^R \nabla \hat{g}^R$ and $\hat{g}^A \nabla \hat{g}^A$. We therefore identify this as a supercurrent contribution. The terms on the second line, however, are proportional to $\nabla \hat{h}$. This current contribution both requires an inhomogeneous distribution function, and is insensitive to the phase-winding of the superconducting condensate, and has to be a resistive current.

In this work, we are primarily interested in generating a spin supercurrent from a nonequilibrium spin accumulation. We therefore limit our attention to systems with a position-independent distribution function \hat{h} that has an excited spin mode. Since we assume $\nabla\hat{h} = 0$, the second line of Eq. (S59) disappears, and only the supercurrent contribution remains:

$$j_s = \frac{1}{8} \text{Re Tr} \left[\hat{h} \hat{\tau}_3 \hat{\sigma} (\hat{g}^R \nabla \hat{g}^R) - \hat{\tau}_3 \hat{\sigma} \hat{h} (\hat{g}^{R\dagger} \nabla \hat{g}^{R\dagger}) \right]. \quad (\text{S60})$$

As for the distribution function, it can be parametrized as

$$\hat{h} = h_0 \hat{\sigma}_0 \hat{\tau}_0 + \mathbf{h}_s \cdot \hat{\sigma} \hat{\tau}_3, \quad (\text{S61})$$

where \mathbf{h}_s points along the net quantization axis of the accumulated spins, and the magnitudes of the modes above are

$$h_0(\epsilon) = \frac{1}{2} \tanh[(\epsilon + eV_s)/2T] + \frac{1}{2} \tanh[(\epsilon - eV_s)/2T], \quad (\text{S62})$$

$$h_s(\epsilon) = \frac{1}{2} \tanh[(\epsilon + eV_s)/2T] - \frac{1}{2} \tanh[(\epsilon - eV_s)/2T]. \quad (\text{S63})$$

Note that the energy mode h_0 and spin mode h_s are odd and even functions of energy, respectively. We have parametrized the spin mode in terms of a spin voltage $V_s := (V_\uparrow - V_\downarrow)/2$, where V_σ are the effective potentials experienced by spin- σ quasiparticles [S12–S14]. The spin mode \mathbf{h}_s is related to the spin accumulation in Eq. (S52) by an energy integral $\rho_s \sim \int d\epsilon N(\epsilon) \mathbf{h}_s(\epsilon)$, where $N(\epsilon)$ is the density of states [S13].

B. Expansion in Pauli matrices

Once we substitute Eq. (S61) into Eq. (S60), there are a few subtleties to be careful about. To handle these, without yet introducing all the details of the singlet/triplet-decomposition, we first expand $\hat{g}^R \nabla \hat{g}^R$ directly in terms of Pauli matrices:

$$\hat{g}^R \nabla \hat{g}^R := \alpha \cdot \hat{\sigma} \hat{\tau}_3 + \beta \cdot \hat{\sigma} \hat{\tau}_0 + \gamma \hat{\sigma}_0 \hat{\tau}_3 + \delta \hat{\sigma}_0 \hat{\tau}_0 + \hat{\epsilon}. \quad (\text{S64})$$

The first four terms parametrizes a general block-diagonal matrix, while the last term $\hat{\epsilon}$ represents off-block-diagonal parts. Since the distribution \hat{h} can always be chosen to be block-diagonal, $\hat{\epsilon}$ does not contribute to the trace in Eq. (S60). The other coefficients are found by taking appropriate traces:

$$\begin{aligned} \alpha &= \frac{1}{4} \text{Tr}[\hat{\sigma} \hat{\tau}_3 \hat{g}^R \nabla \hat{g}^R], & \beta &= \frac{1}{4} \text{Tr}[\hat{\sigma} \hat{\tau}_0 \hat{g}^R \nabla \hat{g}^R], \\ \gamma &= \frac{1}{4} \text{Tr}[\hat{\sigma}_0 \hat{\tau}_3 \hat{g}^R \nabla \hat{g}^R], & \delta &= \frac{1}{4} \text{Tr}[\hat{\sigma}_0 \hat{\tau}_0 \hat{g}^R \nabla \hat{g}^R]. \end{aligned} \quad (\text{S65})$$

We parametrize $\hat{g}^{R\dagger} \nabla \hat{g}^{R\dagger}$ using coefficients $\underline{\alpha}, \underline{\beta}, \underline{\gamma}, \underline{\delta}$ that are defined in the same manner as above.

We will now argue that the parameter δ is identically zero. By differentiating the normalization condition $(\hat{g}^R)^2 = 1$, one can show that the retarded propagator anticommutes with its gradient, $\{\hat{g}^R, \nabla \hat{g}^R\} = 0$. This identity can be rewritten

$$\hat{g}^R (\nabla \hat{g}^R) = -(\nabla \hat{g}^R) \hat{g}^R. \quad (\text{S66})$$

Let us now trace both sides of the equation, and use the cyclic rule $\text{Tr}[\hat{A}\hat{B}] = \text{Tr}[\hat{B}\hat{A}]$ on the right-hand side,

$$\text{Tr}[\hat{g}^R (\nabla \hat{g}^R)] = -\text{Tr}[\hat{g}^R (\nabla \hat{g}^R)]. \quad (\text{S67})$$

Since $\hat{\sigma}_0 \hat{\tau}_0$ is an identity matrix, we see from Eq. (S65) that:

$$\delta = -\delta. \quad (\text{S68})$$

In other words, $\delta = 0$ is always satisfied, as any other conclusion would violate the normalization condition $(\hat{g}^R)^2 = 1$.

Next, to clarify another subtlety, we need to derive some trace identities. By explicitly writing out the matrix products and using $\hat{\sigma} = \text{diag}(\boldsymbol{\sigma}, \boldsymbol{\sigma}^*)$, one can show that

$$\begin{aligned} \text{Tr}[(\mathbf{a} \cdot \hat{\sigma})(\mathbf{b} \cdot \hat{\sigma}) \hat{\sigma} \hat{\tau}_0] &= \text{Tr}[(\mathbf{a} \cdot \boldsymbol{\sigma})(\mathbf{b} \cdot \boldsymbol{\sigma}) \boldsymbol{\sigma}] \\ &+ \text{Tr}[(\mathbf{a} \cdot \boldsymbol{\sigma}^*)(\mathbf{b} \cdot \boldsymbol{\sigma}^*) \boldsymbol{\sigma}^*], \end{aligned} \quad (\text{S69})$$

$$\begin{aligned} \text{Tr}[(\mathbf{a} \cdot \hat{\sigma})(\mathbf{b} \cdot \hat{\sigma}) \hat{\sigma} \hat{\tau}_3] &= \text{Tr}[(\mathbf{a} \cdot \boldsymbol{\sigma})(\mathbf{b} \cdot \boldsymbol{\sigma}) \boldsymbol{\sigma}] \\ &- \text{Tr}[(\mathbf{a} \cdot \boldsymbol{\sigma}^*)(\mathbf{b} \cdot \boldsymbol{\sigma}^*) \boldsymbol{\sigma}^*]. \end{aligned} \quad (\text{S70})$$

Products of spin matrices in general satisfy $(\mathbf{a} \cdot \boldsymbol{\sigma})(\mathbf{b} \cdot \boldsymbol{\sigma}) = (\mathbf{a} \cdot \mathbf{b}) + i(\mathbf{a} \times \mathbf{b}) \cdot \boldsymbol{\sigma}$; multiplying by $\boldsymbol{\sigma}$ and taking the trace, we find the associated trace rule $\text{Tr}[(\mathbf{a} \cdot \boldsymbol{\sigma})(\mathbf{b} \cdot \boldsymbol{\sigma}) \boldsymbol{\sigma}] = +2i(\mathbf{a} \times \mathbf{b})$. However, if we complex-conjugate before taking the trace, we uncover another identity $\text{Tr}[(\mathbf{a} \cdot \boldsymbol{\sigma}^*)(\mathbf{b} \cdot \boldsymbol{\sigma}^*) \boldsymbol{\sigma}^*] = -2i(\mathbf{a} \times \mathbf{b})$. A geometric motivation for the sign difference is that if the basis $\boldsymbol{\sigma} = (\sigma_1, \sigma_2, \sigma_3)$ defines a right-handed coordinate system, then $\boldsymbol{\sigma}^* = (\sigma_1, -\sigma_2, \sigma_3)$ has to define a left-handed one—and this inverts the right-hand rule that cross-products usually satisfy. With the aid of the results above, we see that

$$\text{Tr}[(\mathbf{a} \cdot \hat{\sigma})(\mathbf{b} \cdot \hat{\sigma}) \hat{\sigma} \hat{\tau}_0] = 0, \quad (\text{S71})$$

$$\text{Tr}[(\mathbf{a} \cdot \hat{\sigma})(\mathbf{b} \cdot \hat{\sigma}) \hat{\sigma} \hat{\tau}_3] = 4i(\mathbf{a} \times \mathbf{b}). \quad (\text{S72})$$

This is the subtle trap alluded to above: due to the way we define $\hat{\sigma} = \text{diag}(\boldsymbol{\sigma}, \boldsymbol{\sigma}^*)$, the generalization of the Pauli cross-product identity to matrices in Nambu space requires an extra factor $\hat{\tau}_3$ in the trace to produce a nonzero result.

We now substitute Eqs. (S61) and (S64) into Eq. (S60). With the identities above, we see that the only contributions are:

$$j_s = \frac{1}{2} h_0 \text{Re} [\underline{\alpha} - \underline{\alpha}] + \frac{1}{2} \mathbf{h}_s \times \text{Im} [\underline{\alpha} + \underline{\alpha}]. \quad (\text{S73})$$

By multiplying Eq. (S66) by appropriate Pauli matrices, taking traces, and using $\text{Tr}[\hat{A}\hat{A}^\dagger] = \text{Tr}[\hat{A}^\dagger\hat{A}]$, one can show that $\underline{\alpha} = -\underline{\alpha}^*$. This makes $\underline{\alpha} - \underline{\alpha}$ real and $\underline{\alpha} + \underline{\alpha}$ imaginary, so both contributions are compatible with the normalization condition. We could also use this information to eliminate the underlined coefficients, but this would make it harder to see how mixed singlet/triplet-terms cancel later in the derivation. Interestingly, all spin supercurrent contributions depend on the same coefficient $\underline{\alpha}$, and do not couple to the other traces of $\hat{g}^R \nabla \hat{g}^R$.

The physically observable spin supercurrent is found by integrating the spectral current over all positive and negative energies. We also know that h_0 and \mathbf{h}_s are odd and even functions of energy, respectively. We can therefore let $\underline{\alpha} (+\epsilon) \rightarrow \mp \underline{\alpha} (-\epsilon) = \mp \underline{\alpha}^* (+\epsilon)$ in the spectral current without changing the total spin supercurrent:

$$j_s = \frac{1}{2} h_0 \text{Re} [\underline{\alpha} + \underline{\alpha}^*] + \frac{1}{2} \mathbf{h}_s \times \text{Im} [\underline{\alpha} + \underline{\alpha}^*]. \quad (\text{S74})$$

This form of the result will be useful later, as it makes it clearer which parts of the non-underlined and underlined coefficients cancel for symmetry reasons. Conveniently, this also makes the h_0 and \mathbf{h}_s contributions take very similar forms.

C. Expansion in singlets and triplets

We now proceed with an expansion of the propagators in terms of physically meaningful components. Following the same kind of parametrization as Ref. [S15], we can write

$$\hat{g}^R = \begin{pmatrix} (g_s + \mathbf{g}_t \cdot \boldsymbol{\sigma}) & (f_s + \mathbf{f}_t \cdot \boldsymbol{\sigma})i\sigma_2 \\ -i\sigma_2(\tilde{f}_s - \tilde{\mathbf{f}}_t \cdot \boldsymbol{\sigma}) & -\sigma_2(\tilde{g}_s - \tilde{\mathbf{g}}_t \cdot \boldsymbol{\sigma})\sigma_2 \end{pmatrix}. \quad (\text{S75})$$

Here, f_s represents the spin-singlet pair amplitude, while \mathbf{f}_t is the spin-triplet amplitude. On the other hand, we can interpret g_s and \mathbf{g}_t as the spin-independent and spin-dependent parts of the density of states, respectively [S15]. In our notation, this means that the density of states for particles with spin-projection \mathbf{p} is given by $N = N_0 \text{Re}[g_s + \mathbf{g}_t \cdot \mathbf{p}]$. In equilibrium, the spin accumulation is found by integrating $h_0 \mathbf{g}_t$ over energies, giving another interpretation of \mathbf{g}_t . Outside of equilibrium, we of course get another kind of spin accumulation due to a nonzero spin mode \mathbf{h}_s , which we are interested in here.

Using Eq. (S75) and the identity $\sigma_2 \boldsymbol{\sigma} \sigma_2 = -\boldsymbol{\sigma}^*$, we find that the diagonal components of $\hat{g}^R \nabla \hat{g}^R$ in Nambu space are

$$\begin{aligned} [\hat{g}^R \nabla \hat{g}^R]_{1,1} &= (g_s + \mathbf{g}_t \cdot \boldsymbol{\sigma}) \nabla (g_s + \mathbf{g}_t \cdot \boldsymbol{\sigma}) \\ &\quad + (f_s + \mathbf{f}_t \cdot \boldsymbol{\sigma}) \nabla (\tilde{f}_s - \tilde{\mathbf{f}}_t \cdot \boldsymbol{\sigma}), \\ [\hat{g}^R \nabla \hat{g}^R]_{2,2} &= (\tilde{g}_s + \tilde{\mathbf{g}}_t \cdot \boldsymbol{\sigma}^*) \nabla (\tilde{g}_s + \tilde{\mathbf{g}}_t \cdot \boldsymbol{\sigma}^*) \\ &\quad + (\tilde{f}_s + \tilde{\mathbf{f}}_t \cdot \boldsymbol{\sigma}^*) \nabla (\tilde{f}_s - \tilde{\mathbf{f}}_t \cdot \boldsymbol{\sigma}^*), \end{aligned} \quad (\text{S76})$$

where the subscripts $[\dots]_{i,j}$ are matrix indices in Nambu space. Using the identity $(\mathbf{a} \cdot \boldsymbol{\sigma})(\mathbf{b} \cdot \boldsymbol{\sigma}) = (\mathbf{a} \cdot \mathbf{b}) + i(\mathbf{a} \times \mathbf{b}) \cdot \boldsymbol{\sigma}$ and its conjugate $(\mathbf{a} \cdot \boldsymbol{\sigma}^*)(\mathbf{b} \cdot \boldsymbol{\sigma}^*) = (\mathbf{a} \cdot \mathbf{b}) - i(\mathbf{a} \times \mathbf{b}) \cdot \boldsymbol{\sigma}^*$, we can sort the above into spin-independent and spin-dependent terms,

$$\begin{aligned} [\hat{g}^R \nabla \hat{g}^R]_{1,1} &= (g_s \nabla g_s + \mathbf{g}_t \nabla \mathbf{g}_t + f_s \nabla \tilde{f}_s - \mathbf{f}_t \nabla \tilde{\mathbf{f}}_t) \\ &\quad + (g_s \nabla \mathbf{g}_t + \mathbf{g}_t \nabla g_s + \mathbf{f}_t \nabla \tilde{f}_s - f_s \nabla \tilde{\mathbf{f}}_t) \boldsymbol{\sigma} \\ &\quad + (\mathbf{g}_t \times \nabla \mathbf{g}_t - \mathbf{f}_t \times \nabla \tilde{\mathbf{f}}_t) i \boldsymbol{\sigma}, \\ [\hat{g}^R \nabla \hat{g}^R]_{2,2} &= (\tilde{g}_s \nabla \tilde{g}_s + \tilde{\mathbf{g}}_t \nabla \tilde{\mathbf{g}}_t + \tilde{f}_s \nabla \tilde{f}_s - \tilde{\mathbf{f}}_t \nabla \tilde{\mathbf{f}}_t) \\ &\quad + (\tilde{g}_s \nabla \tilde{\mathbf{g}}_t + \tilde{\mathbf{g}}_t \nabla \tilde{g}_s + \tilde{\mathbf{f}}_t \nabla \tilde{f}_s - \tilde{f}_s \nabla \tilde{\mathbf{f}}_t) \boldsymbol{\sigma}^* \\ &\quad - (\tilde{\mathbf{g}}_t \times \nabla \tilde{\mathbf{g}}_t - \tilde{\mathbf{f}}_t \times \nabla \tilde{\mathbf{f}}_t) i \boldsymbol{\sigma}^*. \end{aligned} \quad (\text{S77})$$

Since we define $\hat{\boldsymbol{\sigma}} = \text{diag}(\boldsymbol{\sigma}, \boldsymbol{\sigma}^*)$, Eq. (S65) tells us that the coefficient α that we require can be expressed as

$$\alpha = \frac{1}{4} \text{Tr} \left\{ \boldsymbol{\sigma} [\hat{g}^R \nabla \hat{g}^R]_{1,1} - \boldsymbol{\sigma}^* [\hat{g}^R \nabla \hat{g}^R]_{2,2} \right\}. \quad (\text{S78})$$

Together with the expansion of $\hat{g}^R \nabla \hat{g}^R$ above, and standard trace identities for Pauli matrices, we then obtain

$$\begin{aligned} 2\alpha &= g_s \nabla \mathbf{g}_t + \mathbf{g}_t \nabla g_s - \tilde{g}_s \nabla \tilde{\mathbf{g}}_t - \tilde{\mathbf{g}}_t \nabla \tilde{g}_s \\ &\quad + \mathbf{f}_t \nabla \tilde{f}_s - f_s \nabla \tilde{\mathbf{f}}_t - \tilde{\mathbf{f}}_t \nabla \tilde{f}_s + \tilde{f}_s \nabla \tilde{\mathbf{f}}_t \\ &\quad + i \mathbf{g}_t \times \nabla \mathbf{g}_t + i \tilde{\mathbf{g}}_t \times \nabla \tilde{\mathbf{g}}_t \\ &\quad - i \mathbf{f}_t \times \nabla \tilde{\mathbf{f}}_t - i \tilde{\mathbf{f}}_t \times \nabla \tilde{\mathbf{f}}_t. \end{aligned} \quad (\text{S79})$$

Let us now calculate the corresponding coefficient $\underline{\alpha}$ from the matrix $\hat{g}^{R\dagger} \nabla \hat{g}^{R\dagger}$. Taking the complex-transpose of Eq. (S75),

$$\hat{g}^{R\dagger} = \begin{pmatrix} (g_s^* + \mathbf{g}_t^* \cdot \boldsymbol{\sigma}) & (\tilde{f}_s^* - \tilde{\mathbf{f}}_t^* \cdot \boldsymbol{\sigma})i\sigma_2 \\ -i\sigma_2(f_s^* + \mathbf{f}_t^* \cdot \boldsymbol{\sigma}) & -\sigma_2(\tilde{g}_s^* - \tilde{\mathbf{g}}_t^* \cdot \boldsymbol{\sigma})\sigma_2 \end{pmatrix}, \quad (\text{S80})$$

we see that $\hat{g}^{R\dagger}$ changed as follows compared to \hat{g}^R :

$$g_s \rightarrow +g_s^*, \quad \mathbf{g}_t \rightarrow +\mathbf{g}_t^*, \quad f_s \rightarrow +\tilde{f}_s^*, \quad \mathbf{f}_t \rightarrow -\tilde{\mathbf{f}}_t^*. \quad (\text{S81})$$

Other than these transformations, the parametrization is clearly identical, and the derivation of $\underline{\alpha}$ becomes identical as well. If we in the end results also choose to let $\epsilon \rightarrow -\epsilon$, corresponding to a combination of complex-conjugation and tilde-conjugation, the net transformation rules become

$$g_s \rightarrow +\tilde{g}_s, \quad \mathbf{g}_t \rightarrow +\tilde{\mathbf{g}}_t, \quad f_s \rightarrow +f_s, \quad \mathbf{f}_t \rightarrow -\mathbf{f}_t. \quad (\text{S82})$$

We can therefore simply perform the changes above to Eq. (S79) to get the corresponding equations for $\underline{\alpha}^*$:

$$\begin{aligned} 2\underline{\alpha}^* &= \tilde{g}_s \nabla \tilde{\mathbf{g}}_t + \tilde{\mathbf{g}}_t \nabla \tilde{g}_s - g_s \nabla \mathbf{g}_t - \mathbf{g}_t \nabla g_s \\ &\quad - \mathbf{f}_t \nabla \tilde{f}_s + f_s \nabla \tilde{\mathbf{f}}_t + \tilde{\mathbf{f}}_t \nabla f_s - \tilde{f}_s \nabla \tilde{\mathbf{f}}_t \\ &\quad + i \tilde{\mathbf{g}}_t \times \nabla \tilde{\mathbf{g}}_t + i \mathbf{g}_t \times \nabla \mathbf{g}_t \\ &\quad - i \mathbf{f}_t \times \nabla \tilde{\mathbf{f}}_t - i \tilde{\mathbf{f}}_t \times \nabla \tilde{\mathbf{f}}_t. \end{aligned} \quad (\text{S83})$$

We are now ready to calculate the spectral spin supercurrent in terms of the singlet/triplet-decomposition. Adding up Eqs. (S79) and (S83), we see that all mixed singlet/triplet terms drop out, and we are left with only the cross-product terms:

$$\alpha + \underline{\alpha}^* = +i \mathbf{g}_t \times \nabla \mathbf{g}_t + i \tilde{\mathbf{g}}_t \times \nabla \tilde{\mathbf{g}}_t - i \tilde{\mathbf{f}}_t \times \nabla \tilde{f}_t - i \mathbf{f}_t \times \nabla \tilde{\mathbf{f}}_t. \quad (\text{S84})$$

Substituting this into Eq. (S74), we immediately see that:

$$\begin{aligned} \mathbf{j}_s &= -\frac{1}{2} h_0 \text{Im} \left[\mathbf{g}_t \times \nabla \mathbf{g}_t + \tilde{\mathbf{g}}_t \times \nabla \tilde{\mathbf{g}}_t - \mathbf{f}_t \times \nabla \tilde{\mathbf{f}}_t - \tilde{\mathbf{f}}_t \times \nabla \mathbf{f}_t \right] \\ &\quad + \frac{1}{2} \mathbf{h}_s \times \text{Re} \left[\mathbf{g}_t \times \nabla \mathbf{g}_t + \tilde{\mathbf{g}}_t \times \nabla \tilde{\mathbf{g}}_t - \mathbf{f}_t \times \nabla \tilde{\mathbf{f}}_t - \tilde{\mathbf{f}}_t \times \nabla \mathbf{f}_t \right]. \end{aligned} \quad (\text{S85})$$

Since h_0 and \mathbf{h}_s are odd and even functions of energy, and the observable spin current is the energy integral of the above, we can let $h_0 \text{Im}[\tilde{A}] \rightarrow h_0 \text{Im}[A]$ and $\mathbf{h}_s \text{Re}[\tilde{A}] \rightarrow \mathbf{h}_s \text{Re}[A]$ without changing any results. Applied to the above, we can summarize our results in the tidy and compact form

$$\begin{aligned} \mathbf{j}_s &= -\text{Im} \left[\mathbf{g}_t \times \nabla \mathbf{g}_t - \mathbf{f}_t \times \nabla \tilde{\mathbf{f}}_t \right] \cdot h_0 \\ &\quad - \text{Re} \left[\mathbf{g}_t \times \nabla \mathbf{g}_t - \mathbf{f}_t \times \nabla \tilde{\mathbf{f}}_t \right] \times \mathbf{h}_s. \end{aligned} \quad (\text{S86})$$

We have shown earlier in the derivation that both contributions are compatible with the normalization condition. The fact that they did not cancel during the last simplification above, shows that both contributions are compatible with the energy symmetries of h_0 and \mathbf{h}_s . Finally, we know that the contents of the brackets $\mathbf{g}_t \times \nabla \mathbf{g}_t - \mathbf{f}_t \times \nabla \tilde{\mathbf{f}}_t$ can be nonzero, since this is the source of equilibrium spin currents.

The final result shows that if one in equilibrium has a spin supercurrent \mathbf{j}_s^{eq} , then a nonequilibrium spin mode \mathbf{h}_s gives rise to a new component $\mathbf{j}_s^{\text{neq}} \sim \mathbf{j}_s^{\text{eq}} \times \mathbf{h}_s$. This can intuitively be interpreted as the injected spins \mathbf{h}_s exerting some kind of torque on the spins transported by the equilibrium current \mathbf{j}_s^{eq} , thus producing a component $\mathbf{j}_s^{\text{neq}}$ that is spin-polarized in a direction perpendicular to both. This analogy is not perfect: it leaves out the Im and Re operations in Eq. (S86), and the fact that the cross-product relation is between *spectral* currents and accumulations. However, the intuition provided by this picture is sufficient to explain the results in the main manuscript.

-
- [S1] J. Rammer and H. Smith, *Rev. Mod. Phys.* **58**, 323 (1986).
- [S2] W. Belzig, F. K. Wilhelm, C. Bruder, G. Schön, and A. D. Zaikin, *Superlattices and Microstructures* **25**, 1251 (1999).
- [S3] V. Chandrasekhar, in *Superconductivity* (Springer, Berlin, Heidelberg, 2008) pp. 279–313.
- [S4] J. A. Ouassou, S. H. Jacobsen, and J. Linder, *Phys. Rev. B* **96**, 094505 (2017).
- [S5] S. H. Jacobsen, I. Kulagina, and J. Linder, *Sci. Rep.* **6**, 23926 (2016).
- [S6] N. B. Kopnin, *Theory of Nonequilibrium Superconductivity* (Clarendon Press, Oxford, United Kingdom, 2001).
- [S7] I. V. Tokatly, *Phys. Rev. B* **96**, 060502 (2017).
- [S8] S. H. Jacobsen, J. A. Ouassou, and J. Linder, *Phys. Rev. B* **92**, 024510 (2015).
- [S9] J. P. Morten, *Spin and charge transport in dirty superconductors*, Master thesis, NTNU, Norway (2005).
- [S10] F. S. Bergeret and I. V. Tokatly, *Phys. Rev. Lett.* **110**, 117003 (2013).
- [S11] F. S. Bergeret and I. V. Tokatly, *Phys. Rev. B* **89**, 134517 (2014).
- [S12] J. A. Ouassou, T. D. Vethaak, and J. Linder, [arXiv:1803.07076](https://arxiv.org/abs/1803.07076).
- [S13] F. S. Bergeret, M. Silaev, P. Virtanen, and T. T. Heikkila, [arXiv:1706.08245](https://arxiv.org/abs/1706.08245).
- [S14] G. E. W. Bauer, E. Saitoh, and B. J. van Wees, *Nat. Mater.* **11**, 391 (2012).
- [S15] M. Eschrig, *Rep. Prog. Phys.* **78**, 104501 (2015).
- [S16] The fact that holes carry opposite spins from electrons can be seen from the field operators. In our formalism, a “spin- σ hole” refers to the quasiparticles counted by $\langle \Psi_\sigma \Psi_\sigma^\dagger \rangle$. This means that the creation operator for spin-up holes is the annihilation operator for spin-up electrons. Annihilating a spin-up electron *reduces* the spin in the system by $\hbar/2$, so a spin-up hole must actually carry net spin in the down-direction. In other words, a “spin-up hole” is “a hole that is left when a spin-up electron is removed”, not “a hole that physically carries spin-up”.